MICROELECTRONIC IMPLANTS FOR CENTRAL AND PERIPHERAL NERVOUS SYSTEM: OVERVIEW OF CIRCUIT AND SYSTEM TECHNOLOGY

EDITED BY: Morris (Ming-Dou) Ker, Takashi Tokuda and Alexandre Schmid
PUBLISHED IN: Frontiers in Neuroscience

frontiers Research Topics

ISSN 1664-8714
ISBN 978-2-88974-023-9
DOI 10.3389/978-2-88974-023-9

About Frontiers

Frontiers is more than just an open-access publisher of scholarly articles: it is a pioneering approach to the world of academia, radically improving the way scholarly research is managed. The grand vision of Frontiers is a world where all people have an equal opportunity to seek, share and generate knowledge. Frontiers provides immediate and permanent online open access to all its publications, but this alone is not enough to realize our grand goals.

Frontiers Journal Series

The Frontiers Journal Series is a multi-tier and interdisciplinary set of open-access, online journals, promising a paradigm shift from the current review, selection and dissemination processes in academic publishing. All Frontiers journals are driven by researchers for researchers; therefore, they constitute a service to the scholarly community. At the same time, the Frontiers Journal Series operates on a revolutionary invention, the tiered publishing system, initially addressing specific communities of scholars, and gradually climbing up to broader public understanding, thus serving the interests of the lay society, too.

Dedication to Quality

Each Frontiers article is a landmark of the highest quality, thanks to genuinely collaborative interactions between authors and review editors, who include some of the world's best academicians. Research must be certified by peers before entering a stream of knowledge that may eventually reach the public - and shape society; therefore, Frontiers only applies the most rigorous and unbiased reviews.
Frontiers revolutionizes research publishing by freely delivering the most outstanding research, evaluated with no bias from both the academic and social point of view. By applying the most advanced information technologies, Frontiers is catapulting scholarly publishing into a new generation.

What are Frontiers Research Topics?

Frontiers Research Topics are very popular trademarks of the Frontiers Journals Series: they are collections of at least ten articles, all centered on a particular subject. With their unique mix of varied contributions from Original Research to Review Articles, Frontiers Research Topics unify the most influential researchers, the latest key findings and historical advances in a hot research area! Find out more on how to host your own Frontiers Research Topic or contribute to one as an author by contacting the Frontiers Editorial Office: frontiersin.org/about/contact

MICROELECTRONIC IMPLANTS FOR CENTRAL AND PERIPHERAL NERVOUS SYSTEM: OVERVIEW OF CIRCUIT AND SYSTEM TECHNOLOGY

Topic Editors:
Morris (Ming-Dou) Ker, National Chiao Tung University, Taiwan
Takashi Tokuda, Tokyo Institute of Technology, Japan
Alexandre Schmid, Swiss Federal Institute of Technology Lausanne, Switzerland

Professor Ker is on the Board of Amazingneuron. The Other Topic Editors Declare no Competing Interests With Regards to the Research Topic Theme.

Citation: Ker, M., Tokuda, T., Schmid, A., eds. (2021). Microelectronic Implants for Central and Peripheral Nervous System: Overview of Circuit and System Technology. Lausanne: Frontiers Media SA.
doi: 10.3389/978-2-88974-023-9

Table of Contents

frontiers in Neuroscience

EDITORIAL
published: 19 November 2021
doi: 10.3389/fnins.2021.794944

Editorial: Microelectronic Implants for Central and Peripheral Nervous System: Overview of Circuit and System Technology

Alexandre Schmid[1]*, *Takashi Tokuda*[2] and *Ming-Dou Ker*[3]

[1] Biomedical and Neuromorphic Microelectronic Systems BNMS, SCI-STI-AXS Station 11, Swiss Federal Institute of Technology EPFL, Lausanne, Switzerland, [2] Institute of Innovative Research (IIR), Tokyo Institute of Technology (Tokyo Tech), Tokyo, Japan, [3] Biomedical Electronics Translational Research Center, National Yang Ming Chiao Tung University, Hsinchu, Taiwan

Keywords: microelectronic implants, neuro-technologies, biomedical circuits and systems, neuroprosthetic systems, bioelectronics

Editorial on the Research Topic

Microelectronic Implants for Central and Peripheral Nervous System: Overview of Circuit and System Technology

1. INTRODUCTION

OPEN ACCESS

Edited and reviewed by:
Laura Ballerini,
International School for Advanced Studies (SISSA), Italy

***Correspondence:**
Alexandre Schmid
alexandre.schmid@epfl.ch

Specialty section:
This article was submitted to Neural Technology, a section of the journal Frontiers in Neuroscience

Received: *14 October 2021*
Accepted: *27 October 2021*
Published: *19 November 2021*

Citation:
Schmid A, Tokuda T and Ker M-D (2021) Editorial: Microelectronic Implants for Central and Peripheral Nervous System: Overview of Circuit and System Technology. Front. Neurosci. 15:794944. doi: 10.3389/fnins.2021.794944

Research on fundamental properties and collaborative operation of neo-cortical microcircuitry has accelerated in the recent years, driven by the conviction that a deeper understanding of human brain will open the way to new medical techniques. Microelectronics has reached a state of maturity, where a single chip provides large amounts of computing power. Recent attempts in combining these two fields have successfully demonstrated some form of responsiveness between microelectronic circuitry and living matter. Novel microelectronic systems are developed as a major component of neurotechnolgy aiming at the closed-loop control of tissues or organs suffering functional malfunction or disease, the restoration of lost limb or organ functionality or bidirectional information passing and interpreting to increase human or amputee capability.

Among several contributors to neurotechnology, microelectronics plays a fundamental role that is evidenced by the emergence of multiple devices, circuit techniques and commercial products. Still, the domain is extremely dynamic and novelty is required to accommodate the usage of new fabrication technologies, the autonomous operation of implantable systems at extremely low power consumption, handling large amounts of data produced by modern and future massively multichannel bio-sensing devices, the extension toward new application fields in the form of therapeutic systems of newly considered diseases or disease prophylaxis. Furthermore, the widening usage of bio-medical and neuroprosthetic systems may result into the emergence of new challenges including the reliability of microelectronics, safety of produced data, invasiveness reduction that should also be tackled at the level of the new circuits and systems.

This Research Topic aims to gather results in recent neurotechnology in the form of a collection of review papers, and also present novel methods with high potential of creating the next generation of technology as an overview.

The focus of this Research Topic relates to ASIC/SoC and microelectronic circuit and system techniques that are applied to the development of advanced implantable bio-electronic and

bio-medical systems, covering but not limited to low-power analog front-end interfaces for recording and stimulation, digital systems aiming at signal processing, feature extraction and pattern detection, power and data telemetry, enhanced ASIC fabrications aiming at new electrical or optical sensing and stimulating, full neuro-prosthetic systems and applications.

A set of ten papers have been selected to appear in this Research Topic on the basis of a thorough peer review process with iterations of manuscript revisions. The manuscripts have been assigned to four major subtopics, being understood that some papers contribute to several sub-topics, as detailed in the following.

2. RECORDING CIRCUITS TECHNIQUES

Implantable recording devices are dedicated and complex systems designed to optimally capture the features of biological signals that are of importance to the subsequent analysis prescribed by the application, research or therapy. Consequently, all methods and circuits that are developed are specific in terms of the electrical specifications that are satisfied. Some techniques are commonly agreed upon to trade-off the bandwidth, gain and power and electronic noise of low-noise front-end amplifiers including multistage amplification, transistor sizing as well as the implementation of signal processing as analog modulation (Bagheri et al., 2017; Luo et al., 2019) for instance. Nevertheless, due to the very different nature of the signals to be recorded, the architecture and designs are not uniform.

Two issues of future implanted recorded systems have been emerging, namely their possible implementation using very-deep submicron fabrication technologies, and their necessary adaptations to support massively large numbers of input channels.

Noshahr et al. present a paper titled "Low-Cutoff Frequency Reduction in Neural Amplifiers: Analysis and Implementation in CMOS 65 nm" and discuss methods aiming at enabling the development of front-end ac-coupled amplifiers in deep-submicron fabrication technologies. Whereas, several bio-signals carry information contents in relatively low frequencies, modern submicron technologies tend to shift the low-corner cut-off frequency of amplifiers to higher values. The reasons of this behavior is identified and modeled and two possible solutions aiming at keeping the low-cutoff frequency low without increasing the circuit size are presented and measured.

Perez-Prieto et al. discuss in their paper titled "Recording Strategies for High Channel Count, Densely Spaced Microelectrode Arrays" many electrical issues that arise in the development of multi-channel recording implantable circuits. A classification of neural recording architectures depending on the position of the analog multiplexer in the signal path is presented. Specifically, time-division multiplexing is systematically analyzed as a suitable technique for analog front-end of implantable biomedical devices. The major architectures of time-division multiplexing at the analog front-end are presented and discussed.

3. STIMULATION CIRCUITS TECHNIQUES

The electrical stimulation of tissues is a proven technique which is the core of several therapeutic devices. Deep-brain and peripheral nerve electrical stimulation is applied in the control of neurological disorders including Parkinson's disease, epilepsy (Rolston et al., 2012).

Wu et al. present in their paper titled "Directions of Deep Brain Stimulation for Epilepsy and Parkinson's Disease" a systematic review of deep-brain stimulation systems aiming at controlling epilepsy and Parkinson's disease. Commercial devices operating in open and closed-loop are presented. Techniques pertaining to recording and stimulation and signal processing are discussed, and an overview of future prospects is presented.

Culaclii et al. discuss the necessity of controlling over arbitrary stimulation waveforms and present a multi-layer system that efficiently generates such stimuli in their paper titled "A Biomimetic, SoC-Based Neural Stimulator for Novel Arbitrary-Waveform Stimulation Protocols." A Specific architecture involving three domains of devices is used to support the control. The system hardware is developed in an implantable version using some discrete components. The system is compatible with neural implants and supports a variety of irregular stimulation waveforms.

Finally, a fully implantable stimulator with sealed packaging and wireless data and power transmission is presented by Jiang et al. in their paper titled "A Versatile Hermetically Sealed Microelectronic Implant for Peripheral Nerve Stimulation Applications." Electrical and in-field characterization results are presented. An architecture consisting of a wearable external station and an implantable stimulator is presented. Three stimulator chips are used that deliver up to 1 mA and 3 mA biphasic pulses to 12 different electrode configurations each. A high-voltage 600 nm CMOS fabrication technology is selected.

4. SYSTEMS WITH CLOSED-LOOP OPERATION

Closed-loop implanted systems have naturally followed the successful development of individual blocks related to recording and stimulation. The decision to deliver electrical stimulation is formed from the some signal processing of the recorded brain signal data, on-chip, hence closing a loop consisting of the disabled tissue and the implanted autonomous control system.

Li et al. present a paper titled "Advances in Neural Recording and Stimulation Integrated Circuits" and discuss the different blocks of a closed-loop implant focusing on a state-of-the-art of implementation circuit techniques and the key issues that each technique aims at solving. An introduction to the basics of neuro-prosthetic systems is presented. The technology, architecture and key issues of neural recorders is discussed. Considerations related to neural recording and stimulation and future trends are proposed.

Additional modules related to artifact removal in signal processing as well as wireless data and power transmission are discussed by Cho et al. in their paper titled "Energy-Efficient

Integrated Circuit Solutions Toward Miniaturized Closed-Loop Neural Interface Systems." A review of state-of-the-art of implantable stimulators is presented along with a discussion of recording systems and the requirement for implantable closed-loop electrical systems.

Stimulation in the optical domain is a recent technology with respect to electrical stimulation, that aims at optogenetics, i.e., the selective optical stimulation of genetically modified cells. A wireless platform aiming at closed-loop optogenetic control in freely moving rodents is presented in the paper titled "A Wireless Electro-Optic Platform for Multimodal Electrophysiology and Optogenetics in Freely Moving Rodents" by Bilodeau et al.. A data reduction rate of 7.77 is achieved by applying real-time compression. The systems records from up to 32 channels and stimulates into four optical channels. Off-the-shelf and FPGA components are used in the development, while signal processing algorithms are embedded to separate action potentials, low field potentials and electromyography signals. The full systems weights 4.7 g and includes a 100 mAh battery.

5. SYSTEMS WITH IMAGING CAPABILITY

Brain imaging has been considered for the sake of studying the activity and operation of some regions. Though, bulky systems based on microscopy were used that limit the freedom of the animal under observation and thus also alter the results. Implantable brain imagers are new systems aiming at disclosing their results obtained in real life conditions, and open a new field of research.

Pakpuwadon et al. present a paper titled "Self-Reset Image Sensor With a Signal-to-Noise Ratio Over 70 dB and Its Application to Brain Surface Imaging" in which a high-dynamic range CMOS sensor is proposed as a suitable solution to detect very small signals. A self-resetting photodiode system is proposed using a modified P+/N-well/P-sub structure that increases the capacity such as to reduce the number of self-reset operations and thus increase stability. An effective signal-to-noise ratio of 70 dB is achieved. Furthermore, an array of the modified photodiodes is developed and tested *in-vivo*.

An implantable fluorescence-imaging device is developed by Rebusi et al. and presented in the paper titled "Simultaneous CMOS-Based Imaging of Calcium Signaling of the Central Amygdala and the Dorsal Raphe Nucleus During Nociception in Freely Moving Mice" that has been used in animal experiments e.g., in the study of pain processing. Custom CMOS imager chips including a 120 by 40 pixel array are mounted on a needle-shape flexible PCB and equipped with optical filters and a blue-light micro-LED. Two such devices are implanted in a mouse to enable simultaneous recordings. Fluorescent imaging experiments are conducted and correlated with behavioral observations of a freely moving animal.

CONCLUSION

Neuro-technology has become a keystone supporting scientific progress of modern neuroscience as well as the emergence of new therapeutic devices. Microelectronics is one major technology enabler of neuro-technology, alongside material science and bio-electronics, advanced signal and image processing. While microelectronics is based on mature fabrication technologies that scale down with time, significant progresses emerge at the circuit and system levels that improve the electrical characteristics of building blocks, which in turns enables the appearance of new application domains and therapeutic methods.

AUTHOR CONTRIBUTIONS

All authors listed have made a substantial, direct, and intellectual contribution to the work and approved it for publication.

ACKNOWLEDGMENTS

The Guest Associate Editors would like to thank all the authors and the reviewers. We would also like to express our sincere thanks to Prof. Idan Segev, Field Chief Editor, Frontiers in Neuroscience, Prof. Laura Ballerini, Specialty Chief Editor Neural Technology and Prof. Michele Giugliano, Assistant Specialty Chief Editor Neural Technology for giving us the opportunity to organize this Research Topic. We also wish to thank the Frontiers support staffs for their efforts in finalizing this Research Topic.

REFERENCES

Bagheri, A., Salam, M. T., Perez Velazquez, J. L., and Genov, R. (2017). Low-frequency noise and offset rejection in dc-coupled neural amplifiers: a review and digitally-assisted design tutorial. *IEEE Trans. Biomed. Circ. Syst.* 11, 161–176. doi: 10.1109/TBCAS.2016.2539518

Luo, D., Zhang, M., and Wang, Z. (2019). A low-noise chopper amplifier designed for multi-channel neural signal acquisition. *IEEE J. Solid State Circ.* 54, 2255–2265. doi: 10.1109/JSSC.2019.2913101

Rolston, J. D., Englot, D. J., Wang, D. D., Shih, T., and Chang, E. F. (2012). Comparison of seizure control outcomes and the safety of vagus nerve, thalamic deep brain, and responsive neurostimulation: evidence from randomized controlled trials. *Neurosurg. Focus* 32:E14. doi: 10.3171/2012.1.FOCUS11335

Conflict of Interest: The authors declare that the research was conducted in the absence of any commercial or financial relationships that could be construed as a potential conflict of interest.

frontiers in Neuroscience

ORIGINAL RESEARCH
published: 21 May 2021
doi: 10.3389/fnins.2021.667708

Simultaneous CMOS-Based Imaging of Calcium Signaling of the Central Amygdala and the Dorsal Raphe Nucleus During Nociception in Freely Moving Mice

*Romeo Rebusi Jr.[1], Joshua Philippe Olorocisimo[1], Jeric Briones[2,3], Yasumi Ohta[1], Makito Haruta[1], Hironari Takehara[1], Hiroyuki Tashiro[4], Kiyotaka Sasagawa[1] and Jun Ohta[1]**

[1] Division of Material Science, Nara Institute of Science and Technology, Ikoma, Japan, [2] Division of Information Science, Nara Institute of Science and Technology, Ikoma, Japan, [3] Advanced Telecommunications Research Institute International, Kyoto, Japan, [4] Department of Health Sciences, Faculty of Medical Sciences, Kyusyu University, Fukuoka, Japan

OPEN ACCESS

Edited by:
Takashi Tokuda,
Tokyo Institute of Technology, Japan

Reviewed by:
Haitao Wu,
Institute of Basic Medical Sciences, China
J. Luis Lujan,
Mayo Clinic College of Medicine and Science, United States

***Correspondence:**
Jun Ohta
ohta@ms.naist.jp

Specialty section:
This article was submitted to Neural Technology, a section of the journal Frontiers in Neuroscience

Received: *14 February 2021*
Accepted: *26 April 2021*
Published: *21 May 2021*

Citation:
Rebusi RJ Jr, Olorocisimo JP, Briones J, Ohta Y, Haruta M, Takehara H, Tashiro H, Sasagawa K and Ohta J (2021) Simultaneous CMOS-Based Imaging of Calcium Signaling of the Central Amygdala and the Dorsal Raphe Nucleus During Nociception in Freely Moving Mice. Front. Neurosci. 15:667708. doi: 10.3389/fnins.2021.667708

Fluorescence imaging devices have been indispensable in elucidating the workings of the brain in living animals, including unrestrained, active ones. Various devices are available, each with their own strengths and weaknesses in terms of many factors. We have developed CMOS-based needle-type imaging devices that are small and lightweight enough to be doubly implanted in freely moving mice. The design also allowed angled implantations to avoid critical areas. We demonstrated the utility of the devices by using them on GCaMP6 mice in a formalin test experiment. Simultaneous implantations to the capsular-lateral central amygdala (CeLC) and dorsal raphe nucleus (DRN) were proven to be safe and did not hinder the execution of the study. Analysis of the collected calcium signaling data, supported by behavior data, showed increased activity in both regions as a result of pain stimulation. Thus, we have successfully demonstrated the various advantages of the device in its application in the pain experiment.

Keywords: fluorescence imaging, pain perception, CMOS-based imaging, formalin test, nociception

INTRODUCTION

Fluorescence imaging brain implants have been indispensable to the field of neurobiology. Their use has given much insight of the inner workings of the brain *in vivo* (Grienberger and Konnerth, 2012). There are a number of types of such devices than can be safely used in living, active animals without compromising the process of a study. These animals are genetically encoded to express fluorescent calcium indicators that signal neuron firing, in a process referred to as calcium signaling. Though all types have their advantages, they also have limitations that must be acknowledged when considering their use. Selecting the appropriate tool can mean the success or failure of doing a study.

Microendoscopes have been used in fluorescence imaging of deep brain tissue. They come in multiple configurations, of differing materials and collection methods (Helmchen et al., 2001;

Silva, 2017; Ozbay et al., 2018; Scott et al., 2018; Klioutchnikov et al., 2020). Resolution of collected images is enhanced by the inclusion of a focusing element or lens. The lens itself can be the endoscope, such as the gradient refraction index (GRIN lens). The available endoscopes can be rigid, such as the GRIN lens or silica-containing fibers, but have been miniaturized enough to be of practical use (Levene et al., 2004; Flusberg et al., 2005). These properties provide minimal invasiveness, but also limit mobility since use of these tools require restrained animals. Movement is necessarily restrained because of the fixed sizeable tabletop equipment required for the excitation light source and fluorescence emission collection.

Miniature head-mountable integrated microscopes are an innovation on the use of microendoscopes (Ziv and Ghosh, 2015; Resendez et al., 2016; Liberti et al., 2017; Jacob et al., 2018). They can be used to acquire high resolution images of brain activity from freely moving animals. The implanted component is a cylindrical lens (e.g., GRIN lens) that refracts light to the microscope module secured on an animal's cranium. Though miniaturized, the sheer bulk needed to accommodate the components gives the device some weight, more than 2 grams in some cases (Helmchen et al., 2001; Ozbay et al., 2018; Scott et al., 2018; Klioutchnikov et al., 2020). This entails consideration for the weight burden on smaller experimental animals, like mice, and the possible effects on brain activity (Ziv and Ghosh, 2015).

Our lab has developed a needle-type implantable device that has the advantages of the aforementioned devices (**Figure 1A**; Ohta et al., 2017; Rustami et al., 2020; Sunaga et al., 2020). Our device uses a complementary metal-oxide semiconductor (CMOS)-based image sensor chip (imaging area of 120 by 40 pixels, 7.5 μm per pixel, hence 300 × 9,000 μm) and a blue-light micro-LED (for green fluorescent protein (GFP) excitation), mounted on a thickened flexible printed-circuit substrate (FPC) (**Figure 1B**). It has a width of 0.7 mm, a thickness of 0.2 mm, an insertion allowance of up to 4.5 mm, and an average weight of 26.6 mg. Its small features and rigidity prevent excessive tissue damage, allow simultaneous implantation of another device, and make possible angled implantations to avoid critical areas and reach difficult sites. Though simultaneous use is still possible with the use of miniature microscopes (de Groot et al., 2020), our devices are much lighter, providing less of a burden on the test animal. The sensor chip allows for imaging of calcium signaling fluorescence, but not to the same resolution as microscopy imaging.

In this study, two of these implantable CMOS-based imaging devices were simultaneously used in mice induced to experience pain via subcutaneous formalin injection. Pain is an immediate and powerful aversive event that has prominent related behavior and can usually activate relevant brain sites with very low latency (review by Woolf, 2010). The devices are implanted adjacent to the capsular-lateral subsection of the central amygdala (CeLC) and the dorsal raphe nucleus (DRN). The central amygdala has been regarded as a center to the processing of pain signals (Bernard et al., 1989; Neugebauer et al., 2004; Ossipov et al., 2010; Veinante et al., 2013) and responsible for pain-related behavior as an output center of the amygdala (Ji et al., 2017). Meanwhile, the DRN has serotonergic connections with the CeLC (Peyron et al., 1997) and has been implicated in the process of pain modulation (Wang and Nakai, 1994; Stamford, 1995; Li et al., 2017; Lopez-Alvarez et al., 2018). Together, they are part of a system responsible for processing aversive stimuli and stress (Spannuth et al., 2011; Groessl et al., 2018; Ren et al., 2018; Zhou et al., 2019).

This study's aim is twofold. First, it is to demonstrate that the simultaneous use of two devices on an unrestrained animal is without risk and also allows the animal behave unhindered. Second, is to provide useful inner-brain imaging data of the pain processing circuitry. This is accomplished through calcium imaging at the relevant sites. Overall, we aim to show that our device can complement established brain imaging implants while also providing unique advantages.

METHODOLOGY

Device Fabrication

The CMOS imaging chips, designed by our laboratory, were cleaned by submersion in acetone (Fujifilm Wako), twice, and then in isopropanol (Fujifilm Wako) for 5 min each. After drying, they were each mounted on a polyimide, gold-circuit-printed FPC substrate (Taiyo Industrial) taped on a glass slide using a thin layer of epoxy resin [low viscosity epoxy resin Z-1 (N), CraftResin]. The blue-light-emitting micro LEDs (ES-VEBCM12A, Epistar), with a central emission wavelength of 470 nm, were also mounted in the same fashion.

The blue-light filter was prepared by first dissolving Valifast Yellow 3150 dye (Orient Chemical Industries) with cyclopentanol (1:1, w/w) overnight in a light-proof vial. In the same container, the mixture was mixed with Norland Optical Adhesive 43 (Norland Products) (2:1, w/w) using a vortex. The resulting adhesive mixture was spin coated (Spincoater model: 1H-D7, Mikasa) on a silicon-coated [CAT-RG catalyst and KE-106 silicone (Shin-Etsu Chemical), 1:10, w/w] cover slip with a size of 23 mm × 23 mm under the following setting: 3 s to 500 rpm–5 sec at 500 rpm–5 s to 2,000 rpm–20 sec at 2,000 rpm–5 s to 0 rpm. The spin coated material was immediately heated on a hot plate at 100°C for 30 min then left to set in room temperature overnight. The filter film was cut with an Nd: YAG laser (Callisto VL-C30RS-GV, TNS Systems) to make a grid of 10,000 × 3,500 μm sheets.

Cut filter sheet were manually placed over the entire imaging area of the CMOS chips. The device was baked in a vacuum oven (AVO-250NS, ETTAS) for 2 h at 120°C and left to cool.

Using a needle, red resist resin (ST-3000L, Fujifilm) was applied on the sides of the CMOS chip. This resin prevented entry of stray blue LED light through the sides of the chip.

The CMOS chip and the LED were connected to the circuitry of the FPC with micro aluminum wires (Tanaka Electronics) using a wire bonder (7400C-79, West Bond). The wiring was sealed by a protective cover of epoxy resin [low viscosity epoxy resin Z-1 (N), CraftResin] and left to set overnight.

The processed device was incised off from the excess FPC material with a blade. The sides at implantable end of the cut FPC

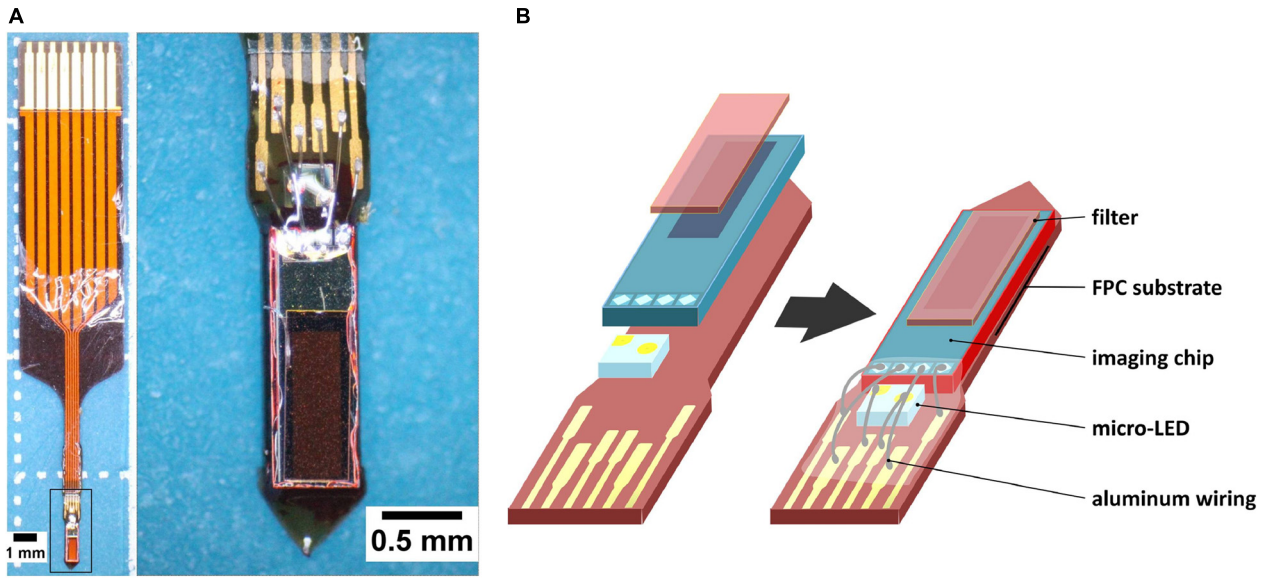

FIGURE 1 | CMOS-based implantable needle-type device for fluorescence imaging. **(A)** Left: Image of the needle-type implantable device as seen under a microscope (28× magnification). This device has undergone all steps of the fabrication process; Right: Higher magnification of the imaging device (from selection, 45×). **(B)** Partial breakdown of the device (left), and the placement of its components (right).

substrate of the device were coated with a thin layer epoxy [low viscosity epoxy resin Z-1 (N), CraftResin] to cover jagged edges.

The devices were lined and bound together with a ribbon of Kapton tape and were enclosed in a parylene coater (PDS 2010, Specialty Coating Systems). They were coated with 5 grams of dichloro-c-cyclophane (GalentisS.r.l.). The thickness of the parylene deposition layer is about 2.5 μm. This transparent, long-lasting coating serves as a bio-protective sheath to prevent infiltration of biological substances into the device that can damage the circuitry.

Implantation

All animal handling procedures were approved by the Nara Institute of Science and Technology (NAIST) Animal Committees, and were performed in accordance with the institutional guidelines of the animal facilities of NAIST.

GCaMP6 mice [strain: FVB-Tg(Thy1-GCaMP6)5Shi., provided RIKEN BRC through the National Bio-Resource Project of the MEXT, Japan (Ohkura et al., 2012)], around 2 months of old of either sex, were implanted with two of our CMOS-based imaging devices (**Figure 2A**). They were positioned adjacent to the CeLC and the DRN, both in the left hemisphere (**Figure 2B**).

The mice were anaesthetized. Hair was removed from the top of their heads and the scalp was disinfected with 4% clorhexidine (Hibitane). They were restrained to a stereotaxic platform (SR-6M, Narishige) using earbars. A heating pad was provided underneath the animals to stabilize body temperature.

Skin was excised from the dorsal side of the head, just enough to access the implantation sites. The cranium was exposed by clearing away tissue and washing with PBS (Fujifilm Wako). After aligning the bregma and lambda, coordinates for the brain site targets were marked on the cranium [CeLC: AP: −0.8 mm, ML: −3.35 mm (left), DV: −4.0 mm; DRN: AP: −5.56 mm, ML: −0.35 mm (left), DV: −3.31 mm; all DV coordinates counted from the dura]. All coordinates were determined using the Paxinos Mouse Brain Atlas (Franklin and Paxinos, 2008) and calibrated in previous trials. Two small micro-screws were shallowly secured into the cranium, spaced some distance from the marked sites. Small cranial windows of around 1 mm in diameter were created on the targets using a dental drill (Hypertec II, Morita) and were cleansed of debris and blood with PBS.

The implants were gently wiped with 70% ethanol (Fujifilm Wako) using cotton swabs and were secured to stereotaxic manipulators (SM-15M, Narishige). They were slowly implanted into the windows, with the CMOS chip facing medially toward the target, up to the predetermined depth. For the DRN, the path of implantation was angled 25° posteriorly to avoid damaging the major superficial blood vessel lying between the entorhinal cortex and the cerebellum (**Figure 2B**).

Once the targets were reached, the cranial windows were sealed with silicone elastomer (Kwik-Cast). The exposed cranium and the surrounding incised skin were sealed with dental cement (Super-Bond kit, Sun Medical). The cement was also used for stabilizing and anchoring the implanted device unto the skull surface and the inserted screws. The manipulators and other restraints were removed. The mouse was allowed to recuperate for at least 12 h in a heated enclosure.

Formalin Test

A modified formalin test was done with the aim of recording brain activity during pain perception, indicated by fluorescence from calcium signaling due to neuronal action potentials.

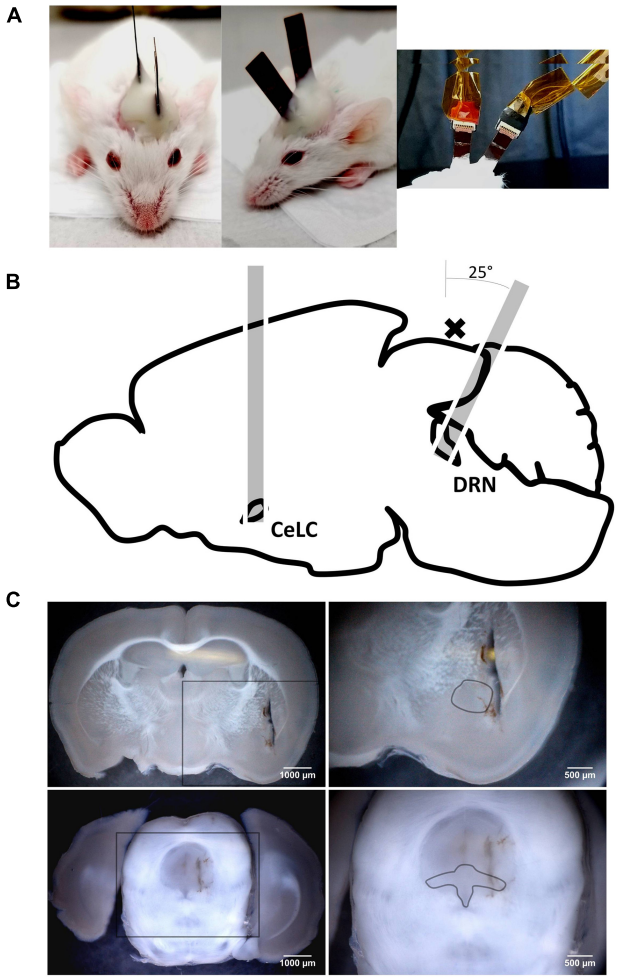

FIGURE 2 | The implanted mouse and the paths of the implants to their targets. **(A)** Left and Middle: A mouse that has just underwent double-implantation, under anesthesia. Note the differing angles of the implanted devices; Right: Implanted devices attached to cables used for supplying power and collecting calcium-signaling fluorescence data. **(B)** Paths of implantation through the brain. The cross (x) indicates the location of a large superficial transverse blood vessel on the brain's surface. **(C)** Coronal sections depicting lesions from implantations and the loci of the brain site targets. Lesions do not reach the dorsal brain surface because the sectioning and the implantation planes are not parallel, more so for the DRN targeting. Upper Left: AP: –1.58 mm, 25×; Upper Right: Zoomed in section from rectangle in upper left image, dashed line approximates the perimeter of the central amygdala (CeA), 45×; Lower Left: AP: –4.36 mm, 25×; Lower Right: Zoomed in section from rectangle in lower left image, dashed line approximates the perimeter of the DRN (dorsal, ventral, and lateral subsections), 45×.

Behavior attributed to pain perception, such as licking, was used to support the validity of the fluorescence imaging data (**Figure 3A**).

The whole recording procedure was done within a darkened canvas tent. This is to prevent the interference of light from sources such as illumination lamps for animal handling, interior overhead lighting, and sunlight passing through windows. Light from such sources are of high enough intensity to permeate the very thin skull, and overlying layers, of the experimental mouse. Such filtered light can still be detected by the implanted devices due to the high sensitivity of the CMOS imaging chip. The orbit and the frontal cranial bone are especially exposed to light penetration. Though the parietal cranium bone is covered with reinforcing dental cement, the cement itself is translucent. Implanted mice were anaesthetized with isoflurane (Fujifilm Wako) using an isoflurane pump (410 Anaesthesia Unit, Univentor). The implants were then connected to cables that were then connected to a slip ring. The rotating slip ring prevented entanglement of the cable pair and served as a bridge between the implants and the power sources (6146 DC Voltage Current Source, ADCMT) and collecting equipment (custom-made, NAIST).

After securing the connections, the mice were kept in an observation enclosure and monitored with a webcam (CMS-V37BK, Sanwa Supply). Illumination was under blue-light that was blocked by the blue-light filter and the red resist coating of the device. Their brain activity and behavior were recorded on a personal computer using specialized custom-made software (CIS_NAIST) and a webcam software (Bandicam) (**Figure 3B**) for a minimum of 10 min to serve as a baseline. Afterward, they were subcutaneously injected using a 30G needle with either 20 µL 2% paraformaldehyde-PBS (Fujifilm Wako) ["Formalin" group (n = 3)] or PBS (Fujifilm Wako) ["PBS" group (n = 3)] at the plantar side of the right hind-paw, contralateral to the side of the implantations. Brain activity and behavior were recorded for a minimum of an hour. For the duration of the experiment, experimenters vacated the tent to prevent affecting behavior.

At the end of the experiment, the mice were sacrificed with an overdose IP injection of sodium pentobarbital (Somnopentyl, ∼0.2 mL, KS Medical). They were perfused with a tubing pump (TP-10SA, AS ONE) with normal saline (Otsuka) and then 4% formaldehyde (Fujifilm Wako). Their brains were extracted and stored in 4% formalin overnight. Coronal sections of the brains (100 µm) were prepared using a vibratome (Linear Slicer PRO7, Dosaka) and were used to confirm successful targeting of the brain sites (**Figure 2C**). Data from animals with unsuccessful implantations were disregarded.

Implanted Brain Temperature Reading

The inner-brain temperature, in Celsius, of an implanted mouse was measured during activation of the blue-light micro-LED at 0.5 mA. Two thermocouples (Cu/constantan (Type T) thermocouple, Muromachi Kikai Co., Ltd., Tokyo, Japan) were bounded unto needle-type devices with Parafilm M (PM-996, Pechiney Plastic Packaging). One thermocouple terminal was located by the LED and another at the device's insertion tip, serving as a reference site away from the LED. The thermocouples were connected to a microcomputer thermometer (BAT 700 1H, Physitemp Instruments LLC).

Mice were anaesthetized and implantations were done into the DRN of one mouse and the CeLC of another as previously described, but with some differences. After implantation, elastomer sealant was not used as a protective cover. Instead, PBS-moistened pieces of Kimwipe were applied on the exposed region surrounding the implant and were held in place with

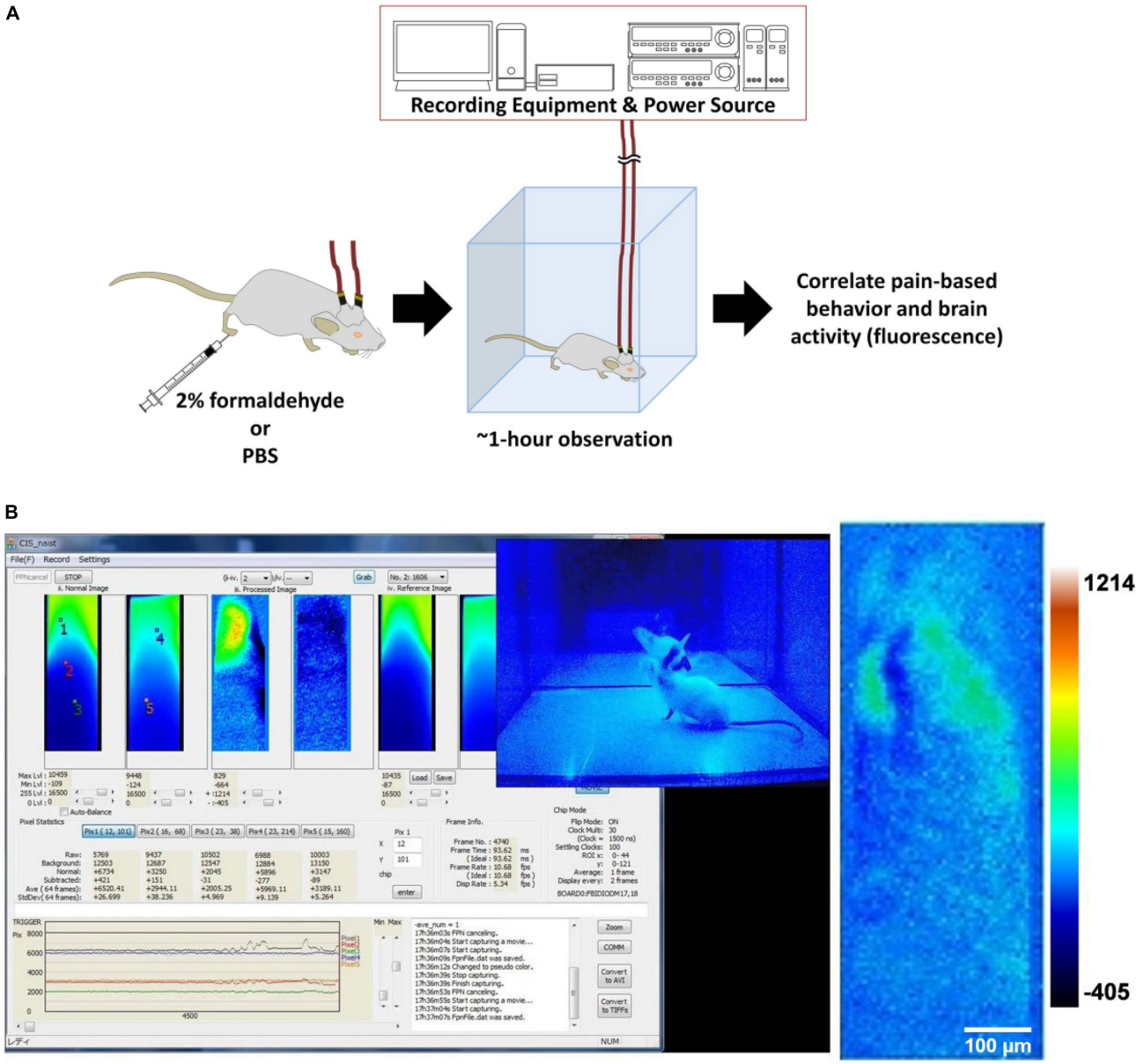

FIGURE 3 | Formalin test with brain activity imaging. **(A)** The experimental design of the modified formalin test. **(B)** Left: Screenshot of the computer monitor during a formalin test. On the screen is the CIS_NAIST software that displays the windows (40 × 120 pixels, 300 × 9,000 µm) for raw, processed, and reference frames of real-time video data, in pairs from left to right. The left of the pair is the fluorescence image from the CeLC, and the right of the pair is from the DRN. Also displayed are the fluorescence level traces at the bottom and frame number information at the middle right. The overlying the CIS_NAIST software window is the video feed of the mouse behavior from the webcam; Right: A sample of a processed image of the CeLC with discernible fluorescent structures. Heatmap values are voltage values that represent ΔF.

Parafilm. The animal's body temperature was allowed to stabilize. Temperature was recorded for 5 min before LED activation, for an hour during activation, and for 5 min afterward.

Data Processing

Videos of the brain fluorescence activity were collected using CIS_NAIST and screen recordings of the working computer. Images of the fluorescence in the CeLC and the DRN were extracted from the time immediately after the injection of the substance and every 10 min thereafter, until the end of the 1-h observation period. The clearest calcium imaging result was selected as a representative example of each sampling group.

Behavior recorded by the webcam was reviewed and pain-related behaviors were taken note of, specifically the licking of the injected site. Behavior was quantified by tallying the amounts of pain-induced licks on the affected paw per 2.5 min blocks within the 1-h observation period. The results were graphed as a number of licks per time block along the passage of time.

Imaging data was acquired using CIS_NAIST, and saved as RAW files. The data was extracted from the files and analyzed using MATLAB (MathWorks). Custom made codes were written in order to process and visualize the data. For processing, the data was first stored as a 3-dimensional matrix (2D spatial pixel array across time), then separated into two for the CeLC and the DRN data. Afterward, the period of injection was determined from webcam recordings, and also by looking at the offset frames in the averaged data set.

Removal of hum noise was performed by making a column vector containing the average values of each row in the pixel array. The average value of that was computed and subtracted to each element of the column vector. The resulting vector was subtracted to each column in the pixel array. This was done in each frame. That is, given a pixel reading $F_t(x, y)$ at frame t, where $x = 1 : n_x, y = 1 : n_y$, the following steps are performed for each t:

(1) Form the column vector $\bar{x}_t$, where $\bar{x}_t(y) = \frac{1}{n_y}\sum_{i=1}^{n_x} F_t(i, y)$ for each $y = 1 : n_y$.
(2) Calculate $\overline{F_t} = \frac{1}{n_x}\sum_{j=1}^{n_y} \bar{x}_t(j)$.
(3) Form the column vector h_t, where $h_t(y) = \overline{F}_t - \bar{x}_t(y)$.
(4) The new reading $F_t^*(x, y)$ is then given by $F_t^*(x, y) = F_t(x, y) - h_t(y)$.

The data was normalized ($\Delta F/F_0$) by getting the average of the frames before injection as the baseline. That is, given $F_t(x, y)$, the baseline F_0 is given by $F_0(x, y) = \frac{1}{t^*}\sum_{t=1}^{t^*} F_t(x, y)$, where t^* is the frame number before injection. The normalized pixel reading $F_t^*(x, y)$ is then given by $F_t^* = \frac{\triangle F}{F_0} = \frac{F_t - F_0}{F_0}$, where $F_t^*(x, y) = \frac{F_t(x,y) - F_0(x,y)}{F_0(x,y)}$.

Based on a previously published study (Takehara et al., 2016), the approximate size of neurons was computed and the regions of interest (ROIs) were selected accordingly. Specifically, it was assumed that the maximum distance between a visible ROI and image sensor surface was 100 μm, and therefore; the full-width at half-maximum (FWHM) would increase 3–4 times compared to a distance of 0 μm. Given the soma and device pixel sizes (8–9 μm and 7.5 μm, respectively) and the 4 times increase in soma size due to the distance from image sensor, then the ROI was computed to be around 6 × 6 pixels. Regions that seemed like neurons based on fluorescent activity were selected as ROIs for further analysis. The average of each ROI was plotted and compared against background values outside the ROIs. A scale bar representing 5% change from baseline was generated. A color plot showing the intensity of each pixel in a frame was graphed to visualize the ROIs. The behavioral data was aligned with the calcium imaging data to see their relationship.

Afterward, the first-differenced calcium traces in each ROI were cross-correlated or auto-correlated. First-difference was applied to ensure stationarity of the data. That is, given a calcium trace reading z_t at time t, the first-differenced calcium trace $\triangle z_t$ at time t is $\triangle z_t = z_{t+1} - z_t$. First-differencing was implemented using **diff()** function of MATLAB. Cross-correlation between CeLC and DRN ROIs was calculated by shifting the DRN data across time. That is, given the CeLC calcium trace reading x_t at time t and the DRN calcium trace reading y_t at time t, the non-normalized cross-correlation coefficient R at lag m is given by

$$R_{x,y}(m) = \begin{cases} \sum_{t=1}^{T-m} x_t y_{t-m} & \text{if } m \geq 0 \\ R_{y,x}(-m) & \text{if } m < 0 \end{cases}.$$

The (normalized) cross-correlation ρ at lag m is then given by $\rho_{x,y}(m) = \frac{1}{\sqrt{R_{x,x}(0)R_{y,y}(0)}} R_{x,y}(m)$. Here, $R_{x,x}(m)$ and $R_{y,y}(m)$ represents the non-normalized auto-correlation at lag m for x_t and y_t, respectively. The DRN time lag with the highest correlation with CeLC $m^* = \text{argmax}_m \rho_{x,y}(m)$ was recorded as the best time lag. Cross-correlation analysis was implemented using **xcorr()** function of MATLAB. The three ROIs from CeLC and three ROIs from DRN were cross-correlated as follows: CeLC vs. DRN, CeLC vs. CeLC, and DRN vs. DRN. Therefore, a total of 27 cross-correlations were analyzed per mouse.

To measure the relationship between brain imaging and behavior, the mutual information coefficient (MI) between these variables was computed. Basically, the mutual information coefficient (Cover and Thomas, 2006) between two (discrete) random variables X and Y is given by

$$I(X;Y) = \sum_{x\in\mathcal{X}}\sum_{y\in\mathcal{Y}} p_{X,Y}(x, y) \log\left(\frac{p_{X,Y}(x, y)}{p_X(x)\, p_Y(y)}\right).$$

Similarly, if X, Y are continuous, then the summation is replaced with integration. However, since brain imaging is a continuous random variable, while the behavior is discrete, MI was measured using an adapted method (Ross, 2014). MI was computed using **discrete_continuous_info_fast()** function of Ross (2014). Since the imaging data was a continuous real-valued dataset, it was binned and averaged across the same 2.5 min window of the behavioral data. This enabled the measurement of mutual information between continuous imaging data and discrete behavioral data, where a higher value indicates more dependence between the two.

Finally, statistical analysis was done using MATLAB. Non-parametric tests were performed: Kruskal-Wallis test for the cross- and auto-correlation analysis and non-parametric two-way ANOVA (Friedman's test) for the brain calcium imaging and licking behavior relationship analysis were performed. P-values less than 0.05 were considered significant. Boxplots with median and interquartile range were graphed also using MATLAB.

RESULTS

Brain Recordings: Fluorescence Imaging and Internal Temperature

No notable complications on the welfare of the experimental mice were encountered during the duration of the study. Implantation surgery was accomplished without issues and all the mice recuperated fully the following day. No signs of distress that may have come from the implantation were observed. Furthermore, there were no indications of encumbrance of the head. Post mortem weighing of the

cement-bound dual implants, excluding the parietal portion of the cranium, gave an average weight of 0.474 g (n = 5). The only signs of discomfort were the pain-related behavior and inflammation reaction of the Formalin group mice after injection and the slight agitation immediately resulting from animal handling.

Images of the calcium signaling from representative examples were chosen (**Figure 4**). The top right corner of the DRN in the Formalin group had an increasing intensity throughout the time course, from the 20-min mark onward, with distinct and prominent fluorescence. The CeLC of the same group, particularly the lower-left of the imaging area, initially displayed some fluorescence that gradually lessened over time.

On the other hand, the PBS group had more uniform and constant images across time. Slight changes in overall fluorescence can still be seen, such as a brighter DRN and CeLC at the 30-min mark. The changes are quite difficult to spot by eye alone. Therefore, a more quantitative approach was taken.

Readings in a double-implanted mouse depict very small increase in deep brain tissue temperature during activation of the blue-light micro-LED (**Figure 5**). At most, there was 0.5°C increase in the portion of the DRN next to the LED. The results also show that proximity to the LED does not necessarily lead to a higher tissue temperature.

Data Analysis

To better visualize changes in CeLC and DRN fluorescence activity, the whole frame average across time was computed in all mice (**Figure 6**, top and middle). In addition, the paw-licking behavior of the mice was also measured simultaneously (**Figure 6**, bottom). Due to the small size of the implantable device, both CeLC and DRN can be visualized at the same time in a freely behaving mouse. Based on the $\Delta F/F_0$ scale bar, the Formalin group generally had higher amplitudes than the PBS group. For example, Formalin Mouse 2 displayed higher fluorescence values compared to PBS Mouse 2 in the CeLC. Furthermore, Formalin Mouse 1 had higher fluorescence intensities than PBS Mouse 1 in

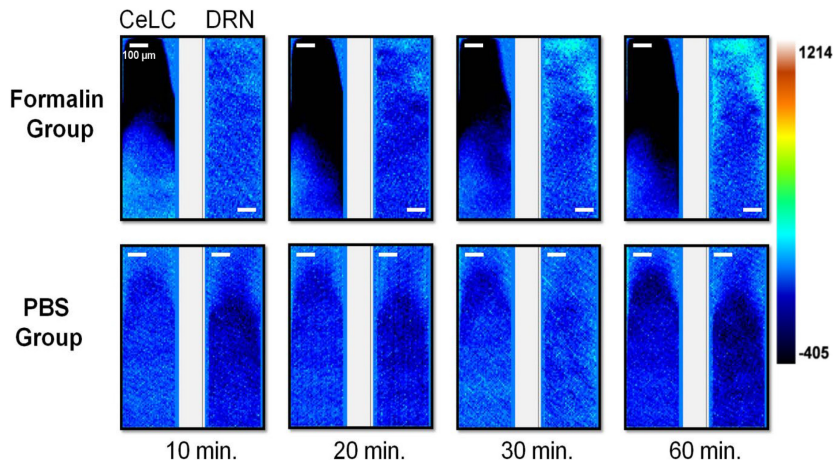

FIGURE 4 | Brain activity fluorescence immediately after injection of formaldehyde or PBS. Neuronal fluorescence from the replicates that demonstrated detectable and distinct signals are presented. Time shown refer to the minutes that has passed after injection of the assigned substance. For all image pairs, CeLC is on the left and the DRN is on the right. Heatmap values are voltage values that represent ΔF.

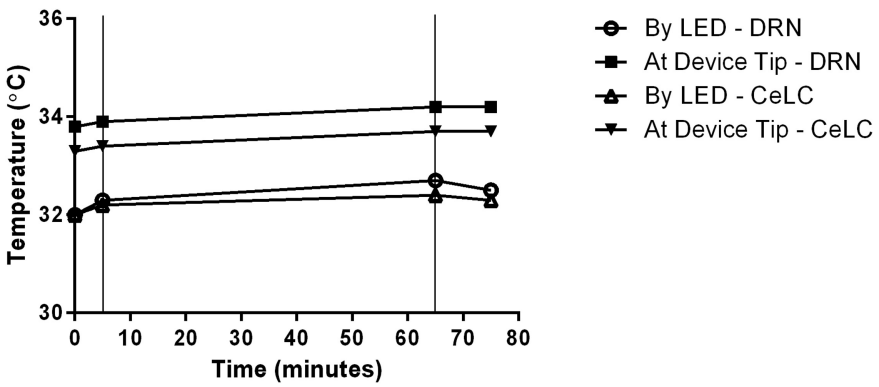

FIGURE 5 | Recorded change of DRN and CeLC temperatures during implantation. Temperature readings were done in the vicinity of the implanted devices, specifically by the LED and at the device insertion tip. Thin vertical lines in the graph indicate start and end points of LED activation time.

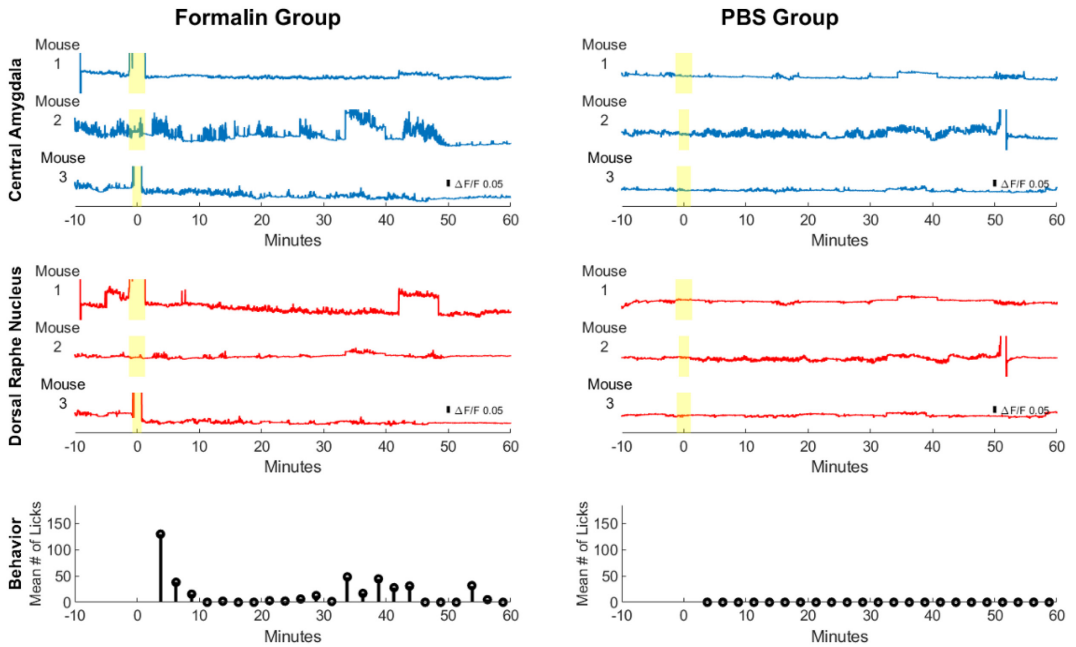

FIGURE 6 | Calcium imaging and behavioral analysis across multiple mice. Brain calcium imaging and behavioral analysis of Formalin- and PBS-injected mice. The yellow highlight marks the injection period. The blue line graphs show calcium measurements of the CeLC across multiple mice, while the red line graphs show calcium measurements of the DRN. At the bottom are the behavioral results for the average number of licks per 2.5 min time block among Formalin mice (n = 4) and PBS mice (n = 3).

the DRN. In addition, the Formalin group had higher frequency of fluorescent peaks for both brain sites. This was most apparent for Mouse 2 and 3 for CeLC and Mouse 1 for DRN. Conversely, the PBS group had graphs that are comparatively flatter. Since this was a proof-of-concept to show that the dual-implantable device works, more mouse samples and further analysis can be done to quantify the difference in amplitudes and frequencies between both groups.

Pain-related behavior was observed from all the mice of the Formalin group, as reflected by the average number of licks. A high number of licks was seen in the initial minutes after injection. The licking behavior then subsided after 10 min. Then, after 30 min licking behavior started to increase again. This bi-phasic response may correspond to the acute and inflammatory phase of formalin injection, as will be discussed later. Interestingly, peaks in licking behavior also corresponded to higher fluorescence activity in the CeLC and DRN. On the other hand, the PBS mice did not display any hindpaw-licking behavior. These results confirm the successful execution of the formalin test.

Another two mice were selected as representatives, one per sampling group, to visualize analysis of multiple regions of interests (ROIs) (**Figure 7**). Slight differences in timing and intensity of fluorescence can be seen in ROIs of the same brain region. For instance, in the Formalin-injected mouse, DRN ROI2 displayed more fluorescence activity than DRN ROI1 at the 20-min mark. It is also observable that the ROIs of the DRN have higher and more distinct spikes than the background. Furthermore, ROI 1 and 2 of the CeLC had higher fluorescence amplitudes than ROI 3. However, CeLC ROI 3 still had higher fluorescence than the CeLC background values.

On the other hand, the PBS-injected mouse had ROI values that are relatively similar with the background. Similar to **Figure 6**, the PBS mouse had a more constant fluorescent activity where its peaks do not deviate too far from the average noise value. The peaks of the Formalin-injected ROIs were more distinct and had higher amplitudes compared to its baseline level before injection.

The relationship between each ROI was explored. The small size and large field of view of the device made it possible to measure cross-correlation of multiple ROIs within and between the CeLC and DRN. First, cross-correlation analysis of the Formalin-injected mouse showed distinct and clear peaks mostly at time lag 0 (**Figure 8**). The only exception was the cross-correlation between CeLC ROI 1 and the DRN ROI 1. The data indicated that when the first-differenced DRN data is shifted 1 frame back, then the correlation with first-differenced CeLC data increases. This means that when the CeLC fluorescence increases, there is a positive correlation that the DRN fluorescence will also increase after 0.094 s. However, this was only true for one ROI of the CeLC. The other two ROIs of the CeLC showed a definite peak at 0 time lag, which indicated that the cross-correlation was highest at 0 s delay.

In contrast, the PBS-injected mouse had less clear and less distinct cross-correlation peaks. It can be seen that most of the cross-correlation graphs are broader, especially for DRN ROI 2. Furthermore, the best time lag is less consistent among the ROIs, with one pair having the highest cross-correlation at 6 frames

(0.562 s) and two pairs of ROIs at 5 frames (0.468 s). This may indicate less synchronization between CeLC and DRN neuronal firing in PBS-injected mouse.

To provide more insight and see if the results are consistent, the cross-correlation of ROIs in each mouse was analyzed (**Figure 9**). Majority of the peak cross-correlations was at time lag 0 (**Figure 9A**). However, it can be observed that PBS mice had several non-zero and non-one time lags. For example, PBS Mouse 1 had a high cross-correlation ($\rho = 0.69$) at -8 frames when analyzing between its CeLC ROI 1 and DRN ROI 2. Then its CeLC ROI 2 and DRN ROI 2 had the best lag at $+3$ frames.

Furthermore, even within the DRN, there was a high cross-correlation at 8, 15, and 4 frame lags for PBS Mouse 1, 2, and 3, respectively. On the other hand, more cross-correlations at time lag 0 can be seen in Formalin-injected mice. For instance, when comparing within the same brain region (i.e., CeLC vs. CeLC or DRN vs. DRN) all ROIs displayed a best time lag of 0, with the exception of DRN ROI 2 and 3 of Formalin Mouse 2. Taken together, this may indicate less synchronization within the DRN of PBS-injected mice.

To compare the difference between the number of frame lags higher than 1 for each mouse group, a two-tailed unpaired *t*-test was performed. The number of frame lags higher than 1 was statistically higher in the PBS group compared to the Formalin group ($p = 0.00773$, Unpaired *t*-test). This confirmed the hypothesis that PBS-injected mice had a higher number of ROIs that were not as synchronized compared to the Formalin-injected mice.

Finally, to measure the relationship between the brain calcium imaging data and licking behavior of mice, we calculated their mutual information (MI). The MI between calcium imaging of PBS mice and their licking behavior is close to 0, showing a lack of a relationship. On the other hand, the Formalin mice displayed higher MI levels across different ROIs and brain areas (**Figure 10A**). This was further confirmed using two-way ANOVA, wherein the Formalin group was significantly different compared to the PBS group ($p < 0.05$). However, no difference was detected between CeLC and DRN within each group.

By using this MI metric, the capability of the dual-implantable device to correlate brain activity and behavior was demonstrated. This showed the potential of the device for use in further experiments and analysis.

DISCUSSION

We have demonstrated that the use of our device in a double-implantation set-up is feasible and will not introduce complications that can affect animal welfare. All trials proceeded successfully with no mice had displaying signs of excessive distress or injury from the implantation. Additionally, internal or core brain temperature of the implanted mice are well within the normal physiological levels of rodents, with the maximum limit at around 38°C (Yarmolenko et al., 2011; Mei et al., 2018). This is true whether the LED was activated or not. Along with the very minute increase in temperature during LED activation, temperature-related necrosis can be said to have not occurred. The relatively low internal body temperature can be attributed to the sleeping state of the recorded mouse (Sela et al., 2021). With the devices' viability and novel features, many methodology changes can be explored. It is important to note that these statements are only applicable to short-term set-ups, those lasting for a few days per run. Nevertheless, the use of the device is still very safe for many methods.

The calcium signal imaging results have shown that there are perceivable qualitative differences in the fluorescence between the Formalin-injected and the PBS-injected group. The increase in signaling of the former group is attributable to nociception itself, as supported by behavioral data. Though the trend is not wholly consistent among mice, there a discernible pattern that can still be observed using our new device. In the images, fluorescent forms or shapes can be seen, especially in that of the DRN of the Formalin group. These forms are surely not individual neurons. They are much larger than the widest span (9–10 μm) of an average soma of neurons found in the selected sites. Light scattering through the tissue cannot be discounted as contributing to the size of the forms as seen on the images, but their effects are assumed to be minimal (Takehara et al., 2016). They are possibly neuronal clusters or ganglia and not glial cells because of the nature of GFP expression in GCaMP6 mice. The actual identity of these fluorescent forms is hard to ascertain because of the low resolution. This is an unavoidable limitation in the use of the CMOS imaging chip, especially the version we are currently using.

The formalin test is a method that can induce a bi-phasic response to pain: an early acute phase (0–5 min post injection) and a later tonic or inflammatory phase. The timing of the latter seems to differ among sources. The phase is mentioned to occur at around 15 min (Hunskaar et al., 1985; Hunskaar and Hole, 1987; Shibata et al., 1989; Rosland et al., 1990) until 60 min post injection (Manning and Mayer, 1995a). This is further complicated by the effect of environmental temperature on the potency of inflammation (Rosland, 1991; Tjølsen et al., 1992). The variability in the timing is reflected in the flattened second peak in the averaged behavior data of the Pain group (**Figure 6**, bottom).

The CeLC is a major component of the pain matrix. It has context-specific paradoxical roles of promoting hypoalgesia (Manning and Mayer, 1995a,b; Kang et al., 1998; Finn et al., 2003; Sabetkasaei et al., 2007; Yu et al., 2007; Veinante et al., 2013) and hyperalgesia. Hyperalgesia is accomplished during inflammation (Carrasquillo and Gereau, 2007; Veinante et al., 2013). Meanwhile, the DRN has also been shown to have an inflammation-specific antinociceptive function (Palazzo et al., 2004; Cucchiaro et al., 2005). Their inflammation-induced activation and the somewhat variable nature of the tonic phase timing might explain the persistent activity spikes of both sites in the Formalin group. This is reflective of the flattened, prolonged second peak, representing the tonic phase, in the Formalin group's behavior data. This does not apply to the first distinct peak of the acute phase. Even if both the fluorescence and the behavior data are indicators of pain perception, the two data sets may not be total complements to each other because of the complex effects of formalin-induced nociception. Even so, together they still provide a holistic portrait for visualizing pain.

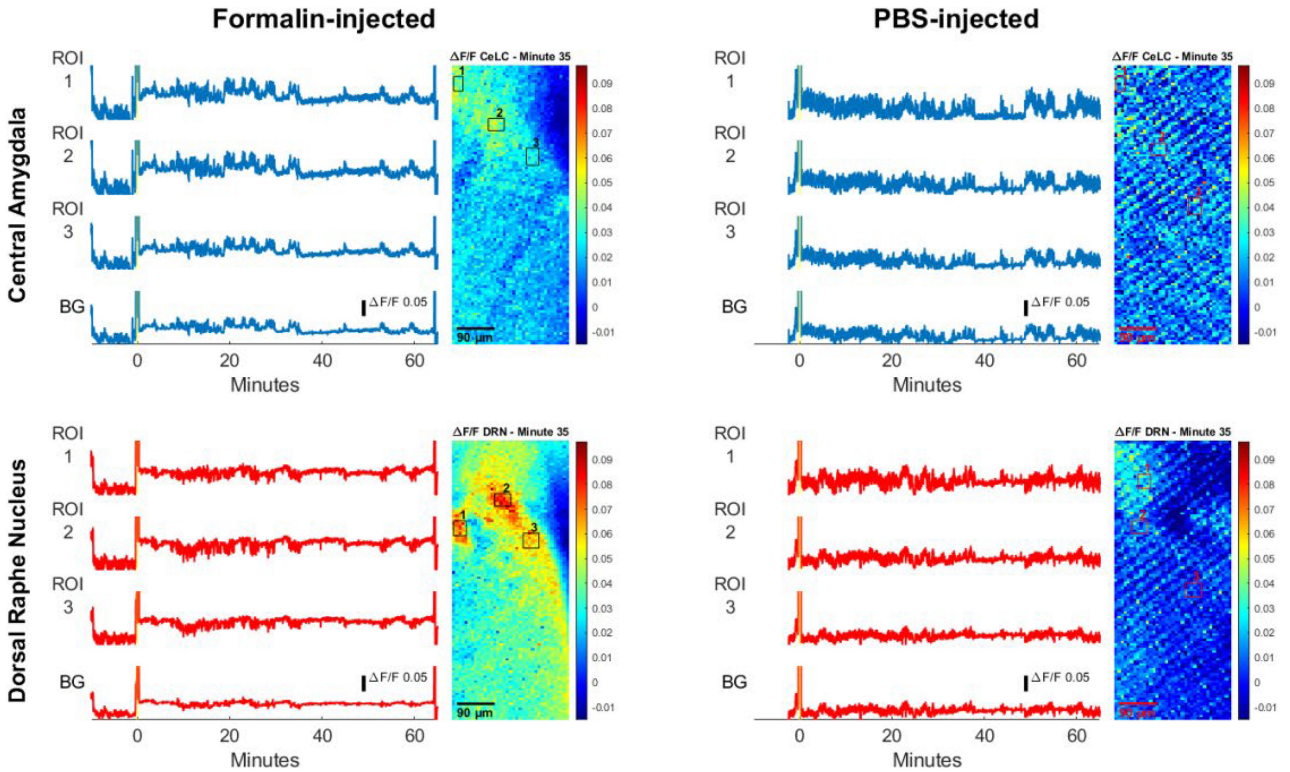

FIGURE 7 | Calcium traces of specific regions of interest (ROIs). Calcium measurement of Formalin-injected mouse and PBS-injected mouse. The yellow bar on the line graph marks the injection period. The blue line graphs show measurements in the CeLC, while the red line graphs show measurements of the DRN. The background values (BG) are the average of all the pixels outside the ROIs. Beside the line graphs are images of sample frames where ROIs are enclosed in black or red boxes.

The qualitative visual data also reflects the results of the behavior analysis. The images of the DRN of the Formalin group display ROIs of higher fluorescence intensity compared to the PBS group. The difference is not fully apparent, especially for the CeLC in the latter half of the observation period. It was expected to fluoresce more prominently, following its central role in modulating pain perception. This weak response to pain stimulation can be attributed to the lateralization of the CeLCs of the two hemispheres. The right CeLC has been observed to be more responsive to nociception to a greater degree (Ji and Neugebauer, 2009; Allen et al., 2021), though this does not mean that the left CeLC is fully inactive (Allen et al., 2021). The descending architecture of the CeLCs are ipsilateral, especially the left one (Manning, 1998; Ji and Neugebauer, 2009). Since the study investigated the left brain hemisphere and induced pain contralaterally, the resulting calcium signaling could not have been strong. The fact that the devices have still detected pain-based trends in fluorescence between the two groups demonstrates its sensitivity.

Cross-correlation analysis showed that the Formalin-injected mice had more max cross-correlations at time lag 0.Though some ROIs displayed best lags at 1 or 2 frames, most other ROIs showed more synchronous activity. In contrast, the PBS-injected mice had more varying frame lags with several values higher than 1 frame delay/advance. The analysis indicated that there may be more asynchronous firing between CeLC and DRN neuronal firing in PBS-injected mice unlike the Formalin-injected mice. This suggests a coupling mechanism between or within the CeLC and the DRN during pain processing. The same mechanism is present in the adjacent cells of the dorsal root ganglion (DRG), a downstream neural pathway of the CeLC and the DRN, during inflammation and nerve damage (Kim et al., 2016). This synchronization was less apparent in naïve mice not exposed to pain.

Additionally, the highly variable time lag values of the cross-correlation coefficients of the ROIs portray a heterogenous population of neurons of differing roles in pain perception. For instance, the central amygdala can increase or decrease pain-related behavior depending on the cell type. Cells expressing protein kinase C-delta played a role in sensitization to nerve injury and increased pain response, while cells expressing somatostatin were inhibited and drove anti-pain behavior (Wilson et al., 2019). Furthermore, adjacent DRN 5-HT neurons are closely coupled and synchronized; however, non-adjacent 5-HT neurons are not. Also, there is a difference in the auto-correlograms of serotenergic and non-serotnergic neurons in the DRN, where non-5-HT cells are more irregular while 5-HT cells are more periodic (Wang and Aghajanian, 1982). Our analysis demonstrates such heterogenous interactions and behavior as well because ROIs within the same brain region, particularly

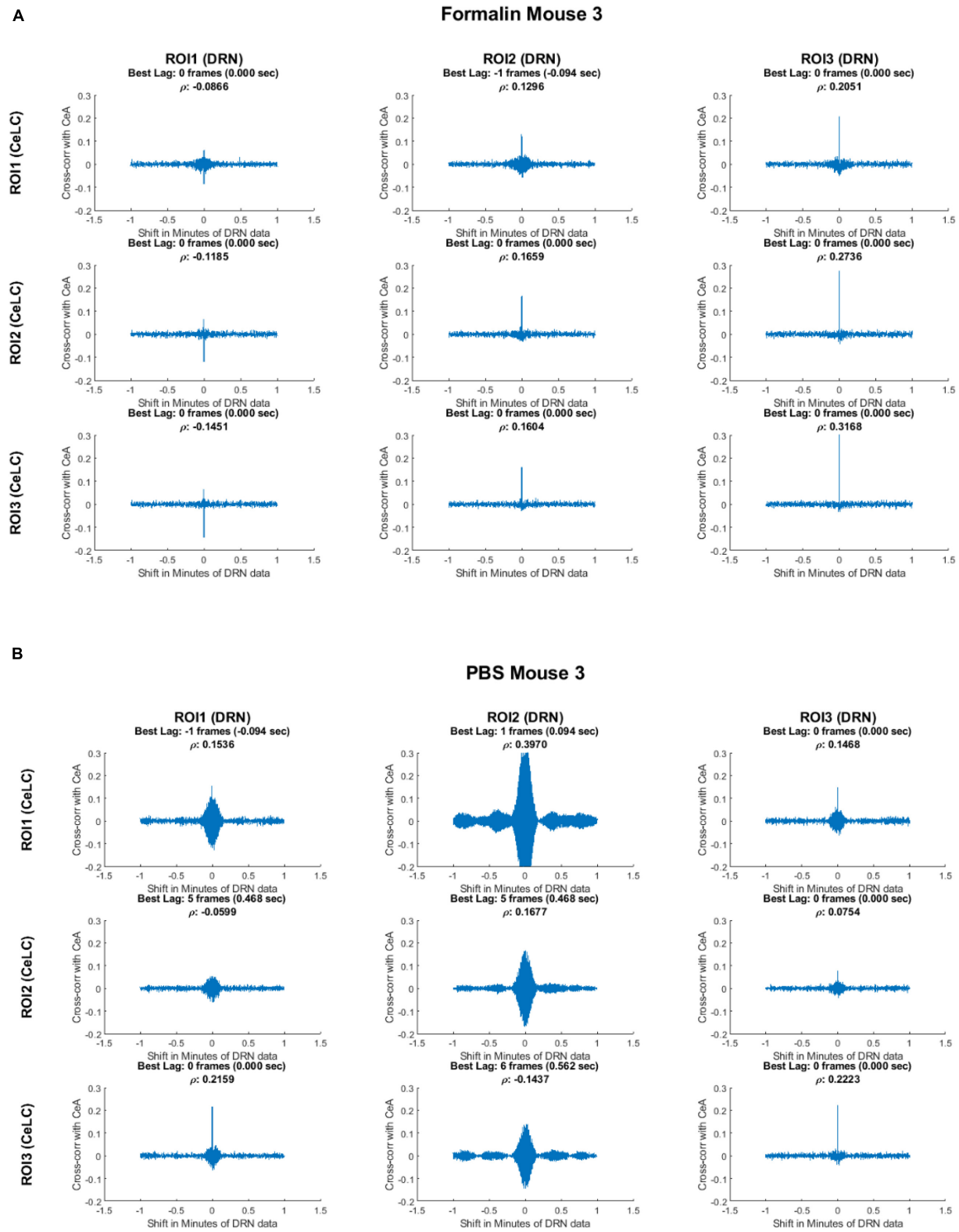

FIGURE 8 | Cross-correlation analysis of two representative mice. Top: Formalin-injected mouse; bottom: PBS-injected mouse. The figure shows the cross-correlation of the first-difference of CeLC fluorescence imaging data with DRN data. The correlation between CeLC and time-shifted DRN (across varying lags) is measured. Peaks indicate high cross-correlation at that specific shift or time lag of the DRN data. The time lag with the highest cross-correlation coefficient (ρ) is indicated at the top of each graph.

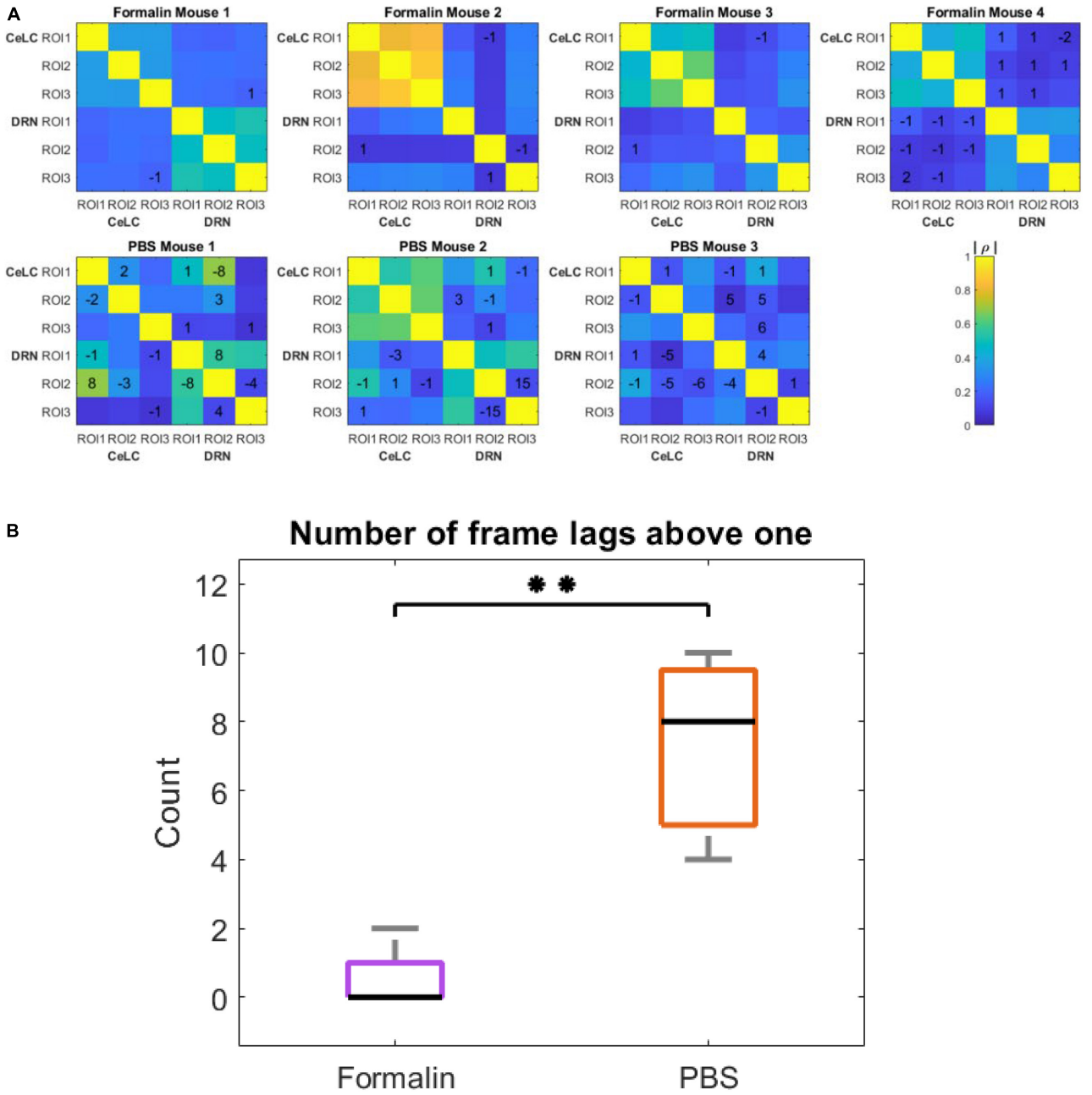

FIGURE 9 | Cross- and auto-correlation analysis in all mice. **(A)** Heatmap showing time lags with the highest cross-correlation coefficients. ROIs from CeLC and ROIs from DRN in each mouse were cross-correlated. The values written indicate the time lag of first-differenced DRN data in frame number that showed the highest cross-correlation with the original unshifted first-differenced CeLC data. No value means the best lag was at 0. The color indicates the cross-correlation coefficient (ρ)from low (blue) to high (yellow) in absolute values. **(B)** Box plot of the number of frame lags that were above 1 in both treatment groups. Kruskal-Wallis test was performed and a significant difference was computed (**p = 0.00773, α = 0.05).

the DRN of PBS mice, showed varying cross-correlograms. In addition, cross-correlation between CeLC and DRN ROIs had different time lags even if the mice were in the same treatment group.

The large gap in the tallied pain-based licking behavior of the groups confirms the successful execution of the formalin test, with the PBS group displaying none. This is reflected in the difference in calcium signaling between the Formalin and the PBS groups, though the peaks of the behavior tally graph and the fluorescence graph do not match after the initial phase. So, even though PBS Mouse 2 demonstrated relatively high CeLC brain activity, it is not indicative of any pain processing, based on behavior. This is further supported by and elucidated in the MI analysis between behavior and calcium signaling result.

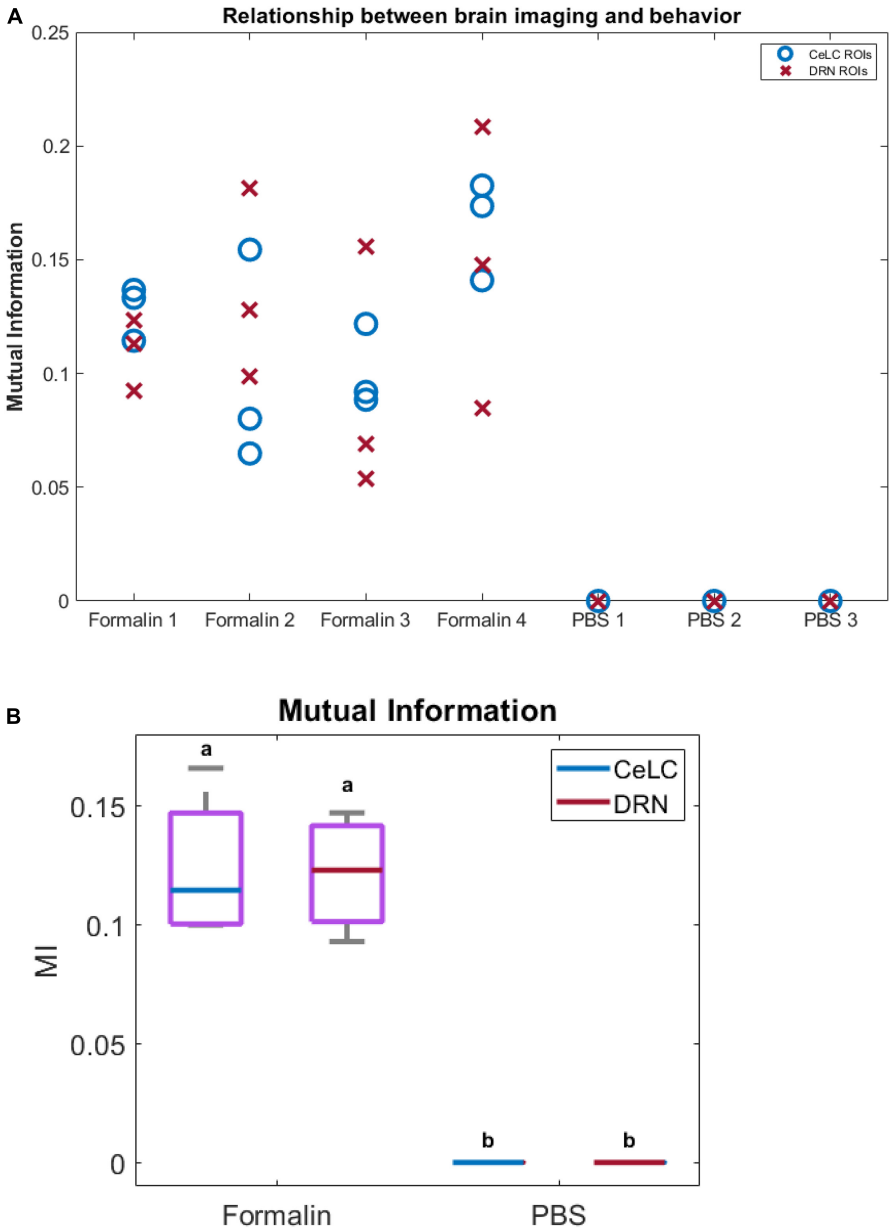

FIGURE 10 | Relationship between brain calcium imaging and licking behavior. Relationship between brain calcium imaging and licking behavior. **(A)** Plot of mutual information between imaging and behavior. Blue circles indicate ROIs from CeLC, while red crosses indicate ROIs from DRN. **(B)** Box plot of the mutual information (MI) when ROIs in each mouse were averaged. PBS mice showed almost 0 MI with behavior, while Formalin mice showed higher MI values. Non-parametric two-way ANOVA showed significant difference between Formalin and PBS groups ($p < 0.05$, $\alpha = 0.05$), but no significant difference between CeLC and DRN within each group.

MI is the amount of shared information between the two data, and shows how related they are with each other. A value of 0 indicates that the two data are independent. MI has several advantages such as being unbiased to the sample size, being model independent, being unrestricted to the data type, being able to detect linear and non-linear interactions, and being multivariate (Ross, 2014; Timme and Lapish, 2018). The analysis showed that the MI between calcium imaging of PBS mice and their licking behavior is close to 0 (**Figure 10A**). This means that the imaging data was not related to any mouse licking behavior in the PBS-injected mice. In contrast, the Formalin mice displayed significantly higher MI levels (**Figure 10B**).

Previous *in vivo* investigations on the mechanisms of pain, using calcium imaging, have mostly been done on the spinal cord level, as a necessity for less injurious methods of visualizing neural activity (Anderson et al., 2018; Miller et al., 2018; Xu and Dong, 2019). Our study is one of the first attempts to simultaneously image pain processing at two

relevant brain regions *in vivo*, addressing the need for multi-site visualization for neuron-network studies (de Melo Reis et al., 2020). Because the protocols we used, from the lens-less CMOS-based fluorescence imaging device usage to the general experimental design modifications, are quite novel, there are many points for improvement that need to be addressed. Long-term double-implantation use of the devices can be explored. The methodology used to demonstrate the device, the formalin test, is very short in duration. It did not allow for the exploration of this aspect of device use. Determining the long-term viability of an implanted device would expand applications to studies involving chronic pain or multi-stage pain-conditioning experiments involving the same experimental animals. Retention of dual-implantation for an extended period can also more ensure better recuperation of the animals and give insight to potential changes to the integrity of the implanted devices. This can be done in future studies because of the parylene coating, which is usually used on medical implants. Because of the modular design of the device, components can easily be upgraded almost independent of each other. There are commercially available CMOS imaging chips of superior performance that can supplant what we have used. As of now, image quality derived from the CMOS chip we have used is relatively of inferior quality compared to that from lens systems. Because of the optics involved in a CMOS-based system vs. a lens system, images from the former will never match the resolving power provided by the latter. Even with an increase in pixel amount, the resolution will not necessarily improve. What this study had provided is a starting point for possible use of better components to better approach data quality of already established tools, but also providing unique advantages. Materials for the FPC substrate can also be made thinner, but more rigid, to ensure better implantation accuracy and safety. The blue-light filter used on our CMOS chips has been developed in our lab (Sunaga et al., 2014) and is still being improved upon through integration of additional filtering layers and better fabrication methods. Thus, there is proof of concept that the dual use of the device can work, but the device has potential still for refinement.

CONCLUSION

We have shown that our developed implantable device can simultaneously be used to image two brain sites in mice while observing behavior, without hindrance or complications. The double implantation of the device was implemented across multiple experimental animals to successfully complete the modified formalin test. The collected fluorescence imaging data has been useful to some degree, enough to show trends and support established findings about pain processing. Though, there is a need for improvement, since at this point, the device is not sensitive enough to provide conclusive visuals. Proper selection of more active brain regions to image may better demonstrate its features. The properties of this implantable CMOS device will make it easy to apply on novel sites and configurations in future experiments.

DATA AVAILABILITY STATEMENT

The raw data supporting the conclusions of this article will be made available by the authors, without undue reservation.

ETHICS STATEMENT

The animal study was reviewed and approved by the Nara Institute of Science and Technology (NAIST) Animal Committees.

AUTHOR CONTRIBUTIONS

All authors listed have made a substantial, direct and intellectual contribution to the work, and approved it for publication.

FUNDING

This work was partially supported by the JSPS KAKENHI, Grant No. JP18H03780 and JST CREST, Grant No. JPMJCR1651. This work was also supported through the activities of VDEC, The University of Tokyo, in collaboration with Cadence Design Systems, Inc.

ACKNOWLEDGMENTS

We would like to greatly thank Prof. Masanobu Takahashi for his contribution to noise reduction in the fluorescence images, and Ms. Mamiko Kawahara for her support in the animal experiments.

REFERENCES

Allen, H. N., Bobnar, H. J., and Kolber, B. J. (2021). Left and right hemispheric lateralization of the amygdala in pain. *Prog. Neurobiol.* 196:101891. doi: 10.1016/j.pneurobio.2020.101891

Anderson, M., Zheng, Q., and Dong, X. (2018). Investigation of pain mechanisms by calcium imaging approaches. *Neurosci. Bull.* 34, 194–199. doi: 10.1007/s12264-017-0139-9

Bernard, J. F., Peschanski, M., and Besson, J. M. (1989). A possible spino (trigemino)-ponto-amygdaloid pathway for pain. *Neurosci. Lett.* 100, 83–88. doi: 10.1016/0304-3940(89)90664-2

Carrasquillo, Y., and Gereau, R. W. (2007). Activation of the extracellular signal-regulated kinase in the amygdala modulates pain perception. *J. Neurosci.* 27, 1543–1551. doi: 10.1523/JNEUROSCI.3536-06.2007

Cover, T. M., and Thomas, J. A. (2006). *Elements of Information Theory*, 2nd Edn. Hoboken, NJ: Wiley-Interscience.

Cucchiaro, G., Chaijale, N., and Commons, K. G. (2005). The dorsal raphe nucleus as a site of action of the antinociceptive and behavioral effects of the α4 nicotinic receptor agonist epibatidine. *J. Pharmacol. Exp. Ther.* 313, 389–394. doi: 10.1124/jpet.104.079368

de Groot, A., van den Boom, B. J., van Genderen, R. M., Coppens, J., van Veldhuijzen, J., Bos, J., et al. (2020). NIN scope, a versatile miniscope for multi-region circuit investigations. *eLife* 9:e49987. doi: 10.7554/eLife.49987

de Melo Reis, R. A., Freitas, H. R., and de Mello, F. G. (2020). Cell calcium imaging as a reliable method to study neuron–glial circuits. *Front. Neurosci.* 14:569361. doi: 10.3389/fnins.2020.569361

Finn, D. P., Chapman, V., Jhaveri, M. D., Samanta, S., Manders, T., Bowden, J., et al. (2003). The role of the central nucleus of the amygdala in nociception and aversion. *NeuroReport* 14, 981–984. doi: 10.1097/01.wnr.0000069062.85441.29

Flusberg, B. A., Cocker, E. D., Piyawattanametha, W., Jung, J. C., Cheung, E. L. M., and Schnitzer, M. J. (2005). Fiber-optic fluorescence imaging. *Nat. Methods* 2, 941–950. doi: 10.1038/nmeth820

Franklin, K. B. J., and Paxinos, G. (2008). *The Mouse Brain in Stereotaxic Coordinates*, 3. Edn. Amsterdam: Elsevier, Academic Press.

Grienberger, C., and Konnerth, A. (2012). Imaging calcium in neurons. *Neuron* 73, 862–885. doi: 10.1016/j.neuron.2012.02.011

Groessl, F., Munsch, T., Meis, S., Griessner, J., Kaczanowska, J., Pliota, P., et al. (2018). Dorsal tegmental dopamine neurons gate associative learning of fear. *Nat. Neurosci.* 21, 952–962. doi: 10.1038/s41593-018-0174-5

Helmchen, F., Fee, M. S., Tank, D. W., and Denk, W. (2001). Two-photon microscope: high-resolution brain imaging in freely moving animals. *Nat. Methods* 14, 713–719.

Hunskaar, S., Fasmer, O. B., and Hole, K. (1985). Formalin test in mice, a useful technique for evaluating mild analgesics. *J. Neurosci. Methods* 14, 69–76. doi: 10.1016/0165-0270(85)90116-5

Hunskaar, S., and Hole, K. (1987). The formalin test in mice: dissociation between inflammatory and non-inflammatory pain. *Pain* 30, 103–114. doi: 10.1016/0304-3959(87)90088-1

Jacob, A. D., Ramsaran, A. I., Mocle, A. J., Tran, L. M., Yan, C., Frankland, P. W., et al. (2018). A compact head-mounted endoscope for in vivo calcium imaging in freely behaving mice. *Curr. Protoc. Neurosci.* 84:e51. doi: 10.1002/cpns.51

Ji, G., and Neugebauer, V. (2009). Hemispheric lateralization of pain processing by amygdala neurons. *J. Neurophysiol.* 102, 2253–2264. doi: 10.1152/jn.00166.2009

Ji, G., Zhang, W., Mahimainathan, L., Narasimhan, M., Kiritoshi, T., Fan, X., et al. (2017). 5-HT 2C receptor knockdown in the amygdala inhibits neuropathic-pain-related plasticity and behaviors. *J. Neurosci.* 37, 1378–1393. doi: 10.1523/JNEUROSCI.2468-16.2016

Kang, W., Wilson, M. A., Bender, M. A., Glorioso, J. C., and Wilson, S. P. (1998). Herpes virus-mediated preproenkephalin gene transfer to the amygdala is antinociceptive. *Brain Res.* 792, 133–135. doi: 10.1016/S0006-8993(98)00194-2

Kim, Y. S., Anderson, M., Park, K., Zheng, Q., Agarwal, A., Gong, C., et al. (2016). Coupled activation of primary sensory neurons contributes to chronic pain. *Neuron* 91, 1085–1096. doi: 10.1016/j.neuron.2016.07.044

Klioutchnikov, A., Wallace, D. J., Frosz, M. H., Zeltner, R., Sawinski, J., Pawlak, V., et al. (2020). Three-photon head-mounted microscope for imaging deep cortical layers in freely moving rats. *Nat. Methods* 17, 509–513. doi: 10.1038/s41592-020-0817-9

Levene, M. J., Dombeck, D. A., Kasischke, K. A., Molloy, R. P., and Webb, W. W. (2004). In vivo multiphoton microscopy of deep brain tissue. *J. Neurophysiol.* 91, 1908–1912. doi: 10.1152/jn.01007.2003

Li, Y., Wang, Y., Xuan, C., Li, Y., Piao, L., Li, J., et al. (2017). Role of the lateral habenula in pain-associated depression. *Front. Behav. Neurosci.* 11:31. doi: 10.3389/fnbeh.2017.00031

Liberti, W. A., Perkins, L. N., Leman, D. P., and Gardner, T. J. (2017). An open source, wireless capable miniature microscope system. *J. Neural Eng.* 14, 045001. doi: 10.1088/1741-2552/aa6806

Lopez-Alvarez, V. M., Puigdomenech, M., Navarro, X., and Cobianchi, S. (2018). Monoaminergic descending pathways contribute to modulation of neuropathic pain by increasing-intensity treadmill exercise after peripheral nerve injury. *Exp. Neurol.* 299, 42–55. doi: 10.1016/j.expneurol.2017.10.007

Manning, B., and Mayer, D. (1995b). The central nucleus of the amygdala contributes to the production of morphine antinociception in the rat tail-flick test. *J. Neurosci.* 15, 8199–8213. doi: 10.1523/JNEUROSCI.15-12-08199.1995

Manning, B. H. (1998). A lateralized deficit in morphine antinociception after unilateral inactivation of the central amygdala. *J. Neurosci.* 18, 9453–9470. doi: 10.1523/JNEUROSCI.18-22-09453.1998

Manning, B. H., and Mayer, D. J. (1995a). The central nucleus of the amygdala contributes to the production of morphine antinociception in the formalin test. *PAIN§* 63, 141–152. doi: 10.1016/0304-3959(95)00027-P

Mei, J., Riedel, N., Grittner, U., Endres, M., Banneke, S., and Emmrich, J. V. (2018). Body temperature measurement in mice during acute illness: implantable temperature transponder versus surface infrared thermometry. *Sci. Rep.* 8:3526. doi: 10.1038/s41598-018-22020-6

Miller, R. E., Kim, Y. S., Tran, P. B., Ishihara, S., Dong, X., Miller, R. J., et al. (2018). Visualization of peripheral neuron sensitization in a surgical mouse model of osteoarthritis by *in vivo* calcium imaging. *Arthritis. Rheumatol.* 70, 88–97. doi: 10.1002/art.40342

Neugebauer, V., Li, W., Bird, G. C., and Han, J. S. (2004). The amygdala and persistent pain. *Neurosci. Rev. J. Bringing Neurobiol. Neurol. Psychiatry* 10, 221–234. doi: 10.1177/1073858403261077

Ohkura, M., Sasaki, T., Sadakari, J., Gengyo-Ando, K., Kagawa-Nagamura, Y., Kobayashi, C., et al. (2012). Genetically encoded green fluorescent Ca2+ indicators with improved detectability for neuronal Ca2+ signals. *PLoS One* 7:e51286. doi: 10.1371/journal.pone.0051286

Ohta, J., Ohta, Y., Takehara, H., Noda, T., Sasagawa, K., Tokuda, T., et al. (2017). Implantable microimaging device for observing brain activities of rodents. *Proc. IEEE* 105, 158–166. doi: 10.1109/JPROC.2016.2585585

Ossipov, M. H., Dussor, G. O., and Porreca, F. (2010). Central modulation of pain. *J. Clin. Invest.* 120, 3779–3787. doi: 10.1172/JCI43766

Ozbay, B. N., Futia, G. L., Ma, M., Bright, V. M., Gopinath, J. T., Hughes, E. G., et al. (2018). Three dimensional two-photon brain imaging in freely moving mice using a miniature fiber coupled microscope with active axial-scanning. *Sci. Rep.* 8:8108. doi: 10.1038/s41598-018-26326-3

Palazzo, E., Genovese, R., Mariani, L., Siniscalco, D., Marabese, I., de Novellis, V., et al. (2004). Metabotropic glutamate receptor 5 and dorsal raphe serotonin release in inflammatory pain in rat. *Eur. J. Pharmacol.* 492, 169–176. doi: 10.1016/j.ejphar.2004.03.063

Peyron, C., Petit, J.-M., Rampon, C., Jouvet, M., and Luppi, P.-H. (1997). Forebrain afferents to the rat dorsal raphe nucleus demonstrated by retrograde and anterograde tracing methods. *Neurosci.* 82, 443–468. doi: 10.1016/S0306-4522(97)00268-6

Ren, J., Friedmann, D., Xiong, J., Liu, C. D., Ferguson, B. R., Weerakkody, T., et al. (2018). Anatomically defined and functionally distinct dorsal raphe serotonin sub-systems. *Cell* 175, 472–487e20. doi: 10.1016/j.cell.2018.07.043

Resendez, S. L., Jennings, J. H., Ung, R. L., Namboodiri, V. M. K., Zhou, Z. C., Otis, J. M., et al. (2016). Visualization of cortical, subcortical and deep brain neural circuit dynamics during naturalistic mammalian behavior with head-mounted microscopes and chronically implanted lenses. *Nat. Protoc.* 11, 566–597. doi: 10.1038/nprot.2016.021

Rosland, J. H. (1991). The formalin test in mice: the influence of ambient temperature. *Pain* 45, 211–216. doi: 10.1016/0304-3959(91)90190-9

Rosland, J. H., Tjølsen, A., Mæhle, B., and Hole, K. (1990). The formalin test in mice: effect of formalin concentration. *Pain* 42, 235–242. doi: 10.1016/0304-3959(90)91167-H

Ross, B. C. (2014). Mutual information between discrete and continuous data sets. *PLoS ONE* 9:e87357. doi: 10.1371/journal.pone.0087357

Rustami, E., Sasagawa, K., Sugie, K., Ohta, Y., Haruta, M., Noda, T., et al. (2020). Needle-type imager sensor with band-pass composite emission filter and parallel fiber-coupled laser excitation. *IEEE Trans. Circ. Syst. Regul. Pap.* 67, 1082–1091. doi: 10.1109/TCSI.2019.2959592

Sabetkasaei, M., Masoudnia, F., Khansefid, N., and Behzadi, G. (2007). Opioid receptors of the central amygdala and morphine-induced antinociception. *Iran. Biomed. J.* 6, 7580.

Scott, B. B., Thiberge, S. Y., Guo, C., Tervo, D. G. R., Brody, C. D., Karpova, A. Y., et al. (2018). Imaging cortical dynamics in GCaMP transgenic rats with a head-mounted widefield macroscope. *Neuron* 100, 1045–1058.e5. doi: 10.1016/j.neuron.2018.09.050

Sela, Y., Hoekstra, M. M., and Franken, P. (2021). Sub-minute prediction of brain temperature based on sleep–wake state in the mouse. *eLife* 10:e62073. doi: 10.7554/eLife.62073

Shibata, M., Ohkubo, T., Takahashi, H., and Inoki, R. (1989). Modified formalin test: characteristic biphasic pain response. *Pain* 38, 347–352. doi: 10.1016/0304-3959(89)90222-4

Silva, A. J. (2017). Miniaturized two-photon microscope: seeing clearer and deeper into the brain. *Light Sci. Appl.* 6:e17104. doi: 10.1038/lsa.2017.104

Spannuth, B. M., Hale, M. W., Evans, A. K., Lukkes, J. L., Campeau, S., and Lowry, C. A. (2011). Investigation of a central nucleus of the amygdala/dorsal raphe nucleus serotonergic circuit implicated in fear-potentiated startle. *Neuroscience* 179, 104–119. doi: 10.1016/j.neuroscience.2011.01.042

Stamford, J. A. (1995). Descending control of pain. *Br. J. Anaesth.* 75, 217–227. doi: 10.1093/bja/75.2.217

Sunaga, Y., Haruta, M., Takehara, H., Ohta, Y., Motoyama, M., Noda, T., et al. (2014). "Implantable CMOS imaging device with absorption filters for green fluorescence imaging," in *Proceeding of the Optical Techniques in Neurosurgery, Neurophotonics, and Optogenetics (International Society for Optics and Photonics), 89280L*, doi: 10.1117/12.2038948

Sunaga, Y., Ohta, Y., Akay, Y. M., Ohta, J., and Akay, M. (2020). Monitoring neural activities in the VTA in response to nicotine intake using a novel implantable microimaging device. *IEEE Access* 8, 68013–68020. doi: 10.1109/ACCESS.2020.2985705

Takehara, H., Katsuragi, Y., Ohta, Y., Motoyama, M., Takehara, H., Noda, T., et al. (2016). Implantable micro-optical semiconductor devices for optical theranostics in deep tissue. *Appl. Phys. Express* 9:047001. doi: 10.7567/APEX.9.047001

Timme, N. M., and Lapish, C. (2018). A tutorial for information theory in neuroscience. *eNeuro* 5:ENEURO.52–ENEURO.18. doi: 10.1523/ENEURO.0052-18.2018

Tjølsen, A., Berge, O.-G., Hunskaar, S., Rosland, J. H., and Hole, K. (1992). The formalin test: an evaluation of the method. *Pain* 51, 5–17. doi: 10.1016/0304-3959(92)90003-T

Veinante, P., Yalcin, I., and Barrot, M. (2013). The amygdala between sensation and affect: a role in pain. *J. Mol. Psychiatry* 1:9. doi: 10.1186/2049-9256-1-9

Wang, Q. P., and Nakai, Y. (1994). The dorsal raphe: an important nucleus in pain modulation. *Brain Res. Bull.* 34, 575–585. doi: 10.1016/0361-9230(94)90143-0

Wang, R. Y., and Aghajanian, G. K. (1982). Correlative firing patterns of serotonergic neurons in rat dorsal raphe nucleus. *J. Neurosci.* 2, 11–16. doi: 10.1523/JNEUROSCI.02-01-00011.1982

Wilson, T. D., Valdivia, S., Khan, A., Ahn, H.-S., Adke, A. P., Martinez Gonzalez, S., et al. (2019). Dual and opposing functions of the central amygdala in the modulation of pain. *Cell Rep.* 29, 332–346.e5. doi: 10.1016/j.celrep.2019.09.011

Woolf, C. J. (2010). What is this thing called pain? *J. Clin. Invest.* 120, 3742–3744. doi: 10.1172/JCI45178

Xu, Q., and Dong, X. (2019). Calcium imaging approaches in investigation of pain mechanism in the spinal cord. *Exp. Neurol.* 317, 129–132. doi: 10.1016/j.expneurol.2019.03.002

Yarmolenko, P. S., Moon, E. J., Landon, C., Manzoor, A., Hochman, D. W., Viglianti, B. L., et al. (2011). Thresholds for thermal damage to normal tissues: an update. *Int. J. Hyperthermia* 27, 320–343. doi: 10.3109/02656736.2010.534527

Yu, O., Parizel, N., Pain, L., Guignard, B., Eclancher, B., Mauss, Y., et al. (2007). Texture analysis of brain MRI evidences the amygdala activation by nociceptive stimuli under deep anesthesia in the propofol–formalin rat model. *Magn. Reson. Imaging* 25, 144–146. doi: 10.1016/j.mri.2006.09.022

Zhou, W., Jin, Y., Meng, Q., Zhu, X., Bai, T., Tian, Y., et al. (2019). A neural circuit for comorbid depressive symptoms in chronic pain. *Nat. Neurosci.* 22, 1649–1658. doi: 10.1038/s41593-019-0468-2

Ziv, Y., and Ghosh, K. K. (2015). Miniature microscopes for large-scale imaging of neuronal activity in freely behaving rodents. *Curr. Opin. Neurobiol.* 32, 141–147. doi: 10.1016/j.conb.2015.04.001

Conflict of Interest: The authors declare that the research was conducted in the absence of any commercial or financial relationships that could be construed as a potential conflict of interest.

The handling editor declared a past co-authorship with the authors.

frontiers in Neuroscience

REVIEW
published: 31 May 2021
doi: 10.3389/fnins.2021.667447

Energy-Efficient Integrated Circuit Solutions Toward Miniaturized Closed-Loop Neural Interface Systems

Jaeouk Cho[1†], *Geunchang Seong*[1†], *Yonghee Chang*[1] *and Chul Kim*[1,2*]

[1] *Biomedical Energy-Efficient Electronics Laboratory, Department of Bio and Brain Engineering, Korea Advanced Institute of Science and Technology, Daejeon, South Korea,* [2] *KAIST Institute for Health Science and Technology, Daejeon, South Korea*

Miniaturized implantable devices play a crucial role in neural interfaces by monitoring and modulating neural activities on the peripheral and central nervous systems. Research efforts toward a compact wireless closed-loop system stimulating the nerve automatically according to the user's condition have been maintained. These systems have several advantages over open-loop stimulation systems such as reduction in both power consumption and side effects of continuous stimulation. Furthermore, a compact and wireless device consuming low energy alleviates foreign body reactions and risk of frequent surgical operations. Unfortunately, however, the miniaturized closed-loop neural interface system induces several hardware design challenges such as neural activity recording with severe stimulation artifact, real-time stimulation artifact removal, and energy-efficient wireless power delivery. Here, we will review recent approaches toward the miniaturized closed-loop neural interface system with integrated circuit (IC) techniques.

Keywords: closed-loop system, neural interface, electroceuticals, ADC-direct front-end, miniaturization, stimulation artifact removal, wireless power transfer

OPEN ACCESS

Edited by:
Alexandre Schmid,
École Polytechnique Fédérale de Lausanne, Switzerland

Reviewed by:
Massimo Barbaro,
University of Cagliari, Italy
Yan Liu,
Shanghai Jiao Tong University, China

***Correspondence:**
Chul Kim
kimchul@kaist.ac.kr

†These authors have contributed equally to this work and share first authorship

Specialty section:
This article was submitted to Neural Technology, a section of the journal Frontiers in Neuroscience

Received: *13 February 2021*
Accepted: *13 April 2021*
Published: *31 May 2021*

Citation:
Cho J, Seong G, Chang Y and Kim C (2021) Energy-Efficient Integrated Circuit Solutions Toward Miniaturized Closed-Loop Neural Interface Systems. Front. Neurosci. 15:667447. doi: 10.3389/fnins.2021.667447

1. INTRODUCTION

As life expectancy increases, the number of patients suffering degenerative brain diseases such as Parkinson's disease (PD) and Alzheimer's disease (AD) is rapidly increasing (Dorsey et al., 2007; Reitz et al., 2011). Several approaches including medication and surgery have been taken to tackle these degenerative brain diseases, and among them, the neural stimulation technique has proved its efficacy. Deep brain stimulation (DBS) has been widely used to suppress tremors of PD patients (Benabid et al., 1987), and the neural stimulation technique is effective to alleviate the symptoms of neurological diseases such as AD, depression, and epilepsy (Cook et al., 2014; Fox et al., 2014; Poewe et al., 2017; Chang et al., 2018). Furthermore, electroceuticals that control neural circuits using electrical pulses are recently gaining increasing interest from researchers (Famm et al., 2013, Levin et al., 2019).

Neural stimulation can be performed in either non-invasive or invasive fashions. Despite the disadvantage of requiring surgical operations, the invasive method is superior to the non-invasive one in specificity (Chen and Chen, 2019). The early stage of the invasive implantable neural stimulation devices began in 1928 with the pacemaker of Mark Lidwell (Aquilina, 2006), followed

by the development of various stimulation devices, including cochlear implantation in 1964 and neurostimulator in 1967 as shown in **Figure 1A** (Simmons et al., 1964; Shealy et al., 1967).

The first generation of invasive stimulation devices have large forms due to large discrete components and battery size, and as a result, would be located outside of the body. Long wire connections between electrodes inside the body and such huge stimulation devices on the outside were required (Hyman, 1932). This led to severe restrictions on patient mobility. To enable normal life of the patients with such devices, studies of stimulation devices using IC technologies started. The use of IC technology was able to decrease overall device size by replacing large discrete components with miniaturized ICs. In 1958, the first wearable pacemaker device using IC technology was developed (Aquilina, 2006; Li et al., 2015), and in 1960, a fully implantable pacemaker with a battery was first applied to a human patient (Lillehei et al., 1960; Mallela et al., 2004). For better stimulation control and long operation time, various studies on multi-channel small form factor stimulation devices and wireless power transmission (WPT) have rapidly increased as shown in **Figure 1B**. Especially, features like closed-loop stimulation (responsive neural stimulation) measuring neural activities and performing stimulation only when necessary are attracting attention because they are able to lessen the side effects of open-loop stimulation (continuous stimulation) and further increase operation time given battery capacity (Bouthour et al., 2019). However, to enable closed-loop stimulation, neural activity recording and stimulation should be performed simultaneously, imposing serious challenges on circuit design.

In this paper, we review state-of-the-art implantable stimulation devices and requirements for implementing closed-loop electrical stimulation systems. In section 2, several neural stimulation devices using the modern technology are introduced. Various stimulation methods and considerations of stimulation designs are presented in section 3, while section 4 describes the requirements of the recording for the closed-loop system. Section 5 explains the origin of stimulation artifacts and techniques to alleviate them. Finally, various modalities for WPT to implants are reviewed in section 6, followed by conclusion in section 7.

2. MINIATURIZED IMPLANTS FOR STIMULATION

Treatment using drugs spreads throughout the entire body, which affects areas other than the desired target, and thus has a potential for side effects. On the other hand, stimulation therapy reduces side effects because the effects of stimulation spread locally (Famm et al., 2013). Stimulation therapy is also effective for people who have resistance to drug effects (Li and Cook, 2018). Therefore, neural stimulation devices have been developed for clinical and research purposes. In **Figure 2**, recent

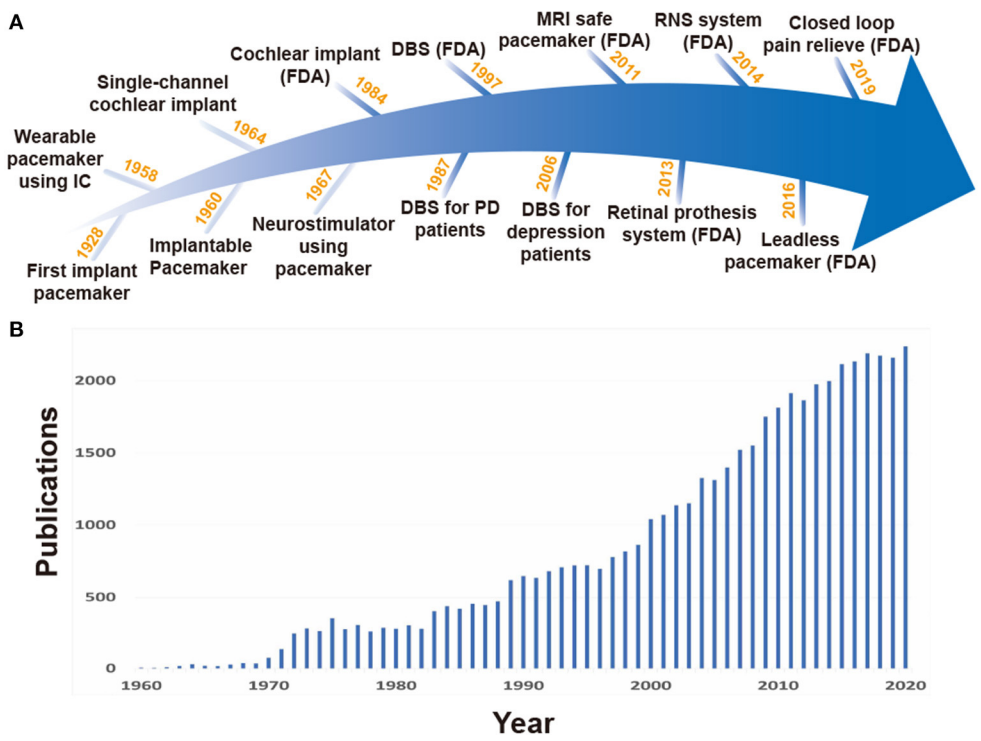

FIGURE 1 | (A) History for stimulation devices. **(B)** Rapid increase in the number of publications on implantable stimulation devices, searched at PubMed (http://www.pubmed.gov).

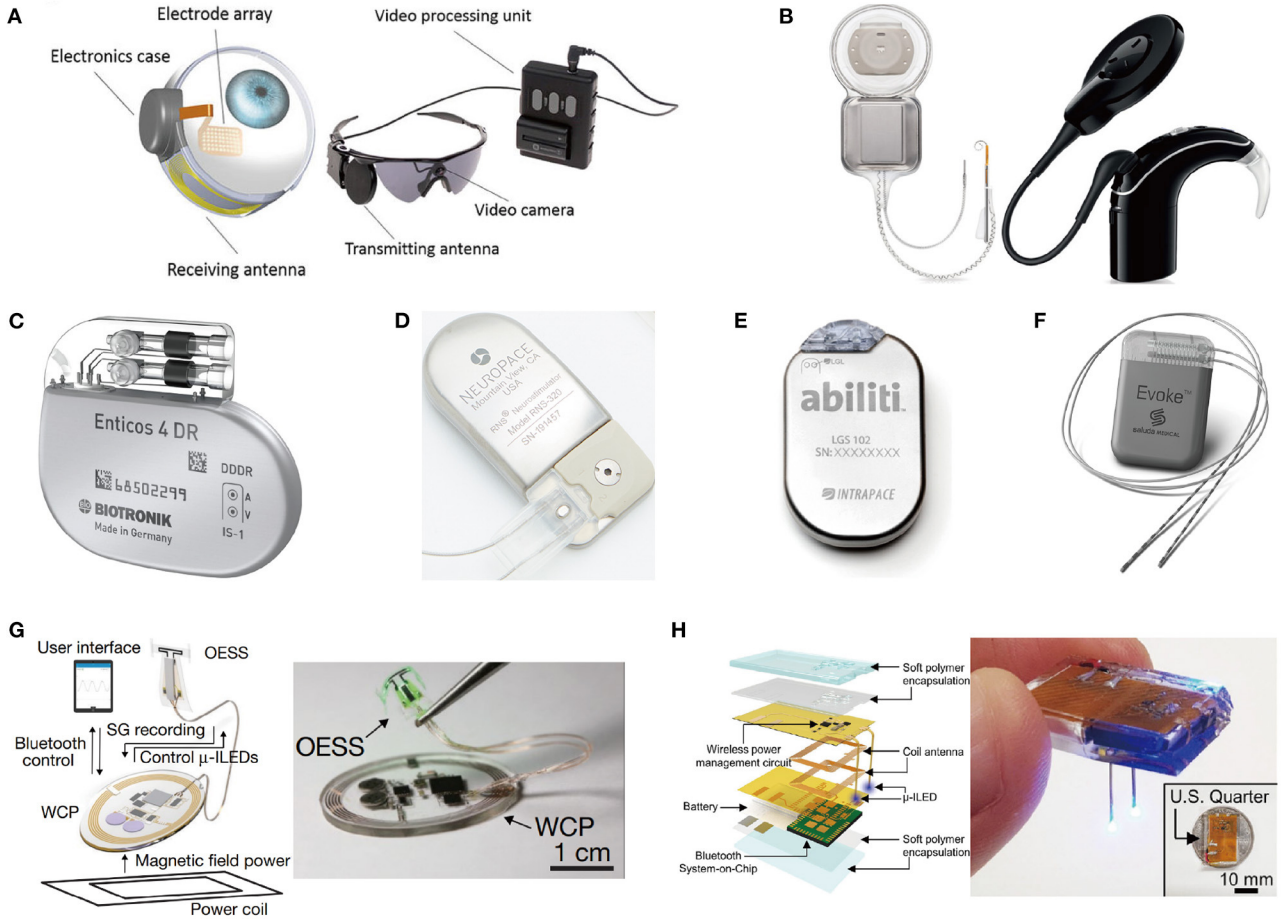

FIGURE 2 | State of the art implant neural stimulation systems: **(A)** Argus II Retinal prosthesis implant operate (Farvardin et al., 2018); **(B)** Cochlear Contour™ cochlear implant system (Parkinson et al., 2002); **(C)** Closed-loop pacemaker of Biotronik (Biotronik, aker); **(D)** Responsive neurostimulator (RNS) system of NeuroPace (Sun et al., 2008); **(E)** Abiliti closed-loop gastric stimulator (Horbach et al., 2015); **(F)** Evoke closed-loop spinal cord stimulation system (Russo et al., 2018); **(G)** Wireless optical peripheral stimulation system for bladder control (Mickle et al., 2019); **(H)** Fully chip-type implanted optical DBS system through the combination of wireless rechargeable battery and stimulator (Kim et al., 2021).

implantable stimulation devices are presented. Devices shown in **Figures 2A,B** have been developed for people whose vision or hearing cannot be treated by surgery or medication. These devices provide stimulation onto impaired parts and generate neural activity as if that impaired part operates as ordinary.

Most stimulation devices use a battery for a power source. However, regular surgery is needed to replace the battery in typically 5–10 years (Helmers et al., 2018; Sette et al., 2019). Periodic surgery increases the risk of infection as well as economic burden on patients (VanEpps and John G, 2016). The easiest solution to alleviate this periodic surgery issue is to adopt a large-capacity battery with large-sized battery. But, a large-sized battery causes protruding and reduces MRI compatibility (Belott, 2019). Besides, it may increase the size of the device, increasing the risk of tissue inflammation and cell death (McConnell et al., 2009; Karumbaiah et al., 2013). Some studies focused on rechargeable batteries using light that can be externally charged with a photovoltaic converter (Algora and Peña, 2009). Unfortunately, however, light cannot penetrate tissue deeply and charging efficiency is therefore poor, leading to rare use. Rather than focusing on battery capacity, reducing the energy consumption of stimulation devices is also a great alternative. Utilizing a closed-loop stimulation can significantly reduce power consumption compared to open-loop stimulation since power consumption of stimulation typically dominates that of the implant. **Figures 2C–F** shows commercialized closed-loop stimulation devices that perform responsive stimulation according to the patient's condition to increase the treatment effects and energy efficiency.

For certain applications, the battery size and weight of the closed-loop stimulation device are still too big and heavy to place near the stimulation site. Therefore, the stimulation device including batteries is needed to be placed apart from impaired parts. This results in long wire connections between electrodes and the device position as shown in **Figure 2F**. Implantation of this wire connection requires general anesthesia, and possibly

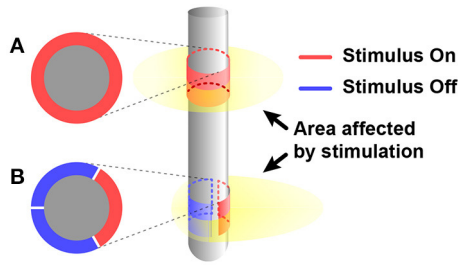

FIGURE 3 | Comparing affected area by electrical stimulus between when using **(A)** conventional ring shape electrode and **(B)** directional electrode.

causes lead dislodgement (Gul and Kayrak, 2011). Thus, research for miniaturization of implants has been actively conducted. The battery is a main culprit for the large size of implants. As such, researchers have recently been trying to use an extremely small-sized rechargeable battery or even trying to eliminate the battery as depicted in **Figures 2G,H**. This is possible since wireless power transmission via inductive or ultrasonic coupling became a main power source (Jow and Ghovanloo, 2007; Luo et al., 2013; Mickle et al., 2019).

3. STIMULATION SYSTEM CONSIDERATIONS

Stimulation systems have utilized various stimulation modalities such as electricity (Farvardin et al., 2018), light (Wells et al., 2005), temperature (Lee J. W. et al., 2018), and ultrasound (Norton, 2003; El-Bialy et al., 2011). Even in electrical stimulation, stimulation methods such as voltage-controlled stimulation (VCS), current-controlled stimulation (CCS), and switched-capacitor based stimulation (SCS) should be considered since stimulation methods affect stimulation safety and design complexity of stimulators. Furthermore, stimulation parameters such as stimulus duration, frequency, and waveform also have significant impacts on the efficacy of stimulation (Simpson and Ghovanloo, 2007; Wongsarnpigoon et al., 2010; Snellings and Grill, 2012).

3.1. Stimulation Modality

Since all nerves in a body are communicating in the form of electricity, electrical stimulation has potential to control a subject's body entirely (Famm et al., 2013). Furthermore, since injected charge can diffuse everywhere in tissue, electrical stimulation features its wide stimulation coverage. Therefore, electrical stimulation has been widely used (Sharpeshkar, 2010). Owing to its long history compared with other stimulation modalities, electrical stimulation has been trimmed and many solutions for various problems such as charge balancing, stimulation safety, and energy-efficiency of stimulation devices have already been suggested (Aquilina, 2006; Zeng et al., 2008). However, wide coverage of electrical stimulation can also serve as an inherent disadvantage on specificity. To improve the specificity of electrical stimulation, differential stimulation with two closely located electrodes is considered since it can decrease incidence area of stimulation (Ha et al., 2016). A directional electrode scheme is also a good solution for specificity. It modifies orientations of stimulus and restricts areas affected by stimulation so that affected areas are more concentrated on the target area other than non-targeted areas. Instead of the conventional ring shape electrode (**Figure 3A**), directional electrodes use unique shapes of electrodes (**Figure 3B**). The common shape of directional electrodes looks like a ring that has been divided in half or other angles and each segment is used as separate electrodes. Even though it shows promising results in simulation, there are still challenges like complicated control of each electrode to shape the electric field (Steigerwald et al., 2019).

Other modalities such as magnetic field and light are also alternatives for better specificity and selectivity. Magnetic stimulation is based on Faraday's law of induction. Alternating current (AC) flowing through a coil generates time-varying magnetic flux, which can couple to tissue at the stimulation site. Then, the flux induces an eddy current at the stimulation site, which can finally evoke neural activities. By adjusting the shape of the lead, the magnetic field is focused on a specific point, allowing for a few hundred μm spatial resolution (Ryu et al., 2020). Optical stimulation requires genetic modification of specific cell types for the formation of light-sensitive ion channels on the cell types. By modulating (excitation or inhibition) activity of the particular cell types using light via small form factor light sources such as micro-LEDs, optical stimulation can increase cell selectivity (Mickle et al., 2019; Kim et al., 2021).

3.2. Principle of the Electric Stimulation

When an electrical stimulus is injected via an electrode, the potential of the electrode, and thus the electric field around the electrode, is changed. While charge distribution is modified by the electric field, ionic flows are created across the cell membrane. Then membrane potential deviates from its original state. If the strength and duration of the stimulus are larger enough to incur membrane potential going beyond a threshold voltage for sodium influx, an action potential occurs (Plonsey and Barr, 2007). The shorter the stimulation time and the longer the distance between the electrode and the target neuron are, the larger the stimulation strength and the longer the duration are required. The minimal magnitude of the current occurring action potential for an infinite duration is called rheobase. It varies depending on cell type, maturity, and geometric condition between a cell and an electrode (Geddes and Bourland, 1985; Kinnischtzke et al., 2012). Therefore, stimulation strength and pulse duration need to be adjusted. In addition to strength and duration, there are other parameters such as stimulus waveform and frequency that affect stimulation performance (Sahin and Tie, 2007; Wongsarnpigoon et al., 2010). Typical parameter ranges in DBS for movement disorder patients are 2–4 V in amplitude, 60–450 μs in pulse width, 130–185 Hz in frequency, and biphasic square wave. Please note that these parameters should be optimized for a specific patient before application (Butson and McIntyre, 2005; Ramasubbu et al., 2018).

The optimal parameter settings are still unresolved issues. In terms of frequency, superiority between high frequency

and low frequency stimulation effects are still debated. Some studies show that higher frequencies are better to suppress epilepsy (Boëx et al., 2007; Yu et al., 2018), while another study shows the opposite (Wang et al., 2016), and a study even suggests that the two methods do not show statistically significant differences (Wongsarnpigoon et al., 2010. In terms of waveform, other than square waveform, ramp or exponential waveforms are also studied. One study shows that, with the same amount of charge, exponential decaying waveform can activate the largest number of neurons among other waveforms (Lee et al., 2014). However, other studies show different results (Merrill et al., 2005; Wongsarnpigoon et al., 2010).

Besides the efficacy, a stimulus waveform is restricted for safety. Continuous direct current (DC) injects a large net charge into tissue and thus induces electrochemical reactions that can cause permanent tissue damage. Traditionally, the known charge density limit was 30 $\mu C/cm^2$ for brain stimulation (Kuncel and Grill, 2004). However, this limit varies based on stimulation parameters such as distance between an electrode and target tissue, pulse frequency, duration, and waveform (Cogan et al., 2016).

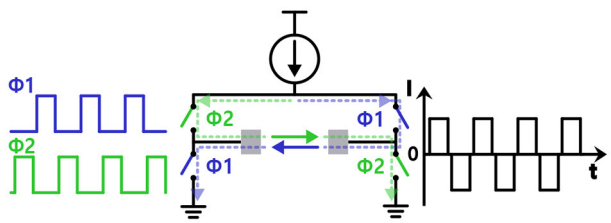

FIGURE 4 | Injecting biphasic current stimulation with a single current source using a H-bridge structure.

Mono-phasic stimulation has no mechanism to actively reverse electrochemical reactions that occurred during the stimulation period. Therefore, its charge injection limit to prevent damage is much smaller than bi-phasic stimulation. Stimulation using waveform of exponential shape shows low damage owing to its fast recovery (Merrill et al., 2005).

Since biphasic waveform is superior to charge balancing and thus is better in terms of tissue damage compared with monophasic waveform, the devices usually apply alternating current (AC) stimulus to avoid net charge flowing into tissue (Merrill et al., 2005; Lee et al., 2013). However, there can be a net current flow due to a mismatch in sourcing and sinking current. Some studies use triphasic or even higher phases stimulus to actively adjust the net charge to zero (Nam et al., 2009; Chu et al., 2013). They detect the mismatch in charge and additionally insert a small stimulus in the opposite direction. Other studies suggest using one single current source to ultimately minimize current mismatch with an H-bridge switch matrix shown in **Figure 4** (Sharpeshkar, 2010). H-bridge circuit makes it possible to supply current in both directions with a circuitry, and thereby in theory, there is no charge mismatch (Zhou et al., 2019). However, in practice, the amount of current provided by a current source always varies depending on a voltage drop across the current source.

3.3. Electrical Stimulation Methods

Figure 5A illustrates three common stimulation methods (Simpson and Ghovanloo, 2007). Voltage-controlled

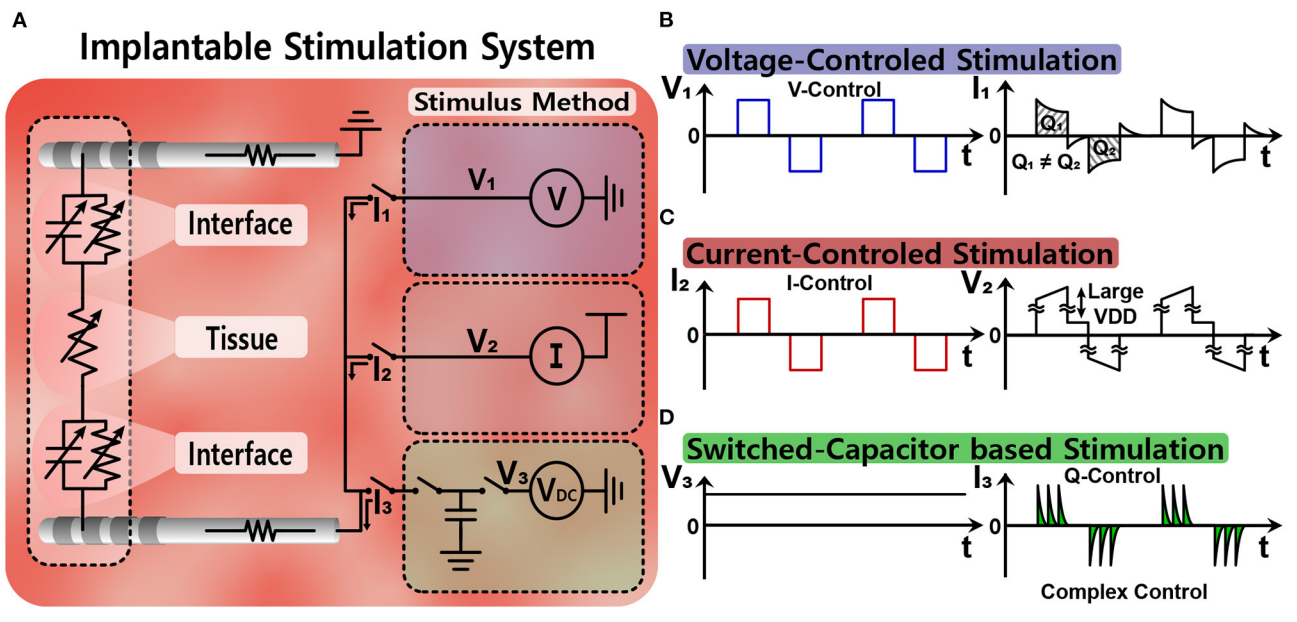

FIGURE 5 | Simple equivalent circuit models of various stimulation methods: **(A)** equivalent circuit models for stimulation, **(B)** voltage-controlled stimulation, **(C)** current-controlled stimulation, and **(D)** switched-capacitor based stimulation.

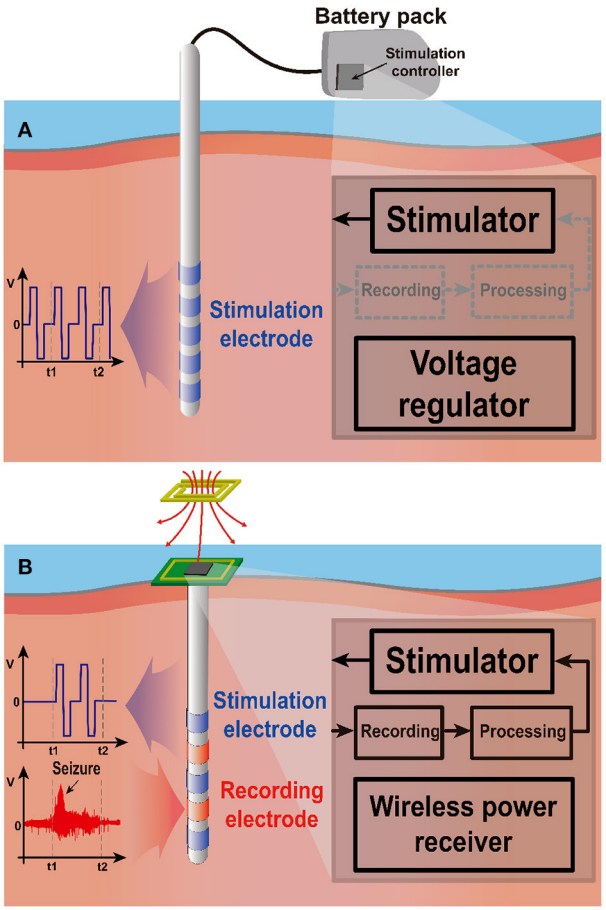

FIGURE 6 | Two stimulation schemes: open-loop and closed-loop stimulation. **(A)** The open-loop system stimulates continuously regardless of the neural activity, requiring large battery pack outside of the stimulation site due to high power consumption. **(B)** The closed-loop system stimulates only when needed, leading to low power consumption. Wireless power transmission can power the implanted stimulation system.

stimulation (VCS) in **Figure 5B** is a simple and power-efficient structure (Wong et al., 2004). However, the injected charge is likely to be unbalanced because impedance of the electrode-tissue interface varies (Vidal and Ghovanloo, 2010; Lee et al., 2014). Current-controlled stimulation (CCS) in **Figure 5C** uses current sources instead, and therefore, accurately manages the amount of current for charge balance (Ha et al., 2018). For a high impedance electrode-tissue interface, however, large supply voltage is essential for a sufficient voltage headroom of the current source and it results in high power consumption (Ghovanloo, 2006). Finally, switched-capacitor based stimulation (SCS) in **Figure 5D** uses multiple capacitors and balances the charge by charging and discharging those capacitors' energy efficiently (Ghovanloo, 2006; Lee et al., 2014). By modifying a DC voltage (V_{DC}) and the number of capacitors, the amount of charge injected can be easily adjusted even on the low supply voltage. However, circuit implementation typically becomes more complicated than other methods and its high energy-efficiency cannot be always guaranteed due to power consumption of multiple switches and control circuits. Furthermore, the SCS method has an inherent limitation in that it can generate only exponential waveform from capacitive charging and discharging. Since different waveforms would result in better outcomes depending on patients, a combination of SCS with other methods may be considered.

3.4. Open-Loop and Closed-Loop Stimulation

Figure 6A depicts the open-loop stimulation system performing continuous preset stimulation regardless of a subject's current state. This has been commonly used in DBS applications to relieve tremor symptoms of PD patients (Bouthour et al., 2019). Since open-loop stimulation systems do not include monitoring function, medical specialists should regularly check the condition of a subject and adjust stimulation parameters. Persistent stimulation can also increase the risk of side effects (Rosin et al., 2011; Vassileva et al., 2018). Moreover, it requires a large amount of power compared with closed-loop stimulation (Little et al., 2013). Thus, a large battery pack is typically required.

On the other hand, closed-loop stimulation shown in **Figure 6B** continuously monitors a subject's conditions to determine whether stimulation is needed. Therefore, the stimulation device can provide responsive neural stimulation. In this way, closed-loop stimulation minimizes side effects due to overstimulation and improves power efficiency by preventing unnecessary stimulation. A study shows that although the current consumption of closed-loop configuration is a bit higher during stimulation 230 μA compared with that of open-loop configuration 220 μA, a system in the closed-loop configuration draws only 60 μA from supply for continuous monitoring during the non-stimulation period such that it significantly increases battery operation time (Khanna et al., 2015). A different study also reports that a closed-loop stimulation system improves power consumption by 331 times compared with an open-loop case for identical seizure inhibitory performance (Salam et al., 2015). Thanks to its lower power consumption, the closed-loop system can be powered by a wireless power transfer (WPT) system. This enables further miniaturization by eliminating battery entirely.

It is important to accurately detect bio-markers that indicate a precursor symptom. If the system fails to capture bio-markers, it results in no or delayed stimulation and decreases treatment effects. Therefore, the system requires the following conditions: First, a monitoring device should record neural activities without distortion under severe stimulation artifact. Second, the artifact should be eliminated without loss of neural information so that the bio-makers can be detected correctly even during stimulation. Finally, all building blocks including monitoring parts must operate at low power due to the limited power delivery of WPT.

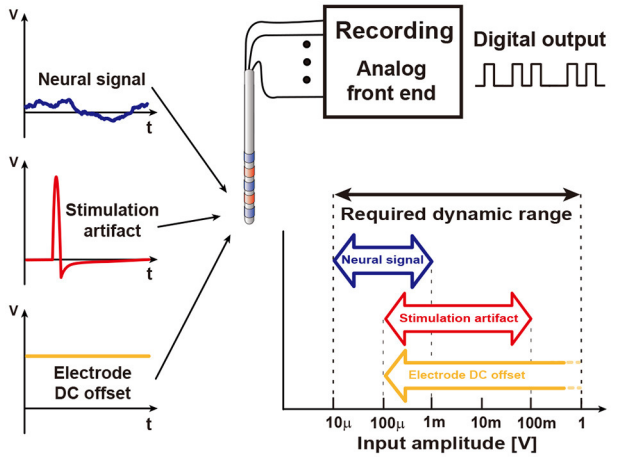

FIGURE 7 | Various inputs to a recording circuit. The amplitudes of these inputs are broad, forcing the recording circuit to have wide dynamic range.

4. DESIGN OF NEURAL RECORDING CIRCUITS FOR CLOSED-LOOP STIMULATION

Closed-loop stimulation systems require neural recording circuits to figure out appropriate timings for stimulation. The design of the recording circuits is more challenging than conventional neural recording circuits due to the existence of the stimulation artifact. In this section, proper architectures for the closed-loop neural recording are studied.

4.1. Requirements for Recording Circuits

The main purpose of recording circuits is to read analog neural signals via electrodes and to perform analog to digital conversion. **Figure 7** illustrates typical incoming signals to an analog front end (AFE). While neural signal ranges in 10 μV–1 mV, other inputs such as stimulation artifacts and electrode DC offset are much greater than neural signal. Thus, several design challenges exist for accurate measurement. Required dynamic range is >100 dB for all incoming inputs without distortion. High dynamic range typically demands high power consumption and large area of the recording circuit. To alleviate dynamic range requirement, researchers should first tackle electrode DC offset (EDO). EDO comes from a half cell potential of electrodes (Weast, 1974; Franks et al., 2005; Ashby and Jones, 2012). The half-cell potential is a function of the electrode materials (e.g., AgCl: 223 mV, Pt: 758 mV, Au: 1.68 V). Differential recording with the same electrodes (at least the material of the electrode) reduces EDO to <100 mV (Denison et al., 2007; Yazicioglu et al., 2007). In addition, EDO can be rejected by adopting an AC coupling method (Harrison and Charles, 2003; Verma et al., 2009; Ng and Xu, 2013) along with a DC servo loop (Kassiri et al., 2016; Luo et al., 2018) at the expense of low frequency components in the neural signal. Even if EDO is fully rejected, >80 dB dynamic range is required under stimulation conditions.

TABLE 1 | Recording system requirements.

Specifications	Target value
DC offset	<100 *mV*
Input range	50–100 *mV*
Input referred noise (1–200 Hz)	<10 μ*Vrms*
Dynamic range	>80 *dB*
DC input impedance	>100 *M*Ω
Power consumption	<10 μ*W/ch*

Low input referenced noise (IRN) is essential for an acceptable signal-to-noise ratio (SNR, typically ≥ 10 dB) since the amplitude of the neural signal is a couple of hundred μV. Low power AFE typically becomes the main noise source. In addition to noise, signal attenuation should be minimized by having >100 MΩ input impedance. Large input impedance also reduces DC input current, which otherwise may cause electrochemical reaction and cell damage (Harrison and Charles, 2003; Merrill et al., 2005; Jochum et al., 2009). Multi-channel recording adds a severe restriction on power consumption. **Table 1** summarizes design requirements.

4.2. Neural Recording With Amplification

Quantization noise (Q-noise) is the inherent noise of an analog-digital converter (ADC), and a major noise source of neural recording. With a high gain amplifier, a small neural signal is amplified to several hundred millivolts to overcome the quantization noise (Harrison and Charles, 2003; Gao et al., 2012; Han et al., 2013; Lee S. et al., 2018). Meanwhile, for low power implementation, supply voltage for a neural amplifier has been extremely lowered to even 0.2 V (Yaul and Chandrakasan, 2016). Due to these two conditions, high gain and low supply voltage, input ranges of the neural amplifiers are severely limited because input signal of the amplifier cannot be greater than a supply voltage divided by the amplifier's voltage gain. This is why this architecture cannot be considered for neural recording in closed-loop neural interfaces, which have large stimulation artifacts as shown in **Figure 8A**.

As an alternative, a structure using a lower gain amplifier and a high-resolution ADC in **Figure 8B** has recently been utilized (Chandrakumar and Marković, 2017, 2018). The gain of the amplifiers is lower than 10. As such, the input range of the neural recording is improved even with a low supply voltage. However, it still has a potential for signal saturation when a large stimulation artifact exists. Furthermore, the benefits from a low gain amplifier are offset by disadvantages such as the area and power consumption for the amplifier.

4.3. ADC-Direct Front-End

Figure 8C shows an ADC-direct front-end structure. It directly converts analog input to digital output without preamplification, leading to an area and power saving effect. Since there is no amplification, the quantization noise (Q-noise) of ADC is directly compared with the small neural signal at input, and thus it is essential for the Q-noise of ADC to be smaller than neural

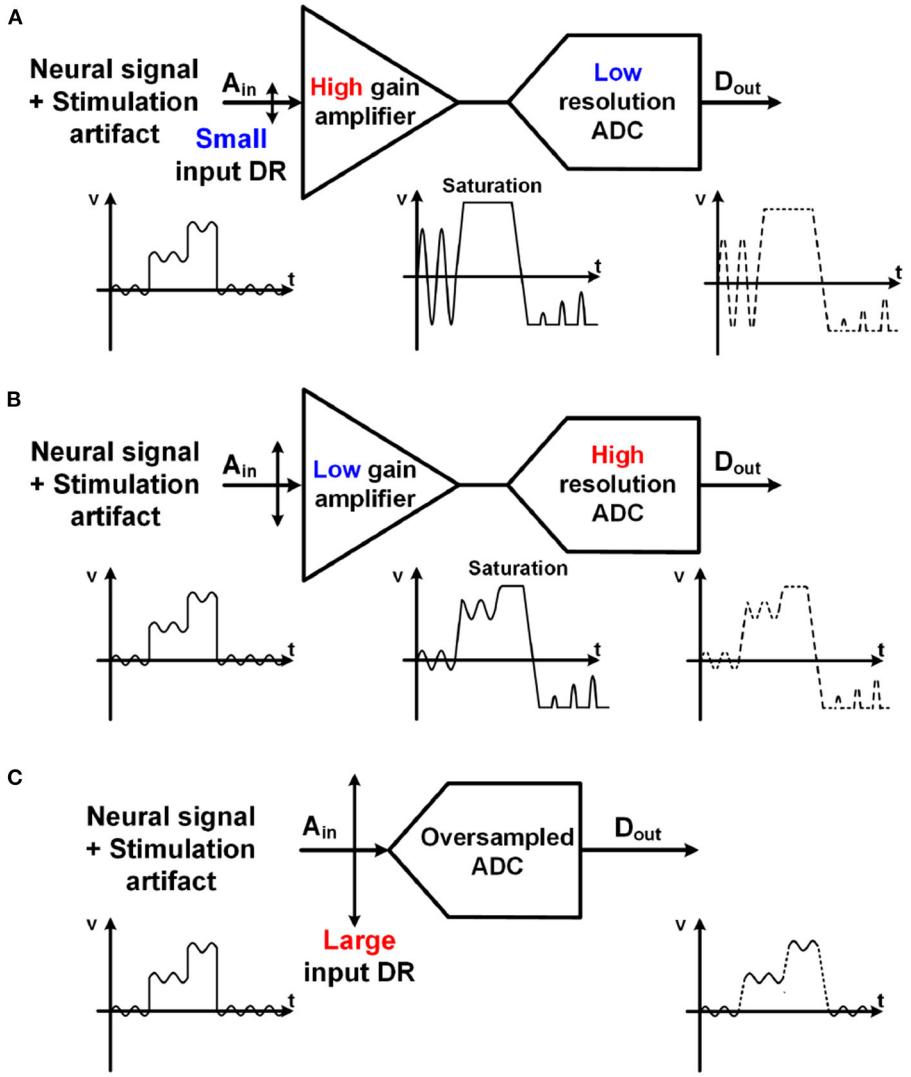

FIGURE 8 | Comparison with various structures for neural recording with stimulation artifact. Both **(A)** a high gain amplifier with a lower resolution ADC and **(B)** a lower gain amplifier with a higher resolution ADC have potential for saturation due to large stimulation artifact. **(C)** Unity gain ADC-direct front-end structure using an oversampling ADC maximizes its input range.

signal. Although a conventional Nyquist sampling rate ADC including a successive-approximation (SAR) ADC may achieve this low Q-noise, an oversampling delta-sigma ADC ($\Delta\Sigma$ADC) is much more energy-efficient to obtain low in-band Q-noise owing to its noise-shaping characteristic. This is why most recent neural recording systems for closed-loop neural interfaces are implemented with noise-shaped delta-sigma ADCs. The oversampling technique utilizes a higher sampling frequency, f_s, than needed and thus reduces the Q-noise in-band because the Q-noise is uniformly spread out over $\pm f_s/2$. To further decrease the noise, loop filters are added in $\Delta\Sigma$ADC. As such, in-band Q-noise is decreased by 3 dB, 9 dB, and 15 dB for every doubling of sampling frequency when zero-order, first-order, and second-order loop filters (integrators) are utilized, respectively. A block diagram for the first-order $\Delta\Sigma$ADC with its spectrum of signal and Q-noise are shown in **Figure 9A**. Neural signal has $1/f^N$ ($2 \leq N \leq 3$) (Reza Pazhouhandeh et al., 2020) low-pass profile in spectrum while in-band Q-noise is minimized owing to noise shaping (Schreier et al., 2005). In addition to low Q-noise, continuous $\Delta\Sigma$ADC includes an inherent anti-aliasing filter. This is because an integrator in $\Delta\Sigma$ADC performs low-pass filtering before sampling (Pavan et al., 2008).

However, a $\Delta\Sigma$ADC is able to be further improved in the input of dynamic range and power consumption by adding an additional integration function in the feedback path as shown in **Figure 9B**. The integrator in the feedback path accurately predicts input signal, A_{in}. Delta function (subtraction) between A_{in} and an estimate from the integrator enable consecutive difference processing. This resolves a famous problem of conventional $\Delta\Sigma$ADC, limit cycle, and minimizes the input

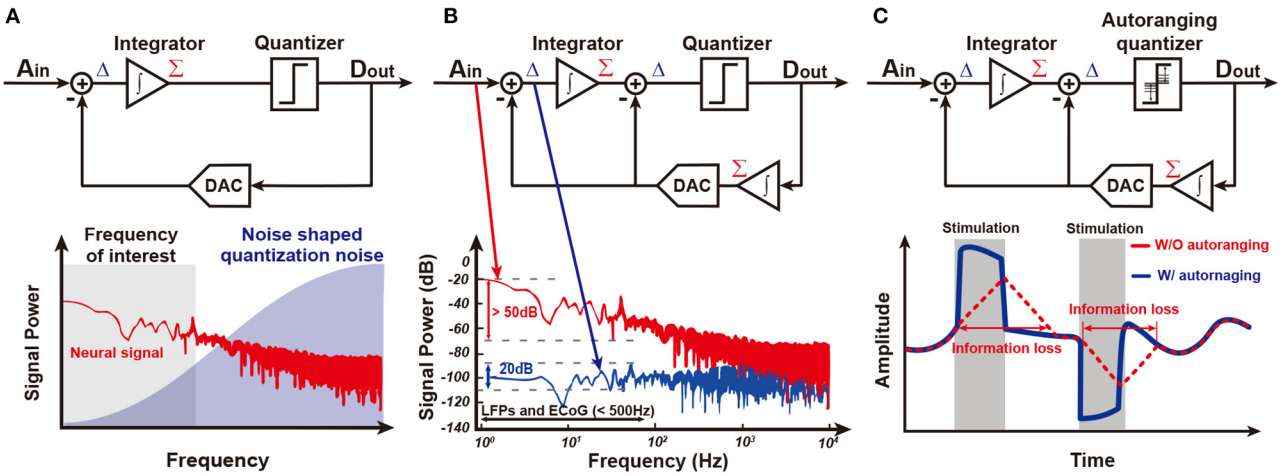

FIGURE 9 | Several $\Delta\Sigma$ structure. **(A)** $\Delta\Sigma$ shapes quantization noise into high frequency. **(B)** An integrator in feedback path of $\Delta\Sigma$ADC reduces the required input integrator's dynamic range. This structure is called $\Delta^2\Sigma$ADC (Kassiri et al., 2017). **(C)** An auto-ranging quantizer in $\Delta^2\Sigma$ makes it possible to follow sudden changes in the input signal (Kim et al., 2018).

signal to the integrator in main path by around 30 dB (Kassiri et al., 2017; Bang et al., 2018; Kim et al., 2018; Reza Pazhouhandeh et al., 2020). Furthermore, the integrator in the main path can be implemented by a low-power open-loop Gm-C filter owing to its small input, allowing for drastic power reduction. This structure is named $\Delta^2\Sigma$ADC.

Although the integrator in the feedback path presents many great advantages, it slows down the speed of prediction. Since updates from the quantizer are averaged by the integrator, prediction speed is limited. This is a serious problem in closed-loop stimulation since the stimulation artifact is large and there is steep variation in amplitude. Actually, utilizing history of the quantizer outputs, ADC detects whether it is slower than input by itself (Kim et al., 2018). If several consecutive outputs of the quantizer, D_{out}, have an equal sign, an ADC needs to tract its input faster, leading to an increase in the update size in the prediction. On the other hand, if consecutive output of the quantizer is alternating, this ADC reaches its input and needs to decrease the update size. This autoranging algorithm improves prediction speed up to 30 times in bandwidth and results in faster than 200 mV/ms tracking speed as shown in **Figure 9C**.

While complementary metal-oxide-semiconductor (CMOS) technology scaling improves the area, speed, and power efficiency of circuitry, the design difficulty of analog circuits becomes more challenging due to the lowered supply voltage of the scaled devices. Thus, rather than using voltage, time or frequency can be a more useful source with modern CMOS devices. A voltage-controlled oscillator (VCO) based ADC that converts input voltage signal to the frequency domain by VCO and processes the converted signal rather than the voltage domain is one of the great examples (Muller et al., 2012, 2015; Huang and Mercier, 2020). Similar to DSM ADC, a VCO-based ADC structure is also implemented as the ADC-Direct front-end structure.

Table 2 shows a comparison of state-of-the-art neural recording AFEs. It is clearly visible that a conventional large gain amplifier with a separate ADC structure has limited input range such that it is difficult to be applied to closed-loop systems due to huge stimulation artifacts. Furthermore, ADC-direct front-ends have better input referred noise performance while consuming lower power and taking up a smaller area.

5. REAL-TIME STIMULATION ARTIFACT REMOVAL

A stimulation artifact typically has a large amplitude and may overlap with the neural signal in spectrum, contaminating neural recording (Zhou et al., 2018). Thus, the stimulation artifact distorts the results of signal processing with contaminated data and leads to the failure of stimulation to be triggered on time (Hartmann et al., 2014). Therefore, real-time stimulation artifact removal is essential for closed-loop stimulation systems.

5.1. Stimulation On-Off Timing Decision

To determine the stimulation on-off timing, a recorded signal is processed as shown in **Figure 10**. First, the recorded signal goes through a preprocessing step. In the input data, there are not only target signals but also additional unwanted signals such as power noise, baseline drift, stimulation artifacts, and non-targeted biological signals included. To remove undesired data, conventional spectral filters including notch filter, high pass filter, or bandpass filter are used. Not only do the recorded data differ in the amplitude of the signal for each patient, but a large amount of data makes it difficult to process the signal. To solve these problems, the input data is normalized by amplitude scaling and the size of the data is reduced by downsampling.

Then, features of the preprocessed data are extracted by using several methods such as principal components analysis (PCA), fast Fourier transform (FFT), and wavelet transform (WT). PCA is used to find orthogonal vectors that best represent the

TABLE 2 | Metric comparison with state-of-the-art.

	JSSC'16 Kassiri	JSSC'18 Chan	JSSC'17 Kassiri	JSSC'18 Kim	JSSC'20 Reza	JSSC'20 Huang
Structure	High gain + ADC	Low gain + ADC	$\Delta^2\sum$ ADC-direct	$\Delta^2\sum$ ADC-direct	$\Delta^2\sum$ ADC-direct	VCO based ADC-direct
Input range (mV_{pp})	4	200	Rail-to-rail	260	1,000	250
IRN ($nV/\sqrt{Hz}$)	133	127	101	44	71	53
Zin (MΩ)	Gate input	1520	1	26	1,465	4
SNDR (dB)	44.5	86	72.2	66.17	69.8	89.2
Power (μW/ch)	9.1	7.3	0.63	0.8	1.7	3.2
Area (mm^2/ch)	0.09	0.113	0.013	0.024	0.023	0.08
NEF	6.9	15.3	2.86	1.81	2.86	4.06
FOMs*	132	160	161	154	155	171

**FOMs: SNDR+ 10log(BW/P).*

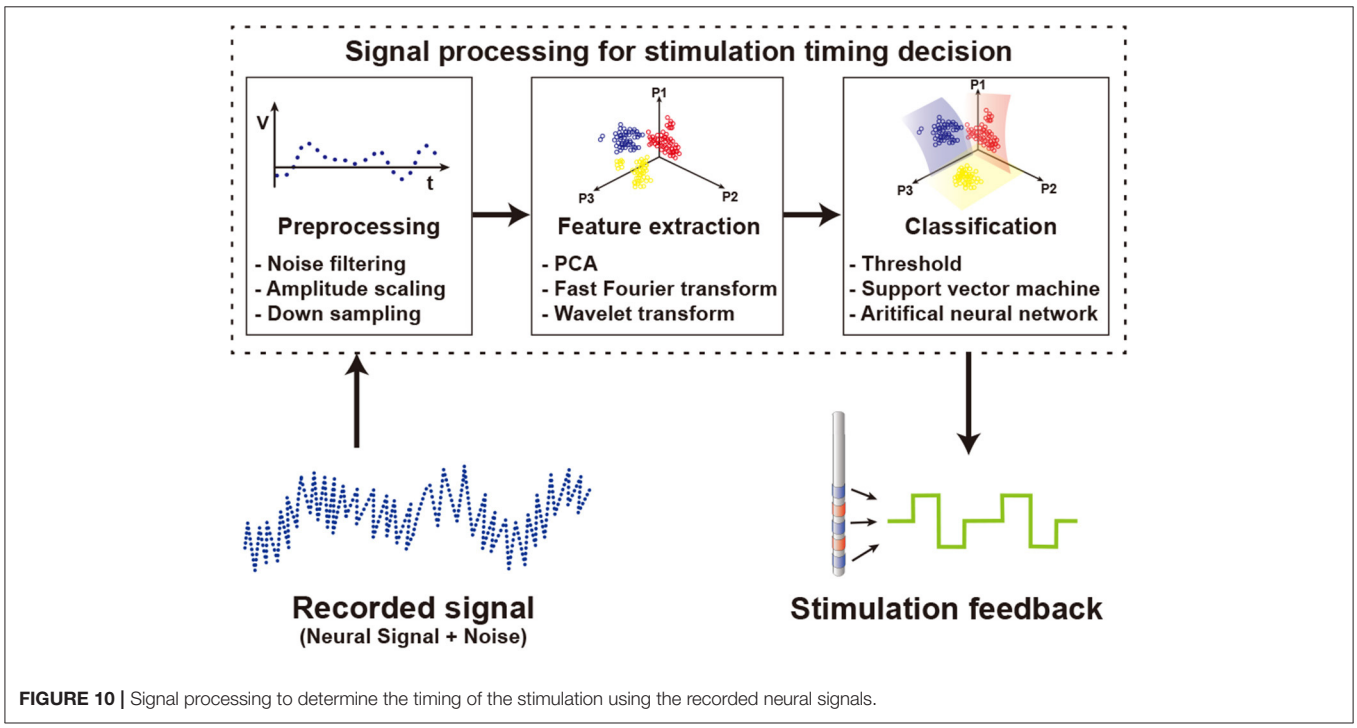

FIGURE 10 | Signal processing to determine the timing of the stimulation using the recorded neural signals.

variance of input data. By selecting the top several principal component vectors and projecting data onto them, the number of features is highly reduced while minimizing the loss of variance of data. An FFT scheme extracts features of data in frequency domain. Since specific spectral band power varies based on brain activities, spectral power information is a commonly used feature in biosignal processing. WT uses a special set of functions called wavelet to decompose signals. While FFT produces features having only frequency domain information, WT produces features including both time and frequency domain information. Generally, a feature set that combines information from various domains shows better performance than using multiple features from a single domain (Mormann et al., 2003; Kuhlmann et al., 2010). At the first glance, an increase in the number of features brings more information, as such classification performance may be better. Unfortunately, however, this is not always the case. A large number of features for classification increase computational loads and typically decrease overall performance. Therefore, it is important to find the most informative feature set. In the case of neural signals, the characteristics of signals vary from patient to patient. Therefore, selecting features optimized for an individual patient shows better performance than using an identical feature set regardless of the patient (Gadhoumi et al., 2013). To find optimal feature sets supporting patient variation and thus ultimately improve seizure classification performance, a study extracts features from temporal, spectral, and spatial domains (Yoo et al., 2013). Finally, the classification process determines whether to stimulate based on the selected feature

set. Threshold based classifiers separate classes if the feature value crosses the threshold (Abdelhalim et al., 2013; Zhou et al., 2019). Since each patient shows unique signal patterns for similar symptoms (Bin Altaf and Yoo, 2016), it is difficult to find a universal optimal threshold value. Therefore, studies adjust and optimize the threshold value for each individual patient after several trials. Other classifiers use machine learning schemes for classification. The support vector machine (SVM), one of the most popular techniques for classification, is a method that maximizes the distance between decision boundary and data in the vicinity of the boundary. Depending on the type of kernel used in the SVM, linear SVM or nonlinear SVM is implemented (Yoo et al., 2013; Bin Altaf and Yoo, 2016). Other than SVM, using artificial neural networks (ANN) as a classifier is also on the rise (Fang et al., 2019; Sayeed et al., 2019). ANN performs classification by connecting nodes at different layers with random weights and optimizing these weights. Though this optimization process can extract optimized features for each patient from raw data without previous feature extraction and selection processes (Alom et al., 2019). However, classifiers with complex algorithms requiring higher computational loads do not always guarantee better results (Kassiri et al., 2017). From a hardware perspective, more complex algorithms require more power and more area. Therefore, based on the purpose of use, an appropriate classifier should be chosen. A study comparing various classifiers for seizure detection shows that area, dynamic power consumption, and signal processing latency are highly different between algorithms. Simple algorithms such as logarithm regression or naive Bayes consume a smaller area and less power than complex algorithms such as SVM or ANN (Page et al., 2014).

5.2. Origin of Stimulation Artifact

Stimulation artifacts can be divided into direct stimulation artifact and residual stimulation artifact based on their cause (Zhou et al., 2018). A direct stimulation artifact is caused by stimulation pulses directly reaching neural recording front-ends. Thus, it is large in amplitude and lasts for the stimulation duration. The waveform of the direct stimulation artifact is not the same as that of the stimulation because there is non-linear parasitic capacitance and resistance between a stimulation electrode and a recording electrode. This makes it difficult to predict stimulation artifacts accurately at neural recording front-ends.

A residual stimulation artifact is created by a residual charge left in double-layer capacitance induced by the stimulation electrode after stimulation. This residual charge contaminates tissue potentials in the vicinity of the stimulation electrode, and thus it is considered as "an artifact." The main causes of this residual charge are (1) current mismatching between the sourcing and sinking current of the stimulator, and (2) electrical characteristic non-linearity of the stimulation electrode during stimulation. The decaying time constant of this residual charge is directly related to the double-layer capacitance and tissue resistance. The typical amplitude of a residual stimulation artifact is a couple of millivolts (Zhou et al., 2018), which is still larger than a neural signal. Therefore, depending on electrode design, a residual stimulation artifact can be long-lasting, and become more serious than a direct stimulation artifact (Hashimoto et al., 2002; Chu et al., 2013).

5.3. Stimulation Artifact Removal Methods

Stimulation artifact removal is important for implementing closed-loop stimulation systems. The first step to reduce a stimulation artifact is to utilize differential recording for a direct stimulation artifact and to adopt charge balancing techniques for a residual stimulation artifact. However, these schemes cannot remove a stimulation artifact entirely. Therefore, additional processes for stimulation artifact removal have been studied as depicted in **Figure 11**.

Spectral filtering shown in **Figure 11A** may be the first method that comes to mind to remove the stimulation artifact. Direct stimulation artifact typically has a strong tone in spectrum. Therefore, spectral filtering may work well (Jech et al., 2006). However, stimulation frequency is an important parameter for stimulation efficacy and as such, it should be adjusted regularly. Furthermore, stimulation and a neural signal may overlap in spectrum with each other (Zhou et al., 2018). In addition, it is difficult to avoid spectral distortion.

Figure 11B shows a blanking and interpolation scheme. Since the stimulation timing is known, it is relatively easy to reject or remove direct stimulation artifact by halting data recording during stimulation or deleting data that contains stimulation artifact (Hartmann et al., 2014; Li et al., 2019). Then, data prediction should be accompanied. Various techniques such as linear (Zhou et al., 2019), cubic spline (Waddell et al., 2009), and gaussian (Caldwell et al., 2020) interpolation are utilized. Depending on the algorithm's complexity, the real-time operation is possible (Zhou et al., 2019). However, interpolation inherently produces artificial data and has a chance to miss abrupt events that may happen during the stimulation period. Therefore, this method is not suitable for stimulation devices that use high-frequency stimulation or have long and unpredictable duration artifacts (Cheng et al., 2017).

Some studies make a template of a stimulation artifact and subtract it in the recording process as shown in **Figure 11C**. The stimulation artifact template is obtained by using various methods such as adaptive filter (Mouthaan et al., 2016), averaging signals (Qian et al., 2016), curve fitting (Drebitz et al., 2020), and equivalent circuit modeling (Trebaul et al., 2016). The earned stimulation artifact template is then applied to the input of an AFE (Wang et al., 2020) or to digitized signal for subtraction at digital signal processing module (Limnuson et al., 2015). Subtraction at the input of an AFE relieves the dynamic range requirement of the AFE at the expense of input impedance and noise performance. Since the template copies only the stimulation artifact, the original neural signal remains after subtraction. However, this scheme heavily depends on the accuracy of the stimulation artifact estimation.

Component decomposition techniques such as principal component analysis (Chang et al., 2019), independent component analysis (Lu et al., 2012), and ensemble empirical mode decomposition (Zeng et al., 2015) to separate stimulation

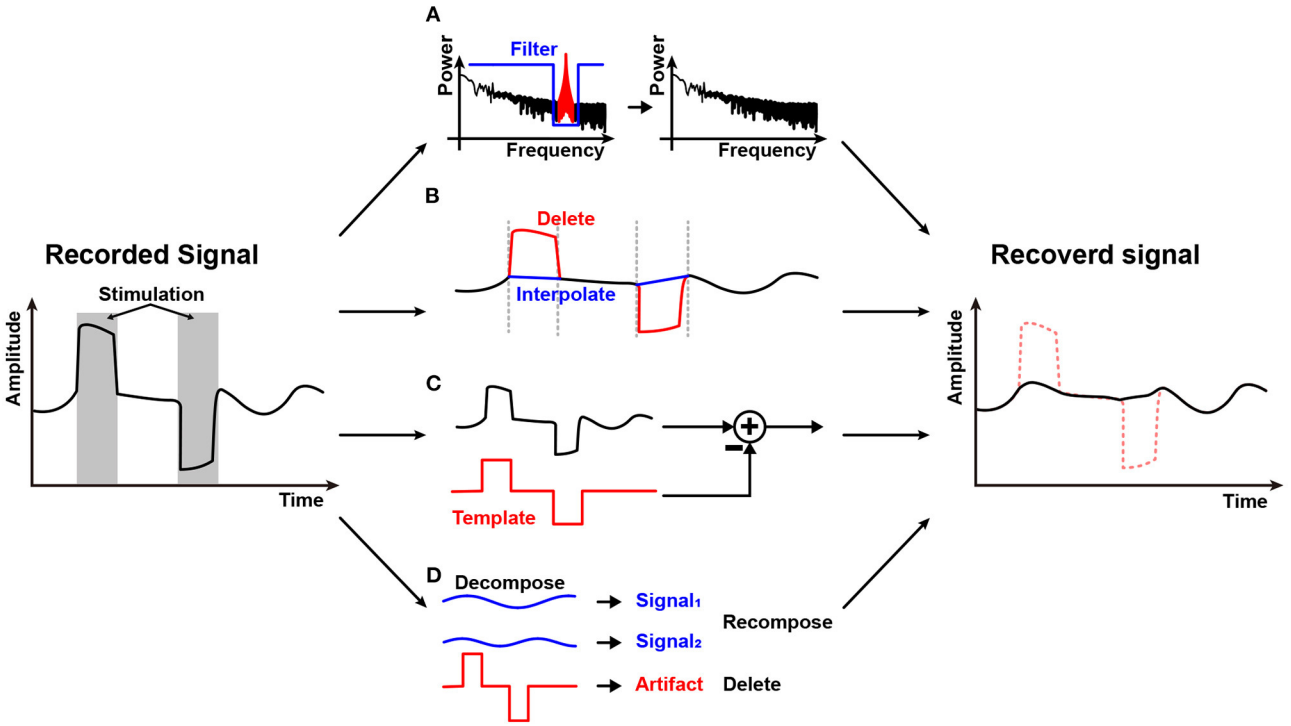

FIGURE 11 | Stimulation artifact removal methods: **(A)** Spectral filtering; **(B)** Blanking and interpolation; **(C)** Template-based subtraction; and **(D)** Components decomposition.

artifact components from contaminated neural signals are illustrated in **Figure 11D**. Since decomposition requires heavy computational resources, this scheme is usually conducted in the digital domain, and in a non-realtime fashion with a high-performance digital processor. This technique is possibly applied together with the aforementioned techniques such as a template method (Wang et al., 2020).

5.4. Avoidance of Stimulation Artifact

Rather than removing the stimulation artifact, as an alternative, schemes for stimulation artifact avoidance are also studied by using different stimulation modalities such as magnetic field or light (Mickle et al., 2019; Ryu et al., 2020). It seems to be obvious that non-electrical stimulation will not generate any electrical artifacts. Unfortunately, however, this is not always true. Magnetic stimulation is fundamentally an electrical stimulation since this relies on induced current by electromotive force. Therefore, it could distort recorded electric signals. Optical stimulation also possibly induces electrical stimulation artifact when photons hit any obstacles due to photovoltaic effect or photoelectrochemical effect (Liu et al., 2018; Kim et al., 2020). In addition, this requires genetic modification for light-sensitivity ion channel expression on target cells, imposing hurdles upon its application to human subjects.

6. WIRELESS POWER TRANSFER FOR MINIATURIZED IMPLANTABLE DEVICES

Reducing implantable devices' volume is essential to prevent inflammation, glial scar, and even cell death inside a human body (Anderson, 1988). To diminish the volume of batteries that account for a significant portion of the implantable device is the most effective way to reduce the device's volume. Moreover, eliminating batteries prevents frequent surgeries for battery replacement (Bock et al., 2012). Since the wireless power transfer (WPT) technique enables continuous power delivery to implantable devices wirelessly, miniaturized implantable devices without batteries become feasible. However, the amount of power delivery by WPT schemes is typically lower than that by battery. Therefore, many implantable devices have been operated by batteries at the expense of large volume. By the fact that closed-loop neural interface systems consume lower power owing to on-demand stimulation compared to open-loop systems, researchers have recently been putting significant efforts into employing WPT schemes for power delivery to the implantable closed-loop systems, especially for a closed-loop deep brain and vagus nerve stimulation (Rhew et al., 2014; Ranjandish and Schmid, 2018). As such, WPT schemes become crucial for implantable closed-loop systems.

Inductive WPT based on Faraday's law of induction is the most historical and steady model among various WPTs. It requires power transmitting (TX) and receiving (RX) coils

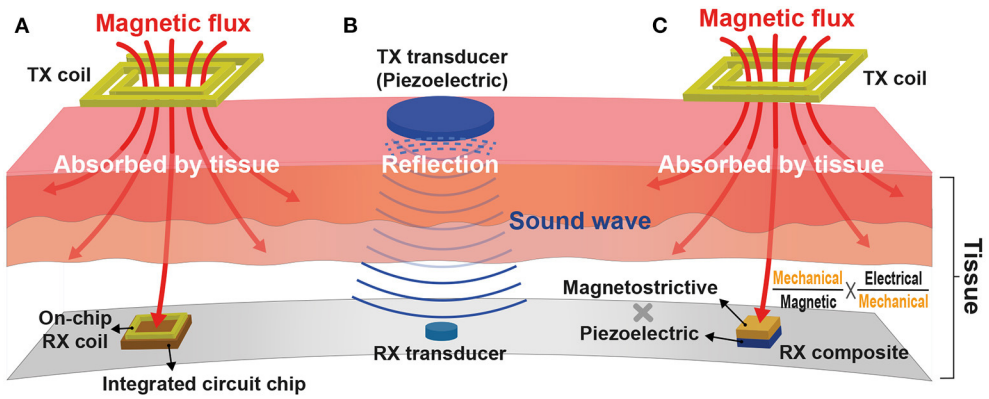

FIGURE 12 | Wireless power transfer (WPT) modalities for a miniaturized implant: **(A)** Inductive WPT using an on-chip power receiving coil; **(B)** Ultrasonic WPT having a short wavelength; and **(C)** Magnetoelectric WPT integrating both inductive and ultrasound WPTs.

inductively coupled via induced magnetic flux at the TX coil. The RX coil is typically implemented on a printed circuit board (PCB) for the coil's great quality factor at the expense of implant size and wire connection between the RX coil and a voltage rectifier and a regulator. To achieve ultimate miniaturization of an implant, this RX coil is recently integrated by on-chip, eliminating all off-chip components as shown in **Figure 12A** (Kim et al., 2016, 2017a,b; Park et al., 2017; Rahmani and Babakhani, 2018a,b). However, the amount of power delivery is directly proportional to RX coil size, and as such, the on-chip RX coil limits the overall amount of power delivered to the implant ($\leq$500μW).

Adopting a higher carrier frequency ($\geq$100 MHz) for power delivery compensates for the reduced amount of power delivery by increasing the magnetic flux variation rate (Kim et al., 2013). Furthermore, a higher carrier frequency allows for a shorter wavelength that provides high spatial-resolution and thus improved WPT energy efficiency (Poon et al., 2010). Unfortunately, however, the tissue absorption rate also rises with the increasing carrier frequency and induces serious safety issues. Considering the fact that sound waves have hundreds of thousands of times shorter wavelengths compared to electromagnetic waves, ultrasonic WPT in **Figure 12B** would be a perfect alternative against inductive WPT. It consists of two miniaturized transducers that convert sound waves to electricity and vice versa (Charthad et al., 2015). Recent studies successfully demonstrate that mm-sized implantable devices using ultrasonic WPT employed at peripheral nerves are able to receive sufficient power ($\leq$3mW) at a few centimeters implant depth ($\leq$10.5cm) (Charthad et al., 2018; Johnson et al., 2018). However, a high acoustic impedance difference between air, bone, and tissue causes sound wave reflection, limiting ultrasonic WPT applications.

Figure 12C illustrates a newly emerged modality, magnetoelectric (ME) WPT. ME WPT consists of magnetostrictive (MS) and piezoelectric (PE) composite. MS converts magnetic to mechanical, and PE converts mechanical to electrical and vice versa (Nan, 1994; Fiebig, 2005). Such a set of conversions resolves the reflection issue of ultrasound and alleviates the miniaturization difficulty of inductive (Singer et al., 2020; Yu et al., 2020b). Nevertheless, ME composite is hard to fabricate, and the composite's low energy conversion ratio is a hurdle to overcome (Truong, 2020; Yu et al., 2020a).

The detailed performance and specification of the state-of-the-art WPTs are compared in **Table 3**. It is visible that ultrasound schemes are superior to inductive coupling schemes from a distance, thanks to their lower carrier frequency. Besides, considering the delivered power and distance shown in the table, it is possible to power an implantable closed-loop system consuming lower than a couple of hundred μW (Khanna et al., 2015; Salam et al., 2015). Please note that power efficiency is related to safety issues. Low power efficiency results in high power loss, possibly on tissues, leading to heating problems. If a 1 mm^3 implant in the brain consumes more than 4 mW, greater than 1 °C temperature increases (Kreith and Black, 1980; Giering et al., 1995; Gosalia et al., 2004; Kim et al., 2007).

7. CONCLUSION

In this article, current state-of-the-art implantable stimulation devices were reviewed. The advantages and disadvantages of various stimulation modalities, methods, parameters, and control schemes were also studied. Based on these considerations, we highlighted the necessity of closed-loop, miniaturized, low-power designs of implantable devices for the subject's safety and devices' performance. Several crucial requirements for neural recording to implement a closed-loop system include high input dynamic range, fast-tracking, low input-referred noise, high input impedance, and low-power consumption. $\Delta\Sigma$ADC direct front-end and VCO-based ADC direct front-end structures are good candidates for those requirements. Problems and causes of stimulation artifact were explained and then several techniques to remove stimulation artifact such as spectral filtering, blanking and interpolation, template-based subtraction, and components decomposition were presented. Finally, representative WPT schemes for

TABLE 3 | Comparison table of the state of the arts WPTs.

	JSSC'17 Kim	IMS'18 Rahmani	JSSC'15 Charthad	CICC'18 Johnson	TBioCAS'20 Yu
Modality	On-chip inductive	On-chip inductive	Ultrasound	Ultrasound	Magnetoelectric
Delivered Power (mW)	0.7	1.2	0.1	0.35	0.09
Power efficiency (%)	0.2	0.1	NR*	NR*	0.064
Link distance (mm)	10	10	30	21.5	30
Volume (mm^3)	2.25	0.64	NR*	6.5	8.2
Frequency (MHz)	144	434	1	2	0.25
Intervening medium	Air	Air	Muscle	Muscle	PBS

NR, Not reported.

eliminating a battery from an implantable device and thus realizing extreme miniaturization were reviewed. In today's era of increasing demand for implantable neuromodulation devices including electroceuticals, a closed-loop neural stimulation device that receives power wirelessly and performs real-time stimulation artifact removal will be an important milestone toward miniaturized neural interfaces.

AUTHOR CONTRIBUTIONS

JC, GS, and CK: paper conception and design and drafting of the manuscript and final approval of the manuscript. JC and CK: stimulation applications and neural recording circuits. GS and CK: stimulation system consideration and stimulation artifact removal. YC and CK: wireless power transfer for miniaturized implantable devices. All authors contributed to the article and approved the submitted version.

FUNDING

This work has been supported by the National Research Foundation of Korea (NRF) grant funded by the Korea government (MSIT) (No.2020R1C1C1009878) and has been supported by the Technology Innovation Program (20012464) funded by the Ministry of Trade, Industry & Energy (MOTIE, Korea).

REFERENCES

Abdelhalim, K., Jafari, H. M., Kokarovtseva, L., Velazquez, J. L. P., and Genov, R. (2013). 64-channel UWB wireless neural vector analyzer SOC with a closed-loop phase synchrony-triggered neurostimulator. *IEEE J. Solid State Circ.* 48, 2494–2510. doi: 10.1109/JSSC.2013.2272952

Algora, C., and Pe na, R. (2009). Recharging the battery of implantable biomedical devices by light. *Artif. Organs* 33, 855–860. doi: 10.1111/j.1525-1594.2009.00803.x

Alom, M. Z., Taha, T. M., Yakopcic, C., Westberg, S., Sidike, P., Nasrin, M. S., et al. (2019). A state-of-the-art survey on deep learning theory and architectures. *Electronics* 8:292. doi: 10.3390/electronics8030292

Anderson, J. M. (1988). Inflammatory response to implants. *ASAIO Trans.* 34, 101–107. doi: 10.1097/00002480-198804000-00005

Aquilina, O. (2006). A brief history of cardiac pacing. *Images Paediatr Cardiol.* 8:17.

Ashby, M. F., and Jones, D. R. (2012). *Engineering Materials 1: An Introduction to Properties, Applications and Design, Vol. 1.* Amsterdam: Elsevier.

Bang, J., Jeon, H., Je, M., and Cho, G. (2018). "6.5μW 92.3dB-DR biopotential-recording front-end with 360MVPP linear input range," in *2018 IEEE Symposium on VLSI Circuits* (Honolulu, HI: IEEE), 239–240. doi: 10.1109/VLSIC.2018.8502264

Belott, P. H. (2019). Cosmetic aspects of device implantation. *Heart Rhythm* 16, 308–311. doi: 10.1016/j.hrthm.2018.08.018

Benabid, A.-L., Pollak, P., Louveau, A., Henry, S., and De Rougemont, J. (1987). Combined (thalamotomy and stimulation) stereotactic surgery of the VIM thalamic nucleus for bilateral Parkinson disease. *Stereot. Funct. Neurosurg.* 50, 344–346. doi: 10.1159/000100803

Bin Altaf, M. A., and Yoo, J. (2016). A 1.83 μJ/classification, 8-channel, patient-specific epileptic seizure classification SoC using a non-linear support vector machine. *IEEE Trans. Biomed. Circ. Syst.* 10, 49–60. doi: 10.1109/TBCAS.2014.2386891

Biotronik (Pacemaker). [*Online*]. Available online at: https://www.biotronik.com/en-gb/products/bradycardia

Bock, D. C., Marschilok, A. C., Takeuchi, K. J., and Takeuchi, E. S. (2012). Batteries used to power implantable biomedical devices. *Electrochim. Acta* 84, 155–164. doi: 10.1016/j.electacta.2012.03.057

Boëx, C., Vulliémoz, S., Spinelli, L., Pollo, C., and Seeck, M. (2007). High and low frequency electrical stimulation in non-lesional temporal lobe epilepsy. *Seizure* 16, 664–669. doi: 10.1016/j.seizure.2007.05.009

Bouthour, W., Mégevand, P., Donoghue, J., Lüscher, C., Birbaumer, N., and Krack, P. (2019). Biomarkers for closed-loop deep brain stimulation in Parkinson disease and beyond. *Nat. Rev. Neurol.* 15, 343–352. doi: 10.1038/s41582-019-0166-4

Butson, C. R., and McIntyre, C. C. (2005). Tissue and electrode capacitance reduce neural activation volumes during deep brain stimulation. *Clin. Neurophysiol.* 116, 2490–2500. doi: 10.1016/j.clinph.2005.06.023

Caldwell, D., Cronin, J., Rao, R., Collins, K., Weaver, K., Ko, A., et al. (2020). Signal recovery from stimulation artifacts in intracranial recordings with dictionary learning. *J. Neural eng.* 17:026023. doi: 10.1088/1741-2552/ab7a4f

Chandrakumar, H., and Marković, D. (2017). A high dynamic-range neural recording chopper amplifier for simultaneous neural recording and stimulation. *IEEE J. Solid-State Circ.* 52, 645–656. doi: 10.1109/JSSC.2016.2645611

Chandrakumar, H., and Marković, D. (2018). A 15.2-ENOB 5-kHz BW 4.5-μW chopped CT $\Delta\Sigma$ -ADC for artifact-tolerant neural recording front ends. *IEEE J. Solid-State Circ.* 53, 3470–3483. doi: 10.1109/JSSC.2018.2876468

Chang, C.-H., Lane, H.-Y., and Lin, C.-H. (2018). Brain stimulation in Alzheimer's disease. *Front. Psychiatry* 9:201. doi: 10.3389/fpsyt.2018.00201

Chang, C.-Y., Hsu, S.-H., Pion-Tonachini, L., and Jung, T.-P. (2019). Evaluation of artifact subspace reconstruction for automatic artifact components removal in multi-channel EEG recordings. *IEEE Trans. Biomed. Eng.* 67, 1114–1121. doi: 10.1109/TBME.2019.2930186

Charthad, J., Chang, T. C., Liu, Z., Sawaby, A., Weber, M. J., Baker, S., et al. (2018). A mm-sized wireless implantable device for electrical stimulation of peripheral nerves. *IEEE Trans. Biomed. Circ. Syst.* 12, 257–270. doi: 10.1109/TBCAS.2018.2799623

Charthad, J., Weber, M. J., Chang, T. C., and Arbabian, A. (2015). A mm-sized implantable medical device (IMD) with ultrasonic power transfer and a hybrid bi-directional data link. *IEEE J. Solid-State Circ.* 50, 1741–1753. doi: 10.1109/JSSC.2015.2427336

Chen, K.-H. S., and Chen, R. (2019). Invasive and noninvasive brain stimulation in Parkinson's disease: clinical effects and future perspectives. *Clin. Pharmacol. Therap.* 106, 763–775. doi: 10.1002/cpt.1542

Cheng, C.-H., Tsai, P.-Y., Yang, T.-Y., Cheng, W.-H., Yen, T.-Y., Luo, Z., et al. (2017). "A fully integrated closed-loop neuromodulation SoC with wireless power and bi-directional data telemetry for real-time human epileptic seizure control," in *2017 Symposium on VLSI Circuits* (Kyoto: IEEE), C44–C45. doi: 10.23919/VLSIC.2017.8008541

Chu, P., Muller, R., Koralek, A., Carmena, J. M., Rabaey, J. M., and Gambini, S. (2013). "Equalization for intracortical microstimulation artifact reduction," in *2013 35th Annual International Conference of the IEEE Engineering in Medicine and Biology Society (EMBC)* (Osaka: IEEE), 245–248. doi: 10.1109/EMBC.2013.6609483

Cogan, S. F., Ludwig, K. A., Welle, C. G., and Takmakov, P. (2016). Tissue damage thresholds during therapeutic electrical stimulation. *J. Neural Eng.* 13:021001. doi: 10.1088/1741-2560/13/2/021001

Cook, I. A., Espinoza, R., and Leuchter, A. F. (2014). Neuromodulation for depression: invasive and noninvasive (deep brain stimulation, transcranial magnetic stimulation, trigeminal nerve stimulation). *Neurosurg. Clin.* 25, 103–116. doi: 10.1016/j.nec.2013.10.002

Denison, T., Consoer, K., Santa, W., Avestruz, A., Cooley, J., and Kelly, A. (2007). A 2 μW 100 nV/$\sqrt{}$Hz chopper-stabilized instrumentation amplifier for chronic measurement of neural field potentials. *IEEE J. Solid-State Circ.* 42, 2934–2945. doi: 10.1109/JSSC.2007.908664

Dorsey, E., Constantinescu, R., Thompson, J., Biglan, K., Holloway, R., Kieburtz, K., et al. (2007). Projected number of people with Parkinson disease in the most populous nations, 2005 through 2030. *Neurology* 68, 384–386. doi: 10.1212/01.wnl.0000247740.47667.03

Drebitz, E., Rausch, L.-P., and Kreiter, A. K. (2020). A novel approach for removing micro-stimulation artifacts and reconstruction of broad-band neuronal signals. *J. Neurosci. Methods* 332:108549. doi: 10.1016/j.jneumeth.2019.108549

El-Bialy, T. H. A., Chen, J., and Tsui, Y. Y. (2011). *Ultrasound Stimulation Devices and Techniques.* US8079966B2. Edmonton, AB: University of Alberta.

Famm, K., Litt, B., Tracey, K. J., Boyden, E. S., and Slaoui, M. (2013). A jump-start for electroceuticals. *Nature* 496, 159–161. doi: 10.1038/496159a

Fang, W.-C., Wang, K.-Y., Fahier, N., Ho, Y.-L., and Huang, Y.-D. (2019). Development and validation of an EEG-based real-time emotion recognition system using edge AI computing platform with convolutional neural network system-on-chip design. *IEEE J. Emerg. Selec. Top. Circ. Syst.* 9, 645–657. doi: 10.1109/JETCAS.2019.2951232

Farvardin, M., Afarid, M., Attarzadeh, A., Johari, M. K., Mehryar, M., Nowroozzadeh, M. H., et al. (2018). The Argus-II Retinal Prosthesis Implantation; From the Global to Local Successful Experience. *Front. Neurosci.* 12:584. doi: 10.3389/fnins.2018.00584

Fiebig, M. (2005). Revival of the magnetoelectric effect. *J. Phys. D* 38:R123. doi: 10.1088/0022-3727/38/8/R01

Fox, M. D., Buckner, R. L., Liu, H., Chakravarty, M. M., Lozano, A. M., and Pascual-Leone, A. (2014). Resting-state networks link invasive and noninvasive brain stimulation across diverse psychiatric and neurological diseases. *Proc. Natl. Acad. Sci. U.S.A.* 111, E4367–E4375. doi: 10.1073/pnas.1405003111

Franks, W., Schenker, I., Schmutz, P., and Hierlemann, A. (2005). Impedance characterization and modeling of electrodes for biomedical applications. *IEEE Trans. Biomed. Eng.* 52, 1295–1302. doi: 10.1109/TBME.2005.847523

Gadhoumi, K., Lina, J.-M., and Gotman, J. (2013). Seizure prediction in patients with mesial temporal lobe epilepsy using EEG measures of state similarity. *Clin. Neurophysiol.* 124, 1745–1754. doi: 10.1016/j.clinph.2013.04.006

Gao, H., Walker, R. M., Nuyujukian, P., Makinwa, K. A. A., Shenoy, K. V., Murmann, B., et al. (2012). HermesE: a 96-channel full data rate direct neural interface in 0.13 μ m CMOS. *IEEE J. Solid-State Circ.* 47, 1043–1055. doi: 10.1109/JSSC.2012.2185338

Geddes, L., and Bourland, J. (1985). The strength-duration curve. *IEEE Trans. Biomed. Eng.* 32, 458–459. doi: 10.1109/TBME.1985.325456

Ghovanloo, M. (2006). "Switched-capacitor based implantable low-power wireless microstimulating systems," in *2006 IEEE International Symposium on Circuits and Systems* (Kos: IEEE), 4. doi: 10.1109/ISCAS.2006.1693055

Giering, K., Minet, O., Lamprecht, I., and Müller, G. (1995). Review of thermal properties of biological tissues. *Laser Induced Interst. Thermother.* 44, 45–65.

Gosalia, K., Weiland, J., Humayun, M., and Lazzi, G. (2004). Thermal elevation in the human eye and head due to the operation of a retinal prosthesis. *IEEE Trans. Biomed. Eng.* 51, 1469–1477. doi: 10.1109/TBME.2004.827548

Gul, E. E., and Kayrak, M. (2011). "Common pacemaker problems: lead and pocket complications," in *Modern Pacemakers-Present and Future*, ed M. R. Das (Rijeka) (Norderstedt: BoD), 299–318.

Ha, S., Akinin, A., Park, J., Kim, C., Wang, H., Maier, C., et al. (2016). Silicon-integrated high-density electrocortical interfaces. *Proc. IEEE* 105, 11–33. doi: 10.1109/JPROC.2016.2587690

Ha, S., Kim, C., Park, J., Cauwenberghs, G., and Mercier, P. P. (2018). A fully integrated RF-Powered energy-replenishing current-controlled stimulator. *IEEE Trans. Biomed. Circ. Syst.* 13, 191–202. doi: 10.1109/TBCAS.2018.2881800

Han, D., Zheng, Y., Rajkumar, R., Dawe, G. S., and Je, M. (2013). A 0.45 V 100-channel neural-recording IC with Sub-μW/channel consumption in 0.18 μm CMOS. *IEEE Trans. Biomed. Circ. Syst.* 7, 735–746. doi: 10.1109/TBCAS.2014.2298860

Harrison, R. R., and Charles, C. (2003). A low-power low-noise CMOS amplifier for neural recording applications. *IEEE J. Solid-State Circ.* 38, 958–965. doi: 10.1109/JSSC.2003.811979

Hartmann, C., Dovšen, S., Amsuess, S., and Farina, D. (2014). Closed-loop control of myoelectric prostheses with electrotactile feedback: influence of stimulation artifact and blanking. *IEEE Trans. Neural Syst. Rehabil. Eng.* 23, 807–816. doi: 10.1109/TNSRE.2014.2357175

Hashimoto, T., Elder, C. M., and Vitek, J. L. (2002). A template subtraction method for stimulus artifact removal in high-frequency deep brain stimulation. *J. Neurosci. Methods* 113, 181–186. doi: 10.1016/S0165-0270(01)00491-5

Helmers, A.-K., Lübbing, I., Deuschl, G., Witt, K., Synowitz, M., Mehdorn, H. M., and Falk, D. (2018). Comparison of the battery life of nonrechargeable generators for deep brain stimulation. *Neuromodulation* 21, 593–596. doi: 10.1111/ner.12720

Horbach, T., Thalheimer, A., Seyfried, F., Eschenbacher, F., Schuhmann, P., and Meyer, G. (2015). abiliti®closed-loop gastric electrical stimulation system for treatment of obesity: clinical results with a 27-month follow-up. *Obes. Surg.* 25, 1779–1787. doi: 10.1007/s11695-015-1620-z

Huang, J., and Mercier, P. P. (2020). A 112-dB SFDR 89-dB SNDR VCO-based sensor front-end enabled by background-calibrated differential pulse code modulation. *IEEE J. Solid-State Circ.* 56, 1046–1057. doi: 10.1109/JSSC.2020.3037833

Hyman, A. S. (1932). Resuscitation of the stopped heart by intracardial therapy: II. Experimental use of an artificial pacemaker. *Arch. Intern. Med.* 50, 283–305. doi: 10.1001/archinte.1932.00150150115012

Jech, R., Ruzicka, E., Urgosik, D., Serranova, T., Volfova, M., Novakova, O., et al. (2006). Deep brain stimulation of the subthalamic nucleus affects resting EEG and visual evoked potentials in Parkinson's disease. *Clin. Neurophysiol.* 117, 1017–1028. doi: 10.1016/j.clinph.2006.01.009

Jochum, T., Denison, T., and Wolf, P. (2009). Integrated circuit amplifiers for multi-electrode intracortical recording. *J. Neural Eng.* 6:012001. doi: 10.1088/1741-2560/6/1/012001

Johnson, B. C., Shen, K., Piech, D., Ghanbari, M. M., Li, K. Y., Neely, R., et al. (2018). "StimDust: A 6.5 mm 3, wireless ultrasonic peripheral nerve stimulator with 82% peak chip efficiency," in *2018 IEEE Custom Integrated Circuits Conference (CICC)* (San Diego, CA: IEEE), 1–4. doi: 10.1109/CICC.2018.8357047

Jow, U.-M., and Ghovanloo, M. (2007). Design and optimization of printed spiral coils for efficient transcutaneous inductive power transmission. *IEEE Trans. Biomed. Circ. Syst.* 1, 193–202. doi: 10.1109/TBCAS.2007.913130

Karumbaiah, L., Saxena, T., Carlson, D., Patil, K., Patkar, R., Gaupp, E. A., et al. (2013). Relationship between intracortical electrode design and chronic recording function. *Biomaterials* 34, 8061–8074. doi: 10.1016/j.biomaterials.2013.07.016

Kassiri, H., Bagheri, A., Soltani, N., Abdelhalim, K., Jafari, H. M., Salam, M. T., et al. (2016). Battery-less Tri-band-radio neuro-monitor and responsive neurostimulator for diagnostics and treatment of neurological disorders. *IEEE J. Solid-State Circ.* 51, 1274–1289. doi: 10.1109/JSSC.2016.2528999

Kassiri, H., Salam, M. T., Pazhouhandeh, M. R., Soltani, N., Perez Velazquez, J. L., Carlen, P., et al. (2017). Rail-to-rail-input dual-radio 64-channel closed-loop neurostimulator. *IEEE J. Solid-State Circ.* 52, 2793–2810. doi: 10.1109/JSSC.2017.2749426

Kassiri, H., Tonekaboni, S., Salam, M. T., Soltani, N., Abdelhalim, K., Velazquez, J. L. P., et al. (2017). Closed-loop neurostimulators: a survey and a seizure-predicting design example for intractable epilepsy treatment. *IEEE Trans. Biomed. Circ. Syst.* 11, 1026–1040. doi: 10.1109/TBCAS.2017.2694638

Khanna, P., Stanslaski, S., Xiao, Y., Ahrens, T., Bourget, D., Swann, N., et al. (2015). "Enabling closed-loop neurostimulation research with downloadable firmware upgrades," in *2015 IEEE Biomedical Circuits and Systems Conference (BioCAS)* (Atlanta, GA: IEEE), 1–6. doi: 10.1109/BioCAS.2015.7348348

Kim, C., Ha, S., Akinin, A., Park, J., Kubendran, R., Wang, H., et al. (2017a). "Design of miniaturized wireless power receivers for mm-sized implants," in *2017 IEEE Custom Integrated Circuits Conference (CICC)* (Austin, TX: IEEE), 1–8. doi: 10.1109/CICC.2017.7993703

Kim, C., Ha, S., Park, J., Akinin, A., Mercier, P. P., and Cauwenberghs, G. (2017b). A 144-MHz fully integrated resonant regulating rectifier with hybrid pulse modulation for mm-sized implants. *IEEE J. Solid-State Circ.* 52, 3043–3055. doi: 10.1109/JSSC.2017.2734901

Kim, C., Joshi, S., Courellis, H., Wang, J., Miller, C., and Cauwenberghs, G. (2018). Sub- μ Vrms-noise sub- μ W/channel ADC-direct neural recording with 200-mV/ms transient recovery through predictive digital autoranging. *IEEE J. Solid-State Circ.* 53, 3101–3110. doi: 10.1109/JSSC.2018.2870555

Kim, C., Park, J., Akinin, A., Ha, S., Kubendran, R., Wang, H., et al. (2016)."A fully integrated 144 MHz wireless-power-receiver-on-chip with an adaptive buck-boost regulating rectifier and low-loss h-tree signal distribution," in *2016 IEEE Symposium on VLSI Circuits (VLSI-Circuits)* (Honolulu, HI: IEEE), 1–2. doi: 10.1109/VLSIC.2016.7573492

Kim, C. Y., Ku, M. J., Qazi, R., Nam, H. J., Park, J. W., Nam, K. S., et al. (2021). Soft subdermal implant capable of wireless battery charging and programmable controls for applications in optogenetics. *Nat. Commun.* 12, 1–13. doi: 10.1038/s41467-020-20803-y

Kim, K., Vöröslakos, M., Seymour, J. P., Wise, K. D., Buzsáki, G., and Yoon, E. (2020). Artifact-free and high-temporal-resolution *in vivo* opto-electrophysiology with microLED optoelectrodes. *Nat. Commun.* 11, 1–12. doi: 10.1038/s41467-020-15769-w

Kim, S., Ho, J. S., and Poon, A. S. (2013). Midfield wireless powering of subwavelength autonomous devices. *Phys. Rev. Lett.* 110:203905. doi: 10.1103/PhysRevLett.110.203905

Kim, S., Tathireddy, P., Normann, R. A., and Solzbacher, F. (2007). Thermal impact of an active 3-d microelectrode array implanted in the brain. *IEEE Trans. Neural Syst. Rehabil. Eng.* 15, 493–501. doi: 10.1109/TNSRE.2007.908429

Kinnischtzke, A. K., Sewall, A. M., Berkepile, J. M., and Fanselow, E. E. (2012). Postnatal maturation of somatostatin-expressing inhibitory cells in the somatosensory cortex of GIN mice. *Front. Neural Circ.* 6:33. doi: 10.3389/fncir.2012.00033

Kreith, F., and Black, W. Z. (1980). *Basic Heat Transfer*. New York, NY: Harper & Row.

Kuhlmann, L., Freestone, D., Lai, A., Burkitt, A. N., Fuller, K., Grayden, D. B., et al. (2010). Patient-specific bivariate-synchrony-based seizure prediction for short prediction horizons. *Epilepsy Res.* 91, 214–231. doi: 10.1016/j.eplepsyres.2010.07.014

Kuncel, A. M., and Grill, W. M. (2004). Selection of stimulus parameters for deep brain stimulation. *Clin. Neurophysiol.* 115, 2431–2441. doi: 10.1016/j.clinph.2004.05.031

Lee, H.-M., Kwon, K. Y., Li, W., and Ghovanloo, M. (2014). A power-efficient switched-capacitor stimulating system for electrical/optical deep brain stimulation. *IEEE J. Solid-State Circ.* 50, 360–374. doi: 10.1109/ISSCC.2014.6757493

Lee, H.-M., Park, H., and Ghovanloo, M. (2013). A power-efficient wireless system with adaptive supply control for deep brain stimulation. *IEEE J. Solid-State Circ.* 48, 2203–2216. doi: 10.1109/JSSC.2013.2266862

Lee, J. W., Jung, H., Cho, H. H., Lee, J. H., and Nam, Y. (2018). Gold nanostar-mediated neural activity control using plasmonic photothermal effects. *Biomaterials* 153, 59–69. doi: 10.1016/j.biomaterials.2017.10.041

Lee, S., George, A. K., Lee, T., Chu, J.-U., Han, S., Kim, J.-H., et al. (2018). "A 110dB-CMRR 100dB-PSRR multi-channel neural-recording amplifier system using differentially regulated rejection ratio enhancement in 0.18 μm CMOS," in *2018 IEEE International Solid-State Circuits Conference-(ISSCC)* (San Francisco, CA: IEEE), 472–474. doi: 10.1109/ISSCC.2018.8310389

Levin, M., Selberg, J., and Rolandi, M. (2019). Endogenous bioelectrics in development, cancer, and regeneration: drugs and bioelectronic devices as electroceuticals for regenerative medicine. *Iscience* 22, 519–533. doi: 10.1016/j.isci.2019.11.023

Li, M. C., and Cook, M. J. (2018). Deep brain stimulation for drug-resistant epilepsy. *Epilepsia* 59, 273–290. doi: 10.1111/epi.13964

Li, X., Serdijn, W. A., Zheng, W., Tian, Y., and Zhang, B. (2015). The injectable neurostimulator: an emerging therapeutic device. *Trends Biotechnol.* 33, 388–394. doi: 10.1016/j.tibtech.2015.04.001

Li, Y., Chen, J., and Yang, Y. (2019). A method for suppressing electrical stimulation artifacts from electromyography. *Int. J. Neural Syst.* 29:1850054. doi: 10.1142/S0129065718500545

Lillehei, C. W., Gott, V. L., Hodges, P. C., Long, D. M., and Bakken, E. E. (1960). Transistor pacemaker for treatment of complete atrioventricular dissociation. *J. Am. Med. Assoc.* 172, 2006–2010. doi: 10.1001/jama.1960.03020180016003

Limnuson, K., Lu, H., Chiel, H. J., and Mohseni, P. (2015). A bidirectional neural interface SoC with an integrated spike recorder, microstimulator, and low-power processor for real-time stimulus artifact rejection. *Anal. Integr. Circ. Signal Process.* 82, 457–470. doi: 10.1007/s10470-015-0489-z

Little, S., Pogosyan, A., Neal, S., Zavala, B., Zrinzo, L., Hariz, M., et al. (2013). Adaptive deep brain stimulation in advanced Parkinson disease. *Ann. Neurol.* 74, 449–457. doi: 10.1002/ana.23951

Liu, X., Lu, Y., Iseri, E., Shi, Y., and Kuzum, D. (2018). A compact closed-loop optogenetics system based on artifact-free transparent graphene electrodes. *Front. Neurosci.* 12:132. doi: 10.3389/fnins.2018.00132

Lu, Y., Cao, P., Sun, J., Wang, J., Li, L., Ren, Q., et al. (2012). Using independent component analysis to remove artifacts in visual cortex responses elicited by electrical stimulation of the optic nerve. *J. Neural Eng.* 9:026002. doi: 10.1088/1741-2560/9/2/026002

Luo, D., Zhang, M., and Wang, Z. (2018). "Design of a low noise neural recording amplifier for closed-loop neuromodulation applications," in *2018 IEEE International Symposium on Circuits and Systems (ISCAS)* (Florence: IEEE), 1–4. doi: 10.1109/ISCAS.2018.8351280

Luo, Y.-S., Wang, J.-R., Huang, W.-J., Tsai, J.-Y., Liao, Y.-F., Tseng, W.-T., et al. (2013). Ultrasonic power/data telemetry and neural stimulator with OOK-PM signaling. *IEEE Trans. Circ. Syst. II* 60, 827–831. doi: 10.1109/TCSII.2013.2286000

Mallela, V. S., Ilankumaran, V., and Rao, N. S. (2004). Trends in cardiac pacemaker batteries. *Indian Pacing Electrophysiol. J.* 4:201.

McConnell, G. C., Rees, H. D., Levey, A. I., Gutekunst, C.-A., Gross, R. E., and Bellamkonda, R. V. (2009). Implanted neural electrodes cause chronic, local inflammation that is correlated with local neurodegeneration. *J. Neural eng.* 6:056003. doi: 10.1088/1741-2560/6/5/056003

Merrill, D. R., Bikson, M., and Jefferys, J. G. (2005). Electrical stimulation of excitable tissue: design of efficacious and safe protocols. *J. Neurosci. Methods* 141, 171–198. doi: 10.1016/j.jneumeth.2004.10.020

Mickle, A. D., Won, S. M., Noh, K. N., Yoon, J., Meacham, K. W., Xue, Y., et al. (2019). A wireless closed-loop system for optogenetic peripheral neuromodulation. *Nature* 565, 361–365. doi: 10.1038/s41586-018-0823-6

Mormann, F., Kreuz, T., Andrzejak, R. G., David, P., Lehnertz, K., and Elger, C. E. (2003). Epileptic seizures are preceded by a decrease in synchronization. *Epilepsy Res.* 53, 173–185. doi: 10.1016/S0920-1211(03)00002-0

Mouthaan, B. E., van't Klooster, M. A., Keizer, D., Hebbink, G. J., Leijten, F. S., et al. (2016). Single pulse electrical stimulation to identify epileptogenic cortex: clinical information obtained from early evoked responses. *Clin. Neurophysiol.* 127, 1088–1098. doi: 10.1016/j.clinph.2015.07.031

Muller, R., Gambini, S., and Rabaey, J. M. (2012). A 0.013 mm^2, 5 μW, DC-coupled neural signal acquisition IC with 0.5 V supply. *IEEE J. Solid-State Circ.* 47, 232–243. doi: 10.1109/JSSC.2011.2163552

Muller, R., Le, H., Li, W., Ledochowitsch, P., Gambini, S., Bjorninen, T., et al. (2015). A minimally invasive 64-channel wireless μECoG implant. *IEEE J. Solid-State Circ.* 50, 344–359. doi: 10.1109/JSSC.2014.2364824

Nam, Y., Brown, E. A., Ross, J. D., Blum, R. A., Wheeler, B. C., and DeWeerth, S. P. (2009). A retrofitted neural recording system with a novel stimulation IC to monitor early neural responses from a stimulating electrode. *J. Neurosci. Methods* 178, 99–102. doi: 10.1016/j.jneumeth.2008.11.017

Nan, C.-W. (1994). Magnetoelectric effect in composites of piezoelectric and piezomagnetic phases. *Phys. Rev. B* 50:6082. doi: 10.1103/PhysRevB.50.6082

Ng, K. A., and Xu, Y. P. (2013). A compact, low input capacitance neural recording amplifier. *IEEE Trans. Biomed. Circ. Syst.* 7, 610–620. doi: 10.1109/TBCAS.2013.2280066

Norton, S. J. (2003). Can ultrasound be used to stimulate nerve tissue? *Biomed. Eng. Online* 2:6. doi: 10.1186/1475-925X-2-6

Page, A., Sagedy, C., Smith, E., Attaran, N., Oates, T., and Mohsenin, T. (2014). A flexible multichannel EEG feature extractor and classifier for seizure detection. *IEEE Trans. Circ. Syst. II* 62, 109–113. doi: 10.1109/TCSII.2014.2385211

Park, J., Kim, C., Akinin, A., Ha, S., Cauwenberghs, G., and Mercier, P. P. (2017). "Wireless powering of mm-scale fully-on-chip neural interfaces," in *2017 IEEE Biomedical Circuits and Systems Conference (BioCAS)* (Turin: IEEE), 1–4. doi: 10.1109/BIOCAS.2017.8325186

Parkinson, A. J., Arcaroli, J., Staller, S. J., Arndt, P. L., Cosgriff, A., and Ebinger, K. (2002). The Nucleus 24 Contour cochlear implant system: adult clinical trial results. *Ear Hear.* 23, 41S–48S. doi: 10.1097/00003446-200202001-00005

Pavan, S., Krishnapura, N., Pandarinathan, R., and Sankar, P. (2008). A power optimized continuous-time $\delta\sigma$ ADC for audio applications. *IEEE J. Solid-State Circ.* 43, 351–360. doi: 10.1109/JSSC.2007.914263

Plonsey, R., and Barr, R. C. (2007). *Bioelectricity: A Quantitative Approach*. Berlin: Springer Science & Business Media.

Poewe, W., Seppi, K., Tanner, C. M., Halliday, G. M., Brundin, P., Volkmann, J., et al. (2017). Parkinson disease. *Nat. Rev. Dis. Primers* 3, 1–21. doi: 10.1038/nrdp.2017.13

Poon, A. S., O'Driscoll, S., and Meng, T. H. (2010). Optimal frequency for wireless power transmission into dispersive tissue. *IEEE Trans. Antenn. Propag.* 58, 1739–1750. doi: 10.1109/TAP.2010.2044310

Qian, X., Chen, Y., Feng, Y., Ma, B., Hao, H., and Li, L. (2016). A method for removal of deep brain stimulation artifact from local field potentials. *IEEE Trans. Neural Syst. Rehabil. Eng.* 25, 2217–2226. doi: 10.1109/TNSRE.2016.2613412

Rahmani, H., and Babakhani, A. (2018a). "A 434 MHz dual-mode power harvesting system with an on-chip coil in 180 nm CMOS SOI for mm-sized implants," in *2018 IEEE/MTT-S International Microwave Symposium-IMS* (Philadelphia, PA: IEEE), 1130–1133. doi: 10.1109/MWSYM.2018.8439642

Rahmani, H., and Babakhani, A. (2018b). A dual-mode RF power harvesting system with an on-chip coil in 180-nm SOI CMOS for millimeter-sized biomedical implants. *IEEE Trans. Microw. Theor. Techn.* 67, 414–428. doi: 10.1109/TMTT.2018.2876239

Ramasubbu, R., Lang, S., and Kiss, Z. H. T. (2018). Dosing of electrical parameters in deep brain stimulation (DBS) for intractable depression: a review of clinical studies. *Front. Psychiatry* 9:302. doi: 10.3389/fpsyt.2018.00302

Ranjandish, R., and Schmid, A. (2018). "Implantable IoT system for closed-loop epilepsy control based on electrical neuromodulation," in *2018 IFIP/IEEE International Conference on Very Large Scale Integration (VLSI-SoC)* (Playa del Carmen: IEEE), 155–158. doi: 10.1109/VLSI-SoC.2018.8645023

Reitz, C., Brayne, C., and Mayeux, R. (2011). Epidemiology of Alzheimer disease. *Nat. Rev. Neurol.* 7, 137–152. doi: 10.1038/nrneurol.2011.2

Reza Pazhouhandeh, M., Chang, M., Valiante, T. A., and Genov, R. (2020). Track-and-zoom neural analog-to-digital converter with blind stimulation artifact rejection. *IEEE J. Solid-State Circ.* 55, 1984–1997. doi: 10.1109/JSSC.2020.2991526

Rhew, H.-G., Jeong, J., Fredenburg, J. A., Dodani, S., Patil, P. G., and Flynn, M. P. (2014). A fully self-contained logarithmic closed-loop deep brain stimulation SoC with wireless telemetry and wireless power management. *IEEE J. Solid-State Circ.* 49, 2213–2227. doi: 10.1109/JSSC.2014.2346779

Rosin, B., Slovik, M., Mitelman, R., Rivlin-Etzion, M., Haber, S. N., Israel, Z., et al. (2011). Closed-loop deep brain stimulation is superior in ameliorating Parkinsonism. *Neuron* 72, 370–384. doi: 10.1016/j.neuron.2011.08.023

Russo, M., Cousins, M. J., Brooker, C., Taylor, N., Boesel, T., Sullivan, R., et al. (2018). Effective relief of pain and associated symptoms with closed-loop spinal cord stimulation system: preliminary results of the Avalon study. *Neuromodulation* 21, 38–47. doi: 10.1111/ner.12684

Ryu, S. B., Paulk, A. C., Yang, J. C., Ganji, M., Dayeh, S. A., Cash, S. S., et al. (2020). Spatially confined responses of mouse visual cortex to intracortical magnetic stimulation from micro-coils. *J. Neural Eng.* 17:056036. doi: 10.1088/1741-2552/abbd22

Sahin, M., and Tie, Y. (2007). Non-rectangular waveforms for neural stimulation with practical electrodes. *J. Neural eng.* 4:227. doi: 10.1088/1741-2560/4/3/008

Salam, M. T., Velazquez, J. L. P., and Genov, R. (2015). Seizure suppression efficacy of closed-loop versus open-loop deep brain stimulation in a rodent model of epilepsy. *IEEE Trans. Neural Syst. Rehabil. Eng.* 24, 710–719. doi: 10.1109/TNSRE.2015.2498973

Sayeed, M. A., Mohanty, S. P., Kougianos, E., and Zaveri, H. P. (2019). Neuro-detect: a machine learning-based fast and accurate seizure detection system in the IoMT. *IEEE Trans. Consum. Electron.* 65, 359–368. doi: 10.1109/TCE.2019.2917895

Schreier, R., Temes, G. C., and Pavan, S. (2005). *Understanding Delta-Sigma Data Converters, Vol. 74*. Piscataway, NJ: IEEE Press. doi: 10.1109/9780470546772

Sette, A., Seigneuret, E., Reymond, F., Chabardes, S., Castrioto, A., Boussat, B., et al. (2019). Battery longevity of neurostimulators in Parkinson disease: a historic cohort study. *Brain Stimul.* 12, 851–857. doi: 10.1016/j.brs.2019.02.006

Sharpeshkar, R. (2010). *Ultra Low Power Bioelectronics: Fundamentals, Biomedical Applications, and Bio-Inspired System*. New York, NY: Cambridge University Press. doi: 10.1017/CBO9780511841446

Shealy, C. N., Mortimer, J. T., and Reswick, J. B. (1967). Electrical inhibition of pain by stimulation of the dorsal columns: preliminary clinical report. *Anesth. Anal.* 46, 489–491. doi: 10.1213/00000539-196707000-00025

Simmons, F. B., Mongeon, C. J., Lewis, W. R., and Huntington, D. A. (1964). Electrical stimulation of acoustical nerve and inferior colliculus: results in man. *Arch. Otolaryngol.* 79, 559–567. doi: 10.1001/archotol.79.6.559

Simpson, J., and Ghovanloo, M. (2007). "An experimental study of voltage, current, and charge controlled stimulation front-end circuitry," in *2007 IEEE International Symposium on Circuits and Systems* (New Orleans, LA: IEEE), 325–328. doi: 10.1109/ISCAS.2007.378401

Singer, A., Dutta, S., Lewis, E., Chen, Z., Chen, J. C., Verma, N., et al. (2020). Magnetoelectric materials for miniature, wireless neural stimulation at therapeutic frequencies. *Neuron* 107, 631–643. doi: 10.1016/j.neuron.2020.05.019

Snellings, A., and Grill, W. M. (2012). Effects of stimulation site and stimulation parameters on bladder inhibition by electrical nerve stimulation. *BJU Int.* 110, 136–143. doi: 10.1111/j.1464-410X.2011.10789.x

Steigerwald, F., Matthies, C., and Volkmann, J. (2019). Directional deep brain stimulation. *Neurotherapeutics* 16, 100–104. doi: 10.1007/s13311-018-0667-7

Sun, F. T., Morrell, M. J., and Wharen, R. E. (2008). Responsive cortical stimulation for the treatment of epilepsy. *Neurotherapeutics* 5, 68–74. doi: 10.1016/j.nurt.2007.10.069

Trebaul, L., Rudrauf, D., Job, A.-S., Maiia, M. D., Popa, I., Barborica, A., et al. (2016). Stimulation artifact correction method for estimation of early cortico-cortical evoked potentials. *J. Neurosci. Methods* 264, 94–102. doi: 10.1016/j.jneumeth.2016.03.002

Truong, B. D. (2020). Fundamental issues in magnetoelectric transducers: magnetic field sensing versus wireless power transfer systems. *IEEE Sensors J.* 20, 5322–5328. doi: 10.1109/JSEN.2020.2967808

VanEpps, J. S., and John G, Y. (2016). Implantable device related infection. *Shock* 46:597. doi: 10.1097/SHK.0000000000000692

Vassileva, A., van Blooijs, D., Leijten, F., and Huiskamp, G. (2018). Neocortical electrical stimulation for epilepsy: closed-loop versus open-loop. *Epilepsy Res.* 141, 95–101. doi: 10.1016/j.eplepsyres.2018.02.010

Verma, N., Shoeb, A., Guttag, J. V., and Chandrakasan, A. P. (2009). "A micro-power EEG acquisition SoC with integrated seizure detection processor for continuous patient monitoring," in *2009 Symposium on VLSI Circuits* (Kyoto: IEEE), 62–63.

Vidal, J., and Ghovanloo, M. (2010). "Towards a switched-capacitor based stimulator for efficient deep-brain stimulation," in *2010 Annual International Conference of the IEEE Engineering in Medicine and Biology* (Buenos Aires: IEEE), 2927–2930. doi: 10.1109/IEMBS.2010.5626290

Waddell, C., Pratt, J. A., Porr, B., and Ewing, S. (2009). "Deep brain stimulation artifact removal through under-sampling and cubic-spline interpolation," in *2009 2nd International Congress on Image and Signal Processing* (Tianjin), 1–5. doi: 10.1109/CISP.2009.5301199

Wang, Y., Liang, J., Xu, C., Wang, Y., Kuang, Y., Xu, Z., et al. (2016). Low-frequency stimulation in anterior nucleus of thalamus alleviates kainate-induced chronic epilepsy and modulates the hippocampal EEG rhythm. *Exp. Neurol*. 276, 22–30. doi: 10.1016/j.expneurol.2015.11.014

Wang, Y., Sun, Q., Luo, H., Chen, X., Wang, X., and Zhang, H. (2020). "26.3 a closed-loop neuromodulation chipset with 2-level classification achieving 1.5 V pp CM interference tolerance, 35dB stimulation artifact rejection in 0.5 ms and 97.8% sensitivity seizure detection," in *2020 IEEE International Solid-State Circuits Conference-(ISSCC)* (San Francisco, CA: IEEE), 406–408. doi: 10.1109/ISSCC19947.2020.9062954

Weast, R. C. (1974). *Handbook of Chemistry and Physics, 55th Edition*. Cleveland: CRC Press.

Wells, J., Kao, C., Mariappan, K., Albea, J., Jansen, E. D., Konrad, P., et al. (2005). Optical stimulation of neural tissue *in vivo*. *Opt. Lett*. 30, 504–506. doi: 10.1364/OL.30.000504

Wong, L. S., Hossain, S., Ta, A., Edvinsson, J., Rivas, D. H., and Naas, H. (2004). A very low-power CMOS mixed-signal IC for implantable pacemaker applications. *IEEE J. Solid-State Circuits* 39, 2446–2456. doi: 10.1109/JSSC.2004.837027

Wongsarnpigoon, A., Woock, J. P., and Grill, W. M. (2010). Efficiency analysis of waveform shape for electrical excitation of nerve fibers. *IEEE Trans. Neural Syst. Rehabil. Eng*. 18, 319–328. doi: 10.1109/TNSRE.2010.2047610

Yaul, F. M., and Chandrakasan, A. P. (2016). "A sub-μW 36nV/$\sqrt{}$Hz chopper amplifier for sensors using a noise-efficient inverter-based 0.2 V-supply input stage," in *2016 IEEE International Solid-State Circuits Conference (ISSCC)* (San Francisco, CA: IEEE), 94–95. doi: 10.1109/ISSCC.2016.7417923

Yazicioglu, R. F., Merken, P., Puers, R., and Van Hoof, C. (2007). A 60 μW 60 nV/$\sqrt{}$Hz readout front-end for portable biopotential acquisition systems. *IEEE J. Solid-State Circ*. 42, 1100–1110. doi: 10.1109/JSSC.2007.894804

Yoo, J., Yan, L., El-Damak, D., Altaf, M. A. B., Shoeb, A. H., and Chandrakasan, A. P. (2013). An 8-channel scalable EEG acquisition SoC with patient-specific seizure classification and recording processor. *IEEE J. Solid-State Circ*. 48, 214–228. doi: 10.1109/JSSC.2012.2221220

Yu, T., Wang, X., Li, Y., Zhang, G., Worrell, G., Chauvel, P., et al. (2018). High-frequency stimulation of anterior nucleus of thalamus desynchronizes epileptic network in humans. *Brain* 141, 2631–2643. doi: 10.1093/brain/awy187

Yu, Z., Chen, J. C., Alrashdan, F. T., Avants, B. W., He, Y., Singer, A., et al. (2020a). MagNI: a magnetoelectrically powered and controlled wireless neurostimulating implant. *IEEE Trans. Biomed. Circ. Syst*. 14, 1241–1252. doi: 10.1109/TBCAS.2020.3037862

Yu, Z., Chen, J. C., Avants, B. W., He, Y., Singer, A., Robinson, J. T., et al. (2020b). "34.3 An 8.2 mm 3 implantable neurostimulator with magnetoelectric power and data transfer," in *2020 IEEE International Solid-State Circuits Conference-(ISSCC)* (San Francisco, CA: IEEE), 510–512. doi: 10.1109/ISSCC19947.2020.9062931

Zeng, F., Rebscher, S., Harrison, W., Sun, X., and Feng, H. (2008). Cochlear implants: system design, integration, and evaluation. *IEEE Rev. Biomed. Eng*. 1, 115–142. doi: 10.1109/RBME.2008.2008250

Zeng, K., Chen, D., Ouyang, G., Wang, L., Liu, X., and Li, X. (2015). An EEMD-ICA approach to enhancing artifact rejection for noisy multivariate neural data. *IEEE Trans. Neural Syst. Rehabil. Eng*. 24, 630-638. doi: 10.1109/TNSRE.2015.2496334

Zhou, A., Johnson, B. C., and Muller, R. (2018). Toward true closed-loop neuromodulation: artifact-free recording during stimulation. *Curr. Opin. Neurobiol*. 50, 119–127. doi: 10.1016/j.conb.2018.01.012

Zhou, A., Santacruz, S. R., Johnson, B. C., Alexandrov, G., Moin, A., Burghardt, F. L., et al. (2019). A wireless and artefact-free 128-channel neuromodulation device for closed-loop stimulation and recording in non-human primates. *Nat. Biomed. Eng*. 3, 15–26. doi: 10.1038/s41551-018-0323-x

Conflict of Interest: The authors declare that the research was conducted in the absence of any commercial or financial relationships that could be construed as a potential conflict of interest.

frontiers in Neuroscience

ORIGINAL RESEARCH
published: 02 June 2021
doi: 10.3389/fnins.2021.667846

Low-Cutoff Frequency Reduction in Neural Amplifiers: Analysis and Implementation in CMOS 65 nm

Fereidoon Hashemi Noshahr[1]*, *Morteza Nabavi*[1], *Benoit Gosselin*[2] and *Mohamad Sawan*[1,3,4]

[1] Polystim Neurotech. Lab., Department of Electrical Engineering, Polytechnique Montreal, Montreal, QC, Canada, [2] Department of Computer and Electrical Engineering, Université Laval, Québec, QC, Canada, [3] School of Engineering, Westlake University, Hangzhou, China, [4] Institute of Advanced Study, Westlake Institute for Advanced Study, Hangzhou, China

Scaling down technology demotes the parameters of AC-coupled neural amplifiers, such as increasing the low-cutoff frequency due to the short-channel effects. To improve the low-cutoff frequency, one solution is to increase the feedback capacitors' value. This solution is not desirable, as the input capacitors have to be increased to maintain the same gain, which increases the area and decreases the input impedance of the neural amplifier. We analytically analyze the small-signal behavior of the neural amplifier and prove that the main reason for the increase of the low-cutoff frequency in advanced CMOS technologies is the reduction of the input resistance of the operational transconductance amplifier (OTA). We also show that the reduction of the input resistance of the OTA is due to the increase in the gate oxide leakage in the input transistors. In this paper, we explore this fact and propose two solutions to reduce the low-cutoff frequency without increasing the value of the feedback capacitor. The first solution is performed by only simulation and is called cross-coupled positive feedback that uses pseudoresistors to provide a negative resistance to increase the input resistance of the OTA. As an advantage, only standard CMOS transistors are used in this method. Simulation results show that a low-cutoff frequency of 1.5 Hz is achieved while the midband gain is 30.4 dB at 1 V. In addition, the power consumption is 0.6 μW. In the second method, we utilize thick-oxide MOS transistors in the input differential pair of the OTA. We designed and fabricated the second method in the 65 nm TSMC CMOS process. Measured results are obtained by *in vitro* recordings on slices of mouse brainstem. The measurement results show that the bandwidth is between 2 Hz and 5.6 kHz. The neural amplifier has 34.3 dB voltage gain in midband and consumes 3.63 μW at 1 V power supply. The measurement results show an input-referred noise of 6.1 μV_{rms} and occupy 0.04 mm^2 silicon area.

Keywords: neural amplifier, low noise, low-power, low-cutoff frequency, compact

OPEN ACCESS

Edited by:
Alexandre Schmid, École Polytechnique Fédérale de Lausanne, Switzerland

Reviewed by:
Srinjoy Mitra, University of Edinburgh, United Kingdom
Julian Oreggioni, Universidad de la República, Uruguay

***Correspondence:**
Fereidoon Hashemi Noshahr
fereidoon.hashemi@polymtl.ca

Specialty section:
This article was submitted to Neural Technology, a section of the journal Frontiers in Neuroscience

Received: *14 February 2021*
Accepted: *04 May 2021*
Published: *02 June 2021*

Citation:
Hashemi Noshahr F, Nabavi M, Gosselin B and Sawan M (2021) Low-Cutoff Frequency Reduction in Neural Amplifiers: Analysis and Implementation in CMOS 65 nm. Front. Neurosci. 15:667846. doi: 10.3389/fnins.2021.667846

1. INTRODUCTION

Neural signal acquisition has a crucial role in understanding the function of the different parts of the brain as well as exploring and treating its various disorders (Stevenson and Kording, 2011). In addition, this data is used in developing the neural prostheses (Sun et al., 2008) and brain machine interfaces (BMI) (Fifer et al., 2012). This is why the demand for new techniques that enable

monitoring brain activity wirelessly through implantable devices is increasing every day (Schwartz et al., 2006; Mollazadeh et al., 2009; Cook et al., 2013). A complete review on neural recording is given in Hashemi Noshahr et al. (2020) and Luan et al. (2020).

Brain signals are very small and have very low bandwidth. For instance, the maximum amplitude of local field potentials (LFP) is typically 1 mV and the frequency range is <1 Hz up to 300 Hz (Van Rijn et al., 1991). On the other hand, the amplitude of the spikes or the neural action potentials (AP) are typically as high as 500 μV and their operational frequency is up to 7 kHz (Najafi and Wise, 1986).

Increasing the number of the neural recording sites, which are called channels, is required in some applications, as the spatial resolution of the capturing signals increases. As an example, the total number of channels reported in Musk (2019) is 3072. The electrochemical reaction at the electrode-tissue interface in each channel generates different DC offset voltages across the various electrodes. These voltages vary typically between 1 and 10 mV and in some cases up to 50 mV (Bagheri et al., 2017). As the offset voltages of the channels have high value, they can saturate the neural amplifier. Therefore, they should be eliminated. The most common approach to block this DC input offset is to utilize large AC-coupling capacitors (Harrison and Charles, 2003; Ng and Xu, 2012). On the other hand, there is an alternative method that blocks these DC offset voltages by using a low-pass filter in the feedback path, which is called DC-coupled input offset rejection. The authors in Enz et al. (1995), Yazicioglu et al. (2008), Muller et al. (2012), Biederman et al. (2013), Lee et al. (2019), Jomehei and Sheikhaei (2019), Cabrera et al. (2020), and Farouk et al. (2020) use this method, however, it requires a huge capacitor or high power consumption amplifier in the feedback path.

To design multichannel neural amplifiers, the following factors should be considered and diminished as much as possible.

1. Power consumption: the brain tissues that are surrounded by implantable neuro-amplifiers must be protected from heat damage. For this purpose, the power dissipation of these amplifiers must be lowered.
2. Chip area: The neural amplifiers are generally huge. This is because they usually utilize large AC-coupled input capacitors. Also, to decrease the flicker-noise power of amplifiers, the size of the MOS transistors is designed to be very large especially in the differential pairs. Therefore, for a specific chip area, to maximize the number of the channels, the amplifiers should be designed in their minimum area.
3. Noise: the neural signals have very low amplitude and bandwidth. The flicker and thermal noise of the neural amplifier circuit is the main source of the noise, which can decrease the signal to noise ratio (SNR) in the output of the amplifiers. This is why they are designed as a low noise amplifier (LNA). In the low frequency, the power of the flicker noise is dominant. To decrease the flicker-noise power, in addition to increasing the size of the transistors and utilizing a PMOS differential pair, the chopper-stabilization technique is used (Denison et al., 2007; Verma et al., 2010; Xu et al., 2011; Yazicioglu et al., 2011; Luo et al., 2019; Samiei and Hashemi, 2019). The chopper-stabilization technique modulates the low-frequency noise of the OTA (flicker noise), as well as the offset voltage to a higher frequency by the chopper switches. These higher frequencies are eliminated with a low pass filter (LPF).

The 65 nm CMOS and finer technologies introduce new challenges as a result of the short channel effects for analog circuits. One of these challenges is decreasing the transconductance (gm) of MOS transistors, which diminishes the voltage gain of the whole amplifier. This can be resolved by designing the neural amplifier in 2 or 3 gain stages (Zou et al., 2009; Rezaee-Dehsorkh et al., 2011). The other destructive effect of short channel effects is increasing the low-cutoff frequency (f_L) of the AC-coupled neural amplifiers. In this paper, we analyze the parameters that affect the low-cutoff frequency and propose two solutions. The first solution utilizes a standard CMOS

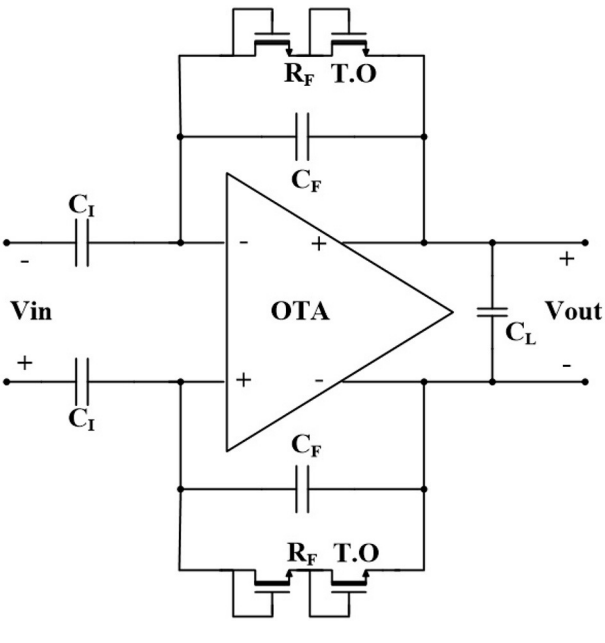

FIGURE 1 | Fully differential capacitive feedback network neural amplifier.

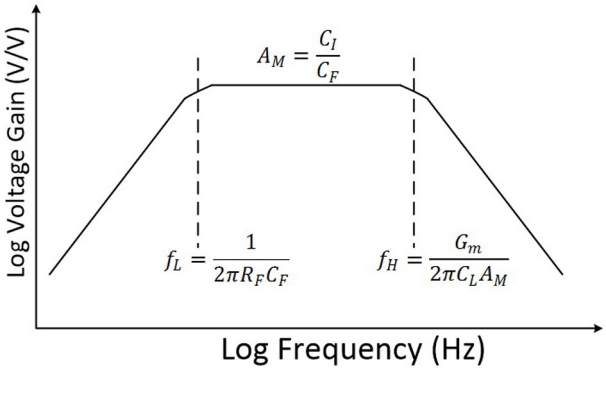

FIGURE 2 | Frequency response of the amplifier.

and improves the low-cutoff frequency by increasing the input resistance. The second method utilizes thick-oxide transistors to increase the input resistance.

The rest of the paper is organized as follows. Section II analyzes the low-cutoff frequency in neural amplifiers. Section III presents the two proposed solutions. The experimental results are provided in Section IV and the paper concludes in section V.

2. LOW-CUTOFF FREQUENCY ANALYSIS

Figure 1 shows the schematic of a fully differential neural amplifier with conventional capacitive feedback network (CFN) architecture. As explained in Harrison and Charles (2003), this architecture is one of the most popular architectures of AC-coupled neural amplifiers in terms of low power consumption, low noise, and compact area. Also, utilizing thick-oxide NMOS pseudoresistors instead of PMOS pseudoresistors, provides a better total harmonic distortion (THD) (Kassiri et al., 2013).

Figure 2 shows the frequency response of this CFN neural amplifier as a bandpass amplifier. Assuming that the voltage gain of the operational transconductance amplifier (OTA) is significantly high, the voltage gain of the amplifier in the midband (A_M) can be approximately calculated by

$$A_M = \frac{C_I}{C_F} \tag{1}$$

where C_I and C_F are input and feedback capacitance of the amplifier, respectively. Also, the low-cutoff frequency (f_L) of the amplifier can be approximated as

$$f_L = \frac{1}{2\pi R_F C_F} \tag{2}$$

where R_F is the dynamic resistance of NMOS pseudoresistors of the amplifier.

As presented in Equation 2, in order to reduce f_L, C_F and R_F should be increased. However, by increasing C_F, it is required to increase C_I to maintain the same gain which results in huge area loss for each channel of a multi channel device. In addition,

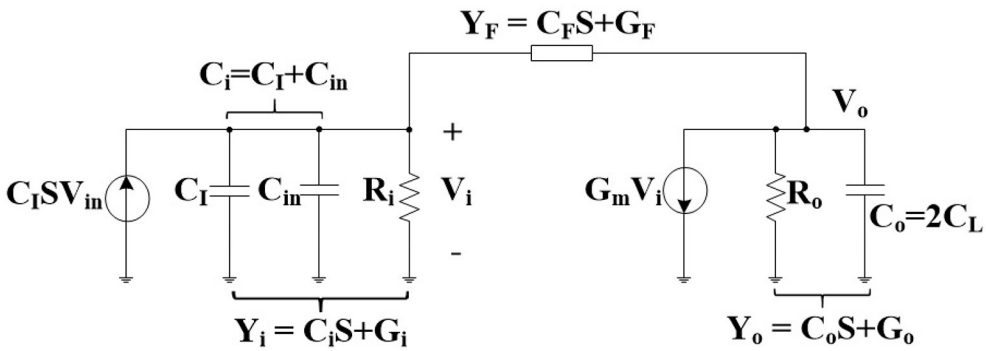

FIGURE 3 | Small signal equivalent of the half-circuit of the neural amplifier.

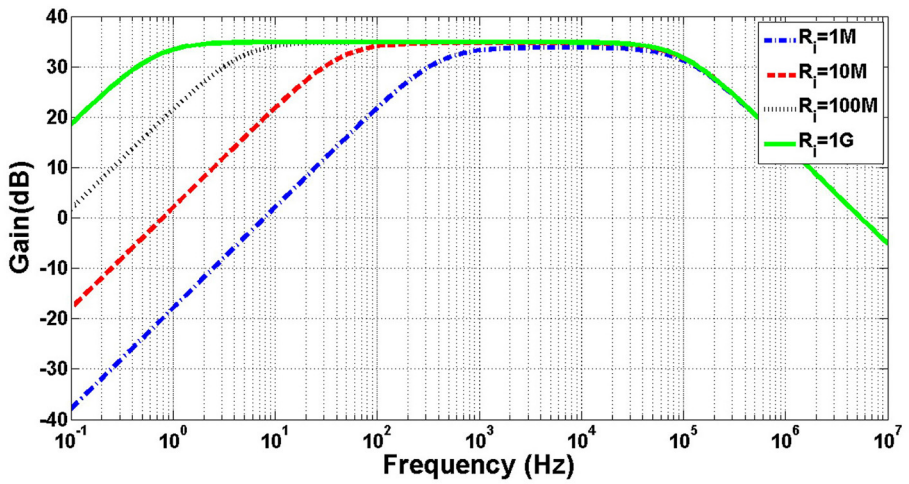

FIGURE 4 | Simulation of frequency response of a neural amplifier with various amounts of R_i.

this results in the reduction of the input impedance of the neural amplifier.

MOS pseudoresistors can be utilized as a feedback resistance (R_F) for their compactness and high resistance. However, the drawback of this technique is that the MOS pseudoresistors provide much less resistance in advanced technology. For example, in an old technology such as 1.5 μm CMOS technology, by utilizing a MOS pseudoresistor for the R_F, a C_F of only 200 fF is enough to achieve a f_L of 0.025 Hz (Harrison and Charles, 2003). However, with the same technique and the same value for C_F, a f_L of 39 Hz is reported in the 180 nm CMOS technology (Shoaran et al., 2014). Moreover, in the 130 nm CMOS technology (Abdelhalim et al., 2013), a higher C_F of 300 fF is used to compensate for the low R_F to provide a f_L of 0.1 Hz. Moreover, in the 65 nm CMOS technology, our simulation results show that when a C_F of 200 fF is used, the f_L is achieved at 472 Hz. To better understand the effects that increase the f_L value in the advanced CMOS technologies, we provide a small signal analysis of the amplifier in the following.

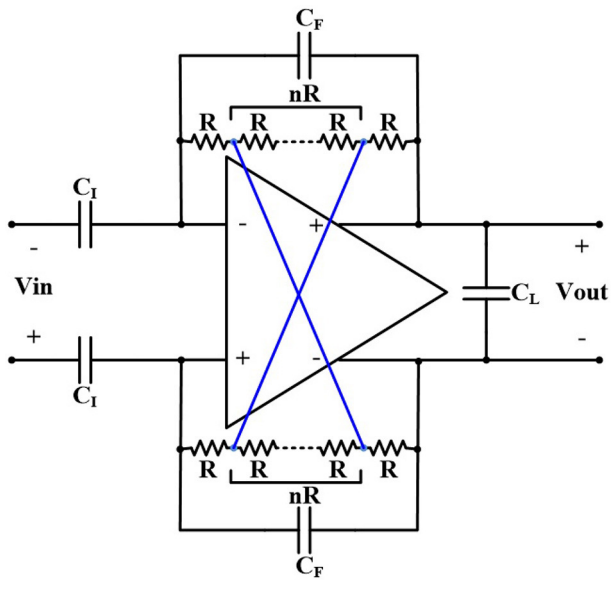

FIGURE 5 | The neural amplifier with cross-coupled positive feedback architecture.

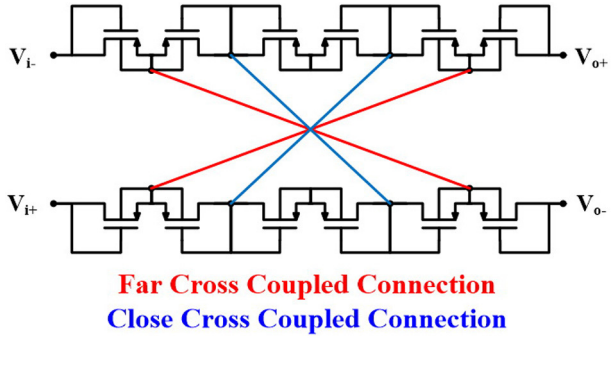

FIGURE 6 | Cross-coupled positive feedback connections.

The equivalent small signal half-circuit of a neural amplifier of **Figure 1** is depicted in **Figure 3**. The OTA can be modeled as a single pole amplifier with a pole at the output node. In this figure, G_m is the transcunductance of the OTA and C_{in}, R_i, and R_o are OTA's input terminal capacitance, resistance, and the output terminal resistance, respectively. We extract the time constant of the first pole as

$$\tau_1 = \frac{1}{p_1} = \tag{3}$$

$$= \frac{C_F(G_o + G_m) + C_oG_F + C_i(G_o + G_F) + G_i(C_o + C_F)}{G_F(G_m + G_o) + G_i(G_F + G_o)}$$

Reduction of the oxide thickness in advanced technologies translates to lower input resistance (i.e., higher G_i) due to higher gate leakage current. By increasing G_i, the denominator in Equation (3) grows much faster than the numerator. Therefore, the time constant (τ_1) increases resulting in lower f_L.

However, for older technologies, we can simplify Equations (3) to (4) with the assumption that OTA's input resistance (R_i) is infinity (i.e., G_i is approximately zero) (Hashemi Noshahr and Sawan, 2017).

$$\tau_1 = \frac{1}{p_1} = R_FC_F + \frac{C_oR_o}{1 + G_mR_o} + \frac{C_i(R_F + R_o)}{1 + G_mR_o} \tag{4}$$

If the gain of the OTA (G_mR_o) is high, the second and third terms of this equation can be considered negligible resulting in Equation (5) where the corresponding frequency to τ_1 is the same as Equation (2). In other words, Equation (5) is a special case of Equation (3) where the gain of the OTA is high and the input resistance of the OTA is infinity.

$$\tau_1 = \frac{1}{p_1} = R_FC_F \tag{5}$$

Figure 4 illustrates the frequency response of the small signal model of the amplifier shown in **Figure 3** for different values of R_i. The DC voltage of the outputs is biased at 0.5 V and thick-oxide NMOS pseudoresistors are utilized for feedback resistors. The values of G_m, R_o, C_I, C_F, C_{in}, and C_o are chosen as 22.4 $\mu\mho$, 157 $M\Omega$, 11.5 pF, 200 fF, 3 pF, and 200 fF, respectively. As shown in this figure, f_L decreases by increasing R_i.

3. PROPOSED SOLUTIONS

In this section, we propose two solutions to decrease the low-cutoff frequency down to 1 Hz of OTA's in advanced CMOS technologies without increasing the feedback capacitance (C_F).

3.1. Cross-Coupled Positive Feedback

Figure 5 shows the architecture of the neural amplifier with cross-coupled positive feedback (CCPF) connections

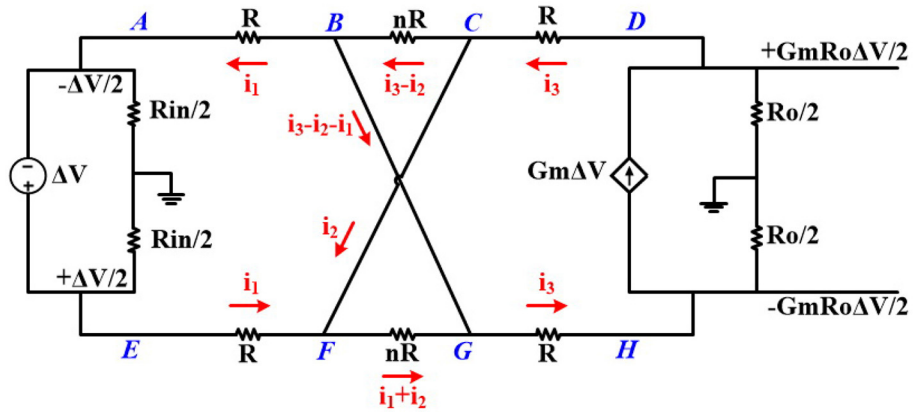

FIGURE 7 | Small signal equivalent circuit of the neural amplifier with a CCPF connection.

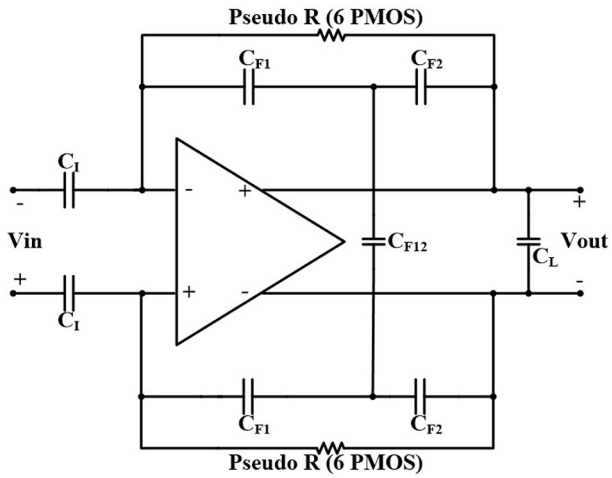

FIGURE 8 | T-capacitor feedback network architecture with CCPF.

in which multiple (n+2) numbers of pseudoresistors are utilized. **Figure 6** shows two implementations of the CCPF connections (far and close connections) in which each pseudoresistor is implemented with a standard PMOS transistor. By knowing the fact that the CCPF provides a negative resistance ($-|R_N|$), the equivalent input resistance of the OTA can be presented by

$$R_{ieq} = R_i \,||\, (-|R_N|) = \frac{R_i|R_N|}{|R_N| - R_i} \tag{6}$$

As presented in Equation (6), to maximize R_{ieq}, $(|R_N| - R_i)$ must be minimized. In other words, to achieve a very high positive equivalent input resistance, the amount of $|R_N|$ must be slightly higher than R_i, and $(|R_N| - R_i)$ should approach zero. However, since this negative resistance is created by positive feedback, the stability of the amplifier limits the lower bound of $(|R_N| - R_i)$.

To verify Equation (6), we calculate the negative resistance of the CCPF. **Figure 7** shows the small signal equivalent circuit of the neural amplifier with a far CCPF connections. For simplicity of calculation, we assume all the pseudoresistors are identical and have the same value.

Performing a KVL in the loops DCBGHD and DCFGHD results in

$$i_3 = i_1 + 2i_2 \tag{7}$$

Also Performing KVL on the loops of ABCFEA and DCBGHD and considering (Equation 7) results in the following two equations

$$(n+2)Ri_1 + nRi_2 = \Delta V \tag{8}$$

$$(n+2)Ri_1 + (n+4)Ri_2 = G_m R_o \Delta V \tag{9}$$

After solving these equations, the value of i_1 will be

$$i_1 = \frac{(n+4) - G_m R_o n}{4(n+2)R} \Delta V \tag{10}$$

As shown in **Figure 7**, $R_N = \frac{\Delta V}{i_1}$ is the equivalent resistance of the whole circuit connected to input terminals of the OTA (nodes A and E), which is parallel to R_{in}. By considering (Equation 10), R_N can be presented as

$$R_N = \frac{4(n+2)R}{(n+4) - G_m R_o n} \tag{11}$$

By knowing that the gain of the OTA ($G_m R_o$) is very high, the dominator of R_N is negative. In practice, the values of the pseudoresistors are not equal and vary based on their currents (or their voltages). Therefore, Equation (11) is not accurate and simulation results are required to calculate the exact value of R_N.

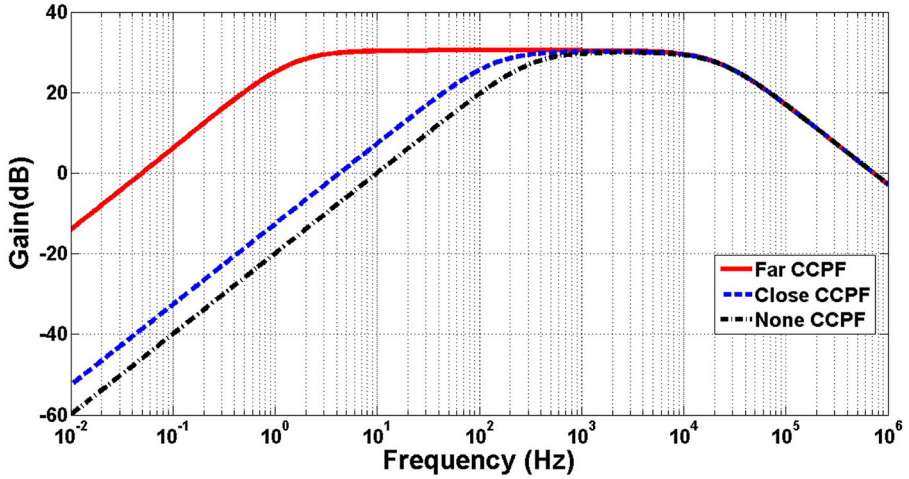

FIGURE 9 | Simulation of frequency response (gain) of the amplifier of **Figure 8** with far, close and no CCPF connection.

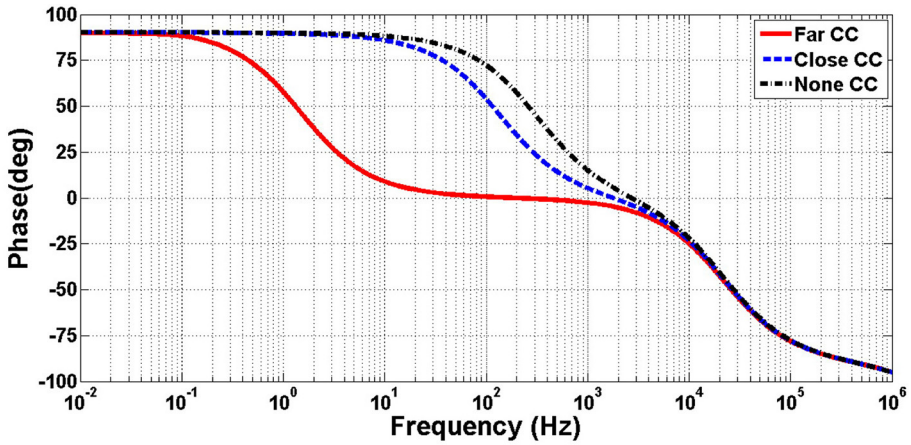

FIGURE 10 | Simulation of frequency response (phase) of the amplifier of **Figure 8** with far, close and no CCPF connection.

The value of the low-cutoff frequency of the amplifier depends on the number and size (W/L) of the pseudoresistors as well as the position of the CCPF connections (far or close). For example, assuming $C_I = 10\ pF$, $C_F = 200\ fF$, $C_L = 1.7\ pF$, and $n = 4$ for a far CCPF connection in the amplifier shown in **Figure 5** achieves a f_L of 0.27 Hz with the midband gain of 31.67 dB, while the total capacitance value of this amplifier is 22 pF. In order to decrease the total capacitance, we exploited a T-capacitor feedback network shown in **Figure 8** (Ng and Xu, 2013). The pseudoresistors and CCPF connections in this figure are implemented similar to **Figure 6** with 6 PMOS transistors.

The midband gain of the amplifier in **Figure 8** is calculated as

$$A_M = \left(\frac{C_I}{C_{F1}}\right)\left(\frac{C_{F1} + C_{F2} + 2C_{F12}}{C_{F12}}\right) \tag{12}$$

We can adjust the capacitances in Equation (12) to keep the total capacitance of the OTA low while maintaining the same gain. For example, in **Figure 8**, by choosing the value of the capacitors as $C_I = 1.4\ pF$, $C_{F1} = C_{F2} = 200\ fF$, $C_{F12} = 400\ fF$, and $C_L = 200\ fF$, the total capacitor value of the amplifier decreases to 4.2 pF, and the low-cutoff frequency increases from 0.27 to 1.5 Hz, which is still in the acceptable range.

Figures 9, **10** illustrates the frequency response of the amplifier in terms of gain and phase, respectively, and in in far, close, and no CCPF connections. The amount of the low-cutoff frequency for far, close, and no CCPF connections are 1.5, 143, and 320 Hz, respectively.

The positive feedback in the CCPF architecture of the amplifier can result in instability. However, by carefully designing the number of pseudoresistors, transistor sizes, and the position of the CCPF connection we can make sure that the negative feedback is dominant and the whole architecture is stable and satisfies at least a 60 degree phase margin. **Figure 11** shows the simulation of open loop frequency response of the amplifier of **Figure 8** with 70 degree phase margin.

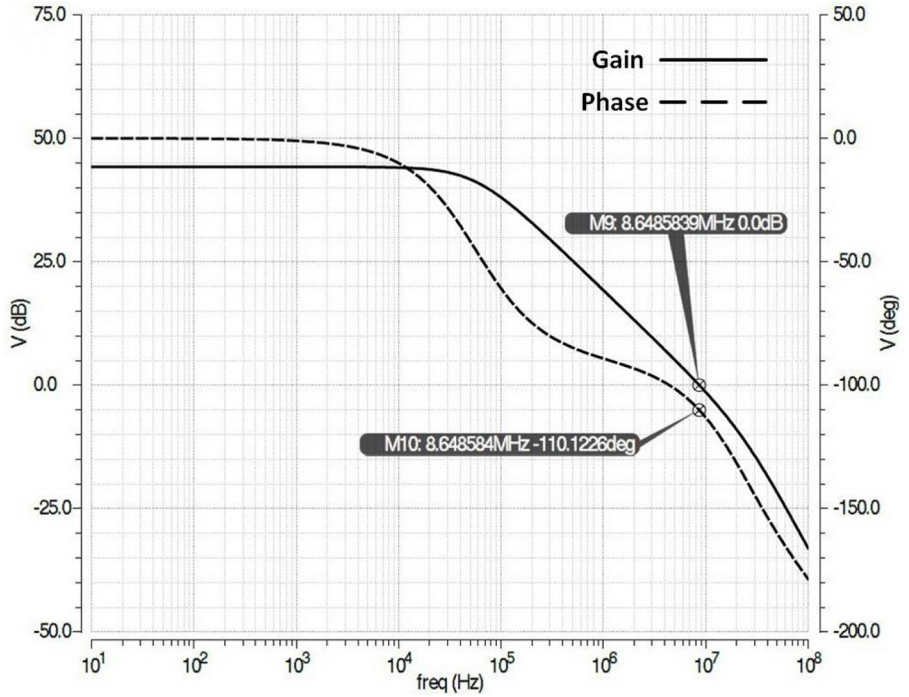

FIGURE 11 | Simulation of open loop frequency response (gain and phase) of the amplifier of **Figure 8** with 70 degree phase margin.

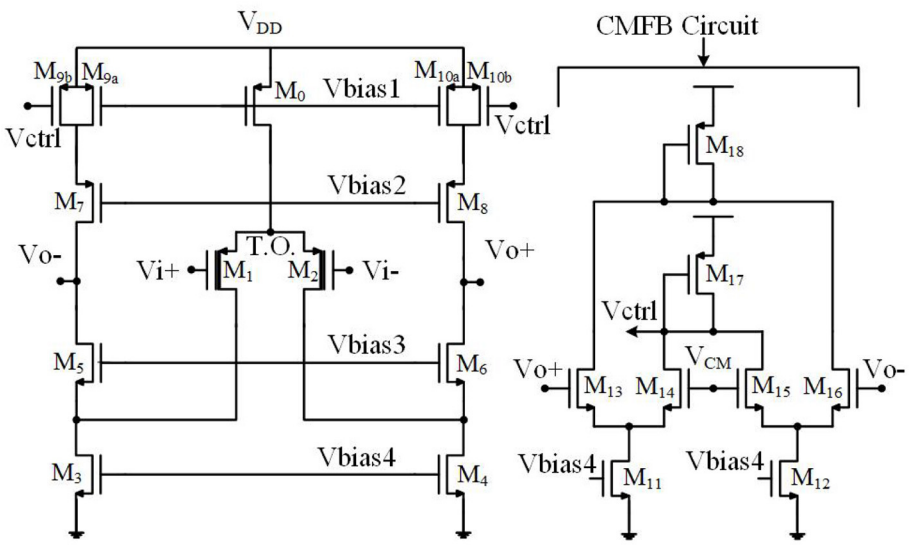

FIGURE 12 | Fully differential folded cascode OTA utilized in neural amplifier.

By adding switches to the CCPF connection we can program (i.e., turn on or off) the connections in the post-fabrication process. In case of multiple pseudoresistors (e.g., 18), the farther CCPF connections might observe instability due to process variation. Therefore, by programming the connections and choosing closer connections, we can avoid instability. In addition, programmability can also give us control over the value of f_L. The closer connections have higher value of f_L and are more stable. On the other hand, the farther connections have lower value of f_L at the cost of less stability.

3.2. Thick Oxide Differential Pair

The second method to increase the input resistance of the OTA without increasing the feedback capacitance is to utilize

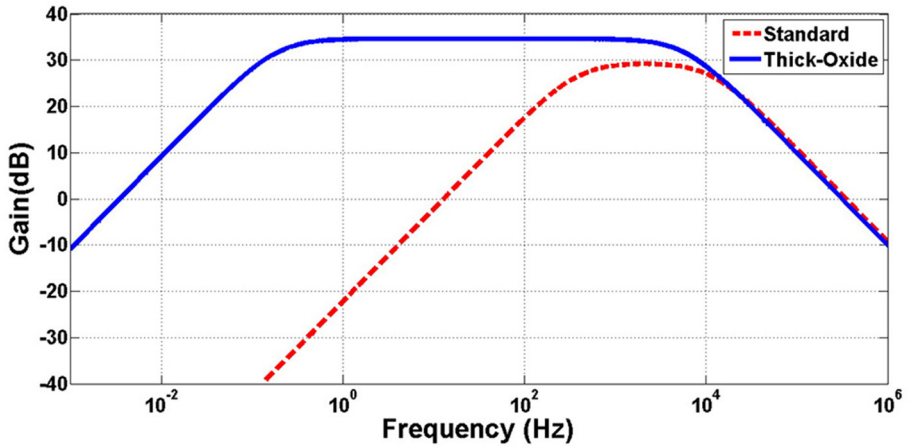

FIGURE 13 | Simulation of frequency response of neural amplifier with thick-oxide and standard PMOS differential pair.

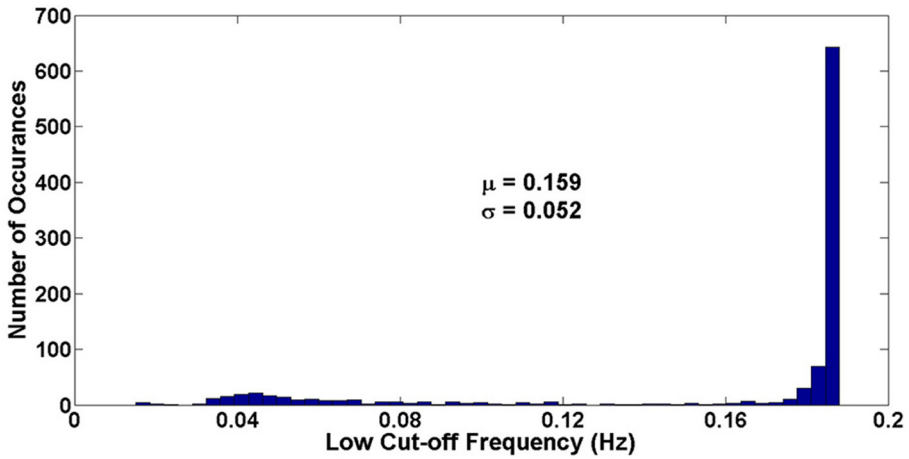

FIGURE 14 | Monte Carlo simulation of low-cutoff frequency of the neural amplifier.

thick-oxide MOS transistors in the input differential pair. **Figure 12** shows the transistor level implementation of the OTA of **Figure 1** with thick-oxide PMOS input differential pair. In this figure, the bulks of NMOS transistors are grounded whereas the bulks of PMOS transistors are connected to their sources. The size of each transistor is shown in **Table 1** and the bias currents are tabulated in **Table 2**.

Figure 13 shows the simulation results of the designed neural amplifier utilizing the OTA of **Figure 12** and the OTA with standard PMOS input differential pair. The gain of the OTA and the whole neural amplifier are 68.2 and 34.6 dB, respectively. As shown in this figure, applying a thick-oxide PMOS in the input differential pair improved the low-cutoff frequency from 360 to 0.19 Hz. These simulation results confirm that increasing the input resistance of the OTA by utilizing thick-oxide PMOS in the differential pair decreases the low-cutoff frequency dramatically.

In order to increase the SNR of the neural amplifier, the first stage of a neural amplifier is designed as an LNA. To reduce the flicker noise of the OTA of **Figure 12**, we optimize the size of the PMOS transistors in the input differential pair (i.e., M_1 and M_2). Also, as mentioned in Harrison and Charles (2003), to minimize the thermal noise, the transistors M_1 and M_2 are biased in the sub-threshold region to maximize their transconductance over drain current called transconductance efficiency (g_m/I_D), and the transistors M_3, M_4, M_{9a}, M_{9b}, M_{10a}, and M_{10_b} are biased in the saturation region to minimize their g_m/I_D.

As mentioned earlier, the bandwidth and operating frequency of neural amplifiers are very low, therefore the dominant noise power is the flicker noise. Also, in the OTA of **Figure 12**, the differential pair transistors are the main source of the flicker noise in comparison with other transistors (Razavi, 2005). Therefore, to analyze the noise of the proposed neural amplifier, we only investigate the effect of the thick-oxide PMOS differential pair. Utilizing thick-oxide PMOS transistors in the differential pair of the OTA decreases the gate-oxide capacitance per unit area (C_{ox}) due to the increased gate oxide thickness (t_{ox}). Utilizing

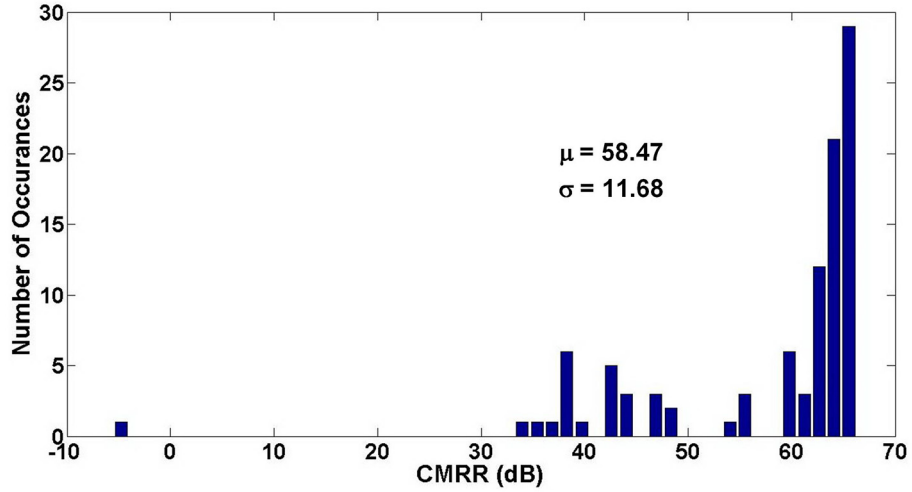

FIGURE 15 | Monte Carlo analysis of CMRR of the neural amplifier.

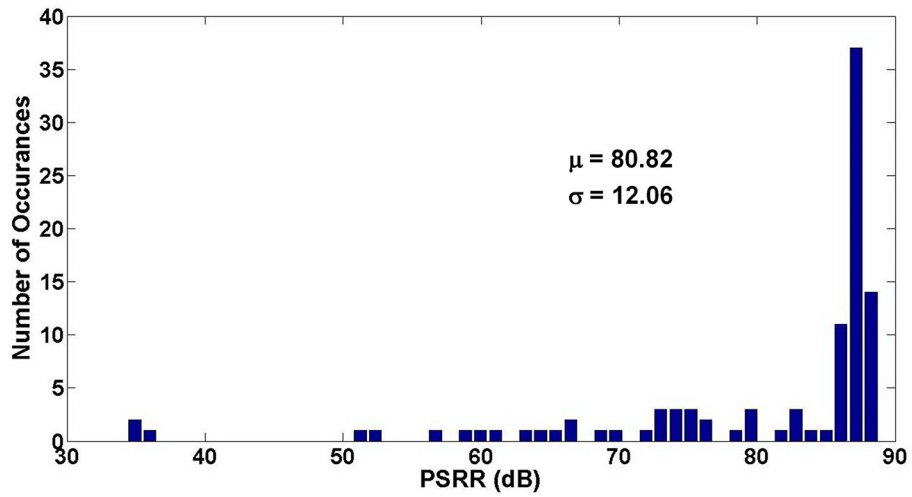

FIGURE 16 | Monte Carlo analysis of PSRR of the neural amplifier.

the thick-oxide PMOS in the input differential pair increases the flicker noise power due to decreasing C_{ox}. The relation between the input-referred noise of the whole neural amplifier ($\overline{V_{ni,amp}^2}$) and the OTA input-referred noise ($\overline{V_{ni}^2}$) is presented as

$$\overline{V_{ni,amp}^2} = \left(\frac{C_I + C_F + C_{in}}{C_I}\right)^2 . \overline{V_{ni}^2} \tag{13}$$

Decreasing the C_{ox} due to utilizing the thick-oxide PMOS differential pair, increases $\overline{V_{ni}^2}$ and decreases the C_{in} in Equation (13). Since the increase in $\overline{V_{ni}^2}$ is much higher than the reduction of its coefficient, the $\overline{V_{ni,amp}^2}$ increases by decreasing the C_{ox}. To compensate this drawback, we can increase the gain of the LNA (C_I/C_F) by increasing C_I to reduce the $\overline{V_{ni,amp}^2}$ in Equation (13). Simulation results show that the minimum input-referred noise voltage of the neural amplifier is 5.9 μV_{rms} in the frequency range between 1 Hz and 5.6 kHz (bandwidth).

Note that to further reduce the noise of the OTA, it is required to apply noise reduction techniques such as the chopper stabilization technique, which is out of the scope of this paper.

Figure 14 shows the Monte Carlo simulation results (N = 1,000) of the low-cutoff frequency. As shown in this figure, the μ is equal to 0.159 Hz and the σ is equal to 0.052, resulting $\frac{3\sigma}{\mu}$ of 0.983.

Figures 15, **16** show the Monte Carlo analysis of CMRR and PSRR of the Neural amplifier. Applying thick-oxide MOS transistors in the input differential pair decreases the gate leakage current significantly and increases the input

impedance of the OTA and consequently the CMRR and PSRR improve.

4. MEASUREMENT AND *IN VITRO* RESULTS

4.1. Measured Performance

The prototype is implemented in the TSMC 65 nm CMOS process. The C_I and C_F are set to 11.5 pF and 208 fF, respectively, in the layout to achieve a gain of 55 V/V (or 34.3 dB) ($A_M = \frac{C_I}{C_F}$). The prototype uses 0.04 mm^2 (270 μm $\times$ 150 μm) of silicon area. The micrograph of the die containing the amplifier is shown in **Figure 17**.

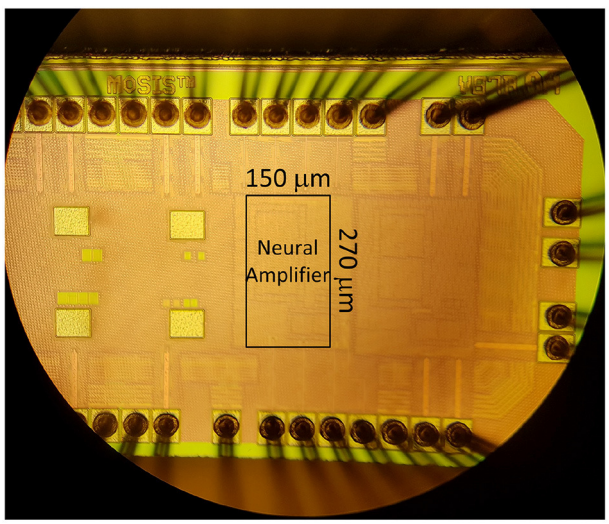

FIGURE 17 | Micrograph of chip containing the neural amplifier with 270 μm $\times$ 150 μm die area.

The measured frequency response from 0.1 Hz to 1 MHz is performed through saline medium to mimic the brain environment as well as the simulation result are illustrated in **Figure 18**. The midband gain is 34.3 dB and the low and high-cutoff frequencies are 2 Hz and 5.6 kHz, respectively. The simulated low-cutoff frequency is 0.19 Hz which is less than that achieved in the measurement result. This deviation is expected as the MOS pseudoresistors are nonlinear and significantly sensitive to their operating point (Harrison and Charles, 2003).

Figure 19 shows the measured input-referred noise voltage spectral density of the neural amplifier. The RMS value of the input referred noise is achieved as 6.1 μV_{rms} by integrating the area under the curve from 1 Hz to 5.6 kHz (amplifier bandwidth) in **Figure 19**. This value is slightly higher than the simulated result (5.9 μV_{rms}).

Table 3 shows a summary of the simulated and measured parameters of the prototype. A comparison of our work and the other published works is presented in **Table 4**. All of the chosen neural amplifiers are AC-coupled. To fairly compare these amplifiers with different gain values, number of stages and technology, we only consider the first stage of each amplifiers.

Measurement results show that the achieved gain is the highest among all in **Table 4**. Note that the gain for Xiao et al. (2010) is reported for two stages. Also, the area of the fabricated chip is less than others. However, we should note that comparing the chip area itself without considering the midband gain is not a fair comparison. The midband gain (A_m) of the amplifier is equal to $\frac{C_I}{C_F}$. The low-cutoff frequency (f_L) is determined by C_F, and C_I is determined by the gain and C_F. Also, note that the main contributor to the chip area is C_I. In other words, for a normalized gain, lower C_F results in less chip area. Therefore, comparing C_F is a better figure of merit for comparing the chip area while the amplifiers have different gains. In this case, the values of C_F of the proposed amplifier and Ng and Xu (2016) are 208 fF and 350 fF, respectively. Note that the gain reported in our work is 34.3 dB, while the gain in Ng and Xu (2016) is 26.4 dB.

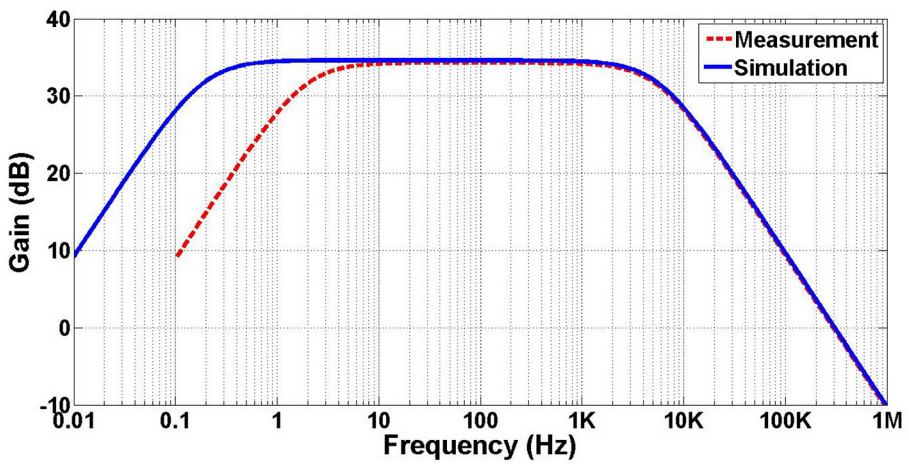

FIGURE 18 | Measured and simulated frequency response of the amplifier. The measured midband gain is 34.3 dB, and the low and high-cutoff frequencies occur at 2 Hz and 5.6 kHz, respectively.

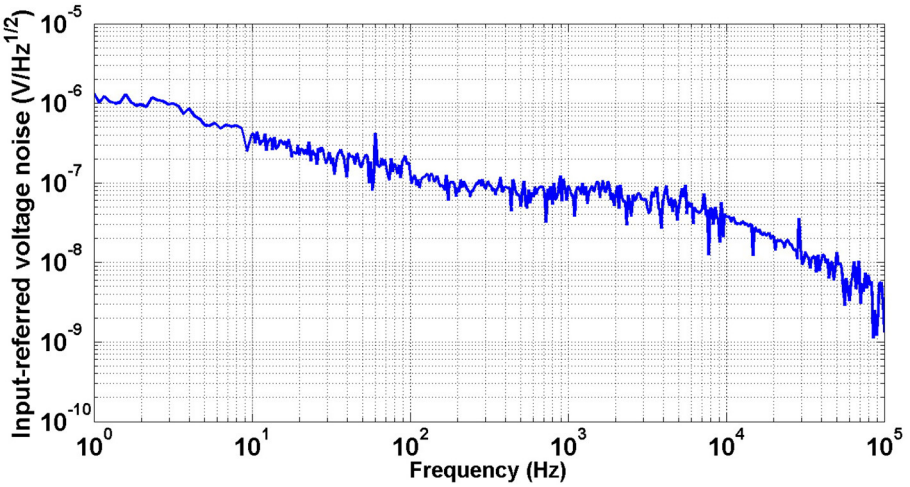

FIGURE 19 | Measured input-referred noise voltage spectrum.

TABLE 1 | Transistor sizes of the neural amplifier.

Transistor	$W/L(\mu m)$	Transistor	$W/L(\mu m)$	Transistor	$W/L(\mu m)$
M_0	$5\frac{4}{10}$	M_5	$2\frac{0.8}{2}$	M_{9b}	$4\frac{1}{20}$
M_1	$24\frac{4}{4}$	M_6	$2\frac{0.8}{2}$	M_{10a}	$4\frac{1}{20}$
M_2	$24\frac{4}{4}$	M_7	$2\frac{0.8}{2}$	M_{10b}	$4\frac{1}{20}$
M_3	$3\frac{1}{20}$	M_8	$2\frac{0.8}{2}$	M_{11}	$2\frac{0.5}{20}$
M_4	$3\frac{1}{20}$	M_{9a}	$4\frac{1}{20}$	M_{12}	$2\frac{0.5}{20}$
M_{13}	$1\frac{1}{1}$	M_{14}	$1\frac{1}{1}$	M_{15}	$1\frac{1}{1}$
M_{16}	$1\frac{1}{1}$	M_{17}	$4\frac{1}{20}$	M_{18}	$4\frac{1}{20}$

TABLE 2 | Bias currents of the neural amplifier.

I_{M0}	$I_{M3,4}$	$I_{M9a,10a}$	$I_{M11,12}$
1.83μA	1.276μA	175nA	390nA

TABLE 3 | Experimental and simulation characteristics of neural amplifier.

Parameter	Simulation	Measured
Supply voltage [V]	1	1
Supply current [μA]	3.63	3.63
Gain [dB]	34.6	34.3
Band width [kHz]	5.8	5.6
Low-cutoff frequency [Hz]	0.19	2
Input-Referred Noise [μV_{rms}]	5.9	6.1
Noise efficiency factor	5.8	6.1
THD (2 mV_{pp} at 1 kHz) [%]	0.18	< 1

This is why the total area of our work is almost the same as that of Ng and Xu (2016).

The amplifier of Song et al. (2013) has been implemented in the 0.18 μm technology with a gain of 26 dB. Its high pass pole is 80 Hz. The value of C_F is not reported, however, the total area of the amplifier is 0.16 mm^2 which is significantly large. In Abdelhalim et al. (2013), neural amplifiers with a gain of 54–60 dB in two gain stages have been implemented in the 0.13 μm process. The first stage (LNA) with the estimated gain of 31.8 dB has 300 fF feedback capacitors with 0.1 Hz low-cutoff frequency. Our analysis shows that the C_F in Abdelhalim et al. (2013) could be reduced to 200 fF if the thick-oxide differential pair is used.

The neural amplifier of Xiao et al. (2010) has employed two gain stages to obtain 49 dB in the 0.13 μm process. The value of the C_F is not reported. However, the estimated amplifier area and f_L are 0.4 mm^2 and 100 Hz, respectively. This amplifier occupies a very large area and has a high low-cutoff frequency. The designs in Biederman et al. (2015) utilize LNA with a gain of 26 dB fabricated in the 65 nm CMOS Technology. It employs a 500 fF feedback capacitor parallel to a pseudoresistor in a conventional CFN architecture similar to our work. The low-cutoff frequency f_L is adjustable, with the minimum value of 10 Hz. The neural amplifier consists of a variable gain amplifier (VGA) and buffer to achieve a gain of 45–60 dB. The amplifier in Ng and Xu (2016) has been implemented with two gain stages with 52.1 dB midband gain in the 65 nm technology. The gain in the first stage, LNA, is 26.4 dB and the f_L is reported as 1 Hz. The LNA exploits a CMOS-inverter-based OTA with 360 fF as C_F. The amplifier designed in Kim and Ko (2019) utilizes relatively small transistors in the OTA. In addition to small transistors, an older process of 0.18 μm is used which they both help decreasing the gate leakage and increase the input resistance of the OTA. This results in a low f_L of 6.4 Hz. However, this comes at the cost of high input-referred noise voltage (10.68 μV_{rms}). CMRR and PSRR in the typical corner simulation are 66.3 and 88 dB, respectively. As mentioned earlier, when thick-oxide CMOS is used, the CMRR and PSRR increase compared to the case when standard CMOS is used. This increase is due to the increased input impedance

TABLE 4 | Comparison of fully integrated neural amplifiers.

Parameter	Song et al. (2013)	Abdelhalim et al. (2013)	Xiao et al. (2010)	Biederman et al. (2015)	Ng and Xu (2016)	Kim and Ko (2019)	This work
Technology [CMOS]	0.18 μm	0.13 μm	0.13 μm	65 nm	65 nm	0.18 μm	65 nm
Area [mm^2]	0.16	N/A	0.4*	N/A	0.042	N/A	0.04
Supply [V]	1.2	1.2	0.8	1	1	0.6	1
Power consumption [μW]	0.43	4.5	0.64	1.2	3.28	0.27	3.63
Gain [dB]	26	31.8	49 **	26	26.4	14-28***	34.3
BW [Hz]	80-15k	0.1-5k	100* - 6.2k	10-8k	1-8.2k	6.4-4.46k	2-5.6k
C_F [fF]	N/A	300	N/A	500	350	100	208
Input-referred noise [μV_{rms}]	8.1	6.5	14	7.5	4.13	10.68	6.1
Noise BW [Hz]	80-15k	10-5k	100* - 6.2k	100-10k	1-8.2k	1-10k	1-5.6k
NEF	1.52	7.2	6.5	3.6	3.19	1.79***	6.1
CMRR [dB]	>60	75	59	N/A	>90 @100Hz	61.3	66.3****
PSRR [dB]	>80	N/A	71	N/A	78 @1kHz	77.2	88****
THD	0.05% @10 mV_{pp}	-51dB @1KHz 0.7 V_{opp}	@1mV_{pp} < 0.4%	N/A	1% 0.7mV_p	0.5% @ 200 mV_{opp}	< 1% @1KHz 2mV_{pp}

*Estimated. **This gain is reported for two stages. All other gains are reported for the first stage. ***Single CCIA. ****Simulation result.

of the OTA. Also, because of less short channel effects in thick-oxide MOS transistors, the linearity and THD of the amplifier are improved.

4.2. *In vitro* Neural Recording

We used this neural amplifier for neural recordings in an *in vitro* experiment on the slices of a mouse brain at the faculty of Dentistry at University of Montreal. A micropipette is used to capture the electrical activity of the brain. The micropipette is filled with NaCl (0.5 mol) without bubbles. This micropipette contains a metal electrode of AgCl which records the extracellular APs of the brainstem of the mouse brain slice. The brain slice is inserted and fixed in a chamber which contains artificial cerebrospinal fluid (ACSF) which is continuously oxygenated and kept humid to mimic a real brain environment and to keep the neurons alive for a few hours. The micropipette is gradually penetrated into the brainstem tissue by means of a microscope and its peripheral tools.

To complete the test setup, the AgCl electrode of the micropipette is connected to the non-inverting input of the prototype amplifier. The connection of the chamber, including the ACSF, is connected to the inverting port of the amplifier as a Vref. It should be noted that shielded wires are utilized to perform these connections. A commercial setup of a neural recording system containing an instrumentation amplifier (A-M systems, Inc.), rack mounted data acquisition equipment and a PC with a spike2 Windows-based software (version 5.19, Cambridge Electronic design) was utilized. The output of the proposed amplifier is connected to the commercial amplifier. The commercial amplifier is a band pass amplifier with a midband gain of 100 (V/V) and with low and high cutoff frequencies of 300 Hz and 5 kHz, respectively. Setting the low-cutoff frequency at 300 Hz allows us to eliminate the LFP and extract the extra cellular APs from the output signal. By using the commercial amplifier as the second stage amplifier, the total gain is achieved at 5,300 V/V. During the test procedure, the amplified signal is sampled with a frequency of 10 kS/s and digitized by the mentioned data acquisition equipment and transferred to the PC. Spike2 was used to observe the captured data in the PC. **Figure 20** illustrates the recorded spontaneous extra cellular APs from the brainstem of the mouse with the proposed neural amplifier.

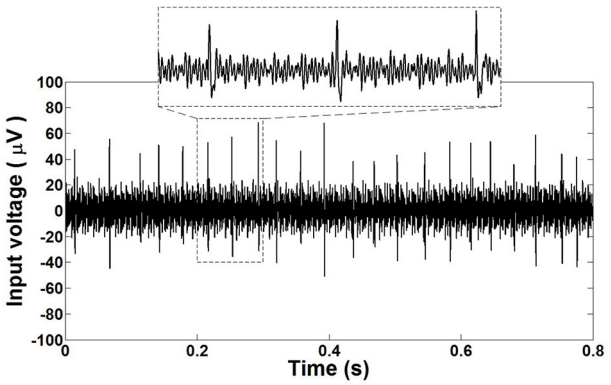

FIGURE 20 | Recorded extracellular APs extracted from the brainstem of a mouse with the fabricated neural amplifier.

5. CONCLUSION

Scaling down technology introduces new challenges in neural amplifier design. One main challenge is the increased low-cutoff frequency (f_L) of the AC-coupled amplifiers, assuming the same feedback capacitance value is used. The simplest

solution is to increase the feedback capacitors. However, this comes at the cost of increased input capacitors for the same gain of the amplifier, which increases the silicon area and decreases the input impedance of the amplifier. Assuming a neural recording implant requires a large array of these amplifiers, the total consumption of the silicon area increases dramatically.

In this paper, we focus on this challenge, find its roots, and propose solutions to improve it. Scaling down the technology increases the leakage current of the differential pair of the OTA due to decreasing the gate oxide thickness (short channel effects). This is translated to decreasing the input resistance (R_i) of OTA. We show, through simulations backed by an analytical analysis, that decreasing R_i is the fundamental reason for the increase in f_L. Two different solutions are presented in this paper to increase R_i: applying a cross-coupled positive feedback architecture and utilizing thick-oxide PMOS transistors in a differential pair of the OTA. The simulations confirm that both of the solutions decrease the f_L. We designed and fabricated the latter solution in the 65 nm TSMC process. The experimental results show that the low-cutoff frequency decreases to 2 Hz with 208 fF feedback capacitor (C_F). The neural amplifier is verified by *in vitro* experiment on mouse brainstem slices.

DATA AVAILABILITY STATEMENT

The original contributions presented in the study are included in the article/supplementary material, further inquiries can be directed to the corresponding author/s.

AUTHOR CONTRIBUTIONS

All authors listed have made a substantial, direct and intellectual contribution to the work, and approved it for publication.

REFERENCES

Abdelhalim, K., Kokarovtseva, L., Velazquez, J. L. P., and Genov, R. (2013). 915-MHz FSK/OOK wireless neural recording SoC with 64 mixed-signal FIR filters. *IEEE J. Solid State Circ.* 48, 2478–2493. doi: 10.1109/JSSC.2013.2272849

Bagheri, A., Salam, M. T., Velazquez, J. L. P., and Genov, R. (2017). Low-frequency noise and offset rejection in DC-coupled neural amplifiers: a review and digitally-assisted design tutorial. *IEEE Trans. Biomed. Circ. Syst.* 11, 161–176. doi: 10.1109/TBCAS.2016.2539518

Biederman, W., Yeager, D. J., Narevsky, N., Koralek, A. C., Carmena, J. M., Alon, E., et al. (2013). A fully-integrated, miniaturized (0.125 mm^2) 10.5 μW wireless neural sensor. *IEEE J. Solid State Circ.* 48, 960–970. doi: 10.1109/JSSC.2013.2238994

Biederman, W., Yeager, D. J., Narevsky, N., Leverett, J., Neely, R., Carmena, J. M., et al. (2015). A 4.78 mm^2 fully-integrated neuromodulation soc combining 64 acquisition channels with digital compression and simultaneous dual stimulation. *IEEE J. Solid State Circ.* 50, 1038–1047. doi: 10.1109/JSSC.2014.2384736

Cabrera, C., Caballero, R., Costa-Rauschert, M. C., Rossi-Aicardi, C., and Oreggioni, J. (2020). "Low-voltage low-noise high-CMRR biopotential integrated preamplifier," in *IEEE Transactions on Circuits and Systems I: Regular Papers*, 1–10.

Cook, M. J., O'Brien, T. J., Berkovic, S. F., Murphy, M., Morokoff, A., Fabinyi, G., et al. (2013). Prediction of seizure likelihood with a long-term, implanted seizure advisory system in patients with drug-resistant epilepsy: a first-in-man study. *Lancet Neurol.* 12, 563–571. doi: 10.1016/S1474-4422(13)70075-9

Denison, T., Consoer, K., Santa, W., Avestruz, A.-T., Cooley, J., and Kelly, A. (2007). A 2 μW 100 nV/$\sqrt{Hz}$ chopper-stabilized instrumentation amplifier for chronic measurement of neural field potentials. *IEEE J. Solid State Circ.* 42, 2934–2945. doi: 10.1109/JSSC.2007.908664

Enz, C. C., Krummenacher, F., and Vittoz, E. A. (1995). An analytical MOS transistor model valid in all regions of operation and dedicated to low-voltage and low-current applications. *Analog Integr. Circ. Signal Process.* 8, 83–114. doi: 10.1007/978-1-4615-2283-6_7

Farouk, T., Dessouky, M., and Elkhatib, M. (2020). A fabrication of a low-power low-noise neural recording amplifier based on flipped voltage follower. *Microelectron. J.* 101:104817. doi: 10.1016/j.mejo.2020.104817

Fifer, M., Acharya, S., Benz, H., Mollazadeh, M., Crone, N., and Thakor, N. (2012). Toward electrocorticographic control of a dexterous upper limb prosthesis: building brain-machine interfaces. *IEEE Pulse* 3, 38–42. doi: 10.1109/MPUL.2011.2175636

Harrison, R. R., and Charles, C. (2003). A Low-power low-noise CMOS amplifier for neural recording applications. *IEEE J. Solid-State Circ.* 38, 958–965. doi: 10.1109/JSSC.2003.811979

Hashemi Noshahr, F., Nabavi, M., and Sawan, M. (2020). Multi-channel neural recording implants: a review. *Sensors* 20:904. doi: 10.3390/s20030904

Hashemi Noshahr, F., and Sawan, M. (2017). "A compact and low power bandpass amplifier for low bandwidth signal applications in 65-nm CMOS," in *IEEE International Symposium on Circuits and Systems (ISCAS)*, (Baltimore, MD: IEEE), 1–4.

Jomehei, M. G., and Sheikhaei, S. (2019). A low-power low-noise CMOS bio-potential amplifier for multi-channel neural recording with active DC-rejection and current sharing. *Microelectron. J.* 83, 197–211. doi: 10.1016/j.mejo.2018.11.021

Kassiri, H., Abdelhalim, K., and Genov, R. (2013). "Low-distortion super-GOhm subthreshold-MOS resistors for CMOS neural amplifiers," in *Biomedical Circuits and Systems Conference (BioCAS)*, (IEEE), 270–273.

Kim, J., and Ko, H. (2019). Self-biased ultralow power current-reused neural amplifier with on-chip analog spike detections. *IEEE Access* 7, 109792–109803. doi: 10.1109/ACCESS.2019.2933674

Lee, B., Jia, Y., Mirbozorgi, S. A., Connolly, M., Tong, X., Zeng, Z., et al. (2019). An inductively-powered wireless neural recording and stimulation system for freely-behaving animals. *IEEE Trans. Biomed. Circ. Syst.* 13, 413–424. doi: 10.1109/TBCAS.2019.2891303

Luan, L., Robinson, J. T., Aazhang, B., Chi, T., Yang, K., Li, X., et al. (2020). Recent advances in electrical neural interface engineering: minimal invasiveness, longevity, and scalability. *Neuron* 108, 302–321. doi: 10.1016/j.neuron.2020.10.011

Luo, D., Zhang, M., and Wang, Z. (2019). A low-noise chopper amplifier designed for multi-channel neural signal acquisition. *IEEE J. Solid State Circ.* 54, 2255–2265. doi: 10.1109/JSSC.2019.2913101

Mollazadeh, M., Murari, K., Cauwenberghs, G., and Thakor, N. V. (2009). Wireless micropower instrumentation for multimodal acquisition of electrical and chemical neural activity. *IEEE Trans. Biomed. Circ. Syst.* 3, 388–397. doi: 10.1109/TBCAS.2009.2031877

Muller, R., Gambini, S., and Rabaey, J. M. (2012). A 0.013 mm^2, 5 μW, DC-Coupled neural signal acquisition IC with 0.5 V supply. *IEEE J. Solid State Circ.* 47, 232–243. doi: 10.1109/JSSC.2011.2163552

Musk, E. (2019). An integrated brain-machine interface platform with thousands of channels. *BioRXiv* 703801. doi: 10.2196/16194

Najafi, K., and Wise, K. D. (1986). An implantable multielectrode array with on-Chip signal processing. *IEEE J. Solid State Circ.* 21, 1035–1044. doi: 10.1109/JSSC.1986.1052646

Ng, K. A., and Xu, Y. P. (2012). "A compact, low input capacitance neural recording amplifier with C_{in}/Gain of 20 fF.V/V," in *Biomedical Circuits and Systems Conference (BioCAS)*, (IEEE), 328–331.

Ng, K. A., and Xu, Y. P. (2013). A compact, low input capacitance neural recording amplifier. *IEEE Trans. Biomed. Circ. Syst.* 7, 610–620. doi: 10.1109/TBCAS.2013.2280066

Ng, K. A., and Xu, Y. P. (2016). A low-power, high cmrr neural amplifier system employing cmos inverter-based otas with cmfb through supply rails. *IEEE J. Solid State Circ.* 51, 724–737. doi: 10.1109/JSSC.2015.2512935

Razavi, B. (2005). *Design of Analog CMOS Integrated Circuits*. New York, NY: McGraw-Hill Education.

Rezaee-Dehsorkh, H., Ravanshad, N., Lotfi, R., Mafinezhad, K., and Sodagar, A. M. (2011). Analysis and design of tunable amplifiers for implantable neural recording applications. *IEEE Trans. Emerg. Sel. Top. Circ. Syst.* 1, 546–556. doi: 10.1109/JETCAS.2011.2174492

Samiei, A., and Hashemi, H. (2019). A chopper stabilized, current feedback, neural recording amplifier. *IEEE Solid State Circ. Lett.* 2, 17–20. doi: 10.1109/LSSC.2019.2916754

Schwartz, A. B., Cui, X. T., Weber, D. J., and Moran, D. W. (2006). Brain-controlled interfaces: movement restoration with neural prosthetics. *Neuron* 52, 205–220. doi: 10.1016/j.neuron.2006.09.019

Shoaran, M., Kamal, M. H., Pollo, C., Vandergheynst, P., and Schmid, A. (2014). Compact low-power cortical recording architecture for compressive multichannel data acquisition. *IEEE Trans. Biomed. Circ. Syst.* 8, 857–870. doi: 10.1109/TBCAS.2014.2304582

Song, S., Rooijakkers, M., Harpe, P., Rabotti, C., Mischi, M., Van Roermund, A., et al. (2013). "A 430nw 64nv/vhz current-reuse telescopic amplifier for neural recording applications," In *2013 IEEE Biomedical Circuits and Systems Conference (BioCAS)*, (Rotterdam: IEEE), 322–325.

Stevenson, I. H. and Kording, K. P. (2011). How advances in neural recording affect data analysis. *Nat. Neurosci.* 14:139. doi: 10.1038/nn.2731

Sun, F., Morrell, M., and Wharen, R. J. (2008). Responsive cortical stimulation for the treatment of epilepsy. *Neurotherapeutics* 5, 68–74. doi: 10.1016/j.nurt.2007.10.069

Van Rijn, A. C. M., Peper, A., and Grimbergen, C. A. (1991). High-quality recording of bioelectric events. *Med. Biol. Eng. Comput.* 29, 433–440. doi: 10.1007/BF02441666

Verma, N., Shoeb, A., Bohorquez, J., Dawson, J., Guttag, J., and Chandrakasan, A. P. (2010). A micro-power EEG acquisition SoC with integrated feature extraction processor for a chronic seizure detection system. *IEEE J. Solid State Circ.* 45, 804–816. doi: 10.1109/JSSC.2010.2042245

Xiao, Z., Tang, C.-M., Dougherty, C. M., and Bashirullah, R. (2010). "A 20μw neural recording tag with supply-current-modulated afe in 0.13 μm cmos," in *2010 IEEE International Solid-State Circuits Conference-(ISSCC)* (IEEE), 122–123.

Xu, J., Yazicioglu, R. F., Grundlehner, B., Harpe, P., Makinwa, K. A., and Van Hoof, C. (2011). A 160 μW 8-channel active electrode system for EEG monitoring. *IEEE Trans. Biomed. Circ. Syst.* 5, 555–567. doi: 10.1109/TBCAS.2011.2170985

Yazicioglu, R. F., Kim, S., Torfs, T., Kim, H., and Van Hoof, C. (2011). A 30 μW analog signal processor ASIC for portable biopotential signal monitoring. *IEEE J. Solid State Circ.* 46, 209–223. doi: 10.1109/JSSC.2010.2085930

Yazicioglu, R. F., Merken, P., Puers, R., and Van Hoof, C. (2008). A 200 μW eight-channel EEG acquisition ASIC for ambulatory EEG systems. *IEEE J. Solid State Circ.* 43, 3025–3038. doi: 10.1109/JSSC.2008.2006462

Zou, X., Xu, X., Yao, L., and Lian, Y. (2009). A 1-v 450-nw fully integrated programmable biomedical sensor interface chip. *IEEE J. Solid State Circ.* 44, 1067–1077. doi: 10.1109/JSSC.2009.2014707

Conflict of Interest: The authors declare that the research was conducted in the absence of any commercial or financial relationships that could be construed as a potential conflict of interest.

frontiers in Neuroscience

REVIEW
published: 14 June 2021
doi: 10.3389/fnins.2021.680938

Directions of Deep Brain Stimulation for Epilepsy and Parkinson's Disease

*Ying-Chang Wu[1], Ying-Siou Liao[1], Wen-Hsiu Yeh[2], Sheng-Fu Liang[1,3] and Fu-Zen Shaw[2,4]**

[1] Department of Computer Science and Information Engineering, National Cheng Kung University, Tainan, Taiwan, [2] Institute of Basic Medical Science, National Cheng Kung University, Tainan, Taiwan, [3] Institute of Medical Informatics, National Cheng Kung University, Tainan, Taiwan, [4] Department of Psychology, National Cheng Kung University, Tainan, Taiwan

Background: Deep brain stimulation (DBS) is an effective treatment for movement disorders and neurological/psychiatric disorders. DBS has been approved for the control of Parkinson disease (PD) and epilepsy.

Objectives: A systematic review and possible future direction of DBS system studies is performed in the open loop and closed-loop configuration on PD and epilepsy.

Methods: We searched Google Scholar database for DBS system and development. DBS search results were categorized into clinical device and research system from the open-loop and closed-loop perspectives.

Results: We performed literature review for DBS on PD and epilepsy in terms of system development by the open loop and closed-loop configuration. This study described development and trends for DBS in terms of electrode, recording, stimulation, and signal processing. The closed-loop DBS system raised a more attention in recent researches.

Conclusion: We overviewed development and progress of DBS. Our results suggest that the closed-loop DBS is important for PD and epilepsy.

Keywords: deep brain stimulation, PD, epilepsy, closed-loop, open loop

OPEN ACCESS

Edited by:
Takashi Tokuda,
Tokyo Institute of Technology, Japan

Reviewed by:
David Haslacher,
Charité–Universitätsmedizin Berlin, Germany
Vassiliy Tsytsarev,
University of Maryland, College Park, United States

***Correspondence:**
Fu-Zen Shaw
fzshaw@gmail.com

Specialty section:
This article was submitted to Neural Technology, a section of the journal Frontiers in Neuroscience

Received: *15 March 2021*
Accepted: *12 May 2021*
Published: *14 June 2021*

Citation:
Wu Y-C, Liao Y-S, Yeh W-H, Liang S-F and Shaw F-Z (2021) Directions of Deep Brain Stimulation for Epilepsy and Parkinson's Disease. Front. Neurosci. 15:680938. doi: 10.3389/fnins.2021.680938

INTRODUCTION

Deep brain stimulation (DBS) has been used since the 1980s for treatment of movement disorders. DBS has several apparent advantages over lesion therapy. It is reversible and provides superior symptom relief with fewer complications than lesions. DBS creates maximal efficacy by adjustment of treatment parameters after implantation and can be applied bilaterally while bilateral lesions usually lead to a high risk of side effects (Okun and Vitek, 2004). First used for Parkinson's disease, DBS is an FDA-approved treatment for Parkinson's disease (PD), essential tremor, and dystonia. It is estimated that DBS devices have been implanted in ∼150,000 patients with movement disorders of the United States (Benabid et al., 1987). This success has encouraged the use of DBS across a broad range of neuropsychiatric disorders. More recently, DBS has been approved for obsessive-compulsive disorder and medically refractory epilepsy. Effect of clinical trials studying the use of DBS for the treatment of major depression (Dandekar et al., 2018) and Alzheimer's disease (Lozano et al., 2016) have limited because of inconsistent outcomes for the majority of the aforementioned neuropsychiatric disorders. Several critical aspects of therapy remain unsolved, in particular, how, where and when stimulation should be delivered according to individual anatomical and pathophysiological differences. This review addresses these factors on patients with epilepsy or Parkinson's disease.

PD typically develops between the ages of 55–65 years. Approximately 0.3% of the general population is affected. Parkinson's disease is a neurodegenerative syndrome involving multiple motor and non-motor neural circuits in the basal ganglia (Lang and Lozano, 1998). Motor manifestations of the disorder commonly include a resting tremor, rigidity (stiffness), slowness of movements (bradykinesia), and shuffling steps. In addition to these classical symptoms, PD also has a multitude of non-motor manifestations, including disturbance of mood (e.g., depression, anxiety), cognition (dementia and frontal-lobe dysfunction), and autonomic dysfunction (e.g., sexual dysfunction or digestive problems). DBS is one of the most effective treatments for advanced PD. Conventional DBS using an open loop architecture targets at the subthalamic nucleus (STN) or globus pallidus interna (GPi) which provides, on average, only 40% improvement in the motor items. Paradoxically, DBS of the STN can worsen motor function by not only influencing pathological but also physiological neural activity (Chen et al., 2006). The potential of conventional DBS is often limited due to stimulation induced side effects. More alternative technologies have been suggested to minimize the worse complications of DBS in PDs.

Epilepsy is a common chronic neurological disorder characterized by spontaneous recurrent seizures and affects around 60 million patients worldwide (Engel, 2016). As many of 40% of these patients have drug-resistant epilepsy (DRE). The international League Against Epilepsy has proposed that DRE can be defined as a failure of adequate trials of at least 2 antiepileptic drugs that are appropriately chosen, used, and tolerated. Approximately 1 million people in the US continue to have seizures despite adequate treatment with antiseizure drugs, and DRE can be associated with severe disability and morbidity. The incidence of sudden unexpected death in epilepsy is higher in patients with medically resistant epilepsy than in a general population (Harden et al., 2017). The first-line treatment for DRE is respective surgery. However, when surgery is contraindicated or ineffective, DBS has emerged as an important treatment option. DBS involves the delivery of a predetermined (open-loop) program of electrical stimulation to deep brain structures via implanted electrodes connected with a pulse generator. DBS of the anterior nucleus of the thalamus (ANT) has been approved for the treatment of refractory epilepsy. Surgical (e.g., infection, hemorrhage and pain) and stimulation-related (e.g., headache, sleep disturbance and increased anxiety or depression) adverse effects are similar to those observed from DBS for movement disorders (Fisher and Velasco, 2014). Compared to PD, spontaneous seizures occur in some unexpected scenarios and are not continuous events to perform an open-loop DBS stimulation in patients with epilepsy due to several side effects. Prevalence of side effects strongly depends on the target nucleus and the anatomy and functionality of the surrounding tissues. As such, more commercial DBS device for PDs use an open-loop architecture (**Table 1**), and closed-loop configuration is highly selected for epilepsy (**Table 2**).

High-frequency DBS was thought to function as a reversible lesion by inhibiting neurons near the stimulating electrode (Laxpati et al., 2014). However, it has advantages over ablation including its reversibility, the ability to adjust stimulation setting to optimize efficacy and minimize side effects, the ability to perform bilateral procedures safely, and low risk of cognitive problems (Yu and Neimat, 2008). A critical aspect of DBS efficacy is patient selection and the appropriate target location based on patient's symptom profile, age and cognitive status. These choices greatly depend on the expertise of the surgical team and vary from center to center. Up to 50% of implanted patients can experience stimulation-induced side effects (Volkmann et al., 2009). Emerging technologies aim to minimize these side effects

TABLE 1 | Open-loop neural stimulation system.

	Medtronic	Abbott	Boston scientific	St. Jude
Device	Activa RC	Infinity 7	Vercise PC	Brio
FDA class	II	III	II	II
Volume (cm^3)	22.0	38.6	33.0	22
Stimulation site	DBS	DBS	DBS	DBS
Application	PD, Epilepsy	PD	PD	PD
Stimulation channels	8	16	16	16
Frequency (Hz)	2–250	2–240	2–250	2–240
Pulse width (μs)	6–450	20–500	20–450	50–500
Battery longevity (years)	9	4–5	15(US)–25(EU)	10
Battery type	Rechargeable	Non-rechargeable	Rechargeable	Rechargeable
MRI-compatible	Yes	Yes	Yes	No
Intensity	0–25.5 mA/0–10.5 V	0–12.75 mA	0–20 mA	0–12.75 mA
Data monitoring	Wireless	Wireless	Wireless	Wireless

DBS, Deep brain stimulation; N/R, Not Reported; PD, Parkinson's disease.

TABLE 2 | Closed-loop neural stimulation system.

	Neuropace	Medtronic	LivaNova
Device	RNS system	Activa PC + S	Aspire SR
FDA class	III	II	II
Volume (cm^3)	12.94	37.0	N/R
Stimulation site	DBS	DBS	Vagus Never stimulation
Application	Epilepsy	PD	Epilepsy
Stimulation channels	8	8	N/R
Frequency (Hz)	1–333	2–250	1–30
Pulse width (μs)	40–1,000	60–450	130–1,000
Battery longevity (years)	2–3.5	3–5	4–7
Battery type	Non-rechargeable	Non-rechargeable	Non-rechargeable
MRI-compatible	No	Yes	Yes
Intensity	0.5–12 mA	0–25.5 mA/0–10.5 V	Current/0–3.5 mA
Data monitoring	Wireless	Wireless	Wireless

DBS, Deep brain stimulation; N/R, Not Reported; PD, Parkinson's disease.

and increase efficacy of DBS. We review studies that provide alternative strategies to state-of-the-art DBS with different control policies. We emphasize important considerations for therapy safety that continuously adapt stimulation parameters according to a disease biomarker in a closed-loop configuration with a higher detection rate. In general, a DBS technology system consists of several components (**Figure 1**): electrical stimulation and required aspects of the closed-loop architecture (including recording, preprocessing, feature extraction, classification). This study reviews existing research efforts in signal acquisition, biomarker algorithms, and system integration to provide a solid foundation toward the future development of smart and fully embedded integrated circuits.

DBS SYSTEM OERVIEW

A DBS system is composed of one or more electrode leads implanted in the brain and extension wires tunneled underneath the skin to an implanted pulse generator (IPG) positioned below the collar bone (Miocinovic et al., 2013). There are two main functions of IPG devices: neural recording and stimulation. Owing to the extremely low amplitude of EEG signals, low-noise and low-power electronic design are necessary for recording and analysis (Ranjandish and Schmid, 2020). Subsequently, we introduce DBS electrodes technology, neural recording amplifier and electrical stimulation system in the following paragraphs.

Electrodes for DBS

Development of DBS electrodes for implantation into the human brain began in the mid-twentieth century in the interest of treating movement-related disorders. The crucial characteristics of an electrode include biocompatibility, inertness, durability, stability over time, surgical feasibility, good conductivity, electrical properties, tractability, appropriate current delivery and spatial configuration. The standard DBS electrode configuration consists of 1.27 mm diameter cylinder with four stimulating electrode contact. Each cylindrical contact is 1 mm in length and 0.5–1.0 mm pitch (Medtronic, Inc.). Each active electrode can emit a continuous spherical electric field radiating outward from the stimulation site. In recent years, several new electrode designs have been proposed allowing to arrange the electrical field perpendicular to the lead as a directional DBS (Steigerwald et al., 2019). For example, more simple models split up the conventional ring contacts in 3–4 segments spanning 90° or 120° to create horizontal current flow. That could modify the current threshold for beneficial and adverse effects, which depends on whether current is injected toward or away from the underlying anatomical structure (Anderson et al., 2018). Industry and clinicians hoped that the directional DBS would reduce

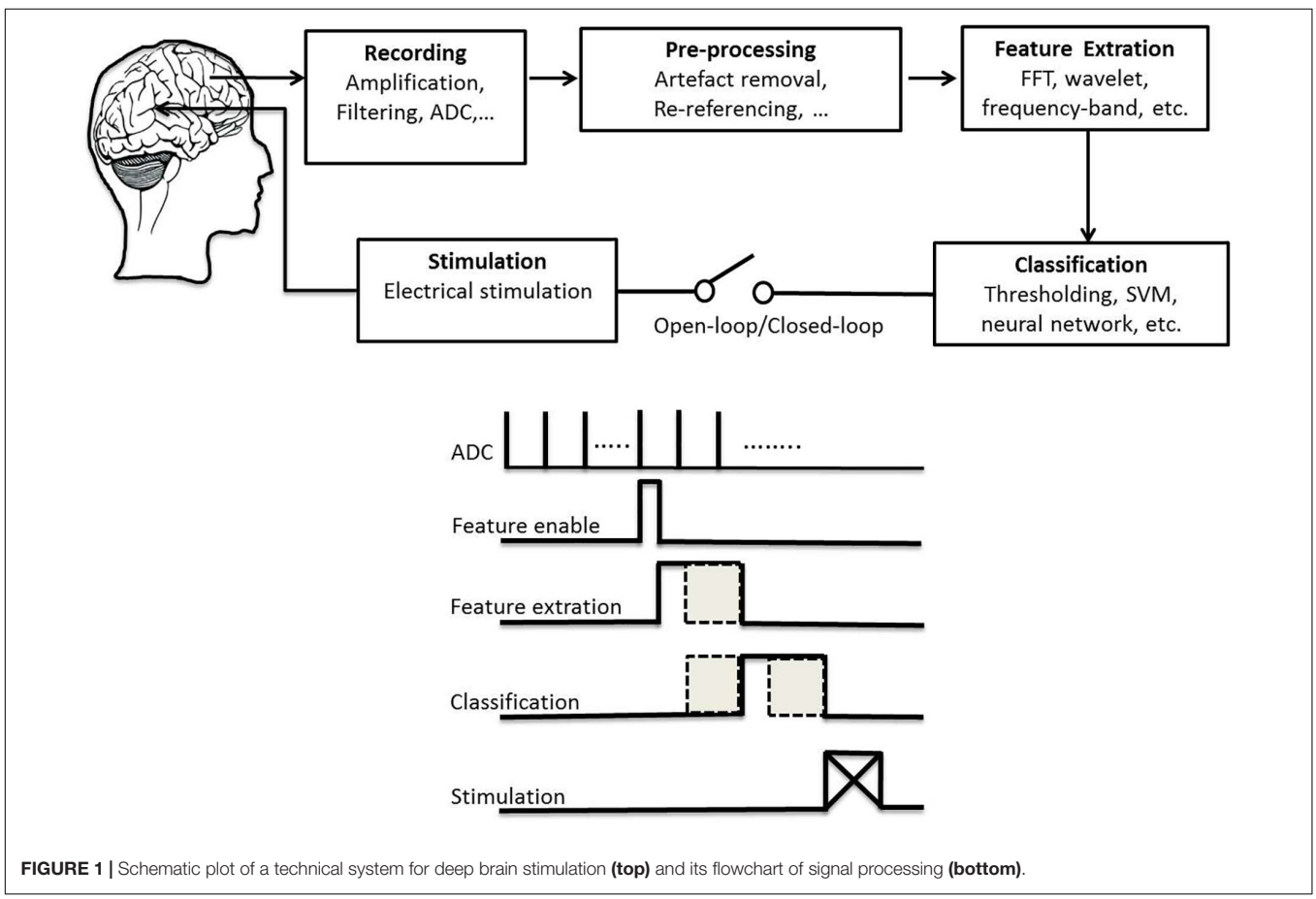

FIGURE 1 | Schematic plot of a technical system for deep brain stimulation **(top)** and its flowchart of signal processing **(bottom)**.

the risk of stimulation-induced adverse effects and optimize the clinical benefit of DBS. These segmented electrodes allow clinicians to modify side-effect thresholds and create a greater margin between symptom suppression and side-effect induction (Dembek et al., 2017).

Once a target is determined, the accuracy of stimulated site is critical so that the volume of tissue activated matches the target structure as best as possible. In addition to directional electrode design, thin-film planar arrays could provide further improvement to spatial specificity of stimulation and recording through reduced contact size and increased contact numbers (Connolly et al., 2015). Advancements in DBS electrode technology have seen large number of electrodes used to emit a directional, rather than uniformly spherical, which allows for unique and simultaneous electrical stimulation at different contacts (Krauss et al., 2020). Compared to silicon-based thin-film array, microwires have a more stable for a long-term recording and stimulation. Recently, three-dimensional microwire arrays combined with CMOS chips are developed for chronic recording and stimulation with a greater success in a long-term treatment (Obaid et al., 2020).

However, increased electrode numbers come with trade-offs. The greater flexibility afforded by segmented electrodes and thin planar arrays considerably increases the degrees of freedom allowed in programming to increase its sensitivity or specificity for DBS. This flexibility increases the burden on the clinical team because parameter selection and optimal stimulation contact most depend on a process of trial and error. Therefore, automated or support tools for assisting clinicians in determining optimal stimulation parameters are sorely needed. For example, it has recently been shown that the use of a disease biomarker, such as heightened rhythmic neural activity, can reduce the amount of time needed for programming segmented electrodes for the PD treatment (Fernández-García et al., 2017). Strategies that consider electrode location and anatomical landmarks in conjunction with individualized neuroimaging could provide additional information needed to reduce the degrees of freedom associated with programming DBS electrodes.

Numerous kinds of materials have been used for DBS electrodes. The choice electrode technology always has strong impact on an implantable neurostimulator's efficacy, efficiency, longevity, precision, and cost. The electrical inefficiency of platinum electrodes causes unnecessary power consumption and reduced battery lifetime. Increasing efficiency can extend implantation life and reduce battery size. Thus modern DBS implants can benefit from more efficient electrode materials (Petrossians et al., 2016). The platinum-iridium alloy expresses superior electrical properties (including minimal toxicity and excellent conduction property) and reveals wonderful mechanical robustness to insertion into brain for DBS.

Materials of the DBS electrodes and geometries are altered to attain low impedance path for charge injection, high charge transfer, and compromised spatial resolution. The electrode fabrication design parameters, e.g., shape, materials, and fabrication technique should be optimized to achieve the best electrode performance. Advantages and disadvantages of microwire or silicon array have been reviewed elsewhere (Ghane-Motlagh and Sawan, 2013). A small electrode size is required for multichannel stimulation, but this increases impedance and affects the signal-to-noise ratio. The electrode array increases insertion force during implementation into the brain. The estimated insertion force and mechanical failure modes are investigated for brittle and ductile materials (Gabran et al., 2014). The mechanical performance of the electrode array is primarily affected by the materials and geometry. A figure of merit in terms of mechanical performance, fabrication cost, geometry of the electrode, and cross sectional area of the electrode, etc., has been proposed to select the best electrode design parameters from different electrode arrays (including silicon, copper, nickel, polyimide materials; Draz et al., 2018).

In addition to different materials and geometries of the electrode, understanding electrochemical behavior of electrode materials and insulation in a long-term process is crucial (Gimsa et al., 2005). Corrosion resistance of the electrode metal is of greatest important for its long-term stability and biocompatibility. The electrode surface is not corroded uniformly because varied spatial distribution of the corrosion of metal and erosion of the plastics insulation regarding to the site dependence of the current density (Gimsa et al., 2006). Erosion of the plastics insulation is known as a severe problem, but it remains largely unknown so far.

Neural Recording Circuits

There are two main functions of implantable biomedical devices: neural recording and stimulation. Electroencephalogram (EEG), electrocorticogram (ECoG), local field potential or action potential is often used in the closed-loop design of an DBS. Because the extremely low amplitude of EEG signals, recording system with low-noise, low-offset, high CMRR and low-power characteristics is necessary for further analysis (Ranjandish and Schmid, 2020). Two principal categories of chopping schemes with instrumentation amplifier are designed. The AC-coupled chopped instrumentation amplifier can effectively reduce 1/f noise and amplifier offset with a CMRR of $>$ 120 dB, an input referred noise density of 57 nV/Hz, and power consumption of 60 μW (Yazicioglu et al., 2007). However, the DC-coupled amplifier limits the electrode offset to only $\pm$ 50 mV. On the other hand, a virtual ground node of the amplifier is designed to reject a large DC offset but scarifying with a CMRR of $\sim$60 dB (Verma et al., 2010), which is a remarkable drawback for multichannel recording. Amplifier circuits for data acquisition using the system on chip have been reviewed in detail elsewhere (Yang and Sawan, 2020).

In the closed-loop system, rejection of stimulation current-induced artifact has been emphasized. Careful placement of stimulation, recording, and reference electrodes, e.g., symmetrical configuration between electrodes, has shown to reduce the stimulation artifact of a common-mode-like signal by differential amplifier with high CMRR. A newer front-end technique has focused on mitigating the effects of stimulation artifacts by preventing saturation in a high-gain preamplifier. Alternatively, disconnecting the front-end via a series switch at the input prevent artifacts from the recording circuitry

(Venkatraman et al., 2009). However, this design can suffer from slow transient settling once reconnected. More advanced technologies to achieve artifact-free recording during stimulation have been reviewed previously (Zhou et al., 2018).

Neural Stimulation Techniques

DBS is very often to activate or inhibit neurons with implantable medical devices. The use of electrical stimulation in clinical practice requires a high degree of safety, stability, and programmability, and also takes into account the issues of voltage-power consumption and heat dissipation. There are two main modes of stimulation: current-mode and voltage-mode. Most of available commercial DBS devices offer the constant voltage stimulators due to higher power efficiency. At this moment, the magnitude of current depends on impedance between tissues and electrodes. The impedance variations in the brain tissue and the electrode-tissue interface always exist in various stages for DBS implementation. Impedance fluctuations have been observed during the first 3 months after surgery (Lempka et al., 2009). A mean 73 Ω/year reduction in impedance in most DBS electrode contacts has been recorded (Satzer et al., 2014). Unbalanced charging is more likely to happen in voltage stimulation and thus relatively lack of safety. Some "excess voltage" may result in gas evolution (e.g., hydrogen evolution at the cathode), redox reactions of organic molecules, and the deposition of potentially harmful materials (e.g., metal ions, chlorine and toxic organic products in the tissue; Gimsa et al., 2005). The constant current stimulation mode is extensively used in DBS. Adaptive currents are used to supply the stimulus current to the load. Total amount of charges injected in the current stimulation mode depend on the magnitude and duration of the stimulation current. Traditionally, the current intensity is set in the range of 0.5–15 mA for 0.3-ms pulse width. Compared with the constant voltage stimulation mode, constant current stimulation mode provides higher controllability and safety; however, lack of power efficiency is worth to be improved (Ortmanns et al., 2007; Sit and Sarpeshkar, 2007; Liu et al., 2008).

Neural stimulation is used to activate or modulate neural activity. When charge is continuously deposited onto an electrode, the resulting electric field becomes strong enough to trigger a response from neighboring neurons. The charge must be removed from the electrode to prevent build up possible permanent tissue damage. Biphasic stimulation is better for this operation rather than monophasic stimulation in DBS (Fung et al., 1998). A traditional charge balanced current stimulation has been widely used. There are at least three problems faced by this topology (Wu et al., 2018): mismatch between the two current sources, excess power consumption for supplied voltage, and large IC area consumption to support one stimulator per electrode. Each stimulator utilizes a single current source for both positive and negative stimulation phases to reduce current mismatch effect and to eliminate the need for calibration (Biederman et al., 2015). An adiabatic, charge-recycling architecture without utilizing off-chip components can minimize power consumption (Arfin and Sarpeshkar, 2011). Multiple supply voltages from DC-DC converter are utilized to minimize the power consumption throughout the stimulation cycle.

Continuous open-loop stimulation of DBS uses static stimulation parameters to measure behavioral or functional outcomes. As we can see in previous studies of PD (**Table 3**) or epilepsy (**Table 4**), continuous open-loop DBS is a popular design at the beginning. Common stimulation parameters of open-loop DBS are $\geq$ 100 Hz at 1–10 V for ANT stimulation for refractory temporal lobe epilepsy, $\geq$ 130 Hz at 1–5 V for hippocampus and STN stimulation for refractory temporal lobe epilepsy, tens to high frequency stimulation at 1–10 V for stimulation of centromedian nucleus of the thalamus for generalized tonic-clonic seizures. For PDs, 130–200 Hz at 2–5 V for STN and GPi stimulation. Cycling of 1 min on and 5 min off at 5 V with 145 Hz stimulation has been suggested for epilepsy. All stimulation parameters are designed in commercial products (**Table 1**). There is no difference between cycling and continuous stimulation and no association between output voltage and seizure reduction (Li and Cook, 2018). DBS-induced side effects can be reduced by minimizing the duration and intensity of stimulation or changing to bipolar mode.

On the other hand, the main motivation of closed-loop stimulation is minimization of treatment side effects by providing only the necessary stimulation required within time window, as determined from a guiding marker. The closed-loop stimulation usually uses a lower intensity and in turns limits any unwanted direct stimulation of nearby fiber tracts, such as those in the internal capsule for STN stimulation. Closed-loop stimulation could be essential not only to reverse direct side effects of stimulation, but also to minimize adverse effects due to combined pharmacological treatment as dyskinesia of dopaminergic medication in PDs (Arlotti et al., 2018). Adverse effects of DBS on sleep might decrease during a closed-loop stimulation of ANT for treatment of epilepsy (Voges et al., 2015).

Several kinds of closed-loop configurations are proposed. Firstly, closed-loop stimulation used feedback from peripheral signals, such accelerometers and/or electromyogram, are applied to automatically determine stimulation timing or intensity. For example, resting tremor is easily recorded using accelerometers providing potential source of feedback to modulate DBS (Cagnan et al., 2017). The scenario using accelerometers is also working in closed-loop seizure control (Chang et al., 2011). Secondly, closed-loop stimulation used local field potentials sensing from the same or nearby electrodes to automatically determine stimulation timing or intensity. For example, beta band ($\sim$20 Hz) of the STN can be tracked at the site of stimulation in PDs (Little et al., 2016). Thirdly, closed-loop stimulation used ECoGs sensing from the cortex to automatically determine stimulation timing or intensity. Gamma activity and beta activity of the motor cortex in the closed-loop stimulation are used to the control of dyskinesias (Swann et al., 2018) and tremor (Herron et al., 2016), respectively. The closed-loop control used DBS of the zona incerta regarding to cortical epileptiform activity is demonstrated to stop seizures in rats (Young et al., 2011).

In patients with epilepsy or PD, many brain areas appear rhythmic activity. In addition to provide an amplitude-related feedback in the closed-loop system, fluctuations in activity timing

TABLE 3 | Recording and stimulation system for PD.

Source	Platform	Channel (s)	Intensity	Control	Filter (Hz)	Clinical results (reduction)
McCreery et al. (2006)	N/A	16	0–0.0265 mA	O	N/A	N/A
Boulet et al. (2006)	N/A	N/A	0–0.35	O	10–200	N/A
Fang et al. (2006)	A-M System	N/A	0–0.2 mA	O	0–130	∼80% initiating time for STN DBS.
Gubellini et al. (2006)	P2MP, Marseille	N/A	0–0.08 mA	O	0–130	N/A
Baunez et al. (2007)	N/A	4	0–0.05 mA	O	0–130	77–85% correct response
Dorval et al. (2008)	N/A	N/A	2.4–4 V	O	0–136	Burst-duration in 67% bursting cells.
Harnack et al. (2008)	PIC16C54	1	0.05–0.6 mA	O	0–131	N/A
Winter et al. (2008)	N/A	N/A	0–0.3 mA	O	0–130	N/A
Lee et al. (2008)	N/A	64	0.003–0.135 mA	C	17–5.3 k	N/A
Paulat et al. (2011)	PIC16C54	N/A	0–0.1 mA	O	N/A	N/A
Nowak et al. (2011)	N/A	1	0–0.5 mA	O	0–130	N/A
Azin et al. (2011)	N/A	4	0–0.0945 mA	C	0–10 k	N/A
Loukas and Brown (2012)	NI DAQ	1	Unipolar (0–10 V), bipolar (± 5 V)	C	13–30	N/A
Forni et al. (2012)	N/A	1	0.05–0.12 mA	O	0–130	44% (2 weeks), 48% (5 weeks) for STN DBS
de Haas et al. (2012)	PICKIT 3	1	0.02–0.1 mA	O	0–131	N/A
Lee et al. (2013)	N/A	4	0.08–2.48 mA	O	N/A	N/A
Poustinchi and Musallam (2013)	N/A	N/A	N/A	O	0.1–100	N/A
Heo et al. (2015)	MSP430F2013,	2	0–3 V	O	N/A	N/A
Parastarfeizabadi et al. (2016)	MCU	1	0–0.2 mA	C	0–130	N/A
Arlotti et al. (2016)	MSP 430	1	0–3 V	C	N/A	∼30%
Herron et al. (2016)	Activa PC + S	1	0–2.5 V	C	N/A	Tremor for 84.5% samples
Little et al. (2016)	N/A	N/A	2.7 ± 0.2 V	C	N/A	N/A
Wu et al. (2017)	IEC 60601-1	1	N/A	C	12–30	N/A
Swann et al. (2018)	Activa PC + S	8	N/A	C	60–90	Energy saving 38–45%
Chen et al. (2018)	FPGA	16	0–0.25 mA	C	30–10 k	N/A
Jia et al. (2018)	N/A	16	0–10 mA	O	N/A	N/A
Zhou et al. (2019)	WAND	128	0–5 mA	C	1–200	N/A
Fleischer et al. (2020)	N/A	N/A	0–0.3 mA	O	100–500	N/A
Xu et al. (2020)	NI DAQ	1	0–0.06 4 mA	C	1–8 k	N/A

C, closed-loop; N/A, not available; O, open-loop.

(i.e., phase coupling) and/or strength (amplitude coupling) are crucial for network operation within different brain regions. Stimulation at a certain phase of neural activity can disrupt synchrony. This phase-specific DBS has shown to be effective in acutely suppressing tremor in a group of patients with essential tremor using ∼40% of total electrical energy associated with conventional high-frequency DBS (Cagnan et al., 2017). This stimulation approach has the potential to minimize DBS-induced side effects by reducing the amount of energy delivered into the brain.

In addition, adapting DBS is also proposed and characterized two approaches (Rosa et al., 2015). One is a binary approach with effective stimulation wither on or off. The other approach is a scalar method with stimulation voltage being varied up to therapeutic values. The stimulated voltage is not rapidly increased. For the binary on-off stimulation, it is managed by the incorporation of a ramping of stimulation onset and offset. With regard to the scalar stimulation approach, the stimulating value at sub-threshold voltages remains to be clarified. Consideration of patient behavior, such as sleep or walking, could also further aid in determining optimal stimulation patterns. For example, high-frequency stimulation at a certain period of the decision-making process impaired patient's behavior, suggesting that adapting stimulation timing according to patient behavior could limit such adverse effects (Herz et al., 2018). In summary, these observations highlight a potential new way for stimulation control. Tailoring stimulation is not only according to pathology and its circuit manifestations, but also according to everyday actions and behaviors of patients.

The present study has collected numerous literatures for DBS technology development in the open-loop and closed-loop manners on PD (**Table 3**) and epilepsy (**Table 4**). Most of studies in the open-loop architecture have described DBS effect on symptom reduction regarding to different stimulation sites. Clinical evaluation for the open-loop DBS effect on several PD symptoms regarding different stimulation sites has been reviewed previously (Benabid et al., 2009; Wong et al., 2019). More information of neurophysiological aspects and stimulation

TABLE 4 | Recording and stimulation system for epilepsy.

Source	Platform	Channel (s)	Clock (MHz)	Intensity	Control	Filter (Hz)	Clinical results (reduction)
Boon et al. (2001)	NCP	N/A	N/A	0–3.5 mA	O	1–143	50% in 1/3, 30–50% in 1/3 and no response in 1/3 samples
Velı̇ıŠek et al. (2002)	A-M Instruments	N/A	N/A	0–0.28 mA	O	0–130	N/A
Cohen-Gadol et al. (2003)	VNS system	N/A	N/A	0–8 mA	O	1–70	75% in 1/5 and 50% in 35% samples
Lopez-Meraz et al. (2004)	Paxions	1	N/A	0.1–0.5 mA	O	1	N/A
Kerrigan et al. (2004)	Medtronic itrel 2	N/A	N/A	1–10 V	O	0–130	50% in 4/5 samples after 3 months
Velasco et al. (2005)	Medtronic itrel 3	N/A	N/A	0–2.28 V	O	N/A	tonic seizures:43% after 24 months,
Cuellar-Herrera et al. (2006)	Paxions	N/A	N/A	0.12–0.66 mA	O	0–130	N/A
Boon et al. (2007)	Dual screen 3628	128	N/A	N/A	O	130–200	100% in 1/10, $>$ 90% in 1/10, $\geq$ 50% in 5/10, 30–49% in 2/10, no response in 1/10 samples
Avestruz et al. (2008)	N/A	4	N/A	0–0.01 mA	C	0–1 k	N/A
Halpern et al. (2009)	Medtronic itrel 2	N/A	N/A	4–5 V	C	90–130	∼45%
Boon et al. (2009)	VNS system	N/A	N/A	0–1 mA	O	N/A	40–50%, 100% in 5–10% samples
Jobst et al. (2010)	Minneapolis, MN	N/A	N/A	0.1–5 V	O	130–150	N/A
Kotagal (2011)	VNS system	N/A	N/A	0.25–3.5 mA	O	1–30 Hz	50% in 35%, 75% in 50% samples
Chen et al. (2011a)	FPGA	1	13.6	N/A	C	N/A	N/A
Chen et al. (2011b)	FPGA	4	402	N/A	C	0–3.2 k	N/A
Azin et al. (2011)	N/A	4	1	0–0.029 mA	O	0–10 k	N/A
Young et al. (2011)	CC2430	1	32	0.02–0.05 mA	C	0.8–72	N/A
Zanos et al. (2011)	Neurochip-2	3	N/A	0–5 mA	C	0.5–5 k	N/A
Chang et al. (2011)	CC2430	1	32	0–0.4 mA	C	0.8–80	N/A
Stanslaski et al. (2012)	Activa PC + S	4	N/A	0–25.5 mA	C	2–250	N/A
Bagheri et al. (2013)	FPGA-based	256	N/A	0.02–0.25 mA	O	0.5–500	92.8%
Chen et al. (2014)	BSP	8	81.92	0–0.03 mA	C	0.8–7 k	N/A
Lin et al. (2014)	N/A	N/A	25	0–0.04 mA	O	N/A	N/A
Liu et al. (2014)	PennBMBI	4	N/A	0–1 mA	C	300–6 k	N/A
Shoaran et al. (2015)	FPGA	16	N/A	N/A	C	30–1.7 k	N/A
Lin et al. (2016)	8051	1	10	8.25–229 μA	O	N/A	N/A
Do Valle et al. (2016)	N/A	8	N/A	N/A	C	0–500	N/A
Irwin et al. (2016)	ATMega 328p	16	8	N/A	C	0.1–20 k	N/A
Kassiri et al. (2017b)	GL060V5	24	10	0.01–1 mA	C	10–5 k	N/A
Xie et al. (2017)	CC2541	32	32	N/A	C	0–7.5 k	N/A
Cheng et al. (2018)	YBSP	16	N/A	0.5–3 mA	C	0.59–117	N/A
Hügle et al. (2018)	MSP430FR5994	N/A	8	N/A	C	N/A	N/A
Li and Cook (2018)	N/A	N/A	N/A	1–10	O	0–130	ANT: 46–90%; HC: 48–95%
Kassiri et al. (2019)	AGL 060V5	16	32	0.05–10 mA	O	N/A	N/A
Pazhouhandeh et al. (2019)	N/A	64	10	0–3 mA	C	0.1–5 k	N/A
Lee et al. (2020)	ATUC3C2256C	8	N/A	0–0.51 mA	C	0–150	N/A

ANT, anterior thalamus; C, closed-loop; HC, hippocampus; N/A, not available; O, open-loop; VNS, vagus nerve stimulation.

sites for open-loop DBS on epilepsy control has been reviewed elsewhere (Yan et al., 2019; Zangiabadi et al., 2019). The closed-loop stimulation system provides relatively limited information on long-term DBS effect yet. It may raise more attention in future evaluation of the closed-loop DBS in clinic.

Signal Processing Unit

For patients with PD or epilepsy, there is two major divisions for system architectures: open loop and closed-loop. In this section, we introduce development of system in terms of platform, recording channel, stimulation intensity and architecture, and verification of animal or humans. **Table 3** lists studies utilized in PDs. **Table 4** summarizes studies of epilepsy. For the open-loop architecture, the signal processing unit is emphasized on signal recording and analysis which is separated from stimulation. In a closed-loop architecture, the signal processing unit and stimulation is interacted each other. As shown in the bottom panel of **Figure 1**, the closed-loop system exhibits a timing-schedule processing from recording, feature enable (by threshold of data length or particular waveform amplitude), feature extraction, and classification. From system development viewpoint, system development for the open loop configuration is progressively decreased (**Figure 2**). Instead, studies of the closed-loop architecture have increased recently in the application

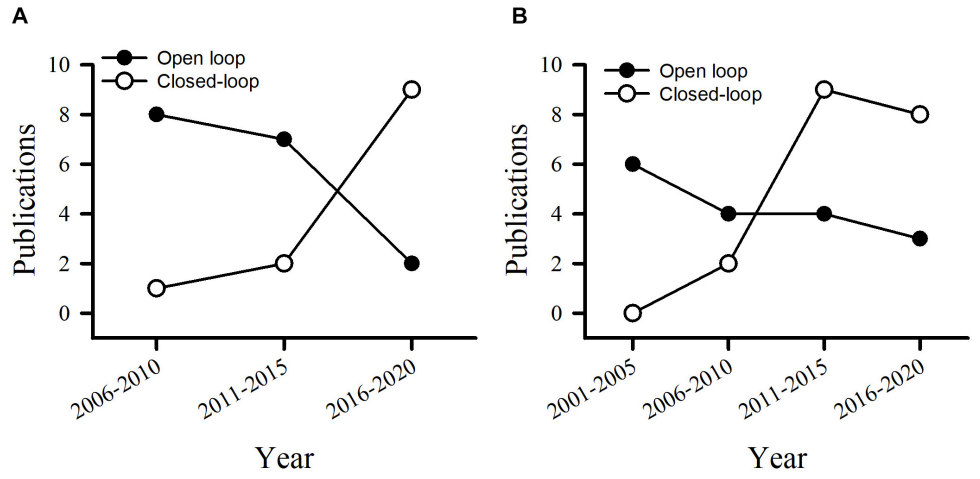

FIGURE 2 | Publications utilizes the open loop and closed-loop architecture in the control of PD **(A)** and epilepsy **(B)**.

of PD (**Figure 2A**) and epilepsy (**Figure 2B**). The closed-loop concept for epilepsy seems to be earlier than PD studies, which reflects more available closed-loop commercial device for epilepsy compared with PD (**Tables 1**, **2**).

There are two major streams for signal processing. One focuses on process and stimulation at the same site or neighboring area. The other is recording and processing of multiple brain regions and/or other accessories which is away from the stimulation region. For the first design, small amount of recording channels is needed and usually integration of recording and stimulation electrodes together. In this system configuration, studies often use features from a local brain region, such as STN or GPi for PD and hippocampus for temporal lobe epilepsy. It has an advantage of better understanding for characteristics of this local brain region in response to PD or epilepsy. However, neurodegeneration within this local region may result in progressive reduction of therapeutic effect. For the second system configuration, these studies have a great capacity to record and analyze signals from bulks of field potentials or neuronal activities from various brain regions. Increased channels and memory with a fast system clock is a crucial requirement. Recently, hundreds of recording electrodes coincident with efficient channel architecture for amplifier and analysis have been developed (Kassiri et al., 2017a; Zhou et al., 2019).

Two major signal processing systems [i.e., microcontroller unit (MCU) and system on a chip (SoC)] are developed. At the early stage, MCU has been developed and widely used since 1980s. The MCU system generally consists of four parts: a central processing core, program storage memory, data storage memory and one or more timers/counters with different resolutions. For example, a mobile single-channel wireless closed-loop epileptic seizure detector uses Texas Instrument's CC2430 module as the MCU and has demonstrated its advantage on seizure control in freely moving rats (Young et al., 2011). To reduce power consumption and minimize the size of the system, configuration of system-on-chip (SoC) has been developed for years. A SoC contains a MCU, a flash memory, necessary capacitors, resistors, oscillators and other components, making it ultra-small and low power consumption. Detail SoC architecture can see in previous reviews (Wu et al., 2018; Yang and Sawan, 2020).

In a closed-loop architecture, feature extraction process with effective classification algorithm plays an important role in attaining efficient control of PD symptoms or seizures. The goal of the feature extraction process is to derive a biomarker from electrophysiological or behavioral signals that are unique during the defined state but not occurring at other states. Frequency domain features are the most commonly used features in previous studies of both PD (**Table 5**) and epilepsy (**Table 6**). Available features in the frequency domain are power or amplitude of particular bands, discrete wavelet analysis for instantaneous power of particular bands, etc. Movement event-related potential has been transferred into 17-dimensional features (Meyer wavelet scales: 9–27) to quantify 13–30 Hz in PD (Loukas and Brown, 2012). Beta frequency power is mostly used as biomarker for the control of PD symptom (**Table 5**). In contrast, frequency powers of various bandwidths are used for seizure detection or prediction in a closed-loop architecture (**Table 6**). Multiple features, such as approximated entropy and coastline, are used in the control of epilepsy.

In addition to feature extraction, various classification methods, such as support vector machine, regression classifiers, linear square classifier, etc., have been used in previous studies (Zhou et al., 2019; Yang and Sawan, 2020). Recently, convolutional neural network (CNN) is composed of convolution, pooling and fully connected layers. Currently, most CNN algorithms are higher complexity and executed using CPU or GPUs. A network architecture called SeizureNet on a low-power processing microcontroller unit to predict seizure (Hügle et al., 2018). There is another low-power CNN processor (TrueNorth developed by IBM) has been used for seizure detection (Merolla et al., 2014). Other detail classifiers in a closed-loop architecture has been reviewed elsewhere (Yang and Sawan, 2020).

TABLE 5 | The closed-loop stimulation system for PD.

Source	Platform	Clock (MHz)	Filter (Hz)	Feature
Lee et al. (2008)	N/A	0.2	17–5.3 k	Amplitude of 10–50 Hz
Azin et al. (2011)	N/A	1	0–10 k	Amplitude of 20–40 Hz
Loukas and Brown (2012)	NI DAQ	N/A	N/A	Meyer'wavelet for instantaneous bandpower (13–30 Hz)
Parastarfeizabadi et al. (2016)	MCU	N/A	0–130	Amplitude of 13–35 Hz
Arlotti et al. (2016)	MSP 430	N/A	N/A	Bandpower (10–16 Hz)
Herron et al. (2016)	Activa PC + S	N/A	N/A	Bandpower (20–32 Hz)
Little et al. (2016)	N/A	N/A	N/A	Bandpower (12–30 Hz)
Wu et al. (2017)	IEC 60601-1	13.56	12–30	Bandpower (4–64 Hz) and entropy
Swann et al. (2018)	Activa PC + S	N/A	60–90	Bandpower (80 ± 2.5 Hz)
Chen et al. (2018)	FPGA	N/A	30–10 k	Amplitude of 20–40 Hz
Zhou et al. (2019)	WAND	166	1–200	Bandpower (0–4 and 4–7 Hz)
Xu et al. (2020)	NI DAQ	N/A	1–8 k	AP probability mapping

AP, action potential; N/A, not applicable.

TABLE 6 | The closed-loop stimulation system for epilepsy.

Source	Platform	Clock (MHz)	Filter (Hz)	Feature
Avestruz et al. (2008)	N/A	N/A	0–500	Bandpower (15–40 Hz)
Halpern et al. (2009)	RNS	N/A	1–333	Bandpower (1–4, 4–8, 8–13, 13–25, and 20–50, > 50 Hz), total power, spike
Chen et al. (2011a)	FPGA	402	N/A	Bandpower (7–9 and 14–18 Hz) and ApEn
Chen et al. (2011b)	FPGA	402	0–3.2 k	Bandpower (7–9 Hz and harmonics) and ApEn
Young et al. (2011)	CC2430	32	0.8–72	Bandpower (7–9 and 14–18 Hz) and ApEn
Zanos et al. (2011)	Neurochip-2	N/A	0.5–5 k	Bandpower (10–20 Hz)
Chang et al. (2011)	CC2430	32	0.8–72	Bandpower (10–20 Hz)
Stanslaski et al. (2012)	Activa PC + S	N/A	0–250	Bandpower (beta band, ∼80 Hz)
Chen et al. (2014)	BSP	3.125	0.8–7 k	entropy and Bandpower (0.8–10 Hz)
Liu et al. (2014)	PennBMBI	N/A	300–6 k	Spike detection
Shoaran et al. (2015)	FPGA	N/A	30–1.7 k	Channel-based coastline features (linelength)
Do Valle et al. (2016)	N/A	8	0–500	Bandpower (0.5–4,:4–8,:8–13, and 13–30 Hz)
Irwin et al. (2016)	ATMega 328p	8	0.1–20 k	Bandpower (75–150 Hz)
Kassiri et al. (2017b)	GL060V5	10	10–5 k	Magnitude and Phase of FIR and Hilbert filter
Xie et al. (2017)	CC2541	32	0–7.5 k	Spike amplitude > 150 μV
Cheng et al. (2018)	BSP	N/A	0.59–117	Bandpower (7–9 and 14–18 Hz)
Hügle et al. (2018)	MSP430FR5994	8	N/A	Intrinsic mode functions
Pazhouhandeh et al. (2019)	N/A	10	0.5–10 k	Bandpower and heart rate
Lee et al. (2020)	MCU	2	0–150	ApEn and power (5, 10, and 15 Hz)

ApEn, approximate entropy; FIR, finite impulse response.

DISCUSSION AND FUTURE PROSPECTS

We are witnessing a rapid expansion in the development of implantable DBS devices for clinical uses. Because of their complexity they are classified by regulatory bodies into the highest risk category for implantable device (Class III) and are required to complete a very rigorous regulatory approval process before clinical use. Preclinical studies (including animal verification) form an important component of this approval process. The present review describes various components in the open loop and closed-loop configuration that are available to researchers when considering to demonstrate device safety and effectiveness.

In the near future, trends of automation and effective information processing, as well as device miniaturization are anticipated. In addition to advanced development of circuit and IC production, low-noise and low-power chopping amplifier and SoC is existing. Numerous systems that can record EEG, ECoG or neuronal activities have increasingly reliable and accurate detection or prediction algorithms. These systems exhibit a great increased capacity for channels and memory size. A closed-loop configuration for DBS or stimulation of the cortex or peripheral nervous system expresses numerous advantages, including minimal adverse effect, reduced potential damage, increased battery life, and preserved daily regular activity. Rechargeable neurotherapy systems are more economical and lower complication than non-rechargeable devices (Chwalek et al., 2015). The main challenge in the design of rechargeable implantable devices is how to efficiently recharge the implantable battery and avoid highly

increased temperatures during the charging process, which may cause skin burns.

The present study has shown an important trend for the closed-loop DBS in PD and epilepsy. Spatial selectivity is enhanced through higher resolution electrodes to increase accuracy. The closed-loop DBS is away from monotonic high-frequency stimulation and advocates dynamic stimulation in response to valuable features. These development directs us closer to the individual therapy that tracks clinical state. However, more sophisticated control requires a greater understanding of pathophysiology to allow the development of useful biomarkers and dictate stimulation. Numerous features are considered as biomarkers compared with a healthy control. It raises a problem about feature reliability throughout the entire DBS progression. Effective DBS alters brain activity progressively then leads to reduction of sensitivity and specificity in electrophysiological feature characteristics and anatomical alteration (Little and Brown, 2012). Meanwhile, intra-subject and inter-subject variability occurs in our day-by-day conditions (Saha and Baumert, 2020). Secure telemetry allows patients continuous wireless upload of data, which would allow more continuous patient assessments and more intricate control using distributed cloud computing system. At the same time, such a system integrates data from other sensors to provide summaries that aid decision-making and prevent clinicians from being overloaded from intensive information. Thus, adapting control algorithms should mature while maintaining tractability.

In the long-term, it is likely that brain stimulation therapies will be disrupted by advancing technology. For example, minimally invasive methods such as transcranial ultrasound are enabling non-invasive ablation of neural circuits for tremor (Lipsman et al., 2013). It may provide many DBS benefits without requirement of cranial surgery 1 day. A hybrid method combined distributed ultrasound systems replacing physically tethered leads may enable a considerable neural interfere to create similar DBS advantages.

AUTHOR CONTRIBUTIONS

Y-CW, S-FL, and F-ZS involved in project administration, study conceptualization, designed the manuscript, and assessed the literature. Y-CW and F-ZS wrote the first draft of the manuscript. Y-CW, W-HY, and F-ZS edited the subsequent drafts and revisions. All authors contributed to the article and approved the submitted version and involved in the supply of the materials.

FUNDING

This work was supported by the Ministry of Science and Technology, Taiwan (MOST108-2321-B-006-024-MY2, MOST109-2627-H-006-005, and MOST109-2634-F-006-013).

REFERENCES

Anderson, D. N., Osting, B., Vorwerk, J., Dorval, A. D., and Butson, C. R. (2018). Optimized programming algorithm for cylindrical and directional deep brain stimulation electrodes. *J. Neural Eng.* 15:026005. doi: 10.1088/1741-2552/aaa14b

Arfin, S. K., and Sarpeshkar, R. (2011). An energy-efficient, adiabatic electrode stimulator with inductive energy recycling and feedback current regulation. *IEEE Trans. Biomed. circ. Syst.* 6, 1–14. doi: 10.1109/tbcas.2011.2166072

Arlotti, M., Marceglia, S., Foffani, G., Volkmann, J., Lozano, A. M., Moro, E., et al. (2018). Eight-hours adaptive deep brain stimulation in patients with Parkinson disease. *Neurology* 90, e971–e976.

Arlotti, M., Rossi, L., Rosa, M., Marceglia, S., and Priori, A. (2016). An external portable device for adaptive deep brain stimulation (aDBS) clinical research in advanced Parkinson's disease. *Med. Eng. Phys.* 38, 498–505. doi: 10.1016/j.medengphy.2016.02.007

Avestruz, A.-T., Santa, W., Carlson, D., Jensen, R., Stanslaski, S., Helfenstine, A., et al. (2008). A 5$\mu $ W/channel spectral analysis IC for chronic bidirectional brain–machine interfaces. *IEEE J. Solid State Circ.* 43, 3006–3024. doi: 10.1109/jssc.2008.2006460

Azin, M., Guggenmos, D. J., Barbay, S., Nudo, R. J., and Mohseni, P. (2011). A battery-powered activity-dependent intracortical microstimulation IC for brain-machine-brain interface. *IEEE J. Solid State Circ.* 46, 731–745. doi: 10.1109/jssc.2011.2108770

Bagheri, A., Gabran, S., Salam, M. T., Velazquez, J. L. P., Mansour, R. R., Salama, M. M., et al. (2013). Massively-parallel neuromonitoring and neurostimulation rodent headset with nanotextured flexible microelectrodes. *IEEE Trans. Biomed. circ. Syst.* 7, 601–609. doi: 10.1109/tbcas.2013.2281772

Baunez, C., Christakou, A., Chudasama, Y., Forni, C., and Robbins, T. W. (2007). Bilateral high-frequency stimulation of the subthalamic nucleus on attentional performance: transient deleterious effects and enhanced motivation in both intact and parkinsonian rats. *Eur. J. Neurosci.* 25, 1187–1194. doi: 10.1111/j.1460-9568.2007.05373.x

Benabid, A. L., Chabardes, C., and Polak, P. (2009). Deep brain stimulation of the subthalamic nucleus for the treatment of Parkinson's disease. *Lancet Neurol.* 8, 67–81.

Benabid, A.-L., Pollak, P., Louveau, A., Henry, S., and De Rougemont, J. (1987). Combined (thalamotomy and stimulation) stereotactic surgery of the VIM thalamic nucleus for bilateral Parkinson disease. *Stereotact. Funct. Neurosurg.* 50, 344–346. doi: 10.1159/000100803

Biederman, W., Yeager, D. J., Narevsky, N., Leverett, J., Neely, R., Carmena, J. M., et al. (2015). A 4.78 mm 2 fully-integrated neuromodulation SoC combining 64 acquisition channels with digital compression and simultaneous dual stimulation. *IEEE J. Solid State Circ.* 50, 1038–1047. doi: 10.1109/jssc.2014.2384736

Boon, P., Raedt, R., De Herdt, V., Wyckhuys, T., and Vonck, K. (2009). Electrical stimulation for the treatment of epilepsy. *Neurotherapeutics* 6, 218–227.

Boon, P., Vonck, K., De Herdt, V., Van Dycke, A., Goethals, M., Goossens, L., et al. (2007). Deep brain stimulation in patients with refractory temporal lobe epilepsy. *Epilepsia* 48, 1551–1560.

Boon, P., Vonck, K., De Reuck, J., and Caemaert, J. (2001). Vagus nerve stimulation for refractory epilepsy. *Seizure* 10, 448–455.

Boulet, S., Lacombe, E., Carcenac, C., Feuerstein, C., Sgambato-Faure, V., Poupard, A., et al. (2006). Subthalamic stimulation-induced forelimb dyskinesias are linked to an increase in glutamate levels in the substantia nigra pars reticulata. *J. Neurosci.* 26, 10768–10776. doi: 10.1523/jneurosci.3065-06.2006

Cagnan, H., Pedrosa, D., Little, S., Pogosyan, A., Cheeran, B., Aziz, T., et al. (2017). Stimulating at the right time: phase-specific deep brain stimulation. *Brain* 140, 132–145. doi: 10.1093/brain/aww286

Chang, D.-W., Liang, S.-F., Young, C.-P., Shaw, F.-Z., Su, A. W., Liu, Y.-D., et al. (2011). A versatile wireless portable monitoring system for brain–behavior approaches. *IEEE J. Emerg. Select. Top. Circ. Syst.* 1, 440–450. doi: 10.1109/jetcas.2011.2181454

Chen, C. C., Brücke, C., Kempf, F., Kupsch, A., Lu, C. S., Lee, S. T., et al. (2006). Deep brain stimulation of the subthalamic nucleus: a two-edged sword. *Curr. Biol.* 16, R952–R953.

Chen, H., Yen-Chung, C., Yshih-Rungeh, Y., Chih-Cheng, H., Kea-Tiong, T., Ping-Hsuan, H., et al. (2018). "Development of a multisite, closed-loop neuromodulator for the theranosis of neural degenerative diseases," in *Proceedings of the 2018 IEEE Symposium on VLSI Technology*, (Honolulu, HI: IEEE), 37–38.

Chen, T.-J., Chiueh, H., Liang, S.-F., Chang, S.-T., Jeng, C., Hsu, Y.-C., et al. (2011a). The implementation of a low-power biomedical signal processor for real-time epileptic seizure detection on absence animal models. *IEEE J. Emerg. Select. Top. Circ. Syst.* 1, 613–621. doi: 10.1109/jetcas.2011.2174472

Chen, T.-J., Jeng, C., Chang, S.-T., Chiueh, H., Liang, S.-F., Hsu, Y.-C., et al. (2011b). "A hardware implementation of real-time epileptic seizure detector on FPGA," in *Proceeedings of the IEEE Biomedical Circuits and Systems Conference (BioCAS) 2011*, (San Diego, CA: IEEE), 25–28.

Chen, W.-M., Chiueh, H., Chen, T.-J., Ho, C.-L., Jeng, C., Ker, M.-D., et al. (2014). A fully integrated 8-channel closed-loop neural-prosthetic CMOS SoC for real-time epileptic seizure control. *IEEE J. Solid State Circ.* 49, 232–247. doi: 10.1109/jssc.2013.2284346

Cheng, C.-H., Tsai, P.-Y., Yang, T.-Y., Cheng, W.-H., Yen, T.-Y., Luo, Z., et al. (2018). A fully integrated 16-channel closed-loop neural-prosthetic CMOS SoC with wireless power and bidirectional data telemetry for real-time efficient human epileptic seizure control. *IEEE J. Solid State Circ.* 53, 3314–3326. doi: 10.1109/jssc.2018.2867293

Chwalek, K., Sood, D., Cantley, W. L., White, J. D., Tang-Schomer, M., and Kaplan, D. L. (2015). Engineered 3D silk-collagen-based model of polarized neural tissue. *J. Visual. Exp.* 104:52970.

Cohen-Gadol, A. A., Britton, J. W., Wetjen, N. M., Marsh, W. R., Meyer, F. B., and Raffel, C. (2003). Neurostimulation therapy for epilepsy: current modalities and future directions. *Mayo Clin. Proc.* 78, 238–248. doi: 10.4065/78.2.238

Connolly, A. T., Vetter, R. J., Hetke, J. F., Teplitzky, B. A., Kipke, D. R., Pellinen, D. S., et al. (2015). A novel lead design for modulation and sensing of deep brain structures. *IEEE Trans. Biomed. Eng.* 63, 148–157. doi: 10.1109/tbme.2015.2492921

Cuellar-Herrera, M., Neri-Bazan, L., and Rocha, L. L. (2006). Behavioral effects of high frequency electrical stimulation of the hippocampus on electrical kindling in rats. *Epilepsy Res.* 72, 10–17. doi: 10.1016/j.eplepsyres.2006.07.002

Dandekar, M., Fenoy, A., Carvalho, A., Soares, J., and Quevedo, J. (2018). Deep brain stimulation for treatment-resistant depression: an integrative review of preclinical and clinical findings and translational implications. *Mol. Psychiatry* 23, 1094–1112. doi: 10.1038/mp.2018.2

de Haas, R., Struikmans, R., Van Der Plasse, G., Van Kerkhof, L., Brakkee, J. H., Kas, M. J., et al. (2012). Wireless implantable micro-stimulation device for high frequency bilateral deep brain stimulation in freely moving mice. *J. Neurosci. Methods* 209, 113–119. doi: 10.1016/j.jneumeth.2012.05.028

Dembek, T. A., Reker, P., Visser-Vandewalle, V., Wirths, J., Treuer, H., Klehr, M., et al. (2017). Directional DBS increases side-effect thresholds—a prospective, double-blind trial. *Mov. Disord.* 32, 1380–1388. doi: 10.1002/mds.27093

Do Valle, B. G., Cash, S. S., and Sodini, C. G. (2016). Low-power, 8-channel EEG recorder and seizure detector ASIC for a subdermal implantable system. *IEEE Trans. Biomed. Circ. Syst.* 10, 1058–1067. doi: 10.1109/tbcas.2016.2517039

Dorval, A. D., Russo, G. S., Hashimoto, T., Xu, W., Grill, W. M., and Vitek, J. L. (2008). Deep brain stimulation reduces neuronal entropy in the MPTP-primate model of Parkinson's disease. *J. Neurophysiol.* 100, 2807–2818. doi: 10.1152/jn.90763.2008

Draz, H. H., Gabran, S. R. I., Basha, M., Mostafa, H., Abu-Elyazeed, M. F., and Zaki, A. (2018). Comparative mechanical analysis of deep brain stimulation electrodes. *BioMed. Eng. OnLine* 17, 1–14. doi: 10.1186/s12938-018-0557-6

Engel, J. Jr. (2016). What can we do for people with drug-resistant epilepsy. *Neurology* 87, 2483–2489. doi: 10.1212/wnl.0000000000003407

Fang, X., Sugiyama, K., Akamine, S., and Namba, H. (2006). Improvements in motor behavioral tests during deep brain stimulation of the subthalamic nucleus in rats with different degrees of unilateral parkinsonism. *Brain Res.* 1120, 202–210. doi: 10.1016/j.brainres.2006.08.073

Fernández-García, C., Foffani, G., Dileone, M., Catalán-Alonso, M., González-Hidalgo, M., Barcía, J., et al. (2017). Directional local field potential recordings for symptom-specific optimization of deep brain stimulation. *Mov. Disord.* 32, 626–628. doi: 10.1002/mds.26949

Fisher, R. S., and Velasco, A. L. (2014). Electrical brain stimulation for epilepsy. *Nat. Rev. Neurol.* 10:261.

Fleischer, M., Endres, H., Sendtner, M., and Volkmann, J. (2020). Development of a fully implantable stimulator for deep brain stimulation in mice. *Front. Neurosci.* 14:726. doi: 10.3389/fnins.2020.00726

Forni, C., Mainard, O., Melon, C., Goguenheim, D., Kerkerian-Le Goff, L., and Salin, P. (2012). Portable microstimulator for chronic deep brain stimulation in freely moving rats. *J. Neurosci. Methods* 209, 50–57. doi: 10.1016/j.jneumeth.2012.05.027

Fung, S. H., Burstein, D., and Born, R. T. (1998). In vivo microelectrode track reconstruction using magnetic resonance imaging. *J. Neurosci. Methods* 80, 215–224. doi: 10.1016/s0165-0270(98)00003-x

Gabran, S. R., Salam, M. T., Dian, J., El-Hayek, Y., Velazquez, J. P., Genov, R., et al. (2014). 3-D flexible nano-textured high-density microelectrode arrays for high-performance neuro-monitoring and neuro-stimulation. *IEEE Trans. Neural Syst. Rehabil. Eng.* 22, 1072–1082. doi: 10.1109/tnsre.2014.2322077

Ghane-Motlagh, B., and Sawan, M. (2013). Design and implementation challenges of microelectrode arrays: a review. *Mater. Sci. Appl.* 4, 483–495. doi: 10.4236/msa.2013.48059

Gimsa, J., Habel, B., Schreber, U., van Rienen, U., Strauss, U., and Gimsa, U. (2005). Choosing electrodes for deep brain stimulation experiments-electrochemical considerations. *J. Neurosci. Methods* 142, 251–265. doi: 10.1016/j.jneumeth.2004.09.001

Gimsa, U., Schreber, U., Habel, B., Flehr, J., van Rienen, U., and Gimsa, J. (2006). Matching geometry and stimulation parameters of electrodes for deep brain stimulation experiments-numerical considerations. *J. Neurosci. Methods* 150, 212–227. doi: 10.1016/j.jneumeth.2005.06.013

Gubellini, P., Eusebio, A., Oueslati, A., Melon, C., Kerkerian-Le Goff, L., and Salin, P. (2006). Chronic high-frequency stimulation of the subthalamic nucleus and L-DOPA treatment in experimental parkinsonism: effects on motor behaviour and striatal glutamate transmission. *Eur. J. Neurosci.* 24, 1802–1814. doi: 10.1111/j.1460-9568.2006.05047.x

Hügle, M., Heller, S., Watter, M., Blum, M., Manzouri, F., Dumpelmann, M., et al. (2018). "Early seizure detection with an energy-efficient convolutional neural network on an implantable microcontroller," in *Proceedings of the 2018 International Joint Conference on Neural Networks (IJCNN)*, (Rio de Janeiro: IEEE), 1–7.

Halpern, C. H., Samadani, U., Litt, B., Jaggi, J. L., and Baltuch, G. H. (2009). "Deep brain stimulation for epilepsy," in *Neuromodulation*, eds E. Krames, P. H. Peckham, and A. Rezai (Amsterdam: Elsevier), 639–649.

Harden, C., Tomson, T., Gloss, D., Buchhalter, J., Cross, J. H., Donner, E., et al. (2017). Practice guideline summary: sudden unexpected death in epilepsy incidence rates and risk factors: report of the guideline development, dissemination, and implementation subcommittee of the American academy of neurology and the American epilepsy society. *Epilepsy Curr.* 17, 180–187. doi: 10.5698/1535-7511.17.3.180

Harnack, D., Meissner, W., Paulat, R., Hilgenfeld, H., Müller, W.-D., Winter, C., et al. (2008). Continuous high-frequency stimulation in freely moving rats: development of an implantable microstimulation system. *J. Neurosci. Methods* 167, 278–291. doi: 10.1016/j.jneumeth.2007.08.019

Heo, M. S., Moon, H. S., Kim, H. C., Park, H. W., Lim, Y. H., and Paek, S. H. (2015). Fully implantable deep brain stimulation system with wireless power transmission for long-term use in rodent models of parkinson's disease. *J. Korean Neurosurg. Soc.* 57:152. doi: 10.3340/jkns.2015.57.3.152

Herron, J. A., Thompson, M. C., Brown, T., Chizeck, H. J., Ojemann, J. G., and Ko, A. L. (2016). Chronic electrocorticography for sensing movement intention and closed-loop deep brain stimulation with wearable sensors in an essential tremor patient. *J. Neurosurg.* 127, 580–587. doi: 10.3171/2016.8.jns16536

Herz, D. M., Little, S., Pedrosa, D. J., Tinkhauser, G., Cheeran, B., Foltynie, T., et al. (2018). Mechanisms underlying decision-making as revealed by deep-brain stimulation in patients with Parkinson's disease. *Curr. Biol.* 28, 1169–1178.e6.

Irwin, Z. T., Thompson, D. E., Schroeder, K. E., Tat, D. M., Hassani, A., Bullard, A. J., et al. (2016). Enabling low-power, multi-modal neural interfaces through a common, low-bandwidth feature space. *IEEE Trans. Neural Syst. Rehabil. Eng.* 24, 521–531. doi: 10.1109/tnsre.2015.2501752

Jia, Y., Mirbozorgi, S. A., Lee, B., Khan, W., Madi, F., Weber, A., et al. (2018). "A mm-sized free-floating wirelessly powered implantable optical stimulating system-on-a-chip," in *Proceedings of the 2018 IEEE International Solid-State Circuits Conference-(ISSCC)*, (San Francisco,CA: IEEE), 468–470.

Jobst, B. C., Darcey, T. M., Thadani, V. M., and Roberts, D. W. (2010). Brain stimulation for the treatment of epilepsy. *Epilepsia* 51, 88–92. doi: 10.1111/j.1528-1167.2010.02618.x

Kassiri, H., Der Chen, F., Salam, M. T., Chang, M., Vatankhahghadim, B., Carlen, P., et al. (2019). Arbitrary-waveform electro-optical intracranial neurostimulator with load-adaptive high-voltage compliance. *IEEE Trans. Neural Syst. Rehabil. Eng.* 27, 582–593. doi: 10.1109/tnsre.2019.2900455

Kassiri, H., Salam, M. T., Pazhouhandeh, M. R., Soltani, N., Velazquez, J. L. P., Carlen, P., et al. (2017a). Rail-to-rail-input dual-radio 64-channel closed-loop neurostimulator. *IEEE J. Solid State Circ.* 52, 2793–2810.

Kassiri, H., Tonekaboni, S., Salam, M. T., Soltani, N., Abdelhalim, K., Velazquez, J. L. P., et al. (2017b). Closed-loop neurostimulators: A survey and a seizure-predicting design example for intractable epilepsy treatment. *IEEE Trans. Biomed. Circ. Syst.* 11, 1026–1040. doi: 10.1109/tbcas.2017.2694638

Kerrigan, J. F., Litt, B., Fisher, R. S., Cranstoun, S., French, J. A., Blum, D. E., et al. (2004). Electrical stimulation of the anterior nucleus of the thalamus for the treatment of intractable epilepsy. *Epilepsia* 45, 346–354. doi: 10.1111/j.0013-9580.2004.01304.x

Kotagal, P. (2011). Neurostimulation: vagus nerve stimulation and beyond. *Sem. Pediatr. Neurol.* 18, 186–194. doi: 10.1016/j.spen.2011.06.005

Krauss, J. K., Lipsman, N., Aziz, T., Boutet, A., Brown, P., Chang, J. W., et al. (2020). Technology of deep brain stimulation: current status and future directions. *Nat. Rev. Neurol.* 7, 75–87. doi: 10.1038/s41582-020-00426-z

Lang, A. E., and Lozano, A. M. (1998). Parkinson's disease. First of two parts. *N. Engl. J. Med.* 339, 1044–1053.

Laxpati, N. G., Kasoff, W. S., and Gross, R. E. (2014). Deep brain stimulation for the treatment of epilepsy: circuits, targets, and trials. *Neurotherapeutics* 11, 508–526. doi: 10.1007/s13311-014-0279-9

Lee, H.-M., Park, H., and Ghovanloo, M. (2013). A power-efficient wireless system with adaptive supply control for deep brain stimulation. *IEEE J. Solid State Circ.* 48, 2203–2216. doi: 10.1109/jssc.2013.2266862

Lee, J., Rhew, H.-G., Kipke, D., and Flynn, M. (2008). "A 64 channelprogrammable closed-loop deep brain stimulator with 8 channel neural amplifier and logarithmic ADC," in *Proceedings of the IEEE Symposium on VLSI Circuits 2008*, (Honolulu, HI: IEEE), 76–77.

Lee, S.-Y., Tsou, C., Liao, Z.-X., Cheng, P.-H., Huang, P.-W., Lee, H.-Y., et al. (2020). A Programmable EEG monitoring SoC with optical and electrical stimulation for epilepsy control. *IEEE Access* 8, 92196–92211.

Lempka, S. F., Miocinovic, S., Johnson, M. D., Vitek, J. L., and McIntyre, C. C. (2009). In vivo impedance spectroscopy of deep brain stimulation electrodes. *J. Neural Eng.* 6:046001.

Li, M. C., and Cook, M. J. (2018). Deep brain stimulation for drug-resistant epilepsy. *Epilepsia* 59, 273–290. doi: 10.1111/epi.13964

Lin, C.-Y., Li, Y.-J., and Ker, M.-D. (2014). Design of high-voltage-tolerant stimulus driver with adaptive loading consideration to suppress epileptic seizure in a 0.18-μm CMOS process. *Anal. Integr. Circ. Signal Process.* 79, 219–226. doi: 10.1007/s10470-014-0282-4

Lin, Y.-P., Yeh, C.-Y., Huang, P.-Y., Wang, Z.-Y., Cheng, H.-H., Li, Y.-T., et al. (2016). A battery-less, implantable neuro-electronic interface for studying the mechanisms of deep brain stimulation in rat models. *IEEE Trans. Biomed. Circ. Syst.* 10, 98–112. doi: 10.1109/tbcas.2015.2403282

Lipsman, N., Schwartz, M. L., Huang, Y., Lee, L., Sankar, T., Chapman, M., et al. (2013). MR-guided focused ultrasound thalamotomy for essential tremor: a proof-of-concept study. *Lancet Neurol.* 12, 462–468. doi: 10.1016/s1474-4422(13)70048-6

Little, S., and Brown, P. (2012). What brain signals are suitable for feedback control of deep brain stimulation in Parkinson's disease? *Ann. N. Y. Acad. Sci.* 1265, 9–24. doi: 10.1111/j.1749-6632.2012.06650.x

Little, S., Tripoliti, E., Beudel, M., Pogosyan, A., Cagnan, H., Herz, D., et al. (2016). Adaptive deep brain stimulation for Parkinson's disease demonstrates reduced speech side effects compared to conventional stimulation in the acute setting. *J. Neurol. Neurosurg. Psychiatry* 87, 1388–1389. doi: 10.1136/jnnp-2016-313518

Liu, X., Demosthenous, A., and Donaldson, N. (2008). An integrated implantable stimulator that is fail-safe without off-chip blocking-capacitors. *IEEE Trans. Biomed. Circ. Syst.* 2, 231–244. doi: 10.1109/tbcas.2008.2003199

Liu, X., Subei, B., Zhang, M., Richardson, A. G., Lucas, T. H., and Van Der Spiegel, J. (2014). "The PennBMBI: a general purpose wireless brain-machine-brain interface system for unrestrained animals," in *Proceedings of the IEEE International Symposium on Circuits and Systems (ISCAS)2014*, (New York, NY: IEEE), 650–653.

Lopez-Meraz, M., Neri-Bazan, L., and Rocha, L. (2004). Low frequency stimulation modifies receptor binding in rat brain. *Epilepsy Res.* 59, 95–105. doi: 10.1016/j.eplepsyres.2004.02.005

Loukas, C., and Brown, P. (2012). A PC-based system for predicting movement from deep brain signals in Parkinson's disease. *Comput. Methods Programs Biomed.* 107, 36–44. doi: 10.1016/j.cmpb.2012.03.011

Lozano, A. M., Fosdick, L., Chakravarty, M. M., Leoutsakos, J.-M., Munro, C., Oh, E., et al. (2016). A phase II study of fornix deep brain stimulation in mild Alzheimer's disease. *J. Alzheimers Dis.* 54, 777–787.

McCreery, D., Lossinsky, A., Pikov, V., and Liu, X. (2006). Microelectrode array for chronic deep-brain microstimulation and recording. *IEEE Trans. Biomed. Eng.* 53, 726–737. doi: 10.1109/tbme.2006.870215

Merolla, P. A., Arthur, J. V., Alvarez-Icaza, R., Cassidy, A. S., Sawada, J., Akopyan, F., et al. (2014). A million spiking-neuron integrated circuit with a scalable communication network and interface. *Science* 345, 668–673. doi: 10.1126/science.1254642

Miocinovic, S., Somayajula, S., Chitnis, S., and Vitek, J. L. (2013). History, applications, and mechanisms of deep brain stimulation. *JAMA Neurol.* 70, 163–171. doi: 10.1001/2013.jamaneurol.45

Nowak, K., Mix, E., Gimsa, J., Strauss, U., Sriperumbudur, K. K., Benecke, R., et al. (2011). Optimizing a rodent model of Parkinson's disease for exploring the effects and mechanisms of deep brain stimulation. *Parkinsons Dis.* 2011:414682.

Obaid, A., Hanna, M.-E., Wu, Y.-W., Kollo, M., Racz, R., Angle, M. R., et al. (2020). Massively parallel microwire arrays integrated with CMOS chips for neural recording. *Sci. Adv.* 6:eaay2789. doi: 10.1126/sciadv.aay2789

Okun, M. S., and Vitek, J. L. (2004). Lesion therapy for Parkinson's disease and other movement disorders: update and controversies. *Mov. Disord.* 19, 375–389. doi: 10.1002/mds.20037

Ortmanns, M., Rocke, A., Gehrke, M., and Tiedtke, H.-J. (2007). A 232-channel epiretinal stimulator ASIC. *IEEE J. Solid State Circ.* 42, 2946–2959. doi: 10.1109/jssc.2007.908693

Parastarfeizabadi, M., Kouzani, A. Z., Gibson, I., and Tye, S. J. (2016). "A miniature closed-loop deep brain stimulation device," in *Prooceedings of the 38th Annual International Conference of the IEEE Engineering in Medicine and Biology Society (EMBC) 2016*, Orlando, FL.

Paulat, R., Meissner, W., Morgenstern, R., Kupsch, A., and Harnack, D. (2011). "Development of an implantable microstimulation system for chronic DBS in rodents," in *Proceedings of the 2011 Annual International Conference of the IEEE Engineering in Medicine and Biology Society*, (Boston, MA: IEEE), 660–662.

Pazhouhandeh, M. R., O'leary, G., Weisspapir, I., Groppe, D., Nguyen, X.-T., Abdelhalim, K., et al. (2019). "22.8 adaptively clock-boosted auto-ranging responsive neurostimulator for emerging neuromodulation applications," in *Proceedings of the 2019 IEEE International Solid-State Circuits Conference-(ISSCC)*, (San Francisco, CA: IEEE), 374–376.

Petrossians, A., Whalen, J. J., and Weiland, J. D. (2016). "Improved electrode material for deep brain stimulation," *38th Annual International Conference of the IEEE Engineering in Medicine and Biology Society (EMBC)*, 1798–1801.

Poustinchi, M., and Musallam, S. (2013). "Towards an implantale intelligent CMOS neurotrophic factor delivery micro neural prosthetic for Parkinson's disease," in *Proceedings of the 6th International IEEE/EMBS Conference on Neural Engineering (NER) 2013*, (San Diego, CA: IEEE), 863–867.

Ranjandish, R., and Schmid, A. (2020). A review of microelectronic systems and circuit techniques for electrical neural recording aimed at closed-loop epilepsy control. *Sensors* 20:5716. doi: 10.3390/s20195716

Rosa, M., Arlotti, M., Ardolino, G., Cogiamanian, F., Marceglia, S., Di Fonzo, A., et al. (2015). Adaptive deep brain stimulation in a freely moving Parkinsonian patient. *Mov. Disord.* 30, 1003–1005. doi: 10.1002/mds.26241

Saha, S., and Baumert, M. (2020). Intra-and inter-subject variability in EEG-based sensorimotor brain computer interface: a review. *Front. Comput. Neurosci.* 13:87. doi: 10.3389/fncom.2019.00087

Satzer, D., Lanctin, D., Eberly, L. E., and Abosch, A. (2014). Variation in deep brain stimulation electrode impedance over years following electrode

implementation. *Stereotac. Funct. Neurosurg.* 92, 94–102. doi: 10.1159/000358014

Shoaran, M., Pollo, C., Schindler, K., and Schmid, A. (2015). A fully integrated IC with 0.85-μw/channel consumption for epileptic iEEG detection. *IEEE Trans. Circ. Syst. II Expr. Briefs* 62, 114–118. doi: 10.1109/tcsii.2014.2387652

Sit, J.-J., and Sarpeshkar, R. (2007). A low-power blocking-capacitor-free charge-balanced electrode-stimulator chip with less than 6 nA DC error for 1-mA full-scale stimulation. *IEEE Trans. Biomed. Circ. Syst.* 1, 172–183. doi: 10.1109/tbcas.2007.911631

Stanslaski, S., Afshar, P., Cong, P., Giftakis, J., Stypulkowski, P., Carlson, D., et al. (2012). Design and validation of a fully implantable, chronic, closed-loop neuromodulation device with concurrent sensing and stimulation. *IEEE Trans. Neural Syst. Rehabil. Eng.* 20, 410–421. doi: 10.1109/tnsre.2012.2183617

Steigerwald, F., Matthies, C., and Volkmann, J. (2019). Directional deep brain stimulation. *Neurotherapeutics* 16, 100–104.

Swann, N. C., De Hemptinne, C., Thompson, M. C., Miocinovic, S., Miller, A. M., Ostrem, J. L., et al. (2018). Adaptive deep brain stimulation for Parkinson's disease using motor cortex sensing. *J. Neural Eng.* 15:046006. doi: 10.1088/1741-2552/aabc9b

Velasco, F., Carrillo-Ruiz, J. D., Brito, F., Velasco, M., Velasco, A. L., Marquez, I., et al. (2005). Double-blind, randomized controlled pilot study of bilateral cerebellar stimulation for treatment of intractable motor seizures. *Epilepsia* 46, 1071–1081. doi: 10.1111/j.1528-1167.2005.70504.x

Velıšek, L., Velıšková, J., and Moshé, S. L. (2002). Electrical stimulation of substantia nigra pars reticulata is anticonvulsant in adult and young male rats. *Exp. Neurol.* 173, 145–152. doi: 10.1006/exnr.2001.7830

Venkatraman, S., Elkabany, K., Long, J. D., Yao, Y., and Carmena, J. M. (2009). A system for neural recording and closed-loop intracortical microstimulation in wake rodents. *IEEE Trans. Biomed. Eng.* 56, 15–22. doi: 10.1109/tbme.2008.2005944

Verma, N., Shoeb, A., Bohorquez, J., Dawson, J., Guttag, J., and Chandrakasan, A. P. (2010). A micro-power EEG acquisition SoC with integrated feature extraction processor for a chronic seizure detection system. *IEEE J. Solid State Circ.* 45, 804–816. doi: 10.1109/jssc.2010.2042245

Voges, B. R., Schmitt, F. C., Hamel, W., House, P. M., Kluge, C., Moll, C. K., et al. (2015). Deep brain stimulation of anterior nucleus thalami disrupts sleep in epilepsy patients. *Epilepsia* 56, e99–e103.

Volkmann, J., Albanese, A., Kulisevsky, J., Tornqvist, A. L., Houeto, J. L., Pidoux, B., et al. (2009). Long-term effects of pallidal or subthalamic deep brain stimulation on quality of life in Parkinson's disease. *Mov. Disord.* 24, 1154–1161.

Winter, C., Flash, S., Klavir, O., Klein, J., Sohr, R., and Joel, D. (2008). The role of the subthalamic nucleus in 'compulsive'behavior in rats. *Eur. J. Neurosci.* 27, 1902–1911. doi: 10.1111/j.1460-9568.2008.06148.x

Wong, J. K., Cauraugh, J. H., Ho, K. W. D., Broderick, M., Ramirez-Zamora, A., Almeida, L., et al. (2019). STN vs. Gpi deep brain stimulation for tremor suppression in Parkinson disease: a systematic review and meta-analysis. *Parkinson. Relat. Disord.* 58, 56–62. doi: 10.1016/j.parkreldis.2018.08.017

Wu, C.-Y., Cheng, C.-H., Ou-Yang, Y.-H., Chen, C.-G., Chen, W.-M., Ker, M.-D., et al. (2017). "Design considerations and clinical applications of closed-loop neural disorder control SoCs," in *Proceedings of the 22nd Asia and South Pacific Design Automation Conference (ASP-DAC)2017*, (Chiba: IEEE), 295–298.

Wu, C.-Y., Tseng, C.-K., and Cheng, C.-H. (2018). Subretinal prosthetic systems and epileptic seizure control systems: chip design, integration, and animal tests. *Jpn. J. Appl. Phys.* 57, 1002A1004.

Xie, K., Zhang, S., Dong, S., Li, S., Yu, C., Xu, K., et al. (2017). Portable wireless electrocorticography system with a flexible microelectrodes array for epilepsy treatment. *Sci. Rep.* 7:7808.

Xu, J., Nguyen, A. T., Wu, T., Zhao, W., Luu, D. K., and Yang, Z. (2020). A wide dynamic range neural data acquisition system with high-precision delta-sigma ADC and on-chip EC-PC spike processor. *IEEE Trans. Biomed. Circ. Syst.* 14, 425–440.

Yan, H., Toyota, E., Anderson, M., Abel, T. J., Donner, E., Kalia, S. K., et al. (2019). A systematic review of deep brain stimulation for the treatment of drug-resistant epilepsy in childhood. *J. Neurosurg. Pedistr.* 23, 274–284. doi: 10.3171/2018.9.peds18417

Yang, J., and Sawan, M. (2020). From seizure detection to smart and fully embedded seizure prediction engine: a review. *IEEE Trans. Biomed. Circ. Syst.* 14, 1008–1023. doi: 10.1109/tbcas.2020.3018465

Yazicioglu, R. F., Merken, P., Puers, R., and Van Hoof, C. (2007). A 60$\mu $ W 60 nV/$\surd $ Hz readout front-end for portable biopotential acquisition systems. *IEEE J. Solid State Circ.* 42, 1100–1110. doi: 10.1109/jssc.2007.894804

Young, C.-P., Liang, S.-F., Chang, D.-W., Liao, Y.-C., Shaw, F.-Z., and Hsieh, C.-H. (2011). A portable wireless online closed-loop seizure controller in freely moving rats. *IEEE Trans. Instr. Measure.* 60, 513–521. doi: 10.1109/tim.2010.2050358

Yu, H., and Neimat, J. S. (2008). The treatment of movement disorders by deep brain stimulation. *Neurotherapeutics* 5, 26–36.

Zanos, S., Richardson, A. G., Shupe, L., Miles, F. P., and Fetz, E. E. (2011). The Neurochip-2: an autonomous head-fixed computer for recording and stimulating in freely behaving monkeys. *IEEE Trans. Neural Syst. Rehabil. Eng.* 19, 427–435. doi: 10.1109/tnsre.2011.2158007

Zangiabadi, N., Ladino, L. D., Sina, F., Orozco-Hernandez, J. P., Carter, A., and Tellez-Zenteno, F. (2019). Deep brain stimulation and drug-resistant epilepsy: a review of the literature. *Front. Neurol.* 10:601. doi: 10.3389/fneur.2019.00601

Zhou, A., Johnson, B. C., and Muller, R. (2018). Toward true closed-loop neuromodulation: artifact-free recording during stimulation. *Curr. Opin. Neurobiol.* 50, 119–127. doi: 10.1016/j.conb.2018.01.012

Zhou, A., Santacruz, S. R., Johnson, B. C., Alexandrov, G., Moin, A., Burghardt, F. L., et al. (2019). A wireless and artefact-free 128-channel neuromodulation device for closed-loop stimulation and recording in non-human primates. *Nat. Biomed. Eng.* 3, 15–26. doi: 10.1038/s41551-018-0323-x

Conflict of Interest: The authors declare that the research was conducted in the absence of any commercial or financial relationships that could be construed as a potential conflict of interest.

frontiers in Neuroscience

ORIGINAL RESEARCH
published: 15 June 2021
doi: 10.3389/fnins.2021.667932

Self-Reset Image Sensor With a Signal-to-Noise Ratio Over 70 dB and Its Application to Brain Surface Imaging

Thanet Pakpuwadon[1], Kiyotaka Sasagawa[1], Mark Christian Guinto[1], Yasumi Ohta[1], Makito Haruta[1], Hironari Takehara[1], Hiroyuki Tashiro[1,2] and Jun Ohta[1]*

[1] Division of Materials Science, Graduate School of Science and Technology, Nara Institute of Science and Technology, Takayama, Japan, [2] Division of Medical Technology, Department of Health Sciences, Faculty of Medical Sciences, Kyushu University, Maidashi, Japan

In this study, we propose a complementary-metal-oxide-semiconductor (CMOS) image sensor with a self-resetting system demonstrating a high signal-to-noise ratio (SNR) to detect small intrinsic signals such as a hemodynamic reaction or neural activity in a mouse brain. The photodiode structure was modified from N-well/P-sub to P+/N-well/P-sub to increase the photodiode capacitance to reduce the number of self-resets required to decrease the unstable stage. Moreover, our new relay board was used for the first time. As a result, an effective SNR of over 70 dB was achieved within the same pixel size and fill factor. The unstable state was drastically reduced. Thus, we will be able to detect neural activity. With its compact size, this device has significant potential to become an intrinsic signal detector in freely moving animals. We also demonstrated *in vivo* imaging with image processing by removing additional noise from the self-reset operation.

Keywords: self-resetting, CMOS image sensor, implantable device, high signal-to-noise ratio, *in vivo* experiment, intrinsic signal, somatosensory cortex, image processing

OPEN ACCESS

Edited by:
Takashi Tokuda,
Tokyo Institute of Technology, Japan

Reviewed by:
Kazuhiro Takahashi,
Toyohashi University of Technology, Japan
Dawen Cai,
University of Michigan, United States

****Correspondence:***
Kiyotaka Sasagawa
sasagawa@ms.naist.jp

Specialty section:
This article was submitted to Neural Technology, a section of the journal Frontiers in Neuroscience

Received: *15 February 2021*
Accepted: *20 May 2021*
Published: *15 June 2021*

Citation:
Pakpuwadon T, Sasagawa K, Guinto MC, Ohta Y, Haruta M, Takehara H, Tashiro H and Ohta J (2021) Self-Reset Image Sensor With a Signal-to-Noise Ratio Over 70 dB and Its Application to Brain Surface Imaging. Front. Neurosci. 15:667932. doi: 10.3389/fnins.2021.667932

INTRODUCTION

The nervous system controls significant body function. It is particularly important to understand its dynamics and functionality to prevent or cure diseases that affect the brain (Hillman, 2007; Haruta et al., 2019). Although numerous methods have been developed to offer various strategies to study brain function, they remain poorly understood because of their complexity, and each method has its limitations. Optical imaging is an important approach for studying the brain. Cell level imaging of an exposed cortex can be performed using a scanning microscope, such as confocal or two-photon microscopy (Yoder and Kleinfeld, 2002; Hillman, 2007; Wilson et al., 2007; Takehara et al., 2014). However, it is not suitable for a wide field of view. Other than that, fluorescence microscopy is a popular brain imaging technique (Grinvald and Hildesheim, 2004; Jung et al., 2004; Wang et al., 2008). All these methods face the same problem. The experimental setup with the microscope made it impossible to study the animal while it is freely moving or demonstrating natural behavior. Observing the brain of an animal behaving naturally is essential in the study of the mechanisms that underlie its function. To overcome these limitations, several groups have developed miniaturized devices (Ferezou et al., 2006; Sawinski et al., 2009; Ghosh et al., 2011; Helmchen et al., 2001). These

are still based on conventional microscope optics. The required equipment obstructs the animals' natural behavior. An implantable optical imaging device based on complementary-metal-oxide-semiconductor (CMOS) technology is an alternative approach to observe neural activities while moving freely (Ohta et al., 2009, 2017; Haruta et al., 2015; Takehara et al., 2015). Previously, our group has reported implantable CMOS image sensors for contact imaging, which are ultra-small and lightweight. Thus, it is suitable for implantation (Ng et al., 2006; Tamura et al., 2008; Haruta et al., 2013, 2014, 2015).

To realize an alternative method for study of a mouse brain without relying on an additional step or preparing the sample with genetic engineering, intrinsic signal imaging was chosen. These signal intensity changes are correlated with different brain states. However, some important reactions in the mouse brain only produce an exceedingly small signal change. Thus, a high performance is required to detect changes of approximately 0.1% in intrinsic brain signals. A high signal-to-noise ratio (SNR) greater than 60 dB is required to monitor these small signals. The peak SNR of a normal active pixel sensor (APS) is typically 40–50 dB (Ohta, 2017). In our previous work, we proposed the use of a self-resetting pixel to achieve a high effective SNR and succeeded in obtaining a high SNR of 64 dB, which can detect the hemodynamic signal from the mouse brain along with the stimulation (Sasagawa et al., 2016a,b; Yamaguchi et al., 2016). However, the experiment could still be improved. It has a chance to receive a better high-definition signal from the brain if the device has a sufficiently high effective SNR. We found that the active circuit used to connect to the V_{rst} has insufficient stability and may cause a signal drop or significantly increase the noise by approximately 3 dB at the first reset. Subsequently, it becomes a floor for the overall SNR. To improve the effective SNR, this voltage drop must be minimized.

To gain an even higher effective SNR, we introduce a modified photodiode structure to increase the photodiode capacity. P-diff/N-well/P-sub was chosen as a photodiode because it has a higher capacity owing to its physical structure having more thin layer area than an N-well/P-sub of the same size. This allows the pixel to handle more electrons within one resetting cycle. In short, it reduces the number of self-resets and avoids the unstable stage. We also used a new relay board with improved performance. Moreover, we developed image processing to reduce artifacts from the self-resetting system. The device implementation concept is illustrated in **Figure 1**.

This article is organized as follows. In section "Self-Reset Imaging Device," we present the proposed pixel circuit, which explains the basic principle, self-reset pixel concept, and the photodiode structure used in this image sensor. Subsequently, the device and its smart relay board fabrication and process are explained. In section "Imaging Device Characteristics," the characteristics of the imaging device are shown. In section "Imaging Experiment," the *in vivo* experimental setup and the image processing procedure are described. Section "Discussion" is for the discussion, touching on the comparison with other sensors, limitations of the device, and the imaging results. After the conclusion in section "Conclusion", the following sections are the additional information, which contains the declaration of conflict of interests, author contributions, and funding.

SELF-RESET IMAGING DEVICE

Image Sensor

Operational Principle

The self-reset image sensor detects the charge accumulated in the pixel and resets the pixel by itself before saturation occurs. As a result, the effective pixel capacity can be increased, and the amount of manageable light can be increased. One of its applications is high-dynamic-range imaging. However, our purpose was to obtain a highly effective SNR. Under high light intensity, photon-shot noise is the dominant noise factor. Its value is proportional to the square root of the amount of incident light, and to achieve a high SNR, it is necessary to avoid pixel saturation and manage a large number of photo carriers. Before discussing the high SNR in the self-resetting sensor, we need to define the parameter that limits the effective SNR. Under high-intensity conditions, photon shot noise is the primary noise. The total self-reset sensor noise $\sigma_{SELFRST}$ is approximately,

$$\sigma_{SELFRST} \simeq \sigma_{SN}\sqrt{\frac{\sigma_{RST}^2}{FWC} + 1}, \tag{1}$$

where σ_{RST} is the pixel reset noise, σ_{SN} is the photon shot noise, and FWC is the full-well pixel capacity. In the case of a sufficiently high FWC, the total noise asymptotically approaches σ_{SN}. The signal components are shown in Eq. 2,

$$V_{sig} = V_{out} + N \cdot A_{out}. \tag{2}$$

From Eq. 2, V_{out} is the pixel output, N is the number of resetting cycles, and A_{out} is the maximum amplitude of the pixel. The effective SNR is described by Eq. 3.

$$SNR_{eff} = \frac{V_{sig}}{\sigma_{SELFRST}}, \tag{3}$$

According to Eqs 1 and 3, we found that the self-reset sensor SNR is nearly the same as that of a normal image sensor under a high light intensity condition. Because the self-resetting system prevents the pixel from saturation, V_{sig} can be as high as the proportional light intensity. After the post-processing for signal reconstruction, the intensity signal can be retrieved by compensating it with an estimated number of resetting cycles. In this demonstration, the number of self-resetting N is unnecessary, especially when the intensity changes are significantly small. One advantage of self-resetting pixels is their effective high dynamic range. However, in this study, we focused on detecting small signals, such as the change from the intrinsic brain signal, where a high dynamic range helps to reach a sufficient SNR.

Pixel Circuit

The entire circuit design is still based on a previous version (Sasagawa et al., 2016a,b; Yamaguchi et al., 2016). We still

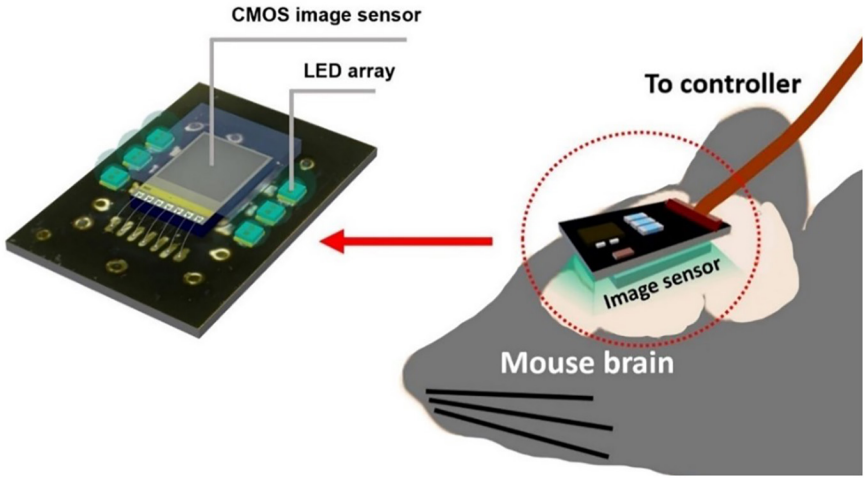

FIGURE 1 | Diagram of an implantable self-reset image sensor for detecting an intrinsic signal from hemodynamics reaction. The proposed image sensor was attached with the relay board surrounded by LEDs.

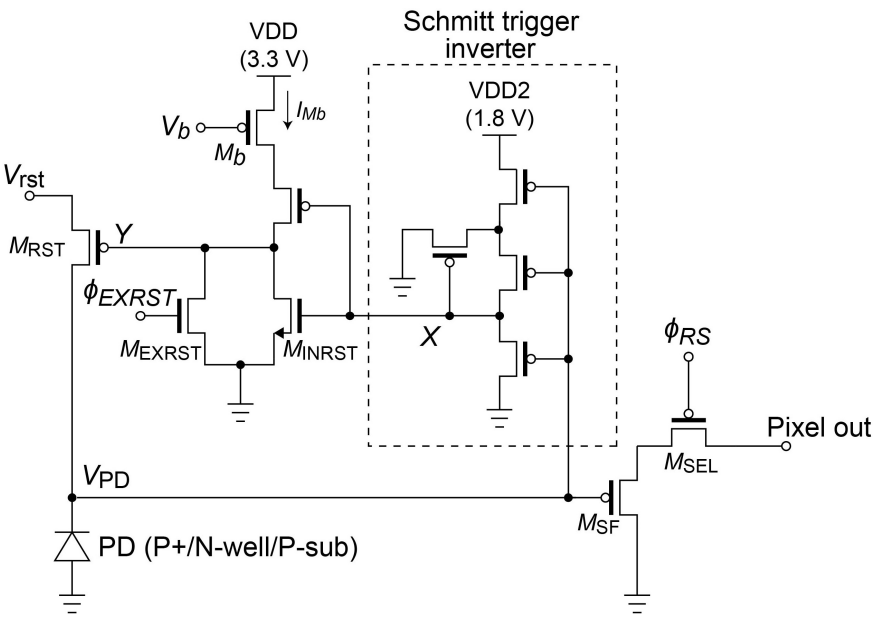

FIGURE 2 | Schematic of the self-reset pixel with a low-voltage driven Schmitt trigger inverter. The PD is composed of P+/N-well/P-sub.

use the same 4-transistor Schmitt trigger inverter as in the previous version. It is driven by a lower voltage VDD2 than the other portions to reduce power consumption. The pixel circuit integrated with the Schmitt trigger inverter is shown in **Figure 2**.

The layout of the proposed pixel with a photodiode is shown in **Figure 3**. In this study, the photodiode type was composed of P+/N-well/P-sub. This structure increases the photodiode capacitance compared to the standard N-well/P-sub structure, which is usually used in 3-transistor APS pixels. However, the pixel size can still be maintained at 15 μm × 15 μm. Eleven transistors were used in the pixel, which is the minimum number for this process.

Pixel Simulation

The operation of the pixel circuit was simulated. V_{rst}, V_B, and VDD2 were set to 2.4, 2.5, and 1.8 V, respectively. In addition, a constant current source of 1 nA was placed in parallel with the PD to simulate the PD photocurrent. The results are shown in **Figure 4**. **Figure 4A** is the period during which several self-resets occur, and **Figure 4B** is the magnified self-reset period plot. After the PD is charged to V_{rst} by an external reset, the V_{PD} is gradually lowered by the photocurrent. When it reaches the Schmitt trigger inverter threshold, node X in **Figure 2** is inverted and becomes HIGH. Furthermore, it is inverted by the inverter circuit, and the reset signal of

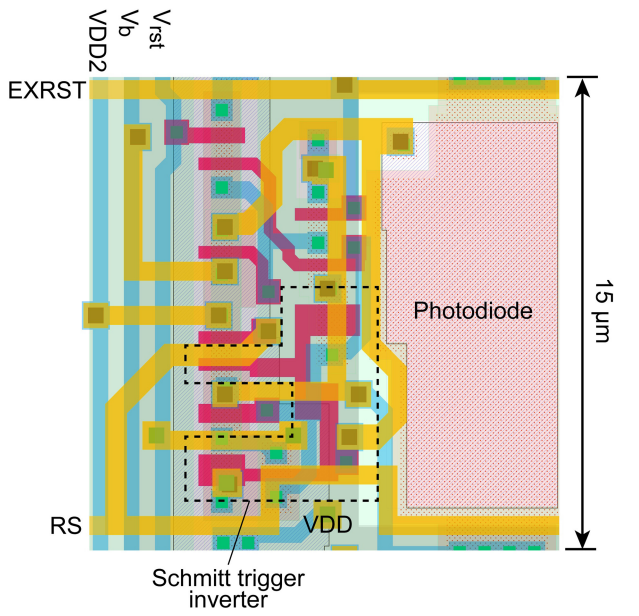

FIGURE 3 | Layout of the pixel with P+/N-well/P-sub photodiode.

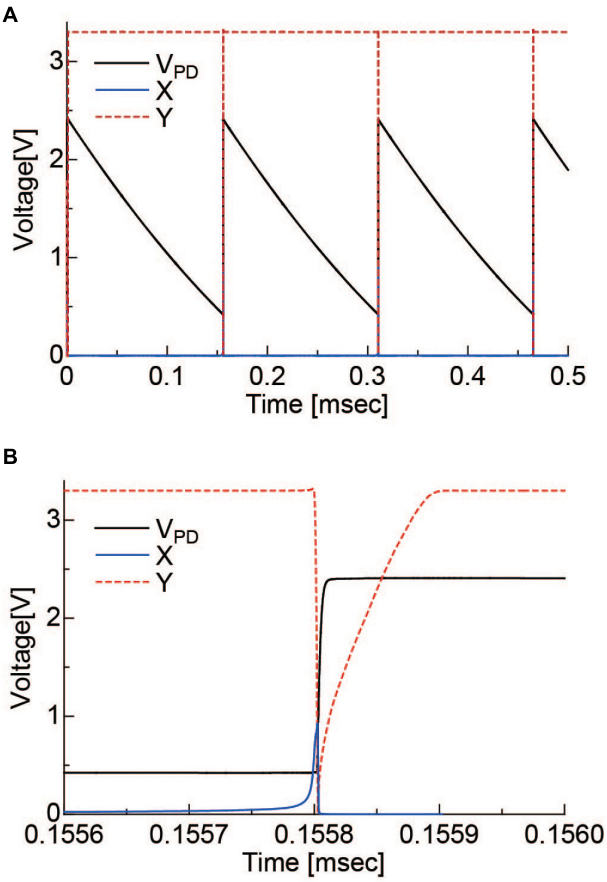

FIGURE 4 | (A) Simulation results of the self-resetting pixel. **(B)** is the magnified plot of the self-resetting region. X, Y correspond to the nodes indicated in **Figure 2**.

node Y becomes LOW. The period of this LOW state was approximately 100 ns. The optical signal could not be detected during this period. When the frame rate is 30 fps and the number of self-resets is 20 times per frame, the output change during this period is $1/1.67 \times 10^4$ of the V_{PD} voltage swing. Under this condition, the SNR exceeds 70 dB, as discussed in section "Pixel Output." Because the photon shot noise, which is the dominant temporary noise, is estimated to be approximately $1/3 \times 10^3$, which indicates that the self-reset time is sufficiently short in this case.

Image Sensor Chip

A graphic of the fabricated chip is shown in **Figure 5**. We used the TSMC 0.35-µm 2-poly 4-metal standard CMOS process. The specifications are listed in **Table 1**. The pixel array is 128 × 128 pixels. The basic configuration of this image sensor is the same as that of our implantable image sensor, and the control line is reduced by generating a control signal from an external clock. However, the analog signal line is externally input. As a result, there are seven signal lines. In particular, the reset voltage (VRST) decreases during self-reset, but this must be minimized. It is difficult to mount a sufficient performance bias inside the chip. The image sensor output is an analog voltage signal.

Fabricated Device

Relay-Board

This custom printed circuit board (PCB) connects the image sensor to the data processing board. Because the image sensor output is an analog signal, it is equipped with a preamplifier circuit. As mentioned in the previous section, the V_{RST} must minimize the voltage drop amplitude and duration as a result of self-reset. Because it is difficult to obtain a sufficient response speed in an active circuit, passive noise filters were inserted into the V_{RST} line on this board. On the other side, the image sensor and six LEDs were mounted as shown in **Figure 6**.

Device Assembly

Because the target application is to be implanted in a mouse brain, we must consider both the thermal condition and waterproof packaging. After connecting the Al wires, epoxy was used to protect all electrode surfaces. Incidental light from the side of the image sensor causes artifacts. To prevent this, a black-colored resist was applied between the LEDs and the sensor. The image sensor was covered with a fiber optic plate (FOP, J5734, Hamamatsu). The FOP is an optical device consisting of a bundle of microoptical fibers. It directly conveys an incident image on its input surface to its output surface. The thickness is 500 µm. This FOP protects the image sensor surface and maintains the distance between the brain surface and the mounted LED because damage owing to its heat may be caused.

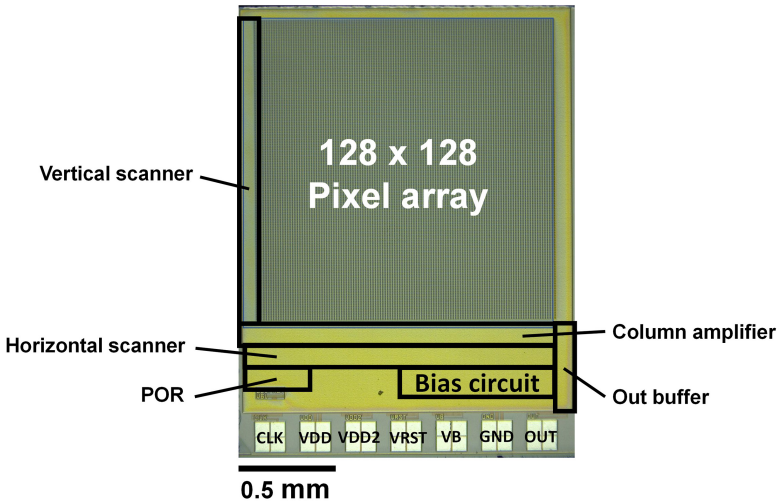

FIGURE 5 | Graphic of the proposed image sensor.

TABLE 1 | Chip specifications.

Technology	TSMC 0.35 μm 2-poly 4-metal standard CMOS process
Chip size	2.7 × 2.1 mm^2
Pixel size	15 × 15 μm^2
Photodiodes	P+/N-well/P-sub
Full well capacity	0.72 Me^-
Fill factor	30%
Pixel number	128 × 128
Operating voltage	3.3 V
Pixel type	3-Tr active pixel sensor with 4-Tr Schmitt trigger inverter for self-resetting

IMAGING DEVICE CHARACTERISTICS

Pixel Output

With the proposed pixel, we set it up as follows: the V_b can control the current flowing through M_b. Thus, the self-resetting time can be adjusted. We optimized it at 2.5 V with a reset duration of approximately 0.1 μs. **Figure 7** shows the output signal as a function of light intensity. In this measurement, the chip was illuminated by a uniform beam with a peak emission wavelength of 530 nm. The signal was observed for one selected pixel. The evaluation was performed at room temperature. When the pixel voltage V_{PD} shown in **Figure 2** becomes lower than the Schmitt trigger inverter threshold, a self-reset is triggered. Thus, the output signal is reset to zero. As a result, the output shape is similar to that of a saw tooth. However, the real illuminated signal can be easily reconstructed when the number of self-resets is known. The reconstructed signal output is plotted in **Figure 7**. For reconstruction, the output amplitude and estimated number of self-resets were added to the signal. From this result, the prototype device has nonlinearity with respect to the light intensity, and the difference in slope is large, especially just before and after the self-reset. Therefore, in the imaging experiment using this device, a look-up table was prepared based on this result, and correction was performed by image processing.

Figure 8 shows the effective SNR as a function of illuminated light power. It was calculated using Eq. 3. **Figure 8A** shows the result of the previous N-well/P-sub structure, and **Figure 8B** shows that of the P+/N-well/P-sub structure. The plot points with a low SNR appear in the high light intensity region, which is at the boundary of the number of self-resets. This can be reduced by correcting the artifacts by self-resetting. The solid line represents the result of fitting with a typical noise curve. As shown in both **Figures 8A,B**, the SNR curve follows the illuminated light power, indicating similar behavior on both low and high luminance. The SNR increases by 20 dB in low illuminance and 10 dB in high illuminance. This is consistent with the fact that light intensity independence noise, such as external resetting and pixel readout, is dominant at low illuminance. Conversely, photon shot noise is dominant at high illuminance. The SNR was improved by applying the noise filter described in the next section, and a high effective SNR of 70 dB or more was achieved in both pixels.

Due to the different photodiode structures, the previous version had a smaller capacity. Therefore, in the low-light range, the SNR is higher than that of the new pixel because it has higher sensitivity due to the smaller capacitance of the photodiode. However, this area was not important for our purposes. Alternatively, the effective SNR in the high-illuminance range is approximately the same. The low photodiode capacity makes self-resetting more frequent and causes the device to become unstable. In particular, noise increases owing to dead time by self-resetting and the residual response nonlinearity error. These issues can be mitigated by a lower number of resets. The number of self-resets at a light intensity of 1.35 mW/cm^2 was 52 for the N-well/P-sub structure and 20 for the P-diff/N-well/P-sub structure. The ratio of PD capacitances in the previous

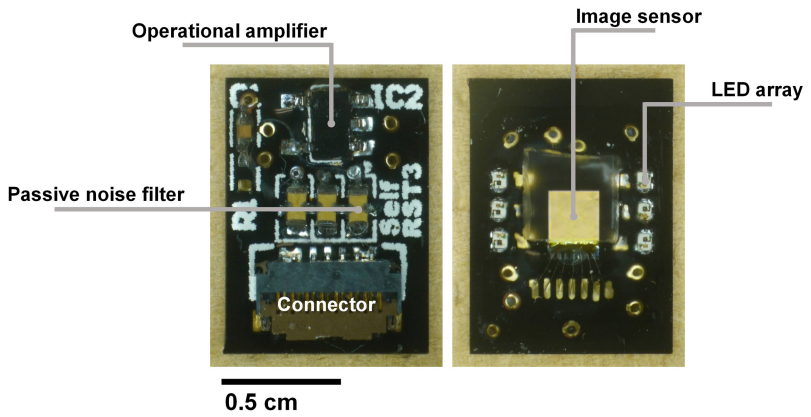

FIGURE 6 | Images of the relay board **(left)** with the preamplifier circuit and passive noise filters placed on this side. **(Right)** The image sensor is mounted between the LED arrays to benefit from the high light intensity. The image sensor surface was covered by the fiber optic plate and sealed with epoxy resin for waterproofing.

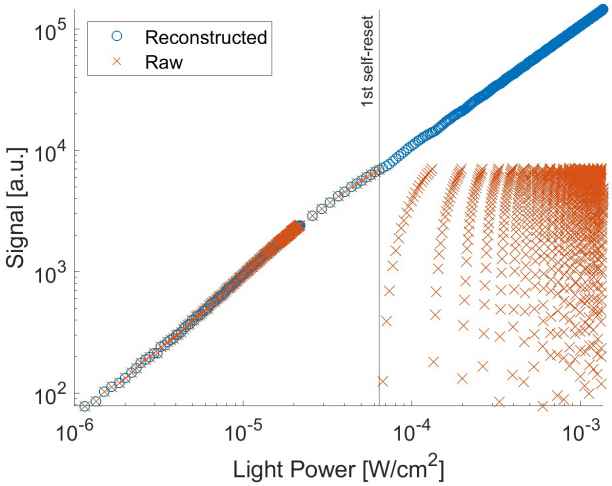

FIGURE 7 | Signal from the pixel with P+/N-well/P-sub photodiode as a function of the light intensity.

and present sensors is approximately 1:2.6 for the self-resetting period. Consequently, the total effective SNR is approximately the same level, but the latest design provides a more stable device.

Performance Improvement by the Relay Board

In our previous work, the noise increased significantly at the first self-reset, and since then, it has been a factor that lowers the overall effective SNR (Sasagawa et al., 2016b; Yamaguchi et al., 2016). It was speculated that this was because the reset potential temporarily dropped, and the V_{RST} potential did not recover to a constant value until the end of the self-reset. Conversely, the new relay board used in this study is equipped with a noise filter (NFM18PS, Murata) on the V_{RST} line. **Figure 9** shows the effective SNR difference with and without a filter. The data of the device with the filter are the same as those in **Figure 8B**. The dashed line represents the curve fitted to the data without the filter. Here, only the offset was changed from the fitted curve for the device with the filter.

Without the filter, there was a significant SNR reduction in the initial self-reset, as in previous devices. However, no significant increase in noise was observed with the filter. As a result, we succeeded in obtaining an SNR improvement of approximately 4 dB. Here, we chose a passive filter to reduce the noise. From the simulation result, the self-reset operation is expected to be completed in 0.1 ns or less. That is, a response bandwidth of approximately 10 GHz or higher is required. It is difficult to achieve such a high-speed response with low-power and active devices. Stable operation is realized by mounting an external filter with a capacity sufficiently larger than the pixel capacity and charging the pixel PD capacity in a short time.

IMAGING EXPERIMENT

Experimental Setup

For the imaging demonstration, intrinsic signal observation was performed on the mouse brain surface. We used wild-type mice (C57BL/6JJmsSlc) from Japan SLC, Inc. The target area was the barrel cortex, a sub-area of the somatosensory cortex. **Figure 10** shows a diagram of the experimental setup. Urethane (10%, Wako Pure Chemical Industries, Inc., Japan) was first administered intraperitoneally at a weight-dependent dose (1 g/kg). The use of urethane as systemic anesthesia allows for extended periods of imaging. It is suitable for sensory stimulation studies since neural responses remain relatively unattenuated and are less variable in time across repeats compared to other anesthetics (Pisauro et al., 2013). The head of the mouse was fixed with the stereotaxic instrument. The sensor was placed on the target area brain surface. We chose bluish-green with a center wavelength of 527 nm (SMLP13EC8TT86, ROHM). All animal experimental procedures were controlled by the Nara Institute of Science and Technology's Animal Care and Experimentation Guidelines.

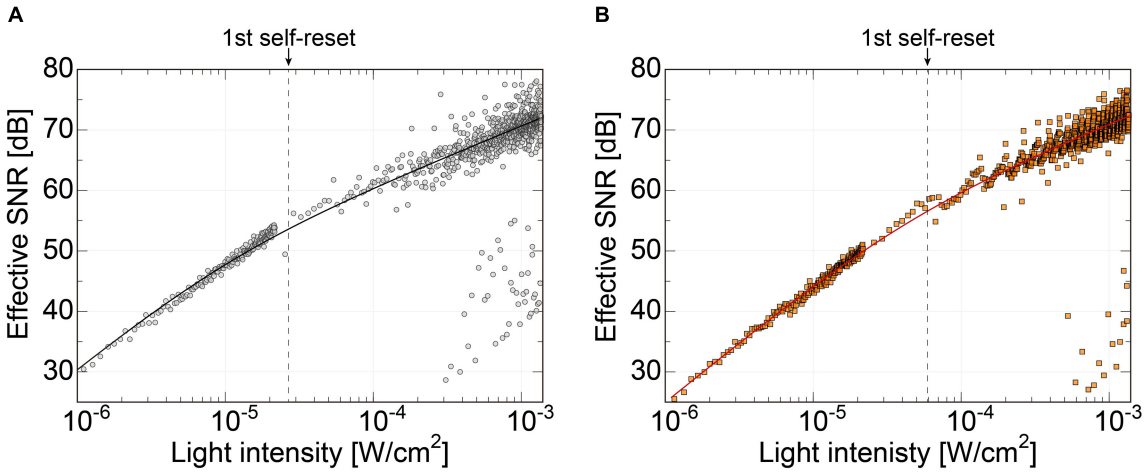

FIGURE 8 | (A) SNR of the pixel with N-well/P-sub photodiode, **(B)** SNR of the pixel with P+/N-well/P-sub photodiode.

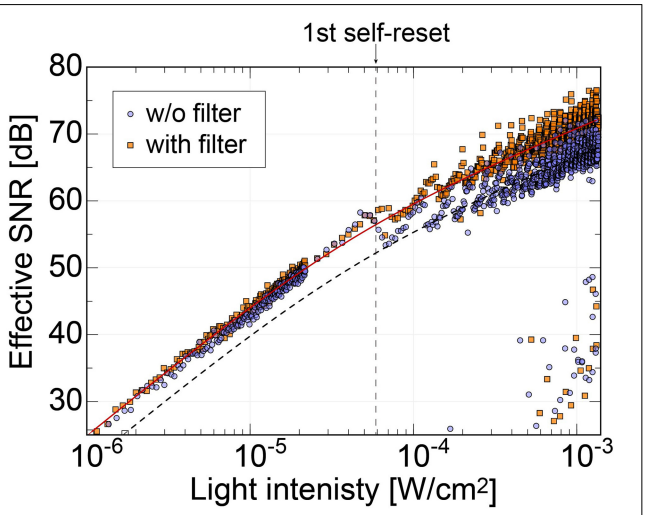

FIGURE 9 | Comparison of the effective SNRs as functions of the incident light intensity between the image sensor using relay boards with and without the noise filter on the Vrst line. The result shows that the SNR dropping behavior at the first self-resetting has been reduced with our latest relay board.

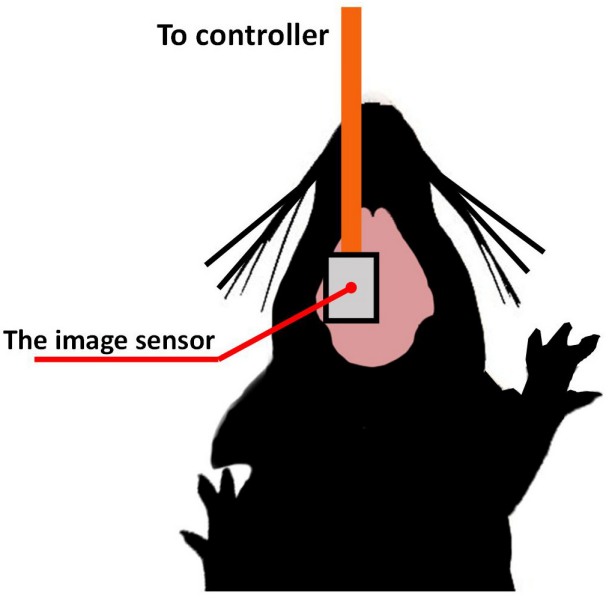

FIGURE 10 | The imaging device is ready to be placed at the left side of the brain on the somatosensory cortex area, while the stimulation was performed on the opposite side.

Imaging Results

Figure 11 shows the mouse brain images. A photograph obtained using a microscope is shown in **Figure 11A**. The red square represents the area where the image sensor was placed. **Figure 11B** shows the raw output image. The frame rate was approximately 15 fps. The LEDs are located on the top and bottom sides of the image. When the light intensity reaches a threshold, the imager resets itself. Thus, the folded intensity fringe pattern appears in the image. This is not a problem for our purpose, that is, to observe the intensity change from a reference image. An important characteristic is the effective SNR for detecting small intrinsic signal intensity changes. In addition, the normal image can be reconstructed by comparing it with a reference image or an estimating algorithm. The number of self-resetting events can be counted when the illumination intensity is gradually increased. The self-resetting number in the central part of **Figure 11B** is three. The reconstructed image is shown in **Figure 11C**.

Our target was to clearly obtain different images from the reference image. In this study, we used MATLAB and an image processing toolbox (MathWorks, Inc.). The processing procedure was as follows:

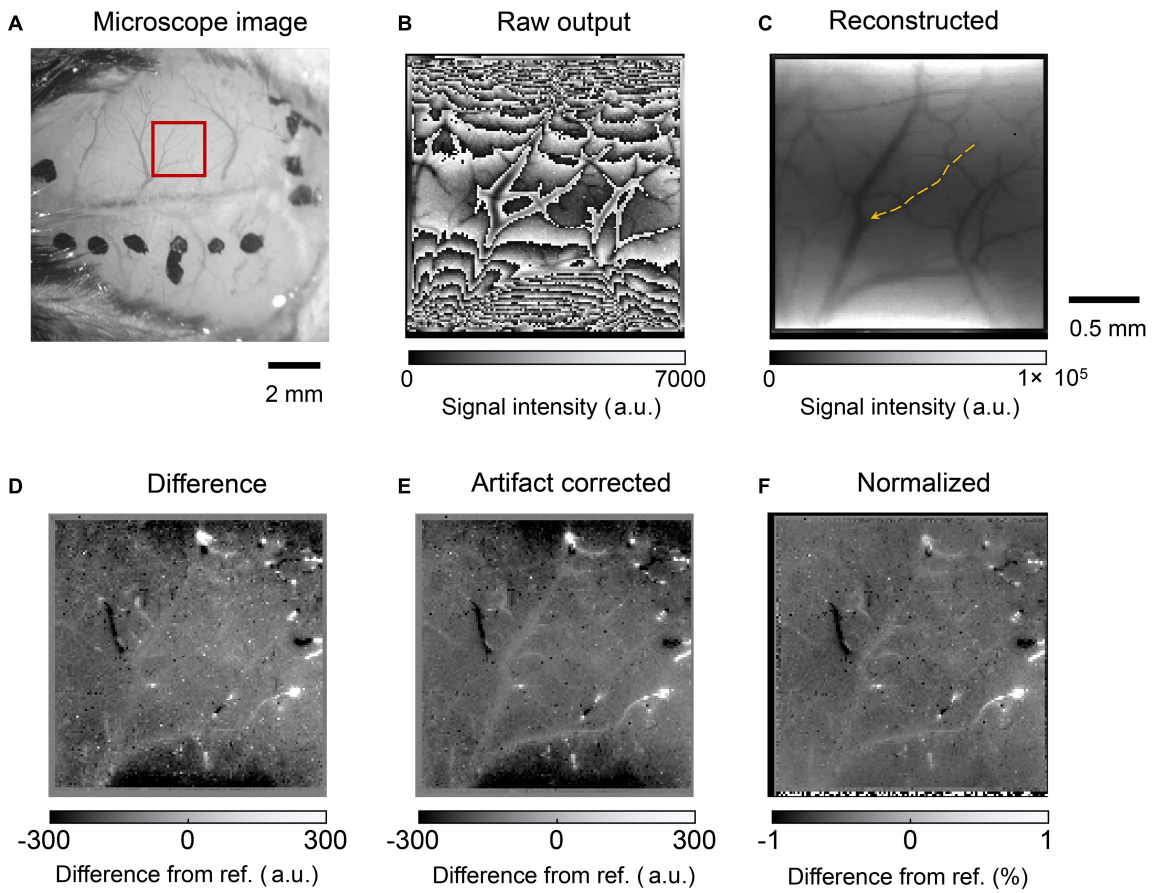

FIGURE 11 | (A) Photograph of the mouse brain surface. The red square shows the position where the image sensor was placed. **(B)** Raw output image from the self-reset sensor. **(C)** Reconstructed image. The orange arrow indicates the blood vessel analyzed in **Figure 12**. **(D)** Difference image from the reference. White and black spots are observed because high output value change occurs when the number of self-resets changes. **(E)** Image after noise and artifact reduction. **(F)** Image normalized by the reconstructed image.

1) Nonlinearity compensation:
   The present pixel shows nonlinearity that cannot be ignored. The correction curve was prepared from the measured output results vs. incident light intensity by polynomial fitting. Nonlinearity was compensated using the result as a look-up table.
2) Intrinsic signal imaging:
   The reference frame was subtracted from each frame; the resulting small intrinsic signal difference in each frame can easily be emphasized and visualized. The reference image used was an average of 1000 frames of sequentially acquired data. The results are shown in **Figure 11D**.
3) Correction of self-resetting artifacts:
   As mentioned above, self-resetting brings the self-resetting artifact as a complex boundary, as shown in **Figure 11B**. The number of self-resetting results in a high output change. However, our target signal was a small change. Thus, it can be easily separated by setting an appropriate threshold. Then, it is compensated by adding or subtracting the output swing value to make it shift off from that level. Here, the swing amplitude is slightly different for each pixel. This time, it was set to 99% of the maximum and minimum values in a series of images.
4) Reduction of pulsation and high-frequency noise:
   The mouse heartbeat was superimposed on the acquired image as a periodic brightness change. For each pixel, a 9–12 Hz component including a mouse beat band and a 15 Hz or higher component, including a high-frequency component, were removed from the frequency spectrum obtained by FFT, and then a waveform was obtained by inverse FFT. The salt and pepper noise that occurs in places at the self-reset boundary is reduced by image processing. An example of the final results is shown in **Figure 11E**.
5) Pixel normalization:
   The observation area illumination is not uniform. To compare it, every frame was divided by the reconstructed reference image shown in **Figure 11F**.

The above results show that the self-reset boundary can be removed by image processing, although a slight noise component

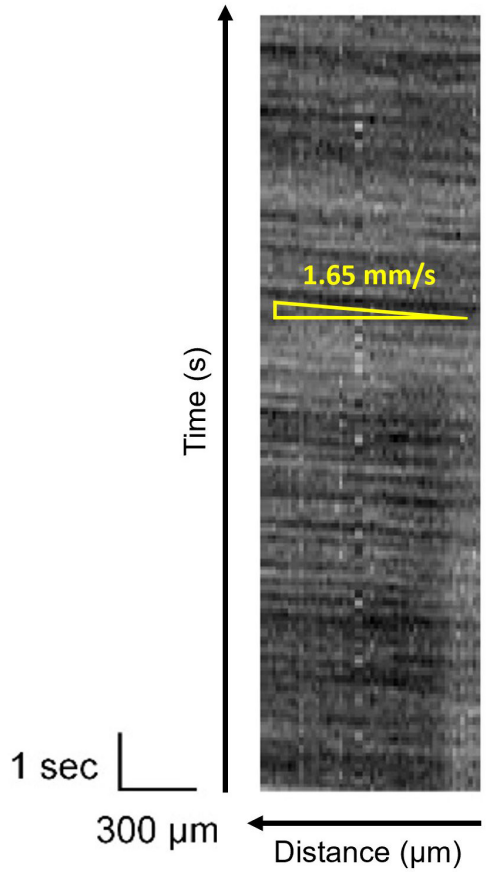

FIGURE 12 | Line scan image of the blood vessel indicated in **Figure 11C**. The movement of red blood cells is shown as dark stripes.

remains. Especially in the boundary part, there is almost no significant noise increase because of the number of self-resets. Furthermore, when the pixel output is used as is, a change in the signal strength difference appears on both sides of the self-reset boundary, but it can be reduced to an invisible level by correcting the nonlinearity. This is in agreement with the SNR curve results shown in **Figure 8**. Significant boundary artifacts owing to self-resets occur when the pixel value that reads the self-reset period overlaps. It is difficult to remove this, and the pixel information with an abnormally large value was removed to manage it in this study.

In the intrinsic imaging, the concentration of blood in a target area is observed, and no information is obtained from the blood vessels. However, the red blood cell flow can be observed in the vessels. It allows estimating blood flow velocity, which is correlated to brain activity (Kleinfeld et al., 1998; Bouchard et al., 2009; Haruta et al., 2014). **Figure 12** shows the temporal change in the brightness of the blood vessel, as shown in **Figure 11C**. It is a line scan along with the blood vessel and plotted as a function of time. This dark stripe corresponds to the higher number of red blood cells. It shows the distance that the red blood cells can travel in time, which reflects the frame rate. The blood velocity can be calculated by dividing $\Delta x(distance)$ by $\Delta t(time)$. Because of the improvement of the effective SNR, the stripe pattern has been observed clearly. Thus, an oblique pattern owing to flow velocity in the blood vessels was observed. The observed blood flow velocity was 1.4–2.8 mm/s. When there is a pulsation, periodic vertical stripes are formed, but this can be clarified by reducing the pulse noise by image processing.

DISCUSSION

Comparison With Other Sensors in the Previous Works

The proposed pixel offers a small size with a high fill factor. Compared to its previous version (Yamaguchi et al., 2016), a base prototype, the SNR is up to 64 dB. With the modified photodiode structure, we succeeded in increasing the SNR to over 70 dB even when the other parameters remained constant, such as pixel size and fill factor. Moreover, this larger FWC strategy also offers a more stable operation. Because a larger FWC reduces the number of self-resets, it can avoid the unstable stage. In particular, compared to other image sensors with a similar self-resetting function (Leñero-Bardallo et al., 2017). Because our pixel has a small circuit part, it is possible to realize a fill factor of the same level or higher, even though it is a relatively small pixel as compared with other self-reset pixels. The proposed image sensor was designed to monitor the brain activity. Thus, the high dynamic range is not as important in that the intensity change is of interest. What matters is the high SNR to detect a relatively small intensity change in brain activities. The effectiveness of sensing the illumination is important in that it can avoid using too high a light intensity to achieve the duty, which can cause the temperature to increase and damage the brain. In addition, methods for estimating the original image from the self-reset sensor image group without a counter have been proposed, and it is possible that these methods will expand the range of applications (Bhandari et al., 2017).

For SNR, Murata and Fujihara et al. presented a pixel with a high SNR of 70 dB (Murata et al., 2020; Fujihara et al., 2021). The pixel size was 16 × 16 µm, and ultra-large capacitances were achieved with in-pixel capacitors. The sensor has a high dynamic range and SNR. However, this requires a special capacitor fabrication technology. Our proposed chip can achieve a similar SNR with a small implantable chip fabricated using a 0.35-µm standard CMOS process. The fill factor can be further increased using a finer process.

Limitations of Pixel Performance

Regarding the frame rate, from the simulation results shown in **Figure 2**, it is estimated that the self-reset artifact can be neglected even if the current pixels are approximately five times faster (∼150 fps). However, for applications that require a high SNR and frame rate, such as voltage-sensitive dye imaging, the self-resetting duration should be shorter. To manage this, a frame rate of approximately 1 kHz or more is required, which is insufficient under the current conditions. However, the simulation predicts that if V_b is changed to shorten the self-reset time, the V_{PD} will

not be firmly reset until V_{RST}. To achieve high-speed operation, it is necessary to make changes such as increasing the reset transistor size.

From this study, it was found that the pixel output nonlinearity with respect to the light intensity can be reduced by correction using the pixel output characteristics acquired in advance. However, when the brightness changes significantly, there are cases in which the error increases. This error can be significantly reduced by improving the nonlinearity. For that purpose, charge transfer to a highly linear capacitance, similar to a general 4-transistor type APS pixel, can be considered.

In vivo Imaging Results

By using FOP in the manufactured device, an almost sufficient spatial resolution was obtained with a pixel size of 15 μm square. In addition, almost no additional noise owing to being mounted on a living body was observed. For the pulsating noise, the frequency component was removed using an FFT. Clear improvements were observed in the captured images, as shown in **Figures 11D–F**. The range of brightness is ±1%, and the results show that slight changes in brightness can be observed. However, this technique can only be used for post-processing. To observe in real time during the experiment, it is necessary to introduce a digital filtering technique.

In **Figure 12**, owing to the high SNR, the change in brightness because of the red blood cell concentration in the blood vessels is clearly visible. In this experiment, the frame rate was set to 15 fps. The resolution of the flow velocity can be improved by increasing the light source brightness and by improving the frame rate. However, it is necessary to consider the heat effects on the observation target.

CONCLUSION

We succeeded in designing and fabricating an image sensor with a self-resetting system, which has an SNR exceeding 70 dB. We increased the pixel capacity to reduce the self-reset frequency and improve operational stability. Moreover, additional noise by self-resetting was decreased by approximately 4 dB after stabilizing the reset voltage during self-reset. Furthermore, image processing reduced artifacts near the boundary of the number of self-resets. The prototype imaging device was applied to the intrinsic signal imaging of a brain surface.

With this device, a high SNR was achieved with a small device that can be mounted on the mouse head. By applying it not only to intrinsic signal imaging but also to voltage-sensitive dye imaging (Ferezou et al., 2006; Tsytsarev et al., 2014), it is expected that it can be applied to brain function observation associated with various behaviors.

DATA AVAILABILITY STATEMENT

The raw data supporting the conclusions of this article will be made available by the authors, without undue reservation.

ETHICS STATEMENT

The animal study was reviewed and approved by the Nara Institute of Science and Technology (NAIST) Animal Committees.

AUTHOR CONTRIBUTIONS

TP contributed to chip design, device fabrication, data analysis, and writing the manuscript. KS contributed to the conception, design, data processing and interpretation, and writing the manuscript. MG contributed to animal experiments and data analysis. YO contributed to the animal experiments. MH, HTk, HTs, and JO contributed to interpretation of the obtained data significance. All authors contributed to the manuscript and approved the submitted version.

FUNDING

This work was supported by the Futaba Foundation, the Japan Society for the Promotion of Science (KAKENHI Grant 18H03519 and 21H03809), the Japan Science and Technology Agency (JST), and Core Research for Evolutional Science and Technology Program (CREST, JPMJCR1654). The CMOS chips were designed with the support of the VLSI Design and Education Centre (VDEC), University of Tokyo, in collaboration with the Cadence Corporation and the Mentor Graphics Corporation.

REFERENCES

Bhandari, A., Krahmer, F., and Raskar, R. (2017). "On unlimited sampling," in *Proceedings of the International Conference on Sampling Theory and Applications (SampTA)*, Tallinn, 31–35. doi: 10.1109/SAMPTA.2017.8024471

Bouchard, M. B., Chen, B. R., Burgess, S. A., and Hillman, E. M. C. (2009). Ultra-fast multispectral optical imaging of cortical oxygenation, blood flow, and intracellular calcium dynamics. *Opt. Express* 17, 15670–15678. doi: 10.1364/OE.17.015670

Ferezou, I., Bolea, S., and Petersen, C. C. H. (2006). Visualizing the cortical representation of whisker touch: voltage-sensitive dye imaging in freely moving mice. *Neuron* 50, 617–629. doi: 10.1016/J.NEURON.2006.03.043

Fujihara, Y., Murata, M., Nakayama, S., Kuroda, R., and Sugawa, S. (2021). An over 120 dB single exposure wide dynamic range CMOS image sensor with two-stage lateral overflow integration capacitor. *IEEE Trans. Electron Devices* 68, 152–157. doi: 10.1109/TED.2020.3038621

Ghosh, K. K., Burns, L. D., Cocker, E. D., Nimmerjahn, A., Ziv, Y., El-Gamal, A., et al. (2011). Miniaturized integration of a fluorescence microscope. *Nat. Methods* 8, 871–878. doi: 10.1038/NMETH.1694

Grinvald, A., and Hildesheim, R. (2004). VSDI: a new era in functional imaging of cortical dynamics. *Nat. Rev. Neurosci.* 5, 874–885. doi: 10.1038/NRN1536

Haruta, M., Kitsumoto, C., Sunaga, Y., Takehara, H., Noda, T., Sasagawa, K., et al. (2013). "An implantable CMOS device for functional brain imaging under freely moving experiments of rats," in *Proceedings of the International*

Conference on Solid State Devices and Materials, Fukuoka, G–1–5. doi: 10.7567/SSDM.2013.G-1-5

Haruta, M., Kitsumoto, C., Sunaga, Y., Takehara, H., Noda, T., Sasagawa, K., et al. (2014). An implantable CMOS device for blood-flow imaging during experiments on freely moving rats. *Jpn. J. Appl. Phys.* 53:04EL05. doi: 10.7567/JJAP.53.04EL05

Haruta, M., Kurauchi, Y., Ohsawa, M., Inami, C., Tanaka, R., Sugie, K., et al. (2019). Chronic brain blood-flow imaging device for a behavioral experiment using mice. *Biomed. Opt. Express* 10, 1557–1566. doi: 10.1364/BOE.10.001557

Haruta, M., Sunaga, Y., Yamaguchi, T., Takehara, H., Noda, T., Sasagawa, K., et al. (2015). Intrinsic signal imaging of brain function using a small implantable CMOS imaging device. *Jpn. J. Appl. Phys.* 54:04DL10. doi: 10.7567/JJAP.54.04DL10

Helmchen, F., Fee, M. S., Tank, D. W., and Denk, W. (2001). A miniature head-mounted two-photon microscope. High-resolution brain imaging in freely moving animals. *Neuron* 31, 903–912. doi: 10.1016/S0896-6273(01)00421-4

Hillman, E. M. (2007). Optical brain imaging in vivo: techniques and applications from animal to man. *J. Biomed. Opt.* 12:051402. doi: 10.1117/1.2789693

Jung, J. C., Mehta, A. D., Aksay, E., Stepnoski, R., and Schnitzer, M. J. (2004). In vivo mammalian brain imaging using one- and two-photon fluorescence microendoscopy. *J. Neurophysiol.* 92, 3121–3133. doi: 10.1152/JN.00234.2004

Kleinfeld, D., Mitra, P. P., Helmchen, F., and Denk, W. (1998). Fluctuations and stimulus-induced changes in blood flow observed in individual capillaries in layers 2 through 4 of rat neocortex. *Proc. Natl. Acad. Sci. U.S.A.* 95, 15741–15746. doi: 10.1073/pnas.95.26.15741

Leñero-Bardallo, J. A., Carmona-Galán, R., and Rodríguez-Vázquez, Á (2017). A wide linear dynamic range image sensor based on asynchronous self-reset and tagging of saturation events. *IEEE J. Solid-State Circuits* 52, 1605–1617. doi: 10.1109/JSSC.2017.2679058

Murata, M., Kuroda, R., Fujihara, Y., Otsuka, Y., Shibata, H., Shibaguchi, T., et al. (2020). A high near-infrared sensitivity over 70-dB SNR CMOS image sensor with lateral overflow integration trench capacitor. *IEEE Trans. Electron Devices* 67, 1653–1659. doi: 10.1109/TED.2020.2975602

Ng, D. C., Tokuda, T., Yamamoto, A., Matsuo, M., Nunoshita, M., Tamura, H., et al. (2006). On-chip biofluorescence imaging inside a brain tissue phantom using a CMOS image sensor for in vivo brain imaging verification. *Sens. Actuators B Chem.* 119, 262–274. doi: 10.1016/J.SNB.2005.12.020

Ohta, J. (2017). *Smart CMOS Image Sensors and Applications*. Boca Raton, FL: CRC press, doi: 10.1201/9781420019155

Ohta, J., Ohta, Y., Takehara, H., Noda, T., Sasagawa, K., Tokuda, T., et al. (2017). Implantable microimaging device for observing brain activities of rodents. *Proc. IEEE* 105, 158–166. doi: 10.1109/JPROC.2016.2585585

Ohta, J., Tokuda, T., Sasagawa, K., and Noda, T. (2009). Implantable CMOS biomedical devices. *Sensors (Basel)* 9, 9073–9093. doi: 10.3390/S91109073

Pisauro, M. A., Dhruv, N. T., Carandini, M., and Benucci, A. (2013). Fast hemodynamic responses in the visual cortex of the awake mouse. *J. Neurosci.* 33, 18343–18351. doi: 10.1523/JNEUROSCI.2130-13.2013

Sasagawa, K., Yamaguchi, T., Haruta, M., Ohta, Y., Takehara, H., Noda, T., et al. (2016a). "Hemodynamic imaging using an implantable self-reset image sensor," in *Proceedings of the IEEE Biomedical Circuits and Systems Conference (BioCAS)*, Shanghai, 452–455. doi: 10.1109/BIOCAS.2016.7833829

Sasagawa, K., Yamaguchi, T., Haruta, M., Sunaga, Y., Takehara, H., Noda, T., et al. (2016b). An implantable CMOS image sensor with self-reset pixels for functional brain imaging. *IEEE Trans. Electron Devices* 63, 215–222. doi: 10.1109/TED.2015.2454435

Sawinski, J., Wallace, D. J., Greenberg, D. S., Grossman, S., Denk, W., and Kerr, J. N. D. (2009). Visually evoked activity in cortical cells imaged in freely moving animals. *Proc. Natl. Acad. Sci. U.S.A.* 106, 19557–19562. doi: 10.1073/PNAS.0903680106

Takehara, H., Nagaoka, A., Noguchi, J., Akagi, T., Kasai, H., and Ichiki, T. (2014). Lab-on-a-brain: implantable micro-optical fluidic devices for neural cell analysis in vivo. *Sci. Rep.* 4:6721. doi: 10.1038/SREP06721

Takehara, H., Ohta, Y., Motoyama, M., Haruta, M., Nagasaki, M., Takehara, H., et al. (2015). Intravital fluorescence imaging of mouse brain using implantable semiconductor devices and epi-illumination of biological tissue. *Biomed. Opt. Express* 6, 1553–1564. doi: 10.1364/BOE.6.001553

Tamura, H., Ng, D. C., Tokuda, T., Honda, N., Nakagawa, T., Mizuno, T., et al. (2008). One-chip sensing device (Biomedical photonic LSI) enabled to assess hippocampal steep and gradual up-regulated proteolytic activities. *J. Neurosci. Methods* 173, 114–120. doi: 10.1016/J.JNEUMETH.2008.06.002

Tsytsarev, V., Liao, L. D., Kong, K. V., Liu, Y. H., Erzurumlu, R. S., Olivo, M., et al. (2014). Recent progress in voltage-sensitive dye imaging for neuroscience. *J. Nanosci. Nanotechnol.* 14, 4733–4744. doi: 10.1166/JNN.2014.9531

Wang, Y., Shyy, J. Y., and Chien, S. (2008). Fluorescence proteins, live-cell imaging, and mechanobiology: seeing is believing. *Annu. Rev. Biomed. Eng.* 10, 1–38. doi: 10.1146/ANNUREV.BIOENG.010308.161731

Wilson, J. M., Dombeck, D. A., Díaz-Ríos, M., Harris-Warrick, R. M., and Brownstone, R. M. (2007). Two-photon calcium imaging of network activity in XFP-expressing neurons in the mouse. *J. Neurophysiol.* 97, 3118–3125. doi: 10.1152/JN.01207.2006

Yamaguchi, T., Takehara, H., Sunaga, Y., Haruta, M., Motoyama, M., Ohta, Y., et al. (2016). Implantable self-reset CMOS image sensor and its application to hemodynamic response detection in living mouse brain. *Jpn. J. Appl. Phys.* 55:04EM02. doi: 10.7567/JJAP.55.04EM02

Yoder, E. J., and Kleinfeld, D. (2002). Cortical imaging through the intact mouse skull using two-photon excitation laser scanning microscopy. *Microsc. Res. Tech.* 56, 304–305. doi: 10.1002/JEMT.10002

Conflict of Interest: The authors declare that the research was conducted in the absence of any commercial or financial relationships that could be construed as a potential conflict of interest.

The handling Editor declared a past co-authorship with the authors.

frontiers in Neuroscience

REVIEW
published: 13 July 2021
doi: 10.3389/fnins.2021.681085

Recording Strategies for High Channel Count, Densely Spaced Microelectrode Arrays

Norberto Pérez-Prieto and Manuel Delgado-Restituto*

Institute of Microelectronics of Seville (IMSE-Centro Nacional de Microelectrónica), Spanish National Research Council, Seville, Spain

Neuroscience research into how complex brain functions are implemented at an extra-cellular level requires *in vivo* neural recording interfaces, including microelectrodes and read-out circuitry, with increased observability and spatial resolution. The trend in neural recording interfaces toward employing high-channel-count probes or 2D microelectrodes arrays with densely spaced recording sites for recording large neuronal populations makes it harder to save on resources. The low-noise, low-power requirement specifications of the analog front-end usually requires large silicon occupation, making the problem even more challenging. One common approach to alleviating this consumption area burden relies on time-division multiplexing techniques in which read-out electronics are shared, either partially or totally, between channels while preserving the spatial and temporal resolution of the recordings. In this approach, shared elements have to operate over a shorter time slot per channel and active area is thus traded off against larger operating frequencies and signal bandwidths. As a result, power consumption is only mildly affected, although other performance metrics such as in-band noise or crosstalk may be degraded, particularly if the whole read-out circuit is multiplexed at the analog front-end input. In this article, we review the different implementation alternatives reported for time-division multiplexing neural recording systems, analyze their advantages and drawbacks, and suggest strategies for improving performance.

Keywords: neuroscience, neural recording, time multiplexing, crosstalk, CMOS technology, prosthetics

OPEN ACCESS

Edited by:
Takashi Tokuda,
Tokyo Institute of Technology, Japan

Reviewed by:
Xin Liu,
University of California, San Diego, United States
Andreas Offenhäusser,
Julich-Forschungszentrum, Helmholtz-Verband Deutscher Forschungszentren (HZ), Germany
Viviana Rincón Montes,
Julich-Forschungszentrum, Helmholtz-Verband Deutscher Forschungszentren (HZ), Germany, in collaboration with reviewer AO

****Correspondence:***
Norberto Pérez-Prieto
norberto@imse-cnm.csic.es

Specialty section:
This article was submitted to Neural Technology, a section of the journal Frontiers in Neuroscience

Received: *15 March 2021*
Accepted: *18 June 2021*
Published: *13 July 2021*

Citation:
Pérez-Prieto N and Delgado-Restituto M (2021) Recording Strategies for High Channel Count, Densely Spaced Microelectrode Arrays. Front. Neurosci. 15:681085. doi: 10.3389/fnins.2021.681085

1. INTRODUCTION

One of the major challenges in neurophysiology is to identify the effective connectivity within the brain and reveal the subjacent drive-response map of the neural system (Friston, 2011; Sakkalis, 2011). This could help to understand the functional mechanisms underlying many neurological disorders which currently do not have effective treatments (Swann et al., 2018; Sisterson et al., 2019) or unravel the neural network involved in specific tasks, including sensory responses, motor activities or intellectual or emotional processes, to implement efficient Brain Machine Interfaces (BMIs) (Vansteensel et al., 2016; Wagner et al., 2018). Neural recording systems based on CMOS technology, in combination with micro-electrode arrays, can achieve very high temporal and spatial resolution and have been proved useful for assessing connectivity at the extracellular single-unit level. The suitability of these devices ultimately depends on the amount and quality of the information which can be extracted from the brain tissue and, accordingly, it is crucial to increase

the number of neural signals which can be accurately and simultaneously recorded *in vivo*. In fact, in the last decades, and similar to the well-known Moore's law for transistor count scaling in dense integrated circuits (ICs), the number of single neuron cells which can be monitored using recording interfaces, either based on intracortical probes or surface sub-dural microelectrode arrays, has increased over the years. This is illustrated in the plot of **Figure 1**, derived from the dataset available in Stevenson (2020). Only intracortical systems published along the last three decades, i.e., approximately since the inception of the first silicon-based structures for neural recording, have been considered. The plot shows that the number of neurons which can be simultaneously recorded has increased exponentially with the year of publication, doubling approximately every 4.65 ± 0.25 years. Anyhow, future forecasts based on this growth trend are questionable, because of fundamental limits in the size and density of microelectrodes, which cannot be decreased arbitrarily without degrading the Signal-to-Noise Ratio (SNR) of the recorded signals (Camunas-Mesa and Quiroga, 2013), or because of the induced displacement in the neural tissue which at last instance may hamper the network connectivity which is aimed to discover.

In the works represented in **Figure 1**, intracortical electrodes are either arranged in parallel microwire bundles (e.g., Obaid et al., 2020), or use micromachined silicon arrays (e.g., Bartolo et al., 2020), or are integrated in planar silicon-based neural probes (e.g., Mora Lopez et al., 2017), or are allocated in flexible polymer-based substrates (e.g., Musk and Neuralink, 2019). Szostak et al. (2017) gives an in-depth review of these techniques. In many cases displayed in **Figure 1**, multiple probes, each with multiple shanks have been used for increasing the number of recording sites. Thus, for instance, in one of the selected works, (Berényi et al., 2014), two silicon-based probes, each with 8 shanks of 32-channels, were used for a total of 512 electrodes. Similarly, in Rajangam et al. (2016), six multielectrode arrays with 96 microwires each were used totalling 576 recording sites. More recently, the trend is toward including more electrodes per individual shank or microwire bundle and, thus, for instance, the Neuropixel probe (Jun et al., 2017) has 960 sites on a single, 10 mm long, non-tapered shank with $70 \times 20\ \mu$m cross-section and the Argo system (Sahasrabuddhe et al., 2020) uses a single microwire bundle with 1300 electrodes (10 mm array diameter, 18 μm wire diameter, 200 μm spacing, 1 mm length), which can be extended to 30,000 channels for surface LFP recordings.

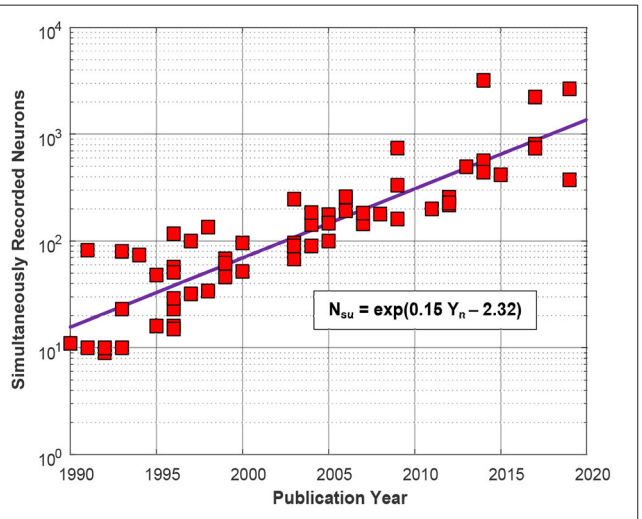

FIGURE 1 | Number of simultaneously recorded neurons, N_{SU}, over the last three decades from a selection of $N = 70$ published works. Variable Y_n is the ordinal number of the years. The coefficient of determination of the fitting model is $R^2 = 84\%$.

Besides the huge amount of data to be processed and transferred, which poses significant challenges in the digital back-end of neural recording systems (Park et al., 2018a), an important bottleneck for implementing high channel count microelectrode arrays stems from the design of the active readout circuitry, which is the focus of this survey. In most of the cases represented in **Figure 1**, intracortical electrodes are passive, i.e., they are made up of recording sites and interconnecting wires, while the main circuitry for the acquisition, conditioning and processing of neural signals, often from multiple probes, is housed in bulky headstages (Shobe et al., 2015; Rajangam et al., 2016). Only recently, seeking to increase the number of recording sites which can addressed from the headstage, some silicon-based intracortical shanks also include active devices such as switches or small amplifiers, as in Raducanu et al. (2017). In order to reduce the form factor of headstages, specific integrated solutions, which almost invariably relies on the use of CMOS technologies, should be used for the implementation of the readout electronics. In this paper, the circuit used for recording the neural signal captured from each individual electrode will be denoted indistinctly as recording channel or neural recording Analog Front-End (AFE), and comprisees all the circuit elements from the input Low-Noise Amplifier (LNA) to the Analog-to-Digital Conversion stage (ADC) (both inclusive). Clearly, in high channel count neural recording systems, the occupation area of individual AFEs should be made as small as possible and, in fact, the density of recording channels has risen from some 5–6 AFEs/mm^2 to more than 80 AFEs/mm^2 in the current state-of-the-art, whilst still satisfying demanding specifications on low noise, high input impedance or low power consumption. The use of Time-Division Multiplexing (TDM) techniques, in which occupation area is traded-off with operation frequency, have played a prominent role on this accomplishment.

TDM makes it possible to totally or partially share AFE elements at different time slots between different electrodes. Compared to other multiplexing techniques such as frequency-division multiplexing (Mikawa et al., 2020), TDM does not suffer from signal overlapping issues in frequency domain, and allows to reusing circuit blocks without penalizing to first order power consumption. This is because although shared elements have to increase their power consumption proportionally to the higher bandwidth requirements in order to preserve the same neural recording sampling rate, such increment is essentially compensated by the fact that only one element is used instead of multiple slower elements. Another advantage of TDM is the improved tolerance against mismatch between recording

channels as a single element is shared between different electrodes, thus reducing discrepancies between the recorded neural signals. Obviously, the more AFE elements are shared by means of multiplexing, the higher the area reduction which can be attained for the complete readout circuitry. In a limit case, the largest area saving could be accomplished if a single AFE is multiplexed between different electrodes (Jun et al., 2017; Raducanu et al., 2017; Sharma et al., 2018), however, as will be shown in this paper, this raises undesired effects which should be tackled.

This work aims to review the implementation strategies and restrictions for time multiplexing neural recording AFEs, and analyses the main advantages and drawbacks of the proposed techniques and architectures. The paper is organized as follows. Section 2 details the main concerns about the AFE-electrode interface. Section 3 introduces AFEs for neural recording applications. Section 4 describes the basics of TDM and section 5 presents a classification of the reported neural recording architectures depending on the position of the analog multiplexer in their signal paths. Section 6 describes the main architectures for TDM at the AFE input, together with their advantages and drawbacks. Finally, section 7 offers some conclusions and suggestions for future research.

2. ELECTRODE-AFE INTERFACE

AFEs in multi-channel systems are usually placed relatively far from the recording electrodes. The interconnection wires between the electrode array and the AFEs severely limit the electrode density and reduce the efficiency of the neural probe's occupation area. However, some silicon-based devices allow the integration of one or more AFE stages along with the electrodes, by splitting the AFE into two parts: one placed on the headstage and the other on the probe shank(s). The most employed stage to be integrated next to the electrodes is the input amplifier (IA). The main advantages and drawbacks of employing or not this active circuitry along with the electrodes can be disclosed in their impact on electrode crosstalk and its noise contribution to the system. The considerations presented throughout this section will apply for recording both local field potentials (LFPs), which are signals comprising the combination of synaptic and network activities within a local brain region with an oscillation frequency from 0.5 to 500 Hz (Muller et al., 2015), and action potentials (APs), which are rapid rises and subsequent falls in voltage or membrane potential across a cellular membrane in a frequency band from 0.25 to 10 kHz (Muller et al., 2015).

2.1. Crosstalk in Electrode-AFE Interfaces

Electrical crosstalk is one of the most significant scaling limitations of multi-channel recording devices. For neural applications, the crosstalk level has to be below 1% of the recorded signal level to make it negligible compared with the background noise (Najafi et al., 1990). This crosstalk can be classified according to where it occurs: electrode crosstalk defines the crosstalk from the electrodes to the AFE, i.e., from the shank to the base of the device; crosstalk takes into account the impact on the multiplexer output of non-activated channels. This last type of crosstalk will be analyzed in section 4.

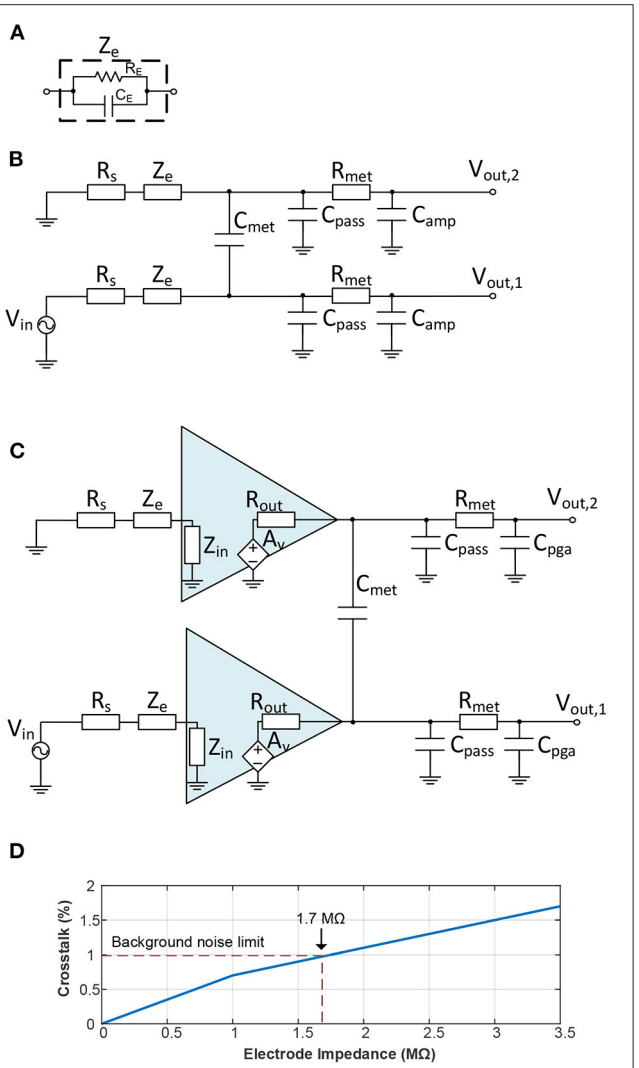

FIGURE 2 | Crosstalk models for electrode-AFE interface. **(A)** Equivalent electrode impedance model. **(B)** Equivalent circuit model for electrode crosstalk without active electrode-AFE interface. **(C)** Equivalent circuit model for electrode crosstalk with active electrode-AFE interface. **(D)** Crosstalk at the electrode-AFE interface against the electrode impedance (Du et al., 2009).

In high-channel-count devices, the space between adjacent electrodes and between interconnection wires is largely reduced while the dielectric layers below and above the electrodes remain constant. The coupling capacitance between electrodes thus increases because of the reduced space, thereby increasing the electrical crosstalk. A simplified scheme which models the crosstalk from the shank to the AFE was proposed in Najafi et al. (1990) and further developed in Du et al. (2009) and Seidl et al. (2012) (see **Figure 2B**). It should be noted that (Seidl et al., 2012) also demonstrated that the switches placed along with the electrodes have a negligible effect on crosstalk, so they were not included in the model. For the AFE to be integrated within

the neural probe, the capacitive coupling between metal lines in the external wires (Du et al., 2009) was also excluded. To further develop this approach, **Figure 2C** shows a model which also includes an amplifier adjacent to the electrodes, similar to Lopez et al. (2014). The circuit elements with their corresponding values (taken from Du et al., 2009; Seidl et al., 2012) are described as follows:

- R_s is the spreading resistance encountered by the current propagating out into the fluid near to the electrode. It has been reported to be about 10 kΩ (Du et al., 2009).
- Z_e represents the equivalent impedance of the electrode-electrolyte interface (from now on simplified as electrode impedance) which is modeled by a resistive R_E and a capacitive C_E component, see **Figure 2A** (Du et al., 2009). This impedance is, then, a frequency-dependent parameter. For this analysis, a 20 μm diameter Pt electrode has been taken with an impedance measured at 1 kHz of about 1.2 MΩ (Seidl et al., 2012).
- C_{met} describes the capacitive coupling between adjacent lines. It was estimated as 0.1 pF (Du et al., 2009).
- C_{pass} is the estimated capacitance of the metal lines with the extracellular fluid. This value was set as 2.7 pF (Du et al., 2009).
- R_{met} represents the equivalent resistance between the metal traces to the input of the amplifier (programmable-gain amplifier, PGA, in the case of the active electrode-AFE interface). Its value was about 500 Ω (Du et al., 2009).
- C_{amp} (only for non-active electrode-AFE interfaces) models the input capacitance of the AFE and was set at about 12 pF (Du et al., 2009).
- C_{pga} (only for active electrode-AFE interfaces) represents the input capacitance of the PGA and it is about 12 pF.
- Z_{in} (only for active electrode-AFE interfaces) is the input impedance of the amplifier next to the electrode. It is above 70 MΩ.
- R_{out} (only for active electrode-AFE interfaces) describes the output resistance of the amplifier next to the electrode. This value is about 50 kΩ.

Simulations carried out in the SPICE software environment in Du et al. (2009), have demonstrated the influence of the electrode impedance in the crosstalk between channels. Electrode impedances larger than 1.7 MΩ produce crosstalks between channels above the 1% (Du et al., 2009), significantly reducing the SNR. This is illustrated in **Figure 2D**, which replicates the analysis provided in Du et al. (2009). It is worth observing that these results also included the influence of the capacitive coupling of the metal lines for the connection with an external AFE, which is not the case of placing the AFE at the base of the probe (Du et al., 2009).

On the other hand, placing the amplifier adjacent to the electrodes isolates the impedance of the electrodes from the interconnection wires (Lopez et al., 2014). This makes the crosstalk dependent on the output resistance of the amplifier due to the fact that this resistance is in this model the equivalent input impedance seen from the interconnection wires (Lopez et al., 2014). Thus, crosstalk results are largely improved (Lopez et al., 2014). For instance, crosstalk values below 0.1% have been reported by including amplifiers along with the electrodes (Mora Lopez et al., 2017).

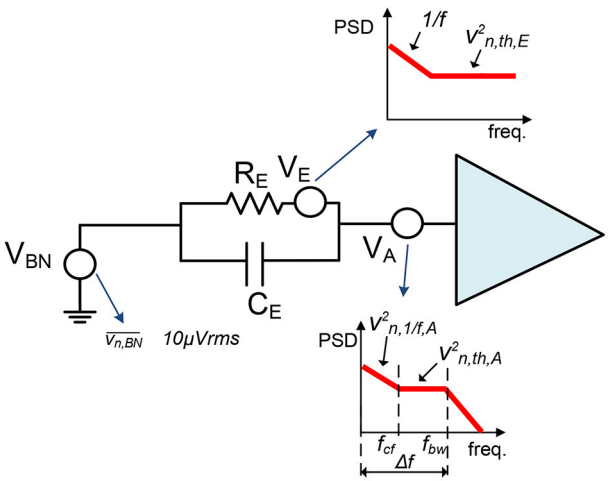

FIGURE 3 | Simplified scheme of the three main noise sources at the Electrode-AFE interface: the biological or background noise (VBN), the electrode noise (VE), and the noise from the recording electronics (VA).

2.2. Noise in Electrode-AFE Interfaces

One of the most significant aspects of neural recording devices is how different noise sources degrade the signal of interest. At the electrode-AFE interface, three main noise sources can be distinguished: biological or background noise, electrode-electrolyte interface noise and the noise from the recording electronics (Obien et al., 2015). This is illustrated in **Figure 3** (Valtierra et al., 2020).

The background noise, V_{BN} in **Figure 3**, comprises the electrical activity of other cells surrounding the recording electrode (Obien et al., 2015). This noise source is usually quoted as $\overline{v_{n,BN}} \approx 10\,\mu V_{rms}$ although its spectral density distribution is not generally defined (Chandrakumar and Markovic, 2017; Valtierra et al., 2020).

The electrode impedance also adds noise to the signal chain, V_E in **Figure 3**. The power spectral density (PSD) function of this noise source at low frequencies (below 10 Hz) is proportional to 1/f (Obien et al., 2015). Above these frequencies, the thermal noise becomes the main noise contributor and its value is given by (Obien et al., 2015):

$$\overline{v^2_{n,E}} = 4 \cdot k \cdot T \cdot Re(Z_e) \cdot \Delta f \tag{1}$$

where k is the Boltzamnn constant, T is the temperature, $Re(Z_e)$ is the real part of the electrode impedance and Δf the recording bandwidth. The resulting PSD is simplified in **Figure 3**.

Finally, the recording electronics, i.e., the AFE, also introduce noise to the signal of interest. The main noise contributor of the AFE is generally the IA because it involves the first amplification stage. The IA's PSD is conventionally divided into three sections: (i) from low frequencies to the corner frequency, f_{cf}, the flicker noise contribution, $v_{n,1/f,A}$, dominates the noise PSD; (ii) from

the corner frequency to the amplifier frequency bandwidth, f_{bw}, the main noise contributor is the thermal noise, $v_{n,th,A}$; and (iii) above this frequency the noise is filtered and can be neglected (Razavi, 2001) (**Figure 3**). Both flicker and thermal noise contributions will depend on the amplifier topology and operation region. In biomedical applications, amplifiers are commonly biased in sub-threshold region (Muller et al., 2015; Delgado-Restituto et al., 2017; Valtierra et al., 2020). Hence, for an IA employing an operational-transconductance amplifier (OTA), the thermal and flicker noise contributions can be respectively estimated by (Valtierra et al., 2020):

$$\overline{v_{n,th,A}^2} = \frac{4 \cdot k \cdot T \cdot \gamma \cdot \eta \cdot V_t}{I_b} \Delta f \tag{2}$$

$$\overline{v_{n,1/f,A}^2} = \frac{K_F}{W \cdot L \cdot C_{ox} \cdot f} \Delta f \tag{3}$$

where V_t is the thermal voltage, η the sub-threshold slope, $gamma = 1/2$ for the sub-threshold region, I_b the current through the OTA, C_{ox} is the gate-oxide capacitance, K_F is a flicker parameter dependent on the specific fabrication process and W and L are the width and length of the OTA.

Integrating this IA adjacent to the electrodes makes the power and area constraints of this stage even more restricted. In terms of the power consumption, neural devices in contact with the tissue have to be designed within the allowed limit of $< 1°C$ of brain tissue heating (Kim et al., 2007). Furthermore, the active area of the shank has to be minimized to increase the number of readout channels (Mora Lopez et al., 2017). Therefore, it can be observed from equations 2 and 3 that the thermal and the flicker noise contribution of the amplifier can be penalized.

In terms of thermal noise, the power consumption of the amplifiers located adjacent to the electrodes increases the shank heating, so the current through these amplifiers, I_b, has to be minimized. From equation 2 can be noted that the thermal noise contribution of the active electrode-AFE interfaces would theoretically be larger than in passive shanks. Nevertheless, as demonstrated by the finite element method simulations carried out in Mora Lopez et al. (2017), this power limitation depends on the structure employed for the probe. Thus, up to 20 mW of power dissipation in the shank can be tolerated without increasing the temperature of the tissue by one degree (Mora Lopez et al., 2017). This keeps the amplifier's power consumption and, consequently, the thermal noise contribution of this stage, at the same level as in conventional AFE structures by properly designing the probe.

In terms of the occupation area, reducing the active area located along with the electrodes makes it possible to increase the number of recording channels and, in turn, the recording density of the neural interface. Keeping the electrode area constant, the area will increase with the size of the amplifier located adjacent to the electrodes, establishing a trade-off between the amplifier's occupation area and the amplifier's flicker noise contribution (see Equation 3). While no such huge impact has been reported in the APs band, the effect of this noise becomes significant for LFP recording. This has been assessed by employing the integrated input-referred noise (IRN), which is the total integrated noise over the band of interest referred to the input of the circuit (Razavi, 2001). This is a widely used measure to evaluate the noise performance of the circuits. In this case, the IRN for the system presented in Mora Lopez et al. (2017) in the AP band is about 6.36 μV_{rms} while the IRN in the LFP band reaches 10.32 μV_{rms}. Therefore, the amplifier adjacent to the electrodes has to be carefully designed in terms of occupation area to not penalize the IRN of the circuit, specially at low frequencies.

3. NEURAL RECORDING AFES

Neural recording AFEs are traditionally made up of an LNA, a PGA, an anti-aliasing filter and an ADC. However, over the years this standard has gradually been adapted according to the requirements of each specific system and with the purpose of optimizing the performance of the circuit. Thus, five different high-performance approaches for neural AFEs have been simplified and illustrated in **Figure 4**.

The conventionally employed AC-coupled topology, continuous-time (CT) AFE (Brenna et al., 2016; Delgado-Restituto et al., 2017; Park et al., 2018a,b), is shown in **Figure 4A**. The basic structure of the LNA is presented in Harrison and Charles (2003). This topology obtains a high input impedance, which is desired to be as high as possible to reduce the attenuation of the signal due to the electrode impedance (Pazhouhandeh et al., 2020b), by reducing the size of the input capacitors. Moreover, the high-pass filter required to reject the input DC offset from electrodes is implemented in the IA, where the pole of the IA transfer function is set by the input capacitors and a pair of feedback resistors. Using pseudoresistors is a common technique for setting this pole at sub-Hz frequencies without penalizing the area of the AFE. However, these resistors conventionally present large temperature and process variations (Sharma et al., 2021). Furthermore, due to the lack of specific techniques for low-frequency noise reduction, IAs are usually made up of large input transistor area. Another significant disadvantage relies on the prone to saturation of the IA to input artifacts due to its high gain and its large time constant.

The chopper stabilization technique is a widely employed method to reduce the low frequency noise components of an amplifier by splitting, in the frequency domain, the flicker noise components from the signal of interest (Enz and Temes, 1996). In recent years, DC-coupled chopper-based AFE topologies (**Figures 4B,C**) have proven their efficiency in further reducing the flicker noise component of the IA. In these architectures, the input impedance is inversely proportional to the chopping frequency and the input capacitor value. Herein, two main impedance boosting techniques have been reported: implementing an impedance boosting loop (IBL) by means of a positive feedback network (Fan et al., 2011) (**Figure 4B**), or/and employing an auxiliary input path (Chandrakumar and Markovic, 2017) (not shown in **Figure 4B**), penalizing the IRN of the system. These DC-coupled topologies also require a mechanism to remove the input DC offset from the electrodes. One widely adopted solution consists of employing a DC SERVO

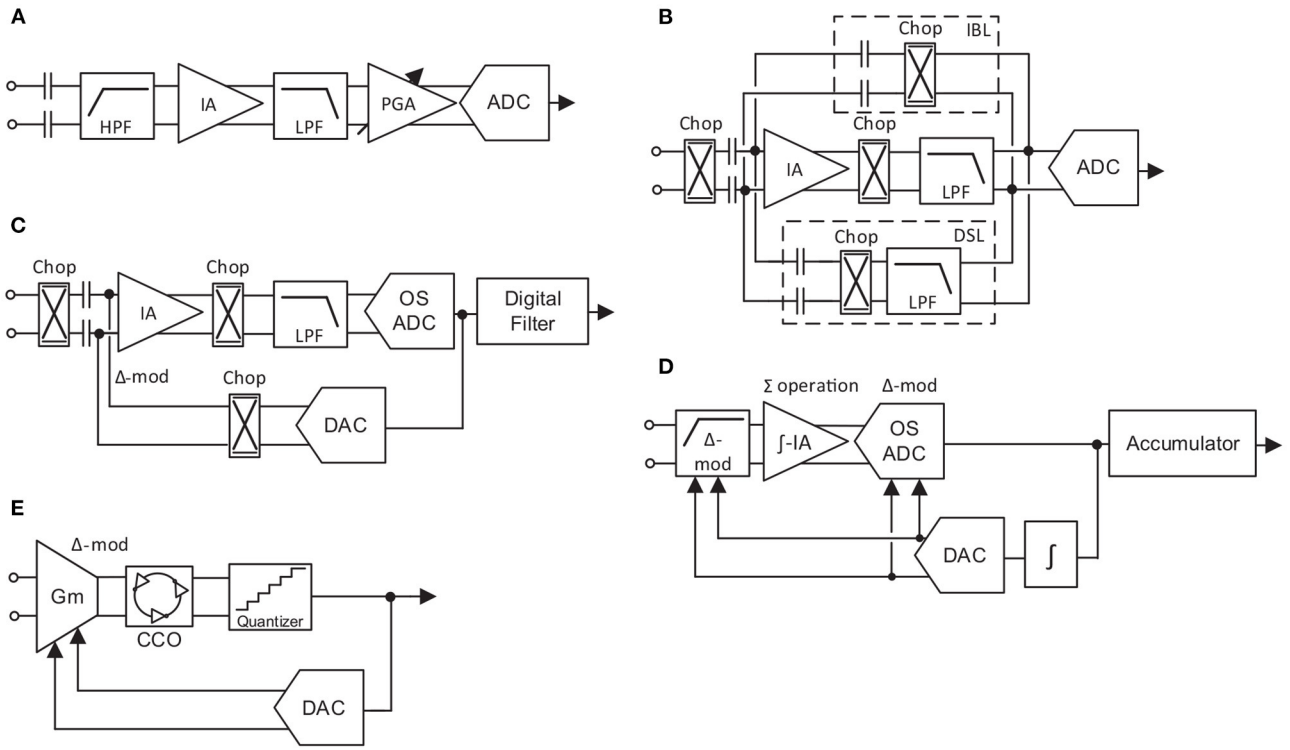

FIGURE 4 | Block diagram of high-performance neural AFEs. **(A)** Continuous-Time AFE topology. **(B)** Chopper-stabilized AFE topology. **(C)** Chopper-based Δ-AFE topology. **(D)** $\Delta^2\Sigma$ AFE topology. **(E)** VCO-Based $\Sigma\Delta$ AFE topology.

LOOP (DSL) (**Figure 4B**) in the analog domain (Fan et al., 2011; Chandrakumar and Markovic, 2017; Lee and Song, 2019; Samiei and Hashemi, 2019) or in the digital domain (Muller et al., 2015) (not illustrated). Another approach is based on employing the Δ-modulation technique. This technique relies on tracking differences between successive samples which inherently implements a high-pass filter. In this way, the applied technique consists of working with Δ-signals by feeding the previous (Johnson et al., 2017) or the predicted (Kim et al., 2018) value of the signal (**Figure 4C**) into the input of the IA by a mixed-signal loop. This method usually increases the dynamic range (DR) of the AFE at the cost of requiring an oversampled ADC (OS ADC).

Besides conventional AFE topologies, some alternatives based on Δ Σ schemes have been presented (Kassiri et al., 2017; Pazhouhandeh et al., 2020a). In contrast with the Δ-modulation technique, the Σ operation relies on the integration of the signal through the summation of successive samples (Carusone et al., 2011). A similar approach of continuous-time Δ Σ AFE is reported in Chandrakumar and Markovic (2018). Some of these architectures are also known as ADC-direct schemes and do not have IAs. Promising architectures based on this technique relies on applying twice the Δ-modulation and are know as Δ^2 Σ AFEs (**Figure 4D**) (Pazhouhandeh et al., 2020a). In these systems, the signal is Δ-modulated at the input, similar to **Figure 4C**). Then, the signal is integrated by the Σ operation carried out during the amplification stage and, finally, Δ-modulated again in the analog-to-digital conversion. Thus, the SNR is largely increased (Pazhouhandeh et al., 2020a). As in the chopper-based AFEs, however, the input impedance depends on the modulation frequency. To improve that, a Δ-modulation opamp-less topology was presented in Pazhouhandeh et al. (2018, 2020b) which increases the input impedance to the GΩs.

Finally, AFEs that rely on a conversion of the signal amplitude to the frequency domain, time/frequency based AFEs, show large efficiency in terms of occupation area (Tu et al., 2017; Jeon et al., 2019). Herein, voltage-controlled oscillators (VCOs) based circuits, which transforms the input signal amplitude into different oscillation frequencies, have recently proven to be an efficient low-power alternative to conventional AFEs (Jiang et al., 2017) and low-frequency filters (Leene and Constandinou, 2017). In these topologies, an AC-coupled input transconductance, G_m, converts the input voltage to current, which is translated to phase by a current-controlled oscillator (CCO) and, finally, converted to the digital domain by a quantizer. Due to the open-loop nature of the AFE, for large input signals the G_m suffers from strong non-linearity, requiring an extra digital circuit calibration at the output of the quantizer. A different approach to implementing VCO-based AFEs is reported in Prabha et al. (2015), Tu et al. (2017), Jeon et al. (2019) and shown in **Figure 4E**. To solve the dynamic range problem, a mixed-signal loop is employed to perform a $\Delta\Sigma$ operation. As in the previously presented

topologies, these Δ-signals at the input eliminate the DC-offset from the electrodes and allow the G_m to work in the linear region for a larger input range. However, the low-frequency noise contribution of the G_m is not reduced and large input transistors are needed to keep it within the system's noise margins.

3.1. Comparison of State-of-the-Art

A comparison of state-of-the-art AFEs and LNAs topologies are illustrated in **Figures 5–7**. It is worth observing that a green-red scale is provided in the figures to evaluate the IRN of each work: the green represents the lowest IRN values and the red the highest IRN values.

Firstly, **Figure 5** represents the evolution of the form factor over the last years for CT LNAs (**Figure 5A**) and for digitally-assisted AFEs (**Figure 5B**). It should be noted that digitally assisted AFEs comprise all AFE architectures presented in section 3, except for CT AFEs. The occupation area saving over the years for CT LNAs (**Figure 5A**) has not been as high as in the case of digitally-assisted AFEs (**Figure 5B**). This is mainly due to the fact that first topologies involving chopper-based amplifiers used to have large input capacitors to improve the IRN results.

On the other hand, **Figure 6** illustrates the noise efficiency factor (NEF), parameter which represents the performance of a circuit in terms of its noise contribution and power consumption, against the area per channel. The NEF is defined as:

$$NEF = v_{ni,rms} \cdot \sqrt{\frac{2 \cdot I_t}{V_t \cdot 4 \cdot k \cdot T \cdot \Delta f \cdot \pi}} \tag{4}$$

where $v_{ni,rms}$ the IRN of the amplifier and I_t the total current through the circuit. This parameter is widely used to illustrate the performance of neural AFEs. Thus, while in **Figure 6A**, this comparison is made for CT LNAs, in **Figure 6B**, this comparison is made digitally-assisted AFEs. Note how the NEF largely depends on the area of the LNA due to the impact of the flicker noise contribution in the case of the CT LNAs (**Figure 6A**). In **Figure 6B**, it can be observed how chopper-stabilized AFEs offer the lowest IRN at the cost of increasing the area per channel. Proposed solutions based on Δ Σ AFEs and mixed-signal feedback offer some of the best performances in terms of noise and area per channel.

Finally, **Figure 7A** compares the channel figure-of-merit (FoM) against the area per channel for different AFE architectures. This FoM represents the performance of the circuit in terms of power, resolution and bandwidth and is given by:

$$Channel\ \ FoM(DR) = \frac{P_{ch}}{2\,BW \cdot 2^{ENOB(DR)}} \tag{5}$$

where P_{ch} is the power consumption per channel and $ENOB(DR) = (DR(\text{dB})\text{- }1.76)/6.02$, represents the equivalent number of bits for the DR of the system. **Figure 7B** compares the LNA supply current with the normalized IRN, which is the result of multiplying the IRN by $\sqrt{BW}$. In both comparisons, CT LNAs show better results than digitally-assisted AFEs, due to the employment of low-power analog blocks instead of complex mixed-signal loops. Moreover, CT LNAs also usually have lower bandwidths than digitally-assisted AFEs, especially those using the chopper-stabilization technique. In **Figure 7B**, the IRN scale has been replaced by a red-blue scale which represents the occupation area per channel.

4. TIME-DIVISION MULTIPLEXING

TDM is a technique widely employed in communication systems. It relies on dividing the data from M-channels into M different time slots of the same output signal. Thus, after multiplexing, the signal from the M channels is shared by the same AFE block/s, reducing the number of instances of each multiplexed block employed by $M - 1$. The main advantage of the TDM technique in neural recording AFEs therefore lies in area saving, which will scale up with the number of multiplexed stages. The technique is carried out by an analog multiplexer, the operating frequency of which, f_{mux}, has to be at least $2 \cdot M$-times faster than the signal bandwidth, fb. The bandwidth of the subsequent block/s therefore has to be about M times larger than in non-multiplexed topologies, leaving the system's overall power consumption the same.

One of the main drawbacks of this technique is related to noise folding. Employing larger bandwidth blocks increases in-band noise, which will be folded to the baseband. Although anti-aliasing filters are used to reduce this spectral folding, if the multiplexer is located in one of the first stages of the AFE, this filter becomes harder to implement and another approach must be adopted. This problem is described in more detail in section 6.

Another noise source to take into account during system design is the crosstalk from an analog multiplexer. This crosstalk can be disclosed in four different components: (i) capacitive coupling between the input metal lines of the multiplexer; (ii) the finite off-resistance of the switches; (iii) time-adjacent channel crosstalk; (iv) capacitive coupling through the parasitic capacitance of the transistor used as a switch. The first three crosstalk sources can be ignored. In the first case, the impact of the capacitive coupling can be avoided by applying layout techniques such as the careful shielding of each input line. In the second, the subthreshold conduction of the switches is negligible due to the large back-bias effect in low-voltage topologies. The off-resistance is in the order of hundreds of GΩ, which does not represent a crosstalk source in the circuit (Seidl et al., 2012). Time-adjacent channel crosstalk reveals the multiplexer's ability to charge/discharge the load capacitors during the active period of a channel. If the multiplexer response is slow, a residual charge will appear between two time-adjacent channels, resulting in crosstalk noise. The time constant defined by the on-resistance of the switches along with the load capacitors of the circuit should therefore be designed to be as small as possible, in order to suppress this crosstalk source.

The effect of the capacitive coupling through the parasitic capacitance of the transistor can have a real impact at the multiplexer output (Chae et al., 2008). Multiplexer crosstalk can be defined as the effect of the turned-off channels at the output of the multiplexer. A complete mathematical analysis of this

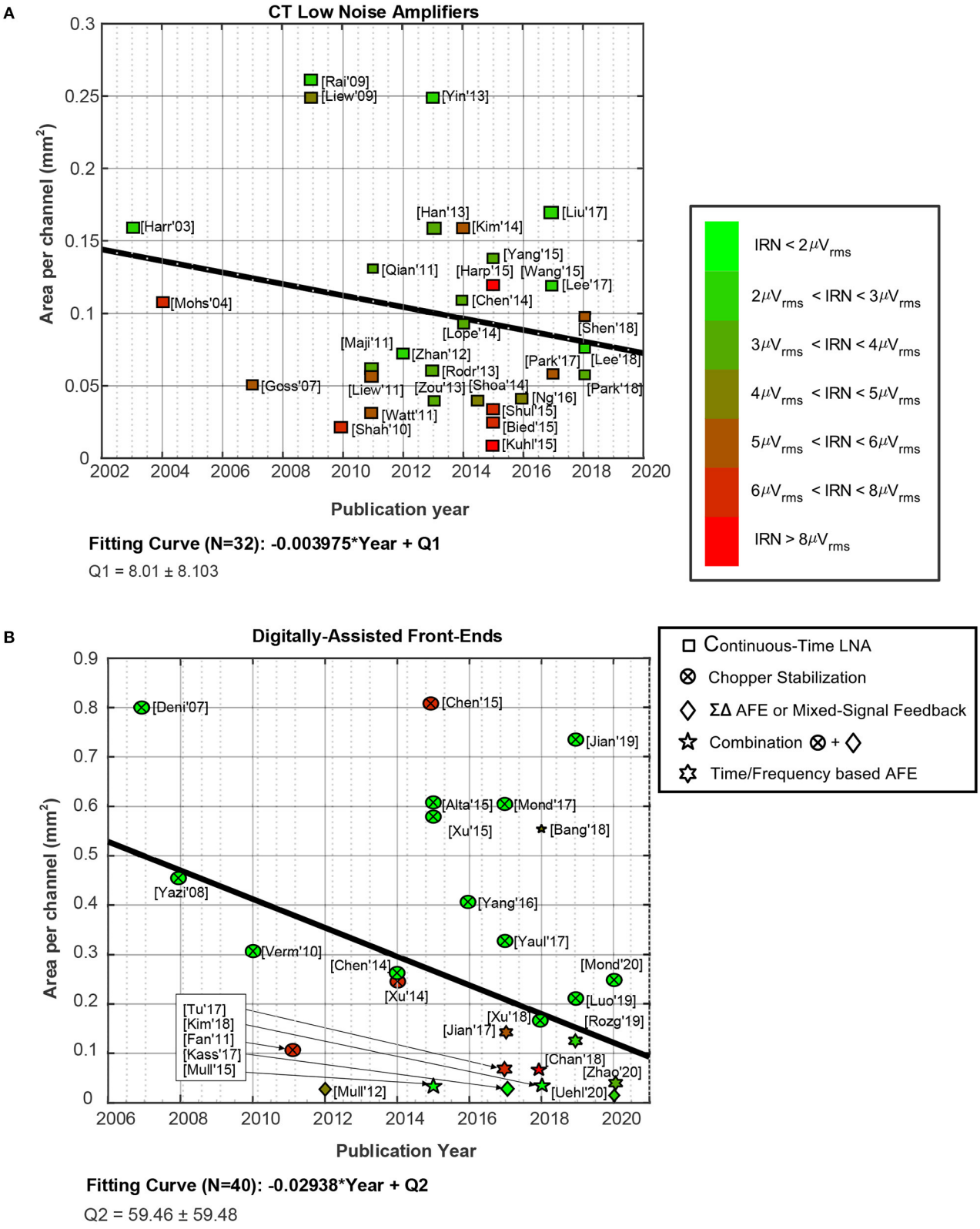

FIGURE 5 | Evolution of the form factor of neural AFEs over the years. The green-red scale indicates the value of the IRN of each reported circuit. Fitting curves represent the trend over the years of the area per channel. **(A)** For CT LNAs. **(B)** For digitally-assisted AFEs.

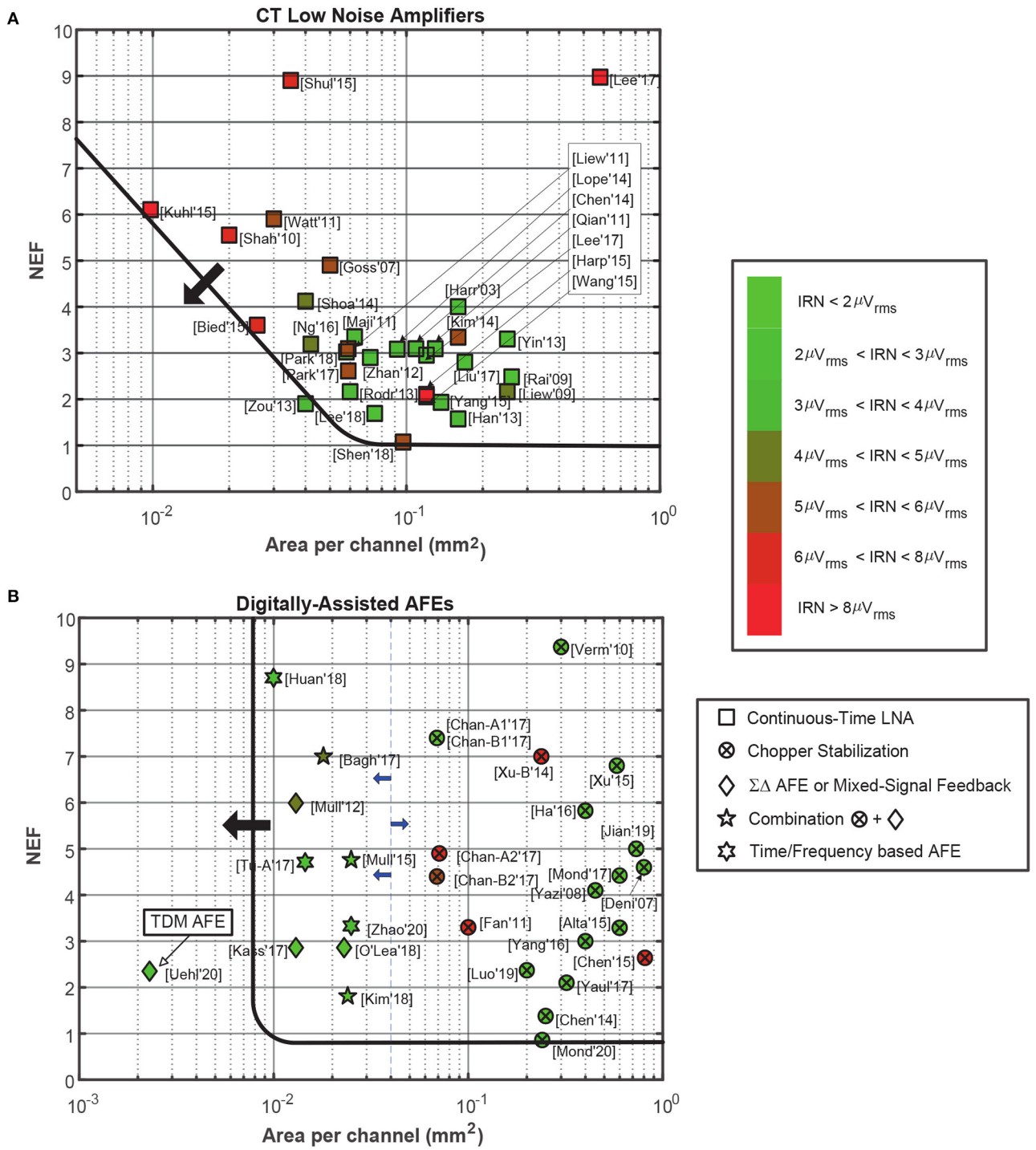

FIGURE 6 | Comparison of state-of-the-art LNAs and AFEs topologies in terms of NEF and area per channel. The green-red scale indicates the value of the IRN for each reported circuit. In both figures, arrows indicate the limit on the trend of current circuits, and how future approaches should be beyond the marked line. **(A)** For CT LNAs. **(B)** For Digitally-Assisted AFEs.

crosstalk effect is provided in Chae et al. (2008). The results from this analysis show that the value of output resistance of the previous stage strongly influences the crosstalk results. For instance, for a resistance value of 4 kΩ, the crosstalk noise is around −110 dB at 10 kHz (Chae et al., 2008). Therefore, by properly setting this value, this crosstalk source can be neglected.

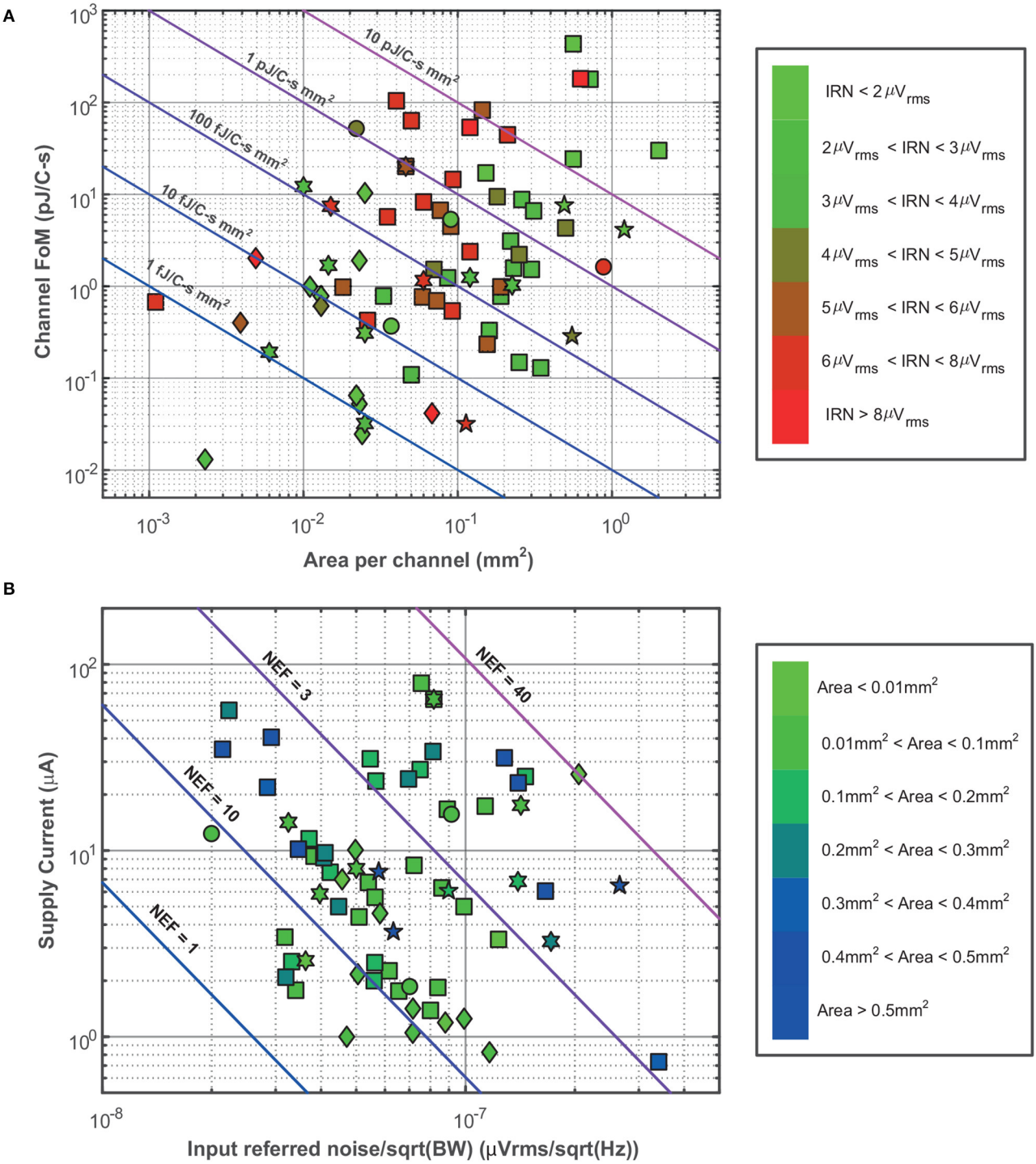

FIGURE 7 | Comparison of state-of-the-art LNAs and AFEs topologies in terms of Channel FoM and normalized IRN. **(A)** Channel FoM vs. area per channel comparison. The green-red scale indicates the value of the IRN of each reported circuit. The lines shows different FoM per area values as references. **(B)** Supply current vs. normalized IRN comparison. The green-blue scale indicates the value of the occupation area of each reported circuit. The lines show different NEF values as references. The employed symbol code is the same as shown in **Figure 6**.

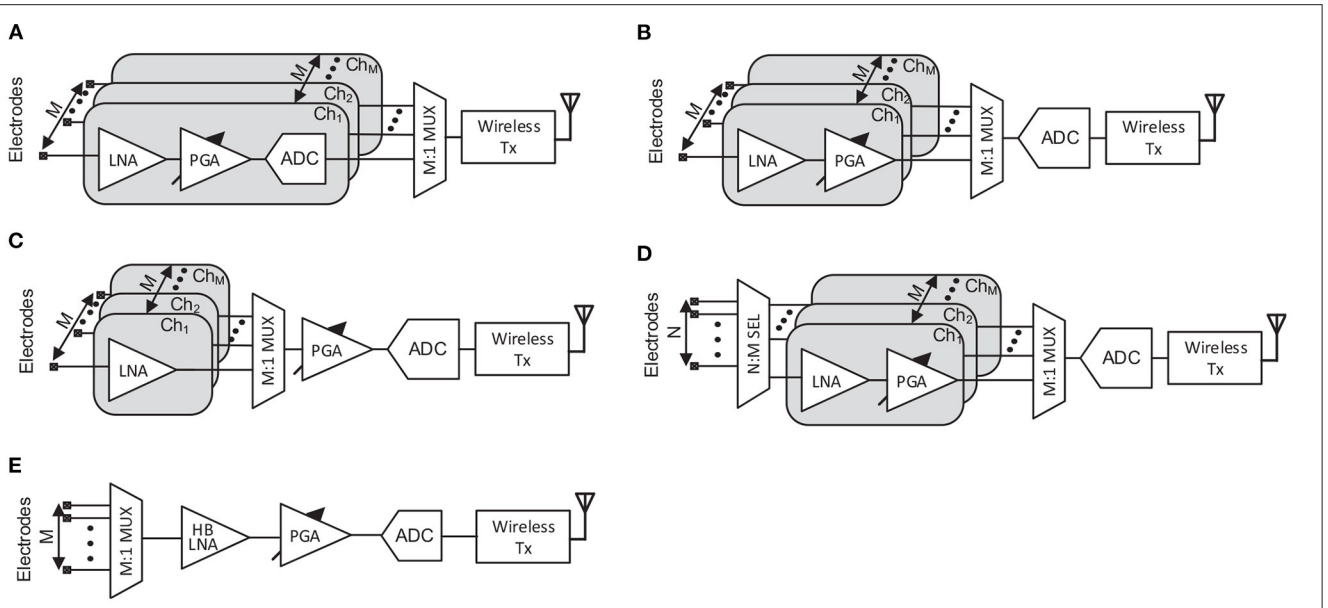

FIGURE 8 | Taxonomy of different AFEs depending on the location of the multiplexer. **(A)** Non-multiplexed AFE topology. **(B)** ADC sharing AFE topology. **(C)** PGA sharing AFE topology. **(D)** Switch array AFE topology. **(E)** Time-division-multiplexing AFE topology.

5. TAXONOMY OF NEURAL RECORDING MULTIPLEXING SYSTEMS

Some of the main building blocks of neural recording AFEs presented in section 3 can be multiplexed to save area. Neural recording multi-channel AFE topologies can thus be classified by the position of the multiplexer in the signal path and, consequently, by the number of multiplexed blocks (**Figure 8**). Note that **Figure 8** does not show the anti-aliasing filter. This is because although this low-pass filter is commonly embedded within the LNA, some works, such as Angotzi et al. (2018), include it in other stages.

5.1. Non-multiplexed AFE Topology

In non-multiplexed AFE topology (see **Figure 8A**), each channel is recorded by a low-rate (low sampling frequency per channel) low-power AFE. For M independent recording channels, M independent AFEs are therefore required. Herein, all the presented architectures in section 3 are suitable for this kind of topology. In terms of the electrode-AFE interface, the constraints of the active area in the shank make the integration of these AFEs along with the electrodes, beforehand, not suitable. Thus, integrating them far from the electrodes relaxes the size and power constraints of the AFE. This enables the inclusion of additional on-chip functionality for the AFE. Employing an AFE per channel also involves mismatch errors in multi-channel topologies (Ng and Xu, 2016). Low-frequency neural signals relax the bandwidth requirements of the AFE's blocks, leading to a reduction of the power consumption of each block. In addition, the design of the non-multiplexed AFE structure must meet the conventional requirements of neural recording AFEs: high input impedance, low-noise, low-power, small occupation area, large common-mode rejection ratio (CMRR), and large DC offset rejection (Muller et al., 2015; Chandrakumar and Markovic, 2017, 2018).

In terms of the ADCs used, despite using a low sampling frequency, conventionally up to few kHz, the need for one ADC per channel requires very careful design in order not to largely increase the area and power consumption of the neural recording IC. Successive-approximation (SAR) ADCs have generally shown good results for this kind of topologies (Gao et al., 2012; Brenna et al., 2016; Delgado-Restituto et al., 2017; Johnson et al., 2017), specially for providing low power consumption for resolutions about 8 to 10 bits (Delgado-Restituto et al., 2016). After conversion, the signal is multiplexed, typically by employing data serializers (Park et al., 2018a,b) (**Figure 8A**). In the digital domain, the signal presents higher noise margins and is more stable against crosstalk and other noise sources than in the analog domain, making it more suitable for multiplexing.

5.2. ADC Sharing and PGA Sharing AFE Topologies

One of the most popular approaches for multi-channel architectures is to use a single ADC shared by all channels (**Figure 8B**). Theoretically, this reduces the form factor and the power consumption of the IC. This topology is based on N structures with M channels per structure sharing a single ADC (N ADCs for the whole system) (Wattanapanitch and Sarpeshkar, 2011; Zou et al., 2013; Bagheri et al., 2014; Yeager et al., 2014; Liu et al., 2017). This approach has the same problems and advantages as the non-multiplexed AFE topology in terms of the AFE-electrode interface. Regarding the electrical properties of the AFE itself, after amplification the signal is directed toward

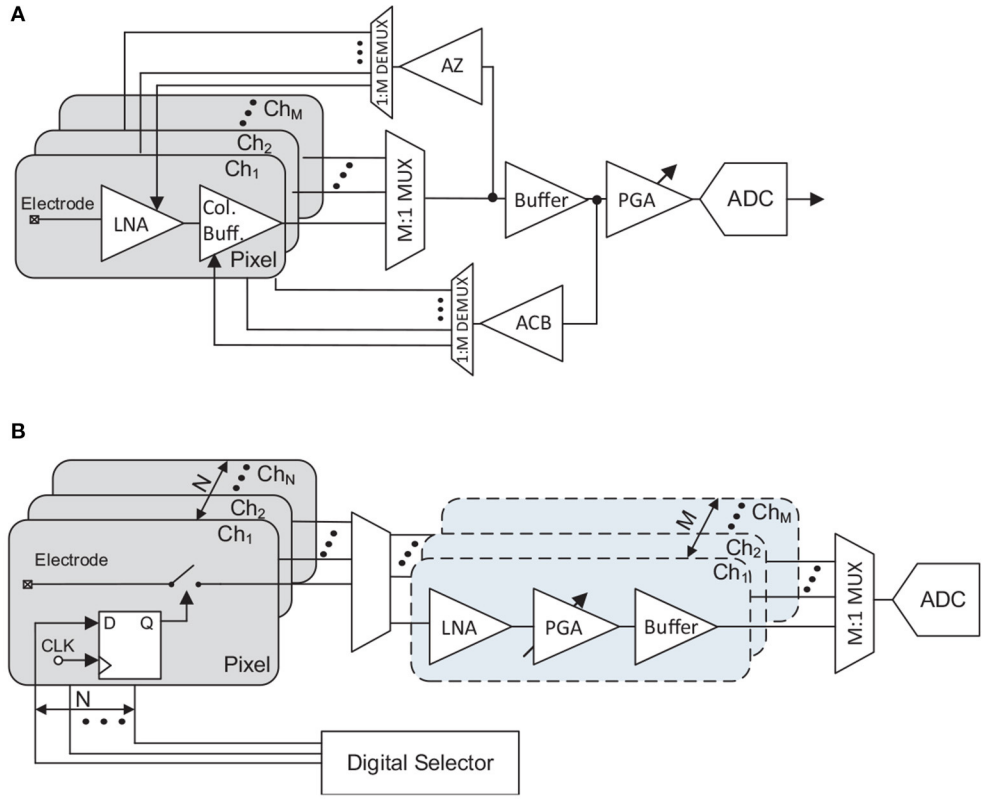

FIGURE 9 | Examples of PGA sharing and switch array AFE topologies. **(A)** Block diagram of the PGA sharing AFE topology presented in Angotzi et al. (2018). **(B)** Block diagram of the switch array AFE topology presented in Dutta et al. (2019).

the ADC by means of TDM. The M times increased sampling frequency increases the power consumption of the ADC and could even require driving buffers at the input of the converter (Noshahr et al., 2020). Most of the topologies presented in section 3 are suitable for being multiplexed at the ADC stage. However, those with a digitally-assisted loop will require memory blocks to store the information for each channel.

A similar scheme to the ADC sharing architectures involves using the same PGA and ADC for the M channels, as shown in **Figure 8C**). In the PGA sharing AFE topology, LNAs can be integrated into the same IC along with the rest of the AFE (Chae et al., 2009; Han et al., 2013; Liu et al., 2016), or along with the electrodes (Johnson et al., 2013; Angotzi et al., 2014, 2018, 2019). An interesting application example of PGA sharing with the LNA adjacent to the electrode is reported in Angotzi et al. (2018) and simplified in **Figure 9A**. In this architecture, the LNAs are integrated within the pixel of the neural probe and basically lie in an open-loop amplifier. To remove the DC offset without increasing the area of the pixel, an out-of-pixel autozero (AZ) amplifier is shared by all the LNAs through time-division-demultiplexing. Moreover, the column buffers are implemented in two stages: a pixel stage (with a column buffer per channel) and a base stage , i.e., not adjacent to the electrodes, which is shared by all the channels. The output of this shared buffer is fed into an amplifier (ACB). The short channel effects are then mitigated by time-division-demultiplexing the signal and feeding it into the pixel's column buffers.

5.3. Switch Array AFE Topology

All presented topologies allow full-frame read-out at the cost of reducing electrode density. To increase the number of electrodes, and therefore to increase the spatial resolution of the probe, a switch-matrix is integrated adjacent to the electrodes. More complex routes are used to rewire a group of electrodes to the available read-out channels (**Figure 8D**). This switch-matrix mainly comprises a large group of routing wires, switches, and a local memory such as a SRAM which allocates the connection status of the electrode (Frey et al., 2010), so that not so much active area is required. As in PGA sharing topologies, this architecture can also include amplifiers along with the electrodes (Huys et al., 2012; Mora Lopez et al., 2017) or just the switch-matrix (Frey et al., 2010; Ballini et al., 2014; Jun et al., 2017; Dutta et al., 2019). In this architecture, also known as static multiplexing, for N electrodes, the switch-matrix only selects M of them (with $N > M$) and interconnects them with the M read-out channels (AFEs). After the amplification stages, the signal is commonly multiplexed as in ADC sharing topologies. A simplified example of a switch array AFE corresponding to the neural probe scheme reported in Dutta et al. (2019) is shown in **Figure 9B**. Note that the switch-matrix incorporates memories

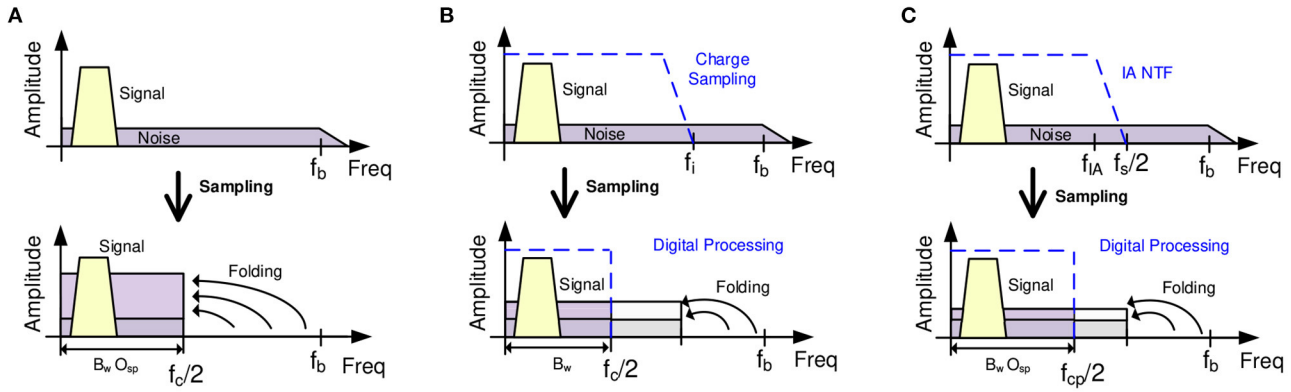

FIGURE 10 | Illustration of the noise folding problem in TDM AFEs. **(A)** Noise folding problem in multiplexing circuits. **(B)** Noise folding in multiplexing circuits applying charge sampling techniques. **(C)** Noise folding in multiplexing circuits applying a narrow-band CDS architecture.

(flip-flops) which select the electrodes to record using a digital selector integrated into the base of the neural probe. In this kind of topology, the overall form factor required defined by the number of readout channels restricts the possibilities of implementing some of the topologies of the section 3.

One of the main issues concerning these structures is the selection of the electrodes to be read and those not to be read. One widely-used solution to this involves a process which firstly records the whole electrode matrix during different time slots. The data is then processed and some groups of electrodes are prioritized to be read by applying an optimization algorithm (which could involve machine learning) based on the previously recorded signals and the main purpose of the recording. Another alternative, presented in Mora Lopez et al. (2017), divides the electrode matrix into a set of subgroups. In this proposal, the electrodes in each subgroup are selected pseudo-randomly, ensuring that all areas of the probe are recorded.

5.4. Time-Division-Multiplexing AFE Topology

One new trend in multi-channel neural recording topologies is to place the multiplexing at the input of a single AFE (**Figure 8E**) which is shared by all channels. This reduces the occupation area per channel and ignores mismatch between recording channels, potentially making the power consumption per channel lower than in conventional topologies (a further breakdown of the AFE time-division-multiplexing specifications and architectures is provided in section 6). For instance, it can be observed in **Figure 6B** how the TDM AFE reported in Uehlin et al. (2020) shows one of the most promising results in terms of area and noise equivalent bandwidth (NEB), which is defined as the bandwidth of a brickwall filter which produce same integrated noise power as that of the analyzed system, for this kind of topologies. The main drawback of these topologies relies on the requirement of a high-bandwidth LNA (HB LNA) to fast-multiplex all the channels, which significantly increases power consumption and in-band noise due to aliasing (Sharma et al., 2018).

6. REVIEW OF TIME-DIVISION-MULTIPLEXING AFES

One of the first reported TDM AFEs was presented in Raducanu et al. (2017). In this architecture, the TDM technique was only used for the amplifiers within the pixel, reducing the number of interconnection wires and increasing the electrode density of the neural probe. The AFE/electrode ratio, however, was still 1:1. Recently, new TDM systems have emerged with multiplexing of the whole AFE (Pérez-Prieto et al., 2019; Sharma et al., 2019; Uehlin et al., 2020). The aim of this kind of architectures is to reduce the power and area of the whole recording interface, but here two major design issues arise: noise folding and DC offset from electrodes.

6.1. Noise Folding in TDM AFEs

For an M-channel multiplexed recording device, the sampling frequency, f_s, has to be M times faster than for a single channel, ($f_c = 2 \cdot f_b$), in order to keep the same throughput rate per channel, i.e., $f_s = M \cdot f_c$. For voltage sampling with a single pole low-pass filter response, the required IA bandwidth will therefore be given by (Sharma et al., 2018):

$$f_{BA} = \frac{\ln(\epsilon) \cdot f_s}{2 \cdot pi} = \frac{\ln(\epsilon) \cdot f_c \cdot M}{2 \cdot pi} \tag{6}$$

where ϵ is the tolerable dynamic settling error. Thus, the NEB for the multiplexed topology will be determined by:

$$NEB_{TDM} = \frac{\pi}{2} \cdot f_{BA} = -f_s \cdot \ln(\epsilon)/4 = -M \cdot f_c \cdot \ln(\epsilon)/4 \tag{7}$$

From equation 7 it can be concluded that the NEB increases proportionally with the number of channels. For APs recording, for example, the NEB in TDM AFEs is $3.5 \cdot M$ higher than for conventional non-multiplexed AFE topologies (Sharma et al., 2018). Accordingly, the out-of-band noise components are folded-back to the baseband which largely increases the system's in-band noise due to aliasing (Raducanu et al., 2017). **Figure 10A**

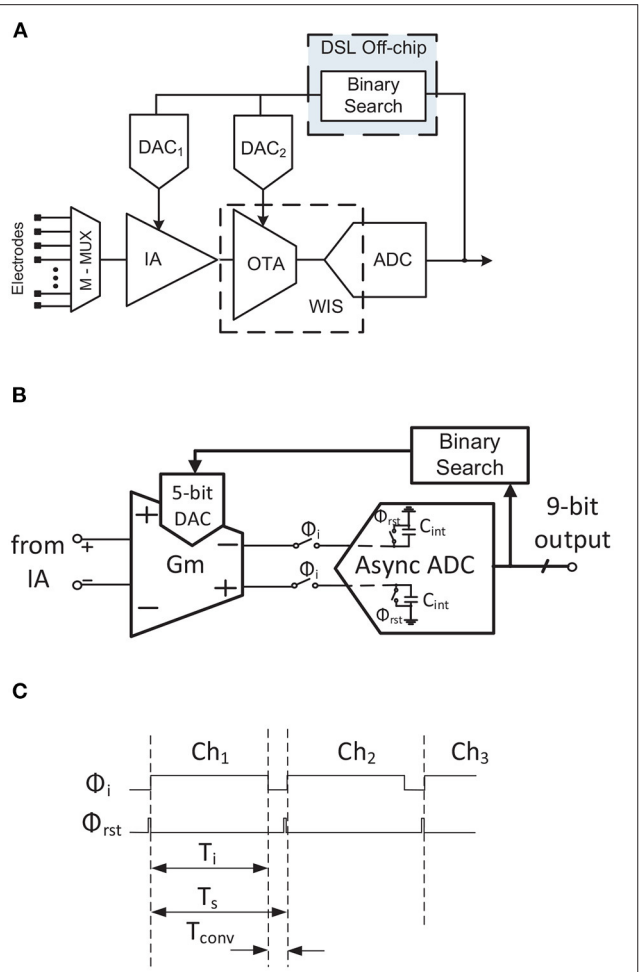

FIGURE 11 | TDM AFE proposed in Sharma et al. (2019). **(A)** Block diagram. **(B)** Simplified schematic of WIS and DC Servo Loop. **(C)** Simplified timing diagram.

illustrates this noise folding process: at the sampling instant, all the noise components above the band of interest which are not filtered ($f_c/2$ in **Figure 10**) are folded-back to the signal bandwidth. To solve this problem, the NEB of the AFE has to be reduced without sacrificing settling accuracy within the time allocated for channel sampling.

The first approach to coping with this problem is to apply charge-sampling (CS) instead of voltage sampling (Raducanu et al., 2017; Smith et al., 2017; Uehlin et al., 2020). The windowed integration sampling solution proposed in Sharma et al. (2018) can be considered as a kind of charge sampling. The main idea of this technique is based on integrating the signal during a period T_i, with $f_i = 1/T_i$ and $f_c < f_i < f_s$, and then sampling the last value. High-frequency noise components are filtered (**Figure 10B**) according to a *sync* filter specifications, i.e., $sin(x)/x$ (Gang and Jiren, 2000), reducing the noise folding effect. In terms of circuit implementation, this technique is performed by a G_m-cell driving a sample-and-hold capacitor, C_{int}, as shown in **Figures 11B**, **12B**. The gain of this block will therefore be given by G_m, T_i and C_{int} (see **Table 1**). However, this technique has some significant drawbacks: (i) the pole of the *sync* filter and the DC gain of the architecture are very sensitive to clock jitter (Gang and Jiren, 2000); (ii) process variations will have a high impact on the system's gain and time constant due to the employment of an open-loop structure; (iii) low-frequency noise components are not reduced; (iv) large common-mode (CM) signals could change the operating point of the G_m stage, which may lead to distortion or even saturation.

Another solution is to use a narrow-band correlated double sampling (CDS) scheme (Pérez-Prieto et al., 2019), **Figure 13B**. In this architecture, the AFE transfer function is reduced by the low-pass filter which the CDS inherently implements, as illustrated in **Figure 10C**. The noise in conventional CDS topologies would normally be doubled due to spectral folding, but since the sampling frequency of the CDS is higher than the CDS amplifier bandwidth, the folded noise components in the bandwidth of interest are reduced as illustrated in **Figure 10C**. Moreover, the flicker noise component is also palliated by the CDS scheme (Enz and Temes, 1996), while the stage power consumption retains approximately the same value as without CDS. In addition to these advantages, since the CDS is a closed-loop structure it has none of the above-mentioned gain accuracy problems, its gain being fixed by the ratio between the input capacitor (C_{in}) and the feedback capacitor (C_{fb}). This makes the system more robust to the influence of large CM signals.

Table 1 briefly compares the two solutions reported for reducing noise folding in TDM AFEs. As can be seen, the main advantages of CDS over CS/WIS are related to CDS being a closed loop architecture. The highest gains, however, are achieved in CS/WIS structures without significantly increasing power consumption, whereas in CDS the power requirement for the same gain is higher.

6.2. DC Offset From the Electrodes in TDM AFEs

DC offset from electrodes is a recurrent problem in DC-coupled AFEs (Fan et al., 2011; Chandrakumar and Markovic, 2017; Samiei and Hashemi, 2019). In any of the presented topologies with an IA per channel, DC offset can usually be rejected using large time constant high-pass filtering. However, analog large time constant filters are not suitable in rapid multiplexing systems, since the filtering would increase crosstalk between channels and would not be fast enough to reject the DC offset from each channel. One solution to this problem could be to limit the gain of the AFE and to increase the resolution of the ADC. However, this extra resolution, together with the high sample rate required for multiplexing, would make the ADC unsuitable for low-power designs.

High-pass filtering the signal through a mixed-signal loop has been adopted as an alternative approach to palliating the DC offset problem in DC-coupled topologies (Muller et al., 2015; Bagheri et al., 2017). In this method, a sub-Hz finite-impulse-response (FIR) or infinite-impulse-response (IIR) filter is fed into the input of the AFE by a digital-to-analog converter (DAC). While the filter can be designed to not penalize the system's power

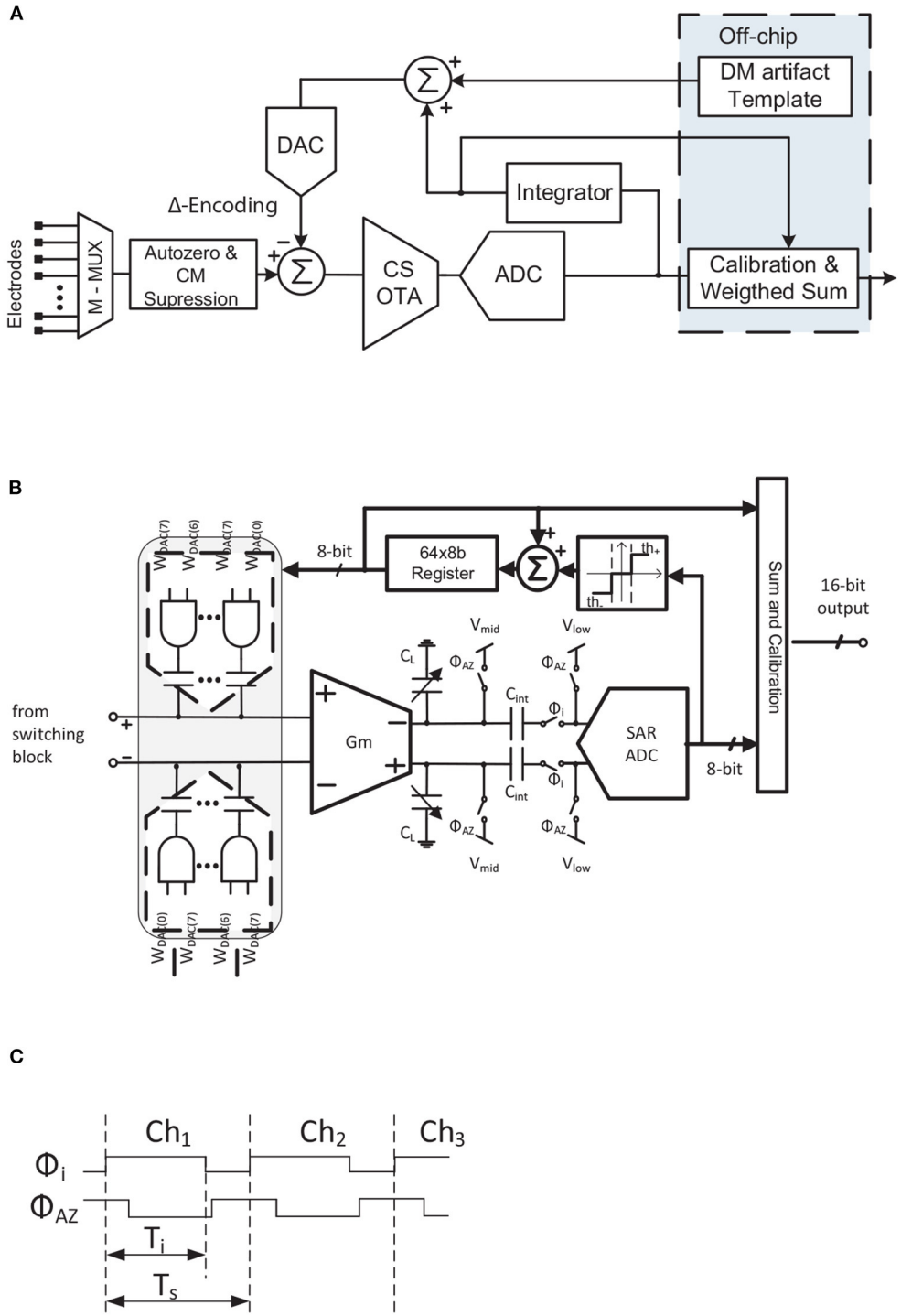

FIGURE 12 | TDM AFE proposed in Smith et al. (2017) and Uehlin et al. (2020). **(A)** Block diagram. **(B)** Simplified schematic of CS amplifier and Δ-Encoding loop. **(C)** Simplified timing diagram of CS amplifier.

consumption and occupation area, the required DAC resolution has to be high enough not to increase the noise at the input of the AFE. The number of bits required will be determined by the resolution of the ADC, the overall gain through the signal path, and the IRN of the AFE. In most practical cases, a DAC of more than 16-bits is required, which strongly compromises

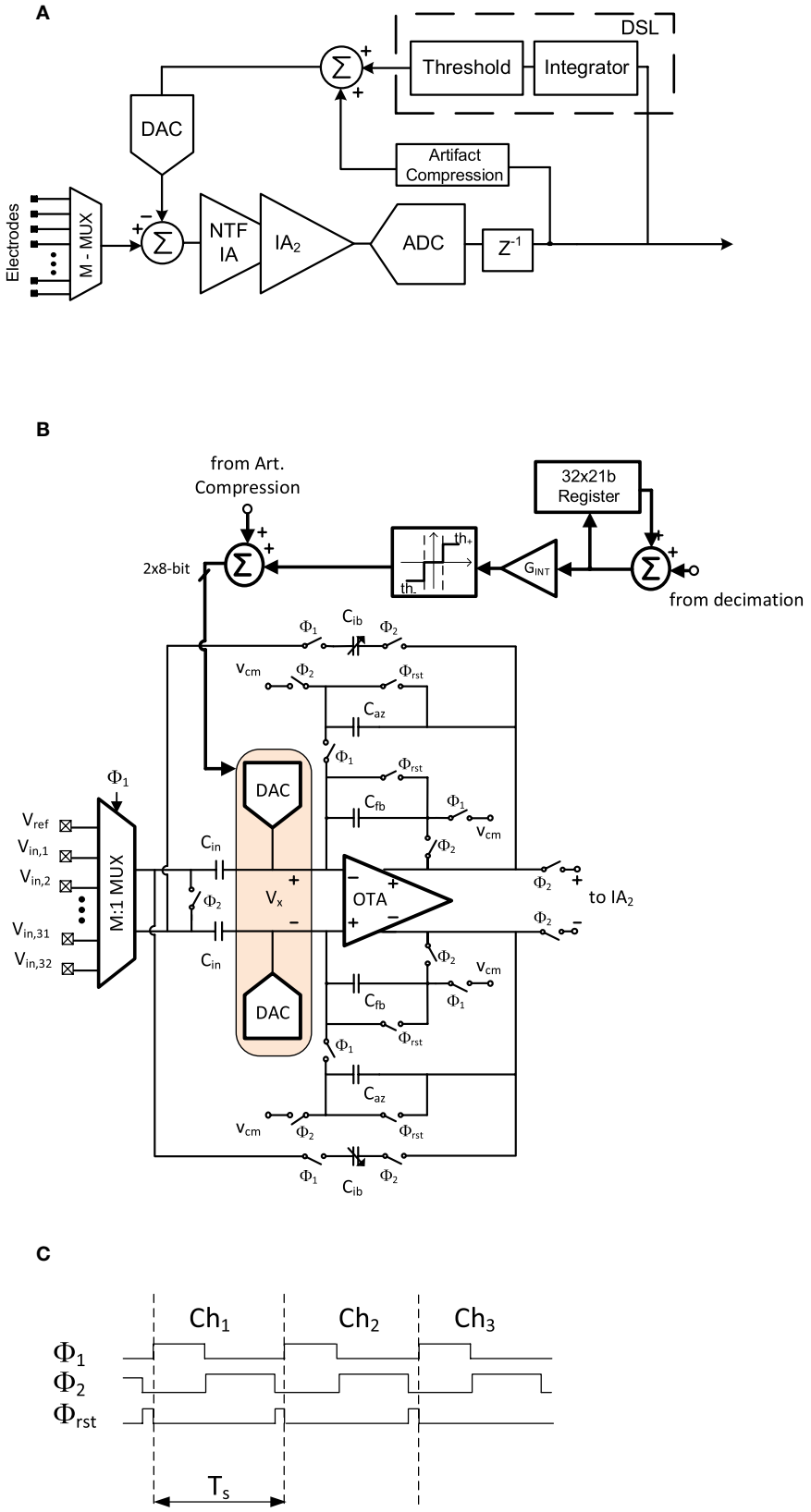

FIGURE 13 | TDM AFE proposed in Pérez-Prieto et al. (2019). **(A)** Block diagram. **(B)** Simplified schematic of CDS amplifier. **(C)** Simplified timing diagram of CDS amplifier.

TABLE 1 | Noise-folding aware structures comparison.

	Architecture	Gain	Noise filtering	Noise folding	Flicker reduction	CMRR insensitive	Clock/process variations	Power requirements
CS / WIS	Open-Loop	$\frac{G_m \cdot T_i}{C_{int}}$	$sync^2$	No	No	No	Weak	Low
CDS	Closed-Loop	$\frac{C_{ia}}{C_{fb}}$	$sync^2$	Yes	Yes	Yes	Robust	Medium

the form factor specification of the neural recording AFE. One proposed solution for implementing this high-resolution DAC is to employ a $\Delta\Sigma$ modulator (Muller et al., 2015; Bagheri et al., 2017). However, this method is not feasible for TDM AFEs because the required oversampling frequency will be multiplied by M, and this will significantly impact the power consumption of the digital part of the IC. An alternative to a high-resolution DAC would be to use a binary search algorithm (Sharma et al., 2019) which initially computes the DC offset codes for each channel and retains the correction values until a threshold condition occurs. At that instant, the binary search recalculates the correction value for each channel. By applying this method, DC offset drifts are palliated without increasing the IRN of the AFE. On the other hand, although the system range is ensured, there will be residual offset at the output of the AFE. This will have to be filtered in the digital domain.

Another proposed solution is based on working with Δ-signals (as illustrated in **Figures 4C–E**). In this approach, the system tracks differences between successive samples, high-pass filtering the input signal. The signal then has to be reconstructed in the digital domain using an integrator/accumulator. This technique can be transferred to TDM AFE topologies by employing registers to store the previously sampled value of each channel. One example of a TDM AFE which exploits this technique is reported in Smith et al. (2017), Uehlin et al. (2020).

6.3. Comparison of TDM AFE Architectures

Despite their promising results, TDM AFE topologies have not to date been researched in depth. In this subsection, three reported TDM AFE architectures are detailed. Block diagrams of these neural AFEs are shown in **Figures 11A**, **12A**, **13A**.

The first architecture, reported in Sharma et al. (2018) and Sharma et al. (2019), is shown in **Figure 11A**. The IA comprises a capacitive feedback single-stage cascaded OTA. An open-loop OTA is employed as a G_m-cell along with the SAR ADC capacitors to implement the WIS filter and to further amplify the signal (**Figure 11B**). This reduces the high-frequency noise components from the IA. The timing diagram of this operation is shown in **Figure 11C**. It can be seen that the integration period, T_i, lasts for most of the sampling period T_s. After that, before the capacitors of the ADC (ϕ_{rst}) are reset and the input channel is changed, the conversion phase, T_{conv}, takes place for only 11% of the sampling period. This short-time conversion is carried out by an asynchronous converter. To remove the DC offset, a binary search algorithm is implemented externally by a Python script. This algorithm recomputes the 9-bit code each second to palliate the input DC offset. This is fast enough to compensate DC drifts at the input. The code is divided into 4-bits for DAC_1 and 5-bits for DAC_2 and maximizes the useful dynamic range of the system while reducing the ADC requirements. It should also be mentioned that both DACs are embedded in the amplifier structure.

A Δ-Encoded TDM AFE was first presented in Smith et al. (2017) and further developed in Uehlin et al. (2020) (**Figure 12A**). In this architecture, after the input multiplexer, an input switching scheme consisting of a set of switches with a couple of input capacitors performs two main functions: (i) autozeroing the inputs to reduce crosstalk between adjacent channels; and (ii) largely suppressing the CM signals. An 8-bit capacitive DAC connected to the input node of the OTA then carries out the Δ-operation by subtracting the signal value previous to the present value. This also minimizes the DC offset, improving the system's dynamic range. Afterwards, the Δ-signal is amplified by a charge-sampling amplifier consisting of an open-loop G_m-cell and capacitors C_L (**Figure 12B**). Note that the value of C_L is variable, mainly to set the gain of the charge-sampling topology and to palliate the ϕ_i clock variations. A timing diagram of this charge-sampling block in normal recording mode is shown in **Figure 12C**. Firstly, the signal is integrated during ϕ_i. Then, in the ϕ_{AZ} phase the capacitors are reset. Once the signal is converted by an 8-bit SAR ADC, it can follow two paths: (i) through the mixed-signal loop to perform the encoding technique and (ii) to the output. The first step of the mixed-signal loop is a user-programmable threshold block which determines the update quantity of the tracking signal. The update values, which can be -1, 0, or $+1$, are added to the previous tracking value. A 64x8-bit register stores the previous values of the correction signal for each channel. This register, together with the tracking update, performs an integration loop. The output signal from this loop feeds the DAC and is also scaled and added to the ADC output in order to reconstruct the signal. The output code thereby increases its resolution from 8 to 16 bits.

Another approach to TDM AFE is shown in **Figure 13A** (Pérez-Prieto et al., 2019). In this architecture, both IAs are implemented using narrow-band CDS architectures to filter the flicker and high-frequency noise components of the circuit and to provide a robust closed-loop structure against CM interferences. The scheme of the first IA is shown in **Figure 13B**. An 8-bit capacitive DAC is connected to each input virtual ground node of the IA, V_x. These DACs close the mixed-signal loop which, in addition to rejecting the DC offset, also implements an artifact compression technique, thus increasing the dynamic range of the circuit. The input impedance of the AFE is boosted by a couple of capacitors, C_{ib}, included in the CDS loop (Fan et al., 2011). The timing diagram of this stage is shown in **Figure 13C**. Before reading the input of the multiplexer, the feedback capacitors are reset in order to reduce crosstalk between adjacent channels. The signal is then amplified and flicker-reduced in phase ϕ_2.

TABLE 2 | Comparison of high-performance AFEs (range of values).

AFE topology	Continuous-time	Chopper-stabilized	Chopper-based ΔΣ	ΔΣ	Time/frequency based	TDM Uehlin et al., 2020
Power/channel (μW/ch)	[0.0015[d]–114.8[c]]	[0.017[i]–2160[j]]	[0.8[p]–9.9[n]]	[0.63[s]–4.79[r]]	[3.2[y]–21[x]]	2.98
IRN normalized ($\mu V_{rms}/\sqrt{Hz}$)	[0.0068[b]–1.354[d]]	[0.0038[i]–0.7518[l]]	[0.0443[p]–0.2656[q]]	[0.0492[r]–0.0716[t]]	[0.0325[x]–0.639[w]]	0.0884
Area/channel (mm^2/ch)	[0.0098[f]–0.26[e]]	[0.017[k]–0.81[j]]	[0.018[n]–0.55[q]]	[0.013[u]–0.023[t]]	[0.01[y]–0.135[v]]	0.0023
Input impedance (MΩ)	[4[b]–61[a]]	[1[j]–5400[h]]	[20[o]–1000[n]]	[1[s]–1000[r]]	[50[w]–∞[v])	92
NEF	[1.07[g]–19.4[c]]	[0.86[m]–126.7[l]]	[1.81[p]–26.03[q]]	[2.86[u]–5.99[r]]	[3.33[z] –57.61[w]]	2.35

[a]Leene and Constandinou, 2017; [b]Zhang et al., 2013 ; [c]Mohseni and Najafi, 2004 ; [d]Harpe et al., 2015 ; [e]Rai et al., 2009 ; [f]Kuhl and Manoli, 2015 ; [g]Shen et al., 2018; [h]Ha and Yoo, 2016; [i]Jiang et al., 2019; [j]Chen et al., 2015; [k]Chandrakumar and Markovic, 2017; [l]Xu et al., 2014; [m]Mondal and Hall, 2020; [n]Bagheri et al., 2017; [o]Chandrakumar and Markovic, 2018; [p]Kim et al., 2018; [q]Bang et al., 2018; [r]Muller et al., 2012; [s]Kassiri et al., 2017; [t]O'Leary et al., 2018; [u]Muller et al., 2015; [v]Jiang et al., 2017; [w]Mohan et al., 2017; [x]Tu et al., 2017; [y]Huang et al., 2018; [z]Zhao et al., 2020.

It is then oversampled and, after analog-to-digital conversion, filtered and decimated. The resolution of the signal is thus increased from 10 to 14 bits. In the mixed-signal loop, the DSL mainly comprises an integrator, the gain of which sets the sub-Hz cutoff frequency. This integrator is voltage-triggered so as not to produce input oscillations.

6.4. Comparison of State-of-the-Art TDM and High-Performance AFEs

Table 2 shows a final comparison between TDM AFEs and the high-performance neural AFEs presented during section 3. Due to the fact that each presented AFE topology comprises several and different works, this comparison has been carried out by employing the lowest and highest reported values for each topology. Thus, it is worth observing how TDM AFEs provide the lowest values in terms of occupation area without significantly penalizing the rest of the AFEs' specifications. This Table corroborates the comparisons of the state-of-the-art previously presented in section 3.

7. DISCUSSION AND FUTURE WORKS

This work has presented a review of recording techniques for high-channel-count, densely-spaced microelectrode arrays. Two of the main concerns when increasing the number of read-out channels in neural recording devices are the occupation area and the power consumption of the silicon-based signal conditioning circuitry. Although the design effort has to be focused on these two factors, other significant neural AFE specifications such as low noise contribution, low crosstalk between channels and high input impedance also have to be satisfied.

Firstly, the issue of whether or not to employ active electrode-AFE interfaces was introduced. With regard to crosstalk, the reported analysis in Du et al. (2009), Seidl et al. (2012), Lopez et al. (2014) has shown how placing the amplifier adjacent to the electrodes significantly minimizes crosstalk between the interconnection wires. However, the power consumption and occupation area of the amplifier are severely limited by the heating and the form factor of the active area. The noise contribution of the active electrode-AFE interface will therefore be larger than for an amplifier placed on the base of the neural probe. With regard to thermal noise, the power constraints of these interfaces depend on the device employed, and this improves the design flexibility to reduce the thermal noise floor. On the other hand, flicker noise is larger for the active interfaces due to the small size of the employed amplifier. The main consideration when using or not using active electrode-AFE interfaces is therefore the reported crosstalk-flicker noise tradeoff.

High-performance neural AFE topologies have been disclosed and briefly introduced and compared. Herein, one commonly employed method for reducing the number of recording blocks is the TDM technique. This paper proposes a classification of neural recording architectures into five different topologies based on the location of the multiplexer in the signal path. Over the last few years, non-multiplexed AFE topologies have been consolidated as one of the best techniques in terms of power consumption and occupation area thanks, among other things, to their design flexibility. Moreover, different schemes of non-multiplexed architectures have been introduced, demonstrating different alternatives for implementing these topologies without penalizing neural AFE specifications. Also, novel TDM AFEs have demonstrated the capability of multiplexing at the AFE input to reduce area and power more than in conventional ADC or/and PGA sharing topologies. Although some strategies, such as charge sampling, have been reported to filter high-frequency noise components, the trade-off between the number of multiplexed channels and the noise increment due to aliasing has to be taken into account in the design process. Furthermore, no TDM structures have been reported with more than 64 channels. This work also provides a state-of-art comparison illustrating how non-multiplexed AFEs and TDM AFEs are generally reported to offer the best performance, while switch array AFEs have the largest number of input channels.

Future advances in neural recording techniques should follow the trends mentioned above. Although not mentioned during this work, one of the main problems associated with these techniques is the processing and transmission of data. Increasing the number of channels considerably increases the amount of data to be processed and transmitted. This increases consumption in the digital part of neural recording systems, making it comparable with that of the analog part. Moreover, as these systems are intended for long-duration implants, the amount of data to be stored could be too big. New techniques for data compression and feature extraction must therefore emerge to address these problems.

AUTHOR CONTRIBUTIONS

NP-P and MD-R conceptualized the study, processed the data and wrote and reviewed the article. All authors contributed to the article and approved the submitted version.

FUNDING

This work has been supported by the Spanish Ministry of Science and Innovation under Grant PID2019-110410RB-I00 and the European Regional Development Fund (ERDF/FEDER)Program.

REFERENCES

Angotzi, G. N., Boi, F., Lecomte, A., Miele, E., Malerba, M., Zucca, S., et al. (2019). SiNAPS: an implantable active pixel sensor CMOS-probe for simultaneous large-scale neural recordings. *Biosens. Bioelectron.* 126, 355–364. doi: 10.1016/j.bios.2018.10.032

Angotzi, G. N., Boi, F., Zordan, S., Bonfanti, A., and Vato, A. (2014). A programmable closed-loop recording and stimulating wireless system for behaving small laboratory animals. *Sci. Rep.* 4, 1–11. doi: 10.1038/srep05963

Angotzi, G. N., Malerba, M., Boi, F., Miele, E., Maccione, A., Amin, H., et al. (2018). A synchronous neural recording platform for multiple high-resolution CMOS probes and passive electrode arrays. *IEEE Trans. Biomed. Circ. Syst.* 12, 532–542. doi: 10.1109/TBCAS.2018.2792046

Bagheri, A., Salam, M. T., Perez Velazquez, J. L., and Genov, R. (2014). "56-channel direct-coupled chopper-stabilized EEG monitoring ASIC with digitally-assisted offset correction at the folding nodes," in *IEEE 2014 Biomedical Circuits and Systems Conference, BioCAS 2014* (Lausanne), 659–662. doi: 10.1109/BioCAS.2014.6981812

Bagheri, A., Salam, M. T., Perez Velazquez, J. L., and Genov, R. (2017). Low-frequency noise and offset rejection in dc-coupled neural amplifiers: a review and digitally-assisted design tutorial. *IEEE Trans. Biomed. Circ. Syst.* 11, 161–176. doi: 10.1109/TBCAS.2016.2539518

Ballini, M., Muller, J., Livi, P., Chen, Y., Frey, U., Stettler, A., et al. (2014). A 1024-channel CMOS microelectrode array with 26,400 electrodes for recording and stimulation of electrogenic cells *in vitro*. *IEEE J. Solid State Circ.* 49, 2705–2719. doi: 10.1109/JSSC.2014.2359219

Bang, J.-S., Jeon, H., Je, M., and Cho, G.-H. (2018). "6.5μw 92.3db-dr biopotentialrecording front-end with 360mvpp linear input range," in *2018 IEEE Symposium on VLSI Circuits* (Honolulu, HI), 239–240. doi: 10.1109/VLSIC.2018.8502264

Bartolo, R., Saunders, R. C., Mitz, A. R., and Averbeck, B. B. (2020). Dimensionality, information and learning in prefrontal cortex. *PLoS Comput. Biol.* 16:e1007514. doi: 10.1371/journal.pcbi.1007514

Berényi, A., Somogyvári, Z., Nagy, A. J., Roux, L., Long, J. D., Fujisawa, S., et al. (2014). Large-scale, high-density (up to 512 channels) recording of local circuits in behaving animals. *J. Neurophysiol.* 111, 1132–1149. doi: 10.1152/jn.00785.2013

Brenna, S., Padovan, F., Neviani, A., Bevilacqua, A., Bonfanti, A., and Lacaita, A. L. (2016). A 64-channel 965-μ W neural recording SoC with UWB wireless transmission in 130-nm CMOS. *IEEE Trans. Circ. Syst. II Express Briefs* 63, 528–532. doi: 10.1109/TCSII.2016.2530882

Camunas-Mesa, L. A., and Quiroga, R. Q. (2013). A detailed and fast model of extracellular recordings. *Neural Comput.* 25, 1191–1212. doi: 10.1162/NECO_a_00433

Carusone, T., Johns, D., and Martin, K. (2011). *Analog Integrated Circuit Design, 2nd Edn*. Hoboken, NJ: Wiley.

Chae, M. S., Liu, W., and Sivaprakasam, M. (2008). Design optimization for integrated neural recording systems. *IEEE J. Solid State Circ.* 43, 1931–1939. doi: 10.1109/JSSC.2008.2001877

Chae, M. S., Yang, Z., Yuce, M. R., Hoang, L., and Liu, W. (2009). A 128-channel 6 mW wireless neural recording IC with spike feature extraction and UWB transmitter. *IEEE Trans. Neural Syst. Rehabil. Eng.* 17, 312–321. doi: 10.1109/TNSRE.2009.2021607

Chandrakumar, H., and Markovic, D. (2017). An 80-mVpp linear-input range, 1.6-G Ω input impedance, low-power chopper amplifier for closed-loop neural recording that is tolerant to 650-mVpp common-mode interference. *IEEE J. Solid State Circ.* 52, 2811–2828. doi: 10.1109/JSSC.2017.2753824

Chandrakumar, H., and Markovic, D. (2018). A 15.2-ENOB 5-kHz BW 4.5-μ W Chopped CT $\Delta\backslash\Sigma$-ADC for artifact-tolerant neural recording front ends. *IEEE J. Solid State Circ.* 53, 3470–3483. doi: 10.1109/JSSC.2018.2876468

Chen, Y.-P., Jeon, D., Lee, Y., Kim, Y., Foo, Z., Lee, I., et al. (2015). An injectable 64 nW ECG mixed-signal SoC in 65 nm for arrhythmia monitoring. *IEEE J. Solid State Circ.* 50, 375–390. doi: 10.1109/JSSC.2014.2364036

Delgado-Restituto, M., Carrasco-Robles, M., Fiorelli, R., Ginés-Arteaga, A. J., and Rodríguez-Vázquez, A. (2016). "A 76nW, 4kS/s 10-bit SAR ADC with offset cancellation for biomedical applications," in *2016 IEEE Asia Pacific Conference on Circuits and Systems (APCCAS)* (Jeju), 421–424. doi: 10.1109/APCCAS.2016.7803992

Delgado-Restituto, M., Rodriguez-Perez, A., Darie, A., Soto-Sanchez, C., Fernandez-Jover, E., and Rodriguez-Vazquez, A. (2017). System-level design of a 64-channel low power neural spike recording sensor. *IEEE Trans. Biomed. Circ. Syst.* 11, 420–433. doi: 10.1109/TBCAS.2016.2618319

Du, J., Riedel-Kruse, I. H., Nawroth, J. C., Roukes, M. L., Laurent, G., and Masmanidis, S. C. (2009). High-resolution three-dimensional extracellular recording of neuronal activity with microfabricated electrode arrays. *J. Neurophysiol.* 101, 1671–1678. doi: 10.1152/jn.90992.2008

Dutta, B., Trautmann, E. M., Welkenhuysen, M., Shenoy, K. V., Andrei, A., Harris, T. D., et al. (2019). "The Neuropixels probe: a CMOS based integrated microsystems platform for neuroscience and brain-computer interfaces," in *Technical Digest - International Electron Devices Meeting, IEDM* (San Francisco, CA), 202–205. doi: 10.1109/IEDM19573.2019.8993611

Enz, C. C., and Temes, G. C. (1996). Circuit techniques for reducing the effects of op-amp imperfections: autozeroing, correlated double sampling, and chopper stabilization. *Proc. IEEE* 84, 1584–1614. doi: 10.1109/5.542410

Fan, Q., Sebastiano, F., Huijsing, J. H., and Makinwa, K. A. (2011). A 1.8 μ W 60 nV/ $\sqrt{Hz}$ capacitively-coupled chopper instrumentation amplifier in 65 nm CMOS for wireless sensor nodes. *IEEE J. Solid State Circ.* 46, 1534–1543. doi: 10.1109/JSSC.2011.2143610

Frey, U., Sedivy, J., Heer, F., Pedron, R., Ballini, M., Mueller, J., et al. (2010). Switch-matrix-based high-density microelectrode array in CMOS technology. *IEEE J. Solid State Circ.* 45, 467–482. doi: 10.1109/JSSC.2009.2035196

Friston, K. J. (2011). Functional and effective connectivity: a review. *Brain Connect.* 1, 13–36. doi: 10.1089/brain.2011.0008

Gang, X., and Jiren, Y. (2000). "Comparison of charge sampling and voltage sampling," in *Proceedings of the 43rd IEEE Midwest Symposium on Circuits and Systems* (Lansing, MI), 440–443.

Gao, H., Walker, R. M., Nuyujukian, P., Makinwa, K. A., Shenoy, K. V., Murmann, B., et al. (2012). HermesE: a 96-channel full data rate direct

neural interface in 0.13 μm CMOS. *IEEE J. Solid State Circ.* 47, 1043–1055. doi: 10.1109/JSSC.2012.2185338

Ha, U., and Yoo, H. (2016). "An EEG-NIRS ear-module SoC for wearable drowsiness monitoring system," in *2016 IEEE Asian Solid-State Circuits Conference (A-SSCC)* (Toyama), 193–196. doi: 10.1109/ASSCC.2016.7844168

Han, D., Zheng, Y., Rajkumar, R., Dawe, G., and Je, M. (2013). "A 0.45V 100-channel neural-recording IC with sub-μW/channel consumption in 0.18μm CMOS," in *Digest of Technical Papers - IEEE International Solid-State Circuits Conference* (San Francisco, CA), 290–291.

Harpe, P., Gao, H., van Dommele, R., Cantatore, E., and van Roermund, A. (2015). "A 3nW signal-acquisition IC integrating an amplifier with 2.1 NEF and a 1.5fJ/conv-step ADC," in *Solid- State Circuits Conference - (ISSCC), 2015 IEEE International* (San Francisco, CA), 1–3. doi: 10.1109/ISSCC.2015.7063086

Harrison, R. R., and Charles, C. (2003). A low-power low-noise CMOS amplifier for neural recording applications. *IEEE J. Solid State Circ.* 38, 958–965. doi: 10.1109/JSSC.2003.811979

Huang, J., Laiwalla, F., Lee, J., Cui, L., Leung, V., Nurmikko, A., et al. (2018). A 0.01-mm2 mostly digital capacitor-less AFE for distributed autonomous neural sensor nodes. *IEEE Solid State Circ. Lett.* 1, 162–165. doi: 10.1109/LSSC.2019.2894932

Huys, R., Braeken, D., Jans, D., Stassen, A., Collaert, N., Wouters, J., et al. (2012). Single-cell recording and stimulation with a 16k micro-nail electrode array integrated on a 0.18 μm CMOS chip. *Lab Chip* 12, 1274–1280. doi: 10.1039/c2lc21037a

Jeon, H., Bang, J. S., Jung, Y., Choi, I., and Je, M. (2019). A high DR, DC-coupled, time-based neural-recording IC with degeneration R-DAC for bidirectional neural interface. *IEEE J. Solid State Circ.* 54, 2658–2670. doi: 10.1109/JSSC.2019.2930903

Jiang, H., Nihtianov, S., and Makinwa, K. A. A. (2019). An energy-efficient 3.7-nV/ $\sqrt{}$ Hz bridge readout IC with a stable bridge offset compensation scheme. *IEEE J. Solid State Circ.* 54, 856–864. doi: 10.1109/JSSC.2018.2885556

Jiang, W., Hokhikyan, V., Chandrakumar, H., Karkare, V., and Marković, D. (2017). A ±50-mV linear-input-range VCO-based neural-recording front-end with digital nonlinearity correction. *IEEE J. Solid State Circ.* 52, 173–184. doi: 10.1109/JSSC.2016.2624989

Johnson, B., Peace, S. T., Cleland, T. A., and Molnar, A. (2013). "A 50μm pitch, 1120-channel, 20kHz frame rate microelectrode array for slice recording," in *2013 IEEE Biomedical Circuits and Systems Conference, BioCAS 2013* (Rotterdam), 109–112. doi: 10.1109/BioCAS.2013.6679651

Johnson, B. C., Gambini, S., Izyumin, I., Moin, A., Zhou, A., Alexandrov, G., et al. (2017). "An implantable 700μW 64-channel neuromodulation IC for simultaneous recording and stimulation with rapid artifact recovery," in *IEEE Symposium on VLSI Circuits, Digest of Technical Papers* (Kyoto), C48–C49. doi: 10.23919/VLSIC.2017.8008543

Jun, J. J., Steinmetz, N. A., Siegle, J. H., Denman, D. J., Bauza, M., Barbarits, B., et al. (2017). Fully integrated silicon probes for high-density recording of neural activity. *Nature* 551, 232–236. doi: 10.1038/nature24636

Kassiri, H., Salam, M. T., Pazhouhandeh, M. R., Member, S., Soltani, N., Luis, J., et al. (2017). Rail-to-rail-input dual-radio 64-channel closed-loop neurostimulator. *IEEE J. Solid State Circ.* 52, 2793–2810. doi: 10.1109/JSSC.2017.2749426

Kim, C., Joshi, S., Courellis, H., Wang, J., Miller, C., and Cauwenberghs, G. (2018). Sub-μ Vrms-noise Sub-μ W/Channel ADC-direct neural recording with 200-mV/ms transient recovery through predictive digital autoranging. *IEEE J. Solid State Circ.* 53, 3101–3110. doi: 10.1109/JSSC.2018.2870555

Kim, S., Tathireddy, P., Normann, R. A., and Solzbacher, F. (2007). Thermal impact of an active 3-d microelectrode array implanted in the brain. *IEEE Trans. Neural Syst. Rehabil. Eng.* 15, 493–501. doi: 10.1109/TNSRE.2007.908429

Kuhl, M., and Manoli, Y. (2015). "A 0.01 mm2 fully-differential 2-stage amplifier with reference-free CMFB using an architecture-switching-scheme for bandwidth variation," in *European Solid-State Circuits Conference (ESSCIRC), ESSCIRC 2015 - 41st* (Graz), 287–290. doi: 10.1109/ESSCIRC.2015.7313883

Lee, C., and Song, J. (2019). A chopper stabilized current-feedback instrumentation amplifier for EEG acquisition applications. *IEEE Access* 7, 11565–11569. doi: 10.1109/ACCESS.2019.2892502

Leene, L. B., and Constandinou, T. G. (2017). Time domain processing techniques using ring oscillator-based filter structures. *IEEE Trans. Circ. Syst I Regular Pap.* 64, 3003–3012. doi: 10.1109/TCSI.2017.2715885

Liu, X., Zhang, M., Xiong, T., Richardson, A. G., Lucas, T. H., Chin, P. S., et al. (2016). A fully integrated wireless compressed sensing neural signal acquisition system for chronic recording and brain machine interface. *IEEE Trans. Biomed. Circ. Syst.* 10, 874–883. doi: 10.1109/TBCAS.2016.2574362

Liu, Y., Luan, S., Williams, I., Rapeaux, A., and Constandinou, T. G. (2017). A 64-channel versatile neural recording SoC with activity-dependent data throughput. *IEEE Trans. Biomed. Circ. Syst.* 11, 1344–1355. doi: 10.1109/TBCAS.2017.2759339

Lopez, C. M., Andrei, A., Mitra, S., Welkenhuysen, M., Eberle, W., Bartic, C., et al. (2014). An implantable 455-active-electrode 52-channel CMOS neural probe. *IEEE J. Solid State Circ.* 49, 248–261. doi: 10.1109/JSSC.2013.2284347

Mikawa, M., Yagi, K., Itakura, K., Onuki, L., and Nakano, N. (2020). "A low-power multi-frequency chopper-stabilized readout with time-domain delta-sigma modulator suitable for neural recording," in *2020 27th IEEE International Conference on Electronics, Circuits and Systems (ICECS)* (Glasgow), 1–4. doi: 10.1109/ICECS49266.2020.9294871

Mohan, R., Zaliasl, S., Gielen, G. G. E., Hoof, C. V., Yazicioglu, R. F., and Helleputte, N. V. (2017). A 0.6-V, 0.015-mm2, time-based ECG readout for ambulatory applications in 40-nm CMOS. *IEEE J. Solid State Circ.* 52, 298–308. doi: 10.1109/JSSC.2016.2615320

Mohseni, P., and Najafi, K. (2004). A fully integrated neural recording amplifier with DC input stabilization. *IEEE Trans. Biomed. Eng.* 51, 832–837. doi: 10.1109/TBME.2004.824126

Mondal, S., and Hall, D. A. (2020). A 13.9-nA ECG amplifier achieving 0.86/0.99 NEF/PEF using AC-coupled OTA-stacking. *IEEE J. Solid State Circ.* 55, 414–425. doi: 10.1109/JSSC.2019.2957193

Mora Lopez, C., Putzeys, J., Raducanu, B. C., Ballini, M., Wang, S., Andrei, A., et al. (2017). A neural probe with up to 966 electrodes and up to 384 configurable channels in 0.13 μm SOI CMOS. *IEEE Trans. Biomed. Circ. Syst.* 11, 510–522. doi: 10.1109/TBCAS.2016.2646901

Muller, R., Gambini, S., and Rabaey, J. M. (2012). A 0.013 mm2, 5 μ W, DC-coupled neural signal acquisition ic with 0.5 v supply. *IEEE J. Solid State Circ.* 47, 232–243. doi: 10.1109/JSSC.2011.2163552

Muller, R., Le, H. P., Li, W., Ledochowitsch, P., Gambini, S., Bjorninen, T., et al. (2015). A minimally invasive 64-channel wireless μeCoG implant. *IEEE J. Solid State Circ.* 50, 344–359. doi: 10.1109/JSSC.2014.2364824

Musk, E., and Neuralink (2019). An integrated brain-machine interface platform with thousands of channels. *J. Med. Internet Res.* 21:e16194. doi: 10.2196/16194

Najafi, K., Ji, J., and Wise, K. D. (1990). Scaling limitations of silicon multichannel recording probes. *IEEE Trans. Biomed. Eng.* 37, 1–11. doi: 10.1109/10.43605

Ng, K. A., and Xu, Y. P. (2016). A low-power, high CMRR neural amplifier system employing MOS inverter-based OTAs with CMFB through supply rails. *IEEE J. Solid State Circ.* 51, 724–737. doi: 10.1109/JSSC.2015.2512935

Noshahr, F. H., Nabavi, M., and Sawan, M. (2020). Multi-channel neural recording implants: a review. *Sensors* 20, 1–29. doi: 10.3390/s20030904

Obaid, A., Hanna, M.-E., Wu, Y.-W., Kollo, M., Racz, R., Angle, M. R., et al. (2020). Massively parallel microwire arrays integrated with cmos chips for neural recording. *Sci. Adv.* 6:eaay2789. doi: 10.1126/sciadv.aay2789

Obien, M., Deligkaris, K., Bullmann, T., Bakkum, D., and Frey, U. (2015). Revealing neuronal function through microelectrode array recordings. *Front. Neurosci.* 8:423. doi: 10.3389/fnins.2014.00423

O'Leary, G., Pazhouhandeh, M. R., Chang,M., Groppe, D., Valiante, T. A., Verma, N., et al. (2018). "A recursive-memory brain-state classifier with 32-channel track-and-zoom 126 ADCs and charge-balanced programmable waveform neurostimulators," in *2018 IEEE International Solid - State Circuits Conference - (ISSCC)* (San Francisco, CA), 296–298. doi: 10.1109/ISSCC.2018.8310301

Park, S. Y., Cho, J., Lee, K., and Yoon, E. (2018a). Dynamic power reduction in scalable neural recording interface using spatiotemporal correlation and temporal sparsity of neural signals. *IEEE J. Solid State Circ.* 53, 1102–1114. doi: 10.1109/JSSC.2017.2787749

Park, S. Y., Cho, J., Na, K., and Yoon, E. (2018b). Modular 128-channel Δ - Δ Σ analog front-end architecture using spectrum equalization scheme for 1024-channel 3-d neural recording microsystems. *IEEE J. Solid State Circ.* 53, 501–514. doi: 10.1109/JSSC.2017.2764053

Pazhouhandeh, M. R., Chang, M., Valiante, T. A., and Genov, R. (2020a). Track-and-zoom neural analog-to-digital converter with blind stimulation artifact rejection. *IEEE J. Solid State Circ.* 55, 1984–1997. doi: 10.1109/JSSC.2020.2991526

Pazhouhandeh, M. R., Kassiri, H., Shoukry, A., Weisspapir, I., Carlen, P. L., and Genov, R. (2020b). Opamp-less sub-μW/channel Δ-modulated neural-ADC with super-GΩ input impedance. *IEEE J. Solid State Circ.* 56, 1565–1575. doi: 10.1109/JSSC.2020.3041289

Pazhouhandeh, M. R., Kassiri, H., Shoukry, A., Wesspapir, I., Carlen, P., and Genov, R. (2018). "Artifact-tolerant Opamp-less delta-modulated bidirectional neuro-interface," in *2018 IEEE Symposium on VLSI Circuits* (Honolulu, HI), 127–128. doi: 10.1109/VLSIC.2018.8502286

Pérez-Prieto, N., Fiorelli, R., Valtierra, J. L., Pérez-García, P., Delgado-Restituto, M., and Rodríguez-Vázquez, A. (2019). "A 32 input multiplexed channel analog front-end with spatial delta encoding technique and differential artifactscompression," in *2019 IEEE Biomedical Circuits and Systems Conference (BioCAS)* (Nara), 1–4. doi: 10.1109/BIOCAS.2019.8919043

Prabha, P., Kim, S. J., Reddy, K., Rao, S., Griesert, N., Rao, A., et al. (2015). A highly digital VCO-Based ADC architecture for current sensing applications. *IEEE J. Solid State Circ.* 50, 1785–1795. doi: 10.1109/JSSC.2015.2414428

Raducanu, B. C., Yazicioglu, R. F., Lopez, C. M., Id, M. B., Putzeys, J., Id, S. W., et al. (2017). Time multiplexed active neural probe with 1356 parallel recording sites. *IEEE Sens. J.* 17, 1–20. doi: 10.3390/s17102388

Rai, S., Holleman, J., Pandey, J. N., Zhang, F., and Otis, B. (2009). "A 500μw neural tag with 2μvrms afe and frequency-multiplying MICS/ISM FSK transmitter," in *2009 IEEE International Solid-State Circuits Conference - Digest of Technical Papers* (San Francisco, CA), 212–213. doi: 10.1109/ISSCC.2009.4977383

Rajangam, S., Tseng, P.-H., Yin, A., Lehew, G., Schwarz, D., Lebedev, M. A., et al. (2016). Wireless cortical brain-machine interface for whole-body navigation in primates. *Sci. Rep.* 6:22170. doi: 10.1038/srep22170

Razavi, B. (2001). *Design of Analog CMOS Integrated Circuits, 1st Edn.* New York, NY: McGraw-Hill.

Sahasrabuddhe, K., Khan, A. A., Singh, A. P., Stern, T. M., Ng, Y., Tadić, A., et al. (2020). The Argo: a high channel count recording system for neural recording *in vivo*. *J. Neural Eng.* 18:015002. doi: 10.1088/1741-2552/abd0ce

Sakkalis, V. (2011). Review of advanced techniques for the estimation of brain connectivity measured with EEG/MEG. *Comput. Biol. Med.* 41, 1110–1117. doi: 10.1016/j.compbiomed.2011.06.020

Samiei, A., and Hashemi, H. (2019). A chopper stabilized, current feedback, neural recording amplifier. *IEEE Solid State Circ. Lett.* 2, 17–20. doi: 10.1109/LSSC.2019.2916754

Seidl, K., Schwaerzle, M., Ulbert, I., Neves, H. P., Paul, O., and Ruther, P. (2012). CMOS-based high-density silicon microprobe arrays for electronic depth control in intracortical neural recording-characterization and application. *J. Microelectromech. Syst.* 21, 1426–1435. doi: 10.1109/JMEMS.2012.2206564

Sharma, K., Pathania, A., Pandey, R., Madan, J., and Sharma, R. (2021). Mos based pseudo-resistors exhibiting tera ohms of incremental resistance for biomedical applications: analysis and proof of concept. *Integration* 76, 25–39. doi: 10.1016/j.vlsi.2020.08.001

Sharma, M., Gardner, A. T., Strathman, H. J., Warren, D. J., Silver, J., and Walker, R. M. (2018). Acquisition of neural action potentials using rapid multiplexing directly at the electrodes. *Micromachines* 9:477. doi: 10.3390/mi9100477

Sharma, M., Strathman, H. J., and Walker, R. M. (2019). Verification of a rapidly multiplexed circuit for scalable action potential recording. *IEEE Trans. Biomed. Circ. Syst.* 13, 1655–1663. doi: 10.1109/TBCAS.2019.2958348

Shen, L., Lu, N., and Sun, N. (2018). A 1-V 0.25- μW inverter stacking amplifier with 1.07 noise efficiency factor. *IEEE J. Solid State Circ.* 53, 896–905. doi: 10.1109/JSSC.2017.2786724

Shobe, J. L., Claar, L. D., Parhami, S., Bakhurin, K. I., and Masmanidis, S. C. (2015). Brain activity mapping at multiple scales with silicon microprobes containing 1,024 electrodes. *J. Neurophysiol.* 114, 2043–2052. doi: 10.1152/jn.00464.2015

Sisterson, N. D., Wozny, T. A., Kokkinos, V., Constantino, A., and Richardson, R. M. (2019). Closed-loop Brain stimulation for drug-resistant epilepsy: towards an evidence-based approach to personalized medicine. *Neurotherapeutics* 16, 119–127. doi: 10.1007/s13311-018-00682-4

Smith, W. A., Uehlin, J. P., Perlmutter, S. I., Rudell, J. C., and Sathe, V. S. (2017). "A scalable, highly-multiplexed delta-encoded Q14 digital feedback ECoG recording amplifier with common and differential-mode artifact suppression," in *IEEE Symposium on VLSI Circuits, Digest of Technical Papers* (Kyoto), C172–C173. doi: 10.23919/VLSIC.2017.8008470

Stevenson, I. H. (2020). *Tracking Advances in Neural Recording*. Available online at: https://stevenson.lab.uconn.edu/scaling/

Swann, N. C., de Hemptinne, C., Thompson, M. C., Miocinovic, S., Miller, A. M., Gilron, R., et al. (2018). Adaptive deep brain stimulation for Parkinson's disease using motor cortex sensing. *J. Neural Eng.* 15:046006. doi: 10.1088/1741-2552/aabc9b

Szostak, K. M., Grand, L., and Constandinou, T. G. (2017). Neural interfaces for intracortical recording: requirements, fabrication methods, and characteristics. *Front. Neurosci.* 11:665. doi: 10.3389/fnins.2017.00665

Tu, C., Wang, Y., and Lin, T. (2017). "A 0.06mm2 $\pm$ 50mV range $-$82dB THD chopper VCO-based sensor readout circuit in 40nm CMOS," in *2017 Symposium on VLSI Circuits* (Kyoto), C84–C85. doi: 10.23919/VLSIC.2017.8008558

Uehlin, J. P., Smith, W. A., Pamula, V. R., Perlmutter, S. I., Rudell, J. C., and Sathe, V. S. (2020). A 0.0023 mm2/ch. Delta-encoded, time-division multiplexed mixed-signal ECoG recording architecture with stimulus artifact suppression. *IEEE Trans. Biomed. Circ. Syst.* 14, 319–331. doi: 10.1109/TBCAS.2019.2963174

Valtierra, J. L., Delgado-Restituto, M., Fiorelli, R., and Rodriguez-Vazquez, A. (2020). A sub-μW reconfigurable front-end for invasive neural recording that exploits the spectral characteristics of the wideband neural signal. *IEEE Trans. Circ. Syst. I Regular Pap.* 67, 1426–1437. doi: 10.1109/TCSI.2020.2968087

Vansteensel, M. J., Pels, E. G., Bleichner, M. G., Branco, M. P., Denison, T., Freudenburg, Z. V., et al. (2016). Fully implanted brain-computer interface in a locked-in patient with ALS. *N. Engl. J. Med.* 375, 2060–2066. doi: 10.1056/NEJMoa1608085

Wagner, F., Mignardot, J. B.,and Le Goff-Mignardot, C., Demesmaeker, R., Komi, S., Capogrosso, M., et al. (2018). Targeted neurotechnology restores walking in humans with spinal cord injury. *Nature* 563, 65–71. doi: 10.1038/s41586-018-0649-2

Wattanapanitch, W., and Sarpeshkar, R. (2011). A low-power 32-channel digitally programmable neural recording integrated circuit. *IEEE Trans. Biomed. Circ. Syst.* 5, 592–602. doi: 10.1109/TBCAS.2011.2163404

Xu, J., Busze, B., Kim, H., Makinwa, K., Van Hoof, C., and Yazicioglu, R. F. (2014). "A 60nV/sqrt (Hz) 15-channel digital active electrode system for portable biopotential signal acquisition," in *Solid-State Circuits Conference Digest of Technical Papers (ISSCC), 2014 IEEE International* (San Francisco, CA), 424–425.

Yeager, D., Biederman, W., Narevsky, N., Leverett, J., Neely, R., Carmena, J., et al. (2014). "A 4.78mm2 fully-integrated neuromodulation SoC combining 64 acquisition channels with digital compression and simultaneous dual stimulation," in *IEEE Symposium on VLSI Circuits, Digest of Technical Papers* (Honolulu, HI), 1–10. doi: 10.1109/JSSC.2014.2384736

Zhang, Y., Zhang, F., Shakhsheer, Y., Silver, J., Klinefelter, A., Nagaraju, M., et al. (2013). A batteryless 19 uw MICS/ISM-band energy harvesting body sensor node soc for exg applications. *IEEE J. Solid State Circ.* 48, 199–213. doi: 10.1109/JSSC.2012.2221217

Zhao, W., Li, S., Xu, B., Yang, X., Tang, X., Shen, L., et al. (2020). A 0.025-mm2 0.8-V 78.5-dB SNDR VCO-based sensor readout circuit in a hybrid PLL- $\Delta\Sigma$ M structure. *IEEE J. Solid State Circ.* 55, 666–679. doi: 10.1109/JSSC.2019.2959479

Zou, X., Liu, L., Cheong, J. H., Yao, L., Li, P., Cheng, M.-Y., et al. (2013). A 100-Channel 1-mW Implantable. *IEEE Trans. Circ. Syst. I* 60, 1–13. doi: 10.1109/TCSI.2013.2249175

Conflict of Interest: The authors declare that the research was conducted in the absence of any commercial or financial relationships that could be construed as a potential conflict of interest.

frontiers in Neuroscience

ORIGINAL RESEARCH
published: 22 July 2021
doi: 10.3389/fnins.2021.681021

A Versatile Hermetically Sealed Microelectronic Implant for Peripheral Nerve Stimulation Applications

*Dai Jiang[1], Fangqi Liu[1], Henry T. Lancashire[2], Timothy A. Perkins[2], Matthew Schormans[1], Anne Vanhoestenberghe[2,3], Nicholas De N. Donaldson[2] and Andreas Demosthenous[1]**

[1] Department of Electronic and Electrical Engineering, University College London, London, United Kingdom, [2] Department of Medical Physics and Biomedical Engineering, University College London, London, United Kingdom, [3] Division of Surgery and Interventional Science, Aspire Centre for Rehabilitation Engineering and Assistive Technology, University College London, London, United Kingdom

OPEN ACCESS

Edited by:
Morris (Ming-Dou) Ker, National Chiao Tung University, Taiwan

Reviewed by:
Aria Samiei, University of Southern California, United States
Yu-Wei Wu, Institute of Molecular Biology, Academia Sinica, Taiwan
Jun Ohta, Nara Institute of Science and Technology (NAIST), Japan

***Correspondence:**
Andreas Demosthenous
a.demosthenous@ucl.ac.uk

Specialty section:
This article was submitted to Neural Technology, a section of the journal Frontiers in Neuroscience

Received: *15 March 2021*
Accepted: *15 June 2021*
Published: *22 July 2021*

Citation:
Jiang D, Liu F, Lancashire HT, Perkins TA, Schormans M, Vanhoestenberghe A, Donaldson NDN and Demosthenous A (2021) A Versatile Hermetically Sealed Microelectronic Implant for Peripheral Nerve Stimulation Applications. Front. Neurosci. 15:681021. doi: 10.3389/fnins.2021.681021

This article presents a versatile neurostimulation platform featuring a fully implantable multi-channel neural stimulator for chronic experimental studies with freely moving large animal models involving peripheral nerves. The implant is hermetically sealed in a ceramic enclosure and encapsulated in medical grade silicone rubber, and then underwent active tests at accelerated aging conditions at 100°C for 15 consecutive days. The stimulator microelectronics are implemented in a 0.6-μm CMOS technology, with a crosstalk reduction scheme to minimize cross-channel interference, and high-speed power and data telemetry for battery-less operation. A wearable transmitter equipped with a Bluetooth Low Energy radio link, and a custom graphical user interface provide real-time, remotely controlled stimulation. Three parallel stimulators provide independent stimulation on three channels, where each stimulator supports six stimulating sites and two return sites through multiplexing, hence the implant can facilitate stimulation at up to 36 different electrode pairs. The design of the electronics, method of hermetic packaging and electrical performance as well as *in vitro* testing with electrodes in saline are presented.

Keywords: hermetic seal package, implantable stimulator, microelectronics, power and data telemetry, wireless stimulation control

INTRODUCTION

Direct interaction with neural pathways through active implantable devices has become an increasingly effective therapeutic approach for treating neurological disorders and organ defects, or replacing lost body function. Traditional clinical applications include cochlear implants for hearing loss, deep brain stimulation (DBS) for epilepsy and Parkinson's disease, and pacemakers for heart defects. More recent research includes epidural spinal cord stimulation for restoring coordinated locomotion in lower limbs (Capogrosso et al., 2016; Formento et al., 2018), peripheral nerve stimulation for creating tactile sensation after amputation (Raspopovic et al., 2014; Zollo et al., 2019), and vagus nerve stimulation for regulating organ function through neuromodulation in order to reinstate a healthy balance (Famm et al., 2013; Pavlov and Tracey, 2017).

Research on implantable active neural interface devices require chronic studies in animal models in order to gain a thorough understanding of the mechanism of neural diseases and disorders. Implantable devices used in these studies require accurate and highly selective neural stimulation at multiple sites. The stimulation should be highly programmable to support closed-loop neural intervention. A variety of implantable stimulator designs has been reported in the literature in the past two decades. They can be divided into three major categories:

1) *Implants adapted from commercially available devices* (Capogrosso et al., 2016; Boutros et al., 2019): Although these implants have proven reliability, they are often limited by their inflexibility, coarse programmability, and low channel count;
2) *Implants without hermetic packaging* (Xu et al., 2015; Lee et al., 2018; Williams et al., 2020): In these implants the electronics are encapsulated in silicone rubber or epoxy. This is a widely adopted approach because of its simple process and low cost. These devices, however, are often used only in short-term animal studies due to the lack of adequate hermetic protection;
3) *In-house made prototype chronic implants:* Some of these devices are packaged in precious metals (Hart et al., 2011; Sun and Morrell, 2014; Zamora et al., 2020) and are expensive for production. Others are simple electronic circuits sealed in miniaturized glass packages (Loeb et al., 2001; Sivaji et al., 2019), where the channel count and programmability are limited.

This article presents the design, implementation, and evaluation of a versatile fully implantable multi-channel stimulator implant for chronic animal studies targeting the peripheral nervous system. The implant is hermetically packaged in a ceramic enclosure and is cost effective as a research platform. Inductive wireless powering removes the need for an implanted battery, avoiding potential battery failure. A bidirectional, high-speed communication channel facilitates real-time programming of the implant from a remote external host computer allowing free movement of the animal. Results from accelerated aging tests at 100°C for 15 consecutive days demonstrate that the implantable stimulator is suitable for chronic implantation.

The rest of the paper is organized as follows. Section "Materials and Methods" describes the design and fabrication of the hardware system, and the operation procedure for remote real-time stimulation control. Section "Results" show the electrical performance of the device as well as its suitability for chronic implantation. Section "Discussion and Conclusion" elaborates on the findings and provides concluding remarks and future directions.

MATERIALS AND METHODS

System Architecture

The wireless multi-channel stimulator system consists of a hermetically sealed, fully implantable stimulator, as shown in **Figure 1C**, and a wearable transmitter, as shown in **Figure 1B**. The implant does not contain a built-in energy source. Power is supplied by the wearable transmitter over a wireless power transfer link comprising two inductively coupled coils, which also provides bidirectional half-duplex communication between the transmitter and the implant. The operation of the transmitter is managed by a CC2640 microcontroller (MCU), which also provides a Bluetooth Low Energy (BLE) radio link. This allows the stimulation from the implant to be controlled from a remote host computer. A custom BLE dongle was designed and fabricated for the radio link of the host computer, as shown in **Figure 1B**. Dedicated software with a graphical user interface (GUI) has been developed for wirelessly controlling the operation of the implantable stimulator from the host computer. In experiments with free-moving animals, the wearable transmitter could be mounted onto the animal subject in a jacket or backpack, with the transmitter (Tx) coil in the inductive link aligned to the implanted receiver (Rx) coil. Researchers can set stimulation parameters on-the-fly from the GUI, where the setting commands are transmitted via an USB-UART interface on the BLE dongle, then over the BLE link to the wearable transmitter, where the commands are relayed to the implant via the inductive link. This arrangement allows real-time control of neurostimulation by the implantable stimulator without the need to attach a cable to the animal subject.

The architecture of the wireless multi-channel stimulator system is shown in **Figure 1A**. The wearable transmitter comprises a rechargeable battery, power management modules, a class-D driver for driving the inductive link, wireless communication modules and a MCU. The implantable stimulator has three parallel stimulators. The primary stimulator facilitates communication and manages the stimulation settings on all the three stimulators. It has a current pulse generator providing biphasic current pulses up to 1 mA, which are multiplexed to six stimulating electrodes and two return electrodes, supporting up to 12 different electrode configurations. The primary stimulator control unit has three parallel finite-state machines (FSMs) for managing the stimulation settings on each stimulator. The FSMs for the two secondary stimulators trigger the local secondary stimulation control units to operate the current pulse generators, where the current amplitude is amplified by a current booster to up to 3 mA. Each secondary stimulator also supports up to 12 electrode configurations. Therefore, the implant can provide three independent channels of parallel current stimulation for up to 36 different electrode pairs.

As shown in **Figure 1B**, the implantable stimulator comprises a hybrid unit, where the stimulation electronics are mounted and sealed inside a ceramic package, a Rx coil printed circuit board (PCB) with a solenoid coil and tuning capacitors for inductive coupling, and three miniature connectors for connecting electrode arrays. The Rx coil PCB also has a neodymium rare earth magnet (8 mm × 3 mm, Duratool) to aid alignment with the Tx coil PCB outside the body, which also has a magnet, as shown in **Figure 1C**. The optimal working distance between the Tx and Rx coils is ∼ 1 cm. The hybrid, Rx coil PCB and connectors are joined with Cooner wires. The length between the hybrid and the Rx coil PCB is ∼ 55 mm, and

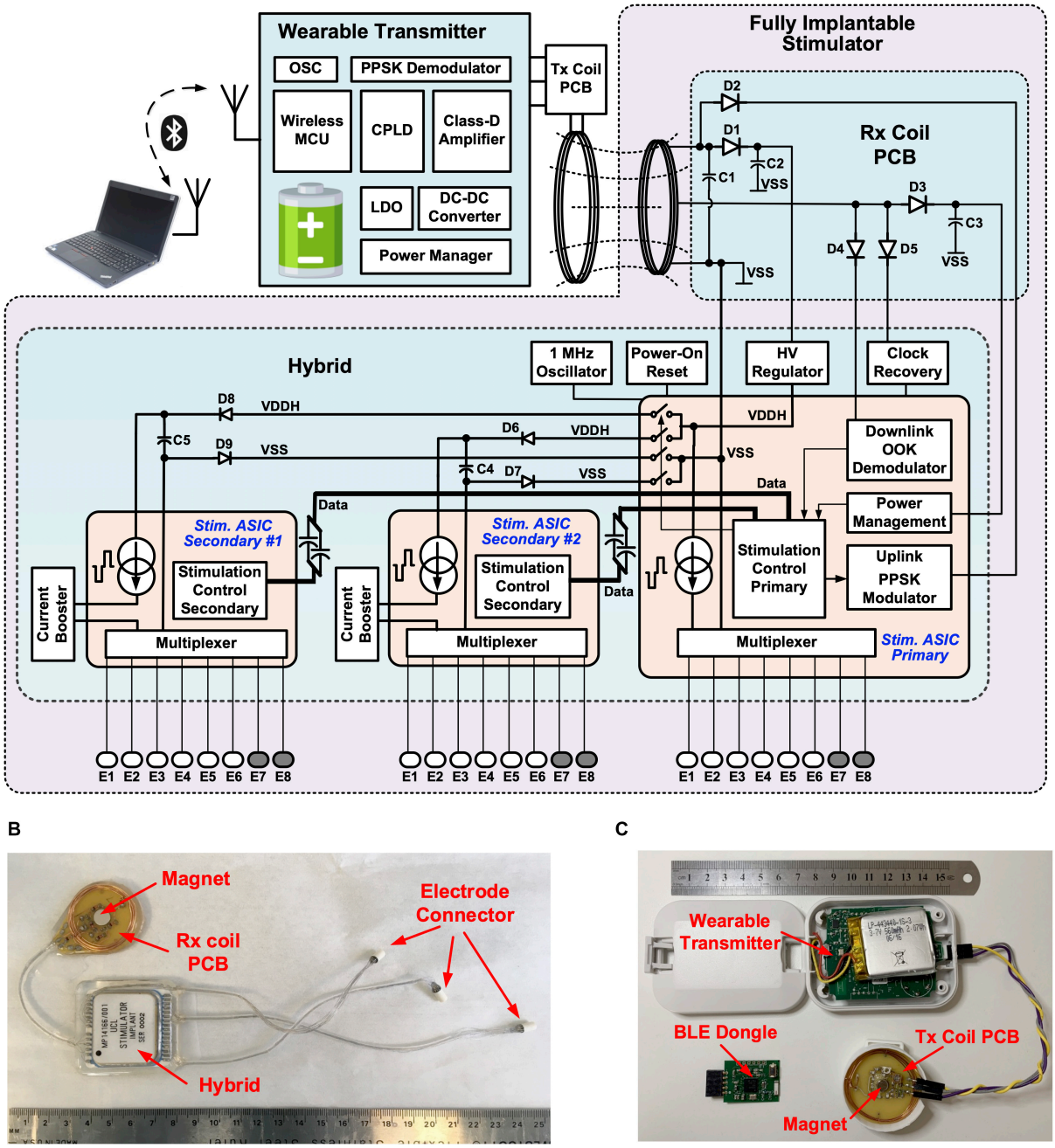

FIGURE 1 | Wireless, fully implantable multi-channel stimulator: **(A)** System architecture; **(B)** Implantable stimulator; **(C)** Wearable transmitter and BLE dongle.

between the hybrid and the connectors is up to 180 mm. This arrangement allows the Rx coil PCB to be implanted close to the skin for strong coupling, whilst the hybrid can be implanted in a relatively deeper, surgically suitable location. In addition, the implantable electrode connectors provide the flexibility of having the electrode cable at any desired length required to reach the targeted nerve. All the units are encapsulated in medical grade silicone rubber. The hermetic package and silicone encapsulation ensure the suitability of the stimulator for chronic implantation.

Stimulator Circuits

The circuits of the three stimulators are integrated onto three application specific integrated circuits (ASICs) using a high-voltage (HV) 0.6 μm CMOS technology. **Figures 2A,B** show the microphotographs of the primary and secondary stimulator

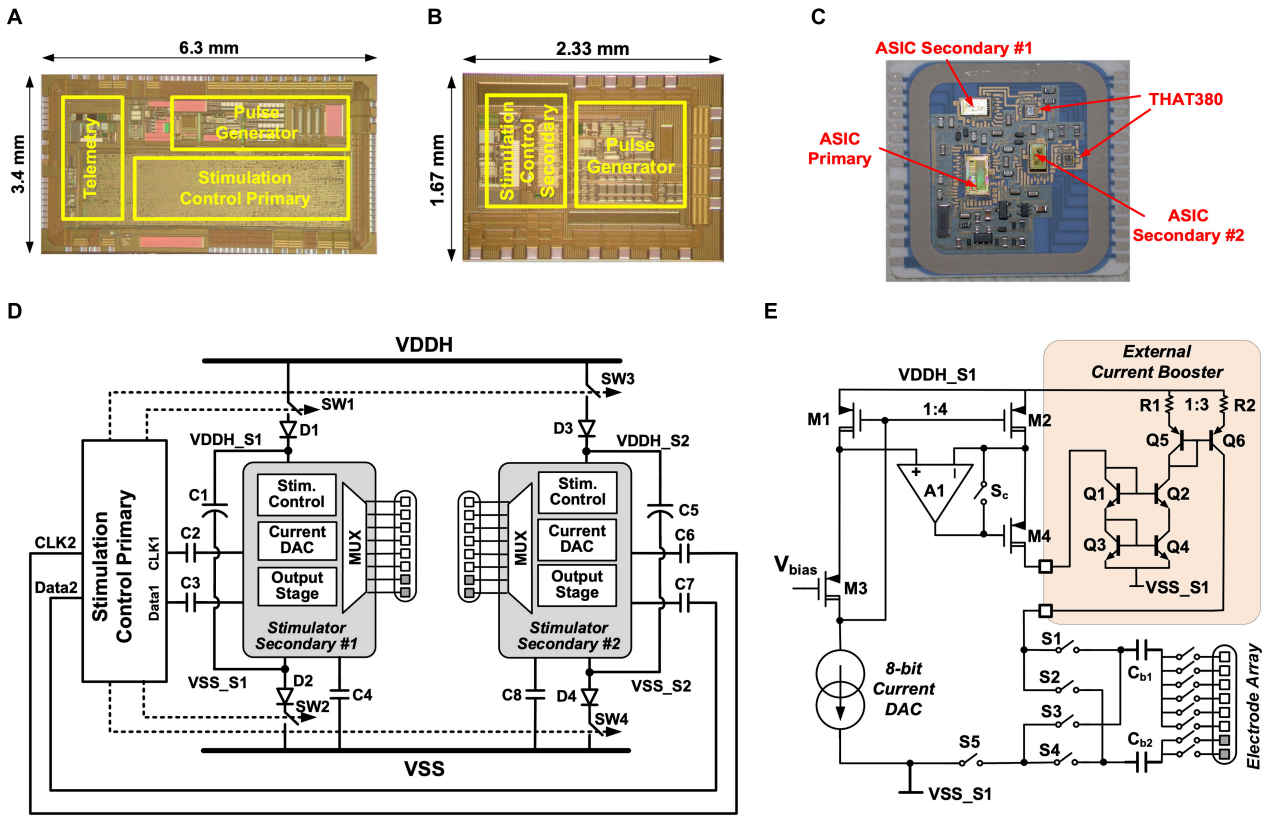

FIGURE 2 | Stimulator circuits: **(A)** Microphotograph of the primary stimulator ASIC; **(B)** Microphotograph of the secondary stimulator ASIC; **(C)** Layout of the stimulator circuits inside the hybrid; **(D)** Schematic of the power isolation scheme for crosstalk reduction; **(E)** Integrated pulse generator on Stimulator Secondary #1 (the circuits for the integrated pulse generator on Stimulator Secondary #2 are identical).

ASICs, respectively. Bare dies of the stimulator ASICs, as well as two commercially available THAT380 ICs, are wire-bonded directly to printed pads inside the hermetically sealed hybrid as shown in **Figure 2C**. In a conventional multi-channel stimulator design, channel interference is addressed by either interleaving the pulses from multiple channels (Zeng et al., 2008), or physically isolating the electrodes (Wong et al., 2007). The former approach correlates the channels hence reduces the degree of stimulation independence, while the latter approach increases the size of the electrode array, which may be limited by surgical constraints. To ensure truly multi-channel stimulation, the implant uses a novel power isolation scheme (Jiang et al., 2015). **Figure 2D** shows the circuit arrangement for this scheme. The two secondary stimulator ASICs are supplied from the 16 V supply rails VDDH and VSS through a switched connection, where the switches are controlled by the primary stimulation control logic. Before the onset of a biphasic pulse from a secondary stimulator, for example, Stimulator Secondary #1, the primary control logic sends the pulse amplitude setting to the secondary stimulation control logic via ac coupled data connections CLK1 and Data1, so that the secondary logic can control the local pulse generator to generate a biphasic pulse at the specified amplitude. During the biphasic pulse, the primary logic switches off SW1 and SW2 to isolate the Secondary #1 ASIC from the other stimulators. This isolation prevents a potential current path from the stimulating electrodes to electrodes connected to other stimulators and minimizes inter-channel electrical crosstalk. During isolation, the secondary ASIC is supplied by the energy storage capacitor, C1. At the completion of the biphasic pulse, SW1 and SW2 are turned on again to recharge C1 until the next biphasic pulse. SW1 and SW2 are implemented in the primary ASIC with complementary HV MOSFETs. When Secondary #1 ASIC is isolated, the voltage at the negative terminal of C1, VSS_S1, may be lower than the substrate voltage of the primary ASIC at VSS. To ensure the NMOS in SW2 remains off, a diode D2 is added in series with SW2. Similarly, the voltage at the positive terminal of C1, VDDH_S1, may be higher than VDDH, which is the bias voltage of the NWELL for the PMOS in SW1. Diode D1 in series with SW1 ensures the PMOS in SW1 remains off. The storage capacitors C1 and C5 are 2.2 μF. When supplying a biphasic pulse at 3 mA with an overall pulse width of 1 ms, the voltage drop across the storage capacitor is (3 mA × 1 ms)/2.2 μF = 1.36 V. The on resistance of SW1, SW2, SW3, and SW4 is 28 Ω each, and the RC time constant when recharging the storage capacitors is 123.3 μs. For the maximum specified pulse frequency is 500 pulse per second (pps), this time constant is sufficiently fast for recharging the storage capacitors during the pulse interval.

Figure 2E shows the circuits of the pulse generator in Stimulator Secondary #1. The pulse generator in each ASIC consists of an 8-bit binary-weighted current digital-to-analog converter (DAC) with a resolution of 1 μA, an output stage with active feedback to amplify the DAC current by four times, and a "H-bridge" formed by S1–S4 to shape the current into a stimulus biphasic pulse. The width of the cathodic phase and anodic phase are programmable so that the biphasic pulse can be either symmetrical or asymmetrical with a longer anodic phase at a lower current amplitude. This is specified by the stimulation settings, which can be programmed from the remote host computer. The anode node between S1 and S3 connects via a 1 μF blocking capacitor (C_{b1}) to a 1-to-6 multiplexer, and the cathode node between S2 and S4 to a 1-to-2 multiplexer, also via a 1 μF blocking capacitor (C_{b2}); thus, the stimulation is selectable between 1 of 6 stimulating electrodes and 1 of 2 return electrodes. In each secondary stimulator a 1:3 current booster outside the ASIC further increases the maximum stimulating current to 3 mA. As shown in **Figure 2E** the current booster is implemented as a source-degenerated current mirror using a discrete matched transistor array (THAT380 IC). Between current pulses, the pulse generator is connected to VDDH and VSS but switches S1, S2, S_c, and S5 are off to isolate the electrodes from VDDH and VSS, preventing stimulating current from other stimulators from flowing into these electrodes. S3 and S4 stay on during the pulse interval for removing any remaining charges on the electrodes due to mismatch or charge leakage.

Power and Data Telemetry

The implantable stimulator is powered by and communicates to the wearable transmitter via a power and data telemetry over an inductive link (Donaldson and Perkins, 1983; Schormans et al., 2018). The circuit arrangement of the power and data telemetry is shown in **Figure 3A**. The inductive link comprises a 5-turn, 32-mm diameter Tx coil and a 7-turn, 28-mm diameter Rx coil. Both coils are solenoids wound using 0.5 mm gauge enameled copper magnet wires. The Tx coil, *L1*, is driven by a class-D amplifier consisting of two NMOS transistors, M1 and M2, using discrete IRLML2030 N-channel power MOSFETs. M1 and M2 are switches turning on and off at 9.6 MHz. Their gates are driven by the secondary sides, S1 and S2, of a toroidal transformer, in opposite polarity. The toroidal transformer arrangement ensures a non-overlap time between the switching on of M1 and M2 to avoid shoot through current. The primary side of the toroidal transformer, P, is driven by a Xilinx XC2V256 complex programmable logic device (CPLD) through a buffer 74AC14. The supply voltage of the class-D amplifier is provided by a dc-dc converter LT1615 with a programmable feedback resistor

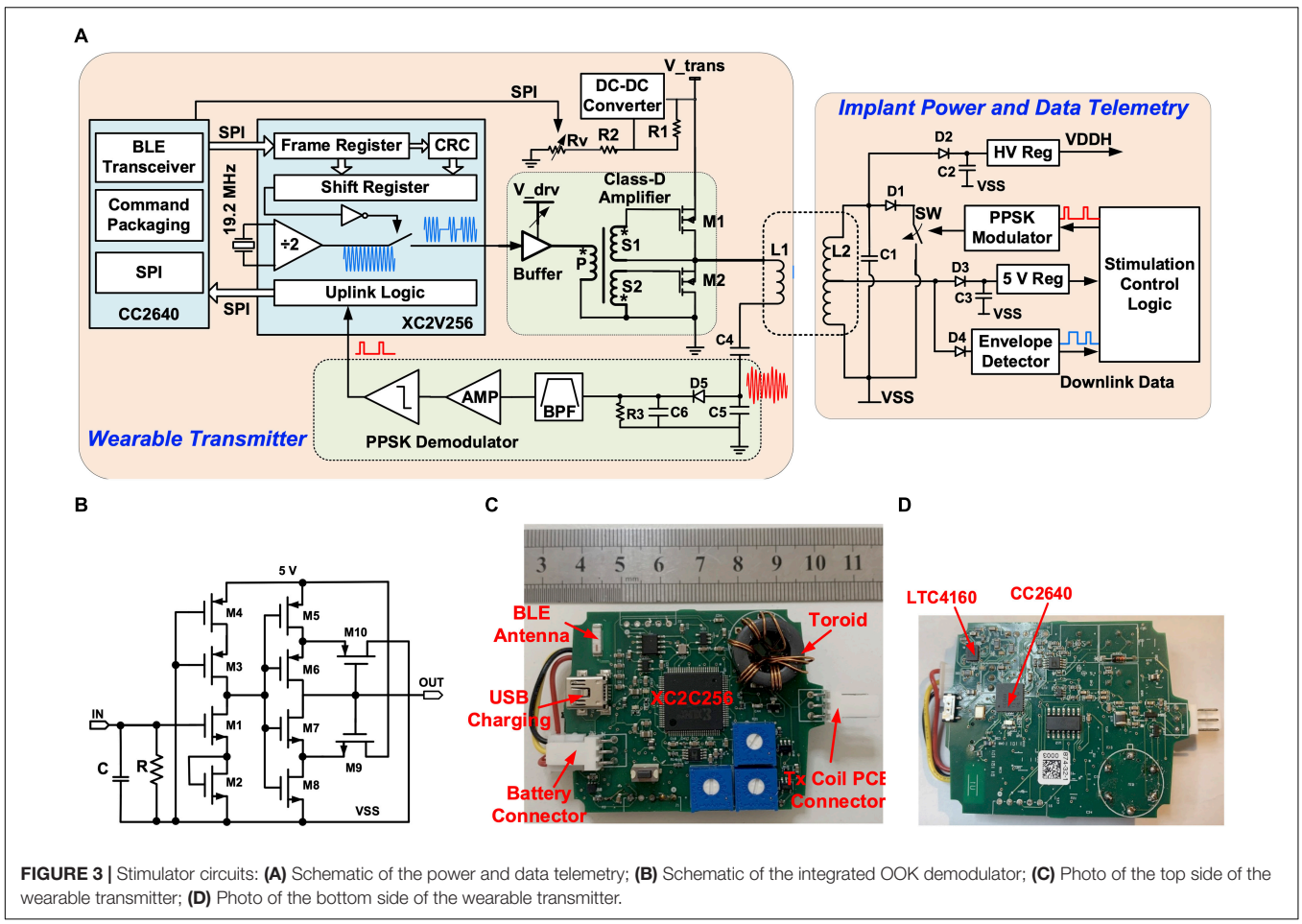

FIGURE 3 | Stimulator circuits: **(A)** Schematic of the power and data telemetry; **(B)** Schematic of the integrated OOK demodulator; **(C)** Photo of the top side of the wearable transmitter; **(D)** Photo of the bottom side of the wearable transmitter.

implemented with a potentiometer AD5220; thus, the transferred power over the inductive link can be controlled by the MCU. The Rx coil, L2, is tuned at 9.6 MHz with capacitor C1. The voltage across coil L2 is rectified by the Schottky diode D2 and a 10 μF capacitor C2, and regulated by a high voltage regulator (MIC5233) to a stable dc supply voltage VDDH of 16 V. There is also a middle tap on L2, where the voltage is rectified by D3 and C3 and then is regulated by a 5 V linear regulator in the primary ASIC to a 5 V supply for the low voltage circuits in the implant. The wearable transmitter is supplied by a lithium polymer battery LP-443440 (3.7 V, 560 mAh). The battery can be recharged from a USB port, regulated by a power management IC (LTC4160).

The inductive link also functions as a bidirectional half-duplex communication channel. The downlink data stream consisting of control commands and stimulation parameters are sent to the implant using on-off keying (OOK) modulation. The uplink data from the implant are transmitted using passive phase-shifted keying (PPSK) modulation (Jiang et al., 2017). During downlink data transfer, the MCU on the wearable transmitter sends stimulation settings received from the host computer over the BLE radio to the CPLD via a serial peripheral interface (SPI). The data frames are shifted in series at 400 kb/s to control an internal switch to turn on and off a 9.6 MHz output signal, which drives the class-D amplifier. On the Rx side, the data stream is recovered from the modulated carrier at the middle tap of L2, where the carrier is first rectified by D4, and then the envelope is extracted by an integrated envelope detector (ENV) and a Schmitt trigger in the primary ASIC. The circuit of the integrated OOK demodulator is shown in **Figure 3B**. The uplink data transfer is implemented with an integrated PPSK modulator. A logic "1" transmitted shorts L2 using an integrated switch SW when the voltage across L2 crosses zero from the negative value and holds for 1.5 carrier cycles. As a result, a current surge is caused in L1 and causes a transient voltage peak on the tuning capacitors C4 and C5. The transient voltage on C5 is demodulated through a passive envelope detector formed by D5, R3, and C6, and then is filtered and amplified. The bitstream is then extracted using a comparator. Details of the PPSK demodulation circuits are presented in Jiang et al. (2017). L1, C4, C5, D5, R3, and C6 are mounted on the Tx coil PCB and the rest of the transmitter circuitry is located inside a wearable unit, as shown in the photos in **Figures 3C,D**. In the implant, L2, C1–C3, and D1–D4 are located on the Rx coil PCB, and the rest of the implant electronics are mounted on the hybrid which is hermetically sealed with a ceramic lid.

Implant Packaging and Encapsulation

The implantable hybrid was constructed from a 36 mm × 38 mm ceramic substrate (96% alumina) with a thickness of 0.635 mm. Two layers of tracks were screen printed in thick film gold (8844-G Au) of 8 ± 1 μm thickness, with solder pads in the top layer over-printed with thick film platinum-gold (5837-G PtAu) of 12 ± 2 μm thickness. Thick film multilayer dielectric (4913-G) was over-printed between the layers and also on top of the top layer, covering all tracks except for the solder pads. A seal ring was formed by screen printing a platinum-gold layer; this also created hermetic feedthroughs for dielectric covered tracks from the hybrid circuit. All discrete components were soldered to the hybrid and flux residue was cleaned by sequential washes in acetone, propan-2-ol (isopropanol), and de-ionized water with ultrasonication. The primary stimulator ASIC, two secondary ASICs and two THAT380 bare dies were wire-bonded to the substrate, as shown in **Figure 2B**, and covered with epoxy glob top (Ablestik 968-2), as shown in **Figure 4A**. The hybrid was dried and sealed hermetically using a custom-made metallized ceramic lid (A473, Kyocera) of 32.13 mm × 28.55 mm size, 6.2 ± 0.5 mm height, and 3 mm thickness, soldered to the screen-printed seal ring while the assembly was placed on a hot plate at 150°C. **Figure 4B** shows the hermetically sealed hybrid.

The circular Rx coil PCB was constructed on an FR4 printed circuit board with a diameter of 34 mm, onto which were mounted discrete passive components in individual hermetic packages, the alignment magnet, and a coil of 0.5 mm gauge enameled copper magnet wire. The PCB was constructed without solder resist and silkscreen, and with exposed copper traces (no pad finish) to improve encapsulant adhesion.

The hybrid and Rx coil PCB were joined with multistrand fluoropolymer insulated stainless steel Cooner Wire (AS632, Cooner Wire Company, Chatsworth, CA, United States), which was also used for electrode connection cables. Connection wires

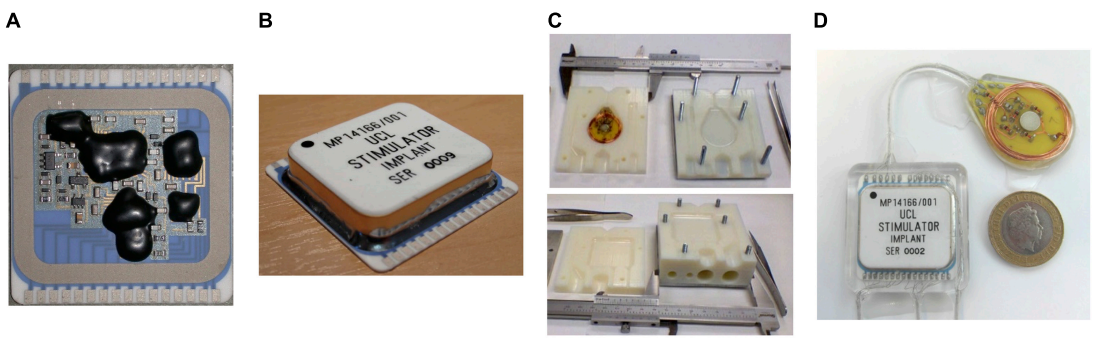

FIGURE 4 | Implant fabrication and encapsulation: **(A)** Stimulator circuits assembled on a ceramic substrate with the bare dies covered in epoxy glob top; **(B)** Stimulation circuits hermetically sealed in a metallized ceramic lid; **(C)** 3D-printed mold for encapsulation: mold for the hybrid (top) and mold for the Rx coil PCB (bottom); **(D)** fully encapsulated implant with a £2 coin as reference for the size.

were threaded through 1 mm bore silicone rubber tubes and soldered to form implantable cables. Three electrode connection cables were formed, one for each parallel stimulator ASIC with the associated two stimulation and six return lines. Electrode cables were terminated with miniature connectors (Nano 360® Plastic Circulars, NCS-11-DD, Omnetics Connector Corporation, Minneapolis, MN, United States).

The hermetically sealed, soldered hybrid and the Rx coil PCB were cleaned by sequential washes in acetone, propan-2-ol, de-ionized water, Leslie's soup, and de-ionized water, with each cleaning stage ultrasound assisted. Leslie's soup is a mixture of 0.5 wt% detergent (Teepol-L, Teepol Products, Kent, United Kingdom), and 25 wt% trisodium phosphate (anhydrous, 13438, Alfa Aesar, Heysham, United Kingdom), in de-ionized water. Cleanliness before encapsulation is essential for the survival of long-term implants (Vanhoestenberghe and Donaldson, 2013; Lonys et al., 2017; Kiele et al., 2020). Following rinsing, the conductivity of the rinse solution was monitored to confirm adequate cleanliness.

The cleaned implants are encapsulated in silicone rubber. A low viscosity, two-part silicone adhesive (EPM-2420, Avantor-NuSil, Radnor, PA, United States) was used to reduce the risk of voids and bubbles. EPM-2420 is mixed in a 1:1, Part A: Part B ratio using a speed mixer for 2 min at 2500 rpm (Dual Asymmetric Centrifugal Laboratory Mixer System, DAC 150 FVZ-K, Synergy Devices Ltd). Two molds were designed in Autodesk Inventor Fusion 2013 for the hybrid and Rx coil PCB. The molds were 3D printed in Verowhite Plus plastic with its gloss finish, to 0.1 mm precision, as shown in **Figure 4C**. Companion "Dural" plates were machined so the mold halves could be bolted together. Implants were held in the cleaned molds using pre-formed silicone spacers. Implants were encapsulated under vacuum (60 mBar) in a centrifuge (up to 200 *g*) to remove air bubbles. Because of the 65°C temperature limit of the Verowhite mold, the silicone rubber was cured at 60°C for 4 h. The implants were extracted from the mold, and sections of Dacron reinforced silicone rubber sheet were glued to the encapsulated implant with EPM-2420 to create suture sites for surgery. Free from the molds, the silicone rubber was further cured for 1 h at 80°C to complete the encapsulation. The encapsulated implant is shown in **Figure 4D**. An alternative medical grade silicone (MED-6215, Avantor-NuSil) is under investigation for long-term implantable devices.

Cleaned miniature connectors are also encapsulated in silicone rubber (Lancashire et al., 2021). Silicone tubing was placed at the base of each connector, surrounding the soldered wire ends. EPM-2420 silicone was degassed at 30 mbar in a vacuum centrifuge for between 1 and 3 min, until bubbles were no longer visible, nor flew onto the wire ends, covering all exposed solder. Silicone was cured at 80°C for 3 h under pressure (2.5 bar) to shrink any bubbles present.

Stimulation Control Procedure

Graphical User Interface

A GUI was developed in Matlab R2020a (MathWorks, Natick, MA, United States) for remotely controlling the stimulation on-the-fly. The GUI controls the Bluetooth connection, implant connection, and stimulation parameter settings. The layout of the GUI is shown in **Figure 5A**. The top panel "Serial Ports Control" controls the Bluetooth and implant connect/disconnect functions, including selecting the COM port number and setting the baud rate. The default baud rate is 9600 b/s. The middle panel "Implant Control" sets the stimulation parameters, where the three identical setting tags, "Stimulator 1," "Stimulator 2," and "Stimulator 3," are provided for each stimulator ASIC. The setting parameters for each stimulator ASIC include selection of the stimulating and return electrodes, the amplitude and width of the biphasic current pulses, the delay between the cathodic and anodic phases, the pulse rate, the shape of charge-balanced biphasic pulses (symmetrical or asymmetrical), and the length of a pulse train. The lower panel "Status Monitor" displays the received stimulation parameters and the expected waveform of current pulses. In the example shown in **Figure 5A**, the setting parameters specify stimulation between electrodes E1 and E8 on Stimulator ASIC Primary, with symmetrical biphasic current pulses with 80 μA (setting step size 4 μA) in amplitude, 10 μs width (setting step size 1 μs) and a pulse period of 1 ms [after reverse exponential conversion (Jiang et al., 2011)]. The expected waveform is shown in the Status Monitor.

Control Procedure

The backend software communicates with the wearable transmitter via a BLE radio link, relayed by the BLE dongle. The communication facilitates four different procedures: establishing connection, sending stimulation parameters, reset implant, and terminating connection, as shown in **Figure 5B** (the operations in the light boxes are executed by the host computer and those in the shaded boxes by the MCU module CC2640 on the wearable transmitter).

The overall communication procedure between the GUI and the implant for controlling multi-channel stimulation is shown in **Figure 5C**. During the "establishing connection" procedure, the link between the implant and the wearable transmitter, and the link between the wearable transmitter and the PC, are established separately. After the implant is powered, it sends a handshake request to the wearable transmitter via the inductive link every 250 μs until it receives confirmation from the transmitter, after which communication over the inductive link is established. The communication between the PC and the wearable transmitter is established after a "connecting" request is sent from the GUI with a specified baud rate and serial port number, where the host computer then wakes up the BLE dongle to establish Bluetooth connection with the wearable transmitter. The MCU on the wearable transmitter classifies the received command and sends a confirmation back to the host computer, hence the communication between the host computer and the implant is established, as shown in **Figure 5B**.

Stimulation from the implant can be controlled from the PC following the "setting parameters" procedure, where stimulation parameters set in the GUI are sent in packets via the Bluetooth link to the transmitter, which repackages the data into frames shown in **Figure 5D** and forward the frames to the implant over the inductive link. The implant verifies the received setting

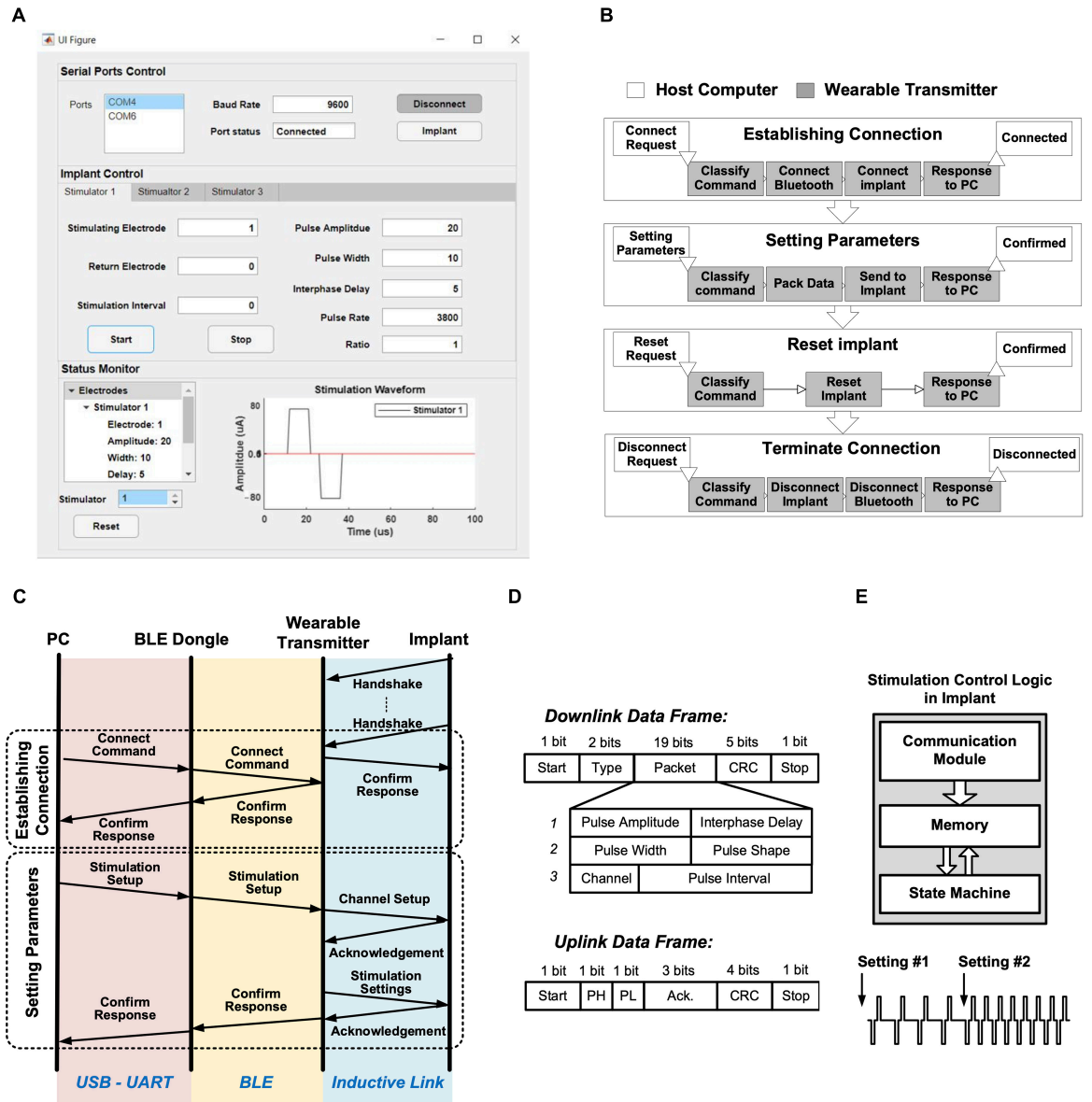

FIGURE 5 | Stimulation control protocol: **(A)** Graphical user interface; **(B)** Four procedures for operating the implant from a host computer, with flowcharts on the wearable transmitter in each procedure; **(C)** Overall communication procedure between the host computer and the implant for establishing connection and setting stimulation parameters; **(D)** Structure of the data frames over the inductive link; **(E)** Block diagram of the stimulation control logic in the implant, with an example of changing stimulation parameters on-the-fly.

parameters using cyclic redundancy check (CRC) in the frames, and sends back an acknowledgment frame to the transmitter with indicating whether the parameters are correctly received or a resend is needed. When all parameters are correctly received, the wearable transmitter sends confirmation back to the host computer to complete the "setting parameters" procedure. This procedure is repeated when changes to the stimulation are needed. After each procedure, the stimulation control logic in the primary stimulator ASIC stores the settings in a built-in memory, where the state-machine for the selected stimulator repeatedly loads the parameters from the memory for continuously generating stimulation pulses as specified, as illustrated in **Figure 5E** (Jiang et al., 2011). **Figure 5E** illustrates the change in stimulation pulses by the two "setting parameters" procedures.

The operation of the implant can be reset by the "reset implant" procedure. When reset is requested from the GUI to the transmitter, as shown in **Figure 5B**, the transmitter will temporarily terminate the power delivery to the implant, which forces the implant to conduct a power-on reset. This safety feature provides an emergency exit to terminate stimulation from the implant during experiments. After an experiment session, the

Bluetooth link between the PC and the transmitter can be released by the "terminate connection" procedure, as shown in **Figure 5B**.

RESULTS

The performance of the fully implantable stimulator was evaluated by electrical and *in vitro* experiments with electrodes in saline, and by accelerated lifetime testing.

Feasibility for Chronic Implantation

The quality of the seal of the implantable hybrid was tested according to the MIL-STD-883 (MIL-STD-883L, 2019) standard test for hermeticity. After sealing the lid, the package was bombed in helium for 2 h at 2 bars, then transferred (maximum delay 1 h) to a mass spectrometer for a fine leak test. The test was considered passed if the leak rate was lower than 5×10^{-8} atm cc/sec helium. After passing this fine leak test, the hybrid was placed in gross leak tank at 125°C for 1 min, and the package was considered to be sufficiently hermetic if no bubbles were observed. Following this procedure, for hybrids that pass the tests, the minimum time for the internal humidity was estimated to reach 60% RH to be at least 151 days, or 47 days minimum to reach 30% RH. Note that the actual times are likely to be much longer because the actual leak rate is likely to be much lower, but the exact leak rates is not available as the MIL-STD-883 standard only specifies a pass/fail fine leak test (Vanhoestenberghe and Donaldson, 2011).

The suitability of the implantable stimulator for chronic implantation was evaluated by accelerated lifetime testing. The test setup is shown in **Figure 6A**. The implant was placed inside a round bottom flask filled with de-ionized water. Deionized water was used to reduce the challenge of evaporation changing saline concentration. The silicone rubber used has low permeability to metal salts (Donaldson et al., 2011) and high permeability to water vapor, the most likely failure mode is driven by the penetration of moisture through the encapsulation layer (Donaldson, 1996). Should there be any ionic contamination on the implant surface (underneath the silicone encapsulation layer), then the osmotic gradient driving water molecules toward the contaminant and contributing to forming a pocket of liquid water, is worse in deionized water than in saline, further accelerating the failure rate. Therefore, for an implant of this type fully encapsulated in silicone, long-term tests in deionized water are appropriate. The flask was continuously heated on a heating mantle (Thermo Fisher Scientific, Waltham, MA, United States) at the boiling temperature for 15 consecutive days. A reflux condenser was installed on the flask to keep the volume of the de-ionized water unchanged. The implant was inductively powered by the first version of the wearable transmitter (Jiang et al., 2016) continuously during the entire course of the accelerated lifetime test. Data packets from the implant were frequently checked to monitor the status of the implant electronics and to ensure the wireless power transfer at a level sufficient for operation. **Figure 6B** shows the Rx coil PCB before the accelerated lifetime test, and **Figure 6C** shows the Rx coil PCB immediately after the implant was extracted from the flask at the end of the 15-day test. No corrosion was observed.

After returning to room temperature, the implant was placed in de-ionized water at room temperature but with the top surface exposed to open air. The implant was inductively coupled with the wearable transmitter and the three stimulators were set to generate current pulses at the maximum amplitude at 500 pps. Immediately after the stimulation starts, a thermal image was taken using a FLIR E4 thermal imaging camera (FLIR Systems, Wilsonville, OR, United States). The surface temperature was 25.5°C, as shown in **Figure 6D**. The implant was allowed to continuously operate for 1 h at the same settings, then the surface temperature was measured again, which increased to 26.7°C, as shown in **Figure 6E**.

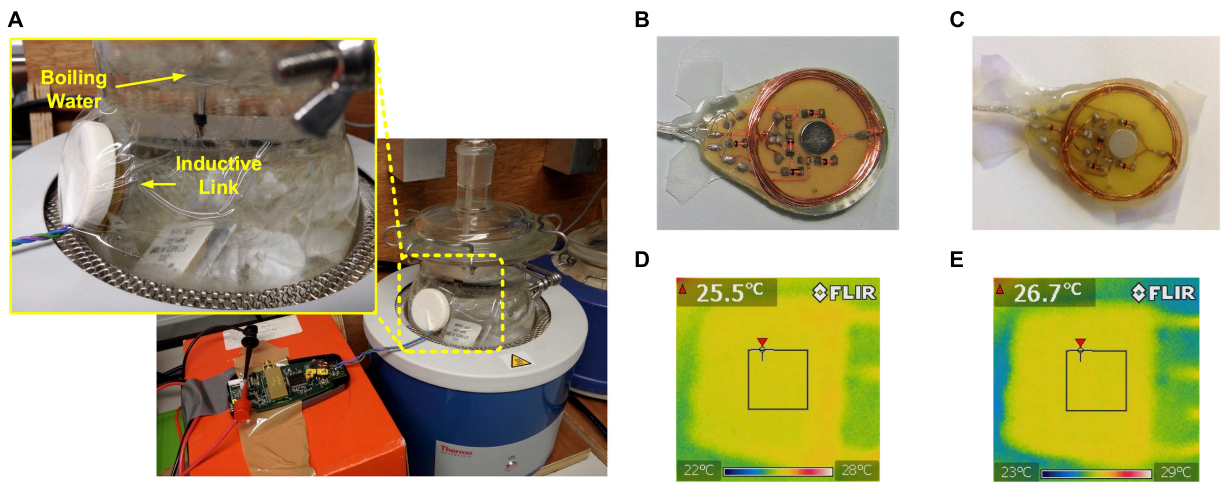

FIGURE 6 | Evaluation of feasibility for chronic implantation. **(A)** Setup of accelerated lifetime test; **(B)** Photo of the Rx coil PCB before the accelerated lifetime test; **(C)** Photo of the Rx coil PCB after accelerated lifetime test for 15 days; **(D)** Thermal image of the implant immediately after switched on at room temperature; **(E)** Thermal image of the implant 1 h after switched on in room temperature.

Electrical Performance Evaluation

The electrical performance of the implantable stimulator was evaluated with *in vitro* experiments both before and after the accelerated lifetime test. No changes were observed. **Figure 7** illustrates the setup of the *in vitro* experiments, where the implant was submerged in saline solution (16.7 mS/cm^2) and was inductively coupled with the wearable transmitter. An epidural electrode array (Courtesy of Fraunhofer IMM) (Capogrosso et al., 2016) was connected to the implant and was also submerged in saline solution. There are 15 gold electrodes in a size of 1.8 mm × 1 mm on a polyimide substrate distributed to the three stimulators. Sensing resistors were connected in series with the electrode array for measuring the current pulses using a DSO-X 2024A oscilloscope (Keysight, Santa Rosa, CA, United States). Stimulation was set from the GUI on a remote host computer. Note that the epidural electrode array was not included in the accelerated lifetime test.

The results shown in **Figures 8A–C**, **9** were recorded after the accelerated lifetime test. **Figure 8A** shows parallel stimulation from the three stimulators. The modulation patterns in this test were prestored in the CPLD on the wearable transmitter, where the remote host selected the patterns by their identification number. All stimulators were set to generate symmetrical biphasic pulses with a pulse width of 200 μs. Pulses on the primary stimulator were at a constant pulse rate of 100 pps but the amplitude was modulated sinusoidally at 4.5 Hz between 250 μA and 1 mA. Pulses on Stimulator Secondary #1 were at a constant amplitude of 800 μA but the pulse rate was modulated sinusoidally at 4.5 Hz between 400 pps and 53 pps. Pulses on Stimulator Secondary #2 were modulated both in frequency and amplitude, where the frequency modulation was the same as that on Stimulator Secondary #1, and the amplitude modulation was a 2-level step change between 700 μA and 1 mA, also at 4.5 Hz. **Figure 8B** demonstrates multiplexing stimulation among electrode pairs on the primary stimulator. In the first 300 ms, stimulation was from electrodes E1 and E8, with a current amplitude of 800 μA at a pulse rate of 100 pps. From 300 ms to 400 ms, the pulse rate was increased to 200 pps, and the pulses were multiplexed between E1 and E2 at a fixed interval of 5 ms, as highlighted in the zoom-in view, effectively providing 100 pps stimulation at both E1 and E2. After 400 ms, the pulse rate was changed back to 100 pps and stimulation was from E2 only. This process repeated after 500 ms between E2 and E3. The tests shown in **Figures 8A,B** were repeated for all the 36 electrode pairs.

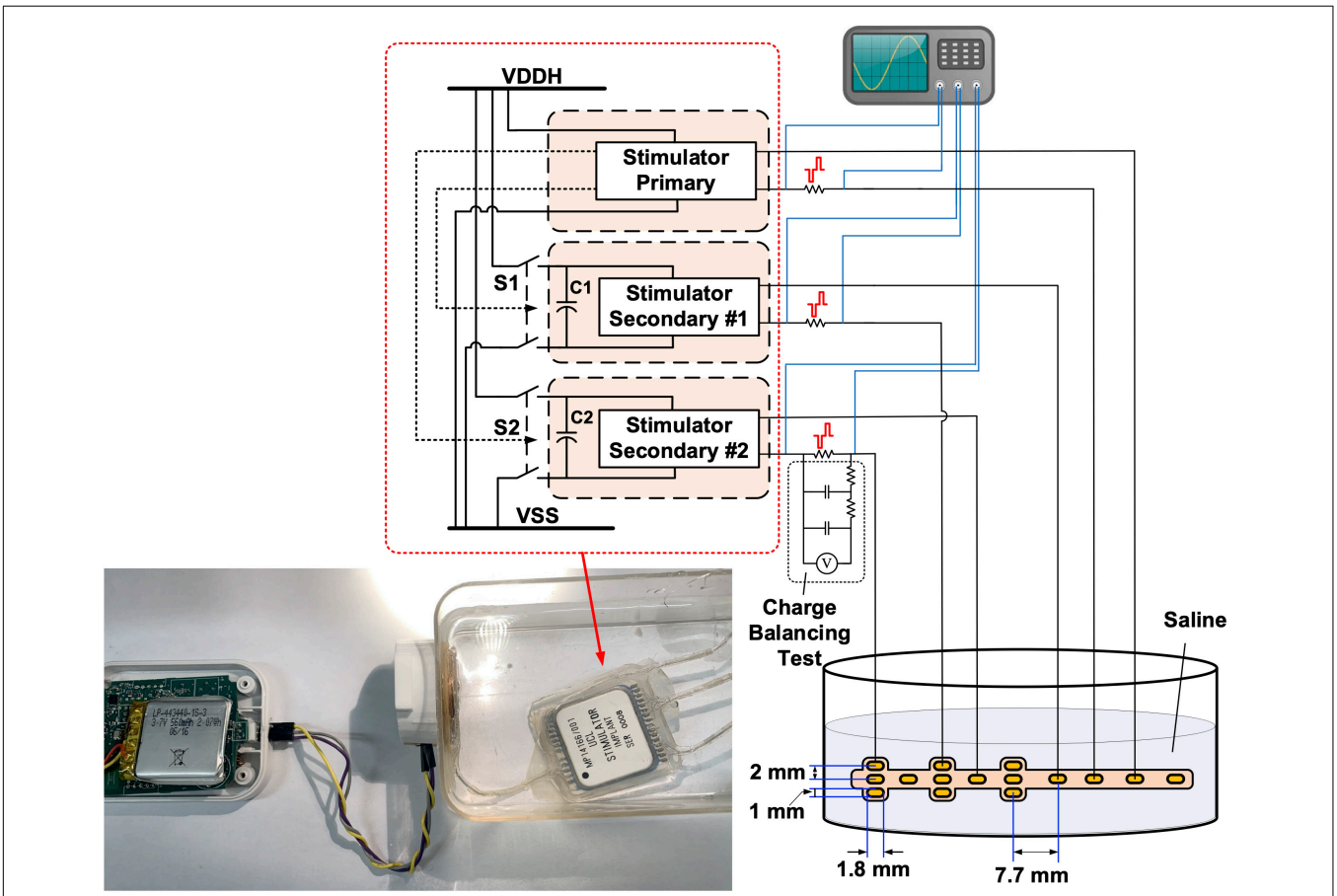

FIGURE 7 | Diagram of the *in vitro* benchtop performance evaluation setup. Insert: photo of the wearable transmitter and implantable stimulator during the in vitro experiment.

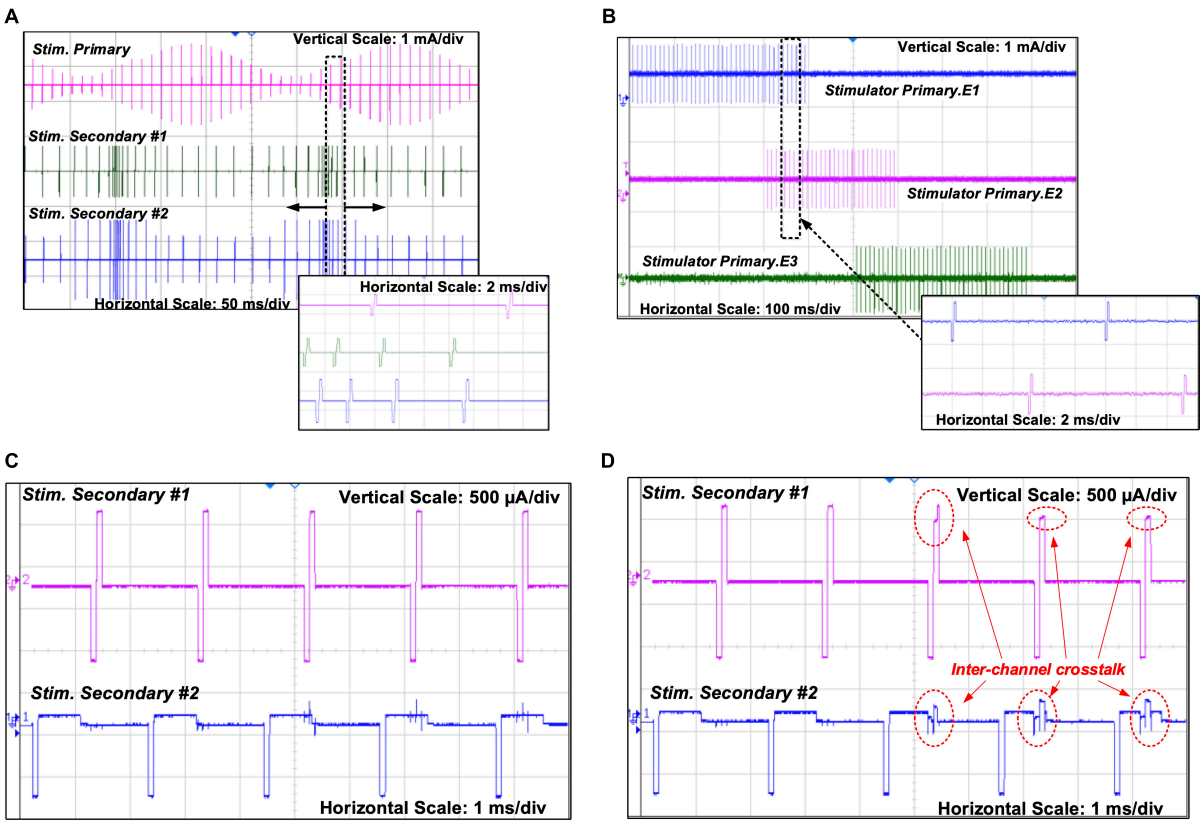

FIGURE 8 | *In vitro* electrical performance evaluation: **(A)** Parallel stimulation on the three stimulators in different modes of modulation; **(B)** Pulses multiplexed among electrodes on the primary stimulator; **(C)** Concurrent stimulating pulses from the two secondary stimulators with minimized crosstalk; **(D)** Concurrent stimulating pulses from a benchtop setup with the same circuits but without the power-isolation scheme.

Figure 8C shows the two secondary stimulators delivering concurrent biphasic pulses to the electrode array in saline solution (16.7 mS/cm^2). The pulses from Stimulator Secondary #1 are symmetrical, and the pulses from Stimulator Secondary #2 have anodic phases 8 times longer in width than the cathodic phases, and 8 times lower in amplitude to retain charge balance. Minimal spikes can be seen on the pulses from Stimulator Secondary #2 when they occur at the same time as the pulses from Stimulator Secondary #1. To compare the crosstalk reduction performance, a benchtop stimulator using the same stimulator ASICs in the same circuit arrangement was tested in the same setup, but the two secondary stimulator ASICs are constantly connected to the power rails without isolation. The measured pulses are shown in **Figure 8D**. Significant distortion can be observed on pulses from both stimulators when they occur at the same time. As shown in **Figure 2E**, the stimulating current between an electrode pair is generated from the current source and passes through the electrode pair via the H-bridge formed by S1 – S4 toward VSS_S1. When current pulses on both the stimulators occur at the same time, if VDDH_S1 and VDDH_S2, as well as VSS_S1 and VSS_S2, are shorted, part of the stimulating current on Stimulator Secondary #2 finds a pathway to VSS_S1 via the stimulating electrode pair on Stimulator Secondary #1, resulting in the distortion on the current pulses, as shown on the last two pulses in **Figure 8D** which are measured on the stimulators on the current path from the electrode pair to VSS_S1 (or VSS_S2), as shown in **Figure 7**. The first two biphasic pulses on Stimulator Secondary #2 in **Figure 8D** occur in the pulse interval on Stimulator Secondary #1, while S1, S2, and S5 in Stimulator Secondary #1 are off, as the crosstalk current pathway does not exist and the measured pulses are intact.

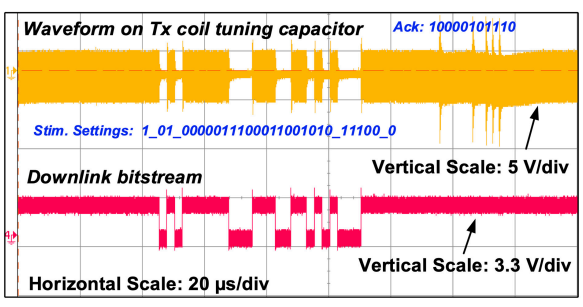

FIGURE 9 | Measured carrier waveform on the Tx tuning capacitor showing both OOK and PPSK modulation, alongside the measured downlink bitstream.

The charge balancing performance of the stimulators was evaluated using the test setup shown in **Figure 7**, where the dc

voltage across the sensing resistor was measured after a second-order low-pass filter with a cut-off frequency of 0.28 Hz. The stimulator under test was set to generate biphasic pulses at 500 pps, with a current amplitude of 1 mA and a pulse width of 100 μs per phase. The stimulation operated continuously for 8 h, and the dc voltage across a 790 Ω sensing resistor was measured every 30 min. The measured voltage remained constant at ∼ 1 μV, suggesting a residue dc current of ∼ 1.27 nA. There are various safety limits for neurostimulation reported in literature on the residue dc current, for example, 25 nA (Sit and Sarpeshkar, 2007) and 100 nA (Huang et al., 1999). The actual safety threshold should be placed in context with the equivalent charge density and the location of the electrodes. Nevertheless, the measured dc current is much lower than these safety limits.

Figure 9 shows the measured modulation on the carrier over the inductive link for sending bitstreams in both directions. The upper waveform is the voltage measured at the input of the envelope detector in the Tx coil PCB, i.e., the voltage across capacitor *C5* in **Figure 3A**, and the lower waveform is the control signal for the OOK modulation switch in the CPLD. It shows a carrier modulated first in OOK to send a 28-bit stimulation setting frame to the implant at 400 kb/s, and then is modulated in PPSK by the implant to send back a 11-bit acknowledgment frame at 600 kb/s.

A battery life test showed the voltage of a fully charged lithium polymer battery (LP-443440, 3.7 V, 600 mAh) dropped from 3.7 V to 3 V after 4 h continuous operation powering and controlling the implantable stimulator.

TABLE 1 | Features and performance of the implant system.

Hybrid dimensions	46 mm × 42.8 mm × 8.8 mm
Weight	35.2 g
Packaging	Hermetically sealed ceramic package with silicone encapsulation
Stimulator ASICs	0.6-μm HV CMOS
Supply voltage	5 V (digital circuits), 16 V (stimulator output stage)
Implant supply	Wireless inductive powering
Wearable transmitter supply	Rechargeable 3.7 V battery
Power consumption (stimulators)	31 mW*
Stimulation type	Biphasic constant current pulsatile stimulation
Stimulation amplitude	Primary ASIC: 8-bit current DAC, 0 μA – 1 mA, step size 4 μA Secondary ASICs: 8-bit current DAC, 0 μA – 3 mA, step size 12 μA
Pulse rate	1–500 pps, resolution ≤0.5 pps
Pulse duration	Cathodic phase: 0–500 μs Anodic phase: 1–8 times cathodic width
Number of stimulators	3, each driving 6 stimulating electrodes and 2 return electrodes
Number of electrode configurations	36
Inductive link parameters	*Primary coil*: 32 mm diameter, 0.5 mm gauge, 5 turns, 1.85 μH *Secondary coil*: 28 mm diameter, 0.5 mm gauge, 7 turns, 2.52 μH
Inductive link working distance	3–11 mm
Received DC supplied voltage	<17 V on the full receiver coil
Inductive link data rate	9.6 MHz carrier frequency, 400 kb/s OOK downlink, 600 kb/s PPSK uplink
Remote control radio link	Bluetooth Low Energy
Control interface	Matlab-based GUI for real-time stimulation control
Stimulator response latency	9.4 ms

**Measured with the three stimulators all generating biphasic pulses at 40 pps with 1 mA in pulses amplitude and 100 μs per phase.*

DISCUSSION AND CONCLUSION

The design, implementation and testing of a wireless fully implantable multichannel neural stimulator was described. The features and performance of the stimulator are summarized in **Table 1**.

The goal of this research was to develop a fully implantable device capable of multisite neural stimulation suitable for chronic studies in free moving animals, where the stimulation can be precisely delivered to the target sites and can be modified wirelessly in real-time from a remote-control host. The feasibility of the implantable stimulator for implantable operation and chronic implantation was evaluated. The device surface temperature rise and the external wearable device battery life for continuous operation were examined. According to BS EN 45502-1:2015 (BSI, 2015), the temperature rise caused by heat dissipation of an implantable device should be lower than 2°C. The tests conducted in this study show a 1.2°C surface temperature rise after 1 h continuous operation at the maximum stimulation capacity, which satisfies the safety criterion. The battery in the wearable device can support the system continuously working for 4 h before the battery voltage drops by 0.7 V to 3 V; 4 h is sufficient for one session of an animal experiment. The 4-h time window could be extended by increasing the supply voltage of the class-D amplifier to increase the reduced power transfer level.

To examine the feasibility of chronic implantation, the implant was evaluated in accelerated lifetime testing at 100°C for 15 consecutive days while powered on continuously. To estimate the equivalent lifetime at body temperature, instead of the empirical "10-degree rule" (Leenson, 1999), the Arrhenius equation (Zhou and Greenbaum, 2010) was used. Activation energies are rarely published, and none for hybrid circuits on alumina were found, but similar work suggests it may range from 0.7 eV to 0.4 eV (Vanhoestenberghe and Donaldson, 2013; Lonys et al., 2015). Using the lowest published activation energy of 0.4 eV, the acceleration factor is 18, or about 270 days at body temperature. For activation energy of 0.7 eV, the acceleration factor is roughly 84, suggesting an equivalent lifetime of ∼ 1,260 days at body temperature, which is sufficient for most chronic animal studies with active implantable devices reported in the literature. The ceramic packaging approach has the advantage of hermetic sealing over polymer packaging methods (Dahan et al., 2012; Au et al., 2020), and is cheaper than approaches using metallic protection.

The electrical performance evaluation demonstrates the stimulator's capability of providing versatile stimulation on multiple channels under real-time remote control. More importantly, it demonstrated that the implantable stimulator can provide truly parallel multichannel stimulation where current pulses on different channels can occur at the same time with minimal channel interference due to crosstalk. This feature allows simultaneous, highly selective stimulation to multiple sites, especially with different stimulation patterns on each site.

The implantable stimulator provides a versatile platform for chronic experimental studies with freely moving animals for applications involving peripheral nerves, such as vagus nerve stimulation, spinal cord injury and hand neural prostheses. Stimulation for up to 36 different electrode pairs can be facilitated and connections to the electrodes are "plug & play" allowing the use of different electrodes to suit each particular application.

Future work could consider the following enhancements in the electronics:

1) *Power Consumption:* As the ASICs are implemented in 0.6 μm CMOS technology, the control logic and the low voltage analog modules such as the 8-bit current DAC are operating at a 5 V supply voltage. The power consumption of these modules is over 20 mW. Implementation in a more advanced CMOS process technology (e.g., 180 nm HV CMOS), allows the supply voltage to the control logic, biasing circuits and the current DAC to be reduced to 1.8 V or lower, reducing the power required. For example, the integrated stimulator presented in Jiang et al. (2021) is implemented 180 nm CMOS and consumes only 1 mW when generating 50 Hz, 50% duty cycle current pulses of 16 mA. The energy consumed by the output stage circuit can be reduced by dynamic compliance voltage techniques (Samiei and Hashemi, 2021) and energy recycling methods (Ha et al., 2019);
2) *Physical Size:* The power isolation scheme requires the substrate of the parallel stimulators to be separated. Using 0.6 μm CMOS technology, the stimulators have to be implemented in separate ASICs. The use of silicon-on-insulator (SOI) CMOS technology would allow a single chip solution for all the stimulator circuits in the implant. In addition, a high-frequency stimulation scheme (Jiang and Demosthenous, 2018) allows on-chip energy storage capacitors, which could further reduce the physical size of the circuit layout. Furthermore, the external current booster using THAT380 was external to the stimulator ASICs, and could be eliminated with a new stimulator ASIC design.
3) *Communication Latency:* In the first version transmitter design (Jiang et al., 2016), an easyRadio ISM module eRA900TRS was used for the communication with the remote host, chosen for its low power consumption, but it was found that the inter packet delay is not optimal. A BLE radio link is chosen for the second version transmitter design. In the 9.4 ms communication latency, 8.3 ms is from the slow UART communication between the host computer and the BLE dongle. This latency could easily be shortened by selecting a higher UART baud rate.

DATA AVAILABILITY STATEMENT

The original contributions presented in the study are included in the article/supplementary material, further inquiries can be directed to the corresponding author/s.

AUTHOR CONTRIBUTIONS

DJ, FL, HL, TP, and AV drafted the manuscript. DJ, FL, and MS developed the hardware and firmware. FL developed the graphical user interface. DJ, HL, TP, and AV conducted implant packaging and encapsulation. DJ, FL, MS, HL, TP, and AV designed and conducted the benchtop device evaluation. ND and AD supervised the research and reviewed the manuscript. All authors contributed to the article and approved the submitted version.

FUNDING

This work was supported in part by the European Commission under projects NEUWalk and CLONS (agreement numbers 258654 and 225929). The open access publication fees were provided by University College London.

ACKNOWLEDGMENTS

The authors would like to thank Prof. David Borton from Brown University for the discussions on the device specifications and Dr. Peter Detemple from Fraunhofer IMM for providing the epidural electrode array for the *in vitro* evaluation.

REFERENCES

Au, S. L. C., Chen, F.-Y. B., Budgett, D. M., Malpas, S. C., Guild, S.-J., and McCormick, D. (2020). Injection molded liquid crystal polymer package for chronic active implantable devices with application to an optogenetic stimulator. *IEEE Trans. Biomed. Eng.* 67, 1357–1365. doi: 10.1109/tbme.2019.2936577

Boutros, P. J., Schoo, D. P., Rahman, M., Valentin, N. S., Chow, M. R., Ayiotis, A. I., et al. (2019). Continuous vestibular implant stimulation partially restores eye-stabilizing reflexes. *JCI Insight* 4:e128397. doi: 10.1172/jci.insight.128397

BSI (2015). *BS EN 45502-1:2015 Implants For Surgery—Active Implantable Medical Devices Part 1: General Requirements For Safety, Marking And For Information to be Provided by the Manufacturer*. London: BSI Standards Limited.

Capogrosso, M., Milekovic, T., Borton, D., Wagner, F., Moraud, E. M., Mignardot, J.-B., et al. (2016). A brain–spine interface alleviating gait deficits after spinal cord injury in primates. *Nature* 539, 284–288. doi: 10.1038/nature20118

Dahan, N., Vanhoestenberghe, A., and Donaldson, N. (2012). Moisture ingress into packages with walls of varying thickness and/or properties: a simple calculation method. *IEEE Trans. Compon. Packaging Manuf. Technol.* 2, 1796–1801. doi: 10.1109/tcpmt.2012.2210425

Donaldson, N. D., and Perkins, T. A. (1983). Analysis of resonant coupled coils in the design of radio frequency transcutaneous links. *Med. Biol. Eng. Comput.* 21, 612–627. doi: 10.1007/bf02442388

Donaldson, N., Baviskar, P., Cunningham, J., and Wilson, D. (2011). The permeability of silicone rubber to metal compounds: relevance to implanted devices. *J. Biomed. Mater. Res. A* 100, 588–598. doi: 10.1002/jbm.a.33257

Donaldson, P. E. K. (1996). The essential role played by adhesion in the technology of neurological prostheses. *Int. J. Adhes. Adhes.* 16, 105–107. doi: 10.1016/0143-7496(95)00031-3

Famm, K., Litt, B., Tracey, K. J., Boyden, E. S., and Slaoui, M. (2013). A jump-start for electroceuticals. *Nature* 496, 159–161. doi: 10.1038/496159a

Formento, E., Minassian, K., Wagner, F., Mignardot, J. B., Le Goff-Mignardot, C. G., Rowald, A., et al. (2018). Electrical spinal cord stimulation must preserve proprioception to enable locomotion in humans with spinal cord injury. *Nat. Neurosci.* 21, 1728–1741. doi: 10.1038/s41593-018-0262-6

Ha, S., Kim, C., Park, J., Cauwenberghs, G., and Mercier, P. P. (2019). A fully integrated RF-powered energy-replenishing current-controlled stimulator. *IEEE Trans. Biomed. Circuits Syst.* 13, 191-202.

Hart, R., Bhadra, N., Montague, F. W., Kilgore, K. L., and Peckham, P. H. (2011). Design and testing of an advanced implantable neuroprosthesis with myoelectric control. *IEEE Trans. Neural Syst. Rehabil. Eng.* 19, 45–53. doi: 10.1109/tnsre.2010.2079952

Huang, C. Q., Shepherd, R. K., Carter, P. M., Seligman, P. M., and Tabor, B. (1999). Electrical stimulation of the auditory nerve: direct current measurement *in vivo*. *IEEE Trans. Biomed. Eng.* 46, 461–469. doi: 10.1109/10.752943

Jiang, D., and Demosthenous, A. (2018). A multichannel high-frequency power-isolated neural stimulator with crosstalk reduction. *IEEE Trans. Biomed. Circuits Syst.* 12, 940–953. doi: 10.1109/tbcas.2018.2832541

Jiang, D., Cirmirakis, D., and Demosthenous, A. (2015). A vestibular prosthesis with highly-isolated parallel multichannel stimulation. *IEEE Trans. Biomed. Circuits Syst.* 9, 124–137. doi: 10.1109/tbcas.2014.2323310

Jiang, D., Cirmirakis, D., Schormans, M., Perkins, T. A., Donaldson, N., and Demosthenous, A. (2017). An integrated passive phase-shift keying modulator for biomedical implants with power telemetry over a single inductive link. *IEEE Trans. Biomed. Circuits Syst.* 11, 64–77. doi: 10.1109/tbcas.2016.2580513

Jiang, D., Demosthenous, A., Perkins, T. A., Liu, X., and Donaldson, N. (2011). A stimulator ASIC featuring versatilemanagement for vestibular prostheses. *IEEE Trans. Biomed. Circuits Syst.* 5, 147–159. doi: 10.1109/tbcas.2011.2138139

Jiang, D., Eder, C., Perkins, T. A., Vanhoestenberghe, A., Schormans, M., Liu, F., et al. (2016). "An implantable wireless multi-channel neural prosthesis for epidural stimulation," in *Proceedings of the IEEE International Symposium on Circuits and Systems (ISCAS)* (Montreal, QC: IEEE), 2026–2029.

Jiang, D., Wu, Y., Almarri, N., Habibollahi, M., Liu, F., Bryson, B., et al. (2021). "An integrated bidirectional multi-channel opto-electro arbitrary waveform stimulator for treating motor neurone disease," in *Proceedings of the IEEE International Symposium on Circuits and Systems (ISCAS)* (Daegu: Republic of Korea).

Kiele, P., Čvančara, P., Langenmair, M., Mueller, M., and Stieglitz, T. (2020). Thin film metallization stacks serve as reliable conductors on ceramic-based substrates for active implants. *IEEE Trans. Compon. Packaging Manuf. Technol.* 10, 1803–1813. doi: 10.1109/tcpmt.2020.3026583

Lancashire, H. T., Habibollahi, M., Jiang, D., and Demosthenous, A. (2021). "Evaluation of commercial connectors for active neural implants," in *Proceedings of the 10th International IEEE EMBS Conference on Neural Engineering (NER)* (Italy).

Lee, B., Koripalli, M. K., Jia, Y., Acosta, J., Sendi, M. S. E., Choi, Y., et al. (2018). An implantable peripheral nerve recording and stimulation system for experiments on freely moving animal subjects. *Sci. Rep.* 8:6115. doi: 10.1038/s41598-018-24465-1

Leenson, I. A. (1999). Old rule of thumb and the arrhenius equation. *J. Chem. Educ.* 76, 1459–1460. doi: 10.1021/ed076p1459

Loeb, G. E., Peck, R. A., Moore, W. H., and Hood, K. (2001). BION^{TM} system for distributed neural prosthetic interfaces. *Med. Eng. Phys.* 23, 9–18. doi: 10.1016/s1350-4533(01)00011-x

Lonys, L., Vanhoestenberghe, A., Huberty, V., Hiernaux, M., Cauche, N., Julémont, N., et al. (2017). In vivo validation of a less invasive gastrostimulator. *Artif. Organs* 41, E213–E221.

Lonys, L., Vanhoestenberghe, A., Julémont, N., Godet, S., Delplancke, M.-P., Mathys, P., et al. (2015). Silicone rubber encapsulation for an endoscopically implantable gastrostimulator. *Med. Biol. Eng. Comput.* 53, 319–329. doi: 10.1007/s11517-014-1236-9

MIL-STD-883L (2019). *Test Method Standard Microcircuits*. Columbus, Ohio: Department of Defence, USA.

Pavlov, V. A., and Tracey, K. J. (2017). Neural regulation of immunity: molecular mechanisms and clinical translation. *Nat. Neurosci.* 20, 156–166. doi: 10.1038/nn.4477

Raspopovic, S., Capogrosso, M., Petrini, F. M., Bonizzato, M., Rigosa, J., Pino, G. D., et al. (2014). Restoring natural sensory feedback in real-time bidirectional hand prostheses. *Sci. Transl. Med.* 6:222ra19. doi: 10.1126/scitranslmed.3006820

Samiei, A., and Hashemi, H. (2021). Energy efficient neural stimulator with dynamic supply modulation. *Electron. Lett.* 57, 173–174. doi: 10.1049/ell2.12024

Schormans, M., Valente, V., and Demosthenous, A. (2018). Practical inductive link design for biomedical wireless power transfer: a tutorial. *IEEE Trans. Biomed. Circuits Syst.* 12, 1112–1130. doi: 10.1109/tbcas.2018.2846020

Sit, J.-J., and Sarpeshkar, R. (2007). A low-power blocking-capacitor-free charge-balanced electrode-stimulator chip with less than 6 nA dc error for 1-mA full-scale stimulation. *IEEE Trans. Biomed. Circuits Syst.* 1, 172–183. doi: 10.1109/tbcas.2007.911631

Sivaji, V., Grasse, D. W., Hays, S. A., Bucksot, J. E., Saini, R., Kilgard, M. P., et al. (2019). ReStore: a wireless peripheral nerve stimulation system. *J. Neurosci. Methods* 320, 26–36. doi: 10.1016/j.jneumeth.2019.02.010

Sun, F. T., and Morrell, M. J. (2014). The RNS system: responsive cortical stimulation for the treatment of refractory partial epilepsy. *Expert Rev. Med. Devices* 11, 563–572. doi: 10.1586/17434440.2014.947274

Vanhoestenberghe, A., and Donaldson, N. (2011). The limits of hermeticity test methods for micropackages. *Artif. Organs* 35, 242–244. doi: 10.1111/j.1525-1594.2011.01222.x

Vanhoestenberghe, A., and Donaldson, N. (2013). Corrosion of silicon integrated circuits and lifetime predictions in implantable electronic devices. *J. Neural Eng.* 10:031002. doi: 10.1088/1741-2560/10/3/031002

Williams, I., Brunton, E., Rapeaux, A., Liu, Y., Luan, S., Nazarpour, K., et al. (2020). SenseBack-an implantable system for bidirectional neural interfacing. *IEEE Trans. Biomed. Circuits Syst.* 14, 1079–1087. doi: 10.1109/tbcas.2020.3022839

Wong, Y. T., Dommel, N., Preston, P., Hallum, L. E., Lehmann, T., Lovell, N. H., et al. (2007). Retinal neurostimulator for a multifocal vision prosthesis. *IEEE Trans. Neural Syst. Rehabil. Eng.* 15, 425–434. doi: 10.1109/tnsre.2007.903958

Xu, Q., Hu, D., Duan, B., and He, J. (2015). A fully implantable stimulator with wireless power and data transmission for experimental investigation of epidural spinal cord stimulation. *IEEE Trans. Neural Syst. Rehabil. Eng.* 23, 683–692. doi: 10.1109/tnsre.2015.2396574

Zamora, M., Toth, R., Ottaway, J., Gillbe, T., Martin, S., Benjaber, M., et al. (2020). DyNeuMo Mk-1: a fully-implantable, motion-adaptive neurostimulator with configurable response algorithms. *bioRxiv* [Preprint]. doi: 10.1101/2020.09.10.292284

Zeng, F.-G., Rebscher, S., Harrison, W. V., Sun, X., and Feng, H. (2008). Cochlear implants: system design, integration and evaluation. *IEEE Rev. Biomed. Eng.* 1, 115–142. doi: 10.1109/RBME.2008.2008250

Zhou, D., and Greenbaum, E. (2010). *Implantable Neural Prostheses 2*. New York, NY: Springer.

Zollo, L., Pino, G. D., Ciancio, A. L., Ranieri, F., Cordella, F., Gentile, C., et al. (2019). Restoring tactile sensations via neural interfaces for real-time force-and-slippage closed-loop control of bionic hands. *Sci. Robot.* 4:eaau9924. doi: 10.1126/scirobotics.aau9924

Conflict of Interest: The authors declare that the research was conducted in the absence of any commercial or financial relationships that could be construed as a potential conflict of interest.

frontiers in Neuroscience

ORIGINAL RESEARCH
published: 29 July 2021
doi: 10.3389/fnins.2021.697731

A Biomimetic, SoC-Based Neural Stimulator for Novel Arbitrary-Waveform Stimulation Protocols

Stanislav Culaclii[1,2], Po-Min Wang[1], Giuliano Taccola[3,4], William Yang[1], Brett Bailey[1], Yan-Peng Chen[1,5], Yi-Kai Lo[1,6] and Wentai Liu[1,5,7,8]**

[1] Department of Bioengineering, University of California, Los Angeles, Los Angeles, CA, United States, [2] Jet Propulsion Laboratory, California Institute of Technology, Pasadena, CA, United States, [3] Neuroscience Department, International School for Advanced Studies, Trieste, Italy, [4] Department of Integrative Biology and Physiology, University of California, Los Angeles, Los Angeles, CA, United States, [5] Department of Electrical Engineering, University of California, Los Angeles, Los Angeles, CA, United States, [6] Niche Biomedical Inc., Los Angeles, CA, United States, [7] California NanoSystems Institute, University of California, Los Angeles, Los Angeles, CA, United States, [8] Brain Research Institute, University of California, Los Angeles, Los Angeles, CA, United States

OPEN ACCESS

Edited by:
Alexandre Schmid,
École Polytechnique Fédérale de Lausanne, Switzerland

Reviewed by:
Gene Yevgeny Fridman,
Johns Hopkins University, United States
Massimo Barbaro,
University of Cagliari, Italy
Soheil Mottaghi,
University of Freiburg, Germany

***Correspondence:**
Stanislav Culaclii
stanislav.c@ucla.edu
Wentai Liu
wentai@ucla.edu

Specialty section:
This article was submitted to Neural Technology, a section of the journal Frontiers in Neuroscience

Received: 20 April 2021
Accepted: 07 July 2021
Published: 29 July 2021

Citation:
Culaclii S, Wang P-M, Taccola G, Yang W, Bailey B, Chen Y-P, Lo Y-K and Liu W (2021) A Biomimetic, SoC-Based Neural Stimulator for Novel Arbitrary-Waveform Stimulation Protocols. Front. Neurosci. 15:697731. doi: 10.3389/fnins.2021.697731

Novel neural stimulation protocols mimicking biological signals and patterns have demonstrated significant advantages as compared to traditional protocols based on uniform periodic square pulses. At the same time, the treatments for neural disorders which employ such protocols require the stimulator to be integrated into miniaturized wearable devices or implantable neural prostheses. Unfortunately, most miniaturized stimulator designs show none or very limited ability to deliver biomimetic protocols due to the architecture of their control logic, which generates the waveform. Most such designs are integrated into a single System-on-Chip (SoC) for the size reduction and the option to implement them as neural implants. But their on-chip stimulation controllers are fixed and limited in memory and computing power, preventing them from accommodating the amplitude and timing variances, and the waveform data parameters necessary to output biomimetic stimulation. To that end, a new stimulator architecture is proposed, which distributes the control logic over three component tiers – software, microcontroller firmware and digital circuits of the SoC, which is compatible with existing and future biomimetic protocols and with integration into implantable neural prosthetics. A portable prototype with the proposed architecture is designed and demonstrated in a bench-top test with various known biomimetic output waveforms. The prototype is also tested *in vivo* to deliver a complex, continuous biomimetic stimulation to a rat model of a spinal-cord injury. By delivering this unique biomimetic stimulation, the device is shown to successfully reestablish the connectivity of the spinal cord post-injury and thus restore motor outputs in the rat model.

Keywords: neural stimulator, biomimetic, SoC, multi-channel, arbitrary waveform, implant, wireless, control logic

INTRODUCTION

Electrical stimulation has been long employed as a treatment for neural disorders, such as Parkinson's (Benabid et al., 1991), epilepsy (Mogul and van Drongelen, 2014); treatment for pain (Gerasimenko et al., 2008); restoration of sensory disorders, such as vision (Weiland et al., 2005) and hearing (Moore and Shannon, 2009); rehabilitation of locomotion for spinal cord injury patients (Taccola et al., 2018), among others. In most applications the stimulation treatment is delivered in the form of charge-controlled, constant-current or voltage pulses, usually repeating as uniform pulse trains (Merrill et al., 2005). Accordingly, most novel neural-prosthetic stimulator designs focus on this type of conventional stimulation waveforms. Such stimulator designs, as in work (Stanslaski et al., 2012), fundamentally employ circuits with constant current or voltage sources and timers to turn the sources on and off with a predefined uniform frequency (**Figures 1A,B**).

Novel stimulation waveforms, shaped unlike the uniform pulse trains, have been shown to be advantageous for specific applications in therapeutics and research. Neural prosthetics require unique design architectures to accommodate such waveforms (**Figure 1**). For example, amplitude ramps, which require dynamic control of amplitude in each stimulation pulse (**Figure 1C**), have been shown to induce asynchronous neural firings in the targeted tissue, leading to a more natural neural activity (Formento et al., 2020). Neural stimulator employed by Wagner et al. (2018) produces stimulation trains with multiple discrete frequencies (**Figure 1D**) to enable locomotion in patients with a spinal cord injury. Brocker et al. (2013), Eles et al. (2020), and Soto-Breceda et al. (2018) demonstrate delivery of a series of pulses with irregular inter-pulse-intervals to reduce synaptic fatigue in retina tissue or improve therapeutic effects in Parkinson's treatments. Stimulators designed for these protocols require a dynamic control of timing of each individual pulse in the series (**Figure 1E**). Energy efficient waveforms with exponential decaying amplitudes (**Figure 1F**) are demonstrated by Lee et al. (2018), and require additional circuitry to control the amplitude of the current pulse during its output. Finally, **Figure 1G** shows a novel biomimetic stimulation waveform from work by Taccola et al. (2020a,b) which was titled Dynamic Stimulation (DS) and was created from an electromyography (EMG) recording of the soleus (Sol) muscle of a healthy rat during stepping. The complex waveform is empirically shown to be significantly more effective than pulse trains in increasing the excitability and neural connectivity of the spinal cord, potentially advantageous in therapy post spinal cord injury. This protocol requires a stimulator architecture which can dynamically control all above parameters of the output current and reproduce a relatively long, continuous, arbitrary waveform data, posing the most complex challenge for stimulator design.

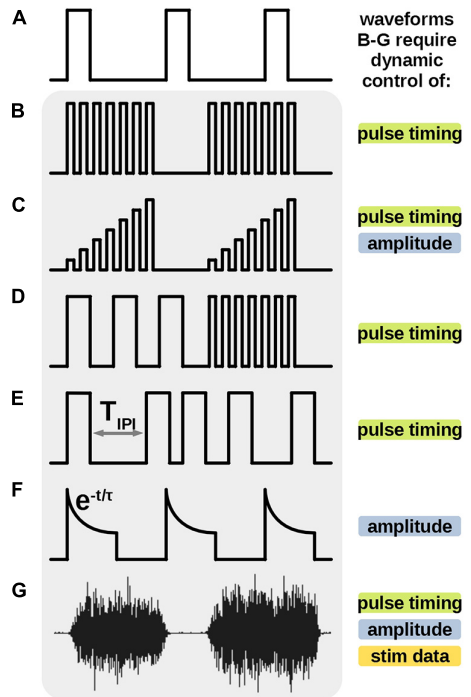

FIGURE 1 | Previously demonstrated novel protocols, uniquely different from the traditional uniform pulse train **(A)** require additional stimulator features to be generated. High frequency bursts **(B,C)** pulse frequency modulation (FM) **(D)** varying inter-pulse-interval **(E)** and the biomimetic waveform (G) require dynamic control of timing of individual stimulus pulses. Amplitude ramp **(C)** energy efficient stimulus **(F)** and biomimetic waveform **(G)** also require dynamic amplitude during the stimulus output. Uniquely, the biomimetic waveform **(G)** requires an ability to store, process and output a relatively large amount of stimulus data points to recreate the protocol. Some, but not all such features were demonstrated in previous works. All these features are available in the proposed stimulator architecture.

At the same time, long-term treatments using the above stimulation protocols often require implementation of the stimulator as an implantable neuroprosthetic, prompting integrated and miniaturized design in the form of a System-on-Chip (SoC) (Stanslaski et al., 2012; Sun and Morrell, 2014; Yip et al., 2015). Although commercial stimulators, such as STG 4008 (Multi Channel Systems, Reutlingen, Germany) used by Taccola et al. (2020a,b) support continuous arbitrary waveforms, they cannot be translated to miniaturized implantable neural prosthetics. Several state-of-the-art SoC-based designs, targeting implantable applications, have been shown to support arbitrary stimulation waveforms (Noorsal et al., 2012; Yip et al., 2015; Kassiri et al., 2017; Piech et al., 2020). Yet, designs (Noorsal et al., 2012; Yip et al., 2015; Kassiri et al., 2017) allow for maximum length of the arbitrary waveform of 8–64 points, limiting the application to controlling the shape of short repeating pulses, rather than stimulating with true complex biomimetic signals. Architecture of the design in Piech et al. (2020) allows for a longer stream of arbitrary parameters for the output stimulus, but limits the output signal's duty cycle to <50% at amplitude resolution of 3-bits, due to the inherent power limitations of the design, in which a millimeter-sized neural implant is remotely powered by ultrasound waves. This restricts the output to a series of discrete stimulus pulses rather than a continuous biomimetic waveform.

A novel stimulator system is proposed to address the need for supporting existing and future novel arbitrary biomimetic waveforms, as well as all other waveforms outlined above,

while also being suitable for implantable applications. The proposed 3-tier control architecture, described in section "System Architecture", distributes the waveform generating logic onto SoC, adopted from prior work (Lo et al., 2016), and the external components of the system. Empowered by an additional firmware layer, it provides flexibility to support a multitude of stimulation protocols, while being compatible with implantable neural prosthetics. A prototype is built and its performance is demonstrated in section "Bench-Top Test" at the benchtop level. Finally, the prototype is tested *in vivo* to increase excitability of the spinal cord and restore connectivity in animal subjects with spinal cord injury, and the results are discussed in section "*In vivo* Tests". This work expands on our previous report (Wang et al., 2019), by adding further design details, signal analysis, new bench-top test results and *in vivo* animal testing.

MATERIALS AND METHODS

Quantifying the Biomimetic Stimulator's Performance

The main requirement for the proposed system is to preserve the key desired features of the biomimetic stimulation protocol. These features are derived and quantified by analysis of the biomimetic signal in the section below. Additional electrical performance considerations, related to the data link and the analog circuitries, are discussed in a further section. The theoretical values and the values measured from the prototyped system are summarized **Table 1**.

Signal Analysis of the Biomimetic Protocol

The novel biomimetic waveform, DS (**Figure 1G**) is used in the *in vivo* test of our proposed stimulator prototype. DS contains two key features – amplitude modulation (AM) and frequency modulation (FM) – which are thought to contribute to its unique efficacy in recruitment of neural networks. A biomimetic stimulator design thus needs to preserve such key modulation characteristics in its output. However, a high-resolution stimulation output requires a hardware design that has a larger size and a higher power consumption, which conflicts with the design requirements of implantable or wearable applications. The miniaturization of critical stimulator components as SoCs results in decreased resolution in timing and output current and reduced memory sizes, which may distort the output stimulus signal and change its key AM and FM modulations, as compared to desktop-sized, non-portable commercial neural stimulators. In order to evaluate the impact of reduced resolution on the key AM and FM features, the DS signals are analyzed (blue trace in **Figure 2A**). The signal is linearly scaled to limit the amplitude peaks to ±225 μA (450 μA peak-to-peak), which was previously found to be therapeutically effective in rat-model experiments similar to the *in vivo* testing in section "*In vivo* Tests". Next, the signal is cropped in time domain from 30 to 3 s, retaining the original 2 ksps sampling rate. The chosen length of the crop at the original sampling rate preserves the frequency variation of the signal. The location of the crop is strategically selected to retain the large amplitude variations of complete EMG bursts (orange trace in **Figure 2A**).

To evaluate effects of the DS signal's transformation on its key features we plot a histogram of peak amplitudes and the fast fourier transform (FFT) of the signal at each step, which are displayed in **Figure 2**. A peak is defined as an extremum (positive or negative) between each pair of consecutive zero-crossings. **Figure 2B** shows that the original signal contains peaks with amplitude values spanning from signal's minimum to maximum. The high count around the 0-amplitude represents noise in the recorded physiological signal. The signal's distinct high-amplitude EMG peaks represent the motoneuron outputs and are fewer compared to low-amplitude peak activity. The histogram's *y*-axis is plotted on a log scale to increase visibility of both high-count and low-count bins. The FFT spectrum is plotted on a 10-log dB scale after the signal is squared to represent its power. The FFT spectrum shows a notch at 60 Hz created by a line noise filter and a relatively higher power in the 100–1000 Hz band as typical of EMG signals.

Figure 2C shows that cropping the signal in time domain by 10× reduces the values on the bin counts in the histogram proportionally, as expected, but the distribution of the peak amplitudes remains the same. The number of points of the FFT plot is reduced proportionally to the signal length but the frequency content is otherwise unchanged. The quantization step shown in **Figure 2D** transfers some peak amplitudes across histogram bins but otherwise no notable difference is seen.

TABLE 1 | Performance of the biomimetic stimulator prototype.

System's Signal Analysis: Theoretical vs. Measured				
Parameter	**Original DS signal**	**Time-cropped and quantized signal**	**Measured system output**	**Δ (Original DS – measured output)**
Amplitude range of positive peaks	181 μA/0.344 V[4]	176 μA/0.334 V[4]	0.376 V	+9.3%[1]
Amplitude range of negative peaks	225 μA/0.428 V[4]	223 μA/0.424 V[4]	0.418 V	−2.3%[1]
Wiener entropy	−2.19 dB	−2.17 dB	−1.87 dB	+3.8%(+0.32 dB)[1]

System's electrical performance				
Parameter	Stimulation data bitrate	Output compliance voltage[3]	Maximum accepted electrode impedance[3]	Charge balance mechanism[3]
Value	133 kbps	± 10 V	24 kΩ+[2]	Passive charge dissipation

[1] *Values include 60 Hz noise and a high-frequency noise aliased into the signal band during the oscilloscope data capture.*
[2] *Upper impedance limit is stated for maximum stimulation current of 500 μA; if current is lowered, the limit increases.*
[3] *Values presented for reference from prior work (Lo et al., 2017).*
[4] *Current values of the signal are converted to voltage through R_S resistor of the Randles Cell model.*

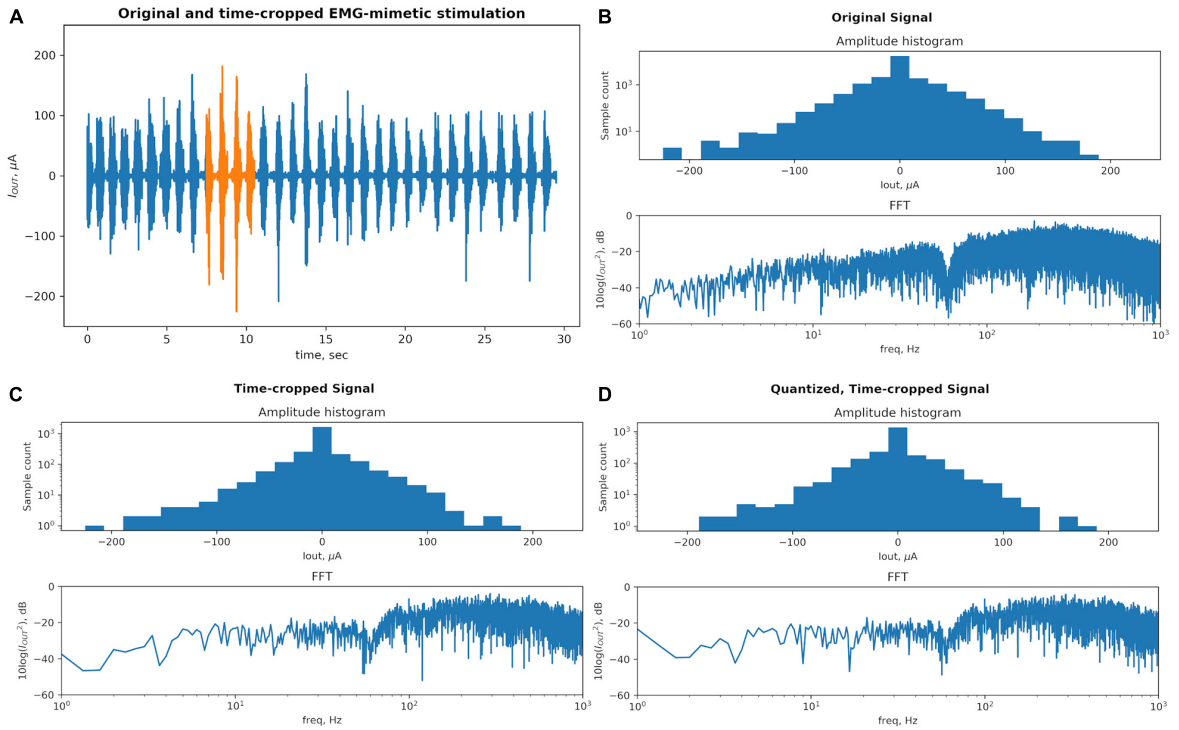

FIGURE 2 | A physiological recording used as a biomimetic stimulation protocol Dynamic Stimulation (DS) is transformed to conform to the typical hardware limitations of the System-on-Chip (SoC)-based stimulators. The key characteristics responsible for therapeutic efficacy of this signal (amplitude and frequency modulations) are preserved through the transformation process. **(A)** Original signal (blue) contains bursts corresponding to rhythmic stepping of an animal on a treadmill. The signal was strategically time-cropped, from 30 to 3 s, to preserve the wide range of peak amplitudes and frequencies while saving memory space in the proposed stimulator system. **(B)** Original signal's statistic of peak amplitudes and frequency content defines a baseline for the comparison. The dip in the spectrum at 60 Hz is created by the "line" noise filter. **(C)** The time-cropped signal's peak amplitude counts and the number of FFT samples are reduced proportionally with the length. The general shape of the histogram and frequency content is notably generally unchanged. A dip at the ~140 μA bin results from a reduced number of high amplitude peaks in the time-cropped signal as it contains less high amplitude bursts as compared to the original signal. **(D)** The quantization step reduces the resolution from the 14-bit precision of the recording amplifier that captured the original signal to the 8-bit output resolution of the neural stimulator SoC employed in this work. The amplitude statistics are and FFT are notably unchanged and this final signal is used in the proposed system and the *in vivo* testing.

In addition to qualitative observations of the histograms, the modulation of the amplitude is also quantified by the range between the largest and the smallest amplitude peaks, measured separately in positive and negative directions. The peak amplitude ranges are 181 and 225 μA for the original DS signal (positive and negative, respectively), and 176 and 223 μA for the pre-processed signal.

The modulation in frequency is quantified by the flatness of the frequency spectrum, which indicates how uniformly the signal power is distributed over its bandwidth. Wiener entropy defines spectral flatness as the ratio of geometrical mean to arithmetic mean of the power in all frequency bins, usually reported in decibels.

$$Wiener\ \ entropy = \frac{\sqrt[N]{\prod_{n=0}^{N-1} x(n)}}{\frac{\sum_{n=0}^{N-1} x(n)}{N}} = \frac{\exp(\frac{1}{N}\sum_{n=0}^{N-1} \ln x\,(n))}{\frac{1}{N}\sum_{n=0}^{N-1} x(n)},$$

$$N = number\ of\ frequency\ bins \quad (1)$$

This measurement will thus be much below 0 dB for a signal with a frequency content concentrated in single or few frequency bands, as is the case for traditional tonic stimulation protocols. The biomimetic protocol should instead measure close to 0 dB, signifying that the frequencies are modulated more evenly across the spectrum. Indeed, the Wiener entropy for the original DS signal and the pre-processed signal are −2.19 and −2.17 dB, respectively. These quantities are recorded are recorded in **Table 1**.

The preliminary signal analysis suggests that the key AM and FM features of the DS waveform can be retained while it is carefully condensed to reduce the resource usage in the proposed stimulator. To ensure that the prototyped stimulator can deliver this signal correctly, its output is measured in section "Bench-Top Test" at bench-top test and compared to the quantities above, and its efficacy is empirically validated *in vivo* in section "*In vivo* Tests."

Electrical Performance of the Biomimetic Stimulator

A key requirement for the implementation of the proposed architecture is to adhere to the maximum bitrate available for its data link. Compared to the conventional, tonic stimulation, the biomimetic protocol contains more information due to

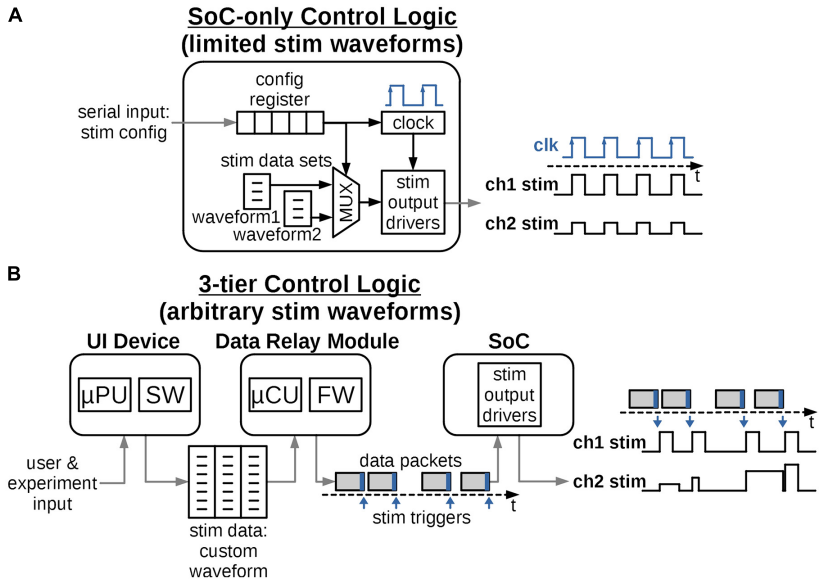

FIGURE 3 | Possible ways to distribute control logic to create the required stimulation waveforms. **(A)** The logic is integrated solely into the digital circuits of the SoC. Provisions are made for a limited set of output waveforms with short, periodically repeating patterns. The design is fixed and future waveform protocols would require challenging and costly redesign of the SoC. **(B)** The control logic is distributed into 3-tiers and accommodates a variety of arbitrary and biomimetic stimulation waveforms. The logic can be reprogrammed for future protocols relatively easily and at low cost.

its longer length and varying amplitude, which needs to be transmitted to the stimulating component (here: the SoC). In the case of a wireless implementation, the available bitrate depends on the data telemetry link employed. Prior art on neural implantable interfaces by Noorsal et al. (2012) and Piech et al. (2020) report transmission bitrates of 2 and 1.85 Mbps, respectively. Additionally, a commercially available medical-band RF transceiver chip ZL70103 (Microchip, Chandler, AZ, United States) can support 800 ksps raw wireless data rate distributed as 70% effective data and 30% communication overhead. Finally, the SoC adopted here includes an on-chip telemetry with a previously demonstrated continuous transmission rate of 2 Mbps, free of overhead aside from what is already included into the native stimulation data packets. The actual command bit rate to the SoC during output of biomimetic protocol is measured in section "Bench-Top Test" and recorded in **Table 1**, to confirm compatibility with reported maximum data rates.

Other commonly cited analog electrical performance measurements of the stimulator, such as output compliance voltage, accepted electrode impedance range, charge cancelation mechanisms, are independent of the proposed control architecture, and are instead specific to the *in vivo* applications targeted by the stimulator. These properties of the adopted stimulator SoC were measured in prior works for application to spinal cord implants and are summarized in **Table 1** for reference.

System Architecture

Neural stimulators take stimulation parameters as an input and administer the stimulation by repeatedly turning its output current or voltage sources on and off at designated times according to control logic. Specifically, traditional implementations of a miniaturized or implantable neural interface typically achieve this by employing an on-chip controller designed to deliver a specific type of stimulation. An external device communicating with the stimulator then only serves the purpose of updating a limited set of stimulator's parameters and triggering a start and stop of a predefined protocol (Stanslaski et al., 2012; Shahdoost et al., 2018; Zhou et al., 2019). Such designs have no or limited abilities to support the next-generation biomimetic protocols discussed in sections "Introduction" and "Quantifying the Biomimetic Stimulator's Performance." If the physiological research evolves to require a significant update to the *in vivo* experiment design, a need to change the default mode of stimulation can arise which can require a difficult hardware revision.

For example, Wagner et al. (2018) collaborated with Medtronic (Minneapolis, MN, United States) to upgrade the hardware of a single-frequency periodic stimulator Activa RC (Medtronic, Minneapolis, MN, United States) to enable support for multiple discrete frequencies as needed during the experiments. Any future changes to experiment requirements, such as a need to modulate amplitude, phase and/or frequency across an arbitrary continuous range, would necessitate further hardware changes, which are especially expensive in implantable systems. This expense can be avoided in a design where the controller of the stimulation waveform is partially distributed outside of the neural interface itself, where the changes can be easily made by firmware and software updates.

To this end, the stimulator architecture proposed here provides the flexibility to support both conventional pulse-train protocols and other existing and future biomimetic protocols by

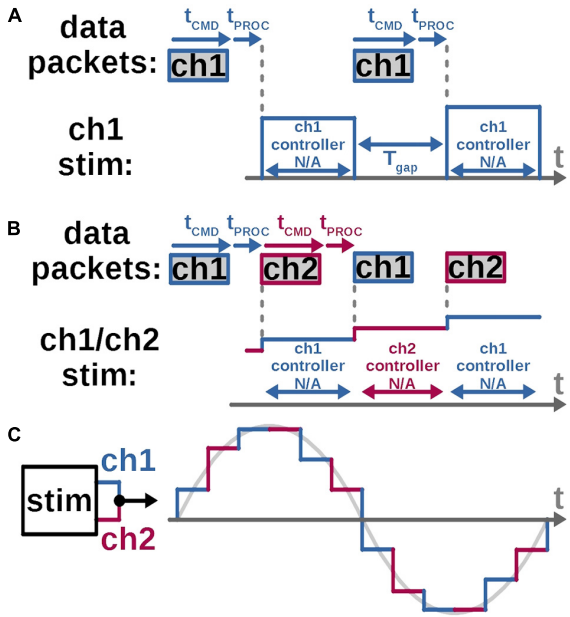

FIGURE 4 | A continuous, gapless arbitrary stimulation waveform is created by interleaving two stimulation channels for each electrode. **(A)** A gap between stimulus pulses arises while using the custom SoC (Lo et al., 2016) adopted for this work, as each channel's local controller is unable to receive parameters of the next stimulus pulse, while outputting the current one. Thus, SoC ch1's local controller can accept a new command only after ch1 completes its current output pulse. The resulting gap between current and next pulses equals command length plus command-processing time. **(B)** While ch1 output is in progress, a command is sent and accepted at ch2's controller, which sets up and fires the next pulse without the gap. **(C)** Arbitrary continuous waveform at each stimulation electrode can be created by connecting it to the output of two channels on the stimulator and assigning odd and even waveform samples to each respective channel.

integrating software, firmware, as well as digital circuitry into a unified control logic.

Logic Architecture for Arbitrary Waveform Generation

Figure 3 shows options for an architecture of a stimulator's control logic. A traditional approach in **Figure 3A** uses on-chip digital circuits to form a memory register and stimulation-specific finite-state machines to generate the output signal. The memory register receives basic configuration parameters from an external device, and the state machine executes "hardwired," fixed stimulation patterns, which are typically periodic square waves with constant frequency, amplitude and pulse-width. While the on-chip digital circuits can be designed to support multiple types of waveforms, this option is constrained by the available chip area, due to high-cost of custom silicon wafer fabrication and utilization of the area by the increasing output-channel count in novel stimulators. Additionally, the set of waveforms remains fixed, and is not adaptable to new stimulation protocols without a major chip redesign.

Figure 3B instead proposes a control architecture distributed among three tiers of devices, all typically present in a miniature neural stimulator system. The system architecture requires the SoC logic to only execute a single stimulation pulse per each data packet received, which relieves the need to define the full stimulation waveform by on-chip circuits. Instead this information is defined and programmed in the external computing device such as a handheld tablet, typically with a graphical interactive User Interface (UI). The UI software takes input from the users or the experiment subjects and generates the necessary, arbitrary-shaped stimulation waveform in a form of a data structure, such as a multidimensional array. The data structure is then transmitted to the Data Relay (DR) module using a ubiquitous link such as Wi-Fi or Bluetooth.

The DR module is located close to the stimulator SoC, either in the same physical enclosure for non-implantable stimulators

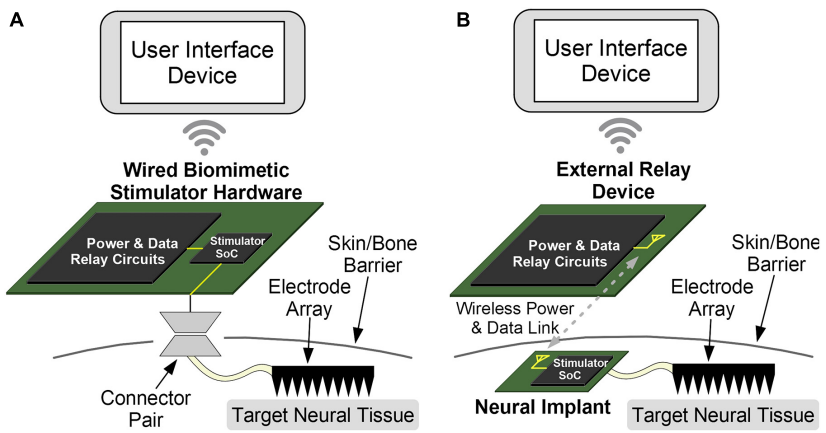

FIGURE 5 | The components of the proposed system can be arranged for wireless or wired implementations. **(A)** While the wired option is easier to implement and provides a stable and constant power, an external connector can disturb normal behavior and has increased risks of infection due to wire-through-skin. This option is best used for prototype testing and acute testing. **(B)** The wireless option is more complex due to challenging wireless data and power links. But the intact skin reduces chances of infection, and chronic experiments can be conducted with normally behaving animals. The wireless approach is further translatable for chronic human therapeutics.

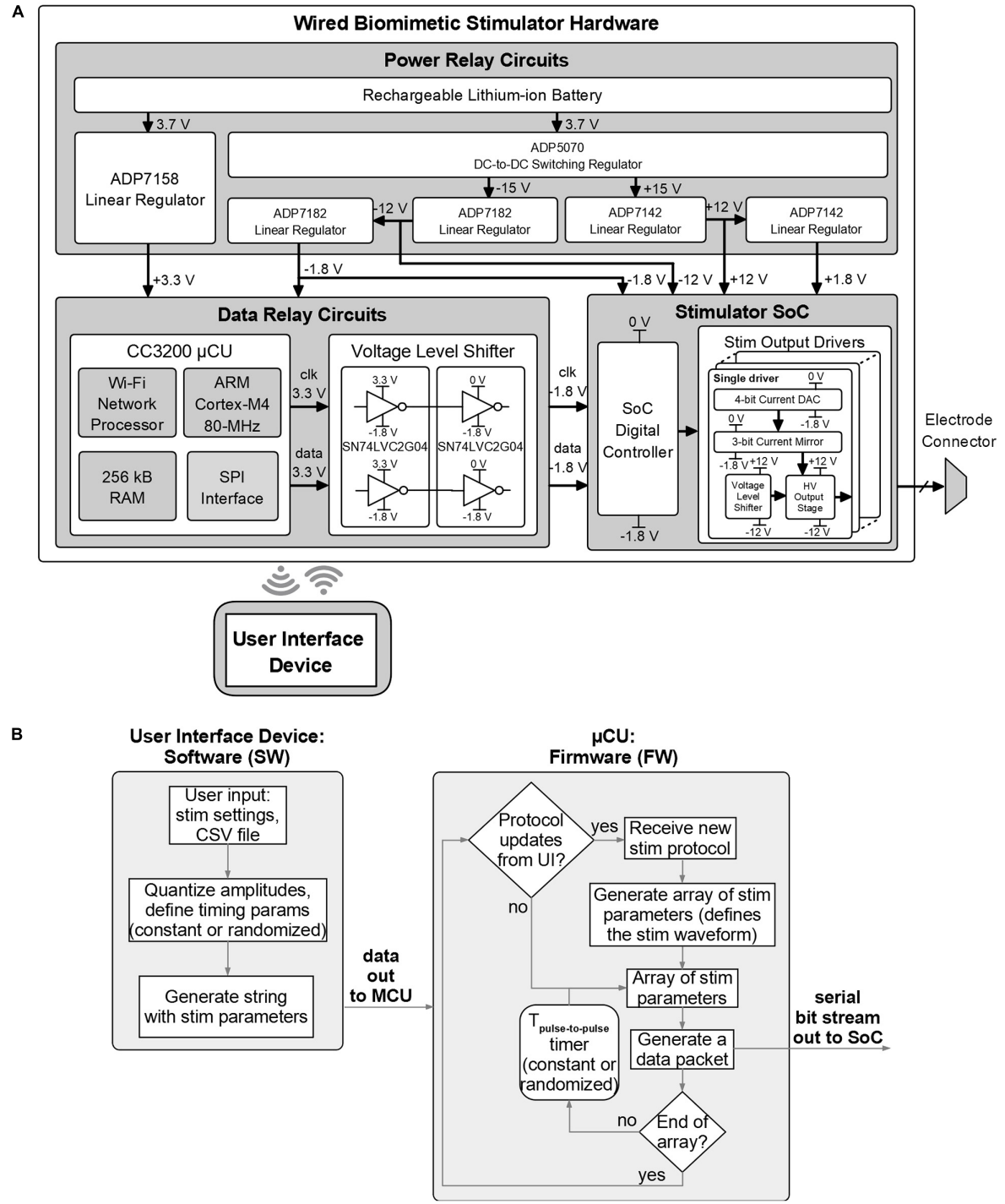

FIGURE 6 | Design details of the biomimetic stimulator prototype. **(A)** Block diagram and schematic of the hardware. Wired arrangement was chosen for initial rapid prototyping and *in vivo* verification. **(B)** Functional blocks of the software and firmware of the prototype.

or just outside of the body for implantable ones. The DR module's purpose is to establish a reliable transmission (wired or wireless) of stimulation information to the SoC in the form of data packets. Each packet contains parameters for a single stimulation pulse for each channel and a trigger command to "fire" the pulse when received by the SoC. The timing of the packets defines the sampling rate of a continuous arbitrary stimulation waveform, such as in section "Quantifying the Biomimetic Stimulator's Performance," or the repetition rate for discrete pulses. As the processing power required to convert a

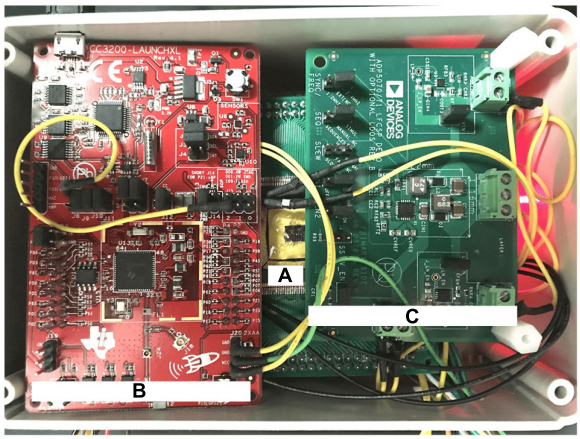

FIGURE 7 | Physical implementation of the wired prototype of the biomimetic stimulator. **(A)** The stimulator SoC in a Quad Flat Package (QFP). **(B)** CC3200 Microcontroller Unit (MCU) from the Data Relay circuits. **(C)** Power relay circuits. Other system components are arranged below the visible ones.

stimulation waveform table to individual data packets is low, the module can be implemented using a low-cost, low-size and low-power Microcontroller Unit (MCU) with a built-in memory. In the implantable configuration, the externally positioned DR is wirelessly linked to the implanted SoC, thus the quality of the wireless link is critical to transmit an uninterrupted stimulation protocol. Reliable wireless connection to the SoC can be readily achieved by one of the integrated data links described in section "Electrical Performance of the Biomimetic Stimulator."

A unique challenge in the proposed architecture can arise due to limitations of the on-chip digital controller which leaves a small gap in time between any two consecutive output stimulus pulses (**Figure 4**). This gap may be irrelevant for stimulation protocols with discrete pulse patterns, but it must be carefully managed for continuous biomimetic stimulation waveforms such as in section "Quantifying the Biomimetic Stimulator's Performance," where the gaps would add undesired frequency content and thus alter the key characteristics of the waveform. The mitigation of this challenge is illustrated in **Figure 4**.

In the SoC stimulator employed in this work (Lo et al., 2016) local digital-control circuits for each stimulation channel are individually collocated with the corresponding output current drivers (Kuanfu and Liu, 2009). This enables independent control of each channel's output timing and amplitude, as demonstrated in section "Bench-Top Test," and scalability for a higher channel count. But the individual memory register at each channel's local controller, which holds that channel's stimulus pulse parameters, does not accept any updates while it's reading these parameters and outputting the corresponding pulse. The command for the following pulse must be thus sent only after the present pulse is completed (**Figure 4A**). This creates a minimum gap between each channel's output pulse equal to the length of the command's bit stream plus the processing time taken by the local controller. To eliminate the gap, two current output channels can be connected together (**Figure 4B**). When the first channel is firing an output pulse, a configuration command is sent to and processed by the second channel's controller, which is set to fire immediately after, without a gap. The gap-less continuous stimulation output with interleaved channels is demonstrated in a bench-top test in section "Bench-Top Test" and the *in vivo* demonstration in section "*In vivo* Tests."

Implementation of the Stimulator Prototype

The multi-tier control architecture can be implemented as either a wired or a wireless neural interface. Both options integrate all three components and are shown in **Figure 5**. The wired arrangement can house the DR circuit on the same substrate, such as a Printed Circuit Board (PCB), as the stimulator SoC and has a physical connection to the stimulating electrode. The wireless implementation instead has an implantable SoC and electrode and usually places the DR module outside of the skin. The UI device can be a detached, handheld device in both cases, making it convenient for the operating user.

While the wired option is easier to implement due to reduced complexity and provides a stable and constant power supply to the SoC, it increases the risk of skin infection due to the protruding physical wire, and is most useful for acute testing of the device or protocols. Even so, the small component-count of this architecture can reduce the size of such "wired" devices and make them portable and convenient for research applications. The wireless configuration requires a wireless data and optionally a wireless power link, although a battery can be implanted as well. This also requires an antenna (for a far-field link) or a coil (for a near-field link). The absence of wires enables chronic applications for therapeutics or testing, assuming a biocompatible packaging for the implanted device. It also allows experiments with freely behaving animals. The Wi-Fi or Bluetooth link between the UI module and the DR module is easily implemented for both options as the two modules are externally positioned and thus are not power or space constrained. The biomimetic stimulator prototype in this work is implemented with the wired option.

Figure 6A shows the detailed block diagram of the prototype's hardware. The hardware is designed in three parts: the power module which provides the required supply voltages, the DR module which receives control from the UI device and sends the necessary command packets to the SoC, and the stimulator SoC whose outputs connect directly to the electrode array. The SoC has an output current range of $-500{+}500\ \mu A$ per channel with 8-bit resolution (including the sign bit), an output compliance voltage of ± 10 V (accounting for headroom required for current sources), can thus accept electrodes with impedance up to $\sim 20\ k\Omega$ at maximum current, and higher for reduced current. The SoC also supports passive charge cancelation to dissipate any residual unbalanced charge during stimulation as needed. These SoC parameters aren't affected by the control architecture, are directly inherited by the system and recorded in **Table 1**.

The DR module employs the CC3200 MCU board with custom firmware which takes input from the UI device via Wi-Fi and outputs data via serial to parallel interface (SPI) to the data level shifters. The voltage level shifters translate MCU's logic

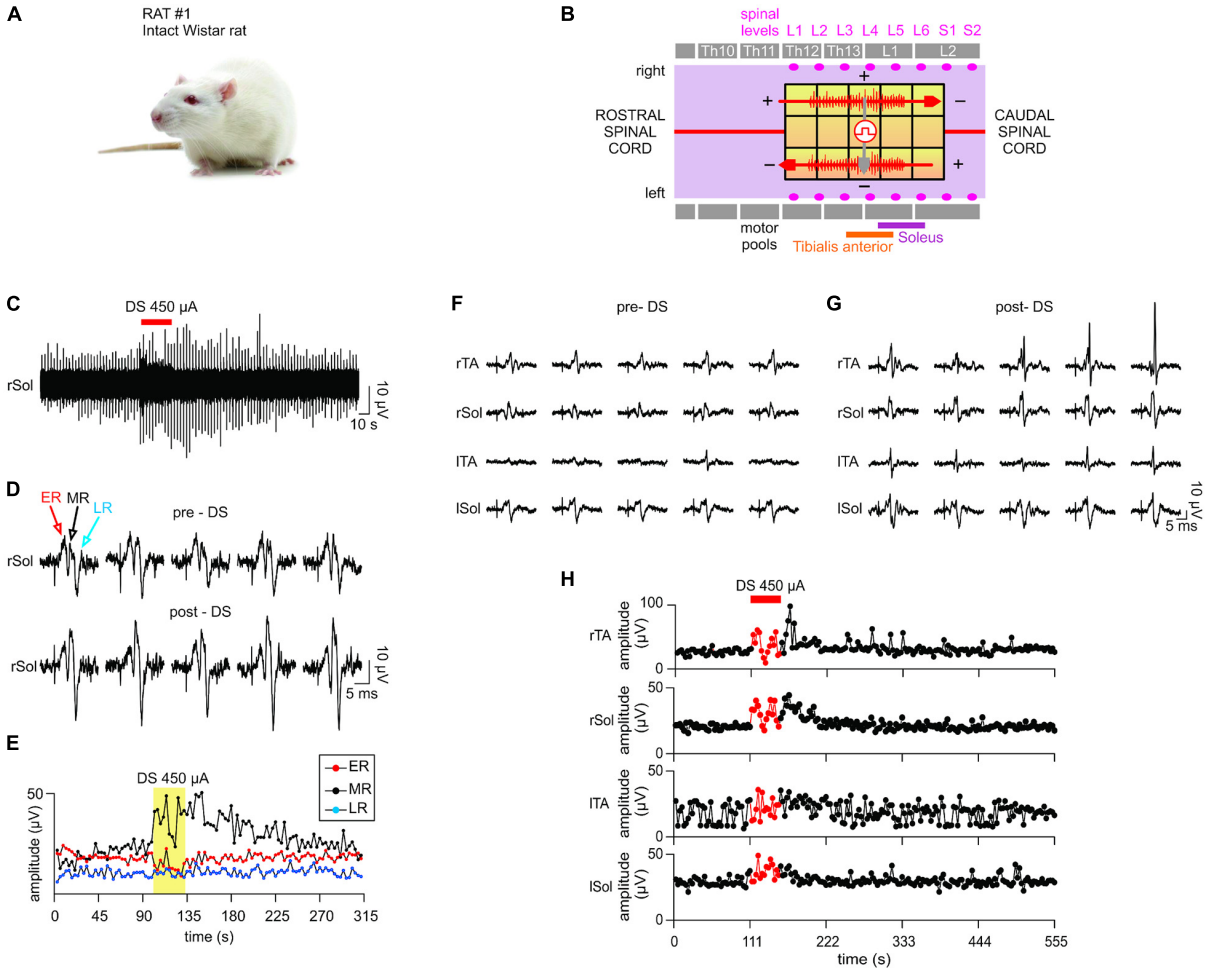

FIGURE 8 | *In vivo* test results I. The stimulator prototype delivers a DS protocol and increases excitability of an intact spinal cord of an animal subject during and post protocol delivery. **(A)** Animal type used in this experiment. **(B)** The diagram of the epidural electrode array shows the electrodes to which stimulation was delivered. Two DS stimuli were delivered simultaneously in a bipolar configuration (red arrows) using the stimulator prototype. An auxiliary stimulation "test pulse" is delivered in the middle of the spinal cord (gray arrow) to test the responsiveness of the motor outputs. The test pulse intensity is adjusted to evoke consistent electromyography (EMG) responses in all muscles. **(C)** DS protocol increases the responsiveness of the motor outputs to test pulses at the right Sol muscle. **(D)** Five evoked response plots were randomly selected from the pre-DS and post-DS recording section to illustrate the resulting range of amplitudes. **(E)** EMG response levels at the right Sol are quantified over time of the experiment. Middle response notably increases due to DS protocol. **(F–H)** The test pulse intensity is reduced to emulate a decreased spinal cord connectivity occurring in cases of spinal cord injury. **(F,G)** While pre-DS responses are relatively decreased or absent, post-DS responses are restored in all muscles. **(H)** Sustained increases of Middle Responses are noted in motor outputs of all four EMG electrodes.

levels (0−3.3 V) to levels compatible with the SoC (−1.8–0 V). The power module converts 3.7 V from a rechargeable battery to five regulated supply voltages: ±12 and ±1.8 V for the SoC and 3.3 and −1.8 V for the DR module. The power module uses an off-the-shelf DC-to-DC converter and five low-dropout voltage regulators by Analog Devices (Norwood, MA, United States). The DC-to-DC converter (ADP5070) generates ±15 V from the battery. The ±15 V are then down-converted to ±12 V to supply the SoC by ADP7142 and ADP7182 regulators, respectively. The ±1.8 V for the SoC are then generated from ±12 V through other ADP7142 and ADP7182 regulators. The 3.3 V for the DR circuits is regulated from the battery directly by ADP7158 regulator. **Figure 7** shows a photo of the wired prototype hardware which is sized 14 cm× 10 cm× 5.5 cm. The SoC is packaged in a Quad Flat Package (QFP) to interface with the peripheral electronics and the stimulation outputs.

Figure 6B shows the functional diagram of the prototype's software for the UI device and firmware for the MCU. The software algorithm translates user input, which describes the chosen stimulator protocol, into a sequence of configuration parameters compatible with the stimulator SoC and sends them to the MCU. The MCU generates one data packet on-the-fly for each stimulus pulse in the protocol sequence and sends it to the SoC by the serial interface, following the logic architecture described in section "System Architecture" and **Figure 3**. The time interval between pulses is controlled by the MCU's timer and can be a constant or a randomized value, as selected in the user input. The MCU firmware periodically checks for presence

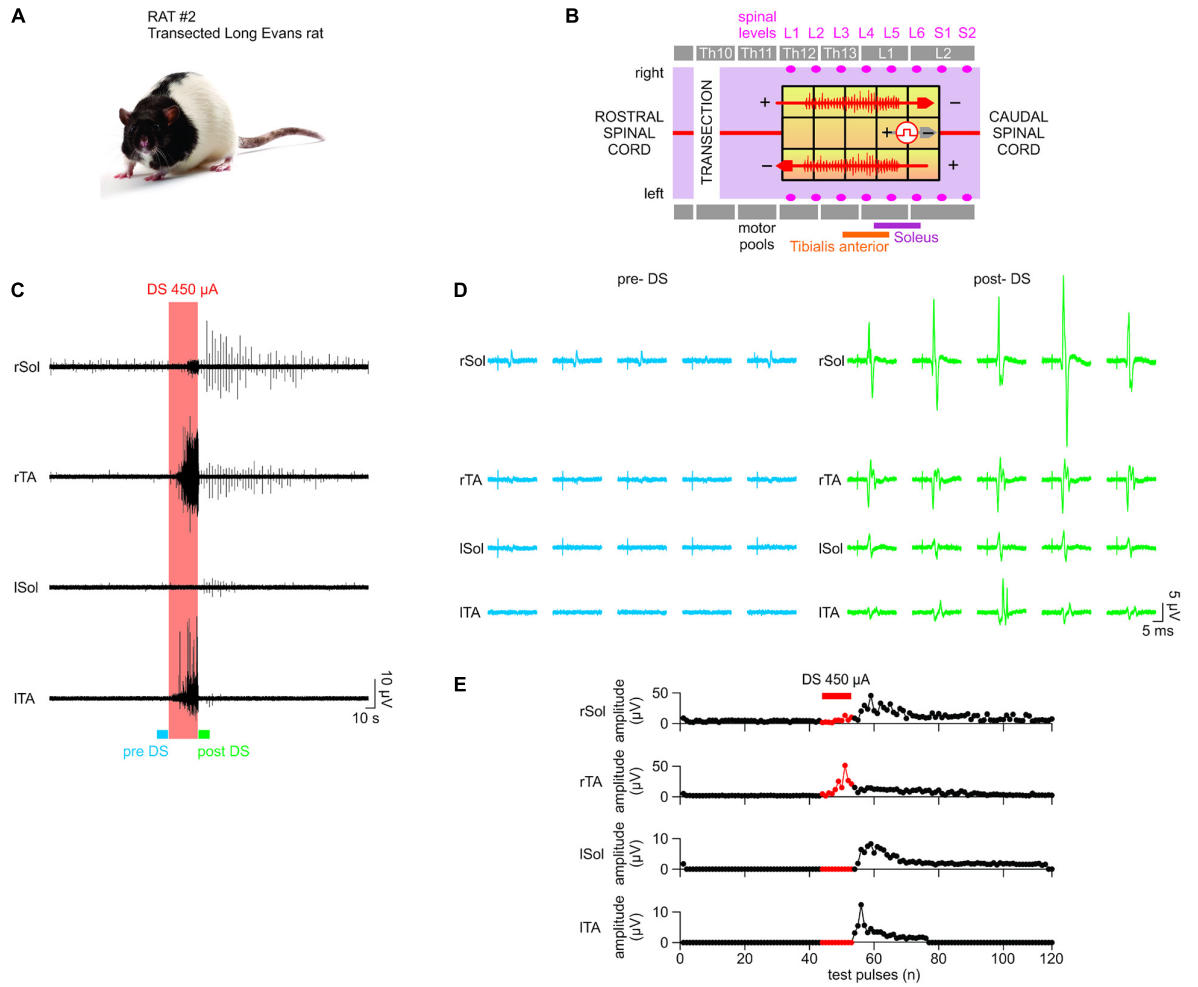

FIGURE 9 | *In vivo* test results II. The stimulator prototype repeats the *in vivo* test in a rat subject with a completely transected spinal cord. **(A)** Animal type used in this experiment. **(B)** Transection is made at the Th10 level (white vertical bar). While the DS protocol is delivered to the same electrode locations as in *in vivo* test I, the test pulse is delivered to different electrodes, which were experimentally chosen to ensure the presence of EMG responses with the spinal cord transection prior to application of DS. **(C–E)** Notably, although consistent responses were not present in the left motor outputs pre-DS, due to the transection, consistent responses appeared on all four EMG electrodes at significantly increased amplitude levels post-DS. This demonstrates the efficacy of the stimulator prototype, which effectively delivers the DS protocol to exploit any spared spinal cord connectivity and restore the motor outputs following a spinal cord injury.

of updated protocols from the UI device, to accommodate a closed-loop experiment setup.

In vivo Animal Preparations and Test Procedures

Experiments were performed on two adult rats (250–300 g body weight, one female Sprague Dawley and one male Long Evans). All procedures received approval by the Animal Research Committee of UCLA, and abide by the guidelines provided by the National Institutes of Health (NIH) Guide for the Care and Use of Laboratory Animals. Initially, the animals have been sedated with isoflurane gas, constantly flowing at 1.5−2.5%, followed by urethane (1.2 mg/Kg, i.p). Afterward, the tibialis anterior (TA) and Sol muscles have been bilaterally implanted with recording wire electrodes (AS 632, Cooner Wire Co., Chatsworth, CA, United States) for intramuscular EMG. The recorded EMG signals were band-pass filtered to a 10 Hz to 5 KHz band, notch filtered at 60 Hz, amplified with gain 100 or 1000 using a differential AC amplifier (DP-304A, Warner Instruments, CT, United States) and finally digitized at 20 or 100 KHz (PowerLab®, ADInstruments, Australia). Electrical stimulation was delivered using a high-density multi-electrode array fabricated with three longitudinal columns and five horizontal rows of platinum-based electrodes (Chang et al., 2014; Taccola et al., 2020b). The array was implanted in the epidural dorsal space from L1 to S1 spinal levels following a Th12 to L2 vertebrae laminectomy, which dorsally expose the spinal cord. The second rat received a complete transection of the spinal cord performed at Th10 spinal level. To determine the threshold intensity for each preparation, rectangular pulses were delivered at 0.33 Hz starting from 100 µA and increasing at 100 µA increments. The threshold was defined as the minimum intensity which elicited a consistent EMG

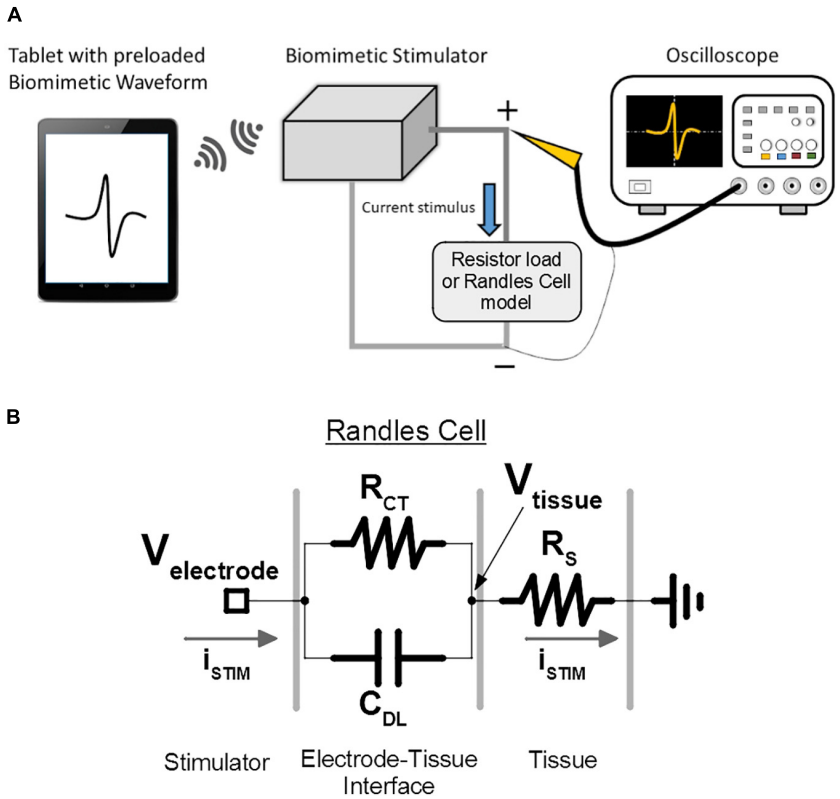

FIGURE 10 | Bench-top test setup is used for verification and demonstration of the prototype of the proposed biomimetic stimulator. **(A)** The illustrated arbitrary waveform is sent to the stimulator, which delivers the current-mode protocol to the emulated loads. The resulting voltage output is captured by the oscilloscope. **(B)** The electrode-tissue interface of the spinal cord epidural electrode is modeled by a Randles cell to investigate the stimulator performance under delivery of DS protocol. V_{tissue} node represents the resulting voltage potential experienced by the neural tissue, which doesn't include the capacitive effects of C_{DL}. $V_{electrode}$ node represents the voltage experienced by the SoC's output current sources, which includes the effect of C_{DL}.

response from all muscles. Lowering the strength of stimulation to sub-threshold level caused seldom deletions in at least one muscle's responses. In the intact Sprague Dawley the threshold was equal to 500 μA, was regularly checked during the course of the experiment and remained consistent. To continuously monitor the motor responses, a 0.33 Hz train of test pulses at threshold was delivered before, during and after the application of DS. The effect of DS was quantified in the first 60 s of its application as the change in the peak amplitude of the responses, expressed as a percentage of the respective pre-DS, baseline values. Additionally, animals were kept under anesthesia over a heating pad (37°C) throughout the duration of each experiment. At the end of all experiments (4 h), animals were sacrificed with isoflurane and sodium pentobarbital (IP, 80–100 mg/Kg) followed by a cervical dislocation.

Both the DS and the square test-pulses were delivered concurrently to the same epidural electrode array but at different electrode locations. The prototype stimulator delivered DS to the four corner electrodes of the array, marked by the red arrows in **Figures 8B, 9B**. As demonstrated previously, this positioning allows this novel protocol and its key properties (section "Quantifying the Biomimetic Stimulator's Performance") to increase the recruitment or excitability of the myelinated fibers of the spinal cord under the full area of the electrode array. Simultaneously, a 0.1 ms-wide square pulse repeating at 0.33 Hz was delivered to electrode locations marked with gray arrows (**Figures 8B, 9B**) by a commercial stimulator STG 4008 (Multi Channel Systems, Reutlingen, Germany). The electrode locations for these square pulses were chosen experimentally in each rat to evoke the EMG responses in the TA and Sol muscles of left and right legs. To ensure consistent EMG responses, the intensity of test-pulses was adjusted as described above and in the section "Results."

RESULTS

Bench-Top Test

The biomimetic stimulator prototype is demonstrated in a bench-top test by generating a variety of waveforms, including a random-period pulse train, a multi-channel arbitrary pulse trains, each with independent parameters, and a continuous biomimetic DS stimulation pattern. The hardware prototype is controlled by the UI app on an Android tablet, which has preloaded test protocols including the biomimetic DS waveform. During the initial functionality demonstration, each stimulation output

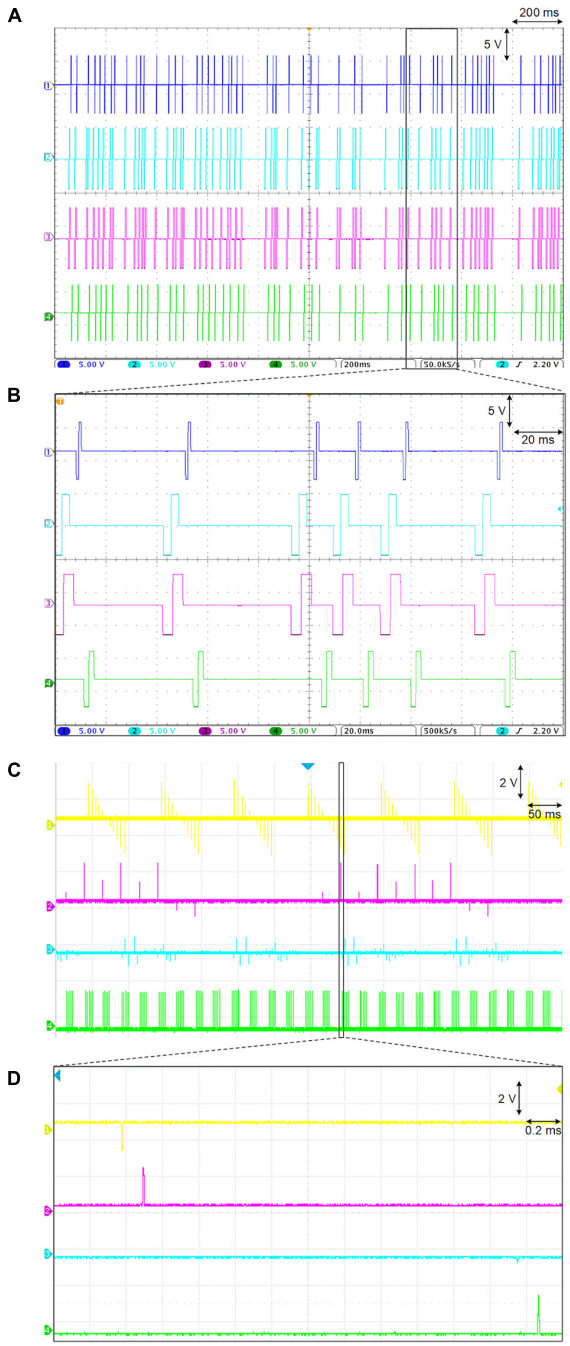

FIGURE 11 | Bench-top test results demonstrate a variety of pulse trains protocols. **(A)** Multi-channel stimulation with random inter-pulse-interval, which follows an exponential distribution. **(B)** Magnified view of panel **(A)** shows the different pulse widths and start delays among different channels. **(C)** Multi-channel stimulation with independent control of waveform, frequency, amplitude and pulse timing. **(D)** Magnified view of panel **(C)**.

channel is connected to a 10 kΩ resistor. The oscilloscope captures the resulting waveforms and thus measures the output-current stimuli delivered to the resistive loads (**Figure 10A**).

Additionally, to better emulate the epidural multi-electrode array used in the *in vivo* experiment during DS protocol output, the resistive load was substituted for a Randles cell circuit (Randles, 1947), which models the electrode-tissue interface (**Figure 10B**) and its capacitive effects. The C_{DL}, R_{CT}, and R_S values of the model were set to 220 nF, 15 and 1.9 kΩ, as measured during the electrode characterization in previous work.

Importantly, the voltage in a tissue is generally not affected by the R_{CT} and C_{DL} effects at the electrode interface. This is because the stimulation current will flow into the R_S of the tissue and out of the ground electrode unaltered by the C_{DL}, following the Kirchhoff's laws. Thus, the voltage potential in the tissue, V_{tissue}, which affects the membrane potentials of the targeted neurons, will be created by the stimulation current and only R_S (reduced in magnitude depending on how far the neuron is located from the site of stimulation). The stimulator's performance is then validated using the recorded V_{tissue} signal. Still, for the above to be valid, $V_{electrode}$ potential must not exceed the compliance voltage of the SoC current sources, otherwise the output current will be distorted from the intended values. This is validated by analysis of $V_{electrode}$ signal recorded during the DS output.

The randomized period pulse train stimulation is demonstrated in **Figures 11A,B** The resulting multi-channel pulse trains exhibit random IPI which follows an exponential random distribution and has been shown to reduce undesired neural adaptation in epiretinal stimulation (Soto-Breceda et al., 2018). The mean period is 30 ms with current amplitudes set to 0.5 mA and pulse width set between 1 and 4 ms among the available channels. Pulse timing offset (phase) can be set among the stimulation channels during this random IPI protocol, which further demonstrates versatility of the prototype's logic architecture. **Figures 11C,D** demonstrates the capability to output multi-channel arbitrary pulse trains, each with independent control of waveform, frequency, and amplitude. This protocol was output simultaneously on 16 channels but only the first four channels are shown due to the limitation of the four-channel oscilloscope. The oscilloscope's channel 1 (yellow) demonstrates a ramp waveform on both anodic and cathodic phases at 200 Hz with a 10 Hz pulse train frequency. Channels 2 (pink) and 3 (blue) demonstrate random firing patterns at low and high frequency (40, 250 Hz). Channel 4 (green) demonstrates a high frequency burst (500 Hz) with a burst-repetition frequency of 40 Hz.

Figure 12 demonstrates the prototype's ability to generate a continuous biomimetic stimulation waveform. The signal is preprocessed as in section "Quantifying the Biomimetic Stimulator's Performance" and loaded into the UI device. The UI device's software further interleaves the signal onto two SoC outputs for gapless waveform. **Figure 12A** shows the resulting DS output (blue) generated by the stimulator as measured at V_{tissue} Randles cell node. The desired DS current-mode protocol (orange) from section "Quantifying the Biomimetic Stimulator's Performance" is then multiplied by the R_S value to convert the data to voltage and to match the scale of the recorded signal. The zoomed in bottom panel shows that the two waveforms are similar, aside from the high-frequency noise aliased into the signal band due to low sampling frequency of the oscilloscope

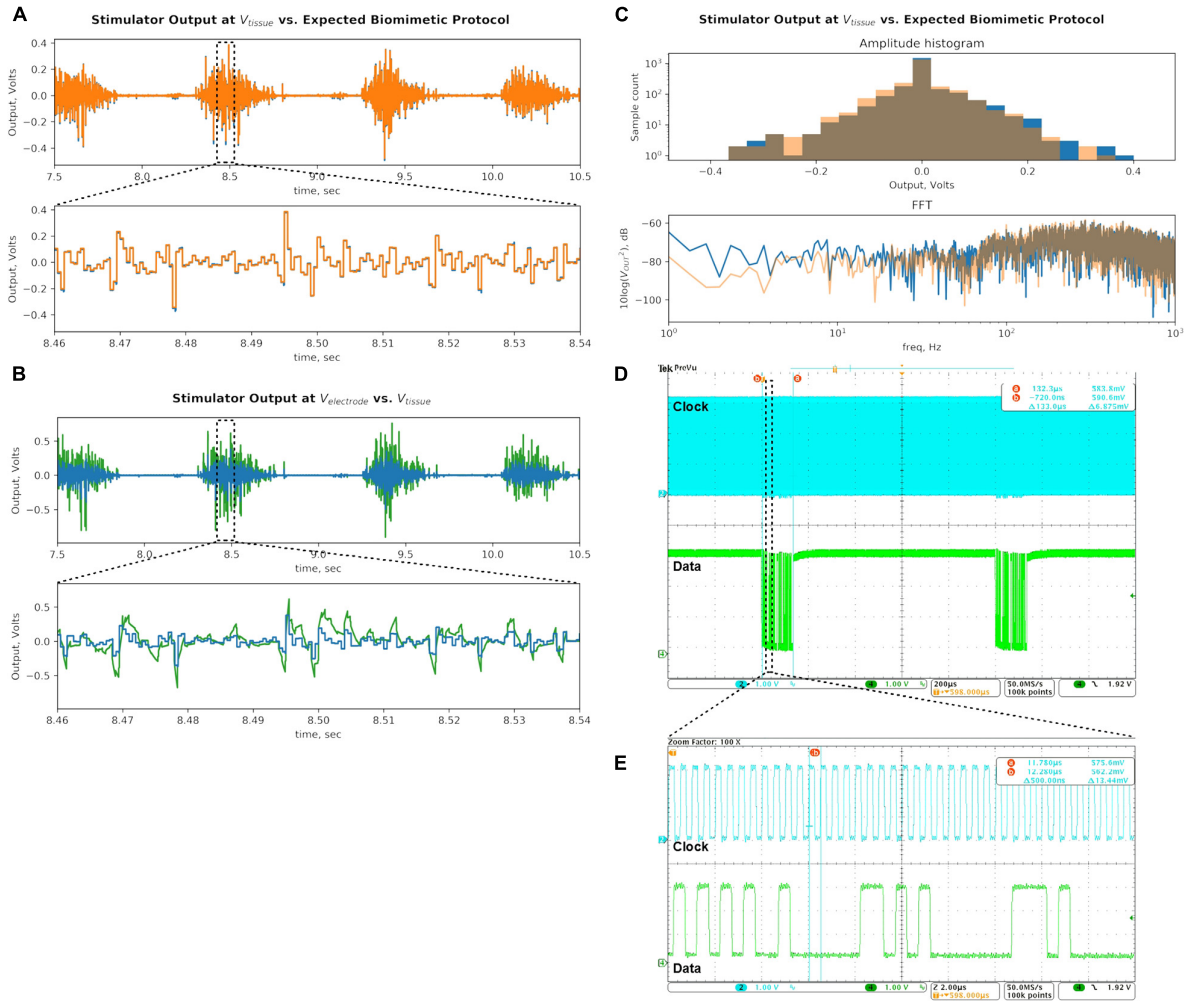

FIGURE 12 | Bench-top demonstration of multi-channel continuous DS waveform mimics a recorded EMG signal, which has been shown to be effective in epidural spinal cord stimulation for restoring motor function. **(A)** Stimulator output recorded at V_{tissue} (blue) is compared to the desired biomimetic protocol waveform (orange). The signals are similar as intended, demonstrating the prototype's ability to deliver gapless and continuous stimulation protocols. **(B)** Output recorded at $V_{electrode}$ (green) is compared to the signal at V_{tissue} (blue). The electrode signal is higher in amplitude due to the added voltage drop across the C_{DL} capacitor, which integrates the output current pulses, but is within the compliance limits of the SoC output current sources with significant margin. **(C)** The DS output of the stimulator (blue) is analyzed against the desired biomimetic protocol (orange).The biomimetic current protocol is multiplied by the R_S value to convert it to voltage units. Histograms of amplitudes of signal peaks and frequency spectrums of the signals are plotted. **(D)** Clock and data digital inputs to the SoC are plotted. Spacing between data packets identifies the sampling rate of the output stimulus signal. Total time period of a packet helps calculate the number of bits it contains, by using the clock period **(E)**. Combination of information in panels **(D,E)** yields the total data bitrate of the DS biomimetic stimulation waveform.

when recording long signals, and its lack of anti-aliasing filter. The signal is quantized as expected and the temporal resolution of 500 μs preserves the original signal's sampling rate of 2 ksps.

Next, **Figure 12B** compares the signal recorded at $V_{electrode}$ (green) against the signal at V_{tissue} (blue). The $V_{electrode}$ signal is larger in amplitude because the R_{CT} and C_{DL} voltage drop is in series with the R_S voltage. The minimum and maximum potentials at the $V_{electrode}$ during DS output are measured to be −0.903 and 0.760 V, respectively. These values are much lower than the ±10 V compliance limits of the SoC current sources, facilitating them to deliver the intended output current. The bottom panel zooms in on the $V_{electrode}$ waveform, which exhibits RC exponential settling as the current pulses are integrated by the C_{DL}, which is also superimposed on the V_{tissue} potential. The charge build-up on the capacitor is frequently discharged when the DS signal changes polarity. This DS protocol output delivered by the stimulator prototype was tested *in vivo* as described in section "*In vivo* Tests."

Following the methods of section "Signal Analysis of the Biomimetic Protocol," the histogram of peak amplitudes, and the frequency spectrum of the signal are plotted in **Figure 12C** (blue). The desired DS signal multiplied by R_S (as above) is also analyzed and superimposed on the plot (orange). The comparison of the two signals demonstrate that the modulations in amplitude and frequency at the output are largely preserved as intended. Still, a few differences are noted.

TABLE 2 | Comparison of state-of-the-art SoC-based arbitrary waveform neural stimulators.

State of art	I_{OUT} max	I_{OUT} resolution, bits	# of stim chan	Continuous gapless stim?	Max. length of arbitrary waveform, (# points)	Demonstrated *in vivo*?
Piech et al. (2020)	400 μA	3-bits	1	No	Not SoC limited[1]	Yes
Yip et al. (2015)	500 μA	6-bits	8	No	8/phase	No
Kassiri et al. (2017)	1.35 mA	8-bits	64	No	32/phase	Yes
Noorsal et al. (2012)	1 mA	5-bits[2]	1024	No	64	Yes
This work	500 μA	8-bits	32	Yes	Not SoC limited[1]	Yes

[1]*Waveform is stored outside of the SoC in an external device and is limited by the PROM size, which can be chosen arbitrarily large with respect to the length of known biomimetic waveforms.*
[2]*Design provides limited control of the shape of the 64-point arbitrary waveform within the I_{OUT} resolution. E.g., each subsequent point can be increased or decreased by 1 LSB relative to the previous or scaled by 0.5× or 2× relative to previous, but the absolute value of each point can't be set.*

The FFT of the prototype's output has higher content in the 60-Hz band due to 60 Hz noise present on the bench top setup. Low frequency band exhibits higher power, possibly due to aliased high-frequency switching noise as explained above. The same added noise likely affected the output signal's histogram (blue) by pushing some of the peaks from their original bins into the neighboring ones. It's noticeable in the −0.250 V bin, where the peak count was low to begin with.

Quantitatively, the range of the amplitude peaks of the output signal are 0.376 and 0.418 V in positive and negative directions, respectively. These values deviate by +9.3% and −2.3% from the corresponding values of the original DS signal. The Wiener entropy for the captured output is −1.87 dB, which deviates by +0.32 dB or 3.8% on a linear scale. The measured values have deviated from the ideal by less than 10%, mostly in the direction of higher levels of modulation in amplitude and frequency. The values are recorded in **Table 1**, and the efficacy of the resulting output signal with respect to the therapeutic effect is empirically verified *in vivo* as described in the next section.

Finally, the command data rate is verified by capturing the data and clock signals at the SoC digital inputs (**Figure 12D**). The number of bits in a data packet can be calculated by measuring the distance between the start and end of the packet (133 μs) and dividing it by the clock period (here: 0.5 μs, **Figure 12E**). Each resulting 266-bit command packet produces two consecutive pulses in an output with 0.5 ms width each (per the gapless schema in section "Logic Architecture for Arbitrary Waveform Generation"). This command repeats with a period of 1 ms. The total data bitrate is 266 bits/packet × 1000 packets/sec = 133 kbps. The value is recorded in the **Table 1** and is well within the bitrate supported by the data links discussed in sections "Quantifying the Biomimetic Stimulator's Performance" and "Simultaneous Power and Data Telemetry in an Implantable Implementation."

In vivo Tests

The efficacy of the proposed architecture was demonstrated *in vivo* with DS protocol. The *in vivo* test is a shorter version of the previously published *in vivo* works with this protocol. As shown, DS delivered by the prototyped device is able to increase the excitability of intact and transected spinal cords in rats. The excitability was concurrently measured by administering a series of current-mode square test-pulses at the spinal cord and recording the amplitude of the EMG responses from leg muscles. The details of the *in vivo* results are described below.

In vivo Test I Results: Intact Spinal Cord

A Sprague Dawley rat with the intact spinal cord (**Figure 8A**) exhibited consistent motor responses in all four EMG electrodes for 0.1-ms test-pulses at threshold amplitude of 500 μA administered to L3/L4 levels (**Figure 8B**). EMG responses from right Sol muscle before, during and after DS protocol, are shown in **Figure 8C**. Zoom-in plots in **Figure 8D** show distinct early response (ER), middle response (MR) and late response (LR) (Gerasimenko et al., 2008) with different amplitudes pre-DS as compared to post-DS. Pre-DS peak values are: ER = 17.98 ± 1.35 μV, MR = 22.67 ± 2.59 μV and LR = 10.06 ± 1.78 μV, averaged for n = 20 repeated pulses, as quantified in **Figure 8E**. Based on the same plot, the change in EMG responses due to the delivery of DS protocol can be calculated as percentage of pre-DS levels. The MRs increased to 167%, while ERs and LRs changed to 77 and 102%, respectively, as averaged for n = 10. The effect of DS on the amplitude of MRs persisted for at least 1 min after its end, peaking at 170%, averaged for n = 20.

The experiment was repeated with test pulses at a reduced, sub-threshold level of 350 μA, while DS was kept at the same level. This test emulates the reduced signaling condition which occurs when an injury to the spinal cord decreases its connectivity. Due to the sub-threshold level of test pulses, pre-DS MRs were minimal (**Figure 8F**) and inconsistent, with noted deletions. Again, the DS protocol increased the responses in all muscles (**Figure 8G**). Average pre-DS MR levels were measured as 27.56 ± 4.01 μV for rTA; 20.52 ± 1.51 μV for rSol; 17.22 ± 8.38 μV for lTA and 29.12 ± 3.52 μV for lSol at n = 20 (**Figure 8H**). During DS the levels increased to rTA = 134%; rSol = 148%; lTA = 124%; lSol = 126% of pre-DS with n = 10. The increase has persisted post-DS, peaking at rTA = 164%; rSol = 153%; lTA = 148%; lSol = 113% of pre-DS levels, with n = 20.

In vivo Test II Results: Transected Spinal Cord

A Long Evans male rat with a transected spinal cord (**Figure 9A**) was used as the test subject. Unlike in the first rat experiment with intact spinal cord, no intensity of test-pulses, including

maximum available 800 μA, was able to produce consistent EMG responses on all four leg muscles pre-DS administration due to spinal cord transection, which intentionally damaged the neural connectivity. Instead, 0.1 ms, 0.33 Hz, and 650 μA test-pulses were delivered to the epidural electrode array (**Figure 9B**), which consistently evoked EMG responses on the right Sol and TA muscles only. It is desired to restore the responses on the left muscles by increasing the spinal cord excitability post-transection using the prototype system with DS protocol (**Figure 9C**). In **Figure 9D**, left, five sample pre-DS responses are shown with average (n = 5) response levels of 3.97 ± 1.02 μV for right Sol and 1.81 ± 2.37 μV for right TA. The asymmetry in the response levels and consistencies among left and right side is most likely due to the transection which unequally affects each specific motor pool.

During DS, responses continued on the right side, but also appeared on the left TA (**Figure 9C**, red box). Post-DS average (n = 5) response levels on the right side increased to 17.41 ± 10.08 μV for rSol and 11.81 ± 3.39 μV for rTA (**Figure 9D**, right). Also, post-DS responses appeared on the left side with average (n = 5) levels of 5.91 ± 2.49 μV for left Sol and 5.97 ± 3.75 μV for left TA. **Figure 9E** shows the EMG peak levels over time. During DS response levels on the right side increased to 127% for right Sol and 896% right TA relative to pre-DS, and remained increased post-DS at 520% right Sol, 599% right TA for up to 1 min. Most notably, the left TA responses, absent pre- and during DS were noticeable post-DS for up to 1 min at 3.06 ± 2.39 μV for n = 23. Also left Sol responses appeared and persisted post-DS for 3 min at 2.67 ± 1.77 μV for n = 59. The test data strongly suggests that the administration of DS, rendered by the prototype system, has successfully increased excitability of the spinal cord and thereby effectively re-established its connectivity after the complete transection.

DISCUSSION

In addition to implantable applications, the prototype can also be advanced to provide biomimetic or other versatile stimulation waveforms in closed-loop neuromodulation. To that end this section includes the relevant design considerations for the wireless link between DR and SoC components and an additional neural recording component.

Comparison to State of the Art

Table 2 compares the proposed architecture and its prototype with other state of the art. To the best of the authors' knowledge, this work is the first *in vivo* demonstration of an SoC-based stimulator architecture which supports a continuous, gapless biomimetic waveform and is fully compatible with integration into implantable neural prosthetics.

Simultaneous Power and Data Telemetry in an Implantable Implementation

In an implantable implementation, the proposed control architecture requires the SoC component to continuously receive data packets containing the biomimetic stimulation protocol, while simultaneously receiving wireless power. The SoC used in this system employs dedicated circuits on-chip to receive data and power transmission using a near-field, inductive coupling. In an implant, the SoC is connected to a pair of coils which receive the data carrier signal at 20 MHz and the inductive power signal at 2 MHz. The 10× difference in frequencies allows on-chip filters to separate the data signal from the 2 MHz interference. The data is transmitted at a rate of 2 Mbps with DPSK modulation and is decoded by the SoC into packets for the digital controller. On-chip quad-level rectifier and regulators convert the power signal into four supply voltages required for SoC operation.

This wireless schema was previously demonstrated in a spinal implant, as well in a high-density epiretinal prosthesis (Lo et al., 2013). Importantly, the data rate of 2 Mbps enabled the epiretinal implant to receive a 1024-pixel (i.e., stimulator channels) image, continuously refreshed at 60 frames per second, with each pixel sample requiring a 19-bit packet, under wireless power. This resulted in a data rate of 1.17 Mbps plus overhead, which is significantly higher than the one measured for the proposed biomimetic stimulator, as indicated in **Table 1**, and thus meets the needs of the implantable implementation.

Stimulation Safety Mechanisms

Importantly, the proposed control logic, which distributes the control over three components of the system, does not increase the risk of delivering an unsafe amount of charge during stimulation. Moreover, three safety mechanisms are built into the proposed system, to further mitigate this risk.

First, the biomimetic signal is chosen to have a zero DC component. This is achieved by recording the EMG (DS) signal with a high pass filter, thus eliminating any arithmetic mean component and resulting in net-zero charge during stimulation. Second, every command sent to the SoC includes one bit which can turn on an optional passive charge dissipation at the electrode. The MCU can periodically enable it at predefined time intervals dissipated any net charge during the stimulation. Third, if any command between UI Device and MCU, or between MCU and SoC is corrupted, the built-in error check mechanism would discard the command. This check is a part of the Wifi standard, and is included as CRC and checksum in our SoC command structure. If the corrupted command is discarded then no corresponding stimulation pulse will occur, thus safely underdelivering the stimulus charge. No reasonable chance exists for a corrupted command to be accepted and erroneously overdeliver an unsafe, large amount of charge.

Stimulation Artifacts in Neural Recordings During Continuous Biomimetic Stimulation

To gain new insights into the mechanisms and efficacy of novel biomimetic stimulation protocols, it can be advantageous to record neural activity concurrently with stimulation to help investigate the neural network's dynamics under these protocols. For example, DS protocol is speculated to increase the excitability of spinal networks and specifically the recruitment of spinal cord's interneurons to generate a more robust motor response. Further

evidence may be acquired by monitoring the cord's neural signals before, during and after DS stimulus. Yet, the stimulation signal injected into the electrode-tissue interface creates an undesired stimulation artifact that is recorded alongside the neural activity. The artifact is frequently larger than the neural signal of interest and can confound the latter (Hottowy et al., 2012). Although solutions to artifact removal have been developed for protocols with periodic stimulation pulses (Stanslaski et al., 2012; Mendrela et al., 2016; Basir-Kazeruni et al., 2017; Culaclii et al., 2018; Zhou et al., 2019), removal of artifacts from continuous complex stimulation waveforms, such as DS, are yet to be demonstrated. Still, a system level approach in Culaclii et al. (2018), which learns the initial artifact template and subsequently subtracts it from the recurring artifacts in the recordings, can be extended to accommodate the continuous artifacts from DS. This approach uses an MCU and data converters which interact with the recording amplifiers to perform the learning and removal. The MCU's memory can be increased as needed to store the continuous artifact spanning the full duration of the DS protocol.

CONCLUSION

A novel architecture is proposed for next generation neural stimulators to support a multitude of irregular, non-tonic stimulation waveforms, simultaneous multi-frequency output on multiple channels, and most notably continuous, gap-less arbitrary biomimetic waveforms from pre-recorded physiological signals. In contrast to the conventional approach which places the waveform generation onto the SoC component only, the proposed architecture additionally integrates firmware and software components and distributes the waveform generating logic over all three resulting domains in the stimulator system. The proposed approach is fully compatible with a design of a neural implant. A portable stimulator prototype is built and tested at bench-top to demonstrate the supported waveforms. The stimulator is also used *in vivo* in animal experiments, where it successfully delivers a biomimetic waveform to exploit the spared connectivity along a transected spinal cord and to restore the motor output in a rat model. The integration of the proposed system as a neural implant and its *in vivo* demonstration in freely behaving animals is planned for future work.

DATA AVAILABILITY STATEMENT

The raw data supporting the conclusions of this article will be made available by the authors, without undue reservation.

ETHICS STATEMENT

The animal study was reviewed and approved by Animal Research Committee of UCLA.

AUTHOR CONTRIBUTIONS

WL and SC: biomimetic stimulator concept and system architecture. SC, P-MW, and Y-KL: circuit design. WY and BB: firmware and software development. Y-PC and SC: stimulation signal analysis. GT, SC, WY, and WL: *in vivo* testing. GT: physiological data interpretation. SC, P-MW, GT, WL, and Y-KL: write the manuscript. All authors contributed to the article and approved the submitted version.

FUNDING

This work was supported in part by NIH 1RF1NS118301-01, Patrick Soon-Shiong Endowment Fund and NIH BRP U01 EB007615.

ACKNOWLEDGMENTS

The authors would like to acknowledge and thank V. R. Edgerton for providing the facilities and animals for the *in vivo* testing described in this work.

REFERENCES

Basir-Kazeruni, S., Vlaski, S., Salami, H., Sayed, A. H., and Marković, D. (2017). "A blind Adaptive Stimulation Artifact Rejection (ASAR) engine for closed-loop implantable neuromodulation systems," in *Proceedings of the 2017 8th International IEEE/EMBS Conference on Neural Engineering (NER)*, Shanghai, 186–189. doi: 10.1109/NER.2017.8008322

Benabid, A. L., Pollak, P., Hoffmann, D., Gervason, C., Hommel, M., Perret, J. E., et al. (1991). Long-term suppression of tremor by chronic stimulation of the ventral intermediate thalamic nucleus. *Lancet* 337, 403–406. doi: 10.1016/0140-6736(91)91175-T

Brocker, D. T., Swan, B. D., Turner, D. A., Gross, R. E., Tatter, S. B., Miller Koop, M., et al. (2013). Improved efficacy of temporally non-regular deep brain stimulation in Parkinson's disease. *Exp. Neurol.* 239, 60–67. doi: 10.1016/j.expneurol.2012.09.008

Chang, C. W., Lo, Y. K., Gad, P., Edgerton, R., and Liu, W. (2014). "Design and fabrication of a multi-electrode array for spinal cord epidural stimulation," in *Proceedings of the 2014 36th Annual International Conference of the IEEE Engineering in Medicine and Biology Society*, Chicago, IL, 6834–6837. doi: 10.1109/EMBC.2014.6945198

Culaclii, S., Kim, B., Lo, Y.-K., Li, L., and Liu, W. (2018). Online artifact cancelation in same-electrode neural stimulation and recording using a combined hardware and software architecture. *IEEE Trans. Biomed. Circuits Syst.* 12, 601–613. doi: 10.1109/TBCAS.2018.2816464

Eles, J. R., Stieger, K. C., and Kozai, T. D. Y. (2020). The temporal pattern of intracortical microstimulation pulses elicits distinct temporal and spatial recruitment of cortical neuropil and neurons. *J. Neural Eng.* 18:015001. doi: 10.1088/1741-2552/abc29c

Formento, E., D'Anna, E., Gribi, S., Lacour, S. P., and Micera, S. (2020). A biomimetic electrical stimulation strategy to induce asynchronous stochastic neural activity. *J. Neural Eng.* 17:046019. doi: 10.1088/1741-2552/aba4fc

Gerasimenko, Y., Roy, R. R., and Edgerton, V. R. (2008). Epidural stimulation: comparison of the spinal circuits that generate and control locomotion in rats, cats and humans. *Exp. Neurol.* 209, 417–425. doi: 10.1016/j.expneurol.2007.07.015

Hottowy, P., Skoczeń, A., Gunning, D. E., Kachiguine, S., Mathieson, K., Sher, A., et al. (2012). Properties and application of a multichannel integrated circuit

for low-artifact, patterned electrical stimulation of neural tissue. *J. Neural Eng.* 9:066005. doi: 10.1088/1741-2560/9/6/066005

Kassiri, H., Salam, M. T., Pazhouhandeh, M. R., Soltani, N., Perez Velazquez, J. L., Carlen, P., et al. (2017). Rail-to-rail-input dual-radio 64-channel closed-loop neurostimulator. *IEEE J. Solid State Circuits* 52, 2793–2810. doi: 10.1109/JSSC.2017.2749426

Kuanfu, C., and Liu, W. (2009). "Highly programmable digital controller for high-density epi-retinal prosthesis," in *Proceedings of the 2009 Annual International Conference of the IEEE Engineering in Medicine and Biology Society*, Minneapolis, MN, 1592–1595. doi: 10.1109/IEMBS.2009.5334120

Lee, H. M., Howell, B., Grill, W. M., and Ghovanloo, M. (2018). Stimulation efficiency with decaying exponential waveforms in a wirelessly powered switched-capacitor discharge stimulation system. *IEEE Trans. Biomed. Eng.* 65, 1095–1106. doi: 10.1109/TBME.2017.2741107

Lo, Y., Kuan, Y., Culaclii, S., Kim, B., Wang, P., Chang, C., et al. (2017). A fully integrated wireless SoC for motor function recovery after spinal cord injury. *IEEE Trans. Biomed. Circuits Syst.* 11, 497–509. doi: 10.1109/TBCAS.2017.2679441

Lo, Y. K., Chang, C. W., Kuan, Y. C., Culaclii, S., Kim, B., Chen, K., et al. (2016). "22.2 A 176-channel 0.5cm3 0.7g wireless implant for motor function recovery after spinal cord injury," in *Proceedings of the 2016 IEEE International Solid-State Circuits Conference (ISSCC)*, San Francisco, CA, 382–383. doi: 10.1109/ISSCC.2016.7418067

Lo, Y. K., Chen, K., Gad, P., and Liu, W. (2013). A fully-integrated high-compliance voltage SoC for epi-retinal and neural prostheses. *IEEE Trans. Biomed. Circuits Syst.* 7, 761–772. doi: 10.1109/TBCAS.2013.2297695

Mendrela, A. E., Cho, J., Fredenburg, J. A., Nagaraj, V., Netoff, T. I., Flynn, M. P., et al. (2016). A bidirectional neural interface circuit with active stimulation artifact cancellation and cross-channel common-mode noise suppression. *IEEE J. Solid State Circuits* 51, 955–965. doi: 10.1109/JSSC.2015.2506651

Merrill, D. R., Bikson, M., and Jefferys, J. G. R. (2005). Electrical stimulation of excitable tissue: design of efficacious and safe protocols. *J. Neurosci. Methods* 141, 171–198. doi: 10.1016/j.jneumeth.2004.10.020

Mogul, D. J., and van Drongelen, W. (2014). Electrical control of epilepsy. *Annu. Rev. Biomed. Eng.* 16, 483–504. doi: 10.1146/annurev-bioeng-071813-104720

Moore, D. R., and Shannon, R. V. (2009). Beyond cochlear implants: awakening the deafened brain. *Nat. Neurosci.* 12, 686–691. doi: 10.1038/nn.2326

Noorsal, E., Sooksood, K., Xu, H., Hornig, R., Becker, J., and Ortmanns, M. (2012). A neural stimulator frontend with high-voltage compliance and programmable pulse shape for epiretinal implants. *IEEE J. Solid State Circuits* 47, 244–256. doi: 10.1109/JSSC.2011.2164667

Piech, D. K., Johnson, B. C., Shen, K., Ghanbari, M. M., Li, K. Y., Neely, R. M., et al. (2020). A wireless millimetre-scale implantable neural stimulator with ultrasonically powered bidirectional communication. *Nat. Biomed. Eng.* 4, 207–222. doi: 10.1038/s41551-020-0518-9

Randles, J. (1947). Kinetics of rapid electrode reactions. *Discuss. Faraday Soc.* 1:11. doi: 10.1039/df9470100011

Shahdoost, S., Frost, S. B., Guggenmos, D. J., Borrell, J. A., Dunham, C., Barbay, S., et al. (2018). A brain-spinal interface (BSI) system-on-chip (SoC) for closed-loop cortically-controlled intraspinal microstimulation. *Analog Integr. Circuits Signal Process.* 95, 1–16. doi: 10.1007/s10470-017-1093-1

Soto-Breceda, A., Kameneva, T., Meffin, H., Maturana, M., and Ibbotson, M. R. (2018). Irregularly timed electrical pulses reduce adaptation of retinal ganglion cells. *J. Neural Eng.* 15:056017. doi: 10.1088/1741-2552/aad46e

Stanslaski, S., Afshar, P., Cong, P., Giftakis, J., Stypulkowski, P., Carlson, D., et al. (2012). Design and validation of a fully implantable, chronic, closed-loop neuromodulation device with concurrent sensing and stimulation. *IEEE Trans. Neural Syst. Rehabil. Eng.* 20, 410–421. doi: 10.1109/TNSRE.2012.2183617

Sun, F. T., and Morrell, M. J. (2014). The RNS system: responsive cortical stimulation for the treatment of refractory partial epilepsy. *Expert Rev. Med. Devices* 11, 563–572. doi: 10.1586/17434440.2014.947274

Taccola, G., Gad, P., Culaclii, S., Ichiyama, R. M., Liu, W., and Edgerton, V. R. (2020a). Using EMG to deliver lumbar dynamic electrical stimulation to facilitate cortico-spinal excitability. *Brain Stimul.* 13, 20–34. doi: 10.1016/j.brs.2019.09.013

Taccola, G., Gad, P., Culaclii, S., Wang, P.-M., Liu, W., and Edgerton, V. R. (2020b). Acute neuromodulation restores spinally-induced motor responses after severe spinal cord injury. *Exp. Neurol.* 327:113246. doi: 10.1016/j.expneurol.2020.113246

Taccola, G., Sayenko, D., Gad, P., Gerasimenko, Y., and Edgerton, V. R. (2018). And yet it moves: recovery of volitional control after spinal cord injury. *Prog. Neurobiol.* 160, 64–81. doi: 10.1016/j.pneurobio.2017.10.004

Wagner, F. B., Mignardot, J.-B., Goff-Mignardot, C. G. L., Demesmaeker, R., Komi, S., Capogrosso, M., et al. (2018). Targeted neurotechnology restores walking in humans with spinal cord injury. *Nature* 563, 65–71. doi: 10.1038/s41586-018-0649-2

Wang, P., Culaclii, S., Yang, W., Long, Y., Massachi, J., Lo, Y., et al. (2019). "A novel biomimetic stimulator system for neural implant," in *Proceedings of the 2019 9th International IEEE/EMBS Conference on Neural Engineering (NER)*, San Francisco, CA, 843–846. doi: 10.1109/NER.2019.8716942

Weiland, J. D., Liu, W., and Humayun, M. S. (2005). Retinal prosthesis. *Annu. Rev. Biomed. Eng.* 7, 361–401. doi: 10.1146/annurev.bioeng.7.060804.100435

Yip, M., Jin, R., Nakajima, H. H., Stankovic, K. M., and Chandrakasan, A. P. (2015). A fully-implantable cochlear implant SoC with piezoelectric middle-ear sensor and arbitrary waveform neural stimulation. *IEEE J. Solid State Circuits* 50, 214–229. doi: 10.1109/JSSC.2014.2355822

Zhou, A., Santacruz, S. R., Johnson, B. C., Alexandrov, G., Moin, A., Burghardt, F. L., et al. (2019). A wireless and artefact-free 128-channel neuromodulation device for closed-loop stimulation and recording in non-human primates. *Nat. Biomed. Eng.* 3:15. doi: 10.1038/s41551-018-0323-x

Conflict of Interest: WL and Y-KL hold shareholder interest in Niche Biomedical Inc. P-MW was employed by the company Niche Biomedical Inc.

The remaining authors declare that the research was conducted in the absence of any commercial or financial relationships that could be construed as a potential conflict of interest.

Publisher's Note: All claims expressed in this article are solely those of the authors and do not necessarily represent those of their affiliated organizations, or those of the publisher, the editors and the reviewers. Any product that may be evaluated in this article, or claim that may be made by its manufacturer, is not guaranteed or endorsed by the publisher.

frontiers in Neuroscience

REVIEW
published: 06 August 2021
doi: 10.3389/fnins.2021.663204

Advances in Neural Recording and Stimulation Integrated Circuits

*Juzhe Li[1], Xu Liu[1], Wei Mao[2], Tao Chen[3] and Hao Yu[2]**

[1] College of Microelectronics, Beijing University of Technology, Beijing, China, [2] School of Microelectronics, Southern University of Science and Technology, Shenzhen, China, [3] Advanced Photonics Institute, Beijing University of Technology, Beijing, China

In the past few decades, driven by the increasing demands in the biomedical field aiming to cure neurological diseases and improve the quality of daily lives of the patients, researchers began to take advantage of the semiconductor technology to develop miniaturized and power-efficient chips for implantable applications. The emergence of the integrated circuits for neural prosthesis improves the treatment process of epilepsy, hearing loss, retinal damage, and other neurological diseases, which brings benefits to many patients. However, considering the safety and accuracy in the neural prosthesis process, there are many research directions. In the process of chip design, designers need to carefully analyze various parameters, and investigate different design techniques. This article presents the advances in neural recording and stimulation integrated circuits, including (1) a brief introduction of the basics of neural prosthesis circuits and the repair process in the bionic neural link, (2) a systematic introduction of the basic architecture and the latest technology of neural recording and stimulation integrated circuits, (3) a summary of the key issues of neural recording and stimulation integrated circuits, and (4) a discussion about the considerations of neural recording and stimulation circuit architecture selection and a discussion of future trends. The overview would help the designers to understand the latest performances in many aspects and to meet the design requirements better.

Keywords: electrical stimulation, biomedical, stimulation artifact, neural recording, closed-loop system

OPEN ACCESS

Edited by:
Ming-Dou Ker, National Chiao Tung University, Taiwan

Reviewed by:
Toshihiko Noda, Toyohashi University of Technology, Japan
Aria Samiei, University of Southern California, United States
Alexandre Schmid, École Polytechnique Fédérale de Lausanne, Switzerland

****Correspondence:***
Hao Yu
yuh3@sustc.edu.cn

Specialty section:
This article was submitted to Neural Technology, a section of the journal Frontiers in Neuroscience

Received: *02 February 2021*
Accepted: *08 July 2021*
Published: *06 August 2021*

Citation:
Li J, Liu X, Mao W, Chen T and Yu H (2021) Advances in Neural Recording and Stimulation Integrated Circuits. Front. Neurosci. 15:663204. doi: 10.3389/fnins.2021.663204

INTRODUCTION OF NEURAL RECORDING AND STIMULATION CIRCUITS

The neural prosthesis chip for biomedical use includes the neural/muscular stimulators and neural recording circuits. In these circuits, the stimulator has been widely used in biomedical applications for decades, such as cardiac pacemaking, cochlear/retinal prosthesis, and cell activation (Chen et al., 2010; Sooksood et al., 2011; Noorsal et al., 2012; Wagner et al., 2018; Lee and Im, 2019; Lin and Ker, 2020; Yen and Ker, 2020). The neural recording circuit is also involved in these applications to sense the neural signal or assess stimulation efficacy and the tissue status to enable closed-loop control in simultaneous neural recording and stimulation (Yoshida and Horch, 1996; Blum et al., 2007; Rolston et al., 2009, 2010; Venkatraman et al., 2009; Xu et al., 2012; Ando et al., 2016; Ramezani et al., 2018; Lancashire et al., 2019; Carmona et al., 2020). The circuits for simultaneous neural recording and stimulation are used in neural prostheses, such as the bionic neural link for limb function restoration (Xu et al., 2012; Sadeghi Najafabadi et al., 2020; Żebrowska et al., 2020).

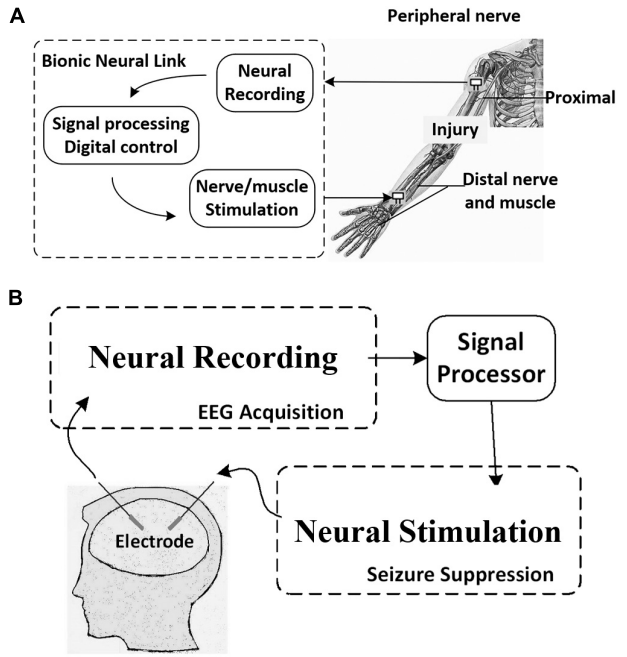

FIGURE 1 | Concept of **(A)** the Bionic Neural Link and **(B)** the epileptic seizure detection and suppression using neural recording and stimulation circuits.

The bionic neural link includes neural recording circuits, stimulation circuits, and action potential (AP) detection circuits (Xu et al., 2017). As shown in **Figure 1A**, once the AP is detected in the circuit, the bionic neural link bypasses the injury and triggers the stimulator to stimulate the distal nerve/muscle and restore the limb function. The integrated circuit (IC) modules and the working theories will be illustrated in detail in the following sections.

ADVANCES IN NEURAL RECORDING AND STIMULATION INTEGRATED CIRCUITS

Neural Stimulation

The essence of electrical stimulation is charge delivery. When the charge accumulation in tissues reaches the threshold, an AP will be produced and muscle contraction will be trigged. The most widely used electrical stimulation method is the current-controlled stimulation (CCS), which benefits from the advantages of controllable charge and high integration. The traditional bidirectional current stimulation scheme is shown in **Figure 2A**, which consists of two highly matched current sources (*Ip* and *In*), an electrode for stimulating charge transfer (V_E is the voltage of electrode), and an electrode for providing a reference voltage V_{CM} (Changhyun and Wise, 1996; Liu et al., 2000; Ortmanns et al., 2007). The electrode–tissue interface can be equivalent to a model with capacitance and resistance. The cathodic stimulation is used for AP triggering and the anodic stimulation is used for charge compensation. In **Figure 2B**, the intermediate delay ensures the transfer of AP. The bidirectional current with high matching is required to ensure that the nerve tissue has no charge accumulation to avoid nerve tissue damage.

Though the CCS has become the most common method, the stimulation voltage is greatly affected by the electrode impedance, especially in multi-channel stimulation cases. The supply voltage needs to ensure the minimum necessary voltage level applicable for various loads, to achieve the required power efficiency. Other stimulation methods such as switched-capacitor stimulation (SCS) can control the amount of stimulus charge better and achieve higher power efficiency. However, it is difficult to integrate the large capacitors into the chip. Recently, the feasibility of high-frequency stimulation has been proved (van Dongen et al., 2015), and a high-frequency switched capacitor stimulation (HFSC) method has been proposed in Hsu and Schmid (2017). As shown in **Figure 2D**, a method using high-frequency switching for stimulation is introduced. Due to the small amount of charge transferred in each switching process, the required capacitance C_{stim} can also be reduced exponentially, which is convenient for on-chip integration and reduces the chip area and cost. The switching timing and the voltage waveform of the electrode (V_E) are shown in **Figure 2E**. The phase difference is introduced between S1 and S2 to remove the dead zone. V_E increases with the number of switching, and AP will be triggered when the charge accumulation reaches the threshold.

During the stimulation process, the bidirectional current cannot match completely, which causes the residual charge in the nerve tissue. The accumulation of residual charge will cause irreparable damage to the nerve tissue. Considering the safety of neural stimulation, the designed stimulator requires minimum residual charge in a single cycle, and the accumulated charge after multiple cycles also needs to be removed in time. The real-time monitoring of V_E is necessary to eliminate the residual charge in time when the voltage does not return to the reference voltage at the end of the stimulation cycle (Ortmanns, 2007). A variety of the accumulated charge balance methods are introduced, such as the electrode short-circuit technology (Rothermel et al., 2009) and the short-time pulse insertion technology (Ortmanns et al., 2007; Yao et al., 2015; Chen et al., 2020). In **Figure 2C**, the electrode short-circuit technology uses switch S to connect the electrode and ground. This method will produce unpredictable discharge time, which depends on the electrode impedance. As for the short-time pulse insertion technique, it can achieve controllable compensation. As shown in **Figure 2F**, when V_E is detected to be out of the reference voltage range at the end of each stimulation cycle, a series of short-time pulses will control the switch for charge compensation to recover the V_E voltage level (Sooksood et al., 2010). However, the frequent short-time pulse stimulation will introduce more switching noise and reduce the signal-to-noise ratio (SNR) of the recorded signal.

A cooperative compensation method is proposed (Butz et al., 2018) to ensure that the residual charge is unable to damage nerve tissue under long-term stimulation by using the "cause-based and consequence-based systems." As shown in **Figure 2H**, the stimulation mode is CCS in this method. The consequence-based system is named Inter-Pulse Charge Control (IPCC) due to its instantaneous compensation properties between the

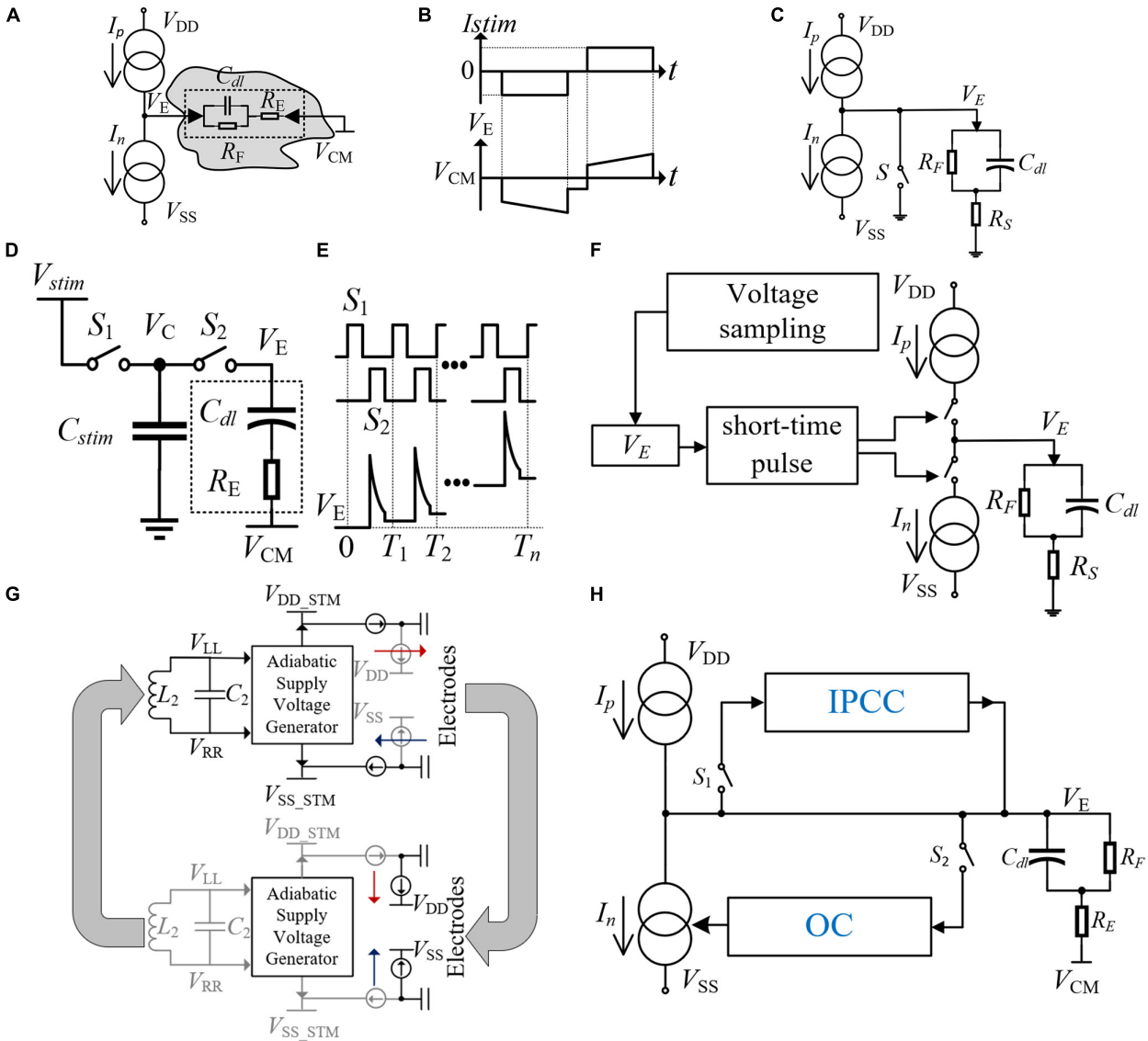

FIGURE 2 | (A) Traditional structure of a bidirectional current stimulator. **(B)** The current and voltage waveforms of the bidirectional current stimulator. **(C)** The structure of the stimulator with an electrode short-circuit technique. **(D)** The structure of the high-frequency switched-capacitor stimulator (HFSC). **(E)** The voltage waveform on the electrode with the switch control signals of the stimulator. **(F)** The structure of a stimulator using the short-time pulse insertion technique. **(G)** The structure of the adiabatic stimulator. **(H)** The structure of the stimulator with IPCC and OC.

stimulations. When the voltage V_E changes greatly at the end of the stimulation cycle, the high-voltage output stage of the IPCC will generate a constant compensation current and compensate the residual charge until V_E returns to the reference voltage. The cause-based compensation method is called offset compensation (OC). A stable feedback system is introduced through the PI control, and the compensation will be performed in the next stimulation cycle. When the OC is working, the PI control will add extra bias current to the cathode current. In the next stimulation cycle, the accumulated charge would be compensated by the improved bidirectional current. After each bidirectional current stimulation, the two compensation methods work independently using S1 and S2 control, which avoids disturbance caused by simultaneous sampling. As the OC time is shorter, the voltage sampling should be finished before the IPCC starts working.

In addition, the power efficiency of the stimulator is also an important design consideration, as higher power efficiency means less thermal power consumption. Excessive thermal power generation will not only cause nerve tissue damage, but also affect the working environment of the stimulator. A new type of adiabatic current-controlled stimulator architecture is adopted in Ha et al. (2019). Under the condition of ensuring better power efficiency, a complete wireless power supply is realized. The adiabatic stimulator can track the change of V_E and minimize the voltage drop across the current source. The adiabatic waveforms

are provided by the on-chip resonant coil, which are directly synthesized by cascading and folding auxiliary rectification stages under the demand of stimulating voltage. In addition, the whole circuit is improved with better energy-saving performance by realizing the function of recovering electric charge from nerve tissue. The process is shown in **Figure 2G**. The stimulation is supplied by $V_{DD\text{-}stm}$ and $V_{DD\text{-}stm}$ at first. After the AP is triggered, reverse current compensation is carried out. In the second stage, the charge inflows to V_{DD} and V_{SS}, which delivers the energy back to the supply rails. Compared with the traditional methods which draw the charge down to a negative power supply or ground, this method prevents energy loss in the stimulation process and improves power efficiency.

Table 1 shows the comparison of the important parameters in the design of neural stimulation circuits. It can be seen that the CCS is still the main stimulation type for the neural stimulators, because the charge injected into the tissue during stimulation can be controlled using CCS. For the power supply, the implantable stimulator requires a wireless power supply with inductive link, while the external wearable stimulator uses a battery. The stimulation safety and energy efficiency are important for neural stimulator design. It is necessary to monitor and remove the residual charge remaining in tissue on time through the voltage detection circuits and the pulse injection circuits or other circuits with better current matching. The performance of peak efficiency refers to the ratio of the maximum output power to the power supply. The highest peak efficiency is 80% among the listed prior works. The maximum stimulation current represents the strength for neural or muscular stimulation. Considering the stimulation effectiveness, most stimulators have the maximum output current not less than 1 mA.

Neural Recording

In a closed-loop neural system, in addition to the stimulator that triggers the AP, neural recording is required to sample local field potentials (LFPs). If the stimulator is regarded as the executor, the neural recording part is the digital back end of the whole system. Different from stimulation signals, LFPs are the electric potentials in the extracellular medium around neurons, which have very small amplitude (μV) and low frequency (1–200 Hz). Due to the microvolt level of the nerve signal, it is not reliable to implement direct digital quantization before amplifying. The most common way is to add a low noise amplifier (LNA) to the front end of the recording (Harrison and Charles, 2003; Harrison et al., 2007) and then to add the digital quantization circuits (Zou et al., 2009; Liu et al., 2017; Yu et al., 2018). As shown in **Figure 3A**, the recording is completed by the cooperation of the LNA and analog-to-digital converter (ADC). The gain of the amplifier is determined by the feedback capacitor C_2 and the input capacitor C_1, and C_L is the load capacitance. The PMOS transistors with diode connection (M_a–M_d) act as pseudo resistors. Besides, a high-pass filter (HPF) with low cutoff frequency is formed with input capacitors. The HPF is used to eliminate the DC offset in neural signals to prevent recording saturation.

In the traditional methods, the HPF is used to block the DC offset by using the input in an ac-coupled form. However, due to the information at low frequency carried by nerve signal, the HPF needs a large input capacitance, which reduces the input impedance of the neural recording circuit. In Jeon et al. (2019), a neural-recording IC using a voltage-controlled oscillator (VCO) is proposed, which can quantize the input signal directly and achieve a high dynamic input range. The circuit structure of the recording is shown in **Figure 3B**. This method is adopted and converts voltage into differential currents by an ac-coupled input transconductance circuit. Then, the current is fed into the current control oscillators (CCOs) CCOP and CCON. According to the phase difference between CCOP and CCON, the quantizer generates the digital output D_{out}. The digital-to-analog converter (DAC) controls the input resistance through a negative feedback, and reduces the difference between I_{in+} and I_{in-}. Due to this negative feedback action, the values of I_{in+} and I_{in-} assume almost the same value even if the input voltage is large, which results in a wide input linear range. In addition, the input of the circuit is directly connected to the gate of the MOSFET, which has a large input impedance and improves the recording stability.

Another new architecture uses a continuous-time delta-sigma modulator (CTDSM) as the recording front end (RFE), and the researcher establishes the structure based on a second-order CTDSM (Nikas et al., 2019). As shown in **Figure 3C**, it has a cascaded integrator and a feedforward compensation

TABLE 1 | Comparison of the parameters in neural stimulation circuits.

	Hsu and Schmid, 2017	Ha et al., 2019	Butz et al., 2018	Noorsal et al., 2012	Lee et al., 2015	Sooksood et al., 2010	Lee et al., 2013	Song et al., 2012
Technology (nm)	HV180	180	350	350	350	PCB	500	130
Stimulation type	HFSC	CCS	CCS	CCS	SCS	CCS	CCS	CCS
Supply voltage (V)	5	0.8	22	20	4	30	5	3.3
Power source	Battery	Inductive link	Battery	Battery	Inductive link	Battery	Inductive link	Battery
Safe voltage detection	N/A	Current matching	IPCC/OC	OC/Short pulse injection	Charge monitoring	OC/Short pulse injections	Charge monitoring	Current matching
Safety window (mV)	N/A	–	±100	±100	N/A	±100	±50	N/A
Peak efficiency (%)	49	63.1	–	62	80.4	–	68	80
Maximum stimulation current (mA)	N/A	0.145	5.12	1	4	1	2.48	1
Power/CH (mW)	0.063	–	11	1.16	–	–	3.75	6.8
Area/CH (mm^2)	0.035	0.0484	1.5	0.2	3	N/A	0.3	1.25

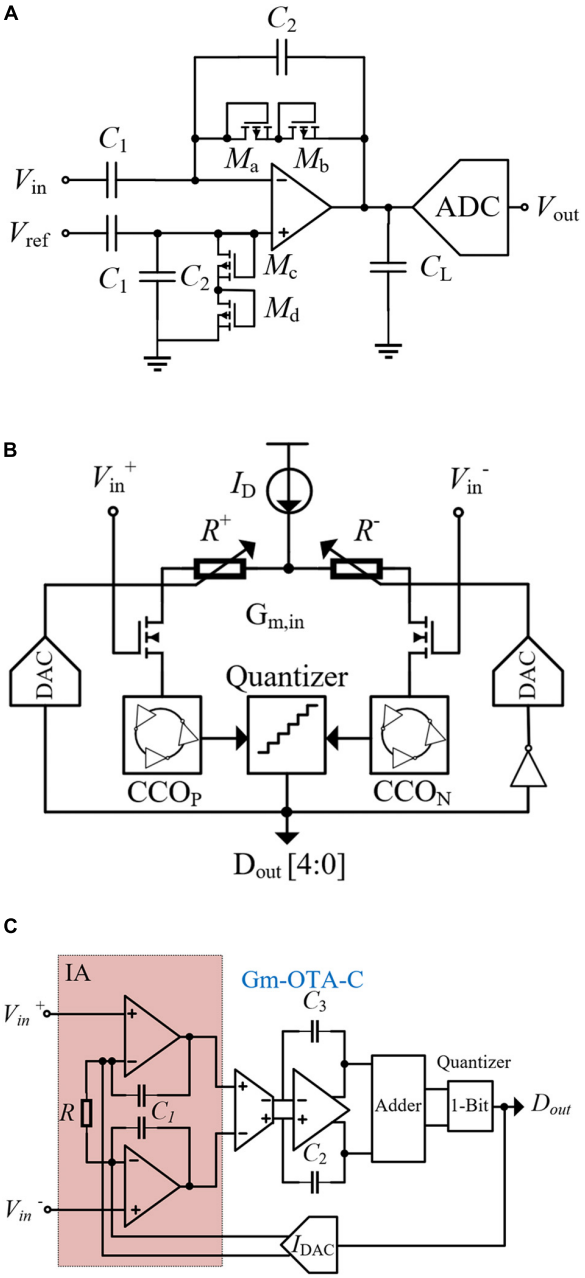

FIGURE 3 | (A) Traditional structure of the neural recorder. **(B)** Structure of the VCO-based neural recorder. **(C)** Structure of the neural recording circuit based on CTDSM.

architecture with distributed feed-in paths and a single-bit quantizer. The first integration stage is realized by using an improved instrumentation amplifier (IA), and the second integrator is implemented with the G_m-C-OTA circuit. The feedforward branches are summed up by the switched capacitor adder, and the quantizer generates digital signals. The feedback IDAC adjusts the bias current of the IA and improves the stability of the first stage. Similar to the way of using voltage-controlled oscillators, the input of the recording is directly connected to the gate of the MOSFET, showing a large input impedance. In addition, both the VCO and CTDSM use quantizer output and feedback DAC modulation, which improves the linear input range of the circuit. The difference recording method has large-signal common-mode rejection. In fact, with the growing demand for neural recording, such as monitoring nerve signals from hundreds of electrodes at the same time, it is necessary to realize intelligent data acquisition systems in the case of low power consumption and small area. Due to the various interface impedance caused by the differences in electrode sizes and materials, a high input impedance front end for neural recording is required. Currently, the recording method based on the gain stage and ADC is gradually replaced. On the contrary, direct conversion to analog front end (AFE) has the advantages of high input impedance, low power consumption, and small area, which would become the future development direction.

Table 2 shows the comparison of neural recording circuits. According to the recorded signals, the designed bandwidth is different. LFP occupies a low-frequency band from 1 to 200 Hz, and AP occupies a higher frequency band from 200 Hz to 10 kHz. The peak input refers to the linear input range of the neural recording, which limits the maximum input range of the circuit. The input-referred noise (IRN) affects the quality of the neural recording. The SNR can be improved by reducing the IRN. To prevent the attenuation of the neural signals, the input impedance (Zin) of the neural recording circuit must be significantly greater than the electrode impedance (Zin > 1G), and the DC current of the electrode should be limited within 100 pA. The high-gain LNA (>40 dB) may cause poor artifact tolerance, as the large-scale artifacts would cause saturation of the amplifier.

In neural recording, the artifact-induced problem of stimulation sometimes emerges and affects the function of biomedical devices for brain stimulation and recording (Asfour et al., 2007; Chen et al., 2011; Lin et al., 2013; Caldwell et al., 2019). As shown in **Figure 1B**, in the closed-loop neural recording and stimulation circuit for epileptic seizure detection and suppression, the stimulator is triggered, and it generates stimulation pulses in certain regions of the brain to suppress the epileptic seizure when an epileptic seizure episode is detected from the intracranial electroencephalogram (iEEG). However, the large stimulation pulse causes the artifact that is subsequently picked up by the recording amplifier as a false AP, and a false stimulation will be triggered. This situation is even worse in the multi-channel neural recording and stimulation circuit (Ng et al., 2012; Joseph et al., 2018).

The detailed artifact origin and the corresponding artifact-removal techniques are presented in the next sections.

KEY ISSUES IN NEURAL RECORDING AND STIMULATION CIRCUITS

Stimulation Induced Artifact in the Closed-Loop System

Most neural/muscular recording and stimulation circuits in biomedical devices consist of multiple recording and stimulation

TABLE 2 | Comparison of the parameters in neural recording circuits.

	Jeon et al., 2019	Samiei and Hashemi, 2019	Nikas et al., 2019	Zou et al., 2009	Shen et al., 2018	Park et al., 2018	Muller et al., 2015	Jiang et al., 2017	Chandrakumar and Markovic, 2018
Technology (nm)	180	180	180	350	180	180	65	40	40
Supply voltage (V)	1.2	0.6/1.2	1.8	1	1.0	0.5/1.0	0.5	0.45/1.2	1.2
Target application	LFP	AP and LFP	LFP	LFP	AP and LFP	AP and LFP	LFP	LFP	AP and LFP
Peak input (mV)	200	–	208	5	–	3	±50	±50	200
Input referred noise (μVrms)	1.3	3.2/2.0	2.3	2.5	5.5	3.32	1.3	5.2	6.35
Zin (Ω)	0.16G	3.0G	∞	–	∞	∞	28M	∞	1.5G
Gain (dB)	N/A	41–59	N/A	60	25.6	37.5–52.9	N/A	N/A	18
Bandwidth (Hz)	200	0.5–5k	250	0.005–292	4–10k	0.4–10.9k	1–500	1–200	1–5k
Power/CH (μW)	3.9	2.6	23	0.895	0.25	1.22	2.3	7	7.3
Area/CH (mm^2)	0.225	0.08	0.694	1	0.29	0.05	0.025	0.135	0.113

channels, AP detection and data processing circuits, stimulation circuitry, and electrodes. During the operation, the large stimulation current causes the tissue potential to change and the tissue potential fluctuation will propagate to the recording site and cause artifacts (McGill et al., 1982). For bipolar stimulation, there are two stimulation electrodes, namely, a working electrode and a reference electrode. During the stimulation, most of the biphasic current flows between the working and the reference electrodes through the stimulated tissue. In the cathodic phase, the electric potential near the working electrode decreases since the stimulator sinks current from the reference electrode. While in the anodic phase, the electric potential near the working electrode increases since the stimulator generates current to the reference electrode through the tissue–electrode interface. The amplitude of this voltage variation is usually from several hundred millivolts to several volts (Xu et al., 2017), which depends on several factors, including the electrode impedance and the power-supply voltage at the output stage of the stimulator. The voltage variation would also be recorded by the neural recording circuit and cause saturation of the recording amplifier, which produces the artifact (Johnson et al., 2017; Jeon et al., 2019). Such a stimulation artifact can be observed in most of the closed-loop recording and stimulation circuits (Yoshida and Horch, 1996; Blum et al., 2007; Venkatraman et al., 2009; Mc Laughlin et al., 2012; Ng et al., 2012; Xu et al., 2012). The amplitude of the recorded artifact spike is determined by several factors such as the distance between the recording and the stimulation sites, the gain of the amplifier, and the electrode impedance (Johnson et al., 2017; Pazhouhandeh et al., 2018; Jeon et al., 2019; Uehlin et al., 2020). The artifact is typically hundreds of millivolts in amplitude, and 10 to 100 times higher than the amplitude of the recorded neural signals (Dabbaghian et al., 2019; Lee and Je, 2020).

Several stimulation artifact cancelation techniques have been reported previously. The blanking technique and digital signal processing (Erez et al., 2010) have been used to cancel the artifact (Olsson et al., 2005; Venkatraman et al., 2009; Kent and Grill, 2011; Myers et al., 2011; Zoladz et al., 2012; Wei-Ming et al., 2013; Yi et al., 2013; Bozorgzadeh et al., 2014; Elyahoodayan et al., 2019). In the blanking technique, the RFE is switched off or disabled (input is shorted to ground) during the stimulation period and turned on after the stimulation is completed to continue the recording. As shown in **Figure 4A**, the recording amplifier and two capacitors (C_1 and C_2) are used to amplify nerve signals. A very large resistor R_1 is used in the feedback path to provide a DC current path to bias the input. The discharge amplifier helps the electrode return to its pre-stimulation voltage after stimulation. The recording amplifier is disabled through S_{blank} during stimulation and enabled after 2 ms when the stimulation ends (Blum et al., 2007). This method is effective in some applications, such as EMG signal acquisition. Because the evoked neural spike usually emerges with a latency, the AP and the artifact spike will not overlap. However, in some other applications, such as neural prosthesis or deep brain stimulation (DBS), the neural responses in the cathodic and anodic stimulation phases also need to be recorded. In such applications, if the blanking technique is employed, the neural signals during the "blanking" period cannot be recorded and thus some important neural information may be missed.

The artifact cancelation using digital signal processing can be divided into two categories: real-time signal processing and signal post-processing, such as active electrode discharge in real-time signal processing (Brown et al., 2008). As shown in **Figure 4B**, $R_{discharge}$ is a variable resistance and the impedance is very large under normal conditions. When a large artifact is detected, $R_{discharge}$ can be changed to a value with low impedance, then the RC time constant of the path is reduced and thus it makes the electrode voltage quickly return to the reference voltage. This method reduces the recovery time from 10 ms to approximately 200 μs, but the problem of artifact recording has not been solved. In signal post-processing, the recorded neural signal together with the artifact are acquired. One processing method is adaptive filtering (Mahajan and Morshed, 2015; Rozgic et al., 2019; Samiei and Hashemi, 2021). The template of the artifact waveform can be obtained by the least-mean-square algorithms, genetic algorithms (Qiu et al., 2015), principal component analysis (Deprez et al., 2017), and wavelet algorithms (Yochum and Binczak, 2015). As shown in **Figure 4D**, the neural signal can be recovered by subtracting the artifact template from the collected signal. One disadvantage of signal

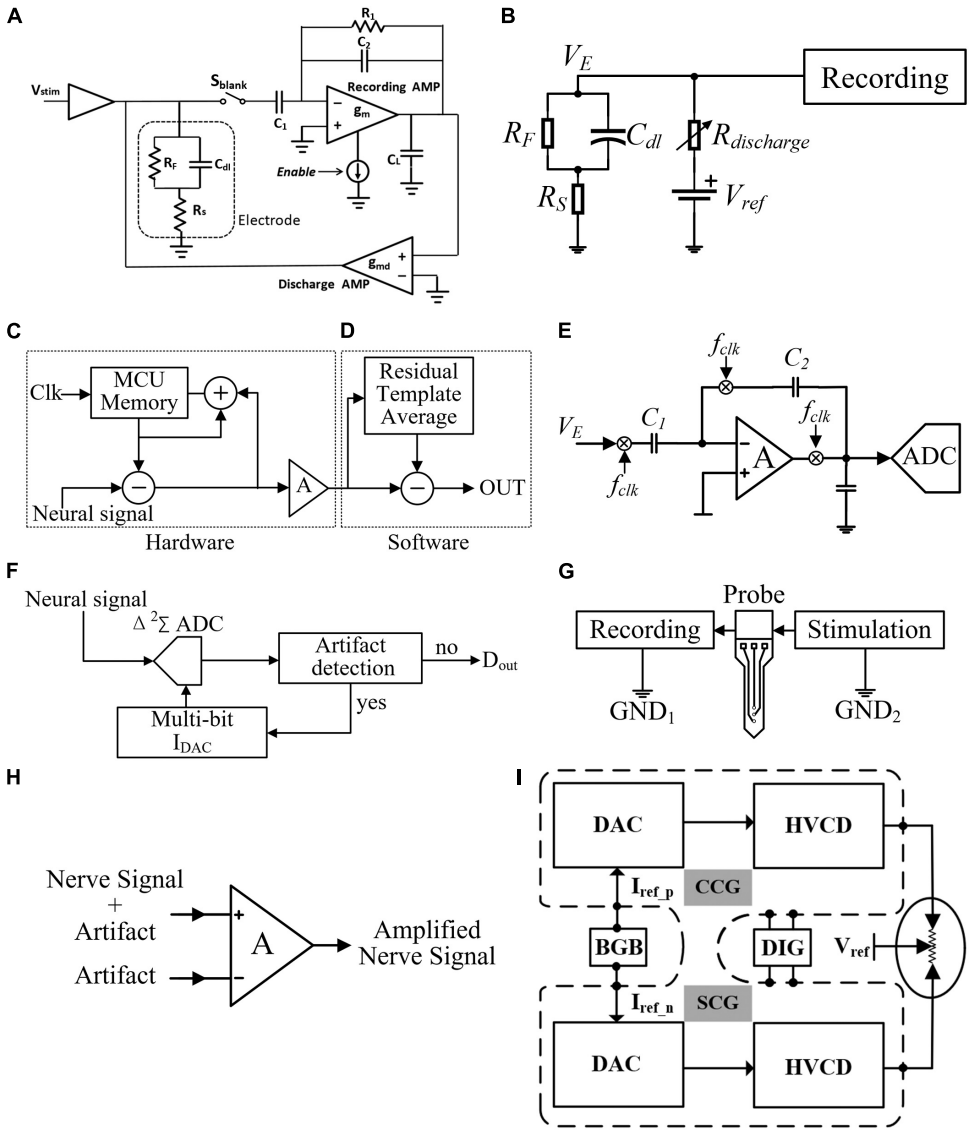

FIGURE 4 | (A) Artifact elimination circuit with blanking technique, **(B)** active electrode discharge technique, **(C)** iterative hardware loops, **(D)** adaptive filtering technique in post-processing, **(E)** chopper technique, **(F)** track-and-zoom (TAZ) neural ADC, **(G)** localized stimulation technique, **(H)** dual electrode in-phase stimulation, and **(I)** RTPPS technique.

post-processing is that the RFE must have a large dynamic range so that the artifact does not saturate the amplifier. The merit of removing artifacts using digital processing compared with blanking is that no neural spikes are missing in the recording. However, the digital processing is computationally intensive. The artifact templates produced by different tissue parts are also inconsistent. Some improved schemes have been proposed in Culaclii et al. (2018), in which both hardware and software are implemented to optimize the system. As shown in **Figure 4C**, the amplitude of artifacts is reduced by iterative hardware loops instead of filtering them completely. The hardware loop stores the artifact as the template and then iteratively updates the template according to the recording difference, until the template converges within the resolution range of the hardware component. Finally, the artifacts are removed by signal post-processing. However, the hardware implementation may introduce the noise caused by other electronic components from the PCB boards. Besides, the software implementation also consumes extra computation resources.

At present, all kinds of signal post-processing methods have become mature. The research focus on artifact suppression has been changed to establishing a high input dynamic range RFE, removing the amplifier saturation caused by artifacts. A common combination composed of a chopper amplifier and the ADC is proposed in Chandrakumar and Markovic (2017; 2018) and Samiei and Hashemi (2019; 2021). As shown in **Figure 4E**, chopping is an effective way to reduce the low-frequency flicker noise of the amplifier. The gain of the capacitive feedback

amplifier is determined by the ratio of C_1 to C_2. To eliminate the influence of the operational amplifiers' low-frequency noise and the DC offset, the chopper is used to up-convert the low-frequency biological signal to the carrier frequency (F_{clk}), away from the DC offset and flicker noise. After band-pass amplification, the up-converted signal is down-converted to its original frequency, and the DC offset and flicker noise are up-converted away from the signal. However, due to the large input capacitor C1, the input impedance is restricted.

A track-and-zoom (TAZ) neural ADC is proposed in Reza Pazhouhandeh et al. (2020). As shown in **Figure 4F**, a recording amplifier and an ADC are combined. When fast artifact transients are detected, the multi-bit DAC will feedback to the TAZ ADC. Then, the dynamic input range of the RFE is exponentially expanded, which prevents the saturation of neural recording and saves chip area and power consumption. In another innovative method, the recording amplifier is replaced by VCO (Jiang et al., 2017; Jeon et al., 2019). As shown in **Figure 3B**, the proposed circuit in this method quantizes the frequency of the sample by counting the phase increment. Applying this method, the neural signals recording can be done in the frequency domain. The feedback DACs compensate the nonlinearity of $G_{m,in}$. Thus, VCOs can keep good linearity in a large input range of neural recording. However, in order to ensure high sensitivity of recording with large input range, the noise of VCOs dominated by flicker noise needs to be further reduced.

Another artifact suppressing technique reported is the localized stimulation (Wong et al., 2007; Yung-Chan et al., 2009), as shown in **Figure 4G**, where the stimulation current returns to a local ground. Although this reduces the artifact amplitude at the input of the recording amplifier and allows the amplifier to quickly recover to the normal state, the artifact is still not effectively suppressed. An improved method is shown in **Figure 4H**. The dual-electrode in-phase stimulation and differential acquisition at the recording electrodes are carried out (Nag et al., 2015). This method uses the common mode suppression characteristics of a differential input to reduce the artifacts. The experimental result showed good artifact suppression effect, but this method requires the electrode impedance to be highly matched. In order to ensure the consistency of the common-mode level, it is necessary to establish an additional accurate impedance matching network.

To avoid impedance mismatching in differential acquisition at the recording electrodes, the referenced and tuned push–pull stimulation (RTPPS) scheme with a tri-polar electrode is proposed (Xu et al., 2017). The problem of the artifact can be solved and no blanking of the recording channels is needed. As shown in **Figure 4I**, the RTPPS uses a tri-polar stimulation configuration with two working electrodes and one reference electrode. The stimulation currents delivered by the two working electrodes are complementary to each other. By doing so, the amplitude of voltage fluctuation at the recording site can be significantly reduced.

Several other artifact cancelation methods have also been proposed. In Liu et al. (2011), neural recording is carried out only in the mid-phase between cathodic and anodic stimulation phases to avoid the artifact. In Dura et al. (2012) and Chu et al. (2013), high-frequency short-duration pulses or other specific patterns are adopted for stimulation. However, the stimulation parameters (i.e., pulse width, amplitude, and frequency) are usually determined by the application and not by the artifact cancelation.

Artifact is a key issue in neural recording. **Table 3** compares various methods of artifact suppression. These methods can be divided into two categories. In the first category, the artifact suppression is done at the RFE by using optimized neural recording circuits, while in the second category, the artifact suppression is implemented by using the digital signal processing after recording. The methods of suppression at the RFE can reduce the maximum artifact amplitude of neural recording and reduce the design complexity. The methods using digital signal processing after recording rely on different algorithms (adaptive filtering, etc.). By comparing the prior works in **Table 3**, it is found that the method (Hardware and Software) using both RFE optimization and digital processing can achieve the highest artifact suppression ratio (100 dB).

Probes in Neural Recording

The purpose of neural recording is to record the activities of neurons; however, how to record a large number of neurons in multiple regions for a long time is a key issue. The implanted probes must contain multiple electrode arrays and ensure the reliability of long-time recording. A 100-electrode neural recording circuit with a Utah probe is proposed in Harrison et al. (2007), and the probe design is shown in **Figure 5A**. This Utah probe uses a 10×10 array of platinum-tipped silicon extracellular electrodes. The silicon-based electrodes were inserted into the cerebral cortex and the researchers can record the electrical activities of nearby neurons. The flipped chip is connected to all 100 electrodes through the back of the Utah array, and it can sample in a plane approximately parallel to the brain surface.

However, the best way to record in layered or deep structures (striatum, hippocampus, or superior colliculus) is to take a dense sample in a plane perpendicular to the brain surface. A breakthrough development named Neuropixels probe is proposed (Jun et al., 2017). This is the first report of a large (10 mm) dense (100 sites per millimeter) implantable nerve recording device. The structure of the probe is shown in **Figure 5B**. The 12×12 μm sites are arranged in a four-column checkerboard and 20 μm center-to-center nearest neighbor spacing. The probe is 10 mm long and contains 960 sites. In addition, it has a user-programmable switch that allows us to address 384 of the 960 sites simultaneously. Titanium carbide (TIN) is selected as the recording site material, which is compatible with CMOS processing and has the advantages of low and uniform impedance. The researchers used two Neuropixels probes to record the activities of more than 700 neurons. This combination of high-performance electrode technology and scalable chip manufacturing opens a way to record the brain-wide neural activities and neuron behaviors.

Chronic recording is essential for understanding the processes that evolve over time, such as learning, memory, and plasticity. In the latest research, the problem of stable recording of a

TABLE 3 | Comparison of the artifact suppression methods.

	Samiei and Hashemi, 2021	Xu et al., 2017	Culaclii et al., 2018	Pazhouhandeh et al., 2018	Uehlin et al., 2020	Rozgic et al., 2019	Reza Pazhouhandeh et al., 2020	Jiang et al., 2017
Technology (nm)	180	180	N/A (SOC)	130	65	40/HV180	130	40
Supply voltage (V)	1/3	1	5.25	1.2/3.3	1.2/2.5	0.6/1.2/1.8	0.6/1.2/3.3	0.45/1.2
Artifact suppression	FE filter	RTPPS	Hardware and software	Differential Acquisition	Digital adaptive filter	Online adaptive filter	Track-and-zoom	Direct digitization
Bandwidth (Hz)	200–9k	200–5.8k	1–10k	–	<32k	1–250	1–500	1–200
ADC type	SAR	N/A	–	Δ	Nyquist Δ-Encode	–	$\Delta^2\Sigma$	SAR
ADC ENOB (bit)	8.6		–	9.7	14	12.8	11.3	12.0
Maximum tolerated artifact (V)	0.7	1	5	0.01	0.11	0.1	0.2	±0.05
Artifact suppression ratio (dB)	–	30	100	78	60	42	N/A	N/A
Power/CH (μW)	4.3	2.4	–	0.73	0.62	8.2	4.913	7
Area/CH (mm^2)	0.66	–	N/A	0.0054	0.0025	0.12	0.023	0.135

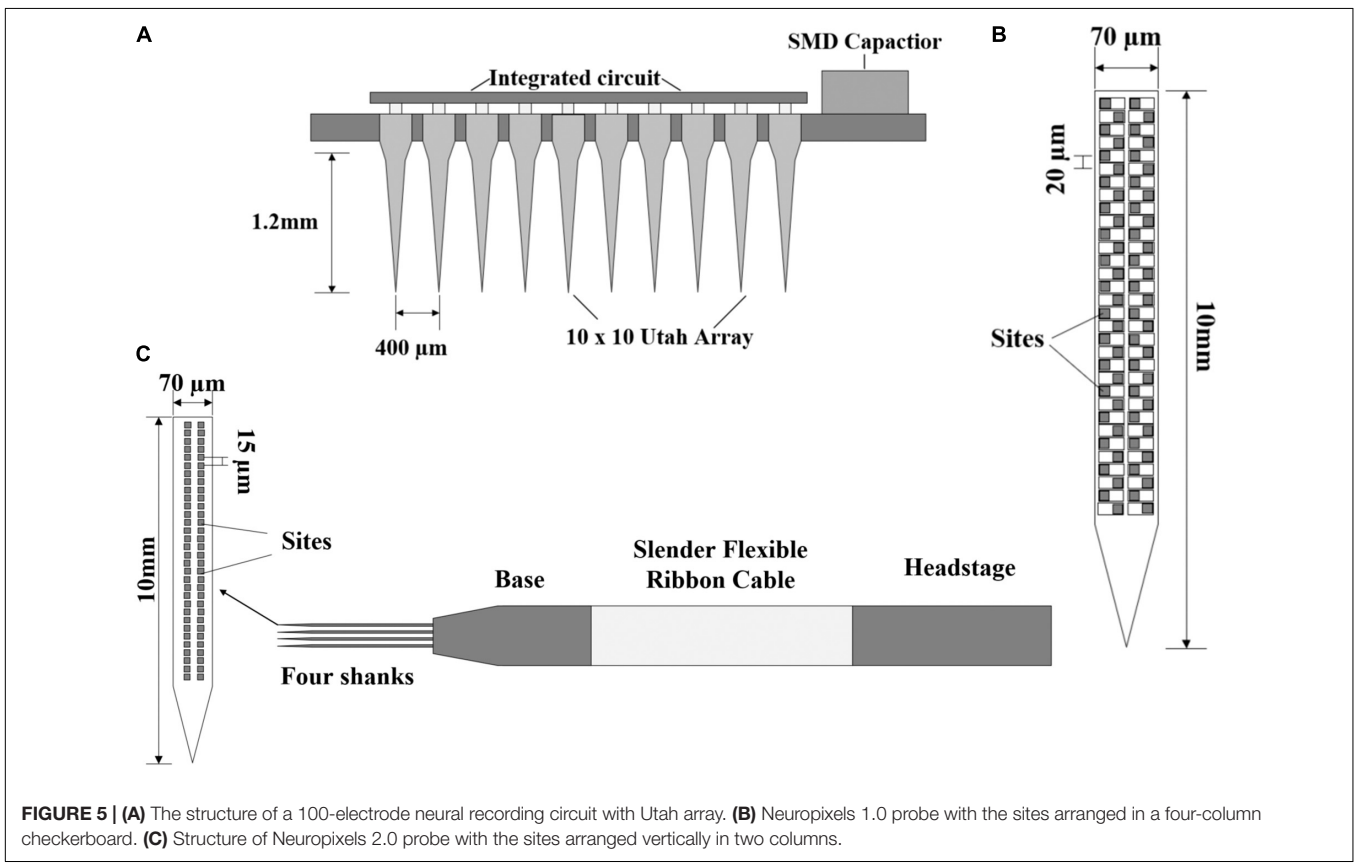

FIGURE 5 | (A) The structure of a 100-electrode neural recording circuit with Utah array. **(B)** Neuropixels 1.0 probe with the sites arranged in a four-column checkerboard. **(C)** Structure of Neuropixels 2.0 probe with the sites arranged vertically in two columns.

single neuron on a long-time scale from several weeks to several months has been overcome (Steinmetz et al., 2021). Based on Neuropixels 1.0, the team has successfully developed a more miniaturized Neuropixels 2.0 with more recording sites. The electrode structure is shown in **Figure 5C**. The probe consists of four slices inserted into the brain and a probe base (the voltage signal is filtered, amplified, multiplexed, and digitized on the base). The weight of the probe plus a headstage is about 1.1 g. The base is fixed on a rigid printed circuit board (PCB) and a slender flexible ribbon cable that plugs into a headstage. Compared with the 20 μm of Neuropixels 1.0, the recording sites are arranged vertically in two columns rather than staggered, and the vertical distance from center to center is 15 μm. The length of the probe is still 10 mm and the number of recording sites per handle is 1,280. The four-shank version supports 5,120 recording sites and the headstage is miniaturized to about one-third of the size of those for Neuropixels 1.0, which is more suitable for chronic recording in a freely moving mouse. Using two four-shank probes, combined with a motion correction algorithm, the success rate of neuron tracking is more than

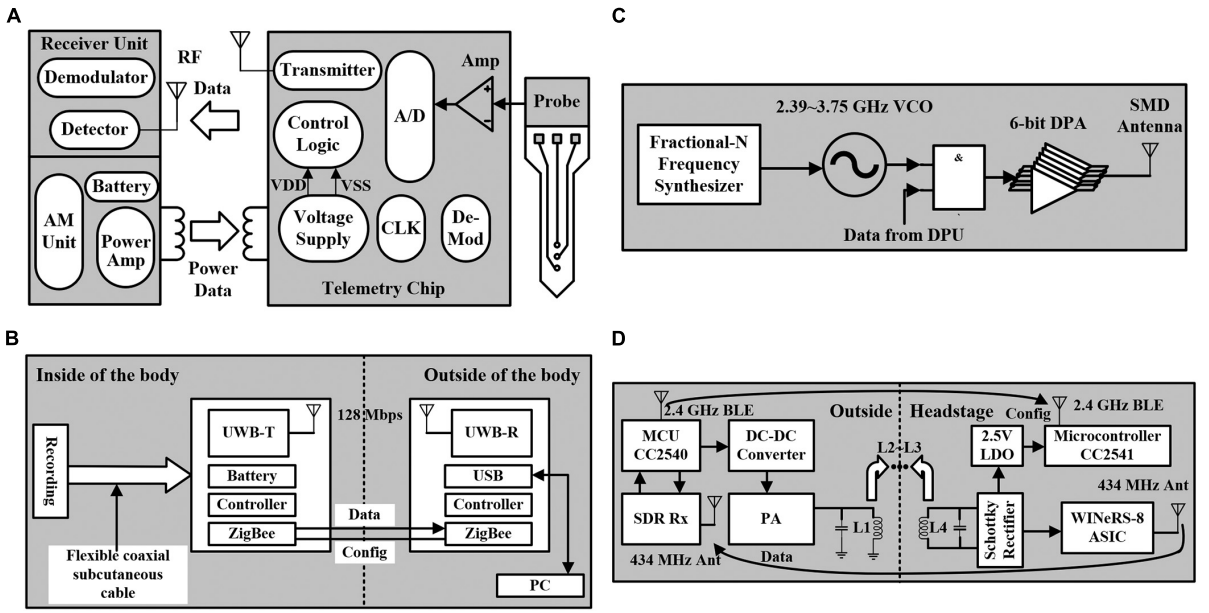

FIGURE 6 | (A) Traditional structure of the wireless powered neural recorder. **(B)** Block diagram of the neural recorder using the UWB transmitter for BMI. **(C)** The block diagram of an energy-efficient wireless transmitter using dual-band on–off keying modulation. **(D)** The block diagram of the four-coil inductively powered wireless neural recording and stimulation system.

90% in 2 weeks and more than 80% successful for up to 2 months. These experimental data are acquired based on chronic recording, and the results prove that the proposed recording electrode (Neuropixels 2.0) is very suitable for brain recording with stable insertion and contact.

Wireless Power Supply and Wireless Communication

In the system-level design of neural stimulation and recording, another necessary module is the power supply. To achieve a complete closed-loop system and satisfy the needs of large-scale electrode array such as the applications in the brain and wireless power supply is necessary for implantable neural chips. The traditional wireless power supply design is shown in **Figure 6A**, which introduces an inductive RF telemetry link (Wise et al., 2004). The outside part includes the receiving unit and the driving unit. The power supply of the implantable chip is provided by the inductors. The neural recording requires multiple channels, and each channel supports several recording sites. The recorded neural signal is converted into a digital signal by the ADC, and transmitted to the outside receiver unit through an RF link. The clock needed for the implantable chip is generated from the RF carrier. The demodulator is used to decode the received data. Then, the data can be transmitted to the computer for storage.

Recent research in nerve prosthesis chips demands high-quality data transmission from multiple neural electrodes. When the data throughput is large in multiple-channel neural recording, wireless transmission is needed as it can reduce the number of connected wires and simplify the interface. A multi-channel neural recording for brain–machine interface (BMI) is proposed (Ando et al., 2016), which adopts an ultra-wideband (UWB) transmitter. The high transmission rate ensures the stable recording of multi-electrodes, and the low output power has stronger anti-interference ability. In addition, the neural recording module and the wireless data transmission module are implanted in the brain and abdomen, respectively. The separated modules are connected by a flexible coaxial subcutaneous cable, which can transmit high data rate signals. The structure of the system is shown in **Figure 6B**, achieving a transmission rate of 128 Mbps, which is enough to support the application of thousands of electrodes. However, the system also has some limitations. The ZigBee module is added to control the implant because the communication direction of UWB can only be unidirectional (from inside to outside). The communication range is only 20 mm, which means that the external communication device must be carried at any time. Besides, the space for implantation is constrained due to the short range.

In the application of multi-electrodes, to break the limitation of power efficiency, the transmitter needs to have a high energy efficiency. Recently, a high energy-efficient wireless transmitter using dual-band on-off keying modulation has been proposed (Lyu et al., 2020), which supports 2.4-GHz and 3.2-GHz bands. The structure of the transmitter is shown in **Figure 6C**, including a fractional-N frequency synthesizer and a 6-bit Class-D digital power amplifier (DPA). The frequency range of the VCO is from 2.39 to 3.75 GHz, covering the working frequency band of the transmitter. The output carrier of the synthesizer is modulated by the coded data from the data processing unit (DPU). Then, the data are sent to the DPA for amplification, and finally transmitted

TABLE 4 | Comparison of the parameters of wireless power supplies.

	Piech et al., 2018	Jia et al., 2017	Mei et al., 2017	Lee et al., 2019	Kassiri et al., 2016	Lee et al., 2016	Lo et al., 2016
Power frequency (Hz)	1.85M	13.56M	346.6M	13.56M	1.5M	13.56M	2M
Distance (cm)	0.5	20	18	18	15	18	–
Coupling	Ultrasound	4 coils	3/4 coils	4 coils	2 coils	3/4 coils	2 coils
Recording	N/A	N/A	EEG	Spike	EEG	Spike	EMG
Stimulation	CCS	CCS	N/A	CCS	CCS	N/A	CCS
Uplink data	LSK	BLE	2.4 GHz RF	OOK/BLE	UWB/FSK	FSK	LSK/WiFi
Downlink data	OOK	BLE	N/A	BLE	ASK	N/A	DPSK/WiFi
Area (mm^2)	3.1 × 1.9 × 0.89	20 × 22 × 11	14 × 25 × 14	19 × 19 × 30	20 × 20	25 × 35 × 8	4.4 × 5.7
Power (mW)	0.15	43	6.4–13	35	6.9	51.4	–
Experiment area (cm^3)	N/A	20 × 46 × 20	61 × 61 × 30	24 × 46 × 20	26 × 45	30 × 28 × 18	0.5 × 0.5 × 0.5

to the SMD antenna for transmission. This structure is based on the interfacing system-on-a-chip (SoC) mode, which achieves a transmission rate of 54 Mbps and a transmission distance of 4 m. Due to the reservation of the wired communication for SPI interface, the circuit can only transmit unilateral wireless data (from inside to outside), which is not applicable for implantation.

Due to the lack of sufficient power budget and two-way wireless communication, most of these devices only support independent neural recording or stimulation function. It is necessary to combine the two functions. A SOC with four-coil inductive power supply is proposed (Lee et al., 2019), which integrates 32-channel neural recording and 4-channel stimulation circuits, and achieves a data transmission rate of 434 MHz. As shown in **Figure 6D**, the four-coil induction power supply mode improves the power efficiency, and the CC2540 micro-controller unit (MCU) connects the DC–DC converter to realize power control. SDR Rx is the external software-defined radio wideband receiver, and PA is a power amplifier. In addition, the MCU sends stimulation parameters and setting parameters to the headstage through the BLE link. The headstage includes a WINeRS-8 ASIC, a Schottky rectifier, an RX MCU (CC2541), and a 2.5-V LDO. The WINeRS-8 ASIC consists of 32-channel neural recording and 4-channel CCS circuits. Because the BLE link does not have enough transmission rate to meet 32-channel applications, a 434-MHz OOK transmitter is added to transmit AFE recorded data. The system integrates the functions of nerve recording and stimulation and achieves a high data transmission rate. However, the four-coil power supply mode limits its application, which can only be used in an energy cage formed by four coils. The BLE link is not based on peer-to-peer communication, but on multiple inputs to multiple outputs mode, which might be vulnerable to radio interference.

The implanted neural chip requires a wireless power supply and a wireless communication system. **Table 4** shows the comparison of the parameters of the circuits with wireless power supplies. The power frequency refers to the frequency of the alternating current (AC) of the induction link, and the external power supply is generally realized by using the inductive coils. The transmission distance is related to the size of the inductive coil, and the transmission distance ranging from 15 to 20 cm can be achieved in the prior works. According to the comparison in **Table 4**, only a few designs incorporate both the function of neural recording and stimulation in one implanted neural chip. The uplink data and downlink data are related to the data transmission mode between internal and external. With the increase of the number of channels, the data transmission rate also needs to be improved consistently.

DISCUSSION

Since several advances in neural recording and stimulation integrated circuits are introduced in this article, it is worthwhile to present a discussion about key indicators for the design, which will help the circuit designer improve the chip performances.

In the design of neural stimulators, the important parameters are safety and efficiency. The essence of stimulation is the injection and recovery of electric charge. For fragile nerves, excessive injection of electric charge will cause irreparable damage. Therefore, we need to restrict the stimulation current and reduce the influence of residual charge in the tissue. CCS is still the mainstream design for neural stimulation. In recent years, the combination of multiple control methods to reduce the residual charge has gradually become the mainstream. As for efficiency, the electrode voltage is highly dependent on the electrode impedance, so more energy loss will be generated. The generation of large energy in the form of heat could be harmful for the tissue around the implantable neural chips. How to effectively reduce heat generation is still an issue for implantable chip design.

For the design of neural recording, accuracy is a key parameter. Due to the small amplitude and low-frequency characteristics of neural signals, the difficulty of sampling is greatly increased. In addition, the impact of the stimulation artifact, the attenuation of neural signals, and the crosstalk of electrical signals are needed to be further researched. There are several irrelevant signals in the collected signals that are difficult to filter out. In the design process, both front-end processing and back-end adaptive filtering are the common ways to solve the problem. In the latest technology, the direct optimization of the AFE has the advantages of achieving high input impedance, high dynamic range, low power consumption, and small area, which would become the future development direction.

At present, the diversity and miniaturization of neural recording and stimulation circuits is a trend. For the requirement of chip implantability, due to the large volume of wired power supply, the application of wireless power supply is necessary. Through wireless transmission, the recorded data are transmitted to the computer terminal, and then the terminal transmits stimulation instructions back after computation. For multi-electrode recording demands, the transmission rate and transmission distance of wireless communication also need to be improved. The trade-off between area and power needs to be carefully considered for different applications. In addition, as the common-mode voltage affects the nerve signals recording, the technique of stimulation artifact suppression is still important to be further researched. The current solution could be divided into two aspects. One is the artifact suppression of the RFE, such as iterative hardware loops or RTPPS technology. The other is to sample the artifact signal followed by filtering or digital post-processing to get the complete neural signal at the neural recording site. The combination of the two schemes for artifact reduction could greatly improve the quality of neural recording in a closed-loop system.

CONCLUSION

In this article, the circuit structures and the latest technologies of neural recording and stimulation circuits are summarized. The key design directions of a closed-loop neural prosthesis chip and advances of neural recording and stimulation integrated circuits are introduced. Due to the different characteristics of neural recording and neural stimulation, we discuss the important parameters in the design process. The various latest technologies mentioned and an analysis of the future trend in this article could help the designers meet their performance requirements in future biomedical device development.

AUTHOR CONTRIBUTIONS

XL and TC: analysis of the electronic integrated circuits. WM, JL, and HY: parameters analysis and writing and revising of the manuscript. All authors contributed to the article and approved the submitted version.

FUNDING

This work was supported by the National Natural Science Foundation of China (Grant No. 61806012), the National Natural Science Foundation of China (NSFC) (Key Program, Grant No. 6203000189), the Innovative Team Program of Education Department of Guangdong Province (Grant No. 2018KCXTD028), the Shenzhen Science and Technology Program (Grant No. KQTD20200201130510 96), and the Key-Area Research and Development Program of Guangdong Province (Grant No. 2019B010142001).

REFERENCES

Ando, H., Takizawa, K., Yoshida, T., Matsushita, K., Hirata, M., and Suzuki, T. (2016). Wireless multichannel neural recording with a 128-Mbps UWB transmitter for an implantable brain-machine interfaces. *IEEE Trans. Biomed. Circ. Syst.* 10, 1068–1078. doi: 10.1109/TBCAS.2016.2514522

Asfour, A., Fiche, C., and Deransart, C. (2007). *"Dedicated electronics for electrical stimulation and EEG recording using the same electrodes: application to the automatic control of epileptic seizures by neurostimulation", in: 2007 IEEE Instrumentation & Measurement Technology Conference IMTC 2007*. New York: IEEE.

Blum, R. A., Ross, J. D., Brown, E. A., and DeWeerth, S. P. (2007). An integrated system for simultaneous, multichannel neuronal stimulation and recording. *IEEE Trans. Circ. Syst. I Regul. Papers* 54, 2608–2618. doi: 10.1109/TCSI.2007.906071

Bozorgzadeh, B., Covey, D. P., Howard, C. D., Garris, P. A., and Mohseni, P. (2014). A neurochemical pattern generator SoC with switched-electrode management for single-chip electrical stimulation and 9.3 μW, 78 pA rms, 400 V/s FSCV Sensing. *IEEE J. Solid-State Circ.* 49, 881–895. doi: 10.1109/jssc.2014.2299434

Brown, E. A., Ross, J. D., Blum, R. A., Yoonkey, N., Wheeler, B. C., and Deweerth, S. P. (2008). Stimulus-artifact elimination in a multi-electrode system. *IEEE Trans. Biomed. Circ. Syst.* 2, 10–21. doi: 10.1109/TBCAS.2008.918285

Butz, N., Taschwer, A., Nessler, S., Manoli, Y., and Kuhl, M. (2018). A 22 V compliant 56 μ W twin-track active charge balancing enabling 100% charge compensation even in monophasic and 36% amplitude correction in biphasic neural stimulators. *IEEE J. Solid-State Circ.* 53, 2298–2310. doi: 10.1109/jssc.2018.2828823

Caldwell, D. J., Ojemann, J. G., and Rao, R. P. N. (2019). Direct electrical stimulation in electrocorticographic brain-computer interfaces: enabling technologies for input to cortex. *Front. Neurosci.* 13:804. doi: 10.3389/fnins.2019.00804

Carmona, L., Diez, P. F., Laciar, E., and Mut, V. (2020). Multisensory stimulation and EEG recording below the hair-line: a new paradigm on brain computer interfaces. *IEEE Trans. Neural. Syst. Rehabil. Eng.* 28, 825–831. doi: 10.1109/TNSRE.2020.2979684

Chandrakumar, H., and Markovic, D. (2017). A high dynamic-range neural recording chopper amplifier for simultaneous neural recording and stimulation. *IEEE J. Solid-State Circ.* 52, 645–656. doi: 10.1109/jssc.2016.2645611

Chandrakumar, H., and Markovic, D. (2018). A 15.2-ENOB 5-kHz BW 4.5- μ W Chopped CT $\Delta\Sigma$ -ADC for artifact-tolerant neural recording front ends. *IEEE J. Solid-State Circ.* 53, 3470–3483. doi: 10.1109/jssc.2018.2876468

Changhyun, K., and Wise, K. D. (1996). A 64-site multishank CMOS low-profile neural stimulating probe. *IEEE J. Solid-State Circ.* 31, 1230–1238. doi: 10.1109/4.535406

Chen, K., Yang, Z., Hoang, L., Weiland, J., Humayun, M., and Liu, W. (2010). An integrated 256-channel epiretinal prosthesis. *IEEE J. Solid-State Circ.* 45, 1946–1956. doi: 10.1109/jssc.2010.2055371

Chen, T.-J., Jeng, C., Chang, S.-T., Chiueh, H., Liang, S.-F., Hsu, Y.-C., et al. (2011). *"A hardware implementation of real-time epileptic seizure detector on FPGA", in: 2011 IEEE Biomedical Circuits and Systems Conference (BioCAS)*. New York: IEEE.

Chen, Z. G., Liu, X., and Wang, Z. (2020). A charge balancing technique for neurostimulators. *Analog Integrated Circuits Signal Proces.* 105, 483–496. doi: 10.1007/s10470-020-01726-6

Chu, P., Muller, R., Koralek, A., Carmena, J. M., Rabaey, J. M., and Gambini, S. (2013). Equalization for intracortical microstimulation artifact reduction. *Annu. Int. Conf. IEEE Eng. Med. Biol. Soc.* 2013, 245–248. doi: 10.1109/EMBC.2013.6609483

Culaclii, S., Kim, B., Lo, Y. K., Li, L., and Liu, W. (2018). Online artifact cancelation in same-electrode neural stimulation and recording using a combined hardware and software architecture. *IEEE Trans. Biomed. Circuits Syst.* 12, 601–613. doi: 10.1109/TBCAS.2018.2816464

Dabbaghian, A., Yousefi, T., Fatmi, S. Z., Shafia, P., and Kassiri, H. (2019). A 9.2-g fully-flexible wireless ambulatory EEG monitoring and diagnostics headband with analog motion artifact detection and compensation. *IEEE Trans. Biomed. Circuits Syst.* 13, 1141–1151. doi: 10.1109/TBCAS.2019.2936327

Deprez, H., Gransier, R., Hofmann, M., van Wieringen, A., Wouters, J., and Moonen, M. (2017). Template subtraction to remove CI stimulation artifacts in auditory steady-state responses in CI subjects. *IEEE Trans. Neural. Syst. Rehabil. Eng.* 25, 1322–1331. doi: 10.1109/TNSRE.2016.2622979

Dura, B., Chen, M. Q., Inan, O. T., Kovacs, G. T., and Giovangrandi, L. (2012). High-frequency electrical stimulation of cardiac cells and application to artifact reduction. *IEEE Trans. Biomed. Eng.* 59, 1381–1390. doi: 10.1109/TBME.2012.2188136

Elyahoodayan, S., Jiang, W., Xu, H., and Song, D. (2019). A multi-channel asynchronous neurostimulator with artifact suppression for neural code-based stimulations. *Front. Neurosci.* 13:1011. doi: 10.3389/fnins.2019.01011

Erez, Y., Tischler, H., Moran, A., and Bar-Gad, I. (2010). Generalized framework for stimulus artifact removal. *J. Neurosci. Methods* 191, 45–59. doi: 10.1016/j.jneumeth.2010.06.005

Ha, S., Kim, C., Park, J., Cauwenberghs, G., and Mercier, P. P. (2019). A fully integrated RF-powered energy-replenishing current-controlled stimulator. *IEEE Trans. Biomed. Circ. Syst.* 13, 191–202. doi: 10.1109/TBCAS.2018.2881800

Harrison, R. R., and Charles, C. (2003). A low-power low-noise cmos for amplifier neural recording applications. *IEEE J. Solid-State Circ.* 38, 958–965. doi: 10.1109/jssc.2003.811979

Harrison, R. R., Watkins, P. T., Kier, R. J., Lovejoy, R. O., Black, D. J., Greger, B., et al. (2007). A low-power integrated circuit for a wireless 100-electrode neural recording system. *IEEE J. Solid-State Circ.* 42, 123–133. doi: 10.1109/jssc.2006.886567

Hsu, W. Y., and Schmid, A. (2017). Compact, energy-efficient high-frequency switched capacitor neural stimulator with active charge balancing. *IEEE Trans. Biomed. Circ. Syst.* 11, 878–888. doi: 10.1109/TBCAS.2017.2694144

Jeon, H., Bang, J.-S., Jung, Y., Choi, I., and Je, M. (2019). A high DR, DC-coupled, time-based neural-recording IC with degeneration R-DAC for bidirectional neural interface. *IEEE J. Solid-State Circ.* 54, 2658–2670. doi: 10.1109/jssc.2019.2930903

Jia, Y., Mirbozorgi, S. A., Wang, Z., Hsu, C. C., Madsen, T. E., Rainnie, D., et al. (2017). Position and orientation insensitive wireless power transmission for enercage-homecage system. *IEEE Trans. Biomed. Eng.* 64, 2439–2449. doi: 10.1109/TBME.2017.2691720

Jiang, W., Hokhikyan, V., Chandrakumar, H., Karkare, V., and Markovic, D. (2017). A ±50-mV linear-input-range VCO-based neural-recording front-end with digital nonlinearity correction. *IEEE J. Solid-State Circ.* 52, 173–184. doi: 10.1109/jssc.2016.2624989

Johnson, B. C., Gambini, S., Izyumin, I., Moin, A., Zhou, A., Alexandrov, G., et al. (2017). *"An implantable 700μW 64-channel neuromodulation IC for simultaneous recording and stimulation with rapid artifact recovery", in: 2017 Symposium on VLSI Circuits*. Honolulu: VLSIC.

Joseph, K., Mottaghi, S., Christ, O., Feuerstein, T. J., and Hofmann, U. G. (2018). When the ostrich-algorithm fails: blanking method affects spike train statistics. *Front. Neurosci.* 12:293. doi: 10.3389/fnins.2018.00293

Jun, J. J., Steinmetz, N. A., Siegle, J. H., Denman, D. J., Bauza, M., Barbarits, B., et al. (2017). Fully integrated silicon probes for high-density recording of neural activity. *Nature* 551, 232–236. doi: 10.1038/nature24636

Kassiri, H., Bagheri, A., Soltani, N., Abdelhalim, K., Jafari, H. M., Salam, M. T., et al. (2016). Battery-less Tri-band-Radio neuro-monitor and responsive neurostimulator for diagnostics and treatment of neurological disorders. *IEEE J. Solid-State Circ.* 51, 1274–1289. doi: 10.1109/jssc.2016.2528999

Kent, A. R., and Grill, W. M. (2011). Instrumentation to record evoked potentials for closed-loop control of deep brain stimulation. *Annu. Int. Conf. IEEE Eng. Med. Biol. Soc.* 2011, 6777–6780. doi: 10.1109/IEMBS.2011.6091671

Lancashire, H. T., Jiang, D., Demosthenous, A., and Donaldson, N. (2019). An ASIC for recording and stimulation in stacked microchannel neural interfaces. *IEEE Trans. Biomed. Circ. Syst.* 13, 259–270. doi: 10.1109/TBCAS.2019.2891284

Lee, B., Jia, Y., Mirbozorgi, S. A., Connolly, M., Tong, X., Zeng, Z., et al. (2019). An inductively-powered wireless neural recording and stimulation system for freely-behaving animals. *IEEE Trans. Biomed. Circ. Syst.* 13, 413–424. doi: 10.1109/TBCAS.2019.2891303

Lee, H.-M., Kwon, K. Y., Li, W., and Ghovanloo, M. (2015). A power-efficient switched-capacitor stimulating system for electrical/optical deep brain stimulation. *IEEE J. Solid-State Circ.* 50, 360–374. doi: 10.1109/jssc.2014.2355814

Lee, H. M., Park, H., and Ghovanloo, M. (2013). A power-efficient wireless system with adaptive supply control for deep brain stimulation. *IEEE J. Solid-State Circ.* 48, 2203–2216. doi: 10.1109/JSSC.2013.2266862

Lee, J. I., and Im, M. (2019). Optimal electric stimulus amplitude improves the selectivity between responses of ON Versus OFF types of retinal ganglion cells. *IEEE Trans. Neural. Syst. Rehabil. Eng.* 27, 2015–2024. doi: 10.1109/TNSRE.2019.2939012

Lee, S. B., Lee, B., Kiani, M., Mahmoudi, B., Gross, R., and Ghovanloo, M. (2016). An inductively-powered wireless neural recording system with a charge sampling analog front-end. *IEEE Sens. J.* 16, 475–484. doi: 10.1109/JSEN.2015.2483747

Lee, T., and Je, M. (2020). Double-high-pass-filter-based electrical-recording front-ends and fluorescence-recording front-ends for monitoring multimodal neural activity. *IEEE Trans. Circ. Syst. II Express Briefs* 67, 876–880. doi: 10.1109/tcsii.2020.2980009

Lin, C. Y., Chen, W. L., and Ker, M. D. (2013). Implantable stimulator for epileptic seizure suppression with loading impedance adaptability. *IEEE Trans. Biomed. Circ. Syst.* 7, 196–203. doi: 10.1109/TBCAS.2012.2200481

Lin, S. P., and Ker, M. D. (2020). Design of stage-selective negative voltage generator to improve on-chip power conversion efficiency for neuron stimulation. *IEEE Trans. Circ. Syst. I Regul. Papers* 67, 4122–4131. doi: 10.1109/TCSI.2020.3012086

Liu, W., Vichienchom, K., Clements, M., DeMarco, S. C., Hughes, C., McGucken, E., et al. (2000). A neuro-stimulus chip with telemetry unit for retinal prosthetic device. *IEEE J. Solid-State Circ.* 35, 1487–1497. doi: 10.1109/4.871327

Liu, X., Demosthenous, A., Jiang, D., Vanhoestenberghe, A., and Donaldson, N. (2011). *"A stimulator ASIC with capability of neural recording during inter-phase delay", in: 2011 Proceedings of the ESSCIRC (ESSCIRC)*. Kraków: ESSCIRC.

Liu, X., Huang, X., Jiang, Y., Xu, H., Guo, J., Hou, H. W., et al. (2017). A microfluidic cytometer for complete blood count with a 3.2-megapixel, 1.1-mum-pitch super-resolution image sensor in 65-nm BSI CMOS. *IEEE Trans. Biomed. Circ. Syst.* 11, 794–803. doi: 10.1109/TBCAS.2017.2697451

Lo, Y. K., Chang, C. W., Kuan, Y. C., Culaclii, S., Kim, B., Chen, K., et al. (2016). *"22.2 A 176-channel 0.5cm3 0.7g wireless implant for motor function recovery after spinal cord injury", in: 2016 IEEE International Solid-State Circuits Conference (ISSCC)*. New York: IEEE, 382–383.

Lyu, L., Ye, D., Xu, R., Mu, G., Zhao, H., Xiang, Y., et al. (2020). A fully-integrated 64-channel wireless neural interfacing SoC achieving 110 dB AFE PSRR and supporting 54 Mb/s symbol rate, meter-range wireless data transmission. *IEEE Trans. Circ. Syst. II Express Briefs* 67, 831–835. doi: 10.1109/tcsii.2020.2982208

Mahajan, R., and Morshed, B. I. (2015). Unsupervised eye blink artifact denoising of EEG data with modified multiscale sample entropy, Kurtosis, and wavelet-ICA. *IEEE J. Biomed. Health Inform.* 19, 158–165. doi: 10.1109/JBHI.2014.2333010

Mc Laughlin, M., Lu, T., Dimitrijevic, A., and Zeng, F. G. (2012). Towards a closed-loop cochlear implant system: application of embedded monitoring of peripheral and central neural activity. *IEEE Trans. Neural. Syst. Rehabil. Eng.* 20, 443–454. doi: 10.1109/TNSRE.2012.2186982

McGill, K. C., Cummins, K. L., Dorfman, L. J., Berlizot, B. B., Leutkemeyer, K., Nishimura, D. G., et al. (1982). On the nature and elimination of stimulus artifact in nerve signals evoked and recorded using surface electrodes. *IEEE Trans. Biomed. Eng.* 29, 129–137. doi: 10.1109/TBME.1982.325019

Mei, H., Thackston, K. A., Bercich, R. A., Jefferys, J. G., and Irazoqui, P. P. (2017). Cavity resonator wireless power transfer system for freely moving animal experiments. *IEEE Trans. Biomed. Eng.* 64, 775–785. doi: 10.1109/TBME.2016.2576469

Muller, R., Le, H.-P., Li, W., Ledochowitsch, P., Gambini, S., Bjorninen, T., et al. (2015). A minimally invasive 64-channel wireless μECoG implant. *IEEE J. Solid-State Circ.* 50, 344–359. doi: 10.1109/jssc.2014.2364824

Myers, F. B., Abilez, O. J., Zarins, C. K., and Lee, L. P. (2011). Stimulation and artifact-free extracellular electrophysiological recording of cells in suspension. *Annu. Int. Conf. IEEE Eng. Med. Biol. Soc.* 2011, 4030–4033. doi: 10.1109/IEMBS.2011.6091001

Nag, S., Sikdar, S. K., Thakor, N. V., Rao, V. R., and Sharma, D. (2015). Sensing of stimulus artifact suppressed signals from electrode interfaces. *IEEE Sens. J.* 15, 3734–3742. doi: 10.1109/jsen.2015.2399248

Ng, K. A., Liu, X., Zhao, J., Xuchuan, L., Yen, S.-C., Je, M., et al. (2012). *"An inductively powered CMOS multichannel bionic neural link for peripheral nerve function restoration", in: 2012 IEEE Asian Solid State Circuits Conference (A-SSCC)*. New York: IEEE.

Nikas, A., Jambunathan, S., Klein, L., Voelker, M., and Ortmanns, M. (2019). A continuous-time delta-sigma modulator using a modified instrumentation amplifier and current reuse DAC for neural recording. *IEEE J. Solid-State Circ.* 54, 2879–2891. doi: 10.1109/jssc.2019.2931811

Noorsal, E., Sooksood, K., Xu, H., Hornig, R., Becker, J., and Ortmanns, M. (2012). A neural stimulator frontend with high-voltage compliance and programmable pulse shape for epiretinal implants. *IEEE J. Solid-State Circ.* 47, 244–256. doi: 10.1109/jssc.2011.2164667

Olsson, R. H. III, Buhl, D. L., Sirota, A. M., Buzsaki, G., and Wise, K. D. (2005). Band-tunable and multiplexed integrated circuits for simultaneous recording and stimulation with microelectrode arrays. *IEEE Trans. Biomed. Eng.* 52, 1303–1311. doi: 10.1109/TBME.2005.847540

Ortmanns, M. (2007). *"Charging Balancing in Functional Electrical Stimulators: A Comparative Study", in: 2007 IEEE International Symposium on Circuits and Systems*. New York: IEEE.

Ortmanns, M., Rocke, A., Gehrke, M., and Tiedtke, H.-J. (2007). A 232-channel epiretinal stimulator ASIC. *IEEE J. Solid-State Circ.* 42, 2946–2959. doi: 10.1109/jssc.2007.908693

Park, S.-Y., Cho, J., Na, K., and Yoon, E. (2018). Modular 128-channel $\ Delta$ - $\ Delta \ Sigma$ analog front-end architecture using spectrum equalization scheme for 1024-channel 3-D neural recording microsystems. *IEEE J. Solid-State Circ.* 53, 501–514. doi: 10.1109/jssc.2017.2764053

Pazhouhandeh, M. R., Kassiri, H., Shoukry, A., Wesspapir, I., Carlen, P., and Genov, R. (2018). *"Artifact-tolerant opamp-less delta-modulated bidirectional neuro-interface", in: 2018 IEEE symposium on VLSI Circuits*. New York: IEEE.

Piech, D. K., Johnson, B. C., Shen, K., Ghanbari, M. M., and Muller, R. (2018). StimDust: A 2.2 mm3, precision wireless neural stimulator with ultrasonic power and communication. *arXiv Neurons Cogn.* **vol&pg,

Qiu, S., Feng, J., Xu, R., Xu, J., Wang, K., He, F., et al. (2015). A stimulus artifact removal technique for SEMG signal processing during functional electrical stimulation. *IEEE Trans. Biomed. Eng.* 62, 1959–1968. doi: 10.1109/TBME.2015.2407834

Ramezani, R., Liu, Y., Dehkhoda, F., Soltan, A., Haci, D., Zhao, H., et al. (2018). On-probe neural interface ASIC for combined electrical recording and optogenetic stimulation. *IEEE Trans. Biomed. Circ. Syst.* 12, 576–588. doi: 10.1109/TBCAS.2018.2818818

Reza Pazhouhandeh, M., Chang, M., Valiante, T. A., and Genov, R. (2020). Track-and-zoom neural analog-to-digital converter with blind stimulation artifact rejection. *IEEE J. Solid-State Circ.* 55, 1984–1997. doi: 10.1109/jssc.2020.2991526

Rolston, J. D., Gross, R. E., and Potter, S. M. (2009). NeuroRighter: closed-loop multielectrode stimulation and recording for freely moving animals and cell cultures. *Annu. Int. Conf. IEEE Eng. Med. Biol. Soc.* 2009, 6489–6492. doi: 10.1109/IEMBS.2009.5333589

Rolston, J. D., Gross, R. E., and Potter, S. M. (2010). Closed-loop, open-source electrophysiology. *Front. Neurosci.* 4:31. doi: 10.3389/fnins.2010.00031

Rothermel, A., Liu, L., Aryan, N. P., Fischer, M., Wuenschmann, J., Kibbel, S., et al. (2009). A CMOS chip with active Pixel Array and specific test features for subretinal implantation. *IEEE J. Solid-State Circ.* 44, 290–300. doi: 10.1109/jssc.2008.2007436

Rozgic, D., Hokhikyan, V., Jiang, W., Akita, I., Basir-Kazeruni, S., Chandrakumar, H., et al. (2019). A 0.338 cm(3), artifact-free, 64-contact neuromodulation platform for simultaneous stimulation and sensing. *IEEE Trans. Biomed. Circ. Syst.* 13, 38–55. doi: 10.1109/TBCAS.2018.2889040

Sadeghi Najafabadi, M., Chen, L., Dutta, K., Norris, A., Feng, B., Schnupp, J. W. H., et al. (2020). Optimal multichannel artifact prediction and removal for neural stimulation and brain machine interfaces. *Front. Neurosci.* 14:709. doi: 10.3389/fnins.2020.00709

Samiei, A., and Hashemi, H. (2019). A chopper stabilized, current feedback, neural recording amplifier. *IEEE Solid-State Circ. Lett.* 2, 17–20. doi: 10.1109/lssc.2019.2916754

Samiei, A., and Hashemi, H. (2021). A bidirectional neural interface SoC with adaptive IIR stimulation artifact cancelers. *IEEE J. Solid-State Circ.* 56, 2142–2157. doi: 10.1109/jssc.2021.3056040

Shen, L., Lu, N., and Sun, N. (2018). A 1-V 0.25-μW inverter stacking amplifier with 1.07 noise efficiency factor. *IEEE J. Solid-State Circ.* 53, 896–905. doi: 10.1109/jssc.2017.2786724

Song, K., Lee, H., Hong, S., Cho, H., Ha, U., and Yoo, H. J. (2012). A sub-10 nA DC-balanced adaptive stimulator IC with multi-modal sensor for compact electro-acupuncture stimulation. *IEEE Trans. Biomed. Circ. Syst.* 6, 533–541. doi: 10.1109/TBCAS.2012.2232292

Sooksood, K., Noorsal, E., Becker, J., and Ortmanns, M. (2011). *"A neural stimulator front-end with arbitrary pulse shape, HV compliance and adaptive supply requiring 0.05mm in 0.35 μm HVCMOS", in: 2011 IEEE International Solid-State Circuits Conference*. New York: IEEE.

Sooksood, K., Stieglitz, T., and Ortmanns, M. (2010). An active approach for charge balancing in functional electrical stimulation. *IEEE Trans. Biomed. Circ. Syst.* 4, 162–170. doi: 10.1109/TBCAS.2010.2040277

Steinmetz, N. A., Aydin, C., Lebedeva, A., Okun, M., Pachitariu, M., Bauza, M., et al. (2021). Neuropixels 2.0: A miniaturized high-density probe for stable, long-term brain recordings. *Science* 372:6539. doi: 10.1126/science.abf4588

Uehlin, J. P., Smith, W. A., Pamula, V. R., Pepin, E. P., Perlmutter, S., Sathe, V., et al. (2020). A single-chip bidirectional neural interface with high-voltage stimulation and adaptive artifact cancellation in standard CMOS. *IEEE J. Solid-State Circ.* 55, 1749–1761. doi: 10.1109/jssc.2020.2991524

van Dongen, M. N., Hoebeek, F. E., Koekkoek, S. K. E., De Zeeuw, C. I., and Serdijn, W. A. (2015). High frequency switched-mode stimulation can evoke post synaptic responses in cerebellar principal neurons. *Front. Neuroeng.* 8:2. doi: 10.3389/fneng.2015.00002

Venkatraman, S., Elkabany, K., Long, J. D., Yao, Y., and Carmena, J. M. (2009). A system for neural recording and closed-loop intracortical microstimulation in awake rodents. *IEEE Trans. Biomed. Eng.* 56, 15–22. doi: 10.1109/TBME.2008.2005944

Wagner, L., Maurits, N., Maat, B., Baskent, D., and Wagner, A. E. (2018). The cochlear implant EEG artifact recorded from an artificial brain for complex acoustic stimuli. *IEEE Trans. Neural. Syst. Rehabil. Eng.* 26, 392–399. doi: 10.1109/TNSRE.2018.2789780

Wei-Ming, C., Herming, C., Tsan-Jieh, C., Chia-Lun, H., Chi, J., Shun-Ting, C., et al. (2013). *"A fully integrated 8-channel closed-loop neural-prosthetic SoC for real-time epileptic seizure control", in: 2013 IEEE International Solid-State Circuits Conference Digest of Technical Papers*. New York: IEEE.

Wise, K. D., Anderson, D. J., Hetke, J. F., Kipke, D. R., and Najafi, K. (2004). Wireless implantable microsystems: high-density electronic interfaces to the nervous system. *Proc. IEEE* 92, 76–97. doi: 10.1109/jproc.2003.820544

Wong, Y. T., Dommel, N., Preston, P., Hallum, L. E., Lehmann, T., Lovell, N. H., et al. (2007). Retinal neurostimulator for a multifocal vision prosthesis. *IEEE Trans. Neural. Syst. Rehabil. Eng.* 15, 425–434. doi: 10.1109/TNSRE.2007.903958

Xu, L., Lei, Y., Peng, L., Lei, L., Xiaodan, Z., Minkyu, J., et al. (2017). An artifact-suppressed stimulator for simultaneous neural recording and stimulation systems. *Annu. Int. Conf. IEEE Eng. Med. Biol. Soc.* 2017, 2118–2121. doi: 10.1109/EMBC.2017.8037272

Xu, Y. P., Yen, S. C., Ng, K. A., Liu, X., and Tan, T. C. (2012). A bionic neural link for peripheral nerve repair. *Annu. Int. Conf. IEEE Eng. Med. Biol. Soc.* 2012, 1335–1338. doi: 10.1109/EMBC.2012.6346184

Yao, L., Li, P., and Je, M. (2015). *"A pulse-width-adaptive active charge balancing circuit with pulse-insertion based residual charge compensation and quantization for electrical stimulation applications", in: 2015 IEEE Asian Solid-State Circuits Conference (A-SSCC)*. New York: IEEE.

Yen, T. Y., and Ker, M. D. (2020). Design of dual-mode stimulus chip with built-in high voltage generator for biomedical applications. *IEEE Trans. Biomed. Circ. Syst.* 14, 961–970. doi: 10.1109/TBCAS.2020.2999398

Yi, X., Jia, J., Deng, S., Shen, S. G., Xie, Q., and Wang, G. (2013). A blink restoration system with contralateral EMG triggered stimulation and real-time artifact blanking. *IEEE Trans. Biomed. Circ. Syst.* 7, 140–148. doi: 10.1109/TBCAS.2013.2255051

Yochum, M., and Binczak, S. (2015). A wavelet based method for electrical stimulation artifacts removal in electromyogram. *Biomed. Signal. Proces. Control* 22, 1–10. doi: 10.1016/j.bspc.2015.06.007

Yoshida, K., and Horch, K. (1996). Closed-loop control of ankle position using muscle afferent feedback with functional neuromuscular stimulation. *IEEE Trans. Biomed. Eng.* 43, 167–176. doi: 10.1109/10.481986

Yu, H., Yan, M., and Huang, X. (2018). *CMOS Integrated Lab-on-a-Chip System for Personalized Biomedical Diagnosis*. Hoboken, NJ: Wiley-IEEE Press.

Yung-Chan, C., Yu-Tao, L., Yeh, S.-R., and Hsin, C. (2009). *"A bidirectional, flexible neuro-electronic interface employing localised stimulation to reduce artifacts", in: 2009 4th International IEEE/EMBS Conference on Neural Engineering*. New York: IEEE.

Żebrowska, M., Dzwiniel, P., and Waleszczyk, W. J. (2020). Removal of the sinusoidal transorbital alternating current stimulation artifact from simultaneous EEG recordings: effects of simple moving average parameters. *Front. Neurosci.* 14:735. doi: 10.3389/fnins.2020.00735

Zoladz, M., Kmon, P., Grybos, P., Szczygiel, R., Kleczek, R., Otfinowski, P., et al. (2012). Design and measurements of low power multichannel chip for recording and stimulation of neural activity. *Annu. Int. Conf. IEEE Eng. Med. Biol. Soc.* 2012, 4470–4474. doi: 10.1109/EMBC.2012.6346959

Zou, X., Xu, X., Yao, L., and Lian, Y. (2009). A 1-V 450-nW fully integrated programmable biomedical sensor interface chip. *IEEE J. Solid-State Circ.* 44, 1067–1077. doi: 10.1109/jssc.2009.2014707

Conflict of Interest: The authors declare that the research was conducted in the absence of any commercial or financial relationships that could be construed as a potential conflict of interest.

Publisher's Note: All claims expressed in this article are solely those of the authors and do not necessarily represent those of their affiliated organizations, or those of the publisher, the editors and the reviewers. Any product that may be evaluated in this article, or claim that may be made by its manufacturer, is not guaranteed or endorsed by the publisher.

frontiers in Neuroscience

ORIGINAL RESEARCH
published: 16 August 2021
doi: 10.3389/fnins.2021.718478

A Wireless Electro-Optic Platform for Multimodal Electrophysiology and Optogenetics in Freely Moving Rodents

Guillaume Bilodeau[1*†], *Gabriel Gagnon-Turcotte*[1†], *Léonard L. Gagnon*[1], *Iason Keramidis*[2], *Igor Timofeev*[2], *Yves De Koninck*[2], *Christian Ethier*[2] *and Benoit Gosselin*[1,2]

[1] *Smart Biomedical Microsystems Laboratory, Department of Electrical Engineering, Université Laval, Québec, QC, Canada,*
[2] *Department of Psychiatry and Neuroscience, CERVO Brain Research Centre, Université Laval, Québec, QC, Canada*

OPEN ACCESS

Edited by:
Takashi Tokuda,
Tokyo Institute of Technology, Japan

Reviewed by:
Vassiliy Tsytsarev,
University of Maryland, College Park, United States
Xin Liu,
University of California, San Diego, United States

***Correspondence:**
Guillaume Bilodeau
guillaume.bilodeau.3@ulaval.ca

[†] These authors have contributed equally to this work and share first authorship

Specialty section:
This article was submitted to Neural Technology, a section of the journal Frontiers in Neuroscience

Received: *31 May 2021*
Accepted: *19 July 2021*
Published: *16 August 2021*

Citation:
Bilodeau G, Gagnon-Turcotte G, Gagnon LL, Keramidis I, Timofeev I, De Koninck Y, Ethier C and Gosselin B (2021) A Wireless Electro-Optic Platform for Multimodal Electrophysiology and Optogenetics in Freely Moving Rodents. Front. Neurosci. 15:718478. doi: 10.3389/fnins.2021.718478

This paper presents the design and the utilization of a wireless electro-optic platform to perform simultaneous multimodal electrophysiological recordings and optogenetic stimulation in freely moving rodents. The developed system can capture neural action potentials (AP), local field potentials (LFP) and electromyography (EMG) signals with up to 32 channels in parallel while providing four optical stimulation channels. The platform is using commercial off-the-shelf components (COTS) and a low-power digital field-programmable gate array (FPGA), to perform digital signal processing to digitally separate in real time the AP, LFP and EMG while performing signal detection and compression for mitigating wireless bandwidth and power consumption limitations. The different signal modalities collected on the 32 channels are time-multiplexed into a single data stream to decrease power consumption and optimize resource utilization. The data reduction strategy is based on signal processing and real-time data compression. Digital filtering, signal detection, and wavelet data compression are used inside the platform to separate the different electrophysiological signal modalities, namely the local field potentials (1–500 Hz), EMG (30–500 Hz), and the action potentials (300–5,000 Hz) and perform data reduction before transmitting the data. The platform achieves a measured data reduction ratio of 7.77 (for a firing rate of 50 AP/second) and weights 4.7 g with a 100-mAh battery, an on/off switch and a protective plastic enclosure. To validate the performance of the platform, we measured distinct electrophysiology signals and performed optogenetics stimulation *in vivo* in freely moving rondents. We recorded AP and LFP signals with the platform using a 16-microelectrode array implanted in the primary motor cortex of a Long Evans rat, both in anesthetized and freely moving conditions. EMG responses to optogenetic Channelrhodopsin-2 induced activation of motor cortex *via* optical fiber were also recorded in freely moving rodents.

Keywords: electrophysiology, optogenetics, photostimulation, freely moving, digital signal processing, wireless, implantable device

1. INTRODUCTION

New tools to study the brain microcircuits of laboratory animals are highly sought after to advance our knowledge of the brain physiology and pathology. The rapid development in optogenetics and electrophysiology have allowed a wide array of different experimental approaches to better understand neural circuits (Balasubramaniam et al., 2018). Optogenetics allows the control of specific genetically modified neurons by light, which improves neural stimulation selectivity and avoids interference with parallel electrophysiological recordings compared to electrical stimulation. Small wireless implantable platforms combining both optogenetic stimulation with electrophysiological recording capability have been designed to study the brain dynamics in small laboratory animals (Gagnon-Turcotte et al., 2017a, 2020; Mesri et al., 2018; Bilodeau et al., 2020). However, performing high-resolution electrophysiology recordings and optical stimulation in small freely moving animal without interfering with their natural behavior remains challenging (Buzsáki et al., 2015).

Assessing multiple electrophysiological signal modalities in parallel is a critical requirement in several experimental settings (Mehring et al., 2003; Jackson et al., 2006; Ethier and Miller, 2015; Watson et al., 2018). Simultaneous recording of LFP and AP signals is crucial in understanding their respective roles, relations, and complementarity (Watson et al., 2018). The information extracted from these two distinct signal modalities has shown to yield better prediction results during reach and grasp tasks in non-human primates (Mehring et al., 2003; Abbaspourazad et al., 2021). Moreover, the development of reliable brain machine interfaces often require to perform parallel recording and stimulation in the motor cortex or other brain structures, while monitoring the EMG signals in muscles (Jackson et al., 2006; Ethier and Miller, 2015). LFP and AP signals are typically recorded from the same electrode implanted in the central nervous system, while EMG is recorded from a separate electrode inserted in the muscle or located under the skin. The amplitudes and frequency bands of AP, LFP, and EMG, respectively range from 300 to 5,000 Hz and 50 to 500 μV (Liu et al., 2013), 1 to 500 Hz and 250 to 5,000 μV (Soltani et al., 2019), and 10 to 300 Hz and 50 to 500 μV (Soltani et al., 2019). Capturing all these waveforms concurrently requires a dedicated strategy. A minimum sampling rate of 10 kS/s is needed, while 25 kS/s is most desirable (Gagnon-Turcotte et al., 2017b), which can produce very high data rates that cannot be handled with low power telemetry in a system including multiple channels. Recording the full neural signal bandwidth on 32 channels in parallel, at 20 kS/s and on 16 bits yields a data rate above 10.24 Mb/s, which cannot be supported by low-power BLE transceivers. Data reduction and/or data compression strategies have proven essential to increase the channel count and resolution, while decreasing the size and the power consumption of such resources constrained devices.

Since the APs are discreet events with high frequency content, data reduction methods mainly focus on this specific modality (Wu and Tang, 2011; Liu et al., 2013; Gagnon-Turcotte et al., 2017b), but each modality has its specific characteristics requiring a custom data reduction scheme. For instance, AP data reduction often initiates by performing high-pass filtering and signal detection (Wu and Tang, 2011; Liu et al., 2013) using a fixed or a dynamic threshold which cannot be performed on continuous low-frequency signals such as LFP. Only the detected APs are transmitted in this scheme, which can greatly reduce the data rate. A combination of AP detection and data compression can yield compression ratios (CR) above 500 (Gagnon-Turcotte et al., 2017b). This type of method, known as *activity dependent* reduction method, can significantly decrease the amount of data, but requires the signal to be high-pass filtered to avoid any LFP contamination, thus, in this approach, the LFPs, which lies at low frequencies, must be separated from the APs right at the beginning.

Neural signal recording systems that rely on custom integrated circuits (IC), often use a sophisticated analog signal processing front-end including different types of analog filters to isolate the preferred signal band directly before digitization (Wu and Tang, 2011; Biederman and al., 2015; Kassiri et al., 2017; Lopez et al., 2017; Gagnon-Turcotte et al., 2018). These solutions can be really effective when recording within only one signal band, or when the data rate is not representing a bottle neck, as it is the case in tethered settings. A custom IC using one dedicated filter and one analog-to-digital converter (ADC) per signal modality has been described before (Liu et al., 2017). This solution, which aims at performing closed-loop control, is trading signal integrity for extracted features. The solutions presented in Perelman and Ginosar (2005) and Bihr and Ortmanns (2012) both use custom chips including two separation filters and 2 ADCs per channel to capture the two separate bands i.e., low- and high-frequency bands simultaneously. This is because the amplitude of the LFP signals can be 10 times higher than the amplitude of extracellularly recorded AP signals. The dynamic range can then be optimized *a posteriori* to reduce the number of bits needed for each modality. However, this approach is limited to only small data reduction factors (e.g., RD < 2 for APs as shown in Bihr and Ortmanns, 2012) at the cost of a lot of additional hardware. Additionally, custom chip solutions typically require longer development time compared to COTS solutions.

Wavelet compression has been applied to AP before in real-time (Schmale et al., 2013; Gagnon-Turcotte et al., 2018). The study presented in Schmale et al. (2013) provides a comparison to determine the best suited wavelet to process AP and LFP, but does not provide insight on how to utilize the results inside a miniaturized device. In contrast, Gagnon-Turcotte et al. (2018) has demonstrated a fully integrated wavelet detection and compression core embedded inside a 10-channel electrophysiology chip for recording AP and LFP separately, but this system cannot capture AP and LFP simultaneously, and was not validated in freely moving rodents.

Here, we present the design of a wireless electro-optic platform providing multimodal electrophysiology recording from 32 channels as well as optogenetic stimulation, and its validation in freely moving laboratory animals. The presented platform, which is based on commercial off-the-shelf components, can (i) extract AP, LFP and/or EMG signals concurrently, over 32 channels, (ii) perform optogenetics

stimulation over four channels along with the electrophysiology recording, and (iii) be utilized in freely moving rodents without any hardwired connection. The system includes a real time digital signal processing core running on a low-power FPGA embedded in the platform to detect and separate the different signal modalities on the fly, and a data compression core to increase the resolution. We validated the system *in vivo* in both anesthetized and freely moving rodents and showed that the system can separate different types of electrophysiological waveforms simultaneously while compressing and transmitting the data wirelessly and in real time.

2. MATERIALS AND METHODS

2.1. System Overview

The concept of the proposed wireless electro-optic platform is shown in **Figure 1A**. A detachable platform is connected to an implantable interface, i.e., an optrode or a microelectrode array (**Figure 1B**), which is secured on the head of a laboratory animal. It can record different types of electrophysiology signals using up to 32 microelectrodes in parallel at 20 ksps (16-bits per samples), and perform optical stimulation using four fiber-coupled LEDs. The presented platform improves the system described in Gagnon-Turcotte et al. (2017b) with a new signal processing core to capture simultaneously multiple electrophysiology signal modalities and a new light-weight format. Additionally, the platform was tested with freely moving rodents. It includes a robust digital signal processing strategy to capture and separate the electrophysiological signal modalities, i.e., LFP/EMG and AP on the fly. Separating these signals in multiple paths inside the system allows to decrease the data rate and the power consumption by performing signal detection and wavelet compression inside the low-power embedded FPGA. Using multiple data paths to separate both LFP and AP inside the platform is the key to perform AP detection and data compression in this design. The system includes a new strategy to extract three signal modalities (i.e., AP, LFP, and EMG) in parallel within the same system. The platform benefits from an optimized integration strategy leveraging a lightweight printed circuit board and a low-power FPGA to implement the custom digital signal processing cores.

The platform encompasses four main building blocks implemented on a rigid-flex printed circuit board (PCB) including (1) a RHD2132 neural recording interface from *Intan Technologies*, USA, (2) a AS1109 4-channel precise LED driver for optical stimulation from *AMS*, Austria, (3) a nRF24l01p 2 Mbps (on-air) wireless transceiver from *Nordic Semiconductor*, Norway, and (4) a small-sized Spartan-6 (XC6LSX16, 8 × 8 mm^2 196-CSPBGA package) low-power field-programmable gate array (FPGA) from *Xilinx*, USA.

2.1.1. Neural Recording Interface

The RHD2132 from *Intan Technologies* provides the platform with a 32-channel neural recording interface which can collect differential signal from 32 electrodes and a common reference, with a maximum amplitude of −5 to 5 mV and a sampling rate of up to 30 ksps. The low-pass cutoff frequency of the bandpass filter is configurable from 100 Hz to 20 kHz, while the high-pass is configurable from 0.1 to 500 Hz, which allows targeting a wide range of electrophysiology signals. It should be noted that every channel reuses the same bandpass filter parameters. The chip uses a small 56 pins QFN package, the size of which is only 8 × 8 mm^2.

2.1.2. Optical Stimulation

The optical stimulation module uses the AS1109 LED driver circuit from *AMS, Austria* which can drive up to 8 LEDs. Each output channel of the chip can supply 0.5–100 mA with a 8-bits resolution. Each LED is driven by two driver output channels in parallel to provide a maximum current of 200 mA to each LED. The system can use 8 LEDs, like the LB G6SP from OSRAM Opto Semiconductors, which can deliver 250 mW/mm^2 at the output of the optical fiber (Gagnon-Turcotte et al., 2017b) when a driving current of 150 mA is provided by the LED driver, for triggering neuronal activity in transgenic animals over-expressing an opsin (LeChasseur et al., 2011). The AS1109 LED driver uses a pins QFN package, the size of which is only 4 × 4 mm.

2.1.3. Wireless Transceiver

The platform uses a nRF24l01p wireless transceiver chip from *Nordic Semiconductor*. This transceiver uses a center frequency of 2.45 GHz in the corresponding Industrial, scientific and medical frequency band and a custom protocol by *Nordic Semiconductor*. It provides a maximum data rate of 2 Mbps in the air, a 11.3 mA current in data transmitting mode and 13.5 mA in receiving mode at 2 Mbps. This wireless transceiver chip allows flexibility with respect to the communication protocol and provides a high effective data rate of up to 1.4 Mbps (Gagnon-Turcotte et al., 2017b) for a low-power consumption. This chip uses a 20 pins QFN package, the size of which is only 4 × 4 mm.

2.1.4. Digital Signal Processing Cores

In this design, a the XC6SLX16 Spartan 6 FPGA from *Xilinx Inc, USA* is utilized to perform signal processing inside the platform in real-time. A custom DSP core module developed and described previously by our group (Gagnon-Turcotte et al., 2017b; Bilodeau et al., 2020) is used to perform signal separation of the LFP, EMG, and AP and AP detection and wavelet signal compression. The FPGA controls all the custom digital cores as well as other modules and chips, i.e., the neural interface, the wireless transceiver and the optical stimulation, using a *Microblaze* microcontroller (MCU) softcore. The block diagram of the system along with the internal modules implemented inside the FPGA are depicted in **Figure 1B**.

2.1.5. PCB System Design

The platform was implemented on a thin rigid-flex printed circuit board as shown in **Figure 2A**. Since the system is designed for enabling experiments in small rodents, it has a low weight (<3.5 g; Gagnon-Turcotte et al., 2017a) and provides sufficient autonomy to accommodate different types of behavioral experiments (30–60 min). All components are mounted on a rigid-flex PCB including two rigid sections and a flexible section. The top rigid section holds the low-power transceiver and the FPGA, while the bottom rigid section holds

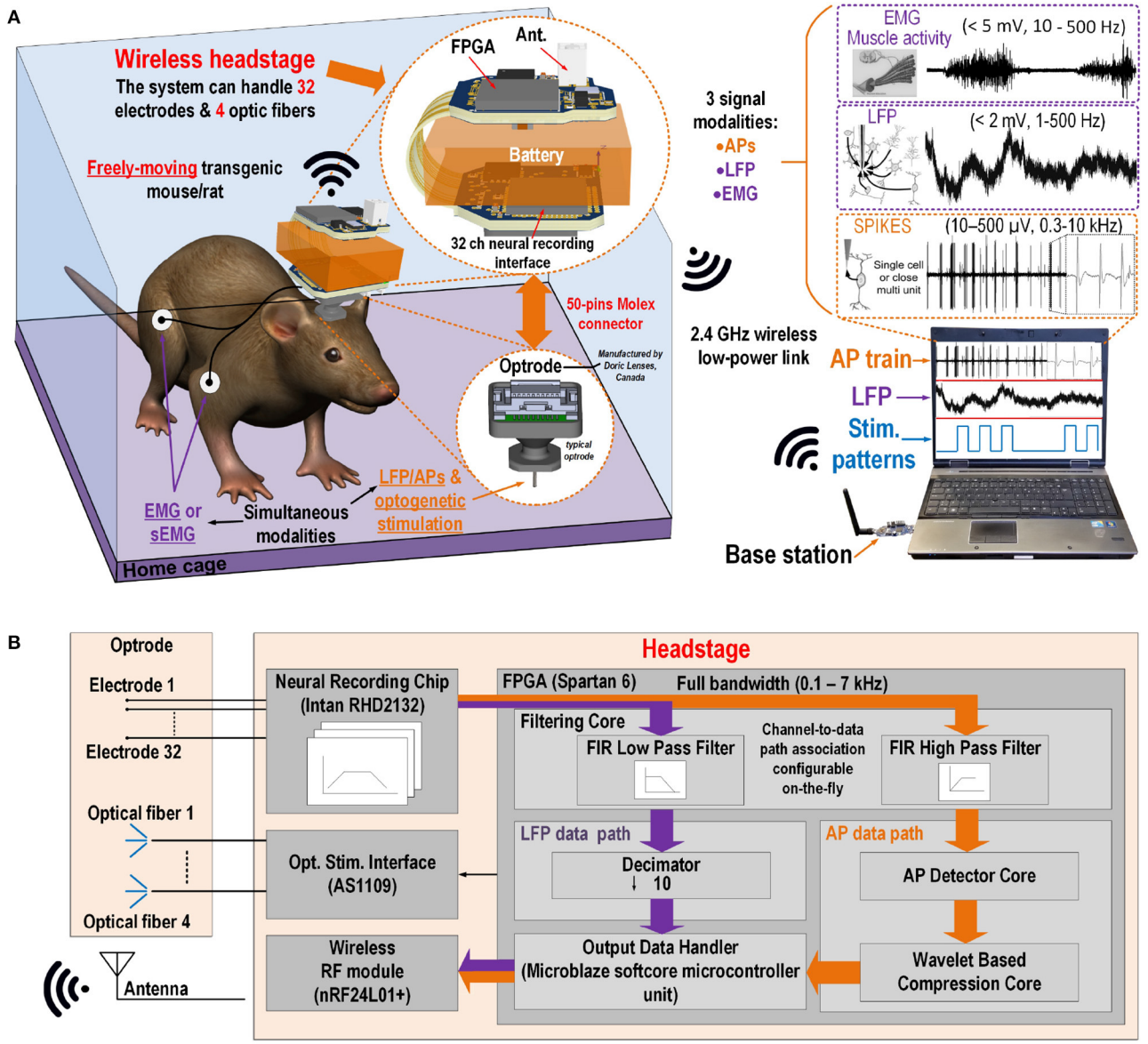

FIGURE 1 | (A) On the left, the concept of the platform connected on an optrode secured on the head of a rodent and to EMG electrodes going to its arm. On the right, the base station with the computer host communicating with the platform. **(B)** System level concept of the platform.

the optical stimulator components (i.e., the LED driver), the neural recording interface and a Molex connector (#0559090574) for connecting the system to an optrode (see **Figure 1B**). The rigid sections are connected to each other using flexible sections. The system is folded around the battery to achieve a very compact size (**Figure 2B**). The final weight of the system is 4.68 g including a 100 mAh battery (Model 051417, MYD Technology), a plastic packaging and an on/off switch. The electronic system represents only 36% of the total weight (∼ 1.7 g), thus lower final weight can be achieved by reducing the battery size and capacity and/or by removing the protective plastic. This specific packaging and battery size are suited for experimental settings involving live laboratory mice or rats.

2.2. Multimodal Extraction Strategy

Our signal extraction strategy allows collecting AP, LFP, and EMG signals in parallel using all or a subset of the 32 channels available.

The separation strategy uses both the analog filters inside the RHD2132 neural recording interface and the digital filters implemented inside the FPGA using Xilinx's IP core. Two types of digital filters are utilized: (1) a high pass filter to extract the AP signal and (2) a low pass filter to extract the low frequency signals (LFP/EMG). The same filter design is used both for the LFP and the EMG for preserving the signal integrity, while the sampling rate of the system is set to 20 ksps ($4 > 2 \times$ the AP bandwidth) for all signal modalities. Then, the LFP/EMG signals are decimated by a factor of 10 (2 ksps). The

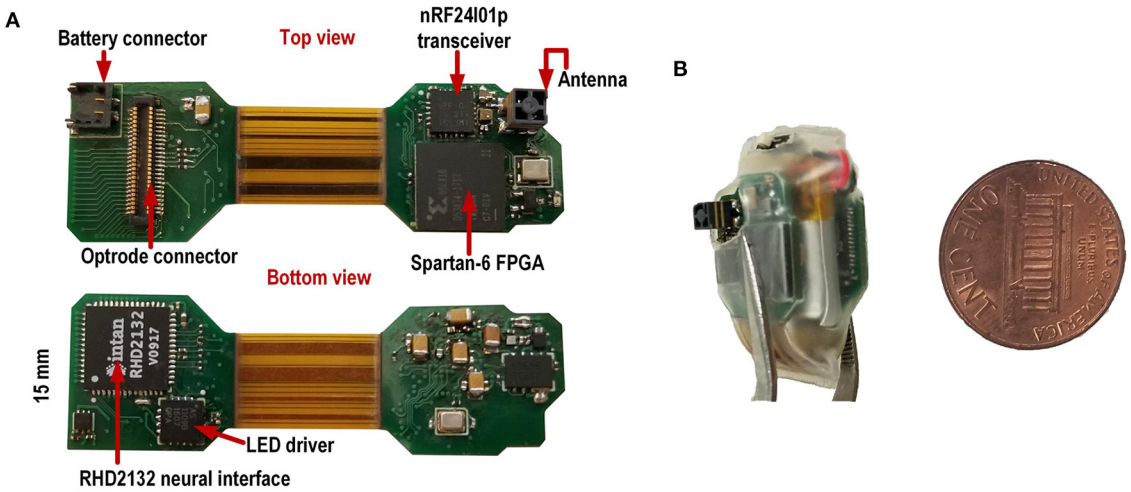

FIGURE 2 | (A) Two-sided view of the rigid-flex PCB when not folded. **(B)** System in its plastic enclosure.

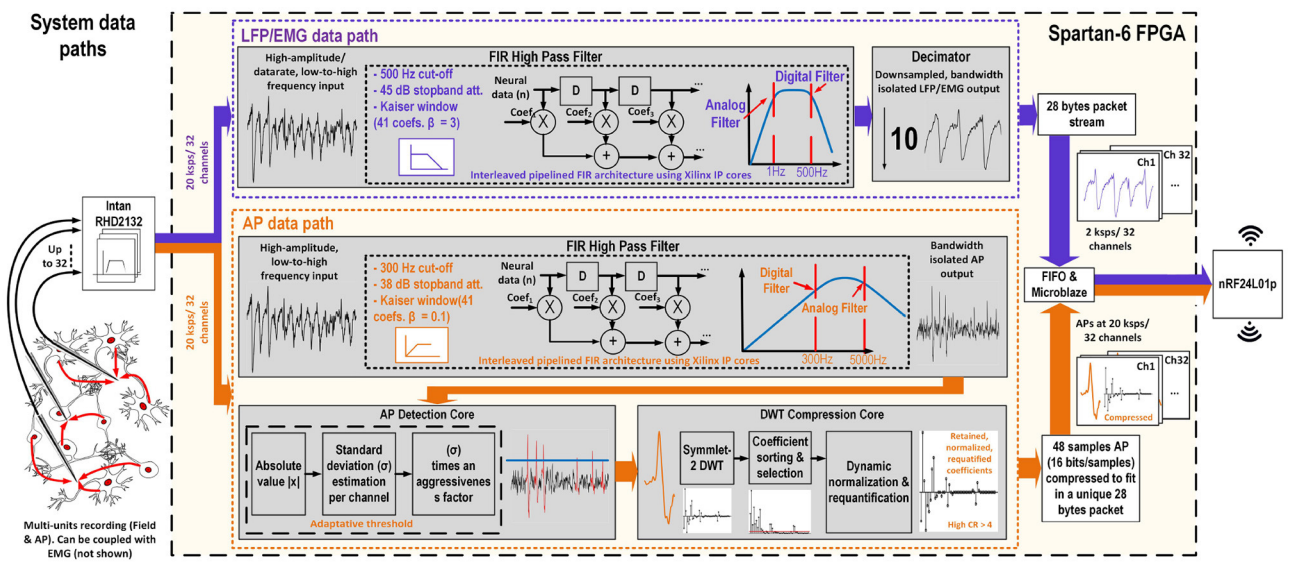

FIGURE 3 | Block diagram of the platform illustrating the data paths for both AP and LFP/EMG signals, and showing the ideal output frequency response for both data paths on the right hand side.

data flow for the AP and the LFP/EMG data is illustrated in **Figure 3**.

First, a tunable analog band-pass filter (0.25–500 Hz 1st order high-pass and 0.1–20 kHz 3rd order Butterworth low-pass) implemented inside the neural recording interface is applied to the neural signal in order to remove any DC offset voltage coming from the electrodes polarization, drift, or high frequency noise and to avoid any aliasing. Then, the FPGA separates the low-frequency from the high-frequency i.e., the AP bands and processes the signals inside two distinct data paths implemented inside the FPGA, as shown in **Figure 3**. The data paths can be described as follow:

- **High frequency band data path for AP signal processing and extraction**: The raw signal is passed through a finite impulse response (FIR) high-pass filter including 41 symmetrical coefficients to remove any frequencies below 300 Hz. The high-pass filtered AP signal is then sent to the AP detection core. Then, the detected and compressed APs are buffered into a FIFO before being sent to the wireless transceiver over the SPI bus. This path corresponds to the bottom branch in **Figure 3**.
- **Low-frequency band data path for LFP and EMG signal processing and extraction**: The raw signal is passed through a FIR low-pass filter including 39 symmetrical coefficients to

remove any frequency content above 500 Hz. The filtered LFP/EMG signal is then decimated by a factor of 10, to bring its sampling rate down to 2 ksps. The decimated signal is then buffered before being sent to the wireless transceiver. This path is presented in the top branch in **Figure 3**.

2.2.1. FIR Filters Implementation

The filter designs are optimized to reduce the area utilization inside the FPGA. Since the LFP/EMG signal amplitude is roughly 10 times larger than the AP signal (a little more in the case of the EMG), the AP high pass filter poses an optimization challenge. The stop band attenuation and the filter main lobe width must be optimized to remove any LFP signal at lower frequencies. However, since the FPGA has limited resources and the filtering has to be done in real time, the number of coefficients in the filter is limited, which in turn limits the stop band attenuation and the main lobe width. On the one hand, an optimization must be done to get the maximum number of filter coefficients without generating a delay larger than the sampling frequency. Additionally, the stop band attenuation at low frequencies must be sufficient to remove any other signal modalities, the amplitude of which would be bigger than the APs, so the AP detector can work properly. On the other hand, the main design parameters of the LFP/EMG filter are the *stop band attenuation* and the *number of coefficients*. The signal processing inside the FPGA and the window design must be optimized to meet these design requirements.

Performing all signal processing and system management inside the platform, requires a minimization of the area utilized in order to fit inside the limited FPGA resources, and to reduce power consumption. Therefore, both low and high pass FIR filters, are implemented by reusing the same data path for the 32 channels through a multiplexing scheme. This way, memory and logic blocks utilization is reduced compared to a parallel implementation, which would result in twice the resource used for each additional channel. In addition, the total latency, meaning the time needed to process 32 channels, should be kept lower than one sampling period ($1/20kHz$). Since the FPGA clock (f_{CLK}) is set to 20 MHz, we can estimate the maximum number of clock cycles (N_{CYCLES}) needed for processing one single sample as follows:$N_{CYCLES} = f_{CLK}/(f_s * 32)$. This leads to a maximum processing time of 31.25 clock cycles per sample to avoid any excessive accumulating delay in the filter. To meet this design requirement while maximizing the filter's order, the coefficients in both filters need to be symmetrical. A symmetrical coefficients filter is designed so the first half of the coefficients are repeated in the second half. Having symmetrical coefficients in the filter results in a smaller latency by reusing the multiplication results of the convolution. Since the filter performs a convolution between the filter and the data, we can show that the outcome of each of the multiplication between a sample and a coefficient can be reused when the sample reaches the second appearance of the coefficient in the filter.

In order to meet the attenuation requirements of the filters without exceeding the maximum number of coefficients allowed, windowing optimization was performed. Both filters were designed following the guidelines presented in Rakshit and Ullah (2014). The maximum number of coefficients per window is set to 41 for both filters, so the FPGA module fulfills the latency requirements. However, this can limit the attenuation and the main lobe width of the filters, which are crucial for the AP filter. A Kaiser window was used as suggested in Rakshit and Ullah (2014) for its smaller main lobe width compared to a Chebychev or a Blackman Harris window for an acceptable stop-band attenuation. The Kaiser window, with a β of 0.1 and 41, yielded the highest attenuation in the low frequency band, and has a low ripple in the pass band.

The main parameters of the LFP/EMG filter are the stop band attenuation, and the filter's main lobe width. The Kaiser window also offers a better attenuation in the stop band of a small main lobe width. A Kaiser window including 41 coefficients and a β of 3 was used for this filter.

2.2.2. AP Detection and Compression

In order to achieve 32 neural recording channels, the platform detects the AP waveforms and compresses them. The APs are detected using a digital adaptive threshold and compressed using a four level discrete wavelet transform (DWT) applied on each AP sample. The utilized detection and the compression strategies were previously presented in detail by our group in Gagnon-Turcotte et al. (2019).

2.3. Control and Software Management

The platform processes the AP and LFP/EMG data using a dedicated DSP module implemented with custom VHDL modules inside the embedded FPGA. These modules are connected to a *Microblaze* softcore MCU *via* an AXI-Lite bus. The system can handle the high level functions, like the communication with the wireless transceiver and the commands interpretation, using a firmware written in C code and running inside the *Microblaze*, while the VHDL custom modules sends their critical notifications through the interrupt controller. The firmware triggers an interrupt when a detected/compressed AP sample or a LFP/EMG sample is ready to be sent to the transceiver.

Each compressed AP (48 samples on 6-bits) is inserted within a single 28 bytes packet, which also includes the type of packet code (8 bits AP packet code), the AP detection timestamp (24 bits), and the channel number (5 bits). Similarly, the LFP/EMG data are packetized and sent within separate packets, each of which includes the packet type (LFP/EMG) and the channel number of the first sample of the packet.

On the base station side, the LFP/EMG data is routed directly to the user interface for plotting and/or storing the data, while the AP data is routed to the decompression module for waveforms reconstruction before the reconstructed signals can be sent to the user interface. The reconstructed AP and LFP/EMG signals are displayed separately inside the user interface using distinct time and amplitude scales.

2.4. Experimental Setups for the *in vivo* Experiments

2.4.1. Multimodal Electrophysiology Recordings

The encapsulated system is used with an adaptor to interface with a 16-microelectrode implant. This adaptor allows to interface a *Molex* connector (on the platform) with an *Omnetics* A79042-001

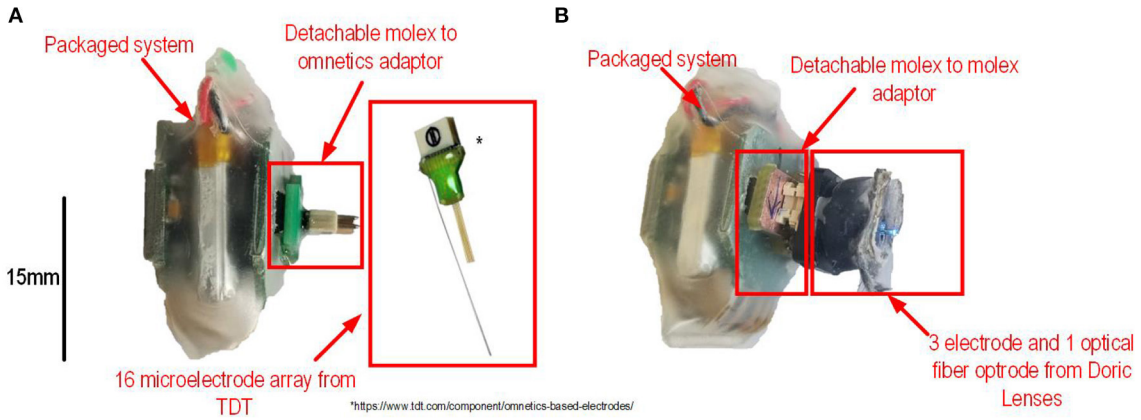

FIGURE 4 | (A) Packaged system connected to a Molex to Omnetics adaptor, a 16 channels microelectrode array and a ground wire. **(B)** Packaged system connected to a Molex to Molex adaptor and a three electrodes and 1 optical fiber optrode from *Doric Lenses*.

including 16 pins (on the microelectrode implant). The implant consists of a 16 electrode *Omnetics* based microwire array from *Tucker-Davis Technologies Inc.* (TDT, 2021). The electrodes are separated in two rows of eight electrodes. Electrodes within rows are separated by 250 μm, and rows were 500 μm apart. Each microwire electrode, the diameter of which is 33 μm, is made from polyimide-insulated tungsten. The implant has one reference wire and uses an *Omnetics* A79043-001 connector to interface with the adaptor. **Figure 4A** shows all the components of the platform before implantation.

All animal manipulations were performed with the approval of Université Laval's Animal Protection Committee (CPAUL) Protocol # VRR-2019-007. A Long-Evans rats (300 g female) was implanted with a 16-channel electrode array made of a 2 × 8 assembly of 33 μm tungsten microwires (Tucker-Davis Technologies Inc.) to acquire electrophysiological data *in vivo*. The tips of the microelectrodes were inserted ∼1.25 mm deep into the left primary motor cortex (centered at 1 and 3 mm anterior and lateral with respect to bregma). A first set of data was recorded peri-operatively during Ketamine-Xylazine anesthesia (10–100 mg/kg). A second set of recordings was performed 7 days later during live behavior with the same rat.

2.4.2. Optogenetic Stimulation and AP Recording

The extracellular signals were recorded with a Fi-Wi opto-electric cannula (3x tungsten 25 μm probes; 1x optical fiber 245 μm 0.37 NA; *Doric Lenses*, Canada) connected to the platform. The setup, which is using a Molex to Molex adaptor and the optrode, is shown in **Figure 4B**. The Thy1::ChR2-EYFP mouse was purchased from the Jackson Labs [B6.Cg-Tg(Thy1::COP4/EYFP)18Gfng/J]. A small craniotomy was made over the CA1 of dorsal hippocampus (rostro-caudal: −2.5, medial-lateral: 2.5, from Bregma) while the mouse was maintained on isoflurane anesthesia. The cannula was lowered above the CA1 pyramidal cells (dorso-ventral: −1.75), 500 ms pulses of light were delivered with a delay of 4.5 s between the pulses while the raw electrophysiological signal was recorded at a sampling rate of 20 ksps.

2.4.3. EMG Responses to Optogenetic Stimulation of the Motor Cotex

A Long-Evans rat was used to conduct an optogenetic stimulation experiment in the motor cortex. Channelrhodopsin-2 was virally expressed in the rat's motor cortical pyramidal neurons following an injection of the AAV2/php.eB-CaMKIIa-hChR2(H134R)-mCherry viral construct, developed at the Canadian Neurophotonics Platform Viral Vector Core Facility (RRID:SCR_016477). In brief, the AAV was prepared in the absence of helper virus. It was purified on an iodixanol gradient from cell culture. The virus was resuspended in PBS 320 mM NaCl + 5% Sorbitol + 0.001% Pluronic F-68. This rat was implanted with a 400-μm optical fiber, tapered over 1.5 mm, to illuminate the infected cortical tissue in the primary motor cortex. Additionally, three pairs of multi-stranded, PFA-coated stainless steel microwires (41AWG, A-M Systems Inc.) were inserted intramuscularly in the right trapezius, extensor carpi radialis and flexor carpi radialis muscles, and tunneled subcutaneously to a connector (Samtec Inc.) secured on the rat's skull using dental acrylic. A custom-made adapter was made to perform simultaneous optogenetic cortical stimulation and EMG recordings using the wireless platform. During this experiment, EMG signals were recorded and transmitted directly to the base station using the wireless platform, which also provided a control signal to drive the activation of an external light source (488 nm laser diode, Doric Lenses Inc.), to which the animal was tethered using an optical patch cord.

3. RESULTS

3.1. Measured Performance and Results

3.1.1. Filters Responses

The measured frequency responses of the AP filter and the LFP/EMG filter are shown in **Figure 5**. The responses address

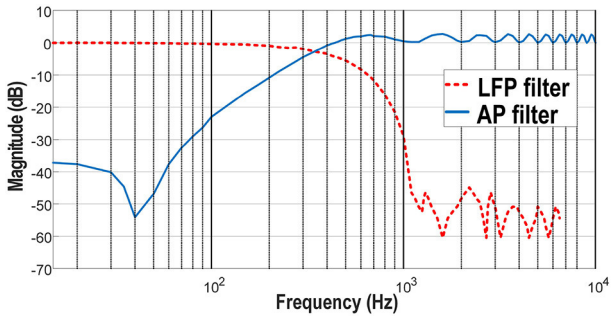

FIGURE 5 | In blue/plain, frequency response of the digital AP high-pass filter. In red/dotted, frequency response of the digital LFP low-pass filter.

TABLE 1 | Platform's characteristics and performance.

Parameter	Value
Nb of recording/stimulation channels	32/4
Targeted signals	AP/LFP/EMG
ADC resolution	16 bits
Sampling rate	20 ksps
Analog low-pass filter cut-off freq.	0.1–20 kHz
Analog high-pass filter cut-off freq.	0.1–500 Hz
Digital low-pass filter cut-off freq.	500 Hz
Digital low-pass filter stop-band att.	45 dB
Digital high-pass filter cut-off freq.	300 Hz
Digital high-pass filter stop-band att.	38 dB
Digital filters coefficient number	40
Combined data reduction ratio*	7.77
Dimensions(LxDxH) packaged	2.8 × 1.5 × 1.1 cm^3
Maximum current per stim. channel	200 mA
Power consumption(w/o stim.)	37 mA
Weight(w/ and w/o battery)	4.4/1.7 g

**AP firing rate of 50 AP/s.*

the design requirements i.e., 500 Hz low pass cut frequency for the LFP filter with −50 dB attenuation in the stop band, and 300 Hz high pass cut frequency with −40 dB attenuation in the stop band. A summary of these characteristics is presented in **Table 1**.

3.1.2. Power Consumption

The system's total current consumption without the filtering core and the dual data path was measured at 36 mA while recording AP and LFP signals that were recorded in the brain of a mouse in the course of previous *in vivo* experiments that were played at the inputs of the platform using a *Tektronix AFG 3101* arbitrary waveform generator over 32 channels. The digital filtering core and additional digital signal processing cores, which are critical to enable multimodal electrophysiological recordings in this application, was found to add only 1 mA (1.2 mW in the FPGA core powered at 1.2-V) while the system is recording from 32 channels over both signal frequency bands. The measured recording autonomy with the dual data path activated over 32 channels in parallel and without light stimulation was 94 min, using a 100-mAh battery.

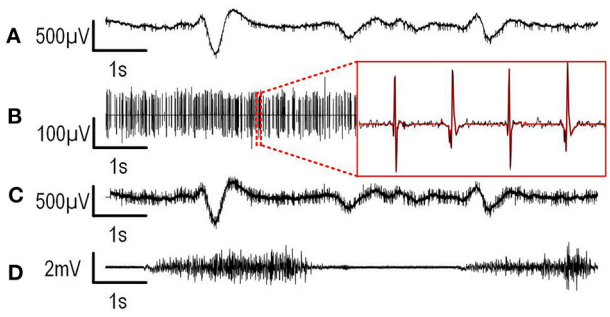

FIGURE 6 | Recordings of synthetic signals are presented. **(A)** Digitally filtered and decimated LFP signal. **(B)** Recorded, digitally filtered, detected, and compressed APs. The magnification shows the uncompressed AP signal (black) superimposed with the decompressed detected APs (red). **(C)** Recorded original raw signal. **(D)** EMG recorded in parallel with the neural signal.

3.1.3. System Performance

The *Combined Data Reduction Ratio* (CDRR) metric presented in **Table 1** was evaluated using a typical firing rate of 50 AP/s, while recording both AP and LFP separately at 20 ksps on 16 bits. This ratio was calculated as follows:

$$CDRR = \frac{f_{SH}}{\frac{NFR \times Samples_{AP}}{CR} + f_{SL}} \quad (1)$$

where f_{SH} is the sampling frequency of the raw signal in ksps, NFR is the neuron firing rate, $Samples_{AP}$ is the number of samples in each AP, CR is the compression ratio for the AP (CR) and f_{SL} is the decimated sampling frequency in the low frequency band. With a f_{SH} of 20 ksps, a NFR of 50 AP/s, a $Samples_{AP}$ of 48 Samples/AP, a CR of 4.17 and a f_{SL} of 2 ksps, the CDRR was 7.77. This metric takes into account the data reduction induced both by the AP detection core and by the wavelet compression core. These characteristics of the system are summarized in **Table 1**.

3.1.4. Synthetic Recording Results

To validate whether the system can effectively record and separate AP, LFP, and EMG signals simultaneously in real time, the EMG, AP and LFP signals recorded in the brain of a mouse in the course of previous *in vivo* experiments were played at the inputs of the platform using a *Tektronix AFG 3101* arbitrary waveform generator. The signal was attenuated using a precise voltage divider, and then applied on 31 recording channels simultaneously, while the last channel (channel 32) was connected to the pre-recorded EMG signal. The EMG signal was recorded on the arm of a human volunteer using Ag/AgCl surface electrodes and then passed through a 60 Hz notch filter in post processing. Both the real EMG signal and synthetic neural signal references were connected to the ground of the system and on the Intan RHD2132 input reference pin. **Figure 6** presents the recorded data on one channel of both LFP and AP

and on the EMG channel. **Figures 6A,B** show the results for the digitally separated signal shown in **Figure 6C**. This former subfigure shows that both the AP and LFP signals were properly extracted, which allows to correctly detect and compress the APs during subsequent steps. **Figure 6D** shows the EMG data that was recorded in parallel on channel 32.

3.2. *In vivo* Results

Four separate experiments were conducted to validate the critical functionalities of the presented system *in vivo* and with freely moving rodents. First, an electrophysiological experiment was performed *in vivo* in an anesthetized rat with a 16-microelectrode array implanted in the primary motor cortex to demonstrate the real-time separation of the APs and LFPs over a high channel count. Secondly, electrophysiology recordings were performed in freely moving conditions with the same implanted rat. Third, EMG recordings and optogenetic stimulation of the motor cortex were performed *in vivo* in a Long-Evans rat expressing ChR2 delivered with a viral construct. In this experiment, three pairs of electrodes were inserted intramuscularly in the right trapezius, extensor carpi radialis and flexor carpi radialis muscles and paired with optogenetic stimulation performed in the primary motor cortex. Finally, the system was used to perform optogenetic stimulation in the brain of a transgenic Thy1::ChR2-EYFP mouse implanted with an optrode manufactured by Doric Lenses, Canada including three recording channels and one stimulation channel. The methods of these *in vivo* tests and their experimental results are reported in the following sections.

3.2.1. Multimodal Electrophysiology Recording Results

To validate the platform ability to properly collect and separate LFP and AP signals during a freely moving experiment, electrophysiological recordings were conducted *in vivo* in an anesthetized and a freely moving rat using a 16 micro-electrode array recording both LFP and AP signals in parallel. AP were detected and compressed using wavelet compression by the system on 16 channels in real time. The LFP signals were decimated by the DSP core that is implemented inside the FPGA. The DSP core could successfully reduce the output data rate of the platform below the maximum data rate which can handle the wireless transceiver. Indeed, we can show that the minimum data rate needed to record the full signal bandwidth over 16 channels in parallel at 20 ksps, without data reduction, is 5.12 Mbps. Our data reduction strategy implemented in the platform reduces the data rate below the maximum effective data rate of the wireless transceiver, which is limited to ∼1.4 Mbps.

3.2.2. Anesthetized Multimodal Recording Results

The data presented in this section comes from recordings that were performed during the implantation procedure described in section 2.4.1, while the rat was anesthetized and remained still. These recordings were taken after the implantation and before solidifying the implant for chronic use. The platform recorded AP and LFP signals on 16 electrodes during this experiment. The APs that were detected and compressed by the platform were wirelessly transmitted to the base station during the experiment.

In order to analyze the AP and LFP signals recorded on the 16 microelectrodes, the AP trains were reconstructed by temporally placing the AP samples according to their timestamps with respect to their detection time point. They were then superimposed with the decimated LFP signals (**Figure 7A**). As expected, under ketamine-xylazine anesthesia cortical activity revealed slow oscillation pattern (major frequency about 1 Hz). The recorded neurons were silent during the depth-positive components and they fired AP during the depth-negative components of the slow oscillations. For channels 2, 14, 15, and 16 large APs (up to 250 μV peak to peak) were detected in separated rapid spike-trains which is expected under ketamine-xylazine anesthesia in the neo-cortex. In the rest of the channels, smaller APs (< 100 μV peak to peak) and spiking activity was recorded. Among the LFP shown in **Figure 7A**, a large low-frequency component can be seen over the 16 channels. **Figure 7B** shows AP and LFP signals superimposed over 20 s of a 30 s recording on electrode 2, with a zoom on a section of the signal, to show the relation between AP firing and phase of LFP. This correspondence between both measured modalities show the correct parallel recording capability of the presented platform when utilized into an *in vivo* setting.

The APs that were detected during 30 s over 16 channels were clustered and superimposed (**Figure 8**). The decompressed APs recorded during the experiments were re-filtered from 300 Hz to 5 kHz and re-centered around their peak value in post-processing. A Principal component analysis (PCA) has been performed on the resulting extracted APs for each channel and followed by a clustering task using the Kmeans algorithm to identify and sort the different AP shapes collected over each electrode, which result from different neurons. While channels 5, 6, and 7 showed small waveforms ($<20\mu$V), most channels showed at least one AP shape that is repeated throughout the recording, indicating that the electrodes were effectively picking up genuine neural activity for these channels. This shows that the AP detection and compression strategy implemented inside the platform and utilized to perform this experiment, works properly along with our signal separation method to capture different signal modalities in parallel over several channels.

The data reduction on the platform during recording was calculated using a 30 s sample of the recording session. The total number of APs detected during 30 s over the 16 channels was 5,547 (**Figure 7A**). Given that each AP includes 48 samples on 16 bits per sample, the decimated sampling frequency of the LFP is 2 ksps and the compression ratio is 4.17. The total data reduction ratio can be calculated as follows:

$$CDRR = \frac{20ksps \times 30s \times 16}{\frac{5547APs \times 48samples/AP}{4.17} + 2ksps \times 30s \times 16} \quad (2)$$

The resulting total data reduction ratio for this experiment was 9.38, which reduces the data rate from 5.12 Mbps, for full bandwidth neural signals, to 0.55 Mbps, which is well

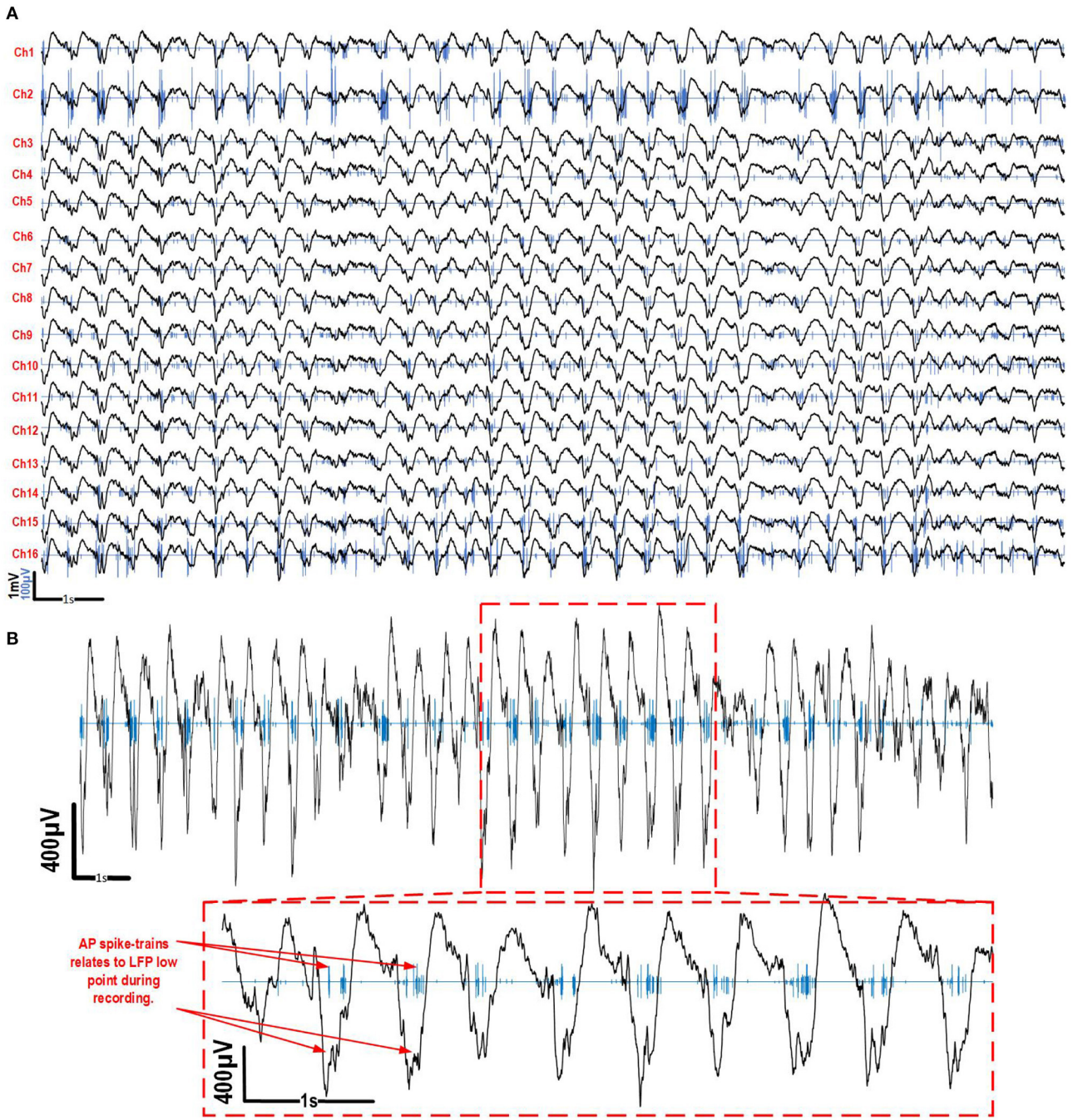

FIGURE 7 | *In vivo* recordings for 16 channels of both LFP and AP in the brain of a freely moving Long-Evans rat under anesthesia. **(A)** 20 s of recording during the experiment with the AP and LFP superimposed. **(B)** A magnification of the signals on channel two during the same recording to highlight the correspondence between AP spike-trains and LFP activity.

below the limits of our low-power wireless transceiver chip after data reduction.

In order to obtain the frequency content of the LFPs during the recording session, a fast Fourier transform (FFT) was performed on the LFP recorded on channel 2 (**Figure 9A**). The result of the FFT was then normalized using the 2-norm method. The typical frequency bands used in the LFP analysis (Liu et al., 2017) are added to **Figure 9A** as an indicator to better analyze the spectrum presented here. **Figure 9B** shows the power distribution in each frequency band. The majority of the activity is contained in the two frequency bands below 10 Hz, which is typical with Ketamine-Xylazine anesthesia in the neocortex.

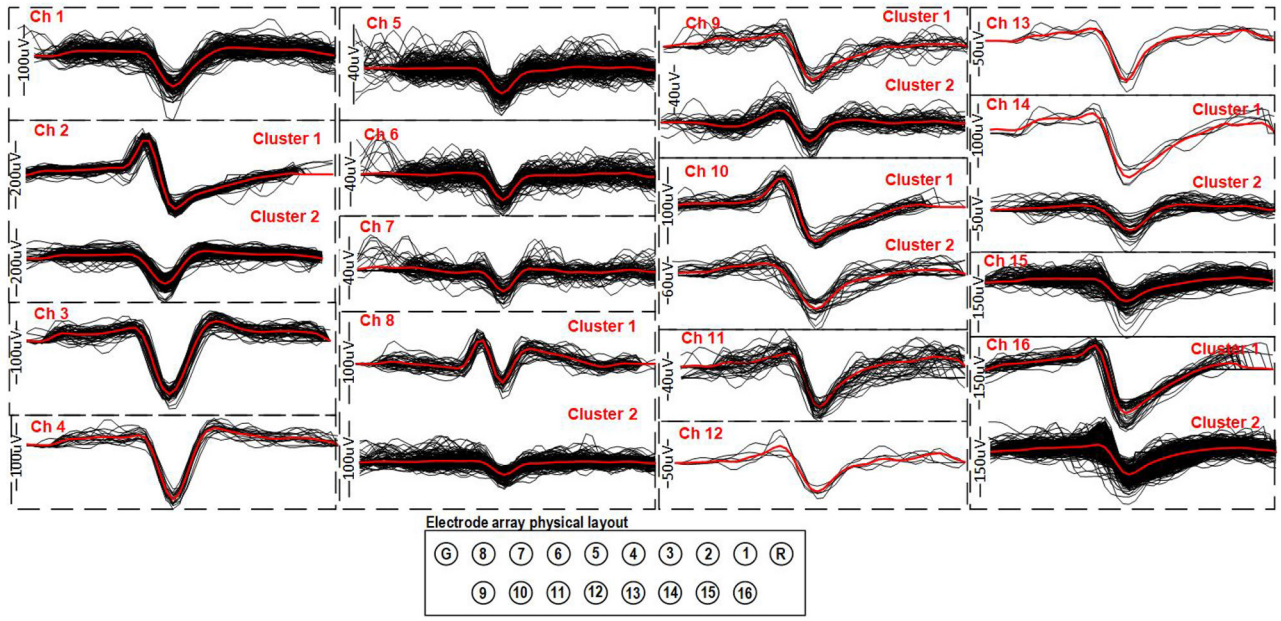

FIGURE 8 | Clustered APs detected for 16 channels recorded simultaneously during a 30 s period. The average AP for each cluster is displayed in red in order to better visualize its shape. Each AP waveform is 2.4 ms.

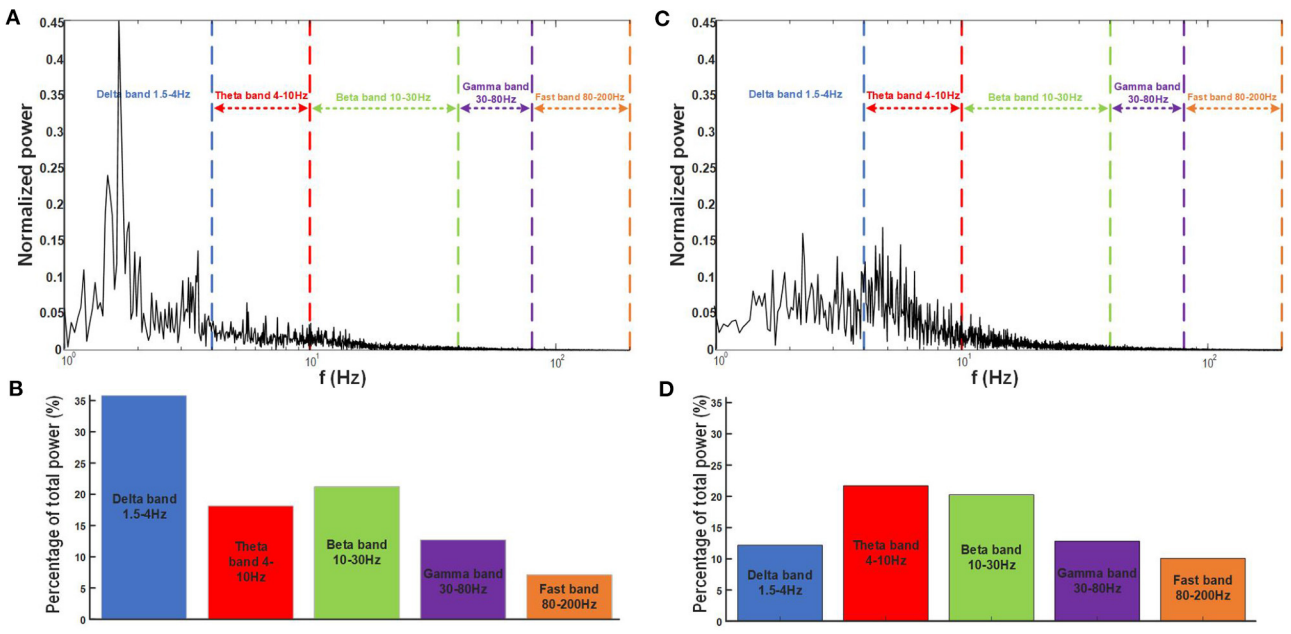

FIGURE 9 | (A) Frequency content for a 30 s LFP recording on one electrode of the 16 electrode implant in the primary motor cotex of the Long-Evans rat under anesthesia with the traditional frequency bands used for analysis identified on the graph. **(B)** Power percentage contained in each band for the specific recording in anesthesia. **(C)** Frequency content for a 20 s LFP recording on the same electrode as in **(A)**, a week after implantation while the rat is freely moving with the traditional frequency bands used for analysis identified on the graph. **(D)** Power percentage contained in each band for the specific recording for the freely moving experiment.

3.2.3. Freely Moving Results

The results presented in this section show the device's ability to record multimodal electrophysiology signals simultaneously in a freely moving laboratory animal. Recordings were taken 1 week after implantation in the same Long-Evans rat that was used in section 2.4.1. AP and LFP signals were simultaneously

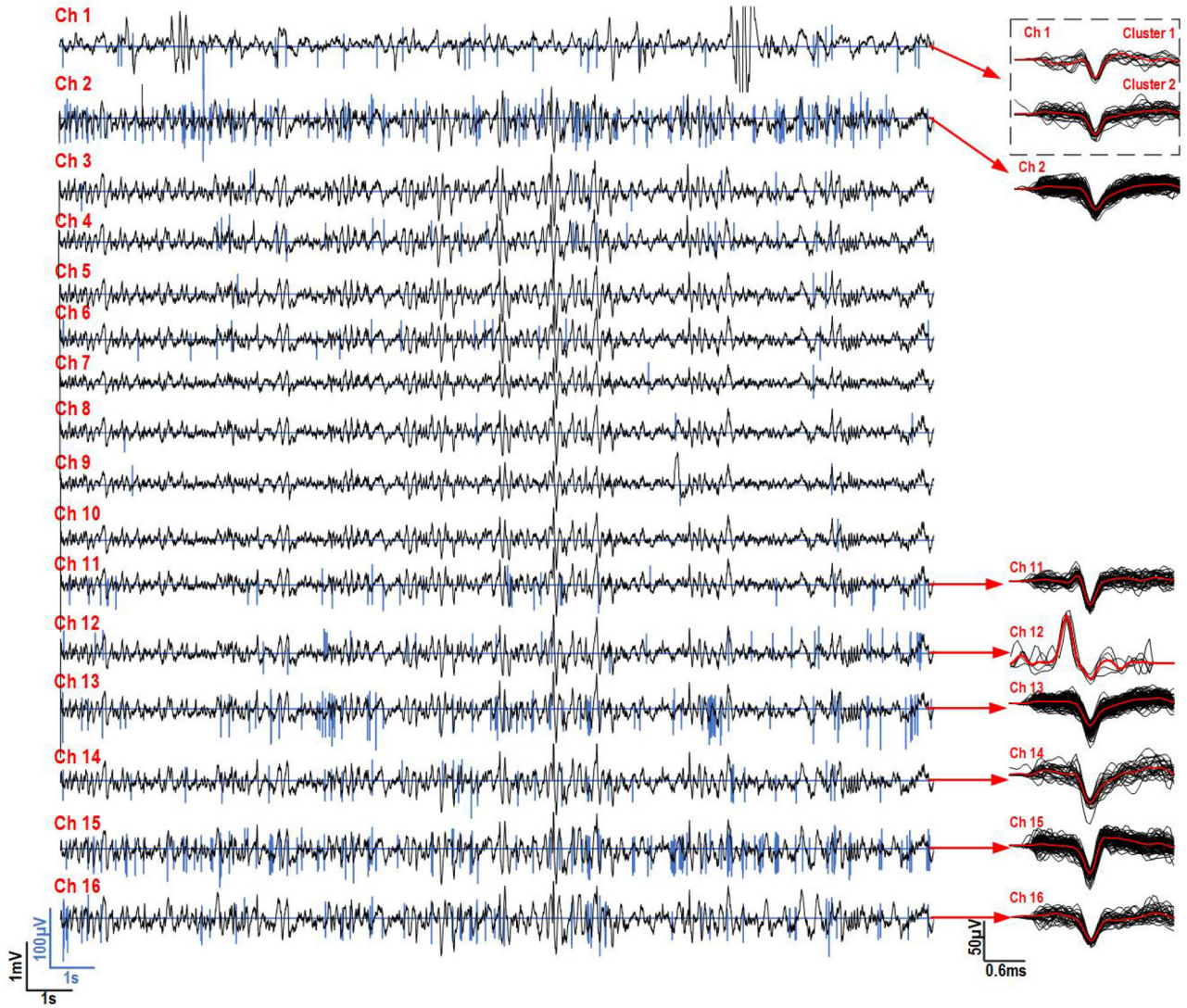

FIGURE 10 | *In vivo* recordings for 16 channels of both LFP and AP in the brain of a freely moving Long-Evans rat with the implant and system on its head. On the left, 20 s of recording during the experiment with the AP and LFP superimposed is shown. On the right, the clustered and superimposed APs are shown along with the average AP waveform (in red) for the channels were some activity was detected is shown.

recorded from the 16 electrodes using the method described in section 3.2.2, while the animal was freely behaving. The packaged system weight 4.68 g, which represents only 1% of the 300 g Long Evans rat.

As in section 3.2.2, the AP and LFP signals recorded on the 16 microelectrodes were reconstructed by temporally replacing the AP samples according to their timestamps with respect to their detection time point and were superimposed with the decimated LFP signals (**Figure 10**). **Figure 10** shows the superimposed results of both signals collected during a 20 s part of the recording. The APs detected on their respective channels were sorted and clustered using a PCA and the Kmeans algorithm to identify and sort the different AP shapes collected over each electrode, which result from different neurons. The result is shown on the right hand side of **Figure 10**. An AP shape was detected consistently during the experiment for channels 1, 2, and 11–16. Little to no activity was detected on the other channels.

In order to compare the frequency content of the LFP during exploration with the frequency content during anesthesia (section 3.2.2), an FFT and 2-norm normalization were performed on the LFP recorded on channel 2 during the freely moving experiment (**Figure 9C**). The power distribution was calculated comparing the total power with the power in each power bands identified in **Figure 9D**. These results show a shift between the frequency content measured during the anesthesia (**Figures 9A,B**) and the beginning of the freely moving

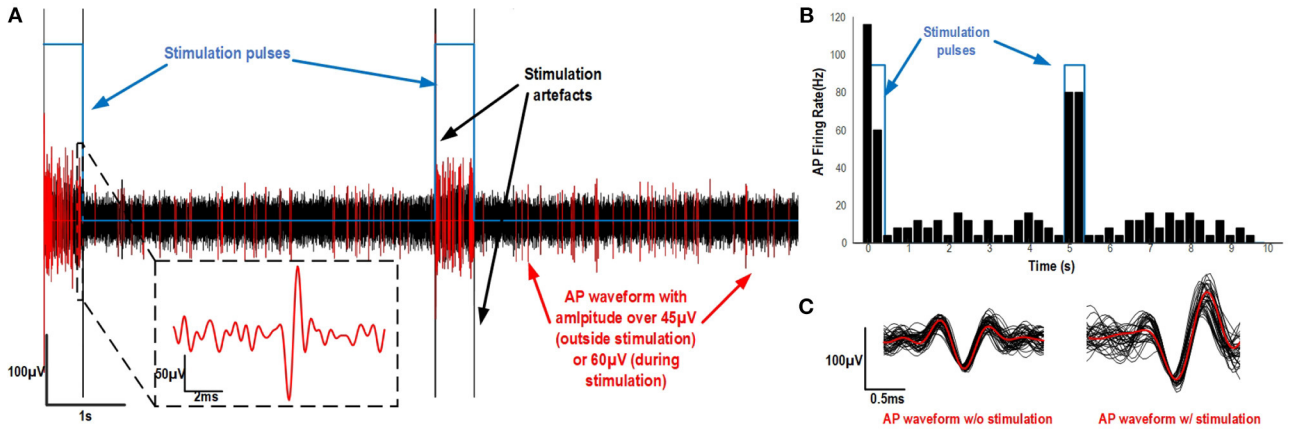

FIGURE 11 | (A) Recorded signal from one electrode of the optrode implanted in the Thy1::ChR2-EYFP transgenic mouse. Five hundred milliseconds of stimulation pulses were applied with a 4.5 s delay between each pulse. The simulation pattern is shown in blue, the recording in black and the detected AP waveforms in red. A zoom on an action potential of about 200 µV is added to better visualize the activity present during the light pulses. **(B)** The AP firing rate at each moment of the experiment. **(C)** The clustered AP waveforms w/o stimulation and during the stimulation pulses.

experiment (**Figures 9C,D**), as expected, during exploration LFP signal was dominated by activities in theta and beta frequency range.

3.3. Optogenetic Stimulation and AP Recording Results

The extracellular activity of CA1 pyramidal neurons was recorded with the system in an anesthetized Thy1::ChR2-EYFP mouse with the setup described in section 2.4.2. The recorded signal was filtered from 300 Hz to 3 kHz for the three recording electrodes. A fixed threshold of 60 µV (inside stimulation pulses) and 45 µV (outside stimulation pulses) was applied after the experiment to better identify the events during the recording and highlight the increase in activity during the optogenetic stimulation shown in blue (**Figure 11A**). The firing rate during the experiment was also calculated for each 0.25 s segment of the recording (**Figure 11B**) and revealed a relation between stimulation and an increase in AP firing rate for the experiment. The APs detected during and in between stimulation were sorted and clustered separately using a PCA and the Kmeans algorithm (**Figure 11C**). The AP shapes identified were higher in amplitude during stimulation as compared to the APs in between the stimulation pulses. Overall, delivering 500 ms light pulses resulted in an increased firing rate and higher AP amplitude during the pulses. The optical stimulation also introduced small stimulation artifacts (likely due to photoelectric effect, shown in **Figure 11A**) in the recorded signal when turning the LED on and off.

3.4. Results of EMG Responses to Optogenetic Stimulation of Motor Cortex

In order to demonstrate the capability of the system to record EMG and to control a stimulation light source, EMG were recorded using the setup described in section 2.4.3. This setup served as a proof-of-concept experiment mainly for the EMG recording, as the platform's capability to generate light for optogenetic stimulation was already demonstrated in section 3.3.

During the experiment, a stimulation train of 10 pulses of 5 ms each 50 ms is repeated every 5.5 s to the optical fiber for 20 s in order to generate sustained activity during every stimulation train. Since the platform measures the signal between 2 wire electrodes and a common reference, which is located far from each muscle, signals are subtracted together to reduce the background noise from the nearby muscle fibers. **Figure 12** shows EMG signals recorded during the experiment. The muscle's EMG activity level increases during the optogenetic stimulation pulse-trains.

4. DISCUSSION

We presented the design of a wireless electro-optic platform and its utilization to perform multimodal neural recording and optical stimulation in parallel with freely moving rodents. The system allows the digital separation of AP and LFP/EMG signals in real time, provides AP detection and AP wavelet compression to minimize the data rate of the wireless link and the overall power consumption. This unique feature, combined with the decimation of the LFP, allows to significantly reduce the amount of data to be transmitted over the low-power wireless data link, while preserving the integrity of the extracted signal modalities. The platform was thoroughly measured and validated in the Smart Biomedical Microsystems Lab and at the CERVO Brain Research center during *in vivo* neurophysiological experiments. Electrophysiology recordings were performed during both anesthetized and freely moving conditions using a 16-channel microelectrode array implanted in the primary motor cortex of a rat. AP and LFP were recorded in parallel using the platform on 16 channels, thanks to the real-time signal separation, AP dectection/compression and LFP decimation, during a behavioral experiment. Optogenetic stimulation along

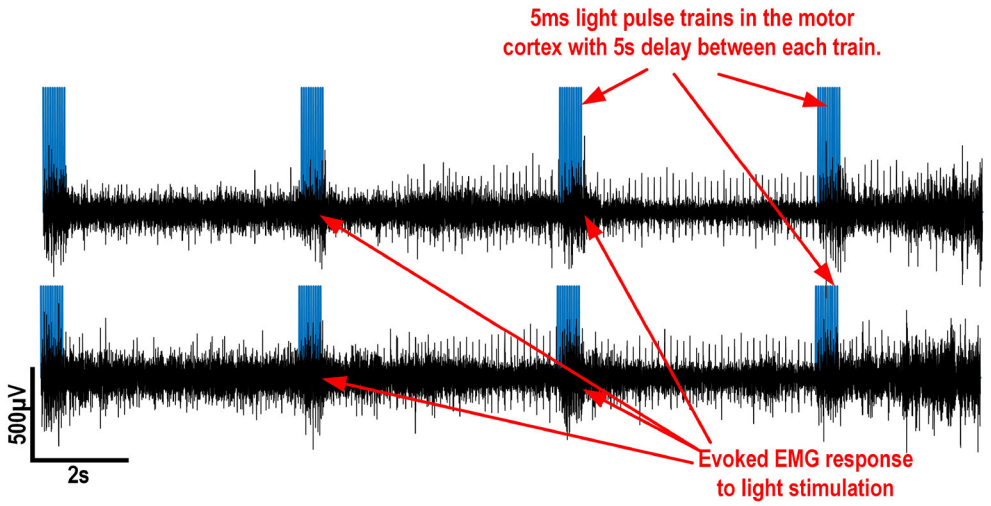

FIGURE 12 | *In vivo* EMG recording in the extensor carpi radialis and flexor carpi radialis muscles of a freely moving rat. The stimulation trains are shown in blue to show when a response should be evoked.

with electrophysiology recordings were performed in parallel in the brain of a transgenic mouse using an optrode including 3 electrodes and 1 optical fiber. EMG recordings along with optical stimulation were also performed respectively in the arm and in the motor cortex of a rat expressing ChR2 *via* a viral vector. These three experiments allowed to validate the platform thoroughly in many experimental scenarios. In future work, we intend to use the presented platform inside a real-time closed-loop scheme where electrophysiological recordings obtained from one specific area will be used to trigger and control optical stimulation into other areas of the brain.

DATA AVAILABILITY STATEMENT

The raw data supporting the conclusions of this article will be made available by the authors, without undue reservation.

ETHICS STATEMENT

The animal study was reviewed and approved by Université Laval's Animal Protection Committee (CPAUL).

AUTHOR CONTRIBUTIONS

GB designed the multimodal extraction strategy and the low-frequency data path. He measured the performance of the system, participated in the *in vivo* validation, analyzed the results, and he wrote this manuscript. GG-T designed the system and the high-frequency data path. He participated in the *in vivo* validation and in the writing of this paper. LG participated in the design of the system. IK participated in the *in vivo* validation and in the writing. YD, IT, and CE supervised the *in vivo* validation and participated in the writing of the paper. BG supervised and participated in the design of the system and participated in the writing of the paper. All authors contributed to the article and approved the submitted version.

FUNDING

We acknowledge the support of the Natural Sciences and Engineering Research Council of Canada (NSERC) [Grant no. RGPIN-2016-05909] and [Grant no. RGPIN-2020-06361] the Weston Family Foundation [Grant nos. TR192089 and RR150149], the The SMAART Collaborative Research and Training Experience Program (CREATE) funded by NSERC, the Canada First Research Excellence Fund Sentinel North Strategy at Laval University, the Fonds de recherche Québec—Nature et technologie (FRQ-NT) [Grant nos. 2018-PR-207644 and 2021-PR-284207], the Microsystems Strategic Alliance of Quebec funded by FRQ-NT, and the Canada Research Chair in Smart Biomedical Microsystems.

ACKNOWLEDGMENTS

We acknowledge the support of the Canada Research Chair in Smart Biomedical Microsystems and we thank CMC Microsystems for providing the design and testing tools.

REFERENCES

Abbaspourazad, H., Choudhury, M., Wong, Y., Pesaran, B., and Shanechi, M. (2021). Multiscale low-dimensional motor cortical state dynamics predict naturalistic reach-and-grasp behavior. *Nat. Commun.* 12:607. doi: 10.1038/s41467-020-20197-x

Balasubramaniam, S., Wirdatmadja, S. A., Barros, M. T., Koucheryavy, Y., Stachowiak, M., and Jornet, J. M. (2018). Wireless communications

for optogenetics-based brain stimulation: present technology and future challenges. *IEEE Commun. Mag.* 56, 218–224. doi: 10.1109/MCOM.2018.1700917

Biederman, W., Yeager, D. J., Narevsky, N., Leverett, J., Neely, R., Carmena, J. M., et al. (2015). A 4.78 mm 2 fully-integrated neuromodulation soc combining 64 acquisition channels with digital compression and simultaneous dual stimulation. *IEEE J. Solid-State Circ.* 50, 1038–1047. doi: 10.1109/JSSC.2014.2384736

Bihr, U., and Ortmanns, M. (2012). "A front-end circuit with active spike and lfp separation via a switched capacitor filter structure for neural recording applications," in *ISCAS 2012 - 2012 IEEE International Symposium on Circuits and Systems*, 2231–2234. doi: 10.1109/ISCAS.2012.6271735

Bilodeau, G., Gagnon-Turcotte, G., Gagnon, L. L., Ethier, C., Timofeev, I., and Gosselin, B. (2020). "A wireless electro-optic headstage with digital signal processing and data compression for multimodal electrophysiology and optogenetic stimulation," in *Proceedings - IEEE International Symposium on Circuits and Systems*, Baltimore, MD, USA 1–5. doi: 10.1109/ISCAS45731.2020.9180912

Buzsáki, G., Stark, E., Berényi, A., Khodagholy, D., Kipke, D. R., Yoon, E., et al. (2015). Tools for probing local circuits: high-density silicon probes combined with optogenetics. *Neuron* 86, 92–105. doi: 10.1016/j.neuron.2015.01.028

Ethier, C., and Miller, L. E. (2015). Brain-controlled muscle stimulation for the restoration of motor function. *Neurobiol. Dis.* 83, 180–190. doi: 10.1016/j.nbd.2014.10.014

Gagnon-Turcotte, G., Bilodeau, G., Tsiakaka, O., and Gosselin, B. (2020). Smart autonomous electro-optic platforms enabling innovative brain therapies. *IEEE Circ. Syst. Mag.* 20, 28–46. doi: 10.1109/MCAS.2020.3027220

Gagnon-Turcotte, G., Gagnon, L. L., Bilodeau, G., and Gosselin, B. (2017a). "Wireless brain computer interfaces enabling synchronized optogenetics and electrophysiology," in *Proceedings - IEEE International Symposium on Circuits and Systems*, (Baltimore, MD), 1–4. doi: 10.1109/ISCAS.2017.8050345

Gagnon-Turcotte, G., Keramidis, I., Ethier, C., De Koninck, Y., and Gosselin, B. (2019). A wireless electro-optic headstage with a 0.13-µm cmos custom integrated dwt neural signal decoder for closed-loop optogenetics. *IEEE Trans. Biomed. Circ. Syst.* 13, 1036–1051. doi: 10.1109/TBCAS.2019.2930498

Gagnon-Turcotte, G., Khiarak, M. N., Ethier, C., De Koninck, Y., and Gosselin, B. (2018). A 0.13-µm CMOS SOC for simultaneous multichannel optogenetics and neural recording. *IEEE J. Solid-State Circ.* 53, 3087–3100. doi: 10.1109/JSSC.2018.2865474

Gagnon-Turcotte, G., Lechasseur, Y., Bories, C., Messaddeq, Y., De Koninck, Y., and Gosselin, B. (2017b). A wireless headstage for combined optogenetics and multichannel electrophysiological recording. *IEEE Trans. Biomed. Circ. Syst.* 11, 1–14. doi: 10.1109/TBCAS.2016.2547864

Jackson, A., Moritz, C. T., Mavoori, J., Lucas, T. H., and Fetz, E. E. (2006). The neurochip bci: Towards a neural prosthesis for upper limb function. *IEEE Trans. Neural Syst. Rehabil. Eng.* 14, 187–190. doi: 10.1109/TNSRE.2006.875547

Kassiri, H., Salam, M. T., Pazhouhandeh, M. R., Soltani, N., Velazquez, J. L. P., Carlen, P., et al. (2017). Rail-to-rail-input dual-radio 64-channel closed-loop neurostimulator. *IEEE J. Solid-State Circ.* 52, 2793–2810. doi: 10.1109/JSSC.2017.2749426

LeChasseur, Y., Dufour, S., Lavertu, G., Bories, C., Deschênes, M., Vallée, R., et al. (2011). A microprobe for parallel optical and electrical recordings from single neurons *in vivo*. *Nat. Methods* 8, 319–325. doi: 10.1038/nmeth.1572

Liu, L., Yao, L., Zou, X., Goh, W. L., and Je, M. (2013). "Neural recording front-end IC using action potential detection and analog buffer with digital delay for data compression," in *Proceedings of the Annual International Conference of the IEEE Engineering in Medicine and Biology Society*, (Osaka), 747–750. doi: 10.1109/EMBC.2013.6609608

Liu, X., Zhang, M., Richardson, A. G., Lucas, T. H., and Spiegel, J. V. D. (2017). Design of a closed-loop, bidirectional brain machine interface system with energy efficient neural feature extraction and PID control. *IEEE Trans. Biomed. Circ. Syst.* 11, 729–742. doi: 10.1109/TBCAS.2016.2622738

Lopez, C. M., Putzeys, J., Raducanu, B. C., Ballini, M., Wang, S., Andrei, A., et al. (2017). A neural probe with up to 966 electrodes and up to 384 configurable channels in 0.13 µm soi cmos. *IEEE Trans. Biomed. Circ. Syst.* 11, 510–522. doi: 10.1109/TBCAS.2016.2646901

Mehring, C., Rickert, J., Vaadia, E., de Oliveira, S. C., Aertsen, A., and Rotter, S. (2003). Inference of hand movements from local field potentials in monkey motor cortex. *Nat. Neurosci.* 6, 1253–1254. doi: 10.1038/nn1158

Mesri, A., Sampietro, M., Cunha, A. B., Ferrari, G., and Martinsen, O. G. (2018). "A laser diode-based wireless optogenetic headstage," in *PRIME 2018 - 14th Conference on Ph.D. Research in Microelectronics and Electronics*, (Prague), 257–260. doi: 10.1109/PRIME.2018.8430348

Perelman, Y., and Ginosar, R. (2005). "An integrated system for multichannel neuronal recording with spike/LFP separation and digital output," in *2nd International IEEE EMBS Conference on Neural Engineering*, (Arlington, VA), 377–380. doi: 10.1109/CNE.2005.1419637

Rakshit, H., and Ullah, M. A. (2014). "A comparative study on window functions for designing efficient fir filter," in *2014 9th International Forum on Strategic Technology*, (Cox's Bazar), 91–96. doi: 10.1109/IFOST.2014.6991079

Schmale, S., Knoop, B., Hoeffmann, J., Peters-Drolshagen, D., and Paul, S. (2013). "Joint compression of neural action potentials and local field potentials," in *Conference Record - Asilomar Conference on Signals, Systems and Computers*, (Pacific Grove, CA), 1823–1827. doi: 10.1109/ACSSC.2013.6810617

Soltani, S., Chauvette, S., Bukhtiyarova, O., Lina, J., Dubé, J., Seigneur, J., et al. (2019). Sleep-wake cycle in young and older mice. *Front. Syst. Neurosci.* 13:51. doi: 10.3389/fnsys.2019.00051

TDT (2021). Available online at: https://www.tdt.com/component/omnetics-based-electrodes/ (accessed April 15, 2021).

Watson, B. O., Ding, M., and Buzsáki, G. (2018). Temporal coupling of field potentials and action potentials in the neocortex. *Eur. J. Neurosci.* 48, 2482–2497. doi: 10.1111/ejn.13807

Wu, J. Y., and Tang, K. T. (2011). "A band-tunable, multichannel amplifier for neural recording with AP/LFP separation and dual-threshold adaptive AP detector," in *Proceedings of the Annual International Conference of the IEEE Engineering in Medicine and Biology Society*, (Boston, MA), 1847–1850.

Conflict of Interest: The authors declare that the research was conducted in the absence of any commercial or financial relationships that could be construed as a potential conflict of interest.

Advantages of publishing in Frontiers

OPEN ACCESS
Articles are free to read for greatest visibility and readership

FAST PUBLICATION
Around 90 days from submission to decision

HIGH QUALITY PEER-REVIEW
Rigorous, collaborative, and constructive peer-review

TRANSPARENT PEER-REVIEW
Editors and reviewers acknowledged by name on published articles

Frontiers
Avenue du Tribunal-Fédéral 34
1005 Lausanne | Switzerland

Visit us: www.frontiersin.org
Contact us: frontiersin.org/about/contact

REPRODUCIBILITY OF RESEARCH
Support open data and methods to enhance research reproducibility

DIGITAL PUBLISHING
Articles designed for optimal readership across devices

FOLLOW US
@frontiersin

IMPACT METRICS
Advanced article metrics track visibility across digital media

EXTENSIVE PROMOTION
Marketing and promotion of impactful research

LOOP RESEARCH NETWORK
Our network increases your article's readership